Precision Spectroscopy of the 2S-6P Transition in Atomic Deuterium

Vitaly Wirthl

München 2022

Precision Spectroscopy of the 2S-6P Transition in Atomic Deuterium

Vitaly Wirthl

Dissertation
an der Fakultät für Physik
der Ludwig–Maximilians–Universität
München

vorgelegt von
Vitaly Wirthl
aus Sankt Petersburg

München, den 24.11.2022

Erstgutachter: Prof. Dr. Thomas Udem
Zweitgutachter: Prof. Dr. Randolf Pohl
Tag der mündlichen Prüfung: 27.1.2023

Zusammenfassung

Die Quantenelektrodynamik (QED) bildet die Grundlage aller anderen Quantenfeldtheorien, auf denen das Standardmodell der Teilchenphysik aufgebaut ist. Derzeit ist klar, dass unser fundamentales Naturverständnis unvollständig ist, sodass erwartet wird, dass das Standardmodell um neue Teilchen oder Wechselwirkungen verändert oder erweitert werden muss. Eine Möglichkeit, diese Grenzen der Grundlagenphysik zu erforschen, ist die Durchführung von Präzisionsmessungen. Diese Arbeit untersucht die Präzisionslaserspektroskopie von Deuterium, wo die Übergangsenergien zwischen verschiedenen Energiezuständen des an den Kern gebundenen Elektrons mit Techniken wie ultrastabilen Lasern und dem Frequenzkamm genau gemessen werden können. Aufgrund der Einfachheit der wasserstoffähnlichen Atome können ihre Energieniveaus anhand der QED-Theorie für gebundene Zustände genau berechnet werden, und mit dem Experiment mit der relativen Genauigkeit in der Größenordnung von 10^{-12} verglichen werden. Ein solcher Vergleich zwischen Theorie und Experiment ist mit der Bestimmung von Naturkonstanten verbunden, die als Parameter in die Theorie eingehen. Erst wenn mehr unabhängige Messungen als Parameter vorliegen, kann die Theorie überprüft werden.

Der Vergleich zwischen Theorie und Laser-Spektroskopie im Deuterium betrifft die Rydberg-Konstante R_∞ und den Deuteronen-Ladungsradius r_d. Dies erfordert mindestens zwei Messungen der verschiedenen Übergangsfrequenzen, um diese Konstanten zu bestimmen, und mehr Messungen, um die Theorie zu testen. Im Gegensatz zum Wasserstoff gibt es bei Deuterium nur wenige ausreichend genaue Messungen der Übergänge. In dieser Arbeit wird die erste Untersuchung des 2S-6P-Übergangs in Deuterium vorgestellt, die mit der bestehenden Frequenzmessung des 1S-2S-Übergangs kombiniert werden kann, um R_∞ und r_d zu erhalten. Zusammen mit der Messung des 2S-2P-Übergangs von myonischem Deuterium stellt diese Bestimmung einen Theorietest dar. Ein solcher Vergleich ist wichtig, um die anhaltende Diskrepanz zwischen dem Ergebnis aus myonischem Deuterium und dem Durchschnitt früherer Daten aus elektronischem Deuterium, sowie die Spannungen zwischen den jüngsten Ergebnissen aus der Wasserstoffspektroskopie, zu beleuchten.

Im Gegensatz zu Wasserstoff wird die Präzisionsspektroskopie des 2S-6P-Übergangs in Deuterium durch die gleichzeitige Anregung unaufgelöster Hyperfeinstruktur-Komponenten erschwert, was zur unaufgelösten Quanteninterferenz führen kann. Diese Arbeit untersucht die möglichen systematischen Effekte, die mit dieser Komplikation verbunden sind. Zusammen mit analytischen störungstheoretischen Modellen werden Supercomputersimulationen durchgeführt, um diese Effekte zu analysieren. Es wird gezeigt, dass die Quanteninterferenz für alle 2S-nP-Übergänge in Deuterium stark unterdrückt wird, wodurch Präzisionsmessungen dieser Übergänge möglich werden. Darüber hinaus wird ein weiterer Effekt in Deuterium im Vergleich zu Wasserstoff untersucht, der sich aus der Lichtkraft ergibt, die auf die Atome in der stehenden Welle des Spektroskopielichts wirkt. Trotz zusätzlicher Zustandsvielfalt durch

die gleichzeitige Anregung unaufgelöster Hyperfeinkomponenten wird gezeigt, dass diese sogenannte "Lichtkraftverschiebung" mit dem gut verstandenen Effekt im Wasserstoff vergleichbar ist.

Die größte Herausforderung bei der Messung des 2S-6P-Ein-Photonen-Übergangs in Deuterium ist die Doppler-Verschiebung erster Ordnung. Ein großer Teil dieser Arbeit befasst sich daher mit dem verbesserten aktiven faserbasierten Retroreflektor (AFR), der eine Technik zur Unterdrückung dieser Verschiebung darstellt. Der zentrale Teil des AFR ist der Faserkollimator, der für die Erzeugung hochwertiger gegenläufiger Laserstrahlen erforderlich ist. Die Entwicklung und Charakterisierung eines solchen Kollimators für die nahe ultraviolette Wellenlänge des 2S-6P-Übergangs ist eine der wichtigsten Errungenschaften des verbesserten AFR. Die Ergebnisse dieser Arbeit können für andere Anwendungen von Interesse sein, bei denen eine hohe Strahlqualität oder wellenfront-zurückverfolgende Strahlen wichtig sind. Darüber hinaus werden die Einschränkungen der AFR untersucht, die sich aus polarisationserhaltenden Singlemode-Fasern ergeben. Neben anderen Verbesserungen wurde eine Polarisationsüberwachung der Spektroskopielaserstrahlen implementiert. Es werden verschiedene Charakterisierungsmessungen vorgestellt, um die Leistungsfähigkeit des verbesserten AFR zu demonstrieren.

Schließlich wird in dieser Arbeit eine vorläufige Messung des 2S-6P-Übergangs in Deuterium vorgestellt. Für diese Messung wurde ein neuer Kryostat in die Apparatur eingebaut, der die Stabilität des Spektroskopiesignals durch reduzierte Temperaturschwankungen verbessert. Die Erzeugung des kryogenen Deuterium-Atomstrahls wurde in Abhängigkeit von der Düsentemperatur analysiert, was eine wichtige Studie für künftige Spektroskopiemessungen darstellt. Darüber hinaus wurden für die Präzisionsmessung verschiedene systematische Effekte untersucht, darunter die Fehlausrichtung des Atomstrahls und die elektrischen Streufelder. Es wird gezeigt, dass eine Präzisionsmessung des 2S-6P-Übergangs in Deuterium mit einer ähnlichen Unsicherheit wie in Wasserstoff machbar ist. Nach der vorläufigen Unsicherheitsabschätzung kann die $2S_{1/2}$-$6P_{1/2}$-Übergangsfrequenz in Deuterium auf 1.7 kHz bestimmt werden, was einer relativen Genauigkeit von 2.3×10^{-12} entspricht. Zusammen mit der 1S-2S-Messung kann dieses Ergebnis bereits die genauesten Bestimmungen des Deuteronenradius und der Rydberg-Konstante aus dem elektronischen Deuterium ermöglichen, sodass die Unsicherheiten für die Rydberg-Konstante und den Deuteronenradius $\delta R_\infty \simeq 5 \times 10^{-5}\,\mathrm{m}^{-1}$ bzw. $\delta r_d \simeq 0.002\,\mathrm{fm}$ betragen. Dieses Ergebnis bildet die Grundlage für eine zukünftige Präzisionsmessung, bei der die 2S-6P-Übergangsfrequenz mit ähnlicher Genauigkeit wie bei Wasserstoff bestimmt werden soll, was $\delta R_\infty \simeq 2 \times 10^{-5}\,\mathrm{m}^{-1}$ und $\delta r_d \simeq 0.0007\,\mathrm{fm}$ entsprechen würde. Der Vergleich mit dem Ergebnis von myonischem Deuterium würde es dann erlauben, die QED-Theorie für gebundene Zustände auf dem Niveau von 9×10^{-13} zu testen.

Abstract

Quantum electrodynamics (QED) forms the basis for all other quantum field theories, upon which the Standard Model of particle physics is constructed. Currently, it is clear that our fundamental understanding of nature is incomplete, such that the Standard Model is expected to be modified or extended by new particles or interactions. One way to explore these frontiers of fundamental physics is to perform precision measurements. This thesis studies the precision laser spectroscopy of deuterium, where the transition energies between different energy states of the electron bound to the nucleus can be accurately measured with techniques such as ultra-stable lasers and the frequency comb. Due to the simplicity of hydrogen-like atoms, their energy levels can be precisely calculated from bound-state QED and confronted with the experiment with the relative accuracy on the order of 10^{-12}. Such a comparison between theory and experiment is linked to the determination of fundamental constants, which enter the theory as parameters. Only if more indepedendent measurements are available than there are parameters, the theory can be tested.

The comparison between theory and laser spectroscopy in deuterium concerns the Rydberg constant R_∞ and the deuteron charge radius r_d. This requires at least two different transition frequency measurements to determine those constants, and more measurements to test the theory. Contrary to hydrogen, only few accurate enough transition frequency measurements are available in deuterium. This thesis presents the first study of the 2S-6P transition in deuterium, which can be combined with the existing 1S-2S transition frequency measurement to obtain R_∞ and r_d. Together with the 2S-2P transition measurement from muonic deuterium, this determination provides a theory test. Such a comparison is important to shine light on the persisting discrepancy between the result from muonic deuterium and the average of previous data from electronic deuterium, as well as tensions between the recent results from hydrogen spectroscopy.

In contrast to hydrogen, precision spectroscopy of the 2S-6P transition in deuterium is complicated by the simultaneous excitation of unresolved hyperfine components, possibly leading to unresolved quantum interference. This thesis studies the possible systematic effects associated with this complication. Along with analytical perturbative models, supercomputer simulations are performed to analyze these effects. It is shown, that quantum interference is strongly suppressed for all 2S-nP transitions in deuterium, making precision measurements of these transitions possible. Furthermore, another effect is studied in deuterium compared to hydrogen, which arises from the light force acting on the atoms in the standing wave of the spectroscopy light. Despite additional state manifolds from the simultaneous excitation of unresolved hyperfine components, it is shown that this so-called "light force shift" is comparable to the well understood effect in hydrogen.

The main challenge of measuring the one-photon 2S-6P transition in deuterium is the first-order Doppler shift. Therefore, a large part of this thesis contributes to the improved

active fiber-based retroreflector (AFR), which is a technique to suppress this shift. The central part of the AFR is the fiber collimator, which is required to produce high-quality counter-propagating laser beams. Designing and characterizing such a collimator for the near ultra-violet wavelength of the 2S-6P transition is one of the main achievements of the improved AFR. The results of this work can be of interest to other applications where a high beam quality or wavefront-retracing beams are important. Furthermore, the limitations of the AFR arising from single-mode polarization-maintaining fibers are investigated. Along with other improvements, a polarization monitor of the spectroscopy laser beams has been implemented. Various characterization measurements are presented to demonstrate the performance of the improved AFR.

Finally, this thesis presents a preliminary measurement of the 2S-6P transition in deuterium. For this measurement, a new cryostat has been installed in the apparatus, which improves the stability of the spectroscopy signal due to reduced temperature fluctuations. The cryogenic deuterium atomic beam generation has been analyzed in dependence on the nozzle temperature, which is an important study for future spectroscopy measurements. Furthermore, for the precision measurement different systematic effects have been investigated, including the atomic beam misalignment and the stray electric fields. It is demonstrated that a precision measurement of the 2S-6P transition in deuterium with a similar uncertainty than in hydrogen is feasible. According to the preliminary uncertainty budget, the $2S_{1/2}$-$6P_{1/2}$ transition frequency in deuterium can be determined to 1.7 kHz, which corresponds to 2.3×10^{-12} relative accuracy. Together with the 1S-2S measurement, already this result can enable the most accurate determinations of the deuteron radius and the Rydberg constant from the electronic deuterium with the uncertainties on the Rydberg constant and the deuteron radius of $\delta R_\infty \simeq 5 \times 10^{-5}\,\mathrm{m}^{-1}$ and $\delta r_d \simeq 0.002\,\mathrm{fm}$, respectively. This result sets the stage for a future precision measurement, where the 2S-6P transition frequency is expected to be determined with the similar accuracy as in hydrogen, which would correspond to $\delta R_\infty \simeq 2 \times 10^{-5}\,\mathrm{m}^{-1}$ and $\delta r_d \simeq 0.0007\,\mathrm{fm}$. The comparison to the result from muonic deuterium would then allow to test bound-state QED at the level of 9×10^{-13}.

Contents

Chapter 1

Introduction

Our fundamental understanding of nature is incomplete. On the cosmological scale, one of the most prominent problems of fundamental physics is that we lack the understanding of 95% of the matter-energy density in the universe (see e.g. [1]). Among these 95% of unknown content, approximately 69% of the total matter-energy density are attributed to dark energy (which is described by the cosmological constant and could be interpreted as the vacuum energy), and 26% to dark matter. Furthermore, we do not understand how the remaining 5% baryonic matter were produced. The early universe was in a hot dense state, where radiation dominated the total energy content. As the universe expanded and cooled down, approximately equal amounts of matter and antimatter should have been produced. However, we do not find any significant amount of antimatter in our universe [2]. Besides, much less visible matter compared to light should have been formed, quantified by the baryon-to-photon ratio η which is measured to be $\eta \sim 10^{-9}$ but deviates by several orders of magnitude from the expected value around $\eta \sim 10^{-18}$ (see e.g. [3]). Another problem for fundamental physics is the non-zero mass of neutrinos, which is observed in neutrino oscillations [4]. Furthermore, fundamental physics is challenged by the vacuum energy discrepancy between the established contribution from particle physics (such as the Higgs field) and the many orders of magnitude smaller observed value in cosmology, which is referred to as the "cosmological constant problem" [5]. To solve the above and other problems, particle physics expects undiscovered particles or interactions beyond the known particles and interactions, which are described by the current theory called the "Standard Model".

At the present stage of fundamental physics, it is an open question how the Standard Model needs to be modified or extended. The complementary approaches for addressing this puzzle can be classified into three categories. One way is to study interactions at highest possible energies, where potentially new particles are produced directly ("high-energy frontier"). Another way is to explore exotic phenomena, which in theory are expected to be rare or forbidden ("intensity frontier"). Yet another way is to look for tiny deviations from theoretical predictions ("precision frontier"). New particles could for instance be responsible for modified potentials, which are probed by low-energy precision measurements.

This thesis aims to contribute to the "precision frontier" of physics, specifically to the precision laser spectroscopy of hydrogen and deuterium, which are some of the simplest atomic systems where theory and experiment can be most accurately compared [6, 7, 8]. Precision physics of simple atoms can be sensitive to light new particles [9], which are not accessible by high-energy experiments due to the ultra-weak coupling of these particles. Precision laser

spectroscopy of hydrogen was accompanied by the invention of the frequency comb technique, which revolutionized the field of optical frequency metrology and enabled even more accurate spectroscopy measurements [10, 11, 12]. Throughout the last decade, hydrogen spectroscopy has continued to be a fruitful building block of fundamental physics [13, 14, 15, 12, 16]. Further examples of simple atomic systems, which are important for fundamental physics, are helium ions [17], helium atoms [18], molecular hydrogen ions [19, 20, 21, 22], as well as exotic atoms such as muonic atoms [23], positronium [24], muonium [25], antiprotonic helium [26], antihydrogen [27], or antihydrogen molecular ions [28].

In general, other areas of searches for new physics using techniques of atomic, molecular and optical (AMO) physics include for instance the following experiments: atom interferometry for the determination of the fine-structure constant [29, 30] or the test of the equivalence principle [31], Penning trap measurements of the magnetic moment of the free electron or positron [32, 33], precision measurements of masses and magnetic moments in ion traps [34, 35, 36, 37, 38], searches for electric dipole moments of particles [39] such as the neutron [40] or the electron [41], certain type of dark matter searches with nuclear magnetic resonance measurements [42], isotope shift spectroscopy for constraints on other types of dark matter candidates [43], optical clock comparisons for tests of Lorentz invariance [44], searches of exotic interactions using quantum sensors [45], and many others (see [46] for a review).

Tests of Quantum Electrodynamics (QED) and fundamental constants

So far, we know four fundamental interactions (forces) which govern the behavior of matter: the electromagnetic interaction, the weak interaction, the strong interaction, and gravity. The fundamental description of the first three forces is rooted in Quantum Field Theory (QFT), upon which the Standard Model is constructed (see e.g. [47]). Gravity is described by General Relativity, which is a classical theory. One of the greatest successes of the Standard Model is the explanation how the electromagnetic and weak interactions originate from the same force (electroweak interaction) described by the Weinberg-Salam theory. The electroweak theory relies on the spontaneous symmetry breaking mechanism predicting the existence of the Higgs boson, which was gloriously discovered at the Large Hadron Collider in 2012 [48, 49]. Though the strong interaction is incorporated into the Standard Model using the framework of QFT (Quantum Chromodynamics theory), it is an open question how it can be unified with the electroweak force, which is explored by possible Grand Unified Theory models. How gravity is related to the other forces is an even more challenging problem, since in the first place, it is an open question whether spacetime is quantized. Hints for answering these questions may be accompanied by the discovery of further particles.

At low energies, for instance in the field of atomic physics which concerns this thesis, the dominant force is electromagnetic, which is described by Quantum Electrodynamics (QED), whereas other forces are often negligible or to a certain extent can effectively be expressed in parameters or functions. QED forms the basis for all other quantum field theories and makes most accurate predictions on precisely measurable quantities such as the magnetic moment of the free electron [50, 51, 52] or the energy levels of simple atoms [6, 7]. Thereby, one may claim that QED provides most accurate tests of the Standard Model [53]. Such comparisons of theory and experiment require accurate determinations of fundamental constants such as the Rydberg constant R_∞, the electron mass m_e or the fine structure constant α, which directly or indirectly enter the theory as parameters. Therefore, precision tests of fundamental physics are closely related to the determination of fundamental constants. Typically, only a

combination of several measurements provides a theory test. For example, in order to test QED with the mentioned electron-magnetic-moment-experiment, other measurements for the determination of α are involved, for instance rubidium or cesium atom interferometry [30, 29] combined with the Rydberg constant R_∞ from hydrogen or deuterium spectroscopy [14, 54] together with atomic masses from ion trap cyclotron frequency measurements [55] and the electron mass. The latter can either be obtained from the measurement of the electron magnetic moment bound to the carbon nucleus [35] or from precision spectroscopy of HD^+ ions [19, 20] combined with proton and deuteron mass measurements [36, 56, 37].

Test of bound-state QED using hydrogen and deuterium spectroscopy

It is important to distinguish between the QED theory describing free particles (e.g. the magnetic moment of the free electron mentioned above), and the so-called "bound-state QED", which describes a relativistic quantum bound problem [6]. While both QED theories originate from the same Lagrangian, bound-state QED has a more complicated structure and involves various effective approaches. Simple atomic systems provide an ideal platform to determine fundamental constants and to test QED in this regime of a bound state between particles. Atomic hydrogen and deuterium are the simplest stable atoms. Laser spectroscopy of these atoms measures the difference between certain energy levels of the bound electron. To this end, the laser frequency is swept over the resonance, which brings the electron from one state to another. From the measured resonance line of the corresponding transition, the energy difference between the initial and excited state can be deduced. QED calculations for these energy levels depend on mainly four parameters, namely the Rydberg constant R_∞, the proton or deuteron root-mean-square charge radii r_p or r_d, the fine structure constant α, as well as the electron-to-proton or electron-to-deuteron mass ratios. The latter two constants are determined from other experiments, for instance from atom interferometry and ion trap experiments mentioned above. For spectroscopy, we are left with two parameters, namely the nuclear size and the Rydberg constant. Therefore, at least two different transitions need to be measured in order to determine both constants. Further transition measurements then test the theory.

One way to visualize the theory test in hydrogen and deuterium is presented in Fig. 1.1. Due to its narrow natural linewidth of only 1.3 Hz and the two-photon first-order Doppler-free spectroscopy, the 1S-2S transition is the most accurately measured transition in hydrogen and deuterium [57, 13, 54]. Combining this result with another transition measurement (shown on the left scale in Fig. 1.1) yields the Rydberg constant and the proton or deuteron radii. Fig. 1.1(a) shows the data from hydrogen spectroscopy, where black points show the values up to the year 2010 (radiofrequency measurements [58, 59, 60] with squared black markers and optical frequency measurements [61, 62, 63, 64, 65, 66] with circular markers). The average of all these values, which contributed to the Committee on Data for Science and Technology (CODATA) 2014 recommended values [72] for the Rydberg constant and the proton radius, is shown in gray ("2014 world data"). In 2010, for the first time, spectroscopy of muonic hydrogen succeeded [73], where the electron is replaced by the 207 times heavier muon. Since the muon is closer to the proton, the energy levels are more sensitive to the proton radius, and thus such a measurement gives the most precise value [67] which is shown in magenta. However, this measurement was four standard deviations (4σ) discrepant with the previous data, which gave rise to the so-called "proton radius puzzle".

The "proton radius puzzle" triggered several new measurements in the last years, which are

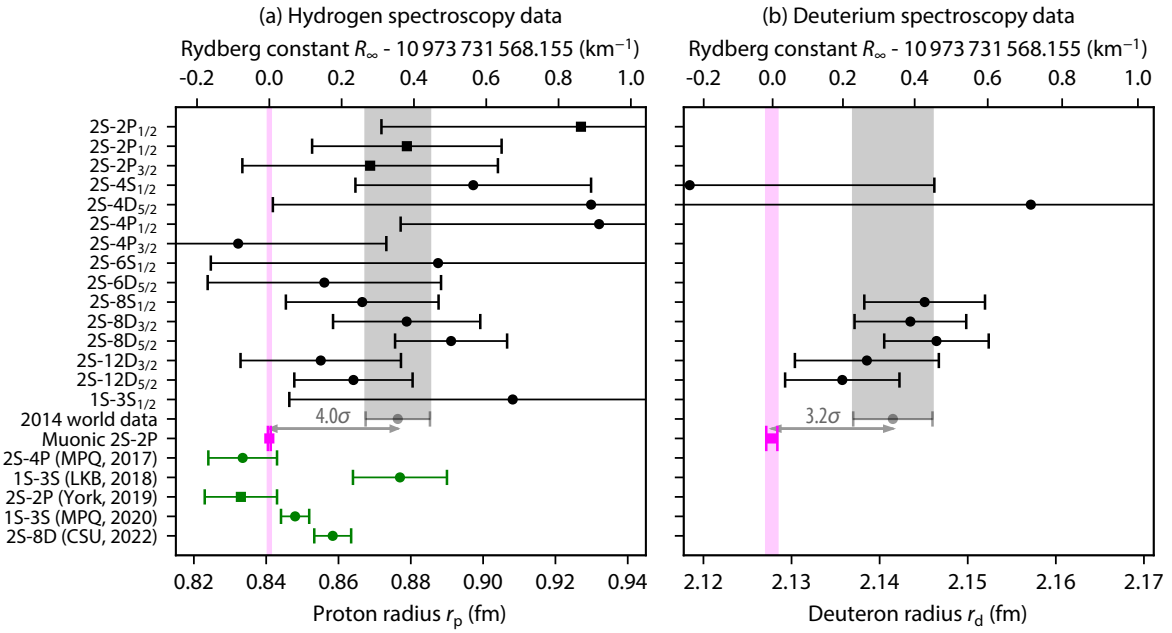

Figure 1.1: Rydberg constant and proton or deuteron charge radii extracted from precision spectroscopy of hydrogen or deuterium, in (a) or (b), respectively. Each point (except "2014 world data") is a combination of the 1S-2S transition measurement in hydrogen or deuterium [57, 13, 54] with a second transition measurement shown on the left scale. Data points up to the year 2010 [58, 59, 60, 61, 62, 63, 64, 65, 66] are shown in black and are averaged in "2014 world data" (in gray). These values are in 4.0σ or 3.2σ discrepancy with the results from muonic hydrogen [67] or deuterium [68, 69] (shown in magenta), which has been called the "proton radius puzzle". Recent spectroscopic measurements from regular (electronic) hydrogen [14, 15, 70, 12, 16] are shown in green, and overall tend to agree with the muonic hydrogen. However, the most recent 2S-8D measurement deviates from muonic hydrogen by 3.1σ, which leaves room to speculate about physics beyond the Standard Model [16], and motivates further measurements. In contrast to hydrogen, so far no recent results are available in deuterium, and a similar discrepancy with muonic deuterium persists. While the recent thesis by Lothar Maisenbacher [71] covers the work on the 2S-6P transition measurement in hydrogen, this thesis contributes towards the result on the Rydberg constant and deuteron radius from the 2S-6P transition in deuterium.

shown in green. The first value came from the 2S-4P transition measurement [14], performed with the predesessor apparatus discussed in this thesis. This result agreed with muonic hydrogen. However, the subsequent result from the 1S-3S measurement [15] gave the larger proton radius. The same transition was measured with a different technique in our group and favors the small radius [12]. Furthermore, the recent radiofrequency Lamb shift measurement agrees with muonic hydrogen [70]. However, the most recent result from the 2S-8D transition deviates from muonic hydrogen by three standard deviations (3.1σ) [16]. This discrepancy illustrates how the spectroscopy of simple atoms is used to test physics beyond the Standard Model, and suggests to speculate about undiscovered bosons which provide an additional coupling between the nucleus and the proton [16]. Such a modified potential could affect certain states more strongly than others, which would effectively result in a Rydberg constant depending on the principal quantum number n [16, 74, 9]. More data is needed to shine light on this discrepancy, with higher n states being more sensitive for contraints on new physics

[74]. This motivates further measurements of 2S-nP transitions in hydrogen and deuterium.

Fig. 1.1(b) gives the overview of data from deuterium spectroscopy. Less data points are available compared to hydrogen, with only a few optical frequency measurements [62, 64, 65]. Only less accurate radiofrequency measurements are available in deuterium as compared to hydrogen [75, 76] (not shown in Fig. 1.1(b)). In 2016, a result from muonic deuterium was published [68]. The uncertainty on the deuteron radius value mainly originates from the theory on nuclear structure corrections ("polarizability"), with the latest result from theory [77] yielding the shown value (in magenta) for the deuteron radius in Fig. 1.1(b), which deviates by 3.2σ from the average value of electronic deuterium. Contrary to hydrogen, no recent results are available from electronic deuterium, such that further measurements are needed to resolve the discrepancy.

Link to nuclear physics and electron scattering experiments

The effect of the finite proton or deuteron charge radius, upon which the energy state of an electron surrounding a proton or a deuteron depends, is only the first-order nuclear structure effect. Depending on the isotope and the level of accuracy, higher-order nuclear structure effects need to be taken into account. The electron can also excite the nucleus, which in turn modifies its energy state. This in-elastic nuclear structure effect is called "polarizability". Since the muon is closer to the nucleus, the nuclear structure effects including the polarizability are greatly enhanced in muonic atoms. Furthermore, the nuclear structure contribution is larger in deuterium than in hydrogen. For muonic deuterium, the theory is therefore limiting the extraction of the deuteron radius. In fact, the muonic deuterium measurement triggered various theory refinements and improved the understanding of certain terms, which were initially [78] thought to be smaller than after further theory calculations [79, 80, 69, 77]. This illustrates how the spectroscopy of simple atomic systems is linked to nuclear physics. For electronic hydrogen, the first-order nuclear structure effect due to the finite proton radius dominates the contribution of nuclear structure effects. However, for electronic deuterium, the higher-order nuclear structure effects significantly contribute to the theoretical prediction of the energy levels [81, 8]. Therefore, similar to muonic deuterium, precision spectroscopy of electronic deuterium is interesting for insights into nuclear forces.

The proton and deuteron radii can also be measured with electron scattering experiments, which provides another link to nuclear physics. In these experiments, the same charge radius as measured in spectroscopy is related to the slope of the form factor at zero momentum transfer [82]. The challenge here is that the experiment cannot be performed at zero momentum transfer, such that an extrapolation is needed to extract the charge radius. Models from nuclear physics can be used to constrain the extrapolation [83]. For the proton radius, new measurements [84, 85] or re-analysis of the old measurements [86, 87] are available with an uncertainty comparable to some recent electronic hydrogen values, with a tendency to agree with the value from muonic hydrogen. In contrast to the proton radius, no recent results are available for the deuteron radius, and the older data [88] is not accurate enough to distinguish between the "small radius" from muonic deuterium and the "large radius" from electronic deuterium. Future scattering experiments [89] promise more accurate results. In general, the comparison of the charge radii from spectroscopy and scattering provides an important link between different fields of physics and tests the understanding of nuclear interactions. Such comparisons are interesting especially in light of planned muon scattering experiments [90, 91]. Furthermore, the recently measured magnetic moment of the muon [92], which chal-

lenges the Standard Model prediction, strengthens the motivation to check for consistency of the theory using the results of different experiments with muons.

In the future, it may be even possible to calculate the nuclear charge radii directly from Quantum Chromodynamics (QCD). One approach for solving QCD problems numerically is called "Lattice QCD". Though the results are currently not accurate enough, rough values for the proton radius are already available from Lattice QCD calculations [93, 94].

Consistency of Rydberg constant determinations

Owing to the precision spectroscopy of simple atoms, the Rydberg constant is the most accurately measured constant of nature, currently known with a fractional uncertainty of 2×10^{-12} [8]. Comparing the Rydberg constant from different atomic systems is therefore a powerful theory test. For example, from Fig. 1.1, we can compare the Rydberg constant as determined from hydrogen spectroscopy to the value from deuterium spectroscopy. This comparison effectively tests the isotope shift theory, which links the proton and deuteron radii [95, 79]: Fig. 1.1(a) and (b) can be overlapped using the same Rydberg constant axis such that the deuteron radius is also determined from hydrogen spectroscopy and the proton radius is also determined from deuterium spectroscopy. Note that the upper scale for the Rydberg constant is identical between Fig. 1.1(a) and (b), demonstrating that the Rydberg constant agrees between muonic hydrogen and muonic deuterium. More data is needed to check for the Rydberg constant consistency between electronic hydrogen and electronic deuterium. Interestingly, the data before 2014 agrees between electronic hydrogen and electronic deuterium, with a similar discrepancy to the results from muonic atoms. New deuterium measurements, with uncertainty comparable or more accurate than the recent hydrogen measurements, are especially interesting in light of the tension from the recent 2S-8D transition measurement in hydrogen [16]. Speculating about a modified potential caused by undiscovered bosons, such potential could be different between hydrogen and deuterium, e.g. if these bosons couple to neutrons differently than to protons.

The comparison of the Rydberg constant from different simple atomic systems becomes increasingly interesting in light of the progress in the field of experimental atomic physics as well as in the field of precise QED calculations. One example is the comparison of the energy levels in hydrogen and antihydrogen, which has become possible only a few years ago [96, 27]. It is anticipated that precision spectroscopy of antihydrogen can reach the similar level of accuracy as in hydrogen, thereby possibly shining light on one of the most pressing problems of fundamental physics – the matter-antimatter-asymmetry of the universe. Light antinuclei, such as the antideuteron, have been produced [97] and in principle, it is thinkable that the technological progress will one day also allow the spectroscopy of antideuterium. What is more close to the not-too-distant future, is the comparison of the Rydberg constant from less exotic two-body atomic systems such as positronium and muonium, though these systems are even more interesting for a QED test in terms the recoil contributions to their hyperfine structure [98, 99, 24, 25]. Furthermore, there are promising efforts towards the laser spectroscopy of helium ions (He^+) [100, 17]. Together with the value for the nuclear charge radius from muonic helium [101], the measurement of the 1S-2S transition in He^+ would yield the Rydberg constant from helium. Recently, there has been also an impressive progress on three-body QED calculations [102, 103, 104, 105, 106, 107], such that systems like hydrogen, deuterium or tritium molecular ions (H_2^+, D_2^+, T_2^+), deuterated molecular hydrogen ions (HD^+) or similar ions with other isotopes (HT^+, DT^+), helium atoms (He) or

lithium ions (Li^+) are already playing [108, 21, 19, 18, 22], or will play an important role in the framework of determining fundamental constants and QED tests. Also four-body QED calculations seem to be within reach [109]. Ultimately, it is important to test the consistency of theory by redundantly comparing the results from different systems, where the Rydberg constant can serve as a common playground. As for hydrogen and deuterium spectroscopy, the goal is to measure as many transitions as possible with an interesting enough accuracy to compare the Rydberg constant within the same system, and to other systems.

Contribution and structure of this thesis

This thesis contributes towards the result for the Rydberg constant and deuteron radius from the 2S-6P transition measurement in deuterium. The 2S-6P measurement in hydrogen with nearly the same apparatus is treated in the recent thesis by Lothar Maisenbacher [71]. Since the 2S-6P spectroscopy of deuterium is similar to hydrogen, this thesis focuses on the differences to what has not been treated already in [71]. Regarding the experimental apparatus, the main contribution of this thesis is the improved active fiber-based retroreflector (AFR), which is used to suppress the first-order Doppler shift. The improved AFR presented here was also used to measure the 2S-6P transition in hydrogen. The results are summarized in the corresponding publication [110], but are extended here to topics which have been omitted or only briefly discussed in [110].

This thesis is structured as follows. In Chapter 2, we discuss the theory and simulations of the 2S-6P transition in atomic deuterium, which are needed to understand and evaluate the spectroscopy measurement. The 2S-nP transitions in deuterium are compared to hydrogen. In contrast to hydrogen, simultaneous excitation of unresolved hyperfine components can not be avoided in deuterium due to the different nuclear spin and the selection rules. Focusing on the differences to the 2S-nP transitions in hydrogen, the complications arising from this simultaneous excitation of unresolved transition lines are investigated. Furthermore, the light force shift is analyzed for the 2S-6P transitions in deuterium. This important effect is associated with the standing wave of two counter-propagating laser beams, which are used to suppress the first-order Doppler shift in the AFR.

Chapter 3 presents the apparatus for probing the 2S-6P transitions in deuterium. After an overview of the experiment, the laser systems including the laser frequency measurement using a frequency comb are described. The numerical modeling of the time-resolved signal in our apparatus is summarized, which is essential to interpret the measurement results in dependence on the mean velocity of atoms, thereby analyzing velocity-dependent effects in the transition frequency measurement. Accurate characterizations of magnetic and electric fields, which are also an important part of the experiment, are presented. The electric field inside the interaction region is measured in-situ using the specially designed fluorescence detector. Finally, the generation of a cryogenic deuterium atomic beam is discussed. Differences between hydrogen and deuterium are here responsible for a modified temperature dependence of the spectroscopy signal, such that the deuterium measurement needs to be performed at a different temperature compared to hydrogen. The temperature dependence of the 2S-6P spectroscopy signal and of the velocity distribution are investigated for deuterium. Compared to the 2S-6P measurement in hydrogen, the apparatus has been upgraded to a high-performance cryostat, which is also presented here.

The improved active fiber-based retroreflector (AFR) for first-order Doppler shift suppression is part of the whole apparatus, but can be viewed as a separate topic, which is

presented in Chapter 4 following the corresponding publication [110]. Since the first-order Doppler shift is the dominant effect when probing the 2S-6P transitions in hydrogen and deuterium, this part of the apparatus is most decisive for an accuracte precision measurement of the transition frequencies. The central part of the AFR is the fiber collimator, which is required to produce high-quality counter-propagating laser beams. Minimizing aberrations produced by the collimator turned out to be particularly challenging for the near ultra-violet (UV) wavelength as required for the 2S-6P transition at 410 nm. Much work has been invested to design a four-lens collimator, which produces a laser beam with a beam quality limited only by the not exactly Gaussian beam profile from the fiber. The topic of aligning the collimator to minimize astigmatism is greatly shortened in [110], but is expanded in this thesis. Furthermore, other improvements such as the improved retroreflection control and the intensity stabilization are presented. In the process of improving the AFR setup, it was found that Rayleigh backscattering in fiber is responsible for an etalon effect, which is important to suppress in our spectroscopy apparatus. This topic was only briefly mentioned in [110], and is therefore treated in detail in this thesis. Finally, a large part of Chapter 4 is dedicated to the polarization monitor of the laser light as seen by atoms during spectroscopy. This topic turned out to be more complicated than initially thought, such that a correction was published [111]. Here, the complications of the polarization monitor are explained in detail.

Chapter 5 presents the preliminary measurement of the 2S-6P transition in deuterium, which was conducted in July 2021. The main purpose of this measurement was the feasibility study for planning a future precision measurement campaign. The preliminary measurement included the temperature characterization of the cryogenic deuterium atomic beam, which is presented along with the apparatus in Chapter 3. Furthermore, around 500 precision spectroscopy line scans were acquired. The preliminary analysis demonstrates the feasibility of the future measurement with a similar uncertainty as the 2S-6P transition measurement in hydrogen. Moreover, already the preliminary measurement may be used to extract the transition frequency with an uncertainty lower than the average of all the previous data in electronic deuterium. So far the preliminary analysis has been performed with a blind offset in the data, such that no value for the Rydberg constant and the deuteron radius is given here. However, the anticipated uncertainty for adding a new data point to Fig. 1.1(b) is presented in Chapter 6, which concludes this thesis.

Chapter 2

Theory and Simulations of the 2S-6P Transition in Atomic Deuterium

In this chapter we refer to the theory and present simulations of the 2S-6P transition in atomic deuterium, which are needed to understand and evaluate the spectroscopy measurement. Much of the theory for probing the 2S-6P transition in atomic deuterium is identical to hydrogen which has been treated in great detail in the thesis by Lothar Maisenbacher [71]. Therefore, we here focus on the differences between the 2S-6P transition in hydrogen and deuterium.

First, a brief overview of the state-of-the-art bound-state QED theory calculations for energy levels in hydrogen and deuterium is given in Section 2.1. Then, the properties of 2S-nP transitions in hydrogen and deuterium are compared in Section 2.2. In contrast to probing the 2S-nP transition hydrogen, simultaneous excitation of unresolved hyperfine components can not be avoided in deuterium due to the different nuclear spin and the selection rules. This complicates the situation and requires to consider three possible imperfections introduced in Section 2.3: the initial state population asymmetry, the residual circularly polarized light fraction, and a possible detection imbalance of fluoresence photons. Following two effects need to be discussed for the 2S-6P transitions in deuterium due to the simultaneous excitation of unresolved hyperfine components. First, the resonance lineshape as well as a possible line center shift for the simulataneous excitation of different unresolved hyperfine transitions, which is discussed in Section 2.4. Second, the possible quantum interference between unresolved components, which is discussed in Section 2.5.

One of the leading systematic uncertainties when probing the 2S-6P transitions in atomic deuterium with our apparatus is associated with the standing wave of two counter-propagating laser beams, which are used to suppress the first-order Doppler shift. The standing light wave produces a light force acting on atoms, which consequently distorts the observed resonance line. This effect, which we denote as the light force shift, is treated in Section 2.6.

2.1 Theory of energy levels in hydrogen and deuterium

The quantum mechanics basics of one-electron atoms are derived in the famous book by H. A. Bethe and E. E. Salpeter [112], originally published in 1957. Since then, much progress

has been made in theory. The state-of-the art bound-state QED calculations for hydrogen and deuterium are summarized in [81] and the CODATA[1] 2018 review [8]. Older, but in some aspects more detailed reviews are for example [113, 6]. Even more details on the bound-state QED theory can for example be found in the books by M. I. Eides, H. Grotch and V. A. Shelyuto [7], as well as the recently published book by U. Jentschura and G. S. Adkins [114]. Numerical tabulation of the transition energies can be for instance found in [115, 116]. Here, we give a brief overview of the theory, summarizing and comparing different contributions to the $1S_{1/2}$-$2S_{1/2}$ and $2S_{1/2}$-$6P_{1/2}$ transition energies in hydrogen and deuterium.

In the following, we do not consider the hyperfine structure, which arises from the interaction of the nuclear magnetic dipole moment with the magnetic field generated by the electron. The hyperfine structure is discussed and tabulated in detail in [116, 117, 115], and does not contribute significantly to the theory uncertainty for the prediction of the energy levels[2]. In this section, we consider the centroid energy E_{nlJ} averaged over the corresponding hyperfine state energies E_{nlJF}, which is defined as [81]:

$$E_{nlJ} = \frac{\sum_F (2F+1) E_{nlJF}}{\sum_F (2F+1)}. \tag{2.1}$$

In the above equation, n is the principal quantum number, l is the orbital angular momentum quantum number of the electron, J is the total angular momentum quantum number of the electron (obtained by adding the electron spin to its orbital angular momentum), and F is the total angular momentum of the atom (obtained by adding the nuclear spin to the total angular momentum of the electron). The centroid energy E_{nlJ} of an electron bound in hydrogen or deuterium can then be written as:

$$E_{nlJ} = hc\, R_\infty \left(-\frac{1}{n^2} + f_{nlJ}(\alpha, \frac{m_e}{m_N}, \dots) + \frac{\delta_{l0}}{n^3} \left(C_{\mathrm{NS}}\, r_N^2 + C_{\mathrm{pol}} + \text{h.o.n.e.} \right) \right). \tag{2.2}$$

The pre-factor hcR_∞, where h is Planck's constant, c the speed of light, and R_∞ the Rydberg constant, converts the energy to SI units. The first term in brackets, $-1/n^2$, is the dominant ("gross") structure of principal quantum number states from the Coulomb potential, already heuristically postulated by N. Bohr in 1913 by using a resonance condition with the de-Broglie wavelength of the electron, and later derived from the Schrödinger equation. The second term f_{nlJ} summarizes all further point-like interaction effects, including relativistic effects, nuclear recoil efects, and QED effects, which mainly depend on the fine-structure constant α and the electron-to-nucleon mass ratio m_e/m_N (other constants enter only with insignificant accuracy). The mass ratios and α can be accurately determined from other

[1] Committee on Data for Science and Technology.

[2] See [116, 115] for the review of off-diagonal contributions to the hyperfine Hamiltonian, which were first calculated in [118] (see also [119, 59] and note that in [59] the off-diagonal contribution for the 2P levels is misprinted as 0.0025 kHz which should be 2.5 kHz). The resulting shifts from off-diagonal contributions to the hyperfine centroid are tabulated for hydrogen in Table 1 of [116] and for deuterium in Table 1 of [117]. This shift $\Delta\nu_{\mathrm{HFS}}^{\mathrm{o.-d.}}$ vanishes for the S levels, and is on the order of 10-20 Hz for the $6P_{1/2}$ and $6P_{3/2}$ levels in deuterium. Another contribution for deuterium levels with $j > 1/2$ is the electric quadrupole hyperfine structure shift $\Delta\nu_{\mathrm{HFS}}^{\mathrm{quad}}$, which does not enter the hyperfine centroid, but is important when considering the individual hyperfine transitions. Both $\Delta\nu_{\mathrm{HFS}}^{\mathrm{o.-d.}}$ and $\Delta\nu_{\mathrm{HFS}}^{\mathrm{quad}}$ are given in Table 2.4 and Table 2.5 for the transitions discussed in this thesis.

experiments [37, 30, 29, 19, 36]. Their recommeded values are [8]:

$$\begin{aligned} m_e/m_p &= 5.446\,170\,214\,87(33) \times 10^{-4}, \\ m_e/m_d &= 2.724\,437\,107\,462(96) \times 10^{-4}, \\ \alpha &= 7.297\,352\,569\,3(11) \times 10^{-3}. \end{aligned} \tag{2.3}$$

The third term in Eq. (2.2) summarizes the nuclear structure effects, and is present only for states with zero angular momentum (S-states where $l = 0$). All nuclear effects have the same scaling $\propto 1/n^3$. The leading term for accounting the nuclear structure is the finite nuclear size effect (elastic nuclear structure effect), which depends on the constant pre-factor C_{NS} given by [120, 81, 8]

$$C_{\mathrm{NS}} = \frac{4m_e^2c^2}{3\hbar^2}\alpha^2 = \frac{4\alpha^2}{3\lambda\!\!\!^{-2}_{\mathrm{C}}} \simeq 4.8 \times 10^{-10}\ [\mathrm{fm}^{-2}], \tag{2.4}$$

where $\lambda\!\!\!^{-}_{\mathrm{C}}$ is the reduced Compton wavelength of the electron, and on the mean-square nuclear charge radius r_N^2, defined as:

$$r_N^2 \equiv \langle r_N^2 \rangle = \int r^2 \rho_N(\vec{r}) \mathrm{d}^3\vec{r} = -6\hbar^2 \frac{\mathrm{d}G_E}{\mathrm{d}q^2}\Big|_{q^2=0}. \tag{2.5}$$

It has been shown [82] that, as the above equation states, the definition of r_N^2 based on the nuclear charge distribution $\rho_N(\vec{r})$ is equivalent to the definition based on the electric form factor G_E, where q is the momentum transfer between the electron and the proton. The form factor can be measured in electron scattering experiments. However, note that the charge radius is defined at zero momentum transfer ($q^2 = 0$), which is impossible to reach in the experiment (the electron cannot scatter from the proton without any momentum transfer, i.e. it does not scatter if no momentum is transferred). Instead, the measurement results for $q^2 > 0$ need to be extrapolated to $q^2 = 0$, such that experiments with q^2 as low as possible are advantageous. Models from nuclear physics can be used to constrain the extrapolation [83]. For the proton radius, new measurements [84, 85] or re-analysis of the old measurements [86, 87] are available. For the deuteron radius, only older less accurate data [88] and proposals for the future [89] are available from scattering experiments.

In muonic atoms, the electron is replaced by the 207 times heavier muon ($m_e \to m_\mu \simeq 207\, m_e$), such that the finite size effect is increased compared to electronic atoms (note that $C_{\mathrm{NS}} \propto m_e^2$). Therefore, most accurate results for the charge radii of the proton and the deuteron are obtained from the spectroscopy of muonic atoms [67, 68], which contribute most significantly for the CODATA 2018 recommended values [8]:

$$r_p = 0.8414(19)\,\mathrm{fm}, \quad r_d = 2.127\,99(74)\,\mathrm{fm}. \tag{2.6}$$

Together with the 1S-2S transition in hydrogen, which is, due to its narrow linewidth and the first-order Doppler-free two-photon spectroscopy, measured most accurately in both hydrogen and deuterium [57, 13, 54], the charge radii from muonic atoms thus dominantly contribute to the recommended value for the Rydberg constant [8]:

$$R_\infty = 10\,973\,731.568\,160(21)\,\mathrm{m}^{-1}. \tag{2.7}$$

We shall also remark that the combination of the 1S-2S isotope shift measurement and theory precisely links deuteron and proton radii [95, 79]:

$$r_d^2 - r_p^2 = 3.820\,70(31)\,\mathrm{fm}^2. \tag{2.8}$$

As has been pointed out in the introduction, converting the proton radius to the deuteron radius and vice versa within the comparison of the spectroscopy results between hydrogen and deuterium, corresponds to testing the consistency of the Rydberg constant determination in hydrogen and deuterium (overlapping Fig. 1.1(a) and (b) using the same Rydberg constant scale), which may also be called a test of the isotope shift theory resulting from the comparison of nuclear structure effects.

The second term C_{pol} accounting for nuclear effects in Eq. (2.2) is the leading term for the so-called "polarizability", which accounts for the excitation of the nucleus (inelastic nuclear structure effect). Furthermore, there are higher order nuclear structure effects (h.o.n.e). We will see below, that for electronic hydrogen only the leading order finite size effect is important, whereas other nuclear effects including polarizability are below the current level of theory uncertainty. However, for electronic deuterium, the polarizability cannot be neglected. For all muonic atoms, including muonic hydrogen, all nuclear effects are much larger, such that even higher order nuclear effects need to be carefully investigated [78].

The leading order for E_{nlJ} is given by the relativistic Dirac equation:

$$\begin{aligned} E_{nlJ} \approx E_D &= m_e c^2 \left(1 + \frac{\alpha^2}{\left(n - J - 1/2 + \sqrt{(J+1/2)^2 - \alpha^2} \right)^2} \right)^{-1/2} - m_e c^2 \\ &= \frac{m_e c^2 \alpha^2}{2} \left(-\frac{1}{n^2} + \alpha^2 \frac{3 + 6J - 8n}{4(1+2J)n^4} + \mathcal{O}(\alpha^4) \right), \end{aligned} \tag{2.9}$$

where in the last step we expanded the equation in series of α. From the Dirac equation, we see how the binding energy of the electron in an atom is linked to its rest mass energy $m_e c^2$. In fact, the Dirac enery includes the electron's rest mass energy, which has been substracted above. Comparing Eq. (2.9) with Eq. (2.2), it is amusing to realize how $m_e c^2$ is manifested in the Rydberg constant (which was empirically found by J. Rydberg in the year 1888, 17 years before Einstein derived the equivalence of energy and mass):

$$hc\, R_\infty = m_e c^2 \times \frac{\alpha^2}{2}. \tag{2.10}$$

Since 2019, h and c are fixed constants of nature [8], such that the measurement of the Rydberg constant is directly linked to measurements of the electron mass m_e and the fine structure constant α.

Eq. (2.9) demonstrates that the order for fine-structure effects is $\alpha^2 \times \mathcal{O}(\alpha^2)$, i.e. 10^{-5} of the binding energy. However, there is an effect which is larger than the fine-structure, namely the nuclear recoil effect. The leading contribution of the nuclear recoil can be understood classicaly: due to the finite nuclear mass m_N, the electron moves not around the nucleus, but both the electron and the nucleus move around their center-of-mass. We can account for this effect by simply considering the motion of the electron in the center-of-mass frame, which requires to replace the electron's mass m_e by the reduced mass m_{red}:

$$m_e \to m_{\mathrm{red}} = \frac{m_e\, m_N}{m_e + m_N}. \tag{2.11}$$

Therefore, the leading order for the recoil effect is simply the subsitution of the binding energy $hcR_\infty = m_e c^2\alpha^2/2$ by $hcR_\infty m_{\mathrm{red}}/m_e = m_{\mathrm{red}}c^2\alpha^2/2$, which is $\sim 5.4 \times 10^{-4}$ for hydrogen and $\sim 2.7 \times 10^{-4}$ for deuterium. This is the leading order difference in transition energies between hydrogen and deuterium. In fact, this is how the isotope deuterium was discovered: H. Urey and colleages observed two lines in spectroscopic measurements [121][1].

The Dirac equation, Eq. (2.9), predicts that states with same n and J but different l have the same energy (Eq. (2.9) does not depend on l). In 1947, Lamb and Retherford measured [123] a difference between the $2S_{1/2}$ and $2P_{1/2}$ states in hydrogen, thereby disproving this prediction. This so-called "Lamb shift" is explained by QED effects, i.e. the interaction with quantum vacuum fluctuations. Today, these effects are precisely calculated, and the theory uncertainty is being constantly improved. The state-of-the-art calculation of the $1S_{1/2}$ ground state in hydrogen and deuterium, following [81, 8], is evaluated in Table 2.1. Fig. 2.1 exemplarily pictures some of the Feynman diagrams for the different effects. Table 2.2 and Table 2.3 summarize and compare the contributions of different effects between the $1S_{1/2}$-$2S_{1/2}$ and $2S_{1/2}$-$6P_{1/2}$ transition frequencies of hydrogen and deuterium.

It is important to recall that theory does not make predictions on numerical values, but rather on expressions which depend on parameters, which we may call "fundamental constants" or "constants of nature". In Table 2.1, Table 2.2 and Table 2.3, the theory result is evaluated for the CODATA 2018 values of the constants α, m_e/m_p or m_e/m_d, R_∞ and r_p or r_d, as listed in Eq. (2.3), Eq. (2.6) and Eq. (2.7). The uncertainty on the total theory predicition is composed from the uncertainty arising from constants, and the theory uncertainty. It shall be remarked that the uncertainty in α and the mass ratios do not significantly contribute to the total uncertainty, i.e. the uncertainty from R_∞ and r_N dominates the overall uncertainty from constants, as well as the total uncertainty. The theory uncertainty is listed in Table 2.1 for the individual effects following [8], which is dominated by the 2-loop QED correction[2].

Furthermore, it shall be remarked that the calculation of the $1S_{1/2}$-$2S_{1/2}$ transition frequency in Table 2.2 has a total uncertainty of around 7 kHz, whereas the measurement has an uncertainty of only 10 Hz (hydrogen) or 25 Hz (deuterium) [54]. However, this does not mean that the theory must be improved in order to be confronted better with the experiment. In fact, it is the opposite case: the experiments determining the fundamental constants must be improved in order to be more accurately confronted with theory. This again illustrates the mentioned situation above: the "theoretical prediction" of transition frequencies involves experimental values of fundamental constants. Note that if we wish to consistently "predict" a certain transition frequency, the measured value of this transition should not be indirectly included into constants entering this calculation. For example, if we predict the 1S-2S transition frequency, the determination of the Rydberg constant entering the calculation should not involve the 1S-2S transition measurement itself, but only other transition measurements.

[1] Following [122], an interesting historic remark: already in the year 1919, Otto Stern hypothesized that hydrogen, which was found to have an atomic mass of 1.0079 atomic units, was a mixture of two isotopes. Otto Stern and his colleage M. Volmer were then trying to find an ∼1% admixture of a heavy hydrogen with mass of 2 to explain the ∼1% higher mass. However, the result was negative. In principle, their idea was qualitatively correct, but they were quantitatively wrong, since the atomic mass of 1.0079 is not purely explained by the heavier hydrogen isotope, and the percentage of deuterium atoms in naturally occuring hydrogen is only around 0.015%.

[2] The theory uncertainty for the 2-loop QED correction has been improved by the recent work [124] not included in the CODATA 2018 review published in [8]. With the result of [124], the 2-loop QED uncertainty is improved to the same order as the 3-loop QED [125].

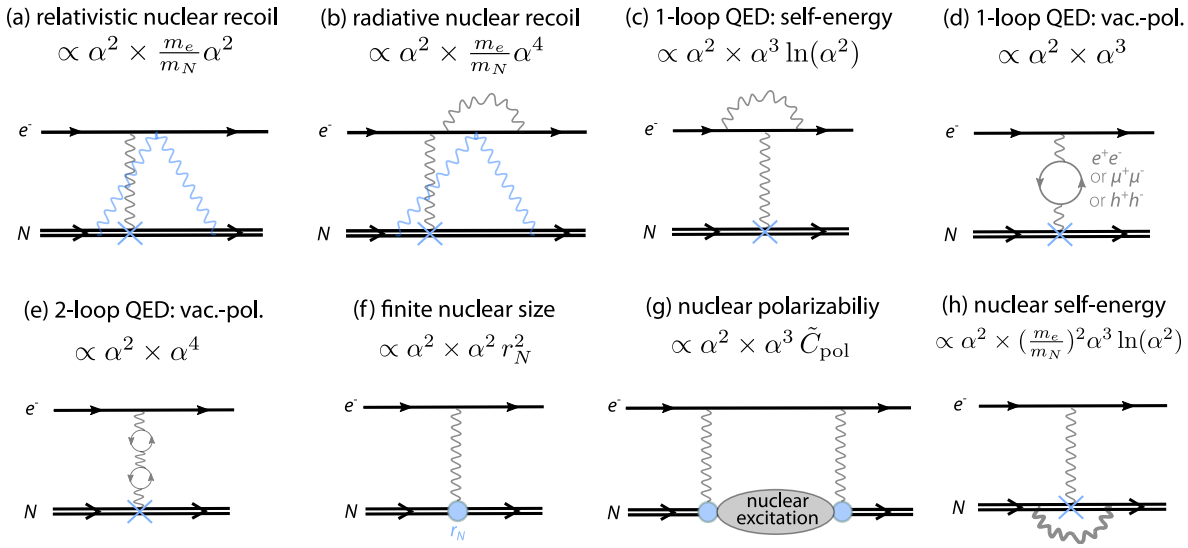

Figure 2.1: Examples of Feynman diagrams for different effects contributing to the energy levels of hydrogen and deuterium. The horizontal axis represents time and the vertical axis represents space. For each diagram, the upper line represents the electron (e^-) and the bottom line represents the nucleus (N). The title in each subfigure names the effect according to the contributions in Table 2.1, Table 2.2 and Table 2.3. Furthermore, the leading order of magnitude in powers of the fine-structure constant α (including the additional factor α^2 from the Rydberg constant according to Eq. (2.10)), and for some cases the other relevant paramater (electron-to-nucleus mass ratio m_e/m_N, mean-square charge radius r_N^2, polarizability coefficient $\tilde{C}_{\mathrm{pol}}$) are given. All diagrams except (f) and (g) consider point-like interactions, with the blue cross denoting the Coulomb vertex. Here, exemplary diagrams with only one Coulomb vertex are shown, whereas for each effect also diagrams with many Coulomb vertices are present. Straight gray wavy curves denote the Coulomb exchange photons between e^- and N. (a) and (b) show the nuclear recoil effects, where the in addition to the Coulomb exchange photon, the blue wavy curve denotes the transverse photon. (c) shows the self-energy of the bound electron, and (d) the effect of vacuum polarization, where the Coulomb exchange is for example affected by eletron-positron, muon-antimuon, or hadron-antihadron pairs. The analogue of the electron self-energy also occurs for the nucleus, which is shown in (h). Both (c) and (d) are called "1-loop QED" effects, and can also occur with more loops: (e) shows an example of the 2-loop vacuum polarization. (f) and (g) show nuclear structure effects. (f) is an example of an elastic nuclear structure effect, also called finite nuclear size effect, which accounts for the finite charge radius of the nucleus. (g) is an example of inelastic nuclear structure effect ("nuclear polarizability"): the nucleus is excited, here accompanied by the two-photon exchange (higher order terms involve more exchange photons, e.g. three-photon exchange).

Otherwise, we would use the measurement of the same transition, which we aim to calculate. In Table 2.2 and Table 2.3 the CODATA 2018 values of fundamental constants are used. For the 2S-6P transition (Table 2.3), no measurement of the same transition enters the CODATA 2018 adjustment of constants. For the 1S-2S transition (Table 2.2), the 1S-2S measurement is included in the CODATA 2018 adjustment of constants. In principle, the 1S-2S measurement should then be excluded from the adjustment of constants in order to make the prediction of this transition frequency. However, this would not substantially change the calculated values since other accurate measurements are available (e.g. 1S-3S measurement combined with the nuclear charge radii from muonic atoms). Besides, Table 2.2 and Table 2.3 mainly serve the purpose to show the contributions of different effects to the transition frequencies.

	Hydrogen $1S_{1/2}$ state energy (in units of hcR_∞)	Deuterium $1S_{1/2}$ state energy (in units of hcR_∞)
Dirac (with $m_e \to m_{\text{red}}$)	$-0.999\,468\,985\,371\,2$	$-0.999\,740\,940\,061\,6$
Rel. nuclear recoil	-6.50853×10^{-9}	-3.26245×10^{-9}
Radiative recoil	$-3.75(22) \times 10^{-12}$	$-1.88(11) \times 10^{-12}$
1-loop QED		
self-energy	2.5482499×10^{-6}	2.5502410×10^{-6}
vacuum-polarization	-6.52969×10^{-8}	-6.535025×10^{-8}
$\mu^+\mu^-$ vacuum-pol.	-1.54×10^{-12}	-1.54×10^{-12}
hadronic vacuum-pol.	-1.03×10^{-12}	-1.03×10^{-12}
2-loop QED	$2.2098(29) \times 10^{-10}$	$2.2116(29) \times 10^{-10}$
3-loop QED	$5.5(2.9) \times 10^{-13}$	$5.5(2.9) \times 10^{-13}$
Finite nuclear size		
$\propto \alpha^4$	3.3654×10^{-10}	2.15437×10^{-9}
$\propto \alpha^5$	$-1.26(5) \times 10^{-14}$	$-4.6(8) \times 10^{-14}$
$\propto \alpha^6$	1.66×10^{-13}	9.53×10^{-13}
$\propto \alpha^7$	$-1.1(4) \times 10^{-15}$	$-1.0(3) \times 10^{-15}$
Nuclear polarizability		
$\propto \alpha^5$	$-2.1(4) \times 10^{-14}$	$-6.62(7) \times 10^{-12}$
$\propto \alpha^6$	$1.2(1.2) \times 10^{-13}$	$-1.6(1.2) \times 10^{-13}$
Nuclear self-energy	$1.40(5) \times 10^{-12}$	$3.7(1) \times 10^{-13}$
Total	$-0.999\,466\,508\,373\,4$	$-0.999\,738\,456\,067\,2$
Theory uncertainty	4.8×10^{-13}	4.5×10^{-13}
Uncert. from constants	2.4×10^{-12}	2.4×10^{-12}
Total uncertainty	2.5×10^{-12}	2.5×10^{-12}

Table 2.1: Contribution of different effects to the theoretical prediction for the hyperfine centroid energy of the $1S_{1/2}$ state in hydrogen and deuterium, following [8, 81]. See Fig. 2.1 for the corresponding examples of Feynman diagrams. Theory does not predict numerical values, but expressions in terms of fundamental constants. Here, the results have been evaluated for their values (mainly α, m_e/m_p or m_e/m_d, and r_p or r_d) according to [8]. The uncertainty is therefore combined from the theory uncertainty and the uncertainty from the measured values of fundamental constants. Note that the terms are evaluated in units of hcR_∞ and hence are independent of R_∞. However, we include the relative uncertainty in R_∞ in the "uncertainty from constants". The total uncertainty is dominated by the relative uncertainty from the Rydberg constant R_∞ and the uncertainty from the proton or deuteron radii r_p and r_d, whereas the contribution of the uncertainty from α, m_e/m_p or m_e/m_d is negligible. For each effect individually, only the theory uncertainty is given.

The first term in Table 2.1 is the evaluation of the Dirac energy from Eq. (2.9) with the replacement $m_e \to m_{\text{red}}$ to account for the leading order recoil effect. This predicts the energy correctly up to the relative fraction of $\sim 10^{-5}$. Next we list the relativistic and higher order nuclear effects[1], which contribute in leading order a binding energy fraction of $\alpha^2 \times m_e/m_N \sim 10^{-8}$ for hydrogen (the contribution is two times lower for deuterium due

[1] The second term in Eq. (8) of [6] or Eq. (5) of [81], plus the Barker-Glover correction (last terms in Eq. (9) and (10) of [8]), plus the relativistic and higher order terms from Eq. (11) and (12) of [8].

	Hydrogen $1S_{1/2}$-$2S_{1/2}$ (Hz)	Deuterium $1S_{1/2}$-$2S_{1/2}$ (Hz)
Dirac (with $m_e \to m_{\rm red}$)	2 466 068 518 610 695	2 466 739 533 830 044
Rel. nuclear recoil	20 264 021	10 156 580
Radiative recoil	10 781	5398
1-loop QED		
self-energy	−7 312 058 467	−7 317 770 941
vacuum-polarization	187 963 502	188 116 977
$\mu^+\mu^-$ vacuum-pol.	4435	4438
hadronic vacuum-pol.	2976	2978
2-loop QED	−635 541	−636 062
3-loop QED	−1594	−1596
Finite nuclear size		
$\propto \alpha^4$	−968 758	−6 201 601
$\propto \alpha^5$	36	133
$\propto \alpha^6$	−470	−2702
$\propto \alpha^7$	3	29
Nuclear polarizability		
$\propto \alpha^5$	59	19 058
$\propto \alpha^6$	−344	473
Nuclear self-energy	−4034	−1059
Total	2 466 061 413 187 299	2 466 732 407 522 147
Theory uncertainty	1396	1271
Uncert. from constants	6437	6395
Total uncertainty	6587	6520

Table 2.2: Similar to Table 2.1, here showing the contribution of different effects to the theoretical prediction for the hyperfine centroid transition frequency of the $1S_{1/2}$-$2S_{1/2}$ transition in hydrogen and deuterium. Theoretical expressions have been evaluated for values of fundamental constants according to [8], here mainly R_∞, α, m_e/m_p or m_e/m_d, and r_p or r_d. The total uncertainty is dominated by the uncertainty from the Rydberg constant R_∞ and the uncertainty from the proton or deuteron radii r_p and r_d, whereas the contribution of the uncertainty from α, m_e/m_p or m_e/m_d is negligible.

to higher mass). Fig. 2.1(a) shows an example of the corresponding diagram. The recoil correction involves an exchange of virtual photons, which happen at different points in time. This is indicated by non-vertical blue wavy curves, which denote the so-called transverse photons [113, 114].

It is interesting to realize, that for the one-photon $2S_{1/2}$-$6P_{1/2}$ transition, the contribution of the relativistic nuclear recoil approximately corresponds to the recoil shift (see Eq. (2.81) and compare Table 2.3 with Table 2.4). This may illustrate the similar physics of the phenomenon: whereas for the internal energy state it is the virtual photon which produces a recoil shift of the energy state, for the probed transition frequency, it is the real photon which produces the recoil and thereby changes the kinetic energy of the atom.

Within the recoil, it is also possible that vacuum fluctuations occur, which is called "radiative nuclear recoil", with an example of self-energy shown in Fig. 2.1(b). These corrections

	Hydrogen $2S_{1/2}$-$6P_{1/2}$ (Hz)	Deuterium $2S_{1/2}$-$6P_{1/2}$ (Hz)
Dirac (with $m_e \to m_{\rm red}$)	730 691 021 696 054	730 889 842 123 184
Rel. nuclear recoil	1 129 173	566 917
Radiative recoil	1540	771
1-loop QED		
self-energy	−1 071 679 859	−1 072 517 882
vacuum-polarization	26 853 088	26 875 014
$\mu^+\mu^-$ vacuum-pol.	634	634
hadronic vacuum-pol.	425	425
2-loop QED	−90 477	−90 551
3-loop QED	−236	−236
Finite nuclear size		
$\propto \alpha^4$	−138 394	−885 943
$\propto \alpha^5$	5	19
$\propto \alpha^6$	−74	−433
$\propto \alpha^7$	<1	4
Nuclear polarizability		
$\propto \alpha^5$	8	2722
$\propto \alpha^6$	−49	68
Nuclear self-energy	−584	−153
Total	730 689 977 771 255	730 888 796 074 559
Theory uncertainty	199	181
Uncert. from constants	1532	1529
Total uncertainty	1545	1539

Table 2.3: Similar to Table 2.2, here showing the contribution of different effects to the theoretical prediction for the hyperfine centroid transition frequency of the $2S_{1/2}$-$6P_{1/2}$ transition in hydrogen and deuterium according to [8]. Note that in deuterium, nuclear polarizability is an order of magnitude larger than the theory uncertainty, whereas in hydrogen the polarizability is negligible. Therefore, precision spectroscopy of deuterium also probes inelastic nuclear effects.

are of order $\alpha^4\, m_e/m_N \sim 10^{-12}$ of the binding energy, and hence also a factor of two smaller for deuterium.

One-loop QED effects are classified into the electron self-energy, Fig. 2.1(c), and vacuum-polarization, Fig. 2.1(d). Note that here only the simplest diagrams with only one Coulomb vertex (blue cross) are depicted, whereas different higher-order diagrams with many Coulomb vertices also need to be evaluated. The one-loop self-energy is the dominant effect for the Lamb-shift, and is of order $\alpha^3 \ln(\alpha^2)/\pi \sim 10^{-6}$ of the binding energy. The similar self-energy effect for the nucleus[1] (see Fig. 2.1(h)) is of order $\alpha(m_e/m_N)^2\alpha^3 \ln(\alpha^2) \sim 10^{-12}$, and due to the $1/m_N^2$ dependency around a factor of 4 smaller for deuterium. The one-loop vacuum-polarization (see Fig. 2.1(d)) from electron-positron (e^+e^-) pairs contributes with a fraction $\alpha^3/\pi \sim 10^{-7}$. Note that also muon-antimuon ($\mu^+\mu^-$) pairs and hadronic pairs in the loop

[1]There is some ambiguity with this correction, since the self-energy also contributes to the nuclear charge radius and nuclear magnetic moment [81, 126].

contribute a small but significant fraction of $\sim 10^{-12}$ each, which is above the total theory uncertainty.

An example of the two-loop QED effect are two consecutive particle-antiparticle pairs within the Coulomb exchange, see Fig. 2.1(e). However, two-loops open many other possibilities for a variety of combinations, see for example Fig. 8 in [113] or Figs. 3 and 6 in [78]. They can be divided into three parts: the two-loop self-energy, the two-loop vacuum polarization (with one example shown in Fig. 2.1(e)), and the mixed self-energy and vacuum-polarization [81]. Note that also many Coulomb vertices are possible. All two-loop QED effects are of order $\alpha^4/\pi^2 \sim 10^{-10}$ of the binding energy. The uncertainty on these effects is dominanting the total theory uncertainty in the tabulation presented here based on [8]. Recent results [124] improve the 2-loop QED uncertainty, such that for the next CODATA review the theory uncertainty is expected to be smaller. The three-loop QED effects are of order $\alpha^5/\pi^3 \sim 10^{-13} - 10^{-12}$, which is on the edge of the current theory uncertainty.

The nuclear structure effects are classified into elastic (finite nuclear size) and inelastic (nuclear polarizability) effects. As for the elastic part, the point-like Coulomb vertex is replaced by the interaction with the nucleus of finite size r_N, symbolically represented by the blue circle in Fig. 2.1(f). The leading order contributes a binding energy fraction of $\alpha^2 r_N^2/\lambda\!\!\!^{-2}_{\mathrm{C}} \sim 10^{-10}$ for hydrogen, and $\sim 10^{-9}$ for deuterium. Higher orders involve an exchange of two or more photons. Interestingly, the two-photon exchange is suppressed [81], such that the next-order contribution from the three-photon exchange is larger than the lower order from the two-photon exchange. For hydrogen, the higher order finite size effects are below the overall theory uncertainty. However, for deuterium, the three-photon contribution to the finite size effect is significant.

If two or more photons are exchanged with the nucleus, an inelastic process can occur, where the nucleus gets excited[1], as illustrated in Fig. 2.1(g). This process depends on nuclear physics effects, which are summarized by the coefficient C_{pol} in Eq. (2.2). For hydrogen, the polarizability effects are negligible. However, for deuterium, the polarizability coefficient was calculated to be significant [81][2]:

$$E^{(5)}_{\mathrm{pol}}(\mathrm{D}) = hcR_\infty \frac{\delta_{l0}}{n^3} C_{\mathrm{pol}} = -21.78 \frac{\delta_{l0}}{n^3} h\,\mathrm{kHz} \pm 1\%, \tag{2.12}$$

which is for the ground state on the order of $\sim 10^{-11}$ of the binding energy. Therefore, precision spectroscopy of electronic deuterium at this level of accuracy is sensitive to nuclear excitations.

Let us now consider the case of determining the constants R_∞ and r_N from the combination of the $1\mathrm{S}_{1/2}$-$2\mathrm{S}_{1/2}$ and $2\mathrm{S}_{1/2}$-$6\mathrm{P}_{1/2}$ transition frequency measurements in hydrogen or deuterium, with the experimental values $\nu^{\text{1S-2S}}_{\mathrm{exp}}$ and $\nu^{\text{2S-6P}}_{\mathrm{exp}}$, respectively. We then have a system of two equations:

$$\nu^{\text{1S-2S}}_{\mathrm{exp}} = cR_\infty \left(A - \frac{7}{8} C_{\mathrm{NS}}\, r_N^2 \right), \quad \nu^{\text{2S-6P}}_{\mathrm{exp}} = cR_\infty \left(B - \frac{1}{8} C_{\mathrm{NS}}\, r_N^2 \right), \tag{2.13}$$

where the right-hand side is the theory prediction for the energy differences, with the constants

[1] Examples of these processes are $p \to n + \pi^+ \to p$ or $p \to \Delta \to p$.

[2] We follow the notation of [81], where the subscript (5) denotes the order in α including the factor α^2 from the Rydberg constant. The lowest order for polarizability is with a two-photon exchange, with a contribution proportional to $\alpha^2 \times \alpha^3 = \alpha^5$.

A and B for hydrogen or deuterium given by:

$$A(\mathrm{H}) = 0.749\,598\,747\,888\,87(80), \quad B(\mathrm{H}) = 0.222\,104\,887\,328\,38(10), \tag{2.14}$$

$$A(\mathrm{D}) = 0.749\,802\,708\,922\,81(78), \quad B(\mathrm{D}) = 0.222\,165\,321\,553\,87(10). \tag{2.15}$$

For the above numerical values, the values for the constants α and m_e/m_p or m_d/m_p have been used from [8] (other constants do not enter with significant accuracy). The uncertainty contribution from these constants is negligible, such that the uncertainty in the above values solely originates from the theory.

The equation system Eq. (2.13) gives the following solutions for R_∞ and r_N:

$$cR_\infty = \frac{\nu_{\mathrm{exp}}^{\mathrm{1S\text{-}2S}} - 7\nu_{\mathrm{exp}}^{\mathrm{2S\text{-}6P}}}{A - 7B}, \quad r_N = 2\sqrt{\frac{2}{C_{\mathrm{NS}}}}\sqrt{\frac{B\,\nu_{\mathrm{exp}}^{\mathrm{1S\text{-}2S}} - A\,\nu_{\mathrm{exp}}^{\mathrm{2S\text{-}6P}}}{\nu_{\mathrm{exp}}^{\mathrm{1S\text{-}2S}} - 7\,\nu_{\mathrm{exp}}^{\mathrm{2S\text{-}6P}}}}. \tag{2.16}$$

With the above expressions, we can derive the uncertainty on the constants, δR_∞ and δr_N, from the uncertainties on the measured transition frequencies, $\delta\nu_{\mathrm{exp}}^{\mathrm{1S\text{-}2S}}$ and $\delta\nu_{\mathrm{exp}}^{\mathrm{2S\text{-}6P}}$. Since the 1S-2S frequency is measured most accuratly, we assume its uncertainty to be negligible compared to the uncertainty of the 2S-6P transition frequency measurement. Therefore, only the derivatives $\partial R_\infty/\partial\nu_{\mathrm{exp}}^{\mathrm{2S\text{-}6P}}$ and $\partial r_N/\partial\nu_{\mathrm{exp}}^{\mathrm{2S\text{-}6P}}$ need to be evaluated, which yields:

$$\delta R_\infty \simeq \frac{1}{1-7/n^2}\,\frac{7\,\delta\nu_{\mathrm{exp}}^{\mathrm{2S\text{-}nP}}}{c}, \quad \delta r_N \simeq \frac{1}{1-7/n^2}\,\frac{3\,\delta\nu_{\mathrm{exp}}^{\mathrm{2S\text{-}nP}}}{C_{\mathrm{NS}}\,cR_\infty\,r_N}, \tag{2.17}$$

where we derived the general result for the 2S-nP or 2S-nD transitions[1]. Measuring transitions with higher n improves the uncertainty on the Rydberg constant and the proton radius for the same uncertainty in the measured transition frequency, but already for $n = 6$, the prefactor in the above equations for δR_∞ and δr_N is 1.24, which is close to the lowest possible value of 1. Currently, the uncertainty of the recommended value for the Rydberg constant is $\delta R_\infty = 0.000\,021\,\mathrm{m}^{-1}$. From the above equation we find that measuring the 2S-6P transition to $\delta\nu_{\mathrm{exp}}^{\mathrm{2S\text{-}6P}} < 0.7\,\mathrm{kHz}$ corresponds to the uncertainty in the Rydberg constant below this value. The uncertainty on the deuteron radius from muonic deuterium is $\delta r_d = 0.000\,78\,\mathrm{fm}$, which corresponds to measuring the 2S-6P transition to approximately the same accuracy of $\delta\nu_{\mathrm{exp}}^{\mathrm{2S\text{-}6P}} \sim 0.7\,\mathrm{kHz}$. The average of all previous electronic deuterium measurements [72] gives the uncertainty in the deuteron radius of $\delta r_d = 0.0025\,\mathrm{fm}$, which corresponds to $\delta\nu_{\mathrm{exp}}^{\mathrm{2S\text{-}6P}} \sim 2.3\,\mathrm{kHz}$.

[1] For this general result, we simply need to plug in $A \simeq 3/4$ and $B \simeq 1/2^2 - 1/n^2$ into the evaluation of the derivatives $\partial R_\infty/\partial\nu_{\mathrm{exp}}^{\mathrm{2S\text{-}6P}}$ and $\partial r_N/\partial\nu_{\mathrm{exp}}^{\mathrm{2S\text{-}6P}}$: note that Eq. (2.13) remains valid for 2S-nP and 2S-nD transitions (but with a different B) because of zero nuclear size effect of P and D levels. For example, evalutating the formula for $n = 8$ with $\nu_{\mathrm{exp}}^{\mathrm{2S\text{-}nP/D}} = 2.0\,\mathrm{kHz}$ in hydrogen yields $\delta r_p = 0.0051\,\mathrm{fm}$ and $\delta R_\infty = 0.000\,052\,\mathrm{m}^{-1}$ which agrees with the values in the recent 2S-8D measurement in hydrogen [16]. For the 1S-2S measurement combined with 1S-nS or 2S-nS measurement, the right equation of Eq. (2.13) is different, such that the prefactor for δR_∞ and δr_N becomes $1/(1-7/n^2+6/n^3)$, e.g. for 1S-2S with 1S-3S the factor is 2.25, such that the 1S-3S transition needs to be measured two times more accurate than the 2S-6P transition to reach the same sensitivity to R_∞ and r_N.

2.2 2S-nP transitions in hydrogen and deuterium

Here, only a concise summary of the properties of the 2S-nP transitions in hydrogen and deuterium is given, with a focus on the comparison between hydrogen and deuterium. For details on various topics which are identical between hydrogen and deuterium, see Chapter 2 of [71].

2.2.1 General properties

The 2S-nP transitions in hydrogen and deuterium are dipole-allowed one-photon transitions between the metastable 2S level (lifetime of 121.5 ms) and the short-lived nP level (e.g. for 6P state the lifetime is 41 ns) at the transition wavelengths between 365 nm ($n = \infty$) and 656 nm ($n = 3$). The transitions have a low saturation intensity and thus a small ac-Stark shift[1]. Combined with the 1S-2S transition frequency measurement, the sensitivity to the Rydberg constant and nuclear radius determinations increases with measuring higher 2S-nP transitions, as has been discussed in Eq. (2.17). Furthermore, the natural linewidth Γ_{nP} decreases with higher n states as $\Gamma_{\mathrm{nP}} \propto n^{-3}$, which is attributed to the n^{-3}-scaling of the transition probability from the nP state to the lower states, see Sec. 63 in [112]. However, the sensitivity to stray electric fields (quadratic dc-Stark shift for very weak electric fields) scales as n^7, such that, depending on the residual electric fields in the detection region, higher n states are more challenging to measure accurately. This scaling can be explained as following: according to second-order perturbation theroy, the quadratic dc-Stark shift (for very weak electric fields) is proportional to μ^2/ϵ, where μ is the dipole moment and ϵ the energy separation betweeen the energy levels, which are mixed through the electric field (see for instance problem 7.12 in [127]). For the $2\mathrm{S}_{1/2}$-$n\mathrm{P}_{1/2}$ transitions, the dc-Stark shift mainly originates from the $n\mathrm{P}_{1/2}$ state perturbing the $n\mathrm{S}_{1/2}$ state or vice versa. The dipole moment between $n\mathrm{P}_{1/2}$ and $n\mathrm{S}_{1/2}$ levels scales as $\mu \propto n^2$ (see Eq. (63.5) in [112]), whereas the energy separation between these states (lowest order Lamb shift) scales as $\epsilon \propto n^{-3}$ (see Eq. (21.3) in [112]), resulting in the n^7-scaling of the dc-Stark shift (see also discussion below Eq. (55.8) in [112], as well as for our case Sec. 2.4. of [71]). For the 2S-6P transition measurement, an accurate control and measurement of stray electric fields is necessary, as discussed in Section 3.5.

For $n < 10$, the natural linewidth of the 2S-nP transitions Γ_{nP} lies in the MHz range, e.g. $\Gamma_{4\mathrm{P}} \sim 13\,\mathrm{MHz}$, $\Gamma_{6\mathrm{P}} \sim 4\,\mathrm{MHz}$, $\Gamma_{9\mathrm{P}} \sim 1\,\mathrm{MHz}$. As we derived from Eq. (2.17), the transitions need to be measured with the accuracy in the kHz range in order to determine R_∞ and r_N with a low enough uncertainty, which corresponds to determining the resonance line center to $\sim 10^{-4}\,\Gamma_{\mathrm{nP}}$. This requires to study various possible effects which shift and/or distort the resonance, as for instance the Doppler shift, quantum inferference or the light force shift.

The level schemes (including the hyperfine structure) for preparing the 2S state and probing the 2S-nP transitions with our apparatus are compared between hydrogen and deuterium in Fig. 2.2. In contrast to hydrogen with a nuclear spin number of $I = 1/2$, deuterium has a nuclear spin number of $I = 1$, which leads to a different hyperfine level structure. The transitions for the preparation of the 2S state are shown in pink, whereas the probed 2S-nP transitions are shown in blue. The excitation takes place with linearly polarized light,

[1] The ac-Stark coefficient for the 2S-6P transition is on the order of $10^{-4}\,\mathrm{Hz}/(\mathrm{W/m^2})$ [71], such that an average intensity of $I_{\text{2S-6P}} \sim P_{\text{2S-6P}}/(\pi W_0^2) \sim 2\,\mathrm{W/m^2}$ (with our laser beam parameters $P_{\text{2S-6P}} = 30\,\mu\mathrm{W}$ and $W_0 = 2.2\,\mathrm{mm}$) results in an ac-Stark shift below 1 mHz.

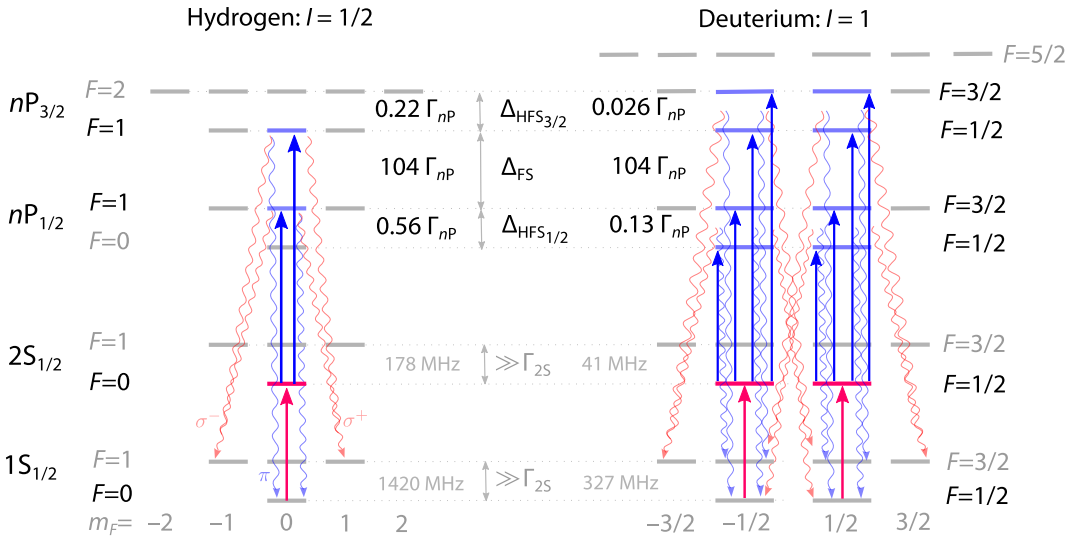

Figure 2.2: Level scheme for probing the 2S-nP transitions in hydrogen in deuterium. The preparation of the 2S initial states is shown in pink. While in hydrogen there is only one initial $2S_{1/2}$ state, in deuterium a superposition of two initial $2S_{1/2}, m_F = \pm 1/2$ states is prepared. The excited 2S-nP transitions with linear polarization along the quantization axis (π transitions) are depicted in blue: while the selection rules in hydrogen forbid the transition to the F=0 level, the analogous transitions to the F=1/2 levels are allowed in deuterium. The Lyman series decays to the ground state from the nP levels are shown in red ($\sigma^{\pm}$ channels) and blue (π channels). Note that the separation between the states is not to scale: nP hyperfine states are not resolved ($\Delta_{\mathrm{HFS}} \ll \Gamma_{nP}$) whereas the nP fine structure states are largely separated ($\Delta_{\mathrm{FS}} \gg \Gamma_{nP}$).

which drives the π transitions. Curved arrows represent the different decay channels from the excited nP states manifold to the 1S ground states ($\sigma^{\pm}$ decays in red and π decays in blue).

For hydrogen, starting from the $1S_{1/2}^{F=0}$ ground state, only the single m_F=0 initial state is present, from which the two-photon transition to the $2S_{1/2}^{F=0}$ level at 243 nm wavelength can be excited. Since the hyperfine splitting of the 1S and 2S levels is much larger than the linewidth Γ_{2S} of the 1S-2S transition[1] and the hyperfine splitting of the 2S state manifold ($\sim$0.2 GHz) is much smaller than the hyperfine splitting of the 1S state manifold ($\sim$1.4 GHz), the $F = 1$ states are unaffected by the excitation laser. Probing the one-photon transitions $2S_{1/2}^{F=0} \rightarrow nP_{1/2}^{F=1}$ and $2S_{1/2}^{F=0} \rightarrow nP_{3/2}^{F=1}$ is also achieved without exciting any other levels since the F=0 $\rightarrow$ F=0 and F=0 $\rightarrow$ F=2 transitions are forbidden by selection rules due to angular momentum conservation [127]. Therefore, only the quantum interference between the resolved fine-structure components $nP_{1/2}^{F=1}$ and $nP_{3/2}^{F=1}$ separated by $\Delta_{\mathrm{FS}} \simeq 104\,\Gamma_{\mathrm{nP}}$ is present. This resolved quantum interference was thoroughly studied in the 2S-4P transition measurement in hydrogen [14, 71]. Effects from the residual circularly polarized light of the linear excitation polarization do not lead to other systematic line shifts except the Zeeman shift, which can be estimated from the upper limits on the circularly polarized light fraction and the magnetic field in the interaction region [14, 71].

To probe the analogous transitions in deuterium, one has to consider the simultaneous excitation of hyperfine transitions. In constrast to hydrogen, two $m_F = \pm 1/2$ initial states

[1] In our apparatus, the observed linewidth is $\Gamma_{2S} \sim 4$ kHz, which is much larger than the natural linewidth of 1.3 Hz due to the broadening caused by the ac-Stark shift and the second-order Doppler shift.

are prepared. The two unresolved hyperfine nP levels, separated[1] by $\Delta_{\mathrm{HFS}_{1/2}} \simeq 0.13\,\Gamma_{\mathrm{nP}}$ and $\Delta_{\mathrm{HFS}_{3/2}} \simeq 0.026\,\Gamma_{\mathrm{nP}}$, are excited simultaneously because in contrast to the analogous case in hydrogen, the $F = 1/2 \to F = 1/2$ transitions are allowed since they do not violate angular momentum conservation [127]. Furthermore, probing the 2S-nP transitions in deuterium requires careful investigation of the unresolved quantum interference between the two hyperfine state manifolds. Examination of these effects requires to consider the initial state population asymmetry, the circularly polarized light fraction of the imperfect linearly polarized excitation light, and the polarization sensitivity of the detector. In the next section all these three imperfections are defined through normalized dimensionless quantities with values ranging from -1 to $+1$, but typically around zero.

Table 2.4 and Table 2.5 summarize and compare the atomic properties of the 2S-6P$_{1/2}$ and 2S-6P$_{3/2}$ transitions in hydrogen in deuterium, respectively. The unperturbed transition frequency $\nu_{A,0}$ is calculated from the QED prediction of the hyperfine centroid $\nu_{\mathrm{A},0}^{\mathrm{HFS\,centr.}}$ based on [8] discussed in the previous section (see Table 2.3), in combination with the hyperfine splittings for the 2S and 6P states from [116], which are added to or substracted from the hyperfine centroid transition frequency with a fraction according to the multiplicity of the corresponding states. For the $2\mathrm{S}_{1/2}^{F=0} \to 6\mathrm{P}_{1/2}^{F=1}$ transition in hydrogen, we find:

$$\nu_{\mathrm{A},0}(\mathrm{H},2\mathrm{S}_{1/2}^{F=0} \to 6\mathrm{P}_{1/2}^{F=1}) = \nu_{\mathrm{A},0}^{\mathrm{HFS\,centr.}} + \frac{3}{4} \times \Delta_{\mathrm{HFS,2S}} + \frac{1}{4} \times \Delta_{\mathrm{HFS}_{1/2}} + \Delta\nu_{\mathrm{HFS}}^{\mathrm{o.\text{-}d.}}, \tag{2.18}$$

where $\nu_{\mathrm{A},0}^{\mathrm{HFS\,centr.}} = 730\,689\,977\,771\,255\,\mathrm{Hz}$ is the hyperfine centroid from Table 2.3, and

$$\Delta_{\mathrm{HFS,2S}} = 177\,556\,838.2(3)\,\mathrm{Hz}, \quad \Delta_{\mathrm{HFS}_{1/2}} = 2\,191\,470(22)\,\mathrm{Hz} \tag{2.19}$$

are the hyperfine splittings of the $2\mathrm{S}_{1/2}$ and $6\mathrm{P}_{1/2}$ states in hydrogen [116], respectively. Note that small off-diagonal hyperfine structure shift $\Delta\nu_{\mathrm{HFS}}^{\mathrm{o.\text{-}d.}}$ needs to be taken into account for the calculation of the specific hyperfine transitions, as first calculated in [118]. This shift is zero for the S states, and is given by the following expression for the $n\mathrm{P}_j^{F=1}$ states [118, 116, 115]:

$$\Delta\nu_{\mathrm{HFS}}^{\mathrm{o.\text{-}d.}} \simeq (j-1)\frac{2\,\alpha^2 c R_\infty}{9\,n^3}\left(\frac{\mu_p}{\mu_\mathrm{B}}\right)^2 C_{\langle IL\rangle}^2, \tag{2.20}$$

where $\mu_p/\mu_\mathrm{B} \simeq 1.521\times10^{-3}$ is the ratio of the proton magnetic moment to the Bohr magneton [8], and $C_{\langle IL\rangle}^2 = 2/9$ is a constant arising from the matrix elements (see Eq. (16) in [118]). The frequency of the $2\mathrm{S}_{1/2}^{F=1/2} \to 6\mathrm{P}_{1/2}^{F=1/2}$ transition in deuterium is given by:

$$\nu_{\mathrm{A},0}(\mathrm{D},2\mathrm{S}_{1/2}^{F=1/2} \to 6\mathrm{P}_{1/2}^{F=1/2}) = \nu_{\mathrm{A},0}^{\mathrm{HFS\,centr.}} + \frac{4}{6} \times \Delta_{\mathrm{HFS,2S}} - \frac{4}{6} \times \Delta_{\mathrm{HFS}_{1/2}} + \Delta\nu_{\mathrm{HFS}}^{\mathrm{o.\text{-}d.}}, \tag{2.21}$$

where $\nu_{\mathrm{A},0}^{\mathrm{HFS\,centr.}} = 730\,888\,796\,074\,559\,\mathrm{Hz}$ is the hyperfine centroid from Table 2.3, and

$$\Delta_{\mathrm{HFS,2S}} = 40\,924\,454(7)\,\mathrm{Hz}, \quad \Delta_{\mathrm{HFS}_{1/2}} = 504\,942(5)\,\mathrm{Hz} \tag{2.22}$$

are the hyperfine splittings of the $2\mathrm{S}_{1/2}$ and $6\mathrm{P}_{1/2}$ states in deuterium [116], respectively. Following [118], the off-diagonal hyperfine structure shift $\Delta\nu_{\mathrm{HFS}}^{\mathrm{o.\text{-}d.}}$ is calculated similar to Eq. (2.20)

[1] Note that the small hyperfine corrections, namely the off-diagonal hyperfine structure shift $\Delta\nu_{\mathrm{HFS}}^{\mathrm{o.\text{-}d.}}$ and (for 6P$_{3/2}$ levels) the electric quadrupole hyperfine shift $\Delta\nu_{\mathrm{HFS}}^{\mathrm{quad}}$, are not taken into account in the level scheme of Fig. 2.2 and the corresponding definition of hyperfine splittings, but included in the calculated transition frequencies $\nu_{\mathrm{A},0}$ in Table 2.4 and Table 2.5.

	Hydrogen	Deuterium	
Transition	$2S_{1/2}^{F=0} \to 6P_{1/2}^{F=1}$	$2S_{1/2}^{F=1/2} \to 6P_{1/2}^{F=1/2}$	$2S_{1/2}^{F=1/2} \to 6P_{1/2}^{F=3/2}$
Transition freq. $\nu_{A,0}$ (kHz)	730 690 111 486.7	730 888 823 020.9	730 888 823 525.8
$6P_{1/2}$ HFS splitting $\Delta_{HFS_{1/2}}$ (Hz)	2 191 470	504 942	
Off-diag. HFS shift $\Delta\nu_{HFS}^{o.-d.}$ (Hz)	−92	−9	−22
Quadrupole HFS shift $\Delta\nu_{HFS}^{quad}$ (Hz)	0	0	0
Dipole moment μ ($e\,a_0$)	$-\frac{9}{512}\sqrt{105}$	$\frac{3}{512}\sqrt{105}$	$-\sqrt{8}\times\frac{3}{512}\sqrt{105}$
eff. value: $\mathrm{sgn}(d_1 d_2)\sqrt{d_1^2+d_2^2}$		$-\frac{9}{512}\sqrt{105}$	
Dipole moment μ (10^{-30} C m)	−1.527 140	0.509 046	−1.439 801
effective value		1.527 140	
Rabi freq. Ω_0 (rad/s $(\mathrm{W/m^2})^{-1/2}$)	$2\pi \times 63\,263.5$	$2\pi \times 21\,087.8$	$2\pi \times 59\,645.4$
effective value		$2\pi\times$ 63 263.5	
Natural linewidth Γ_{6P} (Hz)	3 894 977	3 898 157	3 898 157
Decay rates (dcy/s):			
$\gamma_{e\text{-}2S}$ (to 2S manifold)	$2\pi \times 461\,496$	$2\pi\times$ 454 814	$2\pi\times$ 454 814
γ_{ei} (to initial state(s))	$2\pi \times 153\,471$	$2\pi\times$(16 845+33 690)	$2\pi\times$ (134 760+67 379)
effective value		$2\pi\times$(121 658+63 636)	
$\Gamma_{e\text{-}1S}$ (to 1S manifold)	$2\pi \times 3\,433\,481$	$2\pi\times$ 3 443 342	$2\pi\times$ 3 443 343
Γ_{det} (detected Ly-ϵ)	$2\pi \times 3\,136\,549$	$2\pi\times$ 3 139 110	$2\pi\times$ 3 139 110
Mass of the atom (kg)	1.673533×10^{-27}	3.344495×10^{-27}	
Reduced electron mass (kg)	9.104426×10^{-31}	9.106902×10^{-31}	
Recoil shift $\Delta\nu_{rec}$ (Hz)	1 176 026	588 785	
Recoil velocity v_{rec} (m/s)	0.965016	0.483 010	

Table 2.4: Atomic properties of the $2S_{1/2}$-$6P_{1/2}$ transitions in hydrogen and deuterium. The transitions are assumed to be driven with linearly polarized light as shown in the corresponding level scheme of Fig. 2.2. The values for the transition frequencies $\nu_{A,0}$ are calculated from the hyperfine centroids given in Table 2.3 (based on [8]) in combination with the hyperfine structure (HFS) splittings $\Delta_{HFS_{1/2}}$ and small off-diagonal hyperfine structure shifts $\Delta\nu_{HFS}^{o.-d.}$ following [116]. The electric quadrupole hyperfine structure shift $\Delta\nu_{HFS}^{quad}$ vanishes for hydrogen (since the proton does not have any quadrupole moment), and is also zero for the $j = 1/2$ states in deuterium [117]. The calculations of required matrix elements are based on [128, 129] using non-relativistic quantum mechanics. Note that the written precision of numbers exceeds the available and required accuracy, but is given for possible future comparison of simulations.

by replacing μ_p/μ_B by the ratio $\mu_d/\mu_B \simeq 4.67 \times 10^{-4}$ of the deuteron magnetic moment to the Bohr magneton [8]. For the $nP_j^{F=1/2}$ levels, $C_{\langle IL\rangle}^2 = 2/9$ (same as in hydrogen), and for the $nP_j^{F=3/2}$ levels, $C_{\langle IL\rangle}^2 = 5/9$. Compared to hydrogen, this shift is around an order of magnitude smaller due to the smaller magnetic moment of the nucleus.

The 2S-$6P_{3/2}$ can be calculated in a similar way, or from 2S-$6P_{1/2}$ transitions together with the fine-structure splitting Δ_{FS}. However, for the 2S-$6P_{3/2}$ transitions in deuterium, the electric quadrupole hyperfine structure shift $\Delta\nu_{HFS}^{quad}$ (evaluated from Eq. (1) of [117], which follows the derivation in [128]) has to be taken into account in the calculation of $\nu_{A,0}$ (for hydrogen this shift vanishes due to the zero quadrupole moment of the nucleus, and for $j = 1/2$ this shift vanishes even in the presence of the quadrupole moment [117]).

The transition frequencies $\nu_{A,0}$ differ between hydrogen and deuterium approximately by $\sim 199\,\mathrm{GHz}$. In leading order this difference is determined by a larger reduced electron

	Hydrogen	Deuterium	
Fine-structure splitting Δ_{FS} (Hz)	405 164 408	406 034 692	
Transition	$2S_{1/2}^{F=0} \to 6P_{3/2}^{F=1}$	$2S_{1/2}^{F=1/2} \to 6P_{3/2}^{F=1/2}$	$2S_{1/2}^{F=1/2} \to 6P_{3/2}^{F=3/2}$
Transition freq. $\nu_{\mathrm{A},0}$ (kHz)	730 690 516 651.3	730 889 229 561.0	730 889 229 660.1
$6P_{3/2}$ HFS splitting $\Delta_{\mathrm{HFS}_{3/2}}$ (Hz)	875 992	99 983	
Off-diag. HFS shift $\Delta\nu_{\mathrm{HFS}}^{\mathrm{o.-d.}}$ (Hz)	92	9	22
Quadrupole HFS shift $\Delta\nu_{\mathrm{HFS}}^{\mathrm{quad}}$ (Hz)	0	519	−415
Dipole moment ($e\,a_0$)	$\sqrt{2} \times \frac{9}{512}\sqrt{105}$	$-\sqrt{8} \times \frac{3}{512}\sqrt{105}$	$\sqrt{10} \times \frac{3}{512}\sqrt{105}$
eff. value: $\mathrm{sgn}(d_1 d_2)\sqrt{d_1^2 + d_2^2}$		$\sqrt{2} \times \frac{9}{512}\sqrt{105}$	
Dipole moment (10^{-30} C m)	2.159 701	−1.439 801	1.609 746
effective value		2.159 701	
Rabi freq. Ω_0			
(rad/s $(\mathrm{W/m^2})^{-1/2}$)	$2\pi \times 89\,468.1$	$2\pi \times 59\,645.4$	$2\pi \times 66\,685.5$
effective value		$2\pi\times$ 89 468.1	
Natural linewidth Γ_{6P} (Hz)	3 894 983	3 898 162	3 898 162
Decay rates (dcy/s):			
$\gamma_{\text{e-2S}}$ (to 2S manifold)	$2\pi \times 461\,497$	$2\pi\times$ 454 815	$2\pi\times$ 454 815
γ_{ei} (to initial state(s))	$2\pi \times 306\,073$	$2\pi\times$ (134 760+269 520)	$2\pi\times$ (168 450+84 225)
effective value		$2\pi\times$(153 477+166 578)	
$\Gamma_{\text{e-1S}}$ (to 1S manifold)	$2\pi \times 3\,433\,486$	$2\pi\times$ 3 443 347	$2\pi\times$ 3 443 347
Γ_{det} (detected Ly-ϵ)	$2\pi \times 3\,136\,552$	$2\pi\times$ 3 139 112	$2\pi\times$ 3 139 111
Mass of the atom (kg)	1.673533×10^{-27}	3.344495×10^{-27}	
Recoil shift $\Delta\nu_{\mathrm{rec}}$ (Hz)	1 176 027	588 786	
Recoil velocity v_{rec} (m/s)	0.965016	0.483 010	

Table 2.5: Similar to Table 2.4, here showing the atomic properties of the 2S-$6P_{3/2}$ transitions in hydrogen and deuterium. The transition frequencies differ from the 2S-$6P_{1/2}$ transitions in Table 2.4 by the fine-structure splitting Δ_{FS} as defined in Fig. 2.2, as well as by the small off-diagonal hyperfine structure shift $\Delta\nu_{\mathrm{HFS}}^{\mathrm{o.-d.}}$ and (for deuterium) the electric quadrupole hyperfine structure shift $\Delta\nu_{\mathrm{HFS}}^{\mathrm{quad}}$, which does not vanish for the $j = 3/2$ states in deuterium and has been evaluated following [117].

mass of factor 2.7×10^{-4}, as has been discussed in the previous section. For deuterium, the two hyperfine transitions (separated by the hyperfine splitting) are tabulated separately and effective values for modeling the two hyperfine transitions as a single transition are given for the dipole moments and the decay rates.

Note that the given precision for the numbers in Table 2.4 and Table 2.5 exceeds the available and required accuracy, but is given here for comparisons of underlying simulations. The uncertainty on the prediction of the transition frequencies in discussed in Table 2.3. The hyperfine splittings are known with an uncertainty below 10 Hz [116]. The uncertainty on the decay rates and the natural linewidths is more difficult to estimate. Here, the decay rates are calculated within the dipole approximation from the Einstein coefficients

$$\gamma_{21} \equiv A_{21} = \frac{4\alpha\omega_{12}^3}{3e^2c^2}|\mu_{12}|^2, \tag{2.23}$$

where α is the fine-structure constant, e is the elementary charge, c is the speed of light, ω_{12} is the angular transition frequency between the two levels under consideration and μ_{12} the dipole moment of the corresponding transition [130]. The transition frequencies ω_{12} are obtained for each pair of corresponding levels from the energies based on QED calculations as for instance

compiled in [116]. The relative uncertainty on the decay rates is estimated to be few parts in 10^{-5} (e.g. around 100 Hz for the total decay rate), mainly due to relativistic corrections to the dipole moments, whereas electric quadrupole and magnetic dipole transitions should have a smaller effect for the case of 6P levels[1]. An example of relativistic calculations of transition probabilities is presented in [131].

After the transition frequencies, the hyperfine splittings as well as off-diagonal and electric quadrupole hyperfine shifts, Table 2.4 and Table 2.5 list the absolute values of the transition dipole moment $\mu \equiv |\vec{\mu}|$, which are calculated from the matrix elements using the angular and radial parts of the wavefunction for the corresponding states [128, 129]. Note that this calculation uses non-relativistic quantum mechanics, such that the values are accurate only up to relativistic effects. The given numbers are calculated for the level scheme from Fig. 2.2, i.e. for the corresponding π transitions driven by linearly polarized light. For deuterium, we give the effective value calculated from the quadrature sum of the values for the two hyperfine transitions. This effective value is exactly the same as for hydrogen, as expected: if we consider the two hyperfine transitions effectively as a single transition, we neglect the hyperfine structure arising from nuclear spin, such that the properties of hydrogen and deuterium must be the same (up to the difference in the reduced electron mass which does not enter here).

Using the transition dipole moments, we can calculate the Rabi frequency $\Omega = \vec{\mu} \cdot \vec{E}/\hbar$, which quantifies the coupling between the incoming field $\vec{E}$ and the atomic dipole on resonance. If we assume the polarization of the incoming field to be aligned with the driven dipole transition, we can relate the Rabi frequency to the absolute value of the dipole moment μ and the intensity I of the exciting light field as [127]:

$$\Omega = \frac{\mu|\vec{E}|}{\hbar} = \frac{\mu}{\hbar}\sqrt{\frac{2I}{c\,\epsilon_0}} \equiv \Omega_0 \times \sqrt{I}, \tag{2.24}$$

where c is the speed of light and ϵ_0 is the permittivity of free space. In the above equation we defined the intensity-normalized Rabi frequency Ω_0, which is listed in Table 2.4 and Table 2.5. In the low excitation regime, the number of excited atoms on resonance is proportional to Ω^2 and thus scales linearly with the intensity [127].

Next, Table 2.4 and Table 2.5 list the decay rates. The total decay rate yields[2] the natural linewidth of the transition $\Gamma_{6\mathrm{P}}$, and is composed of the decay rate $\gamma_{\text{e-2S}}$ to the 2S manifold and the decay rate $\Gamma_{\text{e-1S}}$ to the 1S manifold: $\Gamma_{6\mathrm{P}} = \gamma_{\text{e-2S}} + \Gamma_{\text{e-1S}}$.

A fraction of the decay rate $\gamma_{\text{e-2S}}$ is responsible for the decay back to the initial state(s), which we denote as γ_{ei}. For hydrogen, γ_{ei} is the decay rate back to the $2\mathrm{S}_{1/2}^{F=0}$ state, which is the only initial state. For deuterium, there are two $m_F = \pm 1/2$ initial states in the $2\mathrm{S}_{1/2}^{F=1/2}$ manifold. Therefore, γ_{ei} is a sum of the π decay to the same m_F state and the σ decay to the other m_F state. The back decay to the initial states is particularly important to analyze the light force shift discussed in Section 2.6, see Fig. 2.18 and Table 2.6. Weighted with the squared dipole moments of the two hyperfine transitions, $d_1^2 \equiv d_{F=1/2}^2$ and $d_2^2 \equiv d_{F=3/2}^2$, we can also define an effective back decay rate, see Fig. 2.18 and Eq. (2.80). These effective values are approximately the same for hydrogen and deuterium, though slightly higher for deuterium than for hydrogen.

[1] Private communication with Savely Karshenboim.

[2] Note that whereas the decay rate is given in number of decays per second, the natural linewidth is given in Hertz, such that there is a difference of the factor 2π.

The decay rate $\Gamma_{\text{e-1S}}$ to the 1S ground state can either happen via intermediate states (decay cascade) or directly from the 6P state manifold to the 1S state manifold with an emission of a single Lyman-ϵ photon at a wavelength of 94 nm. These Lyman-ϵ decays are shown in Fig. 2.2. In our apparatus, these decays are responsible for ∼99% of the signal [71], such that the corresponding decay rate is listed separately as Γ_{det}.

Finally, Table 2.4 and Table 2.5 compares the recoil shift between hydrogen and deuterium. Due to the two times larger mass of deuterium, the recoil shift is approximately a factor of two smaller in deuterium. However, for precision spectroscopy of the 2S-nP transitions this difference is of no advantage since the recoil shift is precisely known anyway, and the frequency is precisely corrected by this value without increasing the uncertainty of the measurement. Understanding the origin of the recoil shift brings us to the discussion of the resonance condition for the interaction of light with the atom, which we consider next.

2.2.2 Resonance condition

Our goal is to measure the internal energy level difference predicted by the bound-state QED as outlined in Section 2.1, here specifically between the 6P state and the 2S state. This difference is quantified by the unperturbed transition frequency of the atom $\nu_{\text{A},0}$. However, an incoming laser beam photon with a frequency $\nu_{\text{L},0}$ carries energy and momentum, such that when the atom absorbs the photon, not only its internal electronic energy state is changed, but also the external (kinetic) energy and momentum. Evaluating the relativistic energy and momentum conservation in the case of one-photon transitions for an atom with mass m_{A}, velocity vector $\vec{v}$ in the laboratory frame (speed $v \equiv |\vec{v}|$), and the laser beam with wave vector $\vec{k}$ in the laboratory frame, yields the resonance condition [132]:

$$\nu_{\text{L},0} = \nu_{\text{A},0} \left(\frac{\sqrt{1 - v^2/c^2}}{1 - \vec{k} \cdot \vec{v}/(2\pi\nu_{\text{L},0})} \times \frac{1}{1 - \frac{h\nu_{\text{A},0}}{2m_{\text{A}}\, c^2}} \right) = \nu_{\text{A},0} \left(\frac{\sqrt{1-\beta^2}}{1 - \beta\, \cos\alpha} \times \frac{1}{1-\epsilon} \right), \tag{2.25}$$

where in the second step we defined $\beta = v/c$, $\epsilon = h\nu_{\text{A},0}/(2m_{\text{A}}c^2)$, and α as the angle between the atomic beam and the laser beam (in the laboratory frame). The above equation can be expanded as a series in β and ϵ, which gives:

$$\nu_{\text{L},0} = \nu_{\text{A},0} \left(1 + \beta\cos\alpha + \beta^2(-1/2 + \cos^2\alpha) + \mathcal{O}(\beta^3)\right) \times \left(1 + \epsilon + \epsilon^2 + \mathcal{O}(\epsilon^3)\right) \tag{2.26}$$

$$\simeq \nu_{\text{A},0} + \nu_{\text{A},0}\, \beta\cos\alpha + \nu_{\text{A},0}\, \frac{\beta^2}{2} \left(-1 + 2\cos^2\alpha\right) + \nu_{\text{A},0}\, \epsilon, \tag{2.27}$$

where in the second step we kept all terms up to second order in β and first order in ϵ, but neglected mixed terms with $\beta\epsilon$. This is justified by comparing the orders of magnitude of β and ϵ to our accuracy goal of $\sim 10^{-12}\, \nu_{\text{A},0}$: the typical velocity of atoms in our apparatus is $v \sim 200\,\text{m/s}$ which corresponds to $\beta \sim 10^{-6}$. For the 2S-6P transition frequency of $\nu_{\text{A},0} \simeq 731\,\text{THz}$ and the mass of the deuterium atom $m_{\text{A}} \simeq 3.3 \times 10^{-27}\,\text{kg}$ we find $\epsilon \sim 10^{-9}$. Therefore, terms up to $\mathcal{O}(\beta^2)$ are still on the order of interest, while terms with $\mathcal{O}(\epsilon^2)$ or $\mathcal{O}(\epsilon\,\beta)$ can safely be neglected since they lead to shifts below 1 Hz.

The leading shift of $\nu_{\text{A},0}$ relative to $\nu_{\text{L},0}$ in Eq. (2.27) is the first-order Doppler shift $\Delta\nu_{\text{D}}$:

$$\Delta\nu_{\text{D}} = \nu_{\text{A},0}\, \beta\cos\alpha = \nu_{\text{A},0} \frac{v\cos\alpha}{c} = \nu_{\text{A},0} \frac{v\sin\delta\alpha}{c} = \kappa\, v, \tag{2.28}$$

where we introduced $\delta\alpha = \alpha - 90°$ and the Doppler slope κ. Since the full collinear first-order Doppler shift is of the order $10^{-6}\,\nu_{\mathrm{A},0}$, whereas we aim for a factor of 10^6 smaller uncertainty goal, from all the effects, the first-order Doppler shift is most crucial in our apparatus. To suppress the first-order Doppler shift in our experiment, we reduce the velocity of atoms using a liquiud-helium cryostat to the typical velocity of $v \sim 200\,\mathrm{m/s}$. Furthermore, we align the angle α as good as possible to $\alpha \simeq 90°$ and use two counter-propagating beams generated in the active fiber-based retroreflector (AFR), which is treated in Chapter 4. Moreover, we always measure the Doppler slope κ with the time-resolved detection technique (see Section 3.1.1), which allows to measure the transition frequency for groups of atoms with different mean velocities v.

The second term in Eq. (2.27) is the second-order Doppler shift $\Delta\nu_{\mathrm{SOD}}$:

$$\Delta\nu_{\mathrm{SOD}} = \nu_{\mathrm{A},0}\,\beta^2\left(-\frac{1}{2} + \cos^2\alpha\right) = \nu_{\mathrm{A},0}\,\frac{\beta^2}{2}\cos 2\alpha \simeq -\frac{v^2}{2c^2}\nu_{\mathrm{A},0}, \tag{2.29}$$

where we approximated for our case of $\alpha \simeq 90°$. For $v \sim 200\,\mathrm{m/s}$, the above equation yields a shift of $\Delta\nu_{\mathrm{SOD}} \simeq -0.16\,\mathrm{kHz}$, which needs to be taken into account in the uncertainty budget.

Finally, the last term in Eq. (2.27) is identified with the recoil shift:

$$\Delta\nu_{\mathrm{rec}} = \nu_{\mathrm{A},0}\,\epsilon = \frac{h\nu_{\mathrm{A},0}^2}{2m_{\mathrm{D}}c^2}. \tag{2.30}$$

The recoil shift is known with a much better accuracy than required. In our case, the recoil shift is on the order of a MHz. As evident from the above equation, the fractional uncertainty in $\Delta\nu_{\mathrm{rec}}$ corresponds to the quadrature sum of the fractional uncertainties in m_{D} and $\nu_{\mathrm{A},0}$. Therefore, in order to determine the recoil shift to $<1\,\mathrm{Hz}$, we need to know m_{D} and $\nu_{\mathrm{A},0}$ only with a fractional uncertainty of $\sim 10^{-6}$ (h and c are exact). The mass of the deuterium atom m_{D} is composed of the deuteron mass m_d, the electron mass m_e, and the binding energy. Both m_d and m_e are known to 3×10^{-10} in kilograms, but with an order of mangitude higher accuracy in atomic units [8]. Typically, if possible, atomic masses should always be evaluated in atomic units through mass ratios, in order not to loose accuracy. However, for the evaluation of the recoil shift here, even the masses in kilograms have an uncertainty, which is low enough by several orders of magnitude. The binding energy of the deuterium atom in the 2S excited state contributes 2×10^{-9} to the total mass, and can therefore be neglected (note, however, that the constribution of the binding energy is larger than the uncertainty in $m_d + m_e$).

2.3 Imperfections important for 2S-nP transitions in deuterium

2.3.1 Initial state population asymmetry

The $1\mathrm{S}_{1/2}^{F=1/2}$ ground state in deuterium has two $m_F = \pm 1/2$ sub-levels. As shown in Fig. 2.2, we prepare two initial states for probing the 2S-nP transitions, namely the $2\mathrm{S}_{1/2}^{F=1/2}, m_F = \pm 1/2$ states. We define the population asymmetry parameter ι of these initial states $i1 \equiv 2\mathrm{S}_{1/2,m_F=-1/2}^{F=1/2}$ and $i2 \equiv 2\mathrm{S}_{1/2,m_F=+1/2}^{F=1/2}$ with corresponding populations N_{i1} and N_{i2} as:

$$\iota = \frac{N_{i2} - N_{i1}}{N_{i2} + N_{i1}}, \tag{2.31}$$

such that $\iota = \pm 1$ corresponds to the maximal population asymmetry (all the population in the $m_F = +1/2$ or $m_F = -1/2$ state), and $\iota = 0$ corresponds to no population asymmetry. As shown below in Section 2.4 and Section 2.5, the population asymmetry $\iota \neq 0$ can lead in combination with residual circular polarization or an imbalance of decay channel detection to a systematic line shift. Furthermore, even for perfectly linear polarization, the population asymmetry leads to a Zeeman shift, which we analyze in the following.

In the presence of a weak[1] magnetic field B, the energy of the state with quantum numbers l, J, F, m_F is shifted by the Zeeman energy [127]:

$$\Delta E_{\mathrm{Z}} = m_F g_F \mu_{\mathrm{B}} B, \tag{2.32}$$

where $\mu_{\mathrm{B}} = e\hbar/(2m_e) \simeq h \times 1.4\,\mathrm{MHz/G}$ is the Bohr magneton, and the Landé g_F factor is determined from the g_J factor as:

$$g_F \simeq \frac{F(F+1) + J(J+1) - I(I+1)}{2F(F+1)} g_J, \quad g_J \simeq \frac{3}{2} + \frac{S(S+1) - l(l+1)}{2J(J+1)}, \tag{2.33}$$

where $I = 1$ is the nuclear spin number for deuterium, and $S = 1/2$ is the spin number of the electron. The Zeeman splittings relevant for the 1S-2S and 2S-nP transitions in our case are visualized in Fig. 2.3.

For $l = 0, J = 1/2, F = 1/2$ we find from the above equation $g_F = -2/3$, such that the $m_F = \pm 1/2$ states of the $1\mathrm{S}_{1/2}$ and $2\mathrm{S}_{1/2}$ manifolds are separated by $\frac{2}{3}\,\mu_{\mathrm{B}} B \simeq 2\pi \times 934\,\mathrm{kHz/G}$. However, as shown in Fig. 2.3(a), the 1S-2S transition is insensitive to the magnetic field since both levels shift equally. Note that the two-photon transitions with circularly polarized light ($\sigma^{\pm}$ transitions) are forbidden by angular momentum conservation, such that residual circular polarization of the linearly polarized 1S-2S excitation light does not couple the different $m_F = 1/2$ and $m_F = -1/2$ states.

Fig. 2.3(b) shows the Zeeman splittings for the $2\mathrm{S}_{1/2}$-$n\mathrm{P}_{1/2}$ transition. The g_F factors are: $g_F = -2/9$ for the $n\mathrm{P}_{1/2}(F = 1/2)$ state and $g_F = +2/9$ for the $n\mathrm{P}_{1/2}(F = 3/2)$ state. If no asymmetry between the $m_F = \pm 1/2$ states is present ($\iota = 0$), there is no total shift of the resonance line, since the shifts for the $m_F = +1/2$ and $m_F = -1/2$ initial states compensate each other. By weighting the shift of each corresponding hyperfine transition with the squared dipole matrix elements including a population asymmetry ι between the $m_F = \pm 1/2$ inital states, we find the following shift:

$$\Delta\nu_{\iota,\mathrm{Z,2S\text{-}6P}_{1/2}} = \frac{34}{81}\frac{\mu_{\mathrm{B}} B}{h}\iota \simeq \iota \times 0.59\,\mathrm{kHz/mG}. \tag{2.34}$$

For the $2\mathrm{S}_{1/2}$-$n\mathrm{P}_{3/2}$ transition, the g_F factors of the $F = 1/2$ and $F = 3/2$ state manifolds are different in magnitude, as illustrated in Fig. 2.3(c). Similar to the above equation we find:

$$\Delta\nu_{\iota,\mathrm{Z,2S\text{-}6P}_{3/2}} = \frac{361}{405}\frac{\mu_{\mathrm{B}} B}{h}\iota \simeq \iota \times 1.25\,\mathrm{kHz/mG}. \tag{2.35}$$

In the 2S-6P interaction region, the magnetic field is below 1 mG. Therefore, for our accuracy goal, the Zeeman shift from the initial state asymmetry becomes significant only for large asymmetry $\iota > 0.1$. Such asymmetry is orders of magnitude above the expected value as shown below.

[1] The weak-field limit is valid for $\mu_{\mathrm{B}} B \ll \Delta_{\mathrm{HFS}}$, where Δ_{HFS} is the hyperfine splitting: $B \ll 70\,\mathrm{mG}$ for the $6\mathrm{P}_{3/2}$ state, $B \ll 0.4\mathrm{G}$ for $6\mathrm{P}_{1/2}$ state, $B \ll 30\mathrm{G}$ for $2S$ state and $B \ll 240\mathrm{G}$ for $1S$ state. For the 1S-2S transition we thus can use the weak-field limit even in the presence of the earth's magnetic field. For the 2S-6P transition, in our apparatus the magnetic field is compensated and shielded to below 1 mG (see Section 3.4) such that the weak-field limit is also valid.

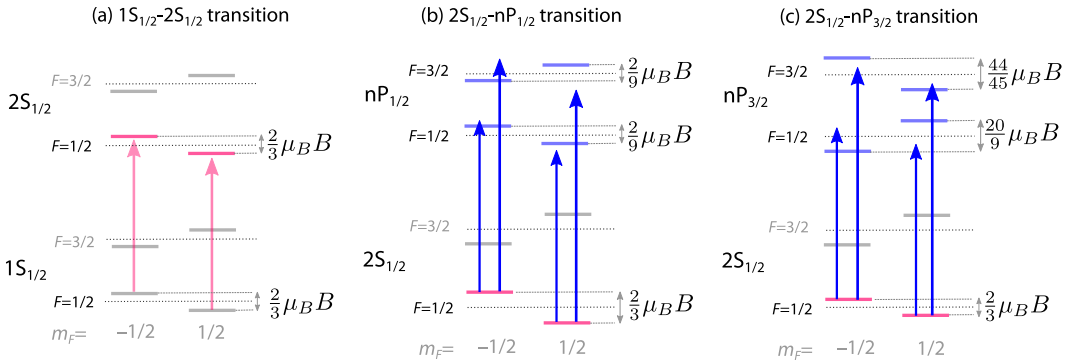

Figure 2.3: Zeeman shifts of the corresponding levels for the (a) $1S_{1/2}$-$2S_{1/2}$, (b) $2S_{1/2}$-$nP_{1/2}$ and (c) $2S_{1/2}$-$nP_{3/2}$ transitions driven with linearly polarized π light according to the scheme shown in Fig. 2.2 (the $F = 5/2$ state manifold of the $nP_{3/2}$ levels is not shown in (c) because this state manifold is not addressed). In the weak magnetic field B, the levels are shifted proportional to $\mu_B B$ according to Eq. (2.32), where μ_B is the Bohr magneton. The $1S_{1/2}$-$2S_{1/2}$ transition is unaffected, since both levels shift equally. For the $2S_{1/2}$-$6P_{1/2}$ and $2S_{1/2}$-$6P_{3/2}$ transitions there is a total Zeeman shift if there is a population asymmetry $\iota \neq 0$ in the initial $m_F = \pm 1/2$ states, see Eq. (2.34) and Eq. (2.35).

The population asymmetry could arise from some spin-polarizing effects in the nozzle during the formation of the atomic beam. However, our nozzle is symmetric, such that only the magnetic field breaks the symmetry by introducing an energy difference of $\Delta E_\iota = \frac{2}{3}\mu_B B$ in the $m_F = \pm 1/2$ initial states. Assuming a Boltzmann distribution, we can make an estimate of the population asymmetry as following:

$$\frac{N_{i1}}{N_{i2}} = \exp\left(-\frac{\Delta E_\iota}{k_B T_N}\right) \simeq 1 - \frac{2\mu_B B}{3 k_B T_N}, \tag{2.36}$$

where k_B is the Boltzmann constant and T_N is the nozzle temperature. Combining the above equation with Eq. (2.31), we find:

$$\iota \simeq \frac{\mu_B B}{3 k_B T_N} \sim 3 \times 10^{-7}, \tag{2.37}$$

where for the numerical value we used $T_N \sim 7\,\mathrm{K}$ and $B \sim 0.1\,\mathrm{G}$ (magnetic field at the nozzle). In the above estimation we assume that the atoms are thermalized in the nozzle. Though we observe some deviation from the thermalized velocity distribution of atoms (see Section 3.6.2), to the leading order the assumption of thermalized atoms is justified.

In the future, one may determine ι experimentally, which is discussed in Appendix A.4.2. Appendix A.2 discusses possible ways to generate an increased initial state asymmetry on purpose for future studies of systematic uncertainty effects associated with ι.

2.3.2 Circularly polarized light

The fraction of circularly polarized light S_3/S_0 is directly obtained from the Stokes parameters (see Appendix A.1). Here, to be more concise in some equations, we will also denote the circularly polarized fraction as s:

$$s \equiv S_3/S_0 = \frac{I_{RHC} - I_{LHC}}{I_{RHC} + I_{LHC}}, \tag{2.38}$$

where S_0 is the total intensity, and S_3 the circularly polarized intensity defined as the difference between the intensity of right- and left-handed circularly polarized light, I_{RHC} and I_{LHC}. Note that s is the only one parameter needed to describe the polarization state of a fully polarized light if one does not care about the linear polarization rotation angle.

We investigated the sources of polarization imperfections and developed a polarization monitor in the apparatus, see Section 4.6. As shown in Fig. 4.30, s is always below 10% in our setup, with typical values around $s \sim 5\%$. However, it is also possible to extract spectroscopy line scans with lower circularly polarized fraction.

Similar to the initial state asymmetry, a residual circular polarization introduces a Zeeman shift. To compute the Zeeman shift of imperfect π linearly polarized light, it is helpful to rotate the quantization basis (as shown below in Fig. 2.8), where linearly polarized light is a superposition of σ^- and σ^+ light. The excitation rate of driving the σ^- and σ^+ transitions is proportional to the intensity of left-handed (I_{RHC}) and right-handed (I_{LHC}) polarized light, whose difference is directly linked to s. Weighting the corresponding hyperfine transitions with s and the squared dipole matrix elements (see Table A.1), the following Zeeman shifts of the 2S-6P$_{1/2}$ and 2S-6P$_{3/2}$ transitions are obtained:

$$\Delta\nu_{s,\mathrm{Z,2S\text{-}6P_{1/2}}} = \frac{28}{81}\frac{\mu_{\mathrm{B}}B}{h}s \simeq s \times 0.48\,\mathrm{kHz/mG}, \tag{2.39}$$

$$\Delta\nu_{s,\mathrm{Z,2S\text{-}6P_{3/2}}} = \frac{181}{162}\frac{\mu_{\mathrm{B}}B}{h}s \simeq s \times 1.56\,\mathrm{kHz/mG}. \tag{2.40}$$

For $s < 0.1$ we obtain Zeeman shifts from residual circular polarization of below 50 Hz (2S-6P$_{1/2}$ transition) and below 160 Hz (2S-6P$_{3/2}$ transition).

The total Zeeman shift is in leading order the sum of the Zeeman shift from the population asymmetry (Eq. (2.34) and Eq. (2.35)) and the Zeeman shift from the residual circular polarization fraction above:

$$\Delta\nu_{\mathrm{Z,2S\text{-}6P_{1/2}}} = \Delta\nu_{\iota,\mathrm{Z,2S\text{-}6P_{1/2}}} + \Delta\nu_{s,\mathrm{Z,2S\text{-}6P_{1/2}}} \simeq (\iota \times 0.59\,\mathrm{kHz} + s \times 0.48\,\mathrm{kHz})/\mathrm{mG}, \tag{2.41}$$

$$\Delta\nu_{\mathrm{Z,2S\text{-}6P_{3/2}}} = \Delta\nu_{\iota,\mathrm{Z,2S\text{-}6P_{3/2}}} + \Delta\nu_{s,\mathrm{Z,2S\text{-}6P_{3/2}}} \simeq (\iota \times 1.25\,\mathrm{kHz} + s \times 0.56\,\mathrm{kHz})/\mathrm{mG}. \tag{2.42}$$

With the estimate from Eq. (2.37), we find $\iota \ll s$, such that the Zeeman shift contribution from non-zero ι can be neglected compared to the contribution from non-zero s.

Unlike in hydrogen, imperfect linear polarization does not only lead to a Zeeman shift, but may also shift the measured line center as we discuss in Section 2.4. However, this effect is suppressed by ι.

2.3.3 Detection imbalance of $\sigma^{\pm}$ and π decays

In comparison to hydrogen, much more decay channels give rise to the signal of the 2S-nP transition measurement in deuterium. The contribution of different σ^+, σ^-, and π decay channels is only symmetric if the initial states $m_F = \pm 1/2$ are equally populated. If not, a possible polarization sensitivity of the detector could lead to a systematic shift. Therefore, a possible detection imbalance of the decay channels is discussed.

To understand how the different decay channels are related to the possible polarization sensitivity of the detector, consider an atom in an excited state which can decay to three different final states via σ^+, σ^- and π decay channels, see left of Fig. 2.4. The projected value of the total atomic angular momentum m_F onto the quantization axis $\hat{z}$ does not

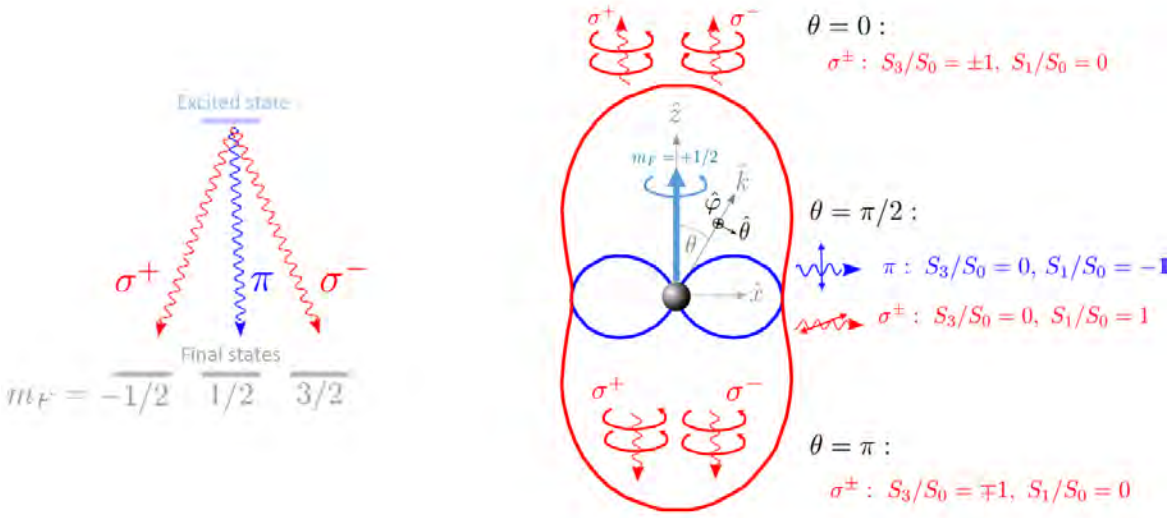

Figure 2.4: Angular distribution and polarization of emitted fluorescence light from an atom. On the left, the considered level scheme is drawn: the atom is in an excited state with projected angular momentum m_F and decays via σ^+, σ^- and π decay to three possible final states with m_F unchanged, or changed by ± 1. The specific value of m_F does not matter, as an example we choose $m_F = 1/2$ and illustrate the $\hbar/2$ unit of projected angular momentum onto the quantization axis $\hat{z}$ with a single curved arrow. Choosing spherical coordinates with azimuthal angle φ and inclination θ for the emitted light propagation vector $\hat{k}$, we can restrict the emission pattern to the $\hat{x}\hat{z}$-plane due to the symmetry of the problem. The intensity of emitted light is proportional to $1 + \cos^2\theta$ for $\sigma^\pm$ decays (red) and to $\sin^2\theta$ for the π decay (blue). The polarization of $\sigma^\pm$ light is fully right- or left-circular at the poles ($S_3/S_0 = \pm 1$) and fully horizontally polarized for $\theta = \pi/2$ ($S_1/S_0 = 1$). Light from the π decay is fully vertically polarized ($S_1/S_0 = -1$).

matter for this discussion, only the difference $\Delta m_F = \{-1, 0, +1\}$ from the excited to the three final states is relevant[1]. To be specific for the case of deuterium, consider that the atom is in the excited state with $m_F = 1/2$. With $\hat{z}$ as the quantization axis and the atom being at the origin of our coordinate system, due to the symmetry we can restrict ourselves to the $\hat{x}\hat{z}$-plane as shown on the right of Fig. 2.4, i.e. in spherical coordinates we set the azimuthal angle $\varphi = 0$. Denoting $\hat{k}$ as the direction of fluorescence light propagation, the inclination angle θ is the angle between $\hat{z}$ and $\hat{k}$. Note that in our experimental setup (see Fig. 3.1) the $\hat{z}$ axis from Fig. 2.4 does not necessarily correspond to the vertical axis of the fluorescence detector: the orientation of the $\hat{x}\hat{z}$-plane from Fig. 2.4 relative to the fluorescence detector depends on the rotation angle of the linear polarization of excitation light.

The circular polarization fractions $(S_3/S_0)_\pi$ and $(S_3/S_0)_{\sigma^\pm}$ of fluorescence light from the π and $\sigma^\pm$ decays, respectively, can be derived (see Appendix A.3) to be the following:

$$(S_3/S_0)_\pi = 0, \quad (S_3/S_0)_{\sigma^\pm} = \pm\frac{2\cos\theta}{1+\cos^2\theta}. \tag{2.43}$$

This result is illustrated on the right of Fig. 2.4: $\sigma^\pm$ decays emit left- or right-handed circular

[1] In fact, it may seem counter-intuitive why Δm_F (and not Δm_l) is responsible for the dipole emission pattern: note that the nuclear spin and the electronic spin do not have a dipole moment. However, the total angular momentum eigenstates obtain a dipole moment due to the coupling to the orbital angular momentum.

polarized light ($S_3/S_0 = \pm 1$) in the directions parallel to the quantization axis ($\theta = 0$), and linear polarization orthogonal to the quantization axis ($\theta = 90°$). As expected from angular momentum conservation, the π decay does not emit any light for $\theta = 0$ and all the light is linearly polarized. For $\theta = 90°$, linearly polarized light emitted from the π and $\sigma^{\pm}$ decays is orthogonal to each other.

The practical property of Stokes parameters is that they can simply be added[1] for superimposed light with different polarizations. Therefore, if all the decays contribute equally, all the relative Stokes parameters add up to zero for all values of θ. The total intensity is independent of θ, such that the fluorescence light is completely unpolarized everywhere and is emitted isotropically. The same is true if the sum of squared matrix elements of σ^+ and σ^- decays is twice as large as the value from the π decay. For deuterium, this is the case for the Lyman decays from the $n\mathrm{P}_{1/2}$ excited states but not from the $n\mathrm{P}_{3/2}$ excited states. Note also that in particular cases, the coherences between the emitted fluorescence photons should be taken into account. For example, if the π fluorescence is described in the different quantization basis, it corresponds to the coherent superposition of σ^+ and σ^- light, which, due to interference, leads to the same emission pattern as the π fluorescence. In the above consideration, we assume no coherence between the fluorescence light from the different decay channels.

One may ask whether one could ignore the polarization sensitivity of the detector, if the emitted fluorescent light is fully unpolarized everywhere. However, the possible systematic bias comes from the different detection efficiencies for individual decays. Though in total the signal from all the decay channels results in unpolarized light, the contribution from each individual decay channel consists of polarized light. One can imagine the polarization-sensitive detector as a partial polarizer: for example, a vertical linear polarizer placed at $\theta = 90°$ transmits more signal from the π decays than from $\sigma^{\pm}$ decays. If their signal lineshape is different, this could lead to a systematic shift.

In general, the detector could be polarization-sensitive in two ways: it could respond asymmetrically to the right- vs left-handed circular polarization and/or to horizontal vs vertical linear polarizations. The first case can be described in the worst case scenario of the detection imbalance of σ^+ and σ^- decays, whereas the detection imbalance of $\sigma^{\pm}$ vs π decays represents the upper limit for the second case. Defining the detection quantum efficiencies of light from σ^+, σ^-, and π decays as ξ^+, ξ^-, and ξ^π, the dimensionless sensitivities $\xi_\circ$ and $\xi_|$, can be defined as:

$$\xi_\circ = \frac{\xi^+ - \xi^-}{\xi^+ + \xi^-}, \quad \xi_| = \frac{\xi^\pm - \xi^\pi}{\xi^\pm + \xi^\pi}, \tag{2.44}$$

where in the latter case $\xi^\pm = \xi^+ = \xi^-$.

Note that since the polarization of light from $\sigma^{\pm}$ decays varies, the above definitions represent the upper limit of the polarization-sensitive detector. If more vertically than horizontally polarized light is detected, then the asymmetry in π vs $\sigma^{\pm}$ detection would be maximal for $\theta = \pi/2$, smaller for other values of θ and vanish at the poles. If we detect more right-handed circular polarized light than left-handed, we would see more signal from σ^+ decay at the north pole ($\theta = 0$), no signal difference at the equator where only linear polarized light can be emitted ($\theta = \pi/2$), and less signal from σ^+ at the south pole ($\theta = \pi$) so that the opposite contribution from the poles would add to zero leading to an unbiased result on average. In

[1] Relative Stokes parameters must be weighted with corresponding intensities and normalized afterwards [133].

general, the polarization sensitivity of the detector can be complicated and depend on the angle θ.

In our apparatus, the detector is built of aluminum, which quickly forms an oxidized layer [134, 135], such that the active area of detector is composed of aluminum oxide. The signal mainly originates from the photoemission of Lyman-ϵ fluorescence photons with a wavelength of 93.8 nm, which corresponds the photon energy of 13.2 eV. In the field of angle-resolved photoemission spectroscopy, it is well known that the photoelectric effect can strongly depend on the polarization of incident light producing the photoelectrons [136, 137]. On the first glance, one may think that the photoelectric effect depends only on the relative amount of s- and p-polarization of the incident light[1], but not on the handedness of light. However, studies have shown that the photocurrent can also depend on the sign of the circularly polarized fraction of light, which is referred to as the circular dichroism asymmetry [136, 137]. Unfortunately, no data on the presence or absence of circular dichroism asymmetry from photoemission on oxidized aluminum seems to be available. In some materials such an asymmetry has been reported to be as large as 24% [138], such that in our case one could make the most conservative assumption of $\xi_\circ < 0.3$. However, as shown in Section 2.5, together with the estimated asymmetry on the population of initial states, the line shift due to unresolved quantum interference is negligible even for the maximum detection imbalance of $\xi_\circ = 1$.

As discussed in Section 2.5, unresolved quantum interference vanishes for π decays, such that $\xi_|$ does not need to be considered for possible line shifts in our case. Nevertheless, for possible future considerations, here we briefly discuss a possible estimation of the upper limit on $\xi_|$, which is related to the difference in the photoemission between s- and p-polarized light. There are studies on the polarisation sensitivity of the photoemission between s- and p-polarized X-rays on oxidized aluminum with energies 65−150 eV [139, 140]. These studies show a polarization-sensitive modulation M of the photocurrent of up to $|M| \sim 25\%$. The results of [140] show that this modulation can be described by the differences in the s- and p-state Fresnel reflectivities R_s and R_p, such that $M = (R_p - R_s)/(2 - R_s - R_p)$. In our case, we may assume a refractive index of $n \sim 1.6 + \mathrm{i} \times 1.2$ based on the value for crystalline oxidized aluminum (sapphire) in [141] (similar to the value from [142]). M is then calculated depending on the incidence angle from R_p and R_s according to the Fresnel equations with the given complex refractive index. In our case, the detector is composed of two aluminum cylinders centered around the interaction region, each with a length of $l \sim 85$ mm and a radius of $r = 28$ mm (see Section 3.5). The fluorescence photons originate in the center of the detector, such that they hit the top or bottom cylinder walls with a maximum incidence angle of $90° - \arctan(r/l) \sim 70°$ w.r.t. the normal of the interface. This incidence angle yields a modulation $|M| \sim 30\%$, with smaller values for smaller incidence angles (M is zero for zero incidence angle where R_s is always equal to R_p). This value can be used as an upper limit on $\xi_|$ (interestingly, this value coincides with the upper limit on $\xi_\circ$ from the discussion above). In reality, $\xi_|$ is expected to be smaller since most fluorescence photons have smaller incidence angles, and the polarization depends on the incidence angle as shown in Appendix A.3, which can be used together with the detector geometry to obtain a lower limit on $\xi_|$. In the future, it may be possible to explore the polarization-sensitivity of our detector by generating a large initial state population asymmetry, see Appendix A.2.

[1] As shown in Appendix A.3.1, the amount of s- and p-polarization is exactly the same for σ^+ and σ^- fluorescence (see Eq. (A.18)), whereas the amount of s- and p-polarization is different between $\sigma^\pm$ and π fluorescence (compare Eq. (A.17) with Eq. (A.18)).

2.4 Simultaneous excitation of unresolved hyperfine levels

Here, we consider the simultaneous excitation of the unresolved $F = 3/2$ and $F = 1/2$ hyperfine levels for the $2S_{1/2}$-nP transitions. We neglect in this section the effects from the decay to final states, which may lead to quantum interference as discussed in Section 2.5.

2.4.1 Sum of two unresolved resonances

Consider a signal I given by the sum of two Lorentzian functions (Lorentzian doublet) with center frequencies separated by Δ_{HFS}, identical linewidths $\Gamma \ll \Delta_{\mathrm{HFS}}$, but different amplitudes D_1^2 and D_2^2:

$$I = \mathcal{L}(\nu_0, D_1, \Gamma) + \mathcal{L}(\nu_0 + \Delta_{\mathrm{HFS}}, D_2, \Gamma), \tag{2.45}$$

where the Lorentzian function $\mathcal{L}$ is defined as:

$$\mathcal{L}(\nu_0, D, \Gamma) = \frac{D^2}{(\delta - \nu_0)^2 + (\Gamma/2)^2}. \tag{2.46}$$

Fig. 2.5 illustrates the corresponding level scheme on the top. On the bottom, the total signal is plotted in red ($\mathcal{L}_1 + \mathcal{L}_2$) with individual contributions shown in blue ($\mathcal{L}_1 = \mathcal{L}(\nu_0, dD_1)$) and orange ($\mathcal{L}_2 = \mathcal{L}(\nu_0 + \Delta_{\mathrm{HFS}}, D_2)$). The parameters were chosen to be similar to the case of the deuterium $2S_{1/2}^{F=1/2}$-nP$_{1/2}$ transition with $D_1^2 = 8D_2^2$ and $\Delta_{\mathrm{HFS}} = 0.13\Gamma$.

In the following, we first discuss why using Eq. (2.45) (Lorentzian doublet fit function) for fitting the typical data with noise is only possible if both the dipole ratio D_2^2/D_1^2 and the hyperfine splitting Δ_{HFS} are known. For 2S-nP transitions the dipole ratio D_2^2/D_1^2 is subject to possible deviations. Therefore, we then discuss the single Lorentzian fit function for the description of data, which can be used even if the dipole ratio D_2^2/D_1^2 cannot be assumed to be exactly known.

For our experimental data we typically use the Voigt fit function (see Eq. (2.73)), which includes the Doppler broadening of the resonance. For the sake of clarity, here we keep the discussion to the case of the Lorentzian fit functions only. The conclusions made here are also valid for the Voigt (doublet) fit functions, though the fit deviations from Fig. 2.7 then depend on the broadening and need to be evaluated separately (see Fig. 2.14).

2.4.1.1 Lorentzian doublet fit function

Since the hyperfine splitting Δ_{HFS} is precisely known, we can consider using the Lorentzian doublet fit function with Δ_{HFS} as a fixed parameter (or a fit function which accounts for both resolved quantum interference and unresolved quantum interference with known Δ_{HFS}, e.g. Eq. 7 and Eq. 12 in [143]). However, for a typical signal with noise as in our experiment, such a fit is not reliable unless the ratio D_2^2/D_1^2 is also given as a fixed parameter. For $D_1^2/D_2^2 \ll 1$ or $D_1^2/D_2^2 \gg 1$, the Lorentzian doublet is equivalent to a single Lorentzian. If the ratio D_2^2/D_1^2 is not fixed, the small function differences between a single Lorentzian and a Lorentzian doublet can vanish in the noise, such that the fit cannot reliably distinguish between a single Lorentzian and a sum of two Lorentzians. This is demonstrated in Fig. 2.6, where a simulation is performed with the signal according to Eq. (2.45) including shot noise. In Fig. 2.6(a), the simulation is performed for 10^7 peak counts and in Fig. 2.6(b) for 10^4 peak counts, which represents the typical count rate in our experiment. The upper plots show an example of a simulated signal for a single line scan along with Lorentzian (blue solid curve)

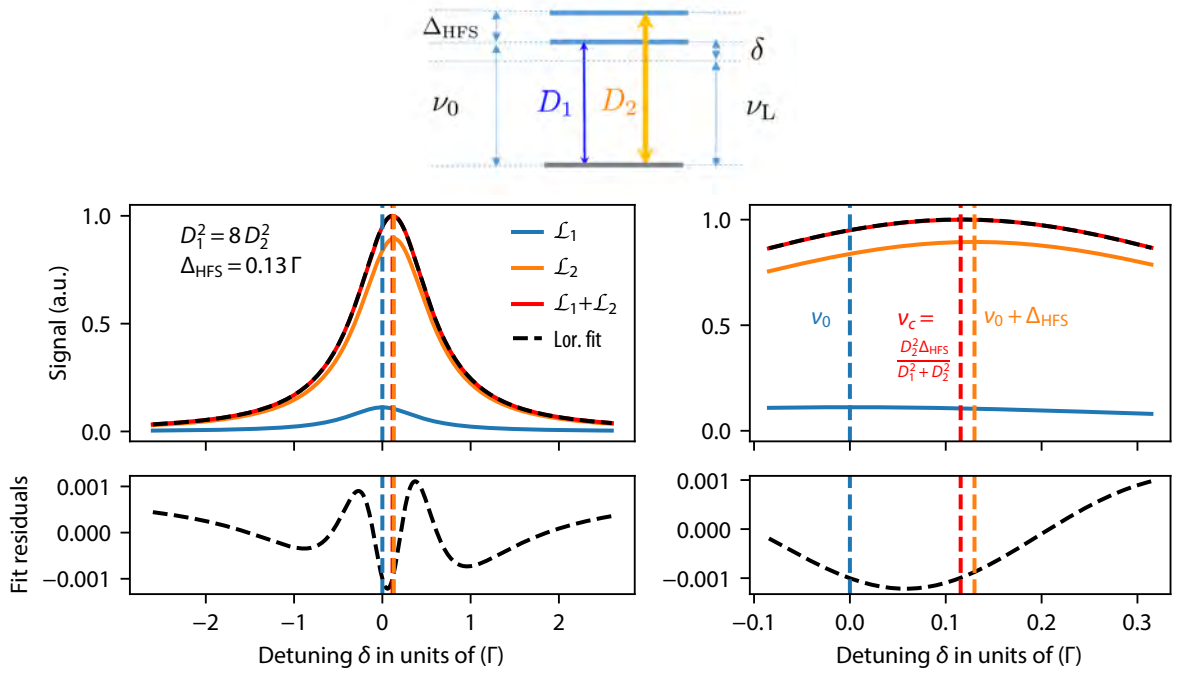

Figure 2.5: Illustration of the signal composed from two unresolved Lorentzian resonances with amplitudes D_1^2 and D_2^2 separated by Δ_{HFS} and with identical linewidths $\Gamma \gg \Delta_{\mathrm{HFS}}$ according to Eq. (2.45). On the top, the level scheme is shown. The bottom plots show the individual Lorentzian signal contributions (blue and orange) as well as the total signal from the sum of the two Lorentzians (red) which are plotted against the laser detuning $\delta = \nu_L - \nu_0$, where ν_L is the laser frequency and ν_0 is the center frequency of the first resonance (blue dashed vertical line). The center frequency of the second resonance is $\nu_0 + \Delta_{\mathrm{HFS}}$ (orange dashed vertical line). The total signal (sum of two Lorentzians) is well approximated by a single Lorentzian with a center frequency at $\nu_c = \nu_0 + D_2^2\Delta_{\mathrm{HFS}}/(D_1^2 + D_2^2)$ (red dashed vertical lines). The fit residuals from a Lorentzian fit to the total signal on the bottom plot reveal the deviations from this approximation.

and Lorentzian doublet (red dashed curve) fits. Below the signal, the average fit residuals for 1000 simulated line scans are shown for the Lorentzian (blue) and Lorentzian doublet (red) fit functions.

When fitting the total signal with a single Lorentzian function, the residuals are on the 10^{-3} level of the peak amplitude. The relative noise is given by $1/\sqrt{N}$ where N is the number of counts, and hence is above the 10^{-3} level for $N < 10^6$. It is therefore expected that if the signal drops well below this level, the Lorentzian doublet fit function does not produce reliable results: the sum of two Lorentzians then equally represents a single Lorentzian such that the fitted amplitude ratio is either $D_1^2/D_2^2 \ll 1$ or $D_1^2/D_2^2 \gg 1$. The averaged residuals hence show a false structure. As a consequence, the Lorentzian doublet fit cannot reliably determine the center frequency, which is demonstrated in the upper histograms of Fig. 2.6(b), where the number of occurences for the difference $\nu_{\mathrm{c,fit}} - \nu_{\mathrm{c}}$ is shown for 1000 simulated line scans. The difference $\nu_{\mathrm{c,fit}} - \nu_{\mathrm{c}}$ is distributed in the range between $-1/9\,\Delta_{\mathrm{HFS}} \simeq -0.014\Gamma$ and $8/9\,\Delta_{\mathrm{HFS}} \simeq 0.116\Gamma$, i.e. the fit finds the center frequency anywhere between the first resonance and the second resonance. The bottom histograms show the results for the fitted ratio D_1^2/D_2^2 for the Lorentzian doublet fit. Whereas for 10^7 peak counts (left) the fit reliably

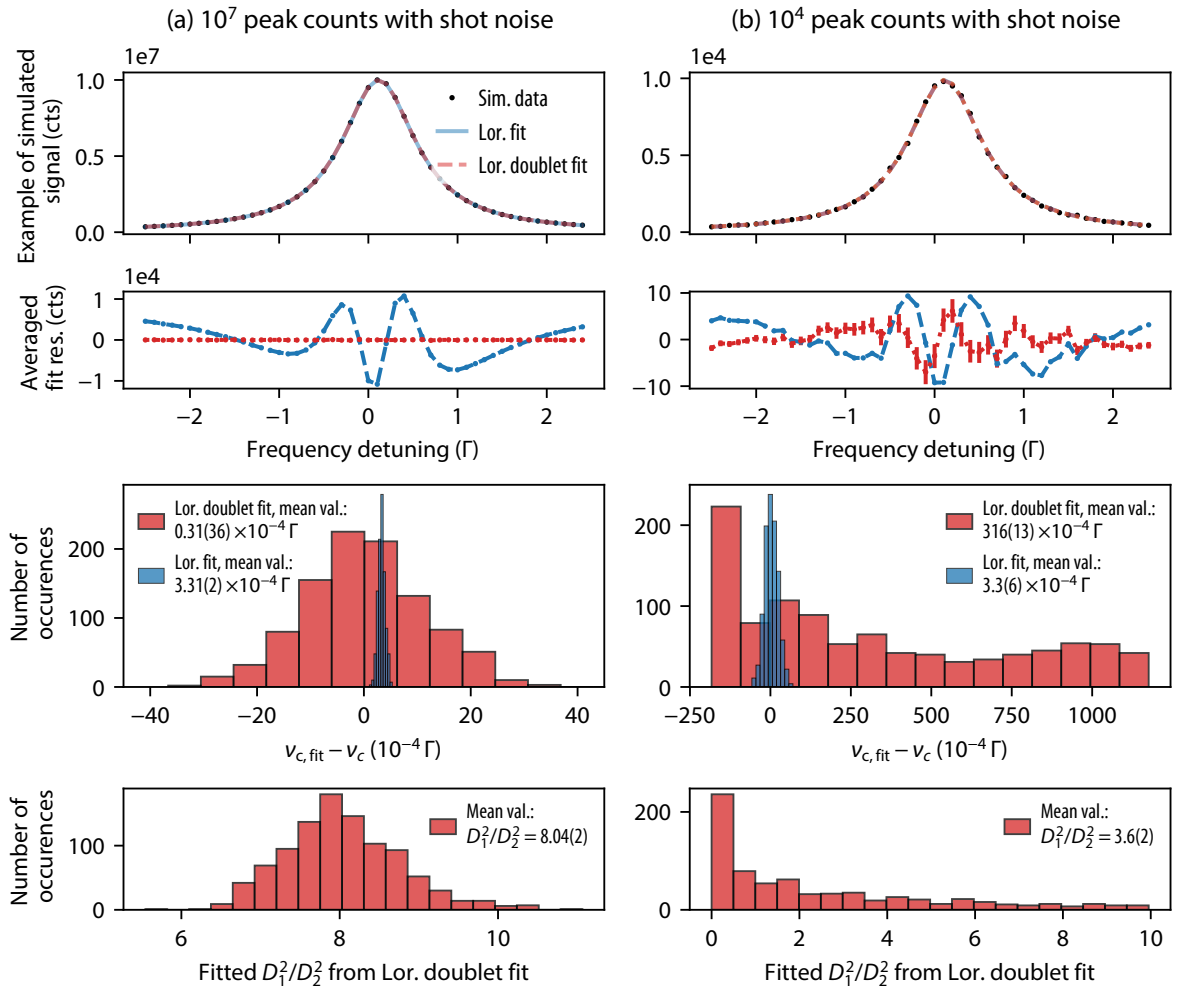

Figure 2.6: Simulated signal from two unresolved Lorentzian resonances as shown in Fig. 2.5 with shot noise. As in Fig. 2.5, the signal is modelled by Eq. (2.45) with $D_1^2 = 8D_2^2$ and $\Delta_{\mathrm{HFS}} = 0.13\Gamma$. Two different functions are used to fit the simulated signal: a single Lorentzian (shown in blue, 3 fit parameters: amplitude D, center frequency $\nu_{\mathrm{c,fit}}$, linewidth Γ), and a Lorentzian doublet with fixed separation Δ_{HFS} and same linewidth (shown in red, 4 fit parameters: dipole strengths D_1, D_2, $\nu_{0,\mathrm{fit}}$, Γ). In (a) the simulation is performed for 10^7 peak counts, in (b) for 10^4 peak counts. The upper plot shows an example of one simulated resonance line. Below, the averaged fit residuals for 1000 simulated resonance lines are plotted. The upper histograms show the frequency difference $\nu_{\mathrm{c,fit}} - \nu_c$, where $\nu_{\mathrm{c,fit}}$ is the fitted resonance center frequency (for the Lorentzian doublet $\nu_{\mathrm{c,fit}} = \nu_{0,\mathrm{fit}} + \nu_c$) and ν_c is defined center frequency from Eq. (2.48). The legend shows the mean values of this frequency difference along with the standard error. Using the sum of Lorentzians as a fit function can reliably reproduce the correct line center frequency for signals with 10^7 peak counts, but it fails for 10^4 peak counts which is also observed in the averaged fit residuals and in the fitted dipole ratio shown in the bottom histogram.

finds the correct ratio, for 10^4 peak counts (right), the fitted ratio is mostly $D_1^2/D_2^2 \ll 1$. It shall be remarked, that the histograms in (b) clearly reveal a non-Gaussian distribution, which also demonstrates the unreliability of the fit. Therefore, for experimental data one would notice the problem with the fit by looking at the distribution of the fit results.

If both the ratio D_1^2/D_2^2 and the hyperfine splitting Δ_{HFS} are known, then the Lorentzian doublet fit function (or similar functions representing unresolved resonances) with fixed parameters D_1^2/D_2^2 and Δ_{HFS} can be used to fit the data. The 2S-8D transitions in hydrogen are such an example [16][1]. In contrast to the 2S-nP transitions in deuterium, there are no possible deviations (e.g. due to circular polarization) from the amplitude ratio, such that it can be fixed to the known value for the fit to the data. For 2S-nP transitions in deuterium, the symmetry may be broken due to the possible population asymmetry between $m_F = -1/2$ and $m_F = +1/2$ initial states such that the observed line center may depend on polarization as discussed in the next section. Therefore, in the following we discuss the single resonance fit. However, as discussed below, the polarization imperfections and the population asymmetry are expected to be small in our case. The results with the single resonance fit (which does not assume any fixed amplitude ratio) function can then be compared to the results with the doublet fit function with a fixed amplitude ratio. If the population asymmetry combined with the polarization imperfections are small, the results should agree.

2.4.1.2 Single Lorentzian fit function

For $\Delta \ll \Gamma$, the sum of two Lorentzians can be approximated by a single Lorentzian:

$$\mathcal{L}(\nu_0, D_1, \Gamma) + \mathcal{L}(\nu_0 + \Delta_{\mathrm{HFS}}, D_2, \Gamma) \approx \mathcal{L}\left(\nu_c, D_1^2 + D_2^2, \Gamma\right). \tag{2.47}$$

The center frequency of this single Lorentzian is given by

$$\nu_{\mathrm{c}} = \nu_0 + \frac{D_2^2}{D_1^2 + D_2^2}\Delta_{\mathrm{HFS}}, \tag{2.48}$$

which we define as the line center of the resonance line composed of two unresolved resonance lines.

Note that the center frequency from Eq. (2.48) does not correspond to the hyperfine centroid as defined in Eq. (2.1). The hyperfine centroid of the $n\mathrm{P}_{1/2}$ levels is $2\Delta_{\mathrm{HFS}}/3$ above the $n\mathrm{P}_{1/2}^{F=1/2}$ states (or $\Delta_{\mathrm{HFS}}/3$ below the $n\mathrm{P}_{1/2}^{F=3/2}$ states), since there are four $n\mathrm{P}_{1/2}^{F=3/2}$ hyperfine sublevels and two $n\mathrm{P}_{1/2}^{F=1/2}$ hyperfine sublevels (see Fig. 2.2). The hyperfine centroid definition simply counts the number of hyperfine sublevels, which does not take into account any excitation scheme. For the excitation of the unresolved hyperfine levels, the observed center frequency depends on the dipole moments of the corresponding transitions (D_1 and D_2 in the above equation).

Furthermore, it shall be remarked, that when we discuss "shifts" of the center frequency from Eq. (2.48) (e.g. "shifts" due to imperfect polarization in Section 2.4.2 or unresolved quantum interference as in Section 2.5), these "shifts" are linked to the definition of the center frequency, and thus may be called "apparent" shifts. Note that whenever the lineshape is asymmetric, as in our case, the center frequency is a matter of definition, and thus also the associated shifts of the center frequency. Different positions at the line can shift differently, as for example in the case of resolved quantum interference [144, 143]. Therefore, it is important to consistently use the same definition of the "center frequency" when discussing the "shifts" of

[1] In [16], following transitions are studied: the $2\mathrm{S}_{1/2}^{F=1}$-$8\mathrm{D}_{5/2}^{F=2,3}$ and $2\mathrm{S}_{1/2}^{F=1}$-$8\mathrm{D}_{3/2}^{F=1,2}$ transitions with a natural linewidth of $\Gamma \simeq 572\,\mathrm{kHz}$ and hyperfine separation of $\Delta_{\mathrm{HFS}} \simeq 143\,\mathrm{kHz}$ ($8\mathrm{D}_{5/2}$) or $\Delta_{\mathrm{HFS}} \simeq 222\,\mathrm{kHz}$ ($8\mathrm{D}_{3/2}$), which is a fraction of 0.25 or 0.39 of the natural linewidth.

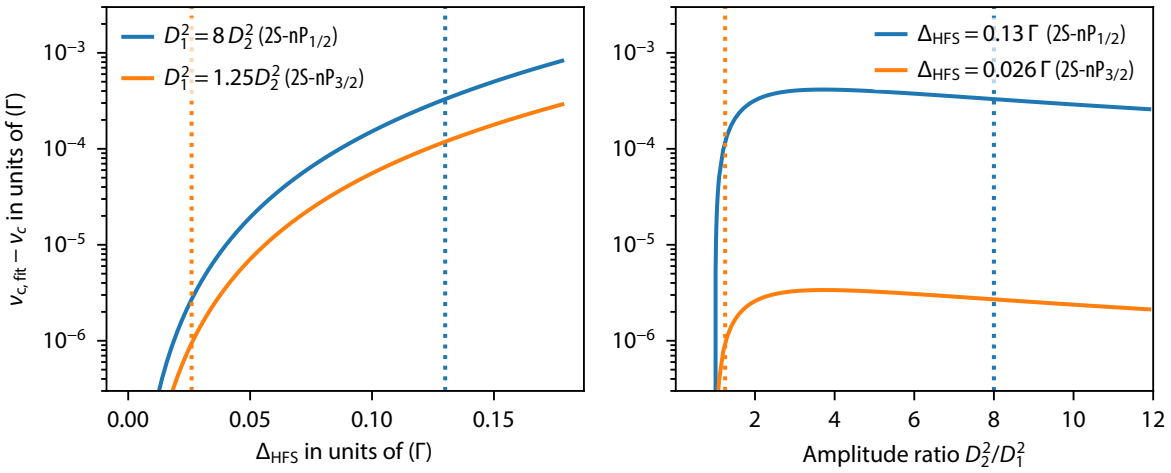

Figure 2.7: Difference $\nu_{c,fit} - \nu_c$ in the line center frequency of the signal modelled by the unresolved Lorentzian doublet according to Eq. (2.45), where $\nu_{c,fit}$ is the line center of the single Lorentzian fit to the signal and ν_c is the line center defined in Eq. (2.48). On the left, the difference $\nu_{c,fit} - \nu_c$ is shown in dependence on the separation Δ_{HFS} for $D_1^2 = 8D_2^2$ (in blue, corresponding to the deuterium 2S-nP$_{1/2}$ transition) and $D_1^2 = 1.25D_2^2$ (in orange, corresponding to the deuterium 2S-nP$_{3/2}$ transition). On the right, the difference $\nu_{c,fit} - \nu_c$ is shown in dependence on the ratio D_2^2/D_1^2 for $\Delta_{HFS} = 0.13\Gamma$ (in blue, corresponding to the deuterium 2S-nP$_{1/2}$ transition) and $\Delta_{HFS} = 0.026\Gamma$ (in orange, corresponding to the deuterium 2S-nP$_{3/2}$ transition). In both plots, the values for Δ_{HFS} or D_2^2/D_1^2 corresponding to the 2S-nP$_{1/2}$ or 2S-nP$_{1/2}$ transition are marked with blue or orange dashed vertical lines, respectively.

the center frequency and when applying these examinations to experimental data. If the exact (asymmetric) lineshape would be used, some "shifts" may in fact not be present at all since they are "absorbed" into the lineshape function. However, as discussed above, in our case the (symmetric) lineshape is advantageous for fitting the data. Therefore, we carefully examine all possible "shifts" associated with such a function, associated with a specifix definition of the center frequency as in Eq. (2.48).

In the example of Fig. 2.5 with $D_1^2 = 8D_2^2$ and $\Delta_{HFS} = 0.13\Gamma$, we find $\nu_c = \nu_0 + 8\Delta_{HFS}/9 \simeq \nu_0 + 0.15556\,\Gamma$, which is shown in Fig. 2.5 as a red dashed vertical line. The center frequency of the first resonance (ν_0) is shown as a blue dashed vertical line, and the center frequency of the second resonance ($\nu_0 + \Delta_{HFS}$) is shown as a orange dashed vertical line. The maximum signal is at $\nu_{max} \simeq \nu_0 + 0.11685\Gamma$, and thus deviates from ν_c by $12.9 \times 10^{-4}\,\Gamma$.

In Fig. 2.5, the total signal (red) is fitted with a single Lorentzian function (black dashed curve). On the bottom, the fit residuals demonstrate the deviations from the total signal fitted with a single Lorentzian. The fitted center frequency of the single Lorentzian is $\nu_{c,fit} \simeq \nu_0 + 0.11589\Gamma$, and thus deviates by $3.3 \times 10^{-4}\,\Gamma$ from ν_c. Fig. 2.7 shows the difference $\nu_{c,fit} - \nu_c$ in dependence on the line separation Δ_{HFS} (left) and the dipole ratio D_2^2/D_1^2 (right), with the cases of $D_1^2 = 8D_2^2$ and $\Delta_{HFS} = 0.13\Gamma$ (corresponding to the 2S-nP$_{1/2}$ transition) or $D_1^2 = 1.25D_2^2$ and $\Delta_{HFS} = 0.026\Gamma$ (corresponding to the 2S-nP$_{3/2}$ transition) marked by dotted vertical lines in blue or in orange, respectively. Since the hyperfine splitting for the 2S-nP$_{3/2}$ transition is smaller and the dipole ratio close to one, the difference $\nu_{c,fit} - \nu_c$ is smaller.

The deviations of the fitted center frequency $\nu_{c,fit}$ to ν_c can be simulated and taken into account. Though these simulations need to include some assumption on the dipole ratio

D_2^2/D_1^2, the calculated deviation does not strongly depend on the exact number as shown in Fig. 2.7. In our case, the deviations are included in the 'Big Model' simulations described in Section 2.5.3 and Section 3.3.2, which use the same fit function and the sampling as in the experiment. Note that since the fit function does not perfectly describe the signal shape, the difference $\nu_{\mathrm{c,fit}} - \nu_c$ may depend on the sampling of the resonance. For the densely spaced equidistant sampling which is used here[1], the dependence on the sampling is on the level of $\sim 10^{-5}\,\Gamma$ and thus negligible. For experimental data with less sampling points, this dependence can be larger.

2.4.2 Line center shift due to imperfect polarization combined with asymmetry of initial states

Comparing the simplified scheme in Fig. 2.5 to the detailed level structure of $2\mathrm{S}_{1/2}^{F=1/2}$-$n\mathrm{P}$ transitions, we find that both resonances (associated with D_1 and D_2) are composed of two resonances each from the two inital states $m_F = \pm 1/2$ of the 2S states ($i1$ and $i2$), which is shown on the left of Fig. 2.8. We define the hyperfine center frequency (orange in Fig. 2.8) as in Eq. (2.48):

$$\nu_c = \nu_0 + \eta \Delta_{\mathrm{HFS}}, \tag{2.49}$$

where ν_0 is the resonance frequency of the $2\mathrm{S}_{1/2}^{F=1/2}$-$n\mathrm{P}_{1/2}^{F=1/2}$ transition, and η is the fraction of the hyperfine splitting Δ_{HFS}, by which the $2\mathrm{S}_{1/2}^{F=1/2}$-$n\mathrm{P}_{1/2}^{F=3/2}$ pulls the total resonance line center. If no imperfections are present, η is given by $\eta = D_2^2/(D_1^2 + D_2^2)$, where D_1 and D_2 are determined by dipole matrix elements of the corresponding transitions. If the initial states are being populated unequally (non-zero ι introduced in Section 2.3.1), there is no line shift unless the energy of the $m_F = \pm 1/2$ states is unequal (Zeeman shift discussed in Section 2.3.1). However, if in addition to non-zero ι there is a residual circular polarized fraction of the excitation light (non-zero s), there is a line shift, which we examine in the following.

Consider first the excitation of $n\mathrm{P}$ levels by perfect linear polarization in the basis where this light is orthogonal to the quantization axis driving the transitions with no change of projected angular momentum, i.e. $\Delta m_F = 0$. This corresponds to π excitation light which is represented in the left of Fig. 2.8 driving the $2\mathrm{S}_{1/2}^{F=1/2} \to n\mathrm{P}^{F=1/2}$ ($i1 \to e1$, $i2 \to e3$) and $2\mathrm{S}_{1/2}^{F=1/2} \to n\mathrm{P}^{F=3/2}$ ($i1 \to e2$, $i2 \to e4$) transitions. Rotating the quantization basis by 90 degrees results in the right level scheme of Fig. 2.8, where the linear polarization is represented by the coherent superposition of σ^+ and σ^- light. This basis is helpful for the examination of polarization imperfections: the strengths of driving the σ^- and σ^+ transitions is proportional to the intensity of left-handed (I_{RHC}) and right-handed (I_{LHC}) polarized light. The residual circular polarized fraction s is proportional to the difference of the right- and left-handed polarized light. The effect of driving the corresponding transitions with a slight imbalance due to the difference $I_{\mathrm{RHC}} - I_{\mathrm{LHC}}$ is then derived in Appendix A.4. This calculation yields for the hyperfine center fractions $\eta_{1/2}$ and $\eta_{3/2}$ of the 2S-$n\mathrm{P}_{1/2}$ and the 2S-$n\mathrm{P}_{3/2}$ transitions, respectively:

$$\eta_{1/2} = \frac{8 + 4\,s\,\iota}{9 + 3\,s\,\iota} \simeq \frac{8}{9} + \frac{4}{27}\,s\,\iota, \quad \eta_{3/2} = \frac{5 + 2.5\,s\,\iota}{9 - 1.5\,s\,\iota} \simeq \frac{5}{9} + \frac{10}{27}\,s\,\iota. \tag{2.50}$$

[1] For simulations of Fig. 2.5, the line was equidistantly sampled between $\pm 2.5\Gamma$ with a frequency spacing of 0.1Γ.

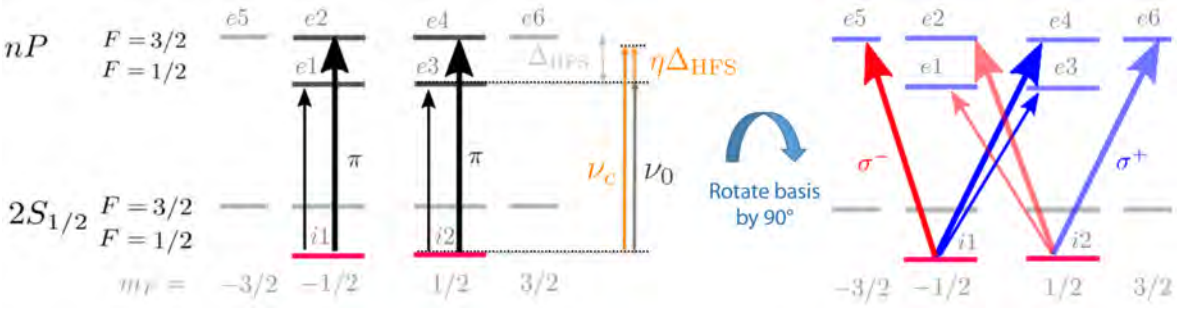

Figure 2.8: Level scheme for driving the $2S_{1/2}^{F=1/2}$-nP transitions (valid for both $n\mathrm{P}_{1/2}$ and $n\mathrm{P}_{3/2}$ levels) with linearly polarized light in two different quantization bases (the energy differences between the levels are not to scale). On the left, the quantization basis is chosen such that linearly polarized light drives the π transitions with $\Delta m_F = 0$. On the right, the quantization basis is rotated by 90°, such that linearly polarized light equally drives the σ^- and σ^+ transitions. This basis is helpful to examine the line shift due to the residual circular polarization, which causes a small imbalance between driving the σ^- and σ^+ transitions. The hyperfine splitting of nP levels is denoted by Δ_{HFS} and the resonance line center frequency $\nu_c = \nu_0 + \eta\Delta_{\mathrm{HFS}}$ of the total resonance line is defined as in Eq. (2.48), where ν_0 is the resonance frequency of the $2S_{1/2}^{F=1/2}$-$n\mathrm{P}_{1/2}^{F=1/2}$ transition, and η is the fraction of the hyperfine splitting by which the $2S_{1/2}^{F=1/2}$-$n\mathrm{P}_{1/2}^{F=3/2}$ transition increases the total resonance line center.

As expected from symmetry, the hyperfine center does not shift if either the $m_F = \pm 1/2$ initial states are populated equally ($\iota = 0$) or the polarization is perfectly linear ($s = 0$). The hyperfine center is shifted only if both imperfections are present. This result is exemplarily illustrated in Fig. 2.9 for the 2S-$n\mathrm{P}_{1/2}$ transition. In Fig. 2.9(a), the observed hyperfine center is plotted as a function of the circular polarization fraction $s = S_3/S_0$ for maximal possible asymmetry, i.e. the initial state $m_F = -1/2$ ($\iota = -1$, solid curve) or $m_F = 1/2$ ($\iota = 1$, dashed curve). For $\iota = -1$ and $s = -1$ as well as for $\iota = +1$ and $s = +1$, only the upper ($F = 3/2$) hyperfine component is excited ($\eta = 1$). For $s = 0$ (perfect linear polarization), the hyperfine center fraction is $\eta_{1/2} = 8/9$. This is the same hyperfine center as for equal initial state population $\iota = 0$ for all possible polarizations, see Fig. 2.9(b). In Fig. 2.9(c), the initial states are populated with an asymmetry $\iota = 1/3$ and the hyperfine center varies by $\sim 0.1\,\Delta_{\mathrm{HFS}}$ between fully right- and left-handed circular polarization.

From Eq. (2.50), the line center shifts $\Delta\nu_{\iota s,1/2}$ (2S-$n\mathrm{P}_{1/2}$ transition) and $\Delta\nu_{\iota s,3/2}$ (2S-$n\mathrm{P}_{3/2}$ transition) from the imperfect polarization combined with the population asymmetry are:

$$\Delta\nu_{\iota s,1/2} \simeq 0.019\,\iota s\Gamma_{\mathrm{nP}} \simeq \iota s \times 75\,\mathrm{kHz} \tag{2.51}$$

$$\Delta\nu_{\iota s,3/2} \simeq 0.010\,\iota s\Gamma_{\mathrm{nP}} \simeq \iota s \times 37\,\mathrm{kHz}, \tag{2.52}$$

where the numerical values are given for the 2S-6P transitions (see Table 2.4 and Table 2.5 for values of $\Gamma_{6\mathrm{P}}$, $\Delta_{\mathrm{HFS}_{1/2}}$, and $\Delta_{\mathrm{HFS}_{3/2}}$). The line shift is around two times smaller for the 2S-$n\mathrm{P}_{3/2}$ transition compared to the 2S-$n\mathrm{P}_{1/2}$ transition. For the 2S-$n\mathrm{P}_{1/2}$ transition, the line shift is smaller than $10^{-4}\,\Gamma_{6\mathrm{P}} \sim 0.4\,\mathrm{kHz}$, if the product of initial state population asymmetry and circular polarization fraction is smaller than $\iota s \lesssim 0.005$. As discussed in Section 4.6, the residual circular polarization fraction s is accurately monitored in our setup and is typically $s \sim 5\%$, such that the initial state population asymmetry has to be $\iota \lesssim 10\%$ in order to satisfy the above condition. As discussed in Eq. (2.37), ι is expected to be many orders of magnitude

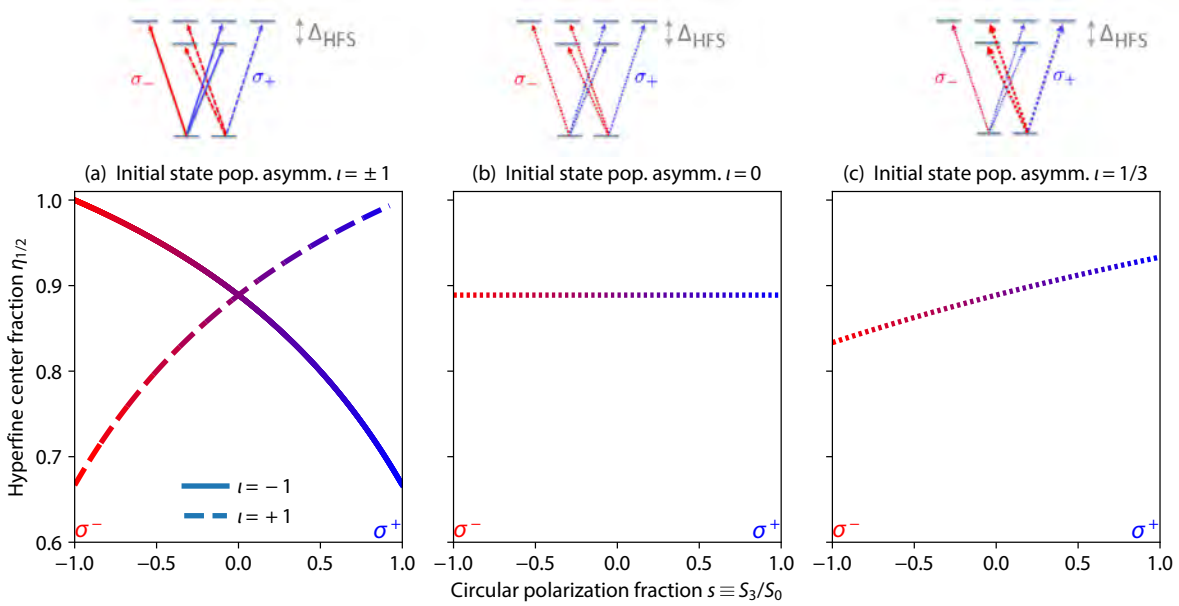

Figure 2.9: Illustrating the result of Eq. (2.50) for the hyperfine center fraction $\eta_{1/2}$ of the 2S-nP$_{1/2}$ transitions in deuterium. The hyperfine center in units of the hyperfine splitting Δ_{HFS} (fraction $\eta_{1/2}$) is plotted in dependence on the circular polarization fraction $s \equiv S_3/S_0$, where the fully left-handed circular polarization ($s = -1$) driving σ^- transitions is shown in red, and fully right-handed ($s = +1$, σ^+ excitation) in blue. The upper level schemes illustrate the driven transitions. In (a), the case of maximal initial state population asymmetry is shown: solid curve represents the $m_F = -1/2$ initial state ($\iota = -1$) and dashed curve the $m_F = +1/2$ initial state ($\iota = 1$). In (b), both states are equally populated ($\iota = 0$), and the hyperfine center is independent of circular polarization s. In (c), two times more atoms are in the $m_F = +1/2$ initial state than in the $m_F = -1/2$ state ($\iota = 1/3$). This results in a hyperfine center shift of around $0.1\,\Delta_{\mathrm{HFS}}$ between fully right- and left-handed circular polarization.

smaller ($\iota < 10^{-6}$), leading to negligible line shifts below 1 Hz according to Eq. (2.51).

2.5 Quantum interference between unresolved transitions

In this section, we include the decay to the final state, which has been neglected in the previous section. It is well known that in quantum mechanics, different paths from the same initial state to the same final state interfere. For the spectrscopy of the 2S-nP transitions in hydrogen and deuterium, this effect is present when considering the excitation from the same inital state accompanied by the decay to the same final state over different excited states originating from the fine structure and hyperfine structure of the nP state manifold. The fine structure leads to the resolved quantum interference, which is the same for hydrogen and deuterium. Here, the focus lies on the effect of quantum interference between the unresolved hyperfine transitions. In other atomic systems, quantum interference between partially resolved hyperfine components has been observed to cause large line shift, which may limit the precision spectroscopy [145, 146]. For the case of 2S-nP transitions in deuterium, we show that quantum interference between unresolved components is highly suppressed, which makes the precision spectroscopy possible with a similar uncertainty than in hydrogen.

We first consider a simple "toy model" to intuitively demostrate the phenomenon of quan-

tum interference and compare the resolved and unresolved case. Then the unresolved quantum interference for 2S-nP transitions in deuterium is evaluated within the perturbative quantum mechanical model. It is found that unresolved quantum interference is doubly suppressed. This suppression is confirmed by the full quantum mechanical model ("Big Model"), which concludes this section.

2.5.1 Simple "toy model"

Consider two interferring dipoles emitters with strengths $D_1 = |\vec{D}_1|$ and $D_2 = |\vec{D}_2|$, resonance frequencies $\nu_1 = \nu_0$ and $\nu_2 = \nu_0 + \Delta$, as well as identical linewidths Γ. Here, we assume for simplicity that the dipoles are aligned ($\vec{D}_1 \cdot \vec{D}_2 = D_1 D_2$). The signal can then be modelled as following:

$$I = \Big| \frac{D_1}{(\delta - \nu_0) + i\Gamma/2} + \frac{D_2}{(\delta - \nu_0 - \Delta) + i\Gamma/2} \Big|^2. \tag{2.53}$$

The above equation can be decomposed into the following terms: two Lorentzians with the two center frequencies ν_0 and $\nu_0 + \Delta$ and a quantum interference term:

$$I = \mathcal{L}(\nu_0, D_1, \Gamma) + \mathcal{L}(\nu_0 + \Delta, D_2, \Gamma) + \mathcal{Q}(\nu_0, D_1, D_2, \Delta, \Gamma), \tag{2.54}$$

where the quantum interference term is given by (see also [143]):

$$\mathcal{Q}(\nu_0, D_1, D_2, \Delta, \Gamma) = 2\, D_1 D_2 \frac{(\delta - \nu_0)(\delta - \nu_0 - \Delta) + (\Gamma/2)^2}{((\delta - \nu_0)^2 + (\Gamma/2)^2)((\delta - \nu_0 - \Delta)^2 + (\Gamma/2)^2)}. \tag{2.55}$$

Fig. 2.10 demostrates the effect of quantum interference in two regimes: (a) $\Delta \gg \Gamma$ (resolved quantum interference), and (b) $\Delta \ll \Gamma$ (unresolved quantum interference). The total signal from Eq. (2.54) is shown in red, the Lorentzian from the first resonance ($\mathcal{L}_1$) in blue, the Lorentzian from the second resonance ($\mathcal{L}_2$) in orange, and the quantum interference term ($\mathcal{Q}$) in gray. Note that when relating the dipole emitters to atoms, $D_1 D_2$ can be either positive or negative, depending on the signs of D_1 and D_2. Therefore, two cases with both signs of the quantum intereference term are shown ($+\mathcal{Q}$ and $-\mathcal{Q}$, solid and dashed curves, respectively).

In the case of resolved quantum interference, $\mathcal{Q}$ has a dispersive form. The contribution of quantum interference distorts the resonance line. This distortion has a distinctive shape, since the quantum interference term has opposite sign contributions below and above the line centers of $\mathcal{L}_1$ and $\mathcal{L}_2$. Therefore, the resolved quantum interference can be accounted for by using a corresponding fit function (e.g. Fano-Lorentzian). Indeed, only one additional parameter, that takes any solid detection angle into account, is needed to describe the effect of resolved quantum interference. For the 2S-nP transitions in hydrogen and deuterium, the resolved quantum intereference occurs between the two fine-structure components (2S-$n\mathrm{P}_{1/2}$ and 2S-$n\mathrm{P}_{3/2}$ transitions, recall Fig. 2.2). Note that compared to Fig. 2.10(a) the line seperation between the 2S-$n\mathrm{P}_{1/2}$ and 2S-$n\mathrm{P}_{3/2}$ transitions is an order of magnitude larger ($\Delta \sim 100\Gamma$), such that the quantum interference is much smaller than in Fig. 2.10(a). The "rule of thumb" line shift due to the resolved quantum interference (when using a fit function which does not automatically take the resolved quantum interference into account) is approximately $\Delta\nu_{\mathrm{res.\,QI}} \sim \Gamma^2/(2\Delta)$ [143], such that the line shifts can be on the order of 5×10^{-3} for the 2S-6P transition. This effect has been studied in great detail in the 2S-4P measurement in hydrogen, see [14, 71] for details, and [143] for a review. For the 2S-6P measurement, the

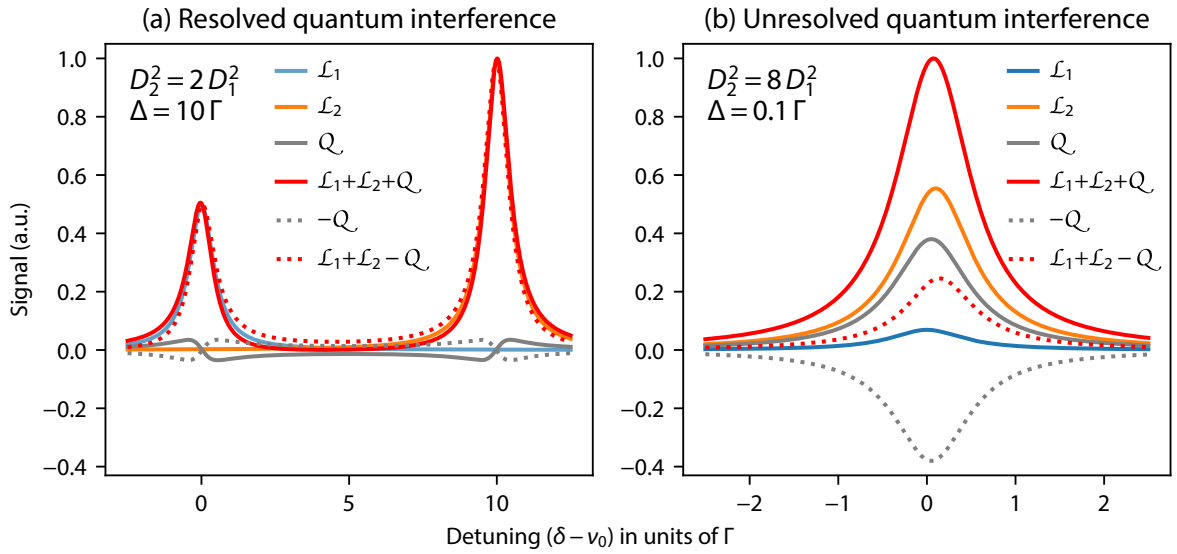

Figure 2.10: Comparison of resolved and unresolved quantum interference using the simple "toy model" for the signal from Eq. (2.54). The total signal (red curves) is a sum of three terms: the Lorentzian of the first resonance ($\mathcal{L}_1$, blue curves), the Lorentzian of the second resonance ($\mathcal{L}_2$, orange curves), and the quantum interference cross term ($\mathcal{Q}$, gray curves). The latter can have different signs, such that two cases are shown,$+\mathcal{Q}$ (solid curves) and $-\mathcal{Q}$ (dashed curves). (a) In the case of resolved quantum interference ($\Delta \gg \Gamma$, here $\Delta = 10\Gamma$), the quantum interference term has a dispersive shape, and therefore leads to distinctive distortions of the total signal, which can be taken into account by using a corresponding fit function. (b) In the case of unresolved quantum interference ($\Delta \ll \Gamma$, here $\Delta = 0.1\Gamma$), the quantum interference term appears as another Lorentzian resonance (see Eq. (2.56)), such that the signal shape is not clearly distinguished from the signal without quantum interference.

effect of resolved quantum intereference is minimized by aligning the polarization of the excitation light to the "magic angle" (see [71] for details). In this thesis, the resolved quantum intereference is not further discussed, since this effect is the same in deuterium as in hydrogen.

In the case of unresolved quantum interference ($\Delta \ll \Gamma$), one can easily prove using a computer algebra system, that the quantum interference term from Eq. (2.55) can be approximated by a Lorentzian with a center frequency at $\nu_0 + \Delta/2$ and dipole strength $2\sqrt{D_1 D_2}$:

$$\mathcal{Q}(\nu_0, D_1, D_2, \Delta, \Gamma) \simeq \operatorname{sgn}(D_1 D_2)\, \mathcal{L}\left(\nu_0 + \Delta/2, 2\sqrt{D_1 D_2}\right). \tag{2.56}$$

Therefore, the quantum interference term appears in first order like another Lorentzian with a dipole strength $D_3 = 2\sqrt{D_1 D_2}$ and a resonance frequency $\nu_3 = \nu_0 + \Delta/2$ lying exactly between the two resonances frequencies of the dipoles D_1 and D_2. The total signal is therefore approximately given by a sum of three Lorentzians:

$$I \simeq \mathcal{L}(\nu_1, D_1) + \mathcal{L}(\nu_2, D_2) + \mathcal{L}(\nu_3, D_3). \tag{2.57}$$

We already showed in Eq. (2.47) that a sum of two Lorentzians with resonance frequencies separated by much smaller values than their linewidth is approximated by a single Lorentzian with a center frequency given by Eq. (2.48):

$$\nu_{\mathrm{c,\,no\,QI}} = \nu_0 + \frac{D_2^2}{D_1^2 + D_2^2}\Delta. \tag{2.58}$$

By mathematical induction, it is clear that any number $n > 2$ of unresolved Lorentzian resonances is also approximated by the single Lorentzian resonance. Therefore, the lineshape with unresolved quantum interference does not have distinctive features compared to the case with no quantum interference.

The line center of the single Lorentzian, which approximates n unresolved Lorentzians, is given by:

$$\nu_{\mathrm{c,n}} = \nu_0 + \frac{\sum_{i=1}^{n} D_i^2 \Delta_i}{\sum_{i=1}^{n} D_i^2}, \tag{2.59}$$

where D_i^2 is the amplitude of the ith Lorentzian and Δ_i is the difference between the line center of the ith Lorentzian to the 1st Lorentzian, which we assume to have the line center ν_0 such that $\Delta_1 = 0$. In Eq. (2.57) we have three Lorentzians with $\Delta_1 = 0$, $\Delta_2 = \Delta$ and $\Delta_3 = \Delta/2$ with $D_3 = 2\sqrt{D_1 D_2}$. The line center with unresolved quantum interference is then given by:

$$\nu_{\mathrm{c,with\ QI}} = \nu_0 + \frac{2D_1 D_2 \Delta/2 + D_2^2 \Delta}{D_1^2 + 2D_1 D_2 + D_2^2} = \nu_0 + \frac{D_2}{D_1 + D_2}\Delta. \tag{2.60}$$

Comparing Eq. (2.60) with Eq. (2.58), we see unresolved quantum interference leads to a different line center for $D_1 \neq D_2$. For example, for $D_2^2 = 9D_1^2$ without quantum interference, the line center is at $\nu_{\mathrm{c,\,no\,QI}} = \nu_0 + 0.9\,\Delta$ independent of the signs of D_1 and D_2. With quantum interference, the line center is either $\nu_{\mathrm{c,\,with\,QI}} = \nu_0 + 0.75\,\Delta$ for $\mathrm{sgn}(D_1 D_2) = +1$ or $\nu_{\mathrm{c,\,with\,QI}} = \nu_0 + 1.5\,\Delta$ for $\mathrm{sgn}(D_1 D_2) = -1$).

For $D_1 = -D_2$, Eq. (2.60) is singular. In this case, quantum interference largerly cancels the total signal ($\mathcal{L}_1 + \mathcal{L}_2 \approx -\mathcal{Q}$). Evaluating Eq. (2.54) for $D_1 = -D_2 \equiv D$, we find:

$$I_{D_1=-D_2} = \frac{D^2}{(\Gamma/2)^2 + (\delta - \nu_0)^2} \times \frac{\Delta^2}{(\Gamma/2)^2 + (\delta - \nu_0 - \Delta)^2}. \tag{2.61}$$

Near the resonance ($\delta \simeq \nu_0$), for $\Delta \ll \Gamma$, the total signal is therefore damped by $\Delta^2/(\Gamma/2)^2$. The signal shape is non-Lorentzian, but symmetric around $\delta = \nu_0 + \Delta/2$.

The simple "toy model" illustrates that unresolved quantum interference can have severe effects on the line center of the total signal. Furthermore, the line shape does not have distinctive properties as in the case of resolved quantum interference, but appears simply as the sum of Lorentzians as in the case of no quantum interference which has been discussed in Section 2.4. Therefore, for noisy data (as has been discussed in Fig. 2.6(b)), the line center can not be determined unless the amplitude ratio and the separation between unresolved lines is given as a known parameter to the fit. Fortunately, we find that for 2S-nP transitions in deuterium, the effect of unresolved quantum interference is largerly suppressed, which makes it possible to determine the line center, and thereby determine the energy difference between 2S and nP levels. We can model and understand this suppression from the quantum mechanical perturbative model, which we discuss in the following.

2.5.2 Quantum mechanical perturbative model

Using quantum mechanical perturbation theory, one can derive the amplitude of the scattered light by an atom, which is excited by the electromagnetic wave of frequency ν_{L} from an initial state $|i\rangle$ to the excited state $|e\rangle$ (having transition frequency ν_{ei}) and decays to the final state $|f\rangle$ to be the following [143]:

$$S_{q,p}^{e,i\to f} \equiv \frac{d_p(i \to e)\, d_q(e \to f)}{\nu_{\mathrm{L}} - \nu_{ei} + i\Gamma_e/2}, \tag{2.62}$$

where $d_p(i \to e)$ and $d_q(e \to f)$ are the dipole moments from the initial to the excited and from the excited to the final states, respectively (see Eq. (A.37) and Eq. (A.49)). p and q denote the spherical components of the emitting and exciting polarization, respectively ($p = 0$ and $q = 0$ corresponds to π-polarized light, whereas $p = \pm 1$ and $q = \pm 1$ corresponds to $\sigma^{\pm}$-polarized light). The linewidth Γ_e is given by the inverse lifetime of the excited state $|e\rangle$.

If the excitation takes place with one of the standard polarizations (e.g. as in our case with linearly polarized light which drives the π transitions, i.e. $p = 0$), the signal is given by [143]:

$$I(\theta) \propto \sum_f \left[\sin^2\theta \left| \sum_e S_{0,p}^{e,i\to f} \right|^2 + \frac{1+\cos^2\theta}{2} \left(\left| \sum_e S_{+1,p}^{e,i\to f} \right|^2 + \left| \sum_e S_{-1,p}^{e,i\to f} \right|^2 \right) \right], \tag{2.63}$$

where θ is the polar angle for the detected signal in the spherical coordinates w.r.t. the corresponding quantization axis (see Fig. 2.4). Note that since the emitted intensity is rotationally symmetric for each of the spherical components q, the dependence on the azimuthal angle does not enter the above equation. If the detector collects all the light (i.e. polarization insensitive detector with a solid angle of 4π), quantum interference vanishes unless the excited states have different principal quantum numbers. Furthermore, even if this condition is not fulfilled, there is a certain value of the angle θ ("magic angle"), for which the contribution of quantum interference cancels. For the resolved quantum interference in our experiment, this angle can be determined from "Big Model" simulations including the simulated detector efficiency (see Fig. 6.8 in [71]). For the case of unresolved quantum interference between the hyperfine components of 2S-nP deuterium transitions, we find that the contribution of quantum interference exactly vanishes for π decays and is doubly suppressed for σ decays, which we show in the following.

The signal contributions of the three decay channels π ($q = 0$) and $\sigma^{\pm}$ ($q = \pm 1$) are added incoherently in Eq. (2.63), and hence we consider them independently. The signal contributions of the different final states also enter Eq. (2.63) as an incoherent sum. Therefore, for each of the two initial states i_1 ($2S_{1/2}^{F=1/2}$, $m_F = -1/2$) or i_2 ($2S_{1/2}^{F=1/2}$, $m_F = +1/2$), we only need to evaluate the interference between the two hyperfine states e_1 and e_2 ($m_F = -1/2$, $nP^{F=1/2}$ and $nP^{F=3/2}$) or e_3 and e_4 ($m_F = 1/2$, $nP^{F=1/2}$ and $nP^{F=3/2}$). Consider first the π decays shown in Fig. 2.11. We exemplarily consider the initial state i_1, from which the excitation to e_1 (blue arrow) and e_2 (orange arrow) takes place. Fig. 2.11(a) shows the decay to the final state f_1 ($2S_{1/2}^{F=1/2}$, $m_F = -1/2$), and Fig. 2.11(b) to the final state f_4 ($2S_{1/2}^{F=3/2}$, $m_F = -1/2$). The contribution from each final state to the signal then corresponds to the model from Eq. (2.54) with $D_1 \equiv D_{1,f}$ and $D_2 \equiv D_{2,f}$ given by:

$$D_{1,f} = d_0(i \to e_1)\, d_0(e_1 \to f), \quad D_{2,f} = d_0(i \to e_2)\, d_0(e_2 \to f). \tag{2.64}$$

Evaluating the above matrix elements (see Table A.1 and Table A.2), we find that the product $D_{1,f}D_{2,f}$ is equal in magnitude but opposite in sign for f_1 and f_4:

$$D_{1,f_1}D_{2,f_1} = -D_{1,f_4}D_{2,f_4}. \tag{2.65}$$

Since the quantum interference term is proportional to D_1D_2 (see Eq. (2.55)), the two quantum interference terms add exactly to zero. Therefore, the unresolved quantum interference vanishes for the π decays of the 2S-nP transitions in deuterium.

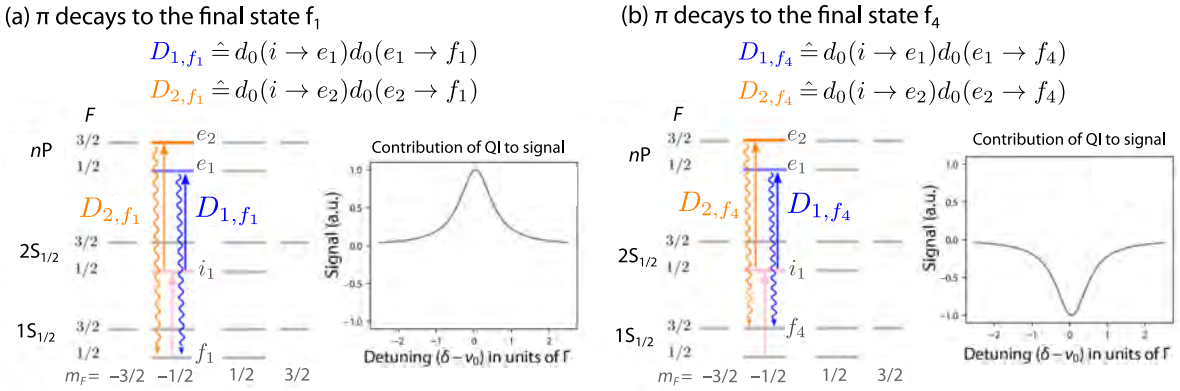

Figure 2.11: Level scheme for evaluating the unresolved quantum interference (QI) for π decays of the 2S-nP transitions in deuterium. The atom is excited from the initial state i_1 ($2S_{1/2}^{F=1/2}$, $m_F = -1/2$) to the two excited states of the nP hyperfine state manifold e_1 (blue) and e_2 (orange). The decay occurs either to the final state f_1 ($1S_{1/2}^{F=1/2}$, $m_F = -1/2$) as shown in (a), or to the final state f_4 as shown in (b). The signal with unresolved quantum interference corresponds in both cases to the model from Eq. (2.54) with $D_1 \equiv D_{1,f}$ and $D_2 \equiv D_{2,f}$ given by Eq. (2.64). The product $D_1 D_2$ is equal in magnitude but opposite in sign for the two final states f_1 and f_4, such that their quantum interference contribution (see Eq. (2.55)) is exactly opposite. Since the signal contribution from different final states adds incoherently to the total signal (see Eq. (2.63)), the quantum interference from the two final states adds to zero. Therefore, the unresolved quantum interference for π decays of 2S-nP transitions in deuterium vanishes.

Fig. 2.12 shows the level schemes for the $\sigma^{\pm}$ decays. Fig. 2.12(a) and (b) consider the decays from the states e_1 and e_2, which have been excited from the initial state i_1. While there is only one possible final state for the σ^+ decay, namely the $1S_{1/2}^{F=3/2}$, $m_F = -3/2$ state which we denote as f_3, there are two possible final states for the σ^- decay, $1S_{1/2}^{F=1/2}$, $m_F = 1/2$ and $1S_{1/2}^{F=3/2}$, $m_F = 1/2$ states, which we denote as f_2 and f_5. Note that the σ^+ and σ^- signal contributions enter the total signal from Eq. (2.63) with the same prefactor. Therefore, the total quantum interference contribution can be analyzed simply by adding the products $D_{1,f} D_{2,f}$ for each final state. Evaluating the corresponding matrix elements (see Table A.1 and Table A.2), we find that the contribution from the σ^- decay exacly cancels the contribution from the σ^+ decay since

$$D_{1,f_3} D_{2,f_3} = -(D_{1,f_2} D_{2,f_2} + D_{1,f_5} D_{2,f_5}). \tag{2.66}$$

In the experiment, this cancellation is present independent of the detector geometry if the σ^+ fluorescence photons are detected with the same quantum efficiency as the σ^- fluorescence photons, i.e. for a detector which does not distinguish between left- and right-handed circularly or elliptically polarized fluorescence light. Furthermore, there is an additional cancellation from the symmetry of the initial states. Fig. 2.12(c) and (d) consider the decays from the states e_3 and e_4, which have been excited from the initial state i_2. The quantum interference contribution for the same decay channel, but different initial state then also cancels, since

$$D_{1,f_3} D_{2,f_3} = -(D_{1,f_1} D_{2,f_1} + D_{1,f_4} D_{2,f_4}) \quad \text{and} \quad D_{1,f_2} D_{2,f_2} + D_{1,f_5} D_{2,f_5} = -D_{1,f_6} D_{2,f_6}. \tag{2.67}$$

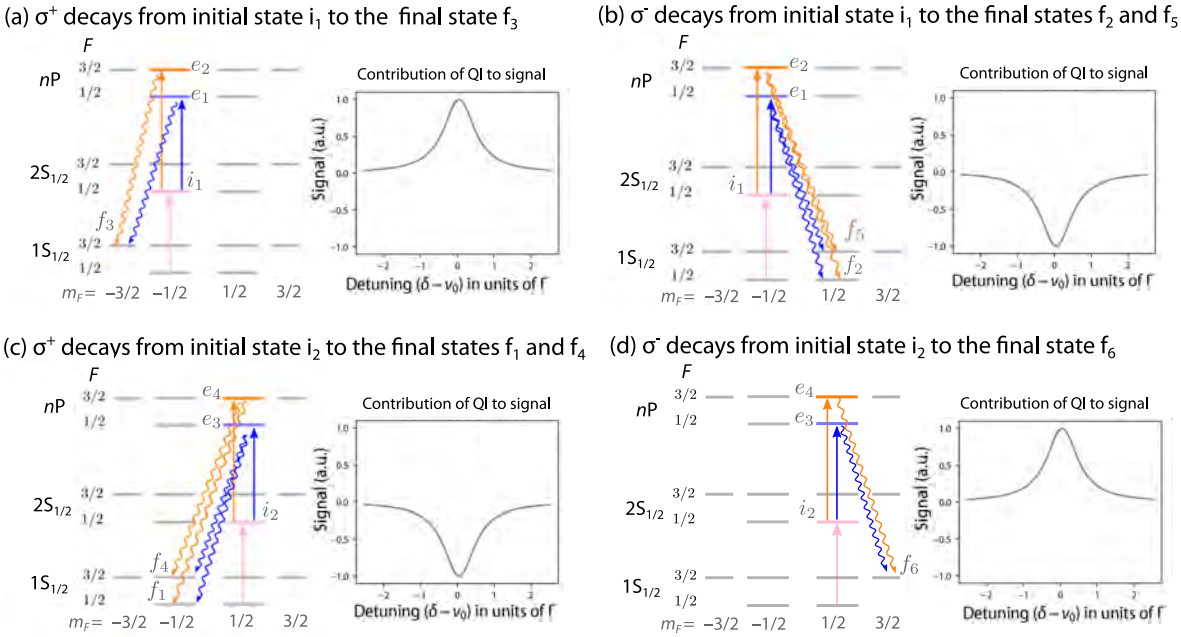

Figure 2.12: Similar to Fig. 2.11, here showing the level scheme for evaluating the unresolved quantum interference (QI) for $\sigma^{\pm}$ decays of the 2S-nP transitions in deuterium. (a) and (b) show the excitation from the i_1 initial state with σ^+ and σ^- decays to the final states f_3 ($1S_{1/2}^{F=3/2}$, $m_F = -3/2$) and f_2 as well as f_5 ($1S_{1/2}^{F=1/2}$ as well as $1S_{1/2}^{F=3/2}$, $m_F = 1/2$). The quantum interference contribution from f_3 is exactly equal to the combined contribution from f_2 and f_5 with the opposite sign, such that the unresolved quantum interference from $\sigma^{\pm}$ decays vanishes as long as the σ^- fluoresence is detected with the same efficiency as the σ^+ fluorescence (i.e. polarization insensitive detector). Similar cancellation occurs when combining the contribution from the same decay component but the different initial state i_2, which is shown in (c) and (d). Therefore, the unresolved quantum interference $\sigma^{\pm}$ decays of 2S-nP transitions in deuterium is doubly suppressed.

Therefore, only if the states i_1 and i_2 are unequally populated (state asymmetry ι introduced in Section 2.3.1) and the detector detects σ^- photons with a different efficiency than σ^+ photons (detection imbalance $\xi_\circ$ introduced in Section 2.3.3) there is an effect from unresolved quantum interference. The hyperfine center fractions $\eta_{1/2}$ and $\eta_{3/2}$ of the 2S-$n\mathrm{P}_{1/2}$ and the 2S-$n\mathrm{P}_{3/2}$ transitions are then calculated to be (see Appendix A.4.3):

$$\eta_{1/2} = \frac{24 + 8\xi_\circ\iota}{27 + 15\xi_\circ\iota} \simeq \frac{8}{9} - \frac{16}{81}\xi_\circ\iota, \quad \eta_{3/2} = \frac{15 + 13\xi_\circ\iota}{27 + 21\xi_\circ\iota} \simeq \frac{5}{9} + \frac{4}{81}\xi_\circ\iota. \tag{2.68}$$

The line center shifts $\Delta\nu_{\iota\xi_\circ,1/2}$ (2S-$n\mathrm{P}_{1/2}$ transition) and $\Delta\nu_{\iota\xi_\circ,3/2}$ (2S-$n\mathrm{P}_{3/2}$ transition) due to the detection imbalance combined with the population asymmetry are then:

$$\begin{aligned} \Delta\nu_{\iota\xi_\circ,1/2} &\simeq -0.026\,\iota\xi_\circ\Gamma_{\mathrm{nP}} \simeq -\iota\xi_\circ \times 100\,\mathrm{kHz}, \\ \Delta\nu_{\iota\xi_\circ,3/2} &\simeq 0.0013\,\iota\xi_\circ\Gamma_{\mathrm{nP}} \simeq \iota\xi_\circ \times 5\,\mathrm{kHz}, \end{aligned} \tag{2.69}$$

where the numerical values are given for the 2S-6P transitions for values of $\Delta_{\mathrm{HFS}_{1/2}}$ and $\Delta_{\mathrm{HFS}_{3/2}}$ from Table 2.4 and Table 2.5. The line shift is a factor of 20 times smaller for the 2S-$n\mathrm{P}_{3/2}$ transition compared to the 2S-$n\mathrm{P}_{1/2}$ transition. For the 2S-$n\mathrm{P}_{1/2}$ transition, the line shift is smaller than $10^{-4}\,\Gamma_{6\mathrm{P}} \sim 0.4\,\mathrm{kHz}$, if the product of initial state population asymmetry

and circular polarization fraction is smaller than $\iota\xi_\circ \lesssim 0.004$. As argued in Section 2.3.3, the most conservative estimation of the detection imbalance is $\xi_\circ < 0.3$. Furthermore, as discussed in Eq. (2.37), ι is expected to be many orders of magnitude smaller ($\iota < 10^{-6}$), leading to negligible line shifts below 1 Hz according to the above equation even for the maximal detection imbalance of $\xi_\circ = 1$.

2.5.3 Full quantum mechanical treatment ("Big Model")

The full quantum mechanical treatment of light interaction with an atom is based on the Liouville-von Neumann equation (also called the master equation in Lindblad form), and is for instance derived in [147]. Here we follow the summary from [143]. The Lioville-von Neumann equation reads:

$$\frac{\partial \rho}{\partial t} = \frac{1}{i\hbar}\left[\hat{H}, \rho\right] - \hat{\mathcal{L}}\rho, \tag{2.70}$$

where $\rho \equiv \rho(t)$ is the density matrix describing the time evolution of atomic states. The Hamiltonian $\hat{H}$ describes the atomic part and the coherent atom-light interaction:

$$\hat{H} = \sum_n |n\rangle\langle n|\hbar\omega_n + \frac{\hbar}{2}\sum_j \left(\hat{S}_j^+ \Omega_j e^{i\omega_L t} + \hat{S}_j^- \Omega_j^* e^{-i\omega_L t}\right), \tag{2.71}$$

where the first sum accounts for all atomic states $|n\rangle$ having an energy $\hbar\omega_n$, and the second sum describes the interaction of the coherent laser field at frequency ω_L for all possible transitions j with projection operators S_j^+ (terms $|i\rangle\langle e|$ for the transition from state $|i\rangle$ to state $|e\rangle$) and its complex conjugate S_j^- (terms $|e\rangle\langle i|$). The Rabi frequencies Ω_j are given by the electric field of the laser and the dipole matrix elements for each transition j, see Eq. (2.24). The spontaneous emission caused by the interaction with the vacuum field is described by the Lindblad operator:

$$\hat{\mathcal{L}}\rho = \frac{1}{2}\sum_{ij}\Gamma_{ij}\left(\hat{S}_i^+\hat{S}_i^- - 2\hat{S}_j^-\rho\hat{S}_i^+ + \rho\hat{S}_i^+\hat{S}_j^-\right), \tag{2.72}$$

where $\Gamma_{ij} = \sqrt{\Gamma_i\Gamma_j}\vec{\epsilon}_i\cdot\vec{\epsilon}_j$ are the cross damping (quantum interference) decay constants given by the decay constants Γ_i and Γ_j, as well as the spherical unit vectors along the corresponding dipole moment $\vec{\epsilon}_i$ and $\vec{\epsilon}_j$, for the transitions i and j, respectively. The projection operators $\hat{S}_i^+$ and $\hat{S}_i^-$ are given by terms $|e\rangle\langle f|$ and $|f\rangle\langle e|$ for each spontaneous decay i from an excited state $|e\rangle$ to the final state $|f\rangle$. In the experiment of this thesis, there are two counter-propagating laser beams, such that in our case a second laser field is added to Eq. (2.71). These and other theoretical details are thoroughly discussed in Sec. 2.3 of [71].

The implementation of Eq. (2.70) for the description of our experiment is based on Arthur Matveev's so far unpublished work ("Master Equation Derivation with External Declaration (MEDWED) code"). In general, the $2S_{1/2}$-6P excitation and resulting decays in deuterium involve $N = 234$ sub-levels, which results in $N^2 = 54756$ entries of the density matrix ρ and thus this much coupled differential equations. Using a computer algebra system[1], the number of equations is reduced to those with non-zero time evolution (i.e. those that lead to non-zero populations or coherences of states). For perfect linear polarization (π excitations only),

[1] The algorithm developed by Arthur Matveev was implemented on two computer algebra systems: Wolfram Mathematica 11.2 and the GiNaC C++ library.

the number of equations is reduced to 1442. The imperfections of polarization described by the circular polarized fraction $s \equiv S_3/S_0$ can be modelled as a superposition of σ^+ and σ^- excitations (see Fig. 2.8), which results in 4229 equations. The initial population asymmetry ι (see Section 2.3.1) in the $2S_{1/2}$, $m_F = -1/2$ and $2S_{1/2}$, $m_F = +1/2$ states is implemented as the initial condition of the corresponding density matrix entries[1].

Here we exemplarily show the simulations of the $2S_{1/2}$-$6P_{1/2}$ transition with two counter-propagating beams crossing the atomic beam at an angle of $\delta\alpha = 1\,\mathrm{mrad}$. The atomic velocity is set to 250 m/s, the 2S-6P laser power is $P_{\text{2S-6P}} = 10\,\mu\mathrm{W}$ with a beam radius $W_0 \simeq 2.2\,\mathrm{mm}$. To account for the broadening of the resonance line (here mainly due to the two overlapping resonances with oppposite Doppler shifts originating from the forward- and backward propagating beams), as for experimental data, we use a Voigt function for fitting the simulated signal:

$$\begin{aligned} \mathrm{V}(\delta, \nu_0, A, \Gamma_\mathrm{L}, \Gamma_\mathrm{G}, y_0) &= \frac{A}{\mathrm{Re}\left[w(\mathrm{i}b)\right]} \mathrm{Re}\left[w(a+\mathrm{i}b)\right] + y_0, \\ \text{with} \quad a &= -\frac{2\sqrt{\ln 2}}{\Gamma_\mathrm{G}}\left(\delta - \nu_0\right) \quad \text{and} \quad b = \sqrt{\ln 2}\,\frac{\Gamma_\mathrm{L}}{\Gamma_\mathrm{G}}, \end{aligned} \tag{2.73}$$

where $w(z) \equiv e^{-z^2}\,\mathrm{erfc}(-\mathrm{i}z)$ is the Faddeeva function (given by the complex complementary error function erfc). Γ_L and Γ_G are the Lorentzian and Gaussian linewidths. The total full-width-half-maximum (FWHM) linewidth Γ_F of a Voigt line shape is approximately given by[2] [148]:

$$\Gamma_\mathrm{F} \simeq 0.5346\,\Gamma_\mathrm{L} + \sqrt{0.2166\Gamma_\mathrm{L}^2 + \Gamma_\mathrm{G}^2}. \tag{2.74}$$

The "Big Model" includes all possible levels and excitations. Therefore, if we consider different decay channels separately, the resolved quantum intereference between the $2S_{1/2}$-$6P_{1/2}$ and $2S_{1/2}$-$6P_{3/2}$ fine-structure components is present. To account for this effect, we also fit the simulated signal with what we call the "Fano-Voigt" function [14, 143] with an asymmetry parameter $\tilde{\eta}$:

$$\mathrm{FV}(\delta, \nu_0, A, \Gamma_\mathrm{L}, \Gamma_\mathrm{G}, y_0, \tilde{\eta}) = \frac{A}{\mathrm{Re}\left[w(\mathrm{i}b)\right]}\left(\mathrm{Re}\left[w(a+\mathrm{i}b)\right] + 2\,\tilde{\eta}\,\mathrm{Im}\left[w(a+\mathrm{i}b)\right]\right) + y_0. \tag{2.75}$$

Fig. 2.13 shows the simulation results for the case of perfect linear polarization of excitation light ($s = 0$), no detection imbalance between σ^+ and σ^- fluorescence ($\xi_\circ = 0$), and an initial state asymmetry of $\iota = 0.25$. Since $s = 0$ and $\xi_\circ = 0$, any value if ι gives the same result. Fig. 2.13(a) shows the signal from π decays, Fig. 2.13(b) the combined signal from σ^+ and σ^- decays, and Fig. 2.13(c) the total signal (sum of π, σ^+, and σ^- decay signals). Since $\xi_\circ = 0$, no effect of unresolved quantum interference is predicted by the perturbative model, which is confirmed by the "Big Model" results. The Fano-Voigt fit result for the hyperfine center is $\nu_{\mathrm{c,fit}} = 450.3(1)\,\mathrm{kHz}$ in agreement between all the decay channels within ∼0.1 kHz. Eq. (2.68) or Eq. (2.50) predict for $\xi_\circ = 0$ or $s = 0$ a hyperfine center of $\nu_c = 8\Delta_{\mathrm{HFS}_{1/2}}/9 \simeq 448.84\,\mathrm{kHz}$

[1] More specifically, $\rho_{7,7} = (1-\iota)/2$ and $\rho_{8,8} = (1+\iota)/2$, where $\rho_{7,7}$ is the density matrix entry describing the population in the $2S_{1/2}$, $m_F = -1/2$ state and $\rho_{8,8}$ in the $2S_{1/2}$, $m_F = +1/2$ state (there are six $1S_{1/2}$ states such that the $2S_{1/2}$ level numbering starts with index 7).

[2] Here we give the expression of the "modified Whiting form" from [148] (coefficients $C_1 = 1.0692$, $C_2 = 0.86639$, $C_3 = 1.0$ in Eq. (4a) of [148]), which results in a maximum inaccuracy of 0.02% of the width Γ_F over the whole range of Γ_L and Γ_G as stated in [148].

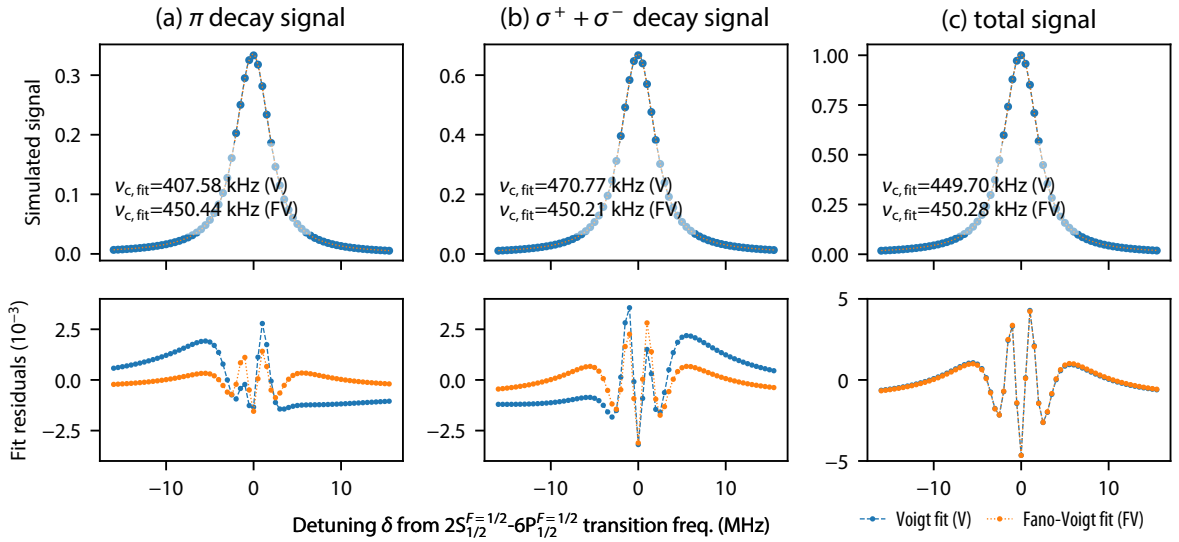

Figure 2.13: Full quantum mechanical model ("Big Model") simulations of the $2S_{1/2}$-$6P_{1/2}$ transition in deuterium (see Table 2.4 for parameters) for a single atomic trajectory. The simulated signal is shown for the signal from π decays in (a), for the combined signal from σ^+ and σ^- decays in (b), and for the total signal in (c), which is the sum of signals from (a) and (b). The atomic velocity is set to 250 m/s, and the simulation is performed with two counter-propagating beams, which cross the atomic beam at an angle of $\delta\alpha = 1$ mrad. The spectroscopy laser parameters are: laser power $P_{\text{2S-6P}} = 10\,\mu\text{W}$, beam radius $W_0 \simeq 2.2$ mm. The detection imbalance between σ^+ and σ^- is set to zero, $\xi_\circ = 0$. Perfect linear polarization is assumed for the excitation ($s \equiv S_3/S_0 = 0$). Since both $\xi_\circ = 0$ and $s = 0$, the simulation results are independent of the population asymmetry ι between the $2S_{1/2}, m_F = \pm 1/2$ initial states. The signal is fitted with a Voigt (blue) or Fano-Voigt (orange) functions, with residuals shown in the bottom plots (in (c) the blue and orange residuals points overlap). The center frequency of the fit gives the hyperfine center $\nu_{\text{c,fit}}$ for the detuning δ, which is counted from the $2S_{1/2}^{F=1/2}$-$6P_{1/2}^{F=1/2}$ transition frequency (corresponding to $\nu_c = \eta_{1/2}\,\Delta_{\text{HFS}_{1/2}}$, i.e. $\nu_0 \equiv 0$ in Eq. (2.49)). The Voigt fit gives a center frequency affected by the resolved quantum interference, which vanishes for the total signal. The Fano-Voigt fit gives a result free from resolved quantum interference, thereby showing that the contribution of unresolved quantum interference vanishes for $\xi_\circ = 0$ and $\iota = 0$ as predicted by the perturbative model, which yields a hyperfine center of $8/9 \times 504.94\,\text{kHz} \simeq 448.84\,\text{kHz}$ (the ~ 1.5 kHz offset is due to the fit of two unresolved resonances, see Fig. 2.14).

(in the following, we set the resonance frequency of the $2S_{1/2}^{F=1/2}$-$6P_{1/2}^{F=1/2}$ transition to zero, $\nu_0 \equiv 0$). The $\sim$1.5 kHz difference between ν_c and $\nu_{\text{c,fit}}$ originates from the fit of a single resonance function to two unresolved resonances, which can be calculated similar to Fig. 2.7 for the Voigt and Fano-Voigt functions. This correction depends on the broadening Γ_{G}, which is evaluated in Fig. 2.14(a) for the case of 2S-nP$_{1/2}$ transitions ($\Delta_{\text{HFS}} = 0.13\Gamma_{\text{L}}$, $D_1^2 = 8D_2^2$) and in Fig. 2.14(b) for the case of 2S-nP$_{3/2}$ transitions ($\Delta_{\text{HFS}} = 0.026\Gamma_{\text{L}}$, $D_1^2 = 1.25D_2^2$). For the simulation of the 2S-6P$_{1/2}$ transitions from Fig. 2.13, where $\Gamma_{\text{G}} \simeq 0.44\Gamma_{\text{L}}$, the deviation is calculated to be $3.76 \times 10^{-4}\,\Gamma_{\text{nP}} \simeq 1.47$ kHz (Fano-Voigt fit) and $2.16 \times 10^{-4}\,\Gamma_{\text{nP}} \simeq 0.84$ kHz (Voigt fit). The remaining differences to the "Big Model" simulation are below 0.1 kHz.

Fig. 2.15 examines the hyperfine center shift due to unresolved quantum interference for $\iota = 0.25$ and non-zero $\xi_\circ$. The signal from the σ^+ decays is multiplied with the factor $k_\xi = \xi^+/\xi^-$ and then summed with the signal from the σ^- decays, i.e. the detector has a sensitivity of ξ^+ for σ^+ photons and ξ^- for σ^- photons, such that a factor k_ξ more (for $k_\xi > 1$)

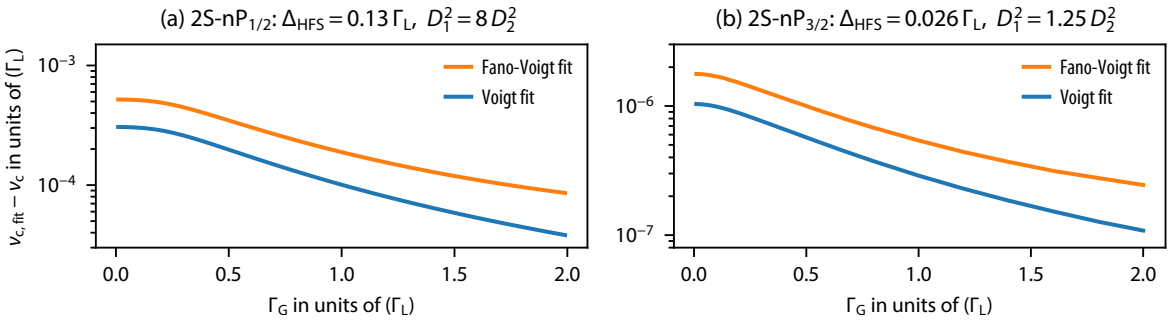

Figure 2.14: Similar to Fig. 2.7, here the difference $\nu_{\mathrm{c,fit}} - \nu_c$ in the line center frequency with the Voigt (blue) and Fano-Voigt (orange) fit functions is shown, where $\nu_{\mathrm{c,fit}}$ is the line center of the single Voigt or Fano-Voigt fit to the signal and ν_c is the line center defined in Eq. (2.48). The correction depends on the broadening Γ_{G}, which is here evaluated in (a) for the case of 2S-nP$_{1/2}$ transitions ($\Delta_{\mathrm{HFS}} = 0.13\Gamma_{\mathrm{L}}$, $D_1^2 = 8D_2^2$) and in (b) for the case of 2S-nP$_{3/2}$ transitions ($\Delta_{\mathrm{HFS}} = 0.026\Gamma_{\mathrm{L}}$, $D_1^2 = 1.25D_2^2$).

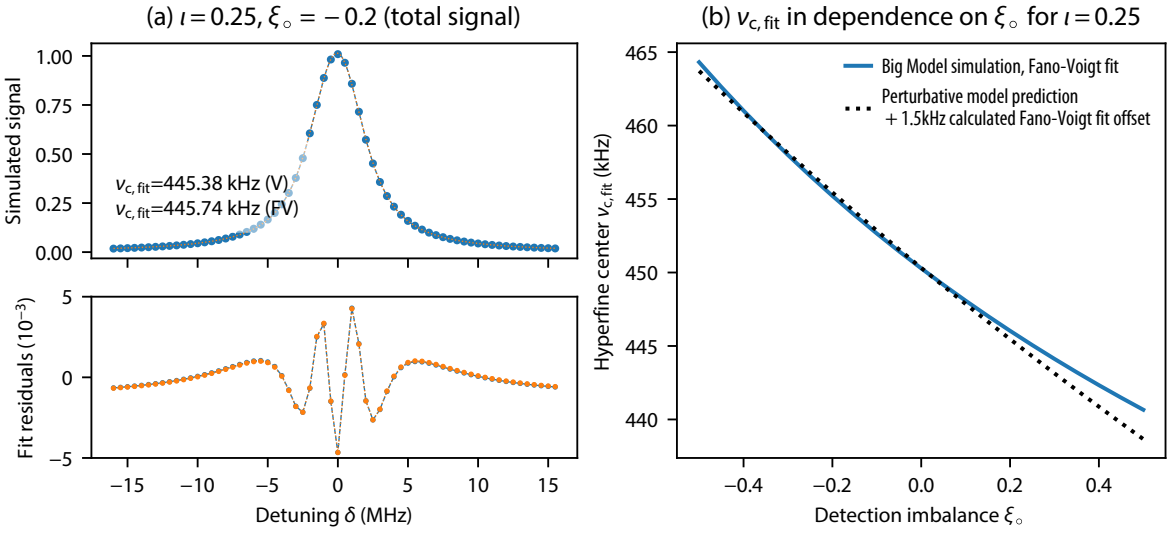

Figure 2.15: Similar to Fig. 2.13 (same simulation parameters), here evaluating the "Big Model" simulation for the non-zero detection imbalance $\xi_\circ$ between the signal from the σ^+ and σ^- decays, which in combination with non-zero population asymmetry ι results in a line shift due to unresolved quantum interference. (a) As an example, the total signal for $\iota = 0.25$ and $\xi_\circ = -0.2$ is shown, where the fit yields a hyperfine center shifted by $\sim$5 kHz compared to $\xi_\circ = 0$ in Fig. 2.13(c), which is in agreement with the prediction from the perturbative model. (b) The hyperfine center $\nu_{\mathrm{fit,c}}$ from the Fano-Voigt fit to the simulated signal (blue curve) is shown in dependence on $\xi_\circ$ for $\iota = 0.25$, and is compared to the prediction of the perturbative model (black dotted curve). The 1.5 kHz offset due to the single Fano-Voigt fit to two unresolved resonances (see Fig. 2.14) is added to the perturbative prediction from Eq. (2.68).

or less (for $k_\xi < 1$) σ^+ photons are detected than σ^- photons. The factor k_ξ converts to $\xi_\circ$ according to Eq. (A.55). In Fig. 2.15(a), the total signal is shown for $\iota = 0.25$ and $\xi_\circ = -0.2$. The perturbative model predicts according to Eq. (2.69) a shift of $\Delta\nu_{\iota\xi_\circ,1/2} \simeq 5$ kHz, in agreement with the "Big Model" simulation. Fig. 2.15(b) shows the fitted hyperfine center $\nu_{\mathrm{c,fit}}$ from the Fano-Voigt fit to the simulated "Big Model" signal (blue curve) in dependence on $\xi_\circ$, which confirms the perturbative model prediction (black dotted curve). The 1.5 kHz

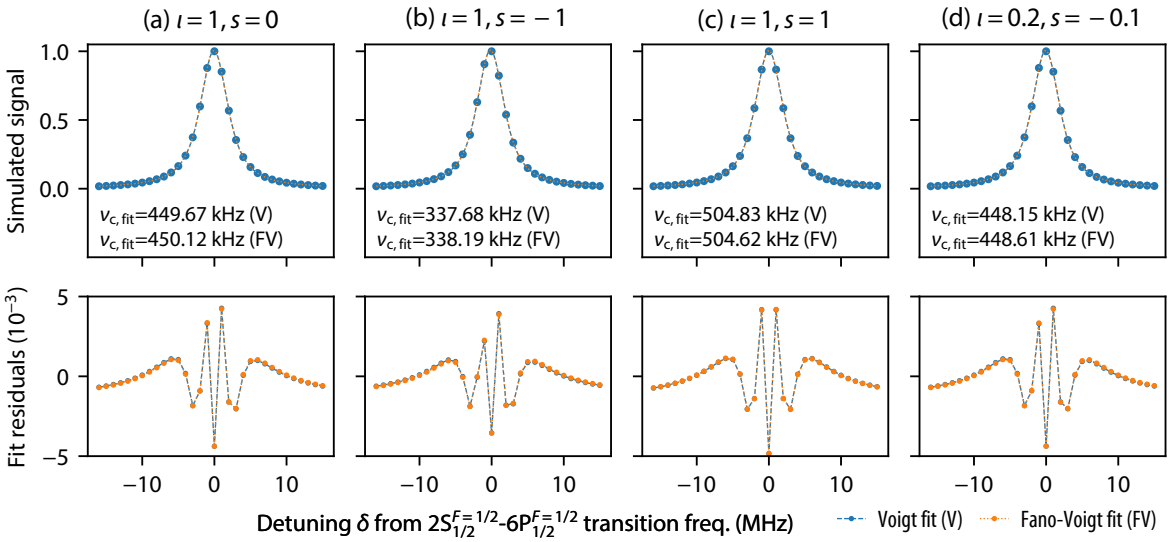

Figure 2.16: Similar to Fig. 2.13 (same simulation parameters), here the "Big Model" simulations of the $2S_{1/2}$-$6P_{1/2}$ transition in deuterium are shown with an initial state asymmetry ι and a different circular polarization fraction $s \equiv S_3/S_0$. (a) Perfect linear polarization ($s = 0$) results in a hyperfine center independent of the state asymmetry ι, even for maximally asymmetric case of $\iota = 1$ shown here. (b) Fully left-handed circular polarization drives only the σ^+ transitions, resulting in a hyperfine center of $\nu_c = 2/3 \times \Delta_{\mathrm{HFS}_{1/2}} \simeq 336.6\,\mathrm{kHz}$ according to Eq. (2.50), in agreement with the "Big Model" simulation, taking the 0.8 kHz (Voigt fit) and 1.5 kHz (Fano-Voigt fit) fit corrections into account. (c) Fully right-handed circular polarization addresses only the $F = 3/2$ hyperfine component of the $6P_{1/2}$ state (recall Fig. 2.8), such that the hyperfine center corresponds to $\nu_c = \Delta_{\mathrm{HFS}_{1/2}} \simeq 505\,\mathrm{kHz}$. (d) $\iota = 0.2$ and $s = -0.1$ results in a line shift of $\Delta\nu_{\iota s,1/2} \simeq 1.5\,\mathrm{kHz}$ compared to the case $s = 0$ or $\iota = 0$, in agreement with the prediction from Eq. (2.51).

offset due to the fit of two unresolved resonances with a single Fano-Voigt function is added to the perturabative model prediction from Eq. (2.68).

Fig. 2.16 shows the "Big Model" simulations with a non-zero circular polarization $s \equiv S_3/S_0$ of the 2S-6P excitation light in combination with the initial state asymmetry ι, which has been discussed in Section 2.4.2. For reference, Fig. 2.16(a) shows the case $s = 0$ for $\iota = 1$, which gives the same result as any non-zero s with $\iota = 0$ or any non-zero ι with $s = 0$. In Fig. 2.16(b), only the σ^- excitation takes place from the $2S_{1/2}$, $m_F = +1/2$ initially populated state ($s = -1$, $\iota = 1$). According to Eq. (2.50), the hyperfine center is $\nu_c = 2/3 \times \Delta_{\mathrm{HFS}_{1/2}} \simeq 336.6\,\mathrm{kHz}$, which agrees with the "Big Model" simulation taking the 0.8 kHz (Voigt fit) and 1.5 kHz (Fano-Voigt fit) fit corrections into account. In Fig. 2.16(c), only the σ^+ excitation takes place from the $2S_{1/2}$, $m_F = +1/2$ initially populated state ($s = 1$, $\iota = 1$). Recalling the right level scheme in Fig. 2.8, only the $F = 3/2$ hyperfine component is excited. Therefore, the hyperfine center is $\nu_c = \Delta_{\mathrm{HFS}_{1/2}}$. In Fig. 2.16(d), both imperfections are small, $\iota = 0.2$ and $s = -0.1$, resulting in a line shift of $\Delta\nu_{\iota s,1/2} \simeq 1.5\,\mathrm{kHz}$ in agreement with the prediction from Eq. (2.51).

In conclusion, the "Big Model" confirms the double suppression of unresolved quantum interference as well as the double suppression of the line shift due to residual circular polarization. Both effects are suppressed by the small initial state asymmetry factor ι. Additionally, the line shift due to unresolved quantum interference is multiplied by the detection imbalance of the detector $\xi_\circ$, such that the effect is suppressed by the combined factor $\iota \times \xi_\circ$,

with Eq. (2.69) predicting the magnitude of the line shift. The line shift due to residual polarization s is suppressed by the combined factor $\iota \times s$, which is calculated with Eq. (2.51).

2.6 Light force shift

To suppress the first-order Doppler shift of the 2S-6P transition, our experiment uses two counter-propagating beams, which cross the atomic beam at an angle of approximately 90°. The details and challenges of achieving the Doppler suppression with such a method are discussed in Chapter 4, which also discusses the possible residual first-order Doppler effect due to imperfections of this technique. Here, we assume a perfect standing wave formed by the two counter-propagating beams (i.e. we assume perfect cancellation of the Doppler effect) and discuss only the effect of the light force acting on the atoms. The standing wave can be viewed as a light grating causing diffraction of an atomic matter wave, just like a mechanical grating causes diffraction of a light wave. The interaction of the atom with this grating causes a shift of the observed resonance line, which we call the light force shift (LFS).

The LFS for the 2S-6P transition in hydrogen has been thoroughly treated in the thesis of Lothar Maisenbacher, see Ch. 3 of [71]. For details, for instance on the coherence properties of atoms and the quantum mechanical description of the atomic beam, we refer to this thesis. Here, the main conclusions on the LFS are summarized and the focus lies on the differences to the 2S-6P transition in deuterium. Based on the work described in [71], in this thesis the LFS model is extended to deuterium and the results are compared to hydrogen.

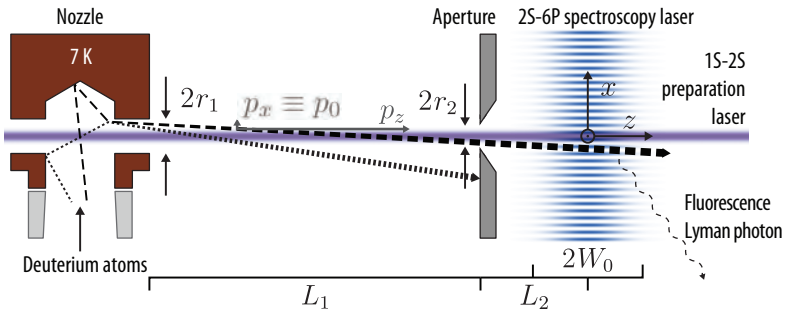

Figure 2.17: The basic scheme of the 2S-6P deuterium spectroscopy experiment as relevant for the theoretical consideration of the light force shift (not to scale). Deuterium atoms escape from the orifice (radius $r_1 = 1\,\mathrm{mm}$) of a copper nozzle (cooled to $T_\mathrm{N} \sim 7\,K$) along the z direction, where they are excited into the initial 2S state $|\mathrm{i}\rangle$ by the 1S-2S preparation laser (243 nm wavelength, shown in purple). An aperture (width $2r_2 = 1.2\,\mathrm{mm}$) is placed $L_1 = 154\,\mathrm{mm}$ after the nozzle to constrain the atomic beam. Following the distance $L_2 = 50\,\mathrm{mm}$ after the aperture, the atoms are excited by two counter-propagating beams of the 2S-6P spectroscopy laser (410 nm wavelength, $1/e^2$ intensity radius $W_0 = 2.2\,\mathrm{mm}$, shown in blue) into the excited 6P state $|\mathrm{e}\rangle$. These two counter-propagating beams form an intensity standing wave (light grating) in the x direction with periodicity of 205 nm. The atom momentum in this direction, $p_x \equiv p_0$, determines the diffraction effect of the atomic matter wave on the light grating, which modifies the interaction and leads to the light force shift while probing the 2S-6P transition. The wiggly line shows a fluorescence photon of the Lyman decay from the 6P excited state $|\mathrm{e}\rangle$ to the 1S ground state $|\mathrm{f}\rangle$, which serves as a signal for the experiment. Figure adapted from [71], where the light force shift for the 2S-6P transition in hydrogen is treated in detail, and upon which the extension of the LFS model to deuterium is based here.

2.6.1 Experimental scheme as relevant for modeling the light force shift

The basic scheme of the experiment as relevant for the theoretical consideration of the LFS is shown in Fig. 2.17. Deuterium atoms are guided into a T-shaped copper nozzle at a temperature of $T_{\mathrm{N}} \sim 7\,K$ and escape through an orifice with $r_1 = 1\,\mathrm{mm}$ radius. The complications of the atomic beam formation (see Section 3.6.1) are not important for the discussion here. Fig. 2.17 shows the x-z plane of the experiment, where the atom has a momentum (p_x, p_y, p_z). The atomic beam is formed along the z direction, where the 1S-2S preparation laser (purple) excites the atoms from the 1S ground state $|\mathrm{f}\rangle$ to the 2S initial state $|\mathrm{i}\rangle$. An aperture with width $2r_2 = 1.2\,\mathrm{mm}$, which is placed at a distance of $L_1 = 154\,\mathrm{mm}$ after the nozzle, constraints the beam, such that only atoms with $p_z \gg p_x, p_y$ are probed. After a further distance of $L_2 = 50\,\mathrm{mm}$ the atoms reach the interaction region where the 2S-6P transition is probed. The atoms are excited from the initial 2S state $|\mathrm{i}\rangle$ into the excited 6P state $|\mathrm{e}\rangle$. This excitation is achieved by the intensity standing wave (periodicity of 205 nm) formed in the x direction by two counter-propagating beams of the spectroscopy laser (410 nm wavelength, $1/e^2$ intensity radius $W_0 = 2.2\,\mathrm{mm}$). The Lyman decay from the 6P state $|\mathrm{e}\rangle$ to the 1S ground state $|\mathrm{f}\rangle$ produces fluorescence photons which serve as a signal to probe the 2S-6P transition.

The decisive parameter for the description of the LFS is the momentum in the x direction, which we denote as $p_x \equiv p_0$. We can restrict the momentum state to the x direction of the standing wave for the following reasons. First, consider the dipole potential produced by the counter-propagating laser beams. Even though the light grating is only present along the x direction, the light wavevector $\vec{K}_{\mathrm{L}}$ is not everywhere exactly parallel to the x axis because the laser beams follow a caustic. However, the contribution of the wavevector along y and z, $K_{\mathrm{L},y}$ and $K_{\mathrm{L},z}$, is much smaller than along x, $K_{\mathrm{L},y}, K_{\mathrm{L},z} \ll K_{\mathrm{L},x} \equiv K_{\mathrm{L}}$. Second, consider spontaneous emission, which can randomly change the momentum state of the atom in all of the three spatial directions. However, the change in the y position of the atom due to the recoil produced by the emission of photons is negligible compared to the beam size. Along the atomic beam axis z, the velocity $v_z \sim 50 \ldots 250\,\mathrm{m/s}$ is much larger than the recoil velocity $v_{\mathrm{rec}} \sim 0.5\,\mathrm{m/s}$, such that the photon recoil does not significantly change v_z and hence the interaction time stays approximately the same.

2.6.2 Transverse coherence length

The description of the light force on atoms is often treated semi-classically, where atoms are described as classical well-localized particles, as for example to describe laser cooling [149]. Furthermore, this treatment successfully describes other experiments, for instance the observation of laser confinement of neutral atoms in a standing wave of light, as well as their channeling into paths between the peaks of the standing wave [150]. However, the description of our experiment requires another approximation, where atoms are almost delocalized and are approximated as plane waves. Which description is applicable to the experiment is determined by the coherence properties of atoms compared to the properties of the interaction with the light grating, which we discuss in the following.

The transverse coherence length $l_{\mathrm{c,t},2}$ of atoms in the 2S-6P interaction region, i.e. after a distance of $L = L_1 + L_2$ after the nozzle, is given by (see Eq. (3.24) of [71]):

$$l_{\mathrm{c,t},2} \simeq \sqrt{l_{\mathrm{c,t},0}^2 + \left(\frac{1}{\pi}\frac{L}{r_1}\lambda_{\mathrm{dB}}\right)^2} \simeq \frac{1}{\pi}\frac{L}{r_1}\lambda_{\mathrm{dB}} \sim 50 \ldots 300\,\mathrm{nm}, \tag{2.76}$$

where $l_{\mathrm{c,t,0}} \sim \lambda_{\mathrm{dB,th}}$ is the coherence length of atoms at the nozzle, which approximately corresponds to thermal de Broglie wavelength $\lambda_{\mathrm{dB,th}} = h/\sqrt{2\pi m_{\mathrm{D}} k_{\mathrm{B}} T_{\mathrm{N}}} \simeq 0.5\,\mathrm{nm}$ of deuterium atoms with mass m_{D} at the nozzle temperature T_{N} (h is the Planck constant and k_{B} is the Boltzmann constant). The de Broglie wavelength $\lambda_{\mathrm{dB}} = h/(m_{\mathrm{D}}\, v) \sim 1 \ldots 4\,\mathrm{nm}$ for velocities $v \sim 50 \ldots 250\,\mathrm{m/s}$ (see Table 3.2) is similar to $\lambda_{\mathrm{dB,th}}$. The factor L/r_1 can be thought of as the geometrical enhancement during propagation, where $L = 204\,\mathrm{mm}$ is the total distance from the nozzle to the interaction region. This enhancement of the coherence length is described by the van Cittert-Zernike theorem, which explains how an incoherent source appears coherent in the far field [151]. The intermediate aperture increases the coherence length by a factor $\sqrt{1 + (L_2\, r_1)^2/(L\, r_2)^2} \simeq 1.1$ (see Eq. (3.31) of [71]), which is close to one and therefore has a negligible effect in our case ($L_2/L \simeq 0.25$ and $r_1/r_2 = 1.67$).

The transverse coherence length $l_{\mathrm{c,t,2}}$ is comparable to the periodicity of the grating ($\lambda_{\mathrm{2S\text{-}6P}}/2 = 205\,\mathrm{nm}$):

$$l_{\mathrm{c,t,2}} \approx \frac{\lambda_{\mathrm{2S\text{-}6P}}}{2}. \tag{2.77}$$

Therefore, it is not appropriate to describe the atoms as classical localized particles. Instead, the atoms must be treated quantum mechanically as delocalized waves. For the quantum mechanical description of an atom in the context of the light force shift, the atomic state should then be described in a combined basis $|n\rangle|p\rangle$, where the internal electronic energy state of the atom $|n\rangle$ is combined with the external momentum state $|p\rangle$. As described above, we can restrict the description of the momentum state to the x direction, such that the combined state is $|n\rangle|p\rangle_x$. The interaction of light with the atoms changes both, the internal and external states: an absorbed or emitted photon changes the external momentum state by the photon momentum $\hbar K_L$, but also drives the transitions between the internal energy levels. The energy difference between the combined states is then determined not only by the internal electronic energy difference, but also by the kinetic energy difference, which depends on the number of photon recoils.

2.6.3 Transverse momentum coherence

An atom with a defined momentum state corresponds to a plane wave which is fully delocalized. In reality, the atomic beam is localized, which corresponds to a superposition of many plane waves following a certain momentum distribution, thereby forming a localized wave packet. However, the coherence between different momentum states can be neglected in our case, and we can treat the superposition of many momentum states as an incoherent sum. This simplification is justified in the following by considerung the transverse momentum coherence scale.

It is important to note that the transverse *momentum* coherence scale is, in constrast to the transverse coherence *length*, not enhanced during propagation [71]. Without an intermediate aperture, the transverse momentum coherence scale $p_{\mathrm{c,t,2}}$ in the interaction region is then equal to the transverse momentum coherence scale $p_{\mathrm{c,t,0}}$ at the nozzle. An intermediate aperture modifies $p_{\mathrm{c,t,0}}$ by the factor of $\sqrt{r_1^2 + r_2^2}/r_2 \simeq 2$ (with $r_1 = 1\,\mathrm{mm}$, $r_2 = 0.6\,\mathrm{mm}$). The expression for $p_{\mathrm{c,t,2}}$ can be obtained from the quantum mechanical description of the atomic beam using the first-order correlation function and the Wigner function which describes the quasiprobability distribution in the position and momentum space [71]:

$$p_{\mathrm{c,t,2}} \simeq \frac{\sqrt{r_1^2 + r_2^2}}{r_2} p_{\mathrm{c,t,0}} \simeq \frac{\sqrt{r_1^2 + r_2^2}}{r_2} \times \frac{2\,\hbar}{r_1} \sim m_{\mathrm{D}} \times 1.2 \times 10^{-4}\,\mathrm{m/s}. \tag{2.78}$$

Intuitively, this momentum coherence scale (i.e. maximum momentum difference two states can have to still interfere) approximately corresponds to the estimate from the Heisenbergs uncertainty principle with $p_{\mathrm{c,t,0}}\, r_1 \sim h$.

The momentum coherence determines the visibility of interference created by the initial momentum difference between the two interfering paths. In our case, this relates to the question whether two different initial momentum states of atoms interfere, or whether they can be treated independently. The tranverse momentum scale of the atom-light interaction is given by the photon momentum $\hbar K_{\mathrm{L}} = m_{\mathrm{D}} v_{\mathrm{rec}} \sim m_{\mathrm{D}} \times 0.5\,\mathrm{m/s}$, where $K_{\mathrm{L}} = 2\pi/\lambda_{\text{2S-6P}}$ is the wavenumber of the 2S-6P spectroscopy laser beams of $\lambda_{\text{2S-6P}} = 410\,\mathrm{nm}$ wavelength, and v_{rec} the recoil velocity. The transverse momentum coherence scale $p_{\mathrm{c,t,2}}$ is several orders of magnitude smaller than this characteristic momentum scale of the light force:

$$p_{\mathrm{c,t,2}} \ll \hbar K_{\mathrm{L}}. \tag{2.79}$$

Therefore, different initial momentum states do not interfere and can be treated as an incoherent superposition: the density matrix in momentum space can be approximated as diagonal because the coherence between different initial momentum states rapidly drops to zero. The light force shift can thus be modelled as an incoherent sum of fully delocalized atoms, i.e. plane waves with a certain initial momentum p_0 along the x direction of the light grating. We only need to consider the case of the light force shift for a single atom with a certain p_0 and can then simply sum the signal contributions of N_{traj} (classical) atom trajectories as described in Section 3.3.1.

2.6.4 Simplified level scheme for modeling the light force shift

We now consider the light force shift for the 2S-6P transition of a single deuterium atom with a certain initial momentum p_0 along the x direction of the light grating. After the derivation of the level scheme, we model the light force shift using the optical Bloch equations. As will be shown below, the leading order LFS is independent of the possible backdecay to the initial state. However, for our uncertainty goal, the effect of the backdecay to the same initial state makes a significant difference, and is crucial to be included into the model. Therefore, we examine the level scheme with possible backdecays to the initial states.

2.6.4.1 Internal initial and excited states with effective backdecay rates

First, let us examine the level scheme of the involved internal initial and excited states. Recalling Fig. 2.2, our 2S-6P transition frequency measurement in deuterium involves two initial $2\mathrm{S}_{1/2}^{F=1/2}$ states: $m_F = -1/2$ and $m_F = +1/2$. From each of the two initial states two 6P states are excited: $6\mathrm{P}_J^{F=1/2}$ and $6\mathrm{P}_J^{F=3/2}$, where $J = 1/2$ or $J = 3/2$ gives the probed fine-structure component. The involved initial and excited states are visualized in Fig. 2.18. From each of the excited states there are two backdecays to the $2\mathrm{S}_{1/2}^{F=1/2}$ states: π backdecays to the same m_F initial state with rates $\gamma_{\mathrm{ei}}^{F=1/2}$ and $\gamma_{\mathrm{ei}}^{F=3/2}$, and σ backdecays to the other m_F initial state with rates $\gamma_{\mathrm{ei_2}}^{F=1/2}$ and $\gamma_{\mathrm{ei_2}}^{F=3/2}$, respectively for the decays from the $6\mathrm{P}_J^{F=1/2}$ and $6\mathrm{P}_J^{F=3/2}$ excited states. It is important to realize that the mixture of the $m_F = -1/2$ and $m_F = +1/2$ initial states is incoherent, such that we can treat these states independently. Since the level scheme is symmetric under swapping the $m_F = -1/2$ and $m_F = +1/2$ states, their excitation and decay patterns are equivalent, as illustrated by the left and center level schemes in Fig. 2.18.

Furthermore, we consider the $F = 1/2$ and $F = 3/2$ excited states effectively as a single excited state[1], as illustrated in the right scheme of Fig. 2.18. In our case we consider the weak excitation regime $(\Omega\, t)^2 \ll 1$, such that the excitation rate is proportional to $\Omega^2 \propto d^2$, where Ω is the Rabi frequency, t the interaction time and d^2 the squared dipole moment. Therefore, the effective π and σ backdecay rates, γ_{ei} and γ_{ei_2}, need then to be weighted according to the squared dipole moments $d^2_{F=1/2}$ and $d^2_{F=3/2}$ for the transitions to the $F = 1/2$ and $F = 3/2$ states:

$$\gamma_{\mathrm{ei}} = \frac{d^2_{F=1/2}\gamma_{\mathrm{ei}}^{F=1/2} + d^2_{F=3/2}\gamma_{\mathrm{ei}}^{F=3/2}}{d^2_{F=1/2} + d^2_{F=3/2}}, \quad \gamma_{\mathrm{ei}_2} = \frac{d^2_{F=1/2}\gamma_{\mathrm{ei}_2}^{F=1/2} + d^2_{F=3/2}\gamma_{\mathrm{ei}_2}^{F=3/2}}{d^2_{F=1/2} + d^2_{F=3/2}}. \tag{2.80}$$

For $J = 1/2$, the squared dipole moment ratio is $d^2_{F=3/2}/d^2_{F=1/2} = 8$ (see Table 2.4), and for $J = 3/2$ it is $d^2_{F=3/2}/d^2_{F=1/2} = 10/8$ (see Table 2.5). The backdecay rates are summarized in Table 2.6, where the effective decay rates γ_{ei} and γ_{ei_2}, as well as the total backdecay rate $\gamma_{\mathrm{ei}} + \gamma_{\mathrm{ei}_2}$ are also given normalized to the total decay rates $\Gamma_{1/2} = 3\,898\,157\,\mathrm{Hz}$ ($J = 1/2$) and $\Gamma_{3/2} = 3\,898\,162\,\mathrm{Hz}$ ($J = 3/2$) (see discussion below Eq. (2.23) regarding the uncertainty of these values). For both the $2\mathrm{S}_{1/2}$-$6\mathrm{P}_{1/2}$ and $2\mathrm{S}_{1/2}$-$6\mathrm{P}_{3/2}$ transitions in deuterium, the total effective backdecay fractions of 4.75% and 8.21% are similar to, but slightly higher than, the corresponding values for hydrogen (3.89% and 7.78%, respectively).

The involved internal initial and excited states are then reduced to the rightmost level scheme in Fig. 2.18. Note that we cannot reduce the scheme to only two levels, since the σ backdecay brings the atom into a different initial state, not the same initial state from which the atom has been excited. Starting from an initial state $|\mathrm{i}\rangle$, the atoms are excited to the state $|\mathrm{e}\rangle$, from which a π backdecay to $|\mathrm{i}\rangle$, or a σ backdecay to another state $|\mathrm{i}_2\rangle$ are possible. If the σ backdecay occurs, the atoms can be excited from $|\mathrm{i}_2\rangle$ to a second excited state $|\mathrm{e}_2\rangle$. We make the approximation that only one backdecay occurs: if a σ backdecay to $|\mathrm{i}_2\rangle$ occured and the atoms are excited to $|\mathrm{e}_2\rangle$, no further backdecays from $|\mathrm{e}_2\rangle$ to $|\mathrm{i}\rangle$ or $|\mathrm{i}_2\rangle$ occur. The approximation of using only a single backdecay has been verified for hydrogen [71] with the Monte Carlo Wavefunction Method (MCWM) [152], where the number of backdecays is not limited[2].

2.6.4.2 Level scheme with combined internal and external states

As discussed above, to examine the light force shift we need to model the atomic state as a combination of the electronic energy level (internal state) and the momentum of the atom (external state). In hydrogen, there is only one initial and excited energy state involved, which leads to only one possible backdecay state manifold. Compared to hydrogen, the situation in deuterium is complicated by two possible backdecay state manifolds. The level scheme with these two possible backdecay state manifolds is shown in Fig. 2.19. Here, the

[1] Note that the effects of quantum interference between the unresolved hyperfine components $F = 1/2$ and $F = 3/2$ are investigated separately using the "Big Model" described in Section 2.5.3. The light force shift is almost identical for the two different hyperfine components. However, at some level of accuracy, also the quantum interference between the unresolved hyperfine components of different momentum states may play a role. To investigate this, the states shown in Fig. 2.19 can be extended in the future by considering both hyperfine components.

[2] The difference in the light force shift between the MCWM model and the optical Bloch equations with only one possible backdecay was found to be less than 30 Hz, corresponding to less than 4% of the light force shift, see Sec. 3.4.1 of [71].

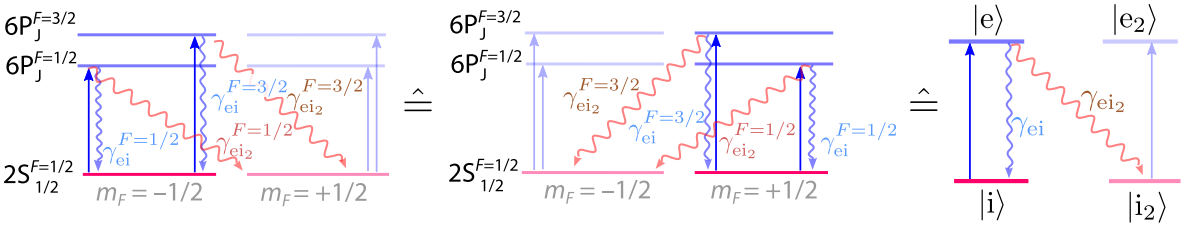

Figure 2.18: Initial and excited states for modeling the light force shift of the $2S_{1/2}^{F=1/2}$-$6P_J$ transitions in deuterium. Recalling Fig. 2.2, two initial states with $m_F = \pm 1/2$ are involved. From each of the two excited state manifolds $6P_J^{F=1/2}$ and $6P_J^{F=3/2}$, where $J = 1/2$ or $J = 3/2$ identifies the probed fine-structure component, there are two possible backdecays to the $2S_{1/2}^{F=1/2}$ states: π backdecays to the same m_F state (shown as blue wiggly arrows, decay rates $\gamma_{ei}^{F=1/2}$ and $\gamma_{ei}^{F=3/2}$) and σ backdecays to the other m_F state (shown as red wiggly arrows, backdecay rates $\gamma_{ei_2}^{F=1/2}$ and $\gamma_{ei_2}^{F=3/2}$). Since the two initial states are in an incoherent superposition, considering the excitation from only one of the initial states is sufficient due to the symmetry, which is illustrated by the equivalence of the left and center level schemes. Furthermore, the two excited states can be modelled effectively as a single excited state, with the effective backdecay rate weighted according to Eq. (2.80). Then the left and center level schemes are reduced to the right level scheme: starting from an initial state $|i\rangle$, the atoms are excited to the state $|e\rangle$, from which a π backdecay to $|i\rangle$, or a σ backdecay to another state $|i_2\rangle$ are possible. After a σ backdecay, the atoms can be excited from $|i_2\rangle$ to a second excited state $|e_2\rangle$.

	π backdecay rates (Hz)			σ backdecay rates (Hz)			Total backdecay rate (Hz)
	$\gamma_{ei}^{F=1/2}$	$\gamma_{ei}^{F=3/2}$	γ_{ei}	$\gamma_{ei_2}^{F=1/2}$	$\gamma_{ei_2}^{F=3/2}$	γ_{ei_2}	$\gamma_{ei} + \gamma_{ei_2}$
$J = 1/2$	16 845	134 760	121 658 $\hat{=}$ 3.12%	33 690	67 379	63 636 $\hat{=}$ 1.63%	185 294 $\hat{=}$ 4.75%
$J = 3/2$	134 760	168 450	153 477 $\hat{=}$ 3.94%	269 520	84 225	166 578 $\hat{=}$ 4.27%	320 055 $\hat{=}$ 8.21%

Table 2.6: Backdecay rates for the $2S_{1/2}^{F=1/2}$-$6P_J$ transitions in deuterium according to the level schemes shown in Fig. 2.18. The effective backdecay rates γ_{ei} and γ_{ei_2} are obtained with the weighting of the dipole moments, see Eq. (2.80), and correspond to the rightmost level scheme of Fig. 2.18. These effective backdecay rates as well as the total effective backdecay rate $\gamma_{ei} + \gamma_{ei_2}$ are also listed in percentage of the total decay rates $\Gamma_{1/2} = 3\,898\,157\,\text{Hz}$ ($J = 1/2$) and $\Gamma_{3/2} = 3\,898\,162\,\text{Hz}$ ($J = 3/2$). The total effective backdecay rates in deuterium are slightly higher compared to hydrogen (3.89% for $J = 1/2$ and 7.78% for $J = 3/2$). Note that the written precision of numbers exceeds the available and required accuracy, but is given for possible future comparison of simulations (see discussion below Eq. (2.23) regarding the relative uncertainty of the decay rates, which is on the order of few parts in 10^{-5}, i.e. the numbers in this table are correct approximately up to the fifth digit).

number of occuring backdecays in each of the two backdecay state manifolds is limited to one ($N_{\text{BD,max}} = 1$). Note that $N_{\text{BD,max}} = 1$ refers to the maximum number of backdecays for a single atom, but there are two possible different backdecays, namely σ or π backdecay, which can happen. The number of photon recoils is limited[1] to two ($N_{\text{k,max}} = 2$). This results in $3 \times (2N_{\text{k,max}} + 1) = 15$ initial and excited states, plus 8 final states. These 23 states are

[1] In [71], $N_{\text{k,max}} = 4$ was used, and with the MCWM model a difference (at the resonance $p_0 = \hbar K_{\text{L}}$ where the LFS is maximal) of only less than 5 Hz to the case $N_{\text{k,max}} = 3$ is reported. Here, we find that the optical Bloch equations model with $N_{\text{k,max}} = 2$ produces values which differ by less than 5% to the case with $N_{\text{k,max}} = 3$.

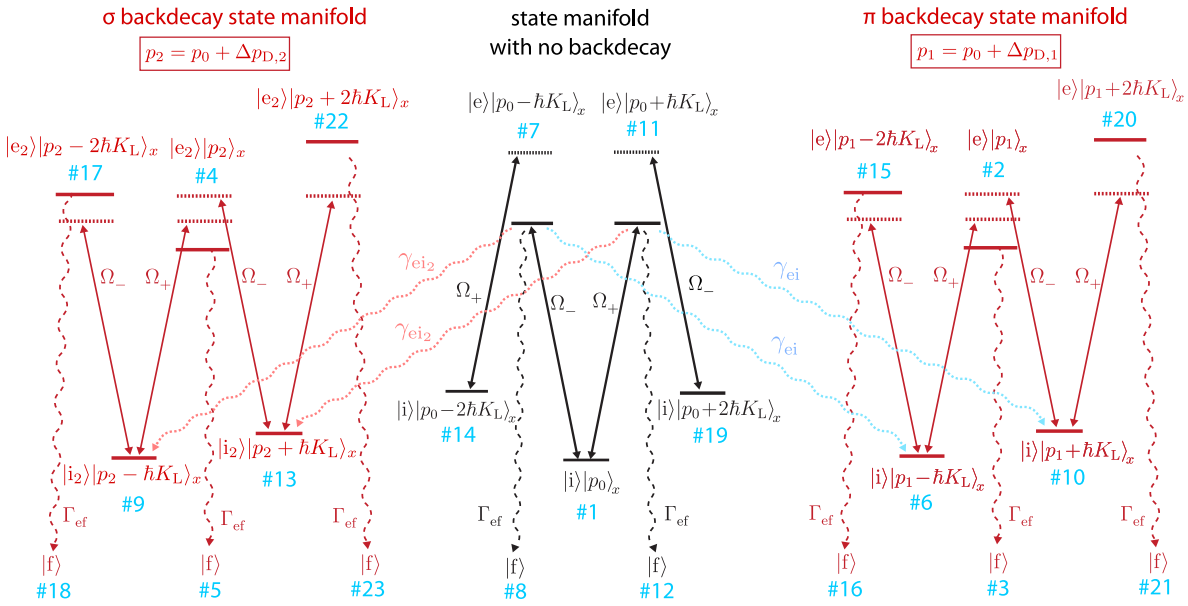

Figure 2.19: Simplified level scheme for modeling the light force shift of the $2S_{1/2}^{F=1/2}$-$6P_J$ transitions in deuterium (not to scale). The atomic state is a combination of the internal states $|n\rangle$ (2S initial states $|i\rangle$ and $|i_2\rangle$, 6P excited states $|e\rangle$ and $|e_2\rangle$, and final state $|f\rangle$) with the external momentum state $|p\rangle_x$ along the x direction of the light grating produced by the counter-propagating laser beams driving the 2S-6P transition (indicated by solid arrows, equal Rabi frequencies $\Omega_+ = \Omega_-$). The atomic state is therefore described in a combined basis $|n\rangle|p\rangle_x$. The interaction with laser light changes the initial atomic momentum p_0 by the recoil momentum $\pm\hbar K_L$, where K_L is the wavenumber. The ladder of states in principle continues to an infinite number of subsequent momentum changes, but is here limited to maximally two photon recoils. The level scheme is shown here in the laboratory frame for the case of $p_0 = 0$ and zero laser detuning such that the laser light is resonant with the transitions $|i\rangle|p_0 = 0\rangle_x \rightarrow |e\rangle| \pm \hbar K_L\rangle_x$ (#1 → #7 and #1 → #11). The dotted horizontal lines mark the laser detuning for other transitions. From the excited states $|e\rangle$, the atom can spontaneously decay to the initial states $|i\rangle$ (π backdecay with rate γ_{ei} from Table 2.6) or $|i_2\rangle$ (σ backdecay with rate γ_{ei_2} from Table 2.6) as illustrated in Fig. 2.18. This randomly changes the atomic momentum by $\Delta p_{D,1}$ or $\Delta p_{D,2} \in [-\hbar K_L, \hbar K_L]$ distributed according to Eq. (2.82) and Eq. (2.83). Furthermore, the atom can spontaneously decay to the final states $|f\rangle$ with a rate Γ_{ef}, which contributes to the signal (the momentum state does not matter for $|f\rangle$ because these states are not coupled by the laser beam).

numbered from #1 to #23.

Consider first the state manifold where no backdecay occurs (center of Fig. 2.19 in black). The atoms start in the internal state $|i\rangle$ with a momentum p_0 along the x axis such that the state is $|i\rangle|p_0\rangle_x$ (state #1). The arrows represent the two counter-propagating laser beams having equal Rabi frequencies $\Omega_+ \equiv \Omega_-$, which drive the transitions to the internal excited state $|e\rangle$. The change of the internal state by the absorption or stimulated emission of these photons changes the atomic momentum by the photon momentum $\pm\hbar K_L = \pm h\nu_L/c$, where $K_L = 2\pi/\lambda_{2S\text{-}6P} = 2\pi\nu_L/c$ is the wavenumber of the counter-propagating 2S-6P spectroscopy laser beams of wavelength $\lambda_{2S\text{-}6P}$ and frequency ν_L . This momentum change corresponds to a change in velocity by $v_{rec} = \hbar K_L/m_D \simeq 0.5\,\mathrm{m/s}$ (recoil velocity), where m_D is the mass of the deuterium atom. Because of energy conservation, the energy levels are shifted by the

kinetic energy difference $h\Delta\nu_{\mathrm{rec}} = m_{\mathrm{D}} v_{\mathrm{rec}}^2/2$, where $\Delta\nu_{\mathrm{rec}}$ is the recoil shift:

$$\Delta\nu_{\mathrm{rec}} = \frac{m_{\mathrm{D}} v_{\mathrm{rec}}^2}{2h} \simeq \frac{h\nu_{\mathrm{A,0}}^2}{2m_{\mathrm{D}}c^2}. \tag{2.81}$$

In the last step, we set the laser frequency ν_{L} to be approximately the same as the frequency $\nu_{\mathrm{A,0}}$ corresponding to the unperturbed energy difference $h\nu_{\mathrm{A,0}}$ between the 2S and 6P levels ($|\mathrm{i}\rangle$ and $|\mathrm{e}\rangle$). More energy is required for the excitation from $|\mathrm{i}\rangle$ to $|\mathrm{e}\rangle$ than the energy difference $h\nu_{\mathrm{A,0}}$ to account for the increase in the kinetic energy of the atom. We here define the laser detuning $\Delta\nu_{\text{2S-6P}}$ to be the detuning from the frequency $\nu_{\mathrm{A,0}} + \Delta\nu_{\mathrm{rec}}$, such that for zero detuning the recoil shift is taken into account. In Fig. 2.19, the level structure is shown for $\Delta\nu_{\text{2S-6P}} = 0$ and $p_0 = 0$, such that there is no Doppler shift when driving the transitions starting from the $|\mathrm{i}\rangle|p_0 = 0\rangle_x$ state, and the laser frequency is on resonance for the transitions $|\mathrm{i}\rangle|p_0 = 0\rangle_x \rightarrow |\mathrm{e}\rangle|\pm\hbar K_{\mathrm{L}}\rangle_x$ (#1 $\rightarrow$ #7 and #1 $\rightarrow$ #11).

Stimulated emission from the excited state $|\mathrm{e}\rangle$ to the initial state $|\mathrm{i}\rangle$ increases the momentum of the atom further by $\pm\hbar K_{\mathrm{L}}$, such that the atom is in the states $|\mathrm{i}\rangle|p_0 \pm 2\hbar K_{\mathrm{L}}\rangle_x$ (#14 and #19). For $p_0 = 0$, these states are shifted in energy by $h \times 4\Delta\nu_{\mathrm{rec}}$ relative to the state $|\mathrm{i}\rangle|p_0 = 0\rangle_x$ (state #1), since the kinetic energy increases by $m_{\mathrm{D}}(2v_{\mathrm{rec}})^2/2 = h \times 4\Delta\nu_{\mathrm{rec}}$. As a result, the laser is not on resonance anymore with the transitions $|\mathrm{i}\rangle|\pm 2\hbar K_{\mathrm{L}}\rangle_x \rightarrow |\mathrm{e}\rangle|\pm\hbar K_{\mathrm{L}}\rangle_x$ (#14 $\rightarrow$ #7 and #19 $\rightarrow$ #11), but is shifted from the resonance by $4\Delta\nu_{\mathrm{rec}}$ which is indicated by the dashed horizontal lines. Thus, no resonant population transfer into states $|\mathrm{i}\rangle|\pm 2\hbar K_{\mathrm{L}}\rangle_x$ (#14 and #19) is possible. However, as we will see below, for a certain values of p_0, the two-photon transitions to these states can become resonant and lead to a large LFS.

From the excited states $|\mathrm{e}\rangle|p_0 \pm \hbar K_{\mathrm{L}}\rangle_x$ (#7 and #11), the atom can either decay with a rate Γ_{ef} to the final states[1] $|\mathrm{f}\rangle$ (#8 and #12) giving rise to the signal (wiggly black dashed arrows), or via a π backdecay (with a rate γ_{ei}, wiggly dotted blue arrows) to the states $|\mathrm{i}\rangle$ (#6 and #10), or via a σ backdecay (with a rate γ_{ei_2}, wiggly dotted red arrows) to the states $|\mathrm{i}_2\rangle$ (#9 and #13).

The decays from the excited 6P states $|\mathrm{e}\rangle$ to the 1S ground states $|\mathrm{f}\rangle$ are responsible for the signal, which in simulations is obtained from the population of all the excited states $|\mathrm{e}\rangle$. The total decay rate $\Gamma = \Gamma_{\text{e-1S}} + \gamma_{\text{e-2S}}$ from the 6P levels is a sum from the decay rate $\Gamma_{\text{e-1S}}$ to the 1S manifold and the decay rate $\gamma_{\text{e-2S}}$ to the 2S manifold ($2\mathrm{S}_{1/2}^{F=1/2}$ and $2\mathrm{S}_{1/2}^{F=3/2}$ states), see Table 2.4 and Table 2.5. Note that we here restrict the decay channels of the 6P states $|\mathrm{e}\rangle$ only to the decays to the $2\mathrm{S}_{1/2}^{F=1/2}$ states $|\mathrm{i}\rangle$ and the 1S ground state $|\mathrm{f}\rangle$, i.e. the decays to the $2\mathrm{S}_{1/2}^{F=3/2}$ levels with the rate $\gamma_{\text{e-2S}} - (\gamma_{\mathrm{ei}} + \gamma_{\mathrm{ei}_2})$ are not included. This approximation is justified by the fact that the $2\mathrm{S}_{1/2}^{F=1/2}$ and $2\mathrm{S}_{1/2}^{F=3/2}$ states are separated by 41 MHz $\gg \Gamma$, such that the $2\mathrm{S}_{1/2}^{F=3/2}$ states are only off-resonantly coupled to the 6P state manifold (see Fig. 2.2). For the simulations of the light force shift, the decay rate Γ_{ef} is set to the difference between the total decay rate and the total effective backdecay rate: $\Gamma_{\mathrm{ef}} = \Gamma - (\gamma_{\mathrm{ei}} + \gamma_{\mathrm{ei}_2})$. Thereby, the linewidth of the excited levels matches the natural linewidth Γ.

The π and σ backdecays open additional state manifolds (shown in red), where again the atomic internal and external states are changed by the interaction with the counter-propagating laser beams. Similar to the state manifold with no backdecay, we consider only momentum changes with up to two photon recoils ($N_{\mathrm{k,max}} = 2$). The backdecays occur via the spontaneous emission following the radiation pattern of the π or σ decays in all spatial

[1] Since the final states are not coupled by the laser beam, their momentum state is of no interest and is therefore left out.

directions. For the light force shift, only the projection onto the x direction matters. We denote the momentum change along x due to the spontaneous backdecay as $\Delta p_{\mathrm{D},1}$ (π backdecay) and $\Delta p_{\mathrm{D},2}$ (σ backdecay). The values are in the range $\Delta p_{\mathrm{D},1}, \Delta p_{\mathrm{D},2} \in [-\hbar K_L, \hbar K_L]$ with normalized probability densities of (see Appendix A.3.3):

$$\mathcal{N}_{\pi}^{\hat{x}}(\Delta p_{\mathrm{D},1}) = \frac{3}{8}\left(1 + \Delta p_{\mathrm{D},1}^2/(\hbar K_{\mathrm{L}})^2\right) \quad (\pi \text{ backdecays}), \tag{2.82}$$

$$\mathcal{N}_{\sigma^{\pm}}^{\hat{x}}(\Delta p_{\mathrm{D},2}) = \frac{3}{16}\left(3 - \Delta p_{\mathrm{D},2}^2/(\hbar K_{\mathrm{L}})^2\right) \quad (\sigma^{\pm} \text{ backdecays}), \tag{2.83}$$

for $|\Delta p_{\mathrm{D},1}/(\hbar K_{\mathrm{L}})| \leq 1$ or $|\Delta p_{\mathrm{D},2}/(\hbar K_{\mathrm{L}})| \leq 1$, and $\mathcal{N}_{\pi}^{\hat{x}}(\Delta p_{\mathrm{D},1}) = 0$ or $\mathcal{N}_{\sigma^{\pm}}^{\hat{x}}(\Delta p_{\mathrm{D},2}) = 0$ else. We first discuss the LFS for certain values of p_0 for fixed $\Delta p_{\mathrm{D},1}$ and $\Delta p_{\mathrm{D},2}$. Next, we evaluate the LFS as a function of $\Delta p_{\mathrm{D},1}$ and $\Delta p_{\mathrm{D},2}$. Finally, we average the LFS over $\Delta p_{\mathrm{D},1}$ and $\Delta p_{\mathrm{D},2}$ according to the probability densities from above, and evaluate the result as a function of p_0. This result then corresponds to the LFS for a given atomic trajectory[1] with a certain p_0. As discussed in Section 2.6.3, in our case the LFS for an atomic beam can be modelled as an incoherent sum of delocalized atoms, i.e. plane waves with a certain initial momentum p_0 along the x direction of the light grating. The signal contributions of N_{traj} atom trajectories (each having a certain value of p_0) can then simply be summed to obtain the LFS for an atomic beam, analogous to the 'Big Model' simulations described in Section 3.3.2.

2.6.5 Light force shift simulation results for single atomic trajectories

2.6.5.1 Light force shift for certain values of initial atomic momentum

We will see below that the effect of backdecay significantly affects the light force shift only for $p_0 \gtrsim 1.2\hbar K_{\mathrm{L}}$ (which for example corresponds for $v_z = 200\,\mathrm{m/s}$ to the transverse angles of $\delta\alpha \simeq v_x/v_z = p_0/(m_{\mathrm{D}} v_z) \gtrsim 2.9\,\mathrm{mrad}$). Though the contribution of the backdecay is important for our accuracy goal, its effect is (for $p_0 \gtrsim 1.2\hbar K_{\mathrm{L}}$) only on the order of few kHz, which is less than a fraction of 10^{-3} of the natural linewidth (3.9 MHz). To discuss the effect of the light force shift for $p_0 \lesssim 1.2\hbar K_{\mathrm{L}}$, which is predominantly produced by the state manifold with no backdecay, we therefore first fix the values $\Delta p_{\mathrm{D},1}$ and $\Delta p_{\mathrm{D},2}$ to some specific numbers ($\Delta p_{\mathrm{D},1} = -0.86\,\hbar K_{\mathrm{L}}$ and $\Delta p_{\mathrm{D},2} = -0.34\,\hbar K_{\mathrm{L}}$, which are two exemplary values from the set of four points used below for the Gaussian quadrature to average over the backdecay momenta).

The level scheme in Fig. 2.19 is used to derive the optical Bloch equations (master equation in the Lindblad form), which have been introduced in Section 2.5.3. Note that they include possible quantum interference between the states shown in Fig. 2.19[2], but not the effects from other electronic states, which are not taken into account in the LFS model, but instead evaluated with the 'Big Model' (e.g. resolved quantum interference between the fine-structure components or unresolved quantum interference between the hyperfine-structure components).

[1] Note that since the "trajectory" has a certain p_0, such a "trajectory" is in fact not localized. However, we may still call such a case a "trajectory", since, as discussed in Section 2.6.3, in our case the localized atomic beam can be described as an incoherent sum of many delocalized "trajectories", each with a certain p_0.

[2] For example, the time evolution of the coherence between the states #7 and #11, $\Delta\rho_{7,11}/\Delta t$ (where $\rho_{i,j}$ is the density matrix entry for states #i and #j) depends on the product of the coherence $\rho_{6,10}$ and the cross-damping constant $\gamma_{6,10}$ between the states #6 and #10, which is a manifestation of quantum interference (cross-damping).

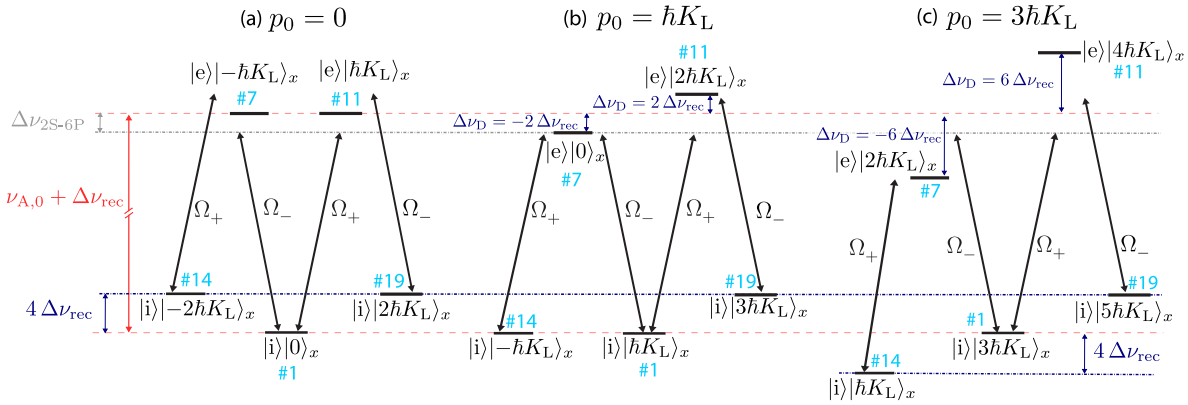

Figure 2.20: Similar to Fig. 2.19, but showing only state manifolds with no backdecay. The laser detuning $\Delta\nu_{2S\text{-}6P}$ (gray dash-dotted line) is defined from the resonance frequency $\nu_{A,0}+\Delta\nu_\mathrm{rec}$ between the 2S ($|\mathrm{i}\rangle$) and 6P ($|\mathrm{e}\rangle$) states for zero p_0, i.e. including the recoil shift. The detuning is here chosen to be $\Delta\nu_{2S\text{-}6P} = -2\Delta\nu_\mathrm{rec}$. Three cases of initial transverse momentum of the atom p_0 are shown: (a) zero p_0 (as in Fig. 2.19) where no Doppler shift is present, (b) $p_0 = \hbar K_\mathrm{L}$ where the Doppler shift is $\pm 2\Delta\nu_\mathrm{rec}$, and (c) $p_0 = 3\hbar K_\mathrm{L}$ resulting in a Doppler shift $\pm 6\Delta\nu_\mathrm{rec}$ (see Eq. (2.85)). For the chosen detuning, the case in (b) shows a resonance of the one-photon transition between the states #1 and #7. Note that the two-photon transition between the states #1 and #14 is on resonance independent of the detuning, which originates from the equal energies of states #1 and #14 (where the two photon recoils lead to the reversed velocity of the atom but with the same magnitude such that its kinetic energy remains unchanged). This case corresponds to the Bragg condition of an atomic matter wave diffracted by the light grating, thereby resulting in a large light force shift. For other values of p_0, the states #1 and #14 always have different energies, and the resulting light force shift is much smaller. The corresponding simulations of resonance lines along with the values for the light force shift $\Delta\nu_{0,\mathrm{LFS}}$ are shown in Fig. 2.21.

The energy between the states is determined by the internal electronic state energy difference and the kinetic energy difference. Therefore, the first-order Doppler shift and the recoil shift are intrinsically included in the LFS model. Recall that we here define the laser detuning $\Delta\nu_{2S\text{-}6P}$ to be the detuning from the frequency $\nu_{A,0} + \Delta\nu_\mathrm{rec}$, i.e. for zero detuning the recoil shift is taken into account. Fig. 2.20 illustrates three specific cases of the energy differences between the levels for the state manifold with no backdecay.

Fig. 2.20(a) shows the case $p_0 = 0$ which corresponds to the center level scheme of Fig. 2.19. In constrast to Fig. 2.19, the detuning is here exemplarily set to $\Delta\nu_{2S\text{-}6P} = -2\Delta\nu_\mathrm{rec}$, and thus below the resonance. Since the transverse velocity of the atom is zero, there is no Doppler shift of the transitions $|\mathrm{i}\rangle|0\rangle_x \to |\mathrm{e}\rangle|\pm\hbar K_\mathrm{L}\rangle_x$ (#1 $\to$ #7 and #1 $\to$ #11). The levels $|\mathrm{i}\rangle|\pm 2\hbar K_\mathrm{L}\rangle_x$ (#14 and #19) are shifted in frequency by $4\Delta\nu_\mathrm{rec}$ since the atomic velocity increases by $\pm 2v_\mathrm{rec}$ and thus the shift due to the increase in kinetic energy is $m_\mathrm{D}(2v_\mathrm{rec})^2/2 = h \times 4\Delta\nu_\mathrm{rec}$. Since $\Omega_+ = \Omega_- \equiv \Omega$, the level scheme is symmetric and can effectively be reduced to only three levels. This corresponds to a Λ system in the context of electromagnetically induced

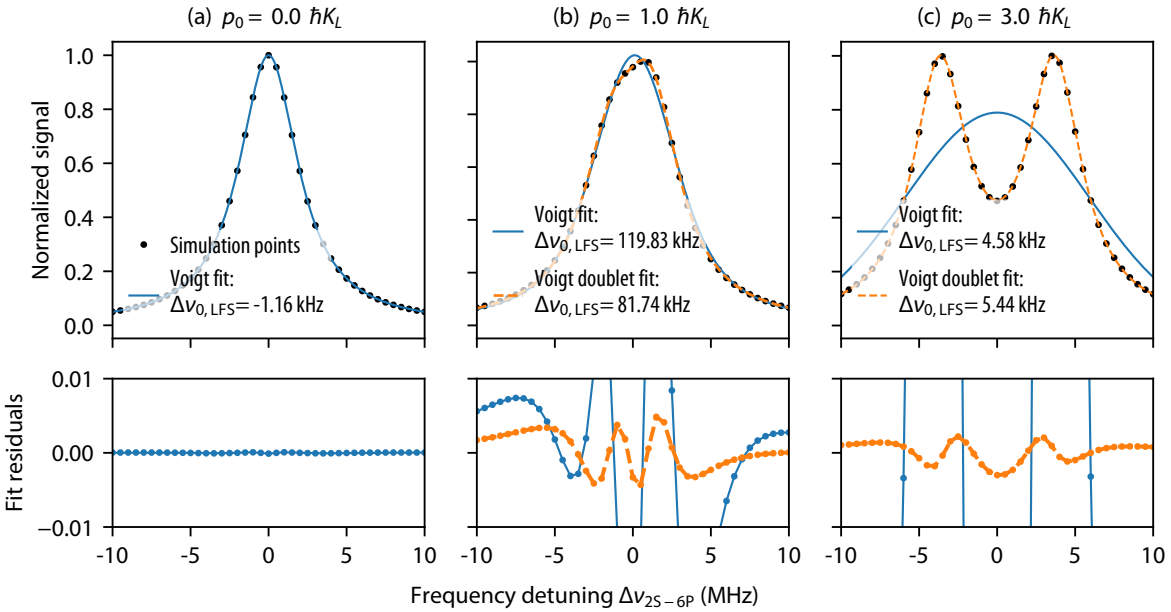

Figure 2.21: Examples of simulated resonance lines of the $2S_{1/2}^{F=1/2}$-$6P_{1/2}$ transition in deuterium with the light force shift model for the three cases of p_0 shown in Fig. 2.20. The simulation points (black markers) were obtained by numerically solving the optical Bloch equations using the level scheme in Fig. 2.19 with $\Delta p_{\mathrm{D},1} = -0.86\,\hbar K_{\mathrm{L}}$ and $\Delta p_{\mathrm{D},2} = -0.34\,\hbar K_{\mathrm{L}}$, $P_{\mathrm{2S\text{-}6P}} = 30\,\mu\mathrm{W}$, $W_0 = 2.2\,\mathrm{mm}$, $v = 200\,\mathrm{m/s}$. For the case of zero p_0 shown in (a), the light force shift (LFS) can be estimated using Eq. (2.84), resulting in $\Delta\nu_{0,\mathrm{LFS}} \simeq -1\,\mathrm{kHz}$. This agrees with the result from the fitted line center using the Voigt (solid blue curve) fit function. The bottom plot shows the residuals, which are for the case of zero p_0 on the level 0.01% (not seen on the shown scale). For non-zero p_0, two Doppler-shifted resonance lines appear, though for $p_0 \lesssim 2\hbar K_{\mathrm{L}}$ there are only partially resolved. Therefore, in (b) and (c) the signal is also fitted with Voigt doublet (orange dashed curve) fit function, and the LFS is calculated from the weighted mean of the two center frequencies according to Eq. (2.86). In (b), the initial transverse atom momentum is equal to the recoil momentum, which results in a resonance shown in Fig. 2.20(b) for the red-shifted transition and leads to a large LFS around 100 kHz. In (c), for $p_0 = 3\hbar K_{\mathrm{L}}$, the Doppler-shifted peaks are well separated, and the small LFS of few kHz is dominated by the backdecay (as demonstrated in Fig. 2.23 below).

transparency [153][1]. In our case, as first pointed out by Lothar Maisenbacher[2], one can analytically derive from this Λ model that the light force shift $\Delta\nu_{0,\mathrm{LFS}}$ of an atom with

[1] In the notation of Fig. 5 in [153], our case corresponds to: $|1\rangle = |\mathrm{i}\rangle|0\rangle_x$ (state #1), $|3\rangle = |\mathrm{e}\rangle| \pm \hbar K_{\mathrm{L}}\rangle_x$ (states #7 and #11), $|2\rangle = |\mathrm{e}\rangle| \pm 2\hbar K_{\mathrm{L}}\rangle_x$ (states #14 and #19), equal probe and control Rabi frequencies $\Omega_{\mathrm{p}} = \Omega_{\mathrm{c}} = \Omega$, detunings $\Delta_1 = \omega_{31} - \omega_{\mathrm{p}} = \Delta\nu_{\mathrm{2S\text{-}6P}}$ and $\Delta_2 = \omega_{32} - \omega_{\mathrm{c}} = 4\Delta\nu_{\mathrm{rec}} + \Delta_1$, equal decay rates $\Gamma_{31} = \Gamma_{32} = \Gamma_{\mathrm{ef}}$. Though the initial level scheme is the same, for electromagnetically induced transparency, typically the case $\Delta_1 = \Delta_2$ with $\Omega_{\mathrm{c}} \gg \Omega_{\mathrm{p}}$ is considered, which is not our case. However, as pointed out by Lothar Maisenbacher (private communication, unpublished), our case can be related to the approximated solution found in [153], where the probe field is treated as a weak perturbation to the system (such that no significant amount of population is transferred into state $|3\rangle$). The absorption is given by the imaginary part of the linear susceptibility $\chi^{(1)}$, from which for our case the light force shift can be deduced.

[2] Private communication (unpublished).

transverse velocity much smaller than the recoil velocity ($p_0 \ll \hbar K_\mathrm{L}$) is given by:

$$\Delta\nu_{0,\mathrm{LFS}}(p_0 \ll \hbar K_\mathrm{L}) = -\frac{|\Omega|^2}{16\,\Delta\nu_\mathrm{rec}} \times \frac{1}{1 - p_0^2/(\hbar K_\mathrm{L})^2}. \tag{2.84}$$

The above equation predicts a negative shift for $p_0 \simeq 0$. Interestingly, one may expect a negative shift from the "naive" semi-classical picture: for negative detunings $\Delta\nu_{\mathrm{2S\text{-}6P}} < 0$, the light force drives the atoms to positions where the intensity has a maximum, whereas for positive detunings $\Delta\nu_{\mathrm{2S\text{-}6P}} > 0$, the atoms are attracted to the intensity minima (see discussion below Eq. (3.16) in [149]). Therefore, there are more atoms for $\Delta\nu_{\mathrm{2S\text{-}6P}} < 0$ which interact with the intensity maxima, and the signal has a maximum for $\Delta\nu_{\mathrm{2S\text{-}6P}} < 0$ such that the center frequency is shifted towards the negative frequency, which results in a negative light force shift $\Delta\nu_{0,\mathrm{LFS}} < 0$.

The simulated resonance line of the $2\mathrm{S}_{1/2}^{F=1/2}$-$6\mathrm{P}_{1/2}$ transition in deuterium for zero p_0 is shown in Fig. 2.21 (black points). The 2S-6P laser parameters are $P_{\mathrm{2S\text{-}6P}} = 30\,\mu\mathrm{W}$ and $W_0 = 2.2\,\mathrm{mm}$, which results in an average intensity of $I_{\mathrm{2S\text{-}6P}} \sim P_{\mathrm{2S\text{-}6P}}/(\pi W_0^2) \sim 2\,\mathrm{W/m^2}$, yielding the Rabi frequency $\Omega \sim 90\,\mathrm{kHz}$ together with Ω_0 from Table 2.4 and Eq. (2.24). With $\Delta\nu_\mathrm{rec} \simeq 589\,\mathrm{kHz}$ the above equation predicts $\Delta\nu_{0,\mathrm{LFS}}(p_0 = 0) \sim -1\,\mathrm{kHz}$, which is in agreement with the value from Fig. 2.21(a), where the light force shift $\Delta\nu_{0,\mathrm{LFS}}$ is given by the center frequency of the Voigt fit function. The fit residuals shown in the bottom are on the level of 0.01% (not resolved on the shown scale), demonstrating that the lineshape is well described by the Voigt function. This shows that, if the atomic beam can be collimated such that $p_0 \ll \hbar K_\mathrm{L}$ for all possible atomic trajectories, the LFS is a small effect, which can easily be evaluated. However, for our atomic beam this is not the case, such that there are trajectories with $p_0 \gtrsim \hbar K_\mathrm{L}$. This case requires a careful detailed examination of the LFS as presented in this thesis. In the future, it may be possible to collimate the atomic beam better using electrostatic quadrupole fields, which quench the metastable 2S atoms inside the 1S-2S preparation laser beam without clipping the laser beam, thereby reducing the LFS.

For non-zero p_0, the levels $|\mathrm{e}\rangle|p_0 \pm \hbar K_\mathrm{L}\rangle_x$ (#7 and #11) are shifted in opposite directions by the first-order Doppler shift given by

$$\Delta\nu_\mathrm{D} = \pm v_x \frac{\nu_{A,0}}{c} = \pm p_0 \frac{\nu_{A,0}}{c\,m_\mathrm{D}} = \pm p_0 \frac{v_\mathrm{rec}}{h} = \pm 2N_{\hbar K}\Delta\nu_\mathrm{rec}, \tag{2.85}$$

where in the last step we expressed the initial momentum in terms of $N_{\hbar K}$ photon recoils, $p_0 = N_{\hbar K}\hbar K_L$. We can then use a Voigt doublet fit function (sum of two Voigt functions with different center frequencies), and characterize the LFS $\Delta\nu_{0,\mathrm{LFS}}$ as the mean from the two center frequencies $\nu_{0,-}$ and $\nu_{0,+}$ weighted with the amplitudes A_- and A_+ of the red-shifted and blue-shifted resonances:

$$\Delta\nu_{0,\mathrm{LFS}} = \frac{A_-\nu_{0,-} + A_+\nu_{0,+}}{A_- + A_+}. \tag{2.86}$$

The two Doppler-shifted resonances are well resolved if their separation $2|\Delta\nu_\mathrm{D}|$ is larger than the natural linewidth: $2|\Delta\nu_\mathrm{D}| \gtrsim \Gamma_{\mathrm{2S\text{-}6P}} = 3.9\,\mathrm{MHz}$. This condition corresponds to $p_0 \gtrsim 2\hbar K_\mathrm{L}$, such that $2|\Delta\nu_\mathrm{D}| \simeq 8\Delta\nu_\mathrm{rec} \simeq 4.7\,\mathrm{MHz} > \Gamma_{\mathrm{2S\text{-}6P}}$. For $p_0 \lesssim 2\hbar K_\mathrm{L}$, the two Doppler-shifted resonances are only partially resolved.

For $p_0 = \hbar K_\mathrm{L}$, the energy of the state #14 ($|\mathrm{i}\rangle|-\hbar K_\mathrm{L}\rangle_x$) after two recoils reducing the transverse velocity of the atom is equal to the energy of the initial state #1 ($|\mathrm{i}\rangle|\hbar K_\mathrm{L}\rangle_x$),

since the kinetic energy remains unchanged, as shown in Fig. 2.20(b). The red-shifted one-photon transition from state #1 to state #7 is resonant for the detuning $\Delta\nu_{\text{2S-6P}} = -2\Delta\nu_{\text{rec}}$. However, the two-photon transition from state #1 to state #14 is resonant independent of the detuning (which corresponds to the two-photon Raman process), such that the atoms can be efficiently pumped from the state #1 ($|\text{i}\rangle|\hbar K_{\text{L}}\rangle_x$) into the state #14 ($|\text{i}\rangle| - \hbar K_{\text{L}}\rangle_x$). This situation corresponds to the Bragg condition for an atomic wave which is resonantly diffracted on the light grating. Fig. 2.21(b) shows the simulated resonance line for this case: since the signal originates from the number of atoms in the excited states #7 and #11 ($|\text{e}\rangle|0\rangle_x$ and $|\text{e}\rangle|2\hbar K_{\text{L}}\rangle_x$), more atoms contribute to the signal for positive detuning than for negative detuning. For negative detuning[1], the atoms are most efficiently "pumped" into the state #14 ($|\text{i}\rangle| - \hbar K_{\text{L}}\rangle_x$). Consequently, the LFS is largest for atoms with p_0 near $\hbar K_{\text{L}}$, here on the order of $\Delta\nu_{0,\text{LFS}} \sim 100\,\text{kHz}$.

The level scheme in Fig. 2.20(c) shows the case $p_0 > \hbar K_{\text{L}}$ exemplarily for $p_0 = 3\hbar K_{\text{L}}$. Since all the involved states have different energies, there is no detuning for which two transitions can be resonantly excited[2]. Consequently, the LFS is smaller again as shown in Fig. 2.21(c). The two Doppler-shifted peaks are well resolved here. Note that the Voigt doublet (orange) fit function does not describe the signal shape perfectly as residuals on the level of 0.1% are clearly visible. From Fig. 2.23, which is discussed below, we will see that the for $p_0 \gtrsim 1.2\hbar K_{\text{L}}$ the LFS is caused by the possible backdecays to the initial state, whereas for $p_0 \lesssim 1.2\hbar K_{\text{L}}$ the effect of backdecay is negligible.

2.6.5.2 Light force shift as a function of backdecay momenta

Let us now consider the LFS as a function of the backdecay momenta $\Delta p_{\text{D},1} \in [-\hbar K_L, \hbar K_L]$ to the π backdecay state manifold and $\Delta p_{\text{D},2} \in [-\hbar K_L, \hbar K_L]$ to the σ backdecay state manifold. Fig. 2.22 shows the LFS as a function of $\Delta p_{\text{D},1}$ in (a) and as a function of $\Delta p_{\text{D},2}$ in (b), where the backdecay momentum to the other state manifold is fixed at $-0.5\hbar K_{\text{L}}$ (dashed curve), zero (solid curve), or $0.5\hbar K_{\text{L}}$ (dotted curve). Different colors represent different values of initial transverse momentum: $p_0 = 0$ (blue), $p_0 = 0.5\hbar K_{\text{L}}$ (orange), and $p_0 = 3\hbar K_{\text{L}}$ (red).

For $p_0 < \hbar K_{\text{L}}$, it is possible that in the level structure of the backdecay state manifolds (red in Fig. 2.19) two states have the same energy. In this case, a resonant behavior of the LFS can occur similar to the state manifold with no backdecay for $p_0 = \hbar K_{\text{L}}$ shown in Fig. 2.20(b). Therefore, for $\Delta p_{\text{D},1} = -p_0$ and $\Delta p_{\text{D},2} = -p_0$, a resonance in the LFS is visible. However, since the backdecay manifold is only a "second-order" effect of the overall LFS, the resonance changes the LFS by $< 5\,\text{kHz}$, which is small compared to the "first-order" effect of the LFS for $p_0 = \hbar K_{\text{L}}$, where $\Delta\nu_{0,\text{LFS}} \sim 100\,\text{kHz}$. Because the effective σ backdecay rate (with momentum change described by $\Delta p_{\text{D},2}$) is around a factor of two smaller (see Table 2.6) than the effective π backdecay rate (with momentum change described by $\Delta p_{\text{D},1}$), the influence of the resonance is smaller in (b) than in (a). Averaged over the whole range of $\Delta p_{\text{D},1}$ or $\Delta p_{\text{D},2}$, the resonance does not contribute significantly to the average value. Apart from the resonance, the LFS stays approximately constant as $\Delta p_{\text{D},1}$ or $\Delta p_{\text{D},2}$ are varied, and is approximately equal to

[1] Note that the state population dynamics is more complicated as may seem at a first glance: for $\Delta\nu_{\text{2S-6P}} = -2\Delta\nu_{\text{rec}}$, atoms are efficiently brought into the state #7, but in this case also the losses to the ground state are largest. The "pumping" from state #1 into state #14 can be analyzed by evaluating the population in state #14. This analysis shows that the population in state #14 is maximal for negative detunings $\Delta\nu_{\text{2S-6P}} < 0$, but not necessarily for $\Delta\nu_{\text{2S-6P}} = -2\Delta\nu_{\text{rec}}$.

[2] Note that here we only consider states with the momentum change by max. $\pm 2\hbar K_{\text{L}}$. If states with larger momentum changes are inclluded in the model, there are more possible resonances.

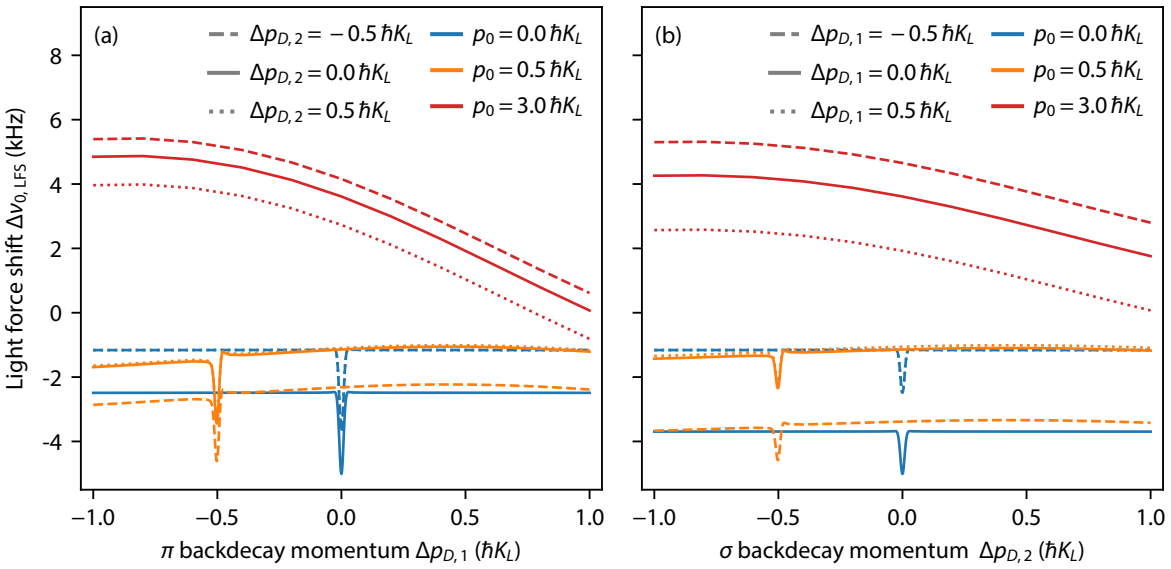

Figure 2.22: Light force shift $\Delta\nu_{0,\mathrm{LFS}}$ of the $2S_{1/2}^{F=1/2}$-$6P_{1/2}$ transition in deuterium as a function of the π and σ backdecay momenta, $\Delta p_{\mathrm{D},1}$ and $\Delta p_{\mathrm{D},2}$, respectively. The simulations were performed by numerically solving the optical Bloch equations using the level scheme in Fig. 2.19 with parameters $P_{\text{2S-6P}} = 30\,\mu\mathrm{W}$, $W_0 = 2.2\,\mathrm{mm}$, $v_z = 200\,\mathrm{m/s}$. In (a), $\Delta p_{\mathrm{D},1}$ is varied while $\Delta p_{\mathrm{D},2}$ is fixed to $-0.5\hbar K_{\mathrm{L}}$ (dashed curve), zero (solid curve), or $0.5\hbar K_{\mathrm{L}}$ (dotted curve). In (b), the situation is reversed and $\Delta p_{\mathrm{D},2}$ is varied while $\Delta p_{\mathrm{D},1}$ is fixed. Three cases of the initial transverse momentum p_0 are shown in different colors: $p_0 = 0$ (blue), $p_0 = 0.5\hbar K_{\mathrm{L}}$ (orange), and $p_0 = 3\hbar K_{\mathrm{L}}$ (red). For $p_0 = 0$, $\Delta\nu_{0,\mathrm{LFS}}$ is determined from a Voigt fit to the simulated resonance line (as in Fig. 2.21(a)), whereas for the latter two cases with $p_0 > 0$, $\Delta\nu_{0,\mathrm{LFS}}$ is determined from Eq. (2.86) using a Voigt doublet fit. For $p_0 < \hbar K_{\mathrm{L}}$, a resonant behavior of the LFS is visible for $\Delta p_{\mathrm{D},1} = -p_0$ and $\Delta p_{\mathrm{D},2} = -p_0$, where a resonant level structure is formed in the backdecay state manifold similar to the case $p_0 = \hbar K_{\mathrm{L}}$ for the state manifold with no backdecay (see Fig. 2.20(b)).

the value with the backdecay not taken into account (where only the state manifold with no backdecay is considered). As the comparison of the LFS with and without backdecay taken into account demonstrates below (see Fig. 2.23), for $p_0 \lesssim 0.8\hbar K_{\mathrm{L}}$ the backdecay changes the LFS only by a small fraction of the overall LFS.

For $p_0 \simeq \hbar K_{\mathrm{L}}$, the LFS is dominated by the resonant Bragg diffraction discussed in Fig. 2.20(b) and Fig. 2.21(b), such that the LFS is largest in this regime. For the chosen parameters ($P_{\text{2S-6P}} = 30\,\mu\mathrm{W}$, $W_0 = 2.2\,\mathrm{mm}$, $v_z = 200\,\mathrm{m/s}$), the value of the LFS is around 100 kHz for $p_0 = \hbar K_{\mathrm{L}}$. The backdecay state manifolds play an even less significant role in this regime compared to $p_0 \lesssim 0.8\hbar K_{\mathrm{L}}$, and therefore this case is not considered in Fig. 2.22 as the LFS is mostly independent of $\Delta p_{\mathrm{D},1}$ and $\Delta p_{\mathrm{D},2}$ (see also Fig. 2.23 below).

For $p_0 \gtrsim 1.2\hbar K_{\mathrm{L}}$, the backdecay is the dominant contribution to the LFS (as demonstrated in Fig. 2.23 below). Fig. 2.22 exemplarily shows for $p_0 = 3\hbar K_{\mathrm{L}}$ (red curves) that the LFS smoothly changes by few kHz as $\Delta p_{\mathrm{D},1}$ or $\Delta p_{\mathrm{D},2}$ are varied.

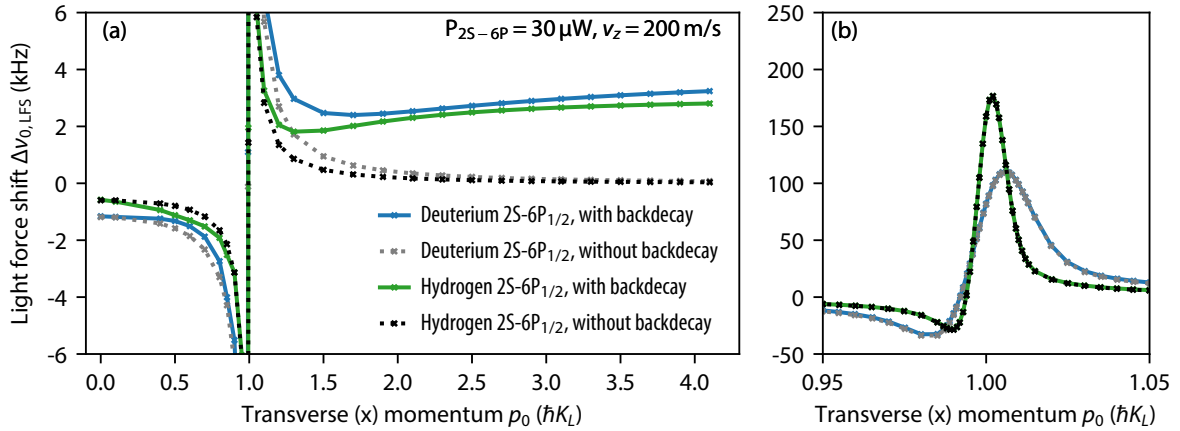

Figure 2.23: Light force shift $\Delta\nu_{0,\mathrm{LFS}}$ (LFS) of the $2S_{1/2}$-$6P_{1/2}$ transition in deuterium (blue solid curves) and hydrogen (green solid curves) as a function of the initial transverse momentum of the atom p_0, which is given in units of the photon momentum $\hbar K_\mathrm{L}$. The LFS is determined from Eq. (2.86), using a Voigt doublet function to fit the resonance lines simulated by numerically solving the optical Bloch equations with the level scheme from Fig. 2.19 with parameters $P_{\text{2S-6P}} = 30\,\mu\mathrm{W}$, $W_0 = 2.2\,\mathrm{mm}$, $v_z = 200\,\mathrm{m/s}$. For each value of p_0, the result was averaged over the backdecay momenta according to the probability density for the corresponding radiation pattern, see Eq. (2.82) and Eq. (2.83) (for hydrogen, only the π backdecay occurs). Gray and black dotted lines show the results with no backdecay, i.e. when only the state manifold with no backdecay (black in Fig. 2.19) is included into the equations. From the comparison in (a) between the LFS with and without backdecay it is clear that the backdecay significantly influences the LFS only for $p_0 \gtrsim 1.2\hbar K_\mathrm{L}$. The slightly higher effective backdecay rates in deuterium (see Table 2.6) lead to a slightly increased LFS compared to hydrogen for $p_0 \gtrsim 1.2\hbar K_\mathrm{L}$. For $p_0 \approx 0$, the LFS is around a factor of two larger for deuterium compared to hydrogen due to the smaller recoil shift (see Table 2.4) and the scaling according to Eq. (2.84). In (b), the LFS around the sharp resonance for $p_0 = \hbar K_\mathrm{L}$ (where the backdecay has no significant effect) is smaller in deuterium compared to hydrogen, which is also related to the smaller recoil shift as described in the main text.

2.6.5.3 Light force shift averaged over the backdecay momenta

To compute the LFS for an atom with a given p_0, the LFS from Fig. 2.22 needs to be averaged[1] over the backdecay momenta $\Delta p_{\mathrm{D},1}$ and $\Delta p_{\mathrm{D},2}$ using probability densities from Eq. (2.82) and Eq. (2.83). These results are shown in Fig. 2.23 and Fig. 2.24.

Fig. 2.23 compares the LFS of the $2S_{1/2}$-$6P_{1/2}$ transition between deuterium and hydrogen, each with (blue and green solid curves) and without (gray and black dotted curves) the backdecay. Note that the effective Rabi frequencies are the same[2] in hydrogen and deuterium (see Table 2.4). Therefore, the simulations were performed for the same parameters of the 2S-6P laser beam (power $P_{\text{2S-6P}} = 30\,\mu\mathrm{W}$, waist $W_0 = 2.2\,\mathrm{mm}$), and the same z-velocity of

[1] The averaging can be efficiently performed with a Gaussian quadrature using only four points (at $\Delta p_{\mathrm{D},1/2} \simeq \pm 0.34\,\hbar K_\mathrm{L}$ and $\Delta p_{\mathrm{D},1/2} \simeq \pm 0.86\,\hbar K_\mathrm{L}$). However, if at these points a resonance is present (e.g. for $p_0 \simeq 0.34\hbar K_\mathrm{L}$ or $p_0 \simeq 0.86\hbar K_\mathrm{L}$), this averaging leads to artifacts.

[2] This is true for low laser powers, i.e. in the low excitation regime, which we consider here. For higher laser powers, because of its higher Rabi frequency, the $2S_{1/2}^{F=1/2}$-$6P_{1/2}^{F=3/2}$ transition in deuterium saturates at lower power compared to the $2S_{1/2}^{F=1/2}$-$6P_{1/2}^{F=1/2}$ transition. Therefore, as soon as saturation plays a role, the effective Rabi frequency for the $2S_{1/2}^{F=1/2}$-$6P_{1/2}$ in deuterium may be different compared to the Rabi frequency of the $2S_{1/2}$-$6P_{1/2}$ transition in hydrogen. Here we neglect these saturation effects.

the atom $v_z = 200\,\mathrm{m/s}$.

The results without backdecay (gray and black dotted curves) were obtained by including only the black center level scheme from Fig. 2.19 (state manifold with no backdecay) into the optical Bloch equations. Fig. 2.23(a) shows that for $p_0 \gtrsim 1.2\hbar K_\mathrm{L}$, the backdecay significantly contributes to the LFS. For $p_0 \gtrsim 3\hbar K_\mathrm{L}$, the LFS is nearly zero if the backdecay is ignored, whereas with backdecay the LFS stays at $2 - 3\,\mathrm{kHz}$. Since the effective backdecay rates in deuterium (see Table 2.6) are slightly higher compared to hydrogen, the LFS is also slightly higher in deuterium in this regime.

For $p_0 \approx 0$, the LFS scales with $1/\Delta\nu_\mathrm{rec}$, see Eq. (2.84). Due to the two times larger mass of the atom and thus two times smaller recoil shift (see Eq. (2.81)), the LFS is two times larger for deuterium for zero p_0. However, for $p_0 \simeq \hbar K_\mathrm{L}$, the smaller recoil shift leads the smaller LFS in deuterium compared to hydrogen, as shown in Fig. 2.23(b). This can be intuitively understood by recalling Fig. 2.20(b): for the larger recoil shift in hydrogen, the separation between the two Doppler-shifted resonances is larger for $p_0 = \hbar K_\mathrm{L}$. Therefore, the misbalance in the signal between the red- and blue-shifted resonances due to the resonant behavior of the LFS is expected to lead to a larger shift of the center frequency compared to the case where the separation between the resonance lines is smaller in deuterium. However, note that due to the larger mass of deuterium, the LFS resonance at $p_0 = \hbar K_\mathrm{L}$ occurs approximately at a two times smaller transverse angle $\delta\alpha \simeq v_x/v_z = p_0/(m_\mathrm{D} v_z)$ (for $v_z = 200\,\mathrm{m/s}$: $\delta\alpha \simeq 4.8\,\mathrm{mrad}$ for hydrogen and $\delta\alpha \simeq 2.4\,\mathrm{mrad}$ for deuterium). Therefore, in an atomic deuterium beam with an angular spread of around $\pm 5\,\mathrm{mrad}$, such as in our experiment, more atoms are subject to this large shift compared to hydrogen (see Fig. 3.11(c) for a typical distribution of $\delta\alpha$ in our atomic beam).

Fig. 2.24(a) and (b) show how the LFS depends on the velocity v_z of atoms along the z direction perpendicular to the light grating along x. Since the transverse velocity v_x is much smaller than v_z ($p_0 \lesssim 4\hbar K_\mathrm{L}$ corresponds to $v_x \lesssim 4\,\mathrm{m/s}$ for hydrogen and $\lesssim 2\,\mathrm{m/s}$ for deuterium), v_z approximately corresponds to the speed of the atoms $v \approx v_z$. Smaller atomic speeds lead to a longer interaction time with the light grating, such that the LFS is generally larger for smaller v_z (i.e. compare the red curve for $v_z = 100\,\mathrm{m/s}$ with the green curve for $v_z = 250\,\mathrm{m/s}$). However, for $p_0 \lesssim 0.8\hbar K_\mathrm{L}$, the LFS is mostly independent of v_z being even slightly smaller for slower atoms.

Fig. 2.24(c) and (d) compare the LFS between the $2\mathrm{S}_{1/2}$-$6\mathrm{P}_{1/2}$ (solid curves, crossed markers) and the $2\mathrm{S}_{1/2}$-$6\mathrm{P}_{3/2}$ (dotted curves, circular markers) transitions in deuterium. Furthermore, the result is shown for different laser powers to demonstrate that the LFS increases with higher laser power as intuitively expected (and predicted by Eq. (2.84) for the case of zero p_0). Since the effective dipole moment is $\sqrt{2}$ larger for the $2\mathrm{S}_{1/2}$-$6\mathrm{P}_{3/2}$ transition compared to $2\mathrm{S}_{1/2}$-$6\mathrm{P}_{1/2}$ transtion (compare Table 2.4 with Table 2.5), the laser power is chosen a factor of two smaller for the $2\mathrm{S}_{1/2}$-$6\mathrm{P}_{3/2}$ transition compared to the $2\mathrm{S}_{1/2}$-$6\mathrm{P}_{1/2}$ transition, such that the Rabi frequencies are equal for the two transitions. As expected from the discussion of the backdecay contribution in Fig. 2.23, the LFS is almost equal for the $2\mathrm{S}_{1/2}$-$6\mathrm{P}_{3/2}$ and $2\mathrm{S}_{1/2}$-$6\mathrm{P}_{1/2}$ transitions in the regime $p_0 \lesssim 1.2\hbar K_\mathrm{L}$ where the backdecay does not significantly contribute to the result. In the opposite regime, for $p_0 \gtrsim 1.2\hbar K_\mathrm{L}$, where the backdecay is the dominant contribution, the LFS is approximately twice as large for the $2\mathrm{S}_{1/2}$-$6\mathrm{P}_{3/2}$ transition compared to the $2\mathrm{S}_{1/2}$-$6\mathrm{P}_{1/2}$ transition (for equal Rabi frequencies, i.e. compare the same colors). Recalling Table 2.6, this difference originates from the two times higher effective backdecay rate.

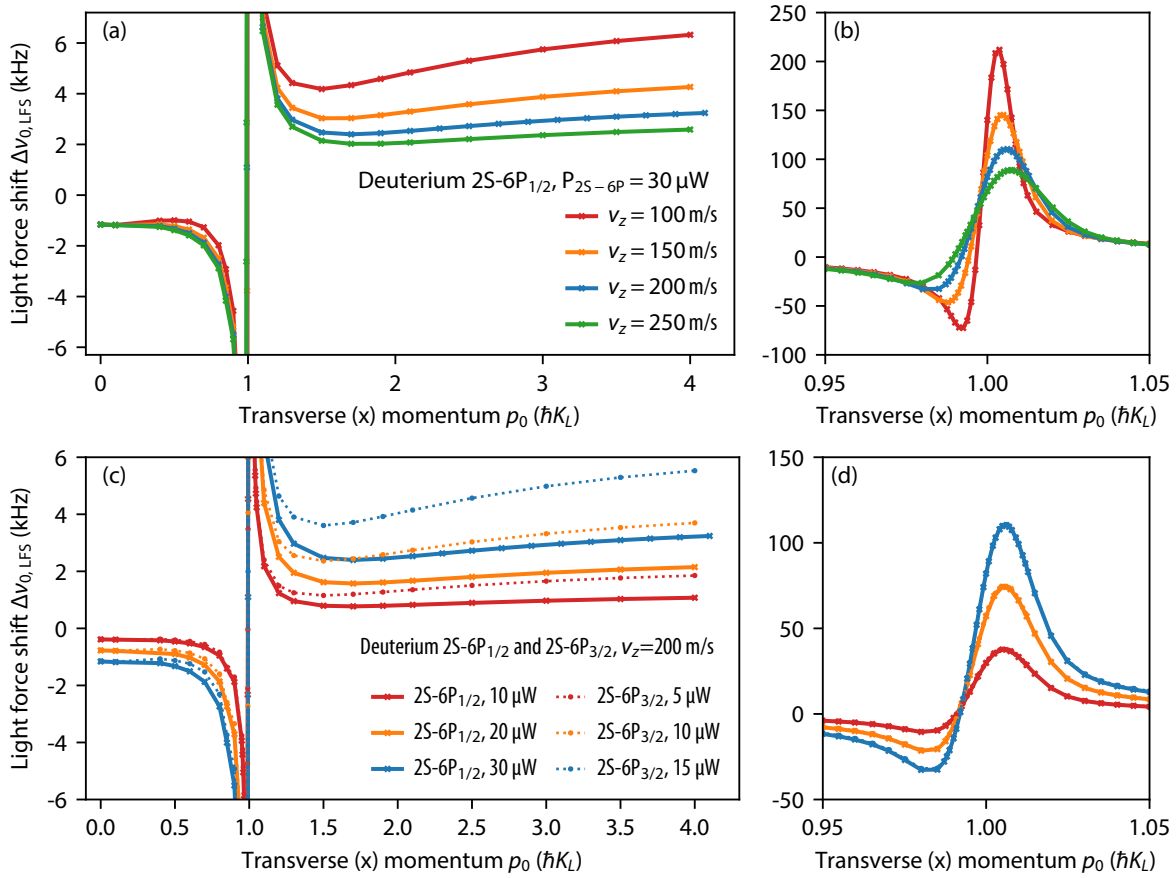

Figure 2.24: Similar to Fig. 2.23, here showing the light force shift of the $2S_{1/2}^{F=1/2}$-$6P_{1/2}$ and $2S_{1/2}^{F=1/2}$-$6P_{3/2}$ transitions in deuterium for different velocities and laser powers. In (a) and (b), the LFS is evaluated for the $2S_{1/2}^{F=1/2}$-$6P_{1/2}$ transition for the laser power of $P_{\text{2S-6P}} = 30\,\mu\text{W}$ (beam waist $W_0 = 2.2\,\text{mm}$) for different velocities, ranging from 100 m/s (red) to 250 m/s (green). The LFS is larger for lower velocities due to the longer interaction time in the light grating. In (c) and (d), the LFS is simulated for the 2S-$6P_{1/2}$ (solid curves, crossed markers) and 2S-$6P_{3/2}$ (dotted curves, circular markers) transitions for three different laser powers. The laser powers are chosen a factor of 2 smaller for the 2S-$6P_{3/2}$ transition to compensate for the $\sqrt{2}$ larger dipole moment (compare Table 2.4 and Table 2.5), thereby equalizing the Rabi frequencies for the $2S_{1/2}$-$6P_{1/2}$ and $2S_{1/2}$-$6P_{3/2}$ transitions. The LFS is then equal for the 2S-$6P_{1/2}$ and 2S-$6P_{3/2}$ transitions for $p_0 \lesssim 1.2\hbar K_{\text{L}}$ where the backdecay does not significantly influence the result. For $p_0 \gtrsim 1.2\hbar K_{\text{L}}$ the LFS is approximately a factor of 2 larger for the 2S-$6P_{3/2}$ transition due to the larger backdecay rate (see Table 2.6).

2.6.6 Light force shift simulation results for an atomic trajectory set

In the previous section, the light force shift has been calculated for a single atomic trajectory in dependence on the speed and transverse momentum assigned to the trajectory. In order to model the light force shift for the atomic beam, first a Monte Carlo simulation of trajectories is performed, as described in Section 3.3.1. Then, for each of the trajectories the signal resonance line is simulated using the optical Bloch equations with the level scheme from Fig. 2.18. The total signal is then calculated from the incoherent sum of individual trajectory signals. The simulation is performed for the time-resolved detection (see Section 3.1.1), such that the total

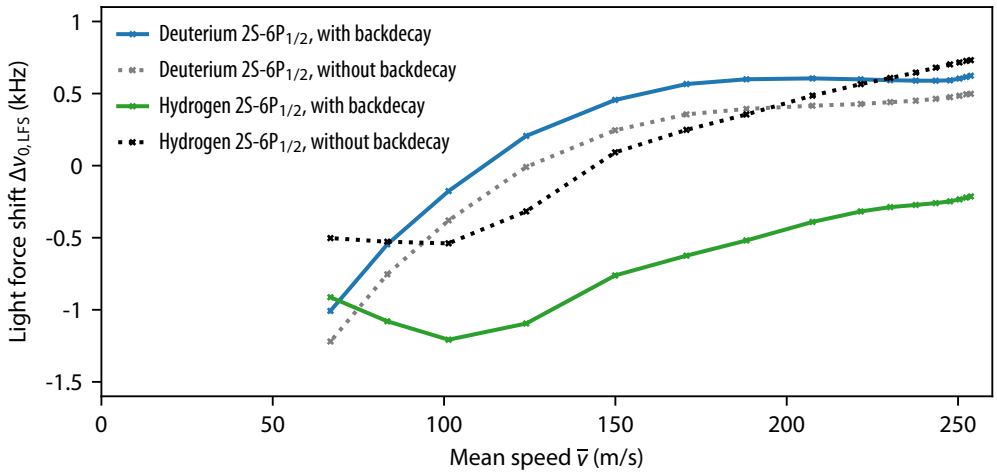

Figure 2.25: Light force shift of the $2S_{1/2}^{F=1/2}$-$6P_{1/2}$ transition in hydrogen (green) and deuterium (blue) for the Monte Carlo simulation of atomic beam trajectories (see Section 3.3.1). For each of the 10^6 trajectories, the signal is calculated from a single trajectory with a certain speed and transverse momentum using the optical Bloch equations with the level scheme from Fig. 2.18. The total time-resolved signal from all trajectories is summed from the signal of individual trajectories and grouped into 16 delays, each having a certain mean speed (see Table 3.2). The simulation parameters are $T_N = 7.1\,\mathrm{K}$, $v_{\mathrm{cutoff}} = 100\,\mathrm{m/s}$, $P_{\mathrm{1S\text{-}2S}} = 1.5\,\mathrm{W}$, $\Delta\nu_{\mathrm{1S\text{-}2S}} = 0.8\,\mathrm{kHz}$, along with the fixed parameters from Table 3.1. Similar to Fig. 2.23, gray and black dotted lines show the results with no backdecay, i.e. when only the state manifold with no backdecay (black in Fig. 2.19) is included into the equations.

signal is grouped into 16 delays, each having a certain mean speed (see Table 3.2). Fig. 2.25 exemplarily shows the result of such simulation with following parameters: nozzle temperature $T_N = 7.1\,\mathrm{K}$, cutoff-velocity $v_{\mathrm{cutoff}} = 100\,\mathrm{m/s}$, 1S-2S intra-cavity laser power $P_{\mathrm{1S\text{-}2S}} = 1.5\,\mathrm{W}$, 1S-2S frequency detuning $\Delta\nu_{\mathrm{1S\text{-}2S}} = 0.8\,\mathrm{kHz}$, along with the fixed parameters from Table 3.1. The light force shift simulation is performed for hydrogen (green) and deuterium (blue). In order to directly compare hydrogen and deuterium, the same trajectory set has been used for hydrogen and deuterium[1]. For deuterium, because of the smaller recoil velocity, there are more atoms with $p_0 > \hbar K_L$, which experience a positive shift. The light force shift is therefore shifted towards the positive frequency shift compared to hydrogen. Furthermore, the light force shift for deuterium is similar to the case for hydrogen with an offset angle, where a similar situation occurs with more atoms subject to a positive shift (see Fig. 6.6 of [71]). Similar to Fig. 2.23, gray and black dotted lines in Fig. 2.25 show the results with no backdecay, i.e. when only the state manifold with no backdecay (black in Fig. 2.19) is included into the equations. For deuterium, the backdecay has less effect because more atoms experience a larger shift near the resonance, which is independent of the backdecay.

[1]Note that for the typical simulation parameter set for hydrogen, the trajectory distribution is very similar to deuterium, since for hydrogen the nozzle temperature is typically set to $T_N = 4.8\,\mathrm{K}$, which compensates the mass difference between the two isotopes (compare Fig. 3.11 with Fig. 5.4. from [71]).

Chapter 3

Hydrogen and Deuterium 2S-6P Spectrometer Apparatus

This chapter presents the apparatus for performing precision spectroscopy of the 2S-nP transitions in hydrogen and deuterium. The apparatus is based on the work of several generations of doctoral students, since the late 1980s, and has been used for various transition frequency measurements, as for instance the celebrated 1S-2S measurement [57]. Starting from 2011, the apparatus was modified to measure the 2S-4P transition, culminating in the important result for the proton radius puzzle [14]. Since 2015, the apparatus was upgraded for the 2S-6P transition. Many details of this apparatus have been covered in the recent thesis by Lothar Maisenbacher [71], which is referenced wherever some part is described only in brevity here. In this thesis, the focus lies on the specific differences for the deuterium measurement, while other parts are presented as an overview. Furthermore, the improved active fiber-based retroreflector, which is integrated into the apparatus for the suppression of the first-order Doppler shift, is detailed in the next chapter, since it presents a major contribution of this thesis and can be treated as a separate topic.

Section 3.1 sets the stage for the rest of the chapter: after the main components of the apparatus are summarized, the key technique of the time-resolved detection for selecting different velocity groups of atoms is explained. Thereafter, the vacuum assembly of the apparatus is presented.

Section 3.2 covers the 1S-2S (243 nm, see Section 3.2.1) and 2S-6P (410 nm, see Section 3.2.2) laser systems of the experiment. These narrow linewidth lasers along with the hydrogen maser-referenced frequency comb measurement of laser frequencies (see Section 3.2.3) are the major ingredients of precision spectroscopy.

The numerical modeling of the experiment, outlined in Section 3.3, is necessary to simulate the mean velocity of the atoms contributing to the signal observed in the time-resolved detection, and therefore is crucial to the whole apparatus. Furthermore, simulations allow to study various systematic effects.

Magnetic and electric fields may lead to systematic Zeeman and dc-Stark shifts, which disturb the precision spectroscopy. Therefore, Section 3.4 describes the magnetic field suppression and presents measurements of the magnetic field in the interaction region. Section 3.5 presents the fluorescence detector, which is also used for in-situ measurements of stray electric fields in the interaction region. In addition, Section 3.5.3 shows the observed non-linearity of the fluorescence detector during the deuterium 2S-6P measurement in July 2021, which is

important for the interpretation of the measured amplitude ratio of the time-resolved signal delay groups.

In Section 3.6, the formation of the cryogenic deuterium atomic beam in the metastable 2S state is discussed. This part of the apparatus reveals the main experimental differences between hydrogen and deuterium spectroscopy. As explained in Section 3.6.1 and demonstrated in Section 3.6.2, the formation of the cryogenic hydrogen and deuterium atomic beams is highly sensitive to the nozzle temperature, with a different optimal temperature for the two isotopes. To this end, a high performance liquid-helium flow cryostat has been installed in February 2020 in the apparatus, which is described in Section 3.6.3.

3.1 Overview of the apparatus and vacuum system

Fig. 3.1 schematically presents an overview of the hydrogen and deuterium 2S-nP experiment (not to scale). Hydrogen (H) or deuterium (D) atoms (symbolized by black arrows) are injected into a T-shaped copper nozzle (NZ) which, depending on the isotope, is cooled to a temperature around 5-7 K using a liquid helium-flow cryostat (see Section 3.6 for details). Atomic beam apertures are properly placed to constrain the atomic beam emerging from the nozzle with a diameter of 2.0 mm. The entrance aperture (EA) is a circular aperture with a fixed diameter of 2.4 mm placed at a distance of 69.0 mm after the nozzle. As described in Section 3.1.2 and shown in Fig. 3.3 in more detail, this entrance aperture separates the high-vacuum region from the main chamber region. Another aperture (VA) is placed at a distance of 153.6 mm after the nozzle, which has a fixed height of 2.0 mm and a variable width typically aligned to 1.2 mm.

The atomic beam is superimposed with the 1S-2S preparation laser beam (PB) with a wavelength of 243 nm which excites the ground state atoms into the metastable 2S state. To enhance the laser power and enable the Doppler-free two-photon excitation from counter-propagating beams, a cavity is formed by the input coupler (also called incoupler) (IC) and output coupler (also called outcoupler) (OC) mirrors separated by 355 mm. The incoupler is a flat mirror with a reflectance of $\sim 97\%$ (transmission 1.7(1)%, and $\sim 1\%$ losses), while the outcoupler is a curved HR mirror with a radius of 4 m and a reflectance of $\sim 99\%$ (transmission of $\sim 1 \times 10^{-4}$, and $\sim 1\%$ losses), which results in a $1/e^2$ beam waist radius of around 0.3 mm. The power enhancement of PE $\sim 30 - 40$ leads to around $1 - 2$ W of 243 nm laser power inside the cavity for 30-50 mW input power before the cavity and a finesse of $\mathcal{F} \sim 150 - 200$, which strongly depends on the degradation of the mirrors throughout the experiment time (to prevent the degradation, the cavity mirrors can be flushed with oxygen in the future, which requires differential pumping). The 1S-2S 243 nm cavity is treated in detail in Section 3.2.1.1.

The 410 nm laser beam for the 2S-6P excitation emerges from a polarization-maintaining (PM) fiber (SF) and is collimated using a four-lens collimator (SC) resulting in a $1/e^2$ beam width radius of 2.2 mm. The 2S-6P excitation takes place in the spectroscopy region (SR) where the 2S-6P laser beam crosses the atomic and 243 nm beams at a distance of 204 mm from the nozzle. The crossing angle is set to approximately 90° in order to suppress the first-order Doppler shift. Furthermore, the beam is retroreflected by the high-reflectivity (HR) mirror (HR) in order to additionally suppress the Doppler shift. This retroreflection is precisely adjusted and actively stabilized, such that the above parts form the improved active-fiber based retroreflector (AFR) which is treated in Chapter 4.

The signal originates mainly from Lyman-ϵ fluorescence photons produced by the decay

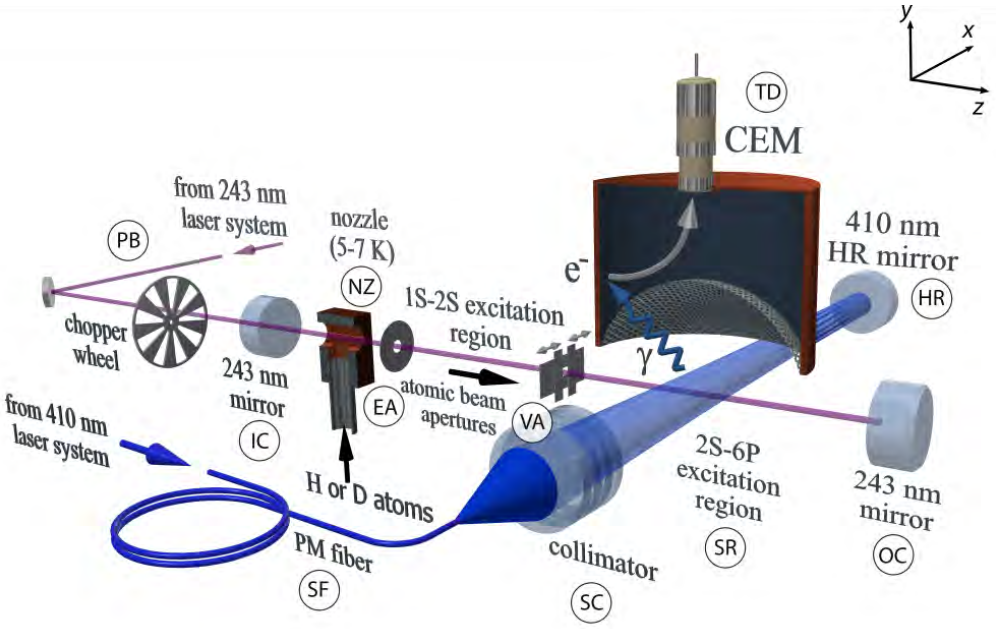

Figure 3.1: Schematic overview of the hydrogen and deuterium 2S-6P spectroscopy experiment (not to scale). Note the coordinate system in the upper right corner of the figure for comparison with Fig. 3.3 for a drawing of the vacuum assembly, Fig. 3.4 for the photograph of the vacuum assembly as well as Fig. 4.2 for a detailed drawing of the active fiber-based retroreflector. Hydrogen (H) or deuterium (D) atoms (indicated by black arrows) escape from the copper nozzle (NZ) and are constrained by the atomic beam apertures (EA) and (VA), where the width of the latter is variable (indicated by gray arrows). The atomic beam is superimposed with the 243 nm preparation laser beam (PB) for the Doppler-free two-photon 1S-2S excitation inside the 243 nm cavity formed by the incoupler (IC) and outcoupler (OC) mirrors. The 410 nm laser beam for the 2S-6P excitation, taking place in the region (SR) where both laser beams cross, emerges from the polarization-maintaining (PM) fiber (SF) and is collimated with the four-lens collimator (SC). The 2S-6P laser beam crosses the atomic beam at an angle of 90° and is retroreflected by the high-reflectivity (HR) mirror to suppress the first-order Doppler-shift. These are the key ingredients of the active fiber-based retroreflector (AFR) treated in Chapter 4. The 2S-6P spectroscopy signal emerges from the fluorescence photons γ (mainly with a wavelength of 94 nm arising from the decay of the short-lived 6P state with a lifetime of 41 ns to the 1S ground state), which passes the Faraday-cage mesh and hits the aluminum wall of the cylindrical detector. The electron e^- generated by the photoelectric effect is pulled into the channeltron electron multiplier (CEM), resulting in a measurable electronic pulse either at the top detector (TD) or at the bottom detector (not shown here). The key technique of the experiment is to perform this detection time-resolved and triggered to the chopper wheel which periodically stops the 1S-2S excitation, see Section 3.1.1. The signal is divided into subsequent delay time groups, thereby probing different velocity groups of atoms.

from the short-lived 6P state to the 1S ground state (branching ratio of 88%) which have a wavelength of 94 nm in the extreme ultraviolet. These photons reach the cylindrical aluminum detector walls (diameter 26.2 mm) through the Faraday-cage meshes, which shield the interaction region from electric fields arising from the high-voltage applied to the channeltron electron multipliers (CEM). Through the photoelectric effect, the fluorescence photons eject electrons from the aluminum, which are pulled into the CEM and ultimately result in electronically counted pulses. Only the top detector (TD) is shown in Fig. 3.1.

The key technique of the experiment, invented by D. Leibfried [154], is to periodically

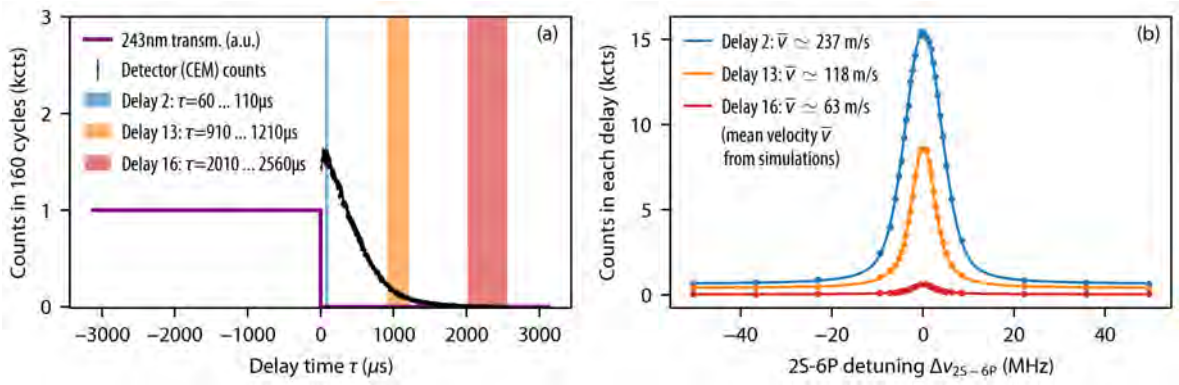

Figure 3.2: Time-resolved detection of the deuterium 2S-6P fluorescence signal. (a) The purple line shows the 243 nm transmission (in a.u.) over the delay time τ: the 1S-2S excitation is periodically stopped with a frequency of 160 Hz resulting in a time period of 3125 µs when no more 2S atoms are being generated. Starting from the time point when the laser light is switched off ($\tau = 0$ µs), the channeltron electron multiplier (CEM) detectors are switched on, with the signal being counted in 5 µs bins over the delay time (black data points). The counts are summed over 160 chopper cycles corresponding to 1 s, and then grouped into 16 delays, with the delays 2 (blue), 13 (orange), and 16 (red) marked here. (b) The time-resolved detection from (a) is repeated for 30 different frequency detunings (the data in (a) shows the signal on resonance), resulting in resonance lines ('line scans') for each delay. Different delays correspond to different velocity groups of atoms: longer delays (longer waiting times after the 2S excitation is blocked) correspond to atoms with lower mean velocity $\overline{v}$ since the faster 2S atoms escape the detection region. The mean velocity is obtained from numerical modelling of the experiment, see Section 3.3 and Table 3.2.

block the 1S-2S excitation beam by a chopper wheel and to record the time-resolved signal during the triggered time periods (delays) when the 1S-2S laser light is blocked. As soon as the 1S-2S excitation light is blocked, the faster 2S atoms begin to escape the 2S-6P interaction region, such that with increasing delay times slower 2S atoms are probed. Grouping the signal into subsequent delay times allows then to access different velocity groups of probed atoms, which is described in the next section.

3.1.1 Time-resolved detection

Fig. 3.2 demonstrates the time-resolved detection of the 2S-6P fluorescence signal. The chopper is operated at a frequency of 160 Hz, resulting in a 'bright' phase of 3125 µs, where the 243 nm light is on, and a 'dark' phase of 3125 µs, where the 243 nm light is off. The purple line in Fig. 3.2(a) shows the transmission of the 243 nm cavity (in a.u.) over the delay time τ which is here defined such that the bright phase lasts from $\tau = -3125 \ldots 0$ µs and the dark phase from $\tau = 0 \ldots 3125$ µs.

During the bright phase the detectors are switched off using a high-voltage (HV) switch, since the high count rate on the order of 10 Mcts/s from photoionization of 2S atoms (producing 1.7 eV electrons) would otherwise saturate the detectors (see Sec. 4.6 in [71]). There is a small delay of 2 µs of the falling chopper trigger such that the HV switch rises at $\tau = 2$ µs. The rise-time of the CEM is on the order of 5 µs.

The signal is recorded in 1024 time bins with 5 µs each (black data points) ranging from $\tau = 0 \ldots 3125$ µs in the dark phase and $\tau = -3125 \ldots -1130$ µs in the bright phase to verify the detector switching (not shown here). The signal is summed over 160 chopper cycles

corresponding to 1 s gate time. Starting from $\tau = 10\,\mu s$ to $\tau = 2560\,\mu s$ the signal of the dark phase is grouped into 16 delays, with delay 2 (blue), 13 (orange), and 16 (red) examplary marked in Fig. 3.2(a). The data for the remaining time of the dark phase does not show any signal, but is nevertheless always recorded.

The detection in Fig. 3.2(a) is shown examplary for the frequency point on resonance, and is repeated for 30 different frequency points to measure the resonance line ('line scan') of the 2S-6P transition, as shown in Fig. 3.2(b). Thereby, a resonance line center frequency is determined for each delay corresponding to different velocity groups of atoms. As soon as the 243 nm laser beam is blocked and hence the 2S excitation is stopped, the 2S atoms start to escape the detection region such that longer delay times correspond to slower atoms. To find the mean velocity of atoms for each delays, numerical modelling of the experiment is used, see Section 3.3 and Table 3.2 for the summary of the delay times and mean velocities of atoms for a given parameter set.

Much effort was provided by Lothar Maisenbacher to write the data acquision software in Python ('Pythonic Hydrogen') which controls the apparatus and records the time-resolved data from the detectors, as well as photodetector voltages along with various auxiliary signals. This software as well as many important details of triggering and high-voltage switching of the detectors are described in Sec. 4.6 and 4.7 of his thesis [71].

3.1.2 Vacuum system

The vacuum assembly of the experiment is shown in Fig. 3.3 on a to-scale 3D engineering drawing, while Fig. 3.4 shows a photograph of the assembled vacuum chamber. Note the coordinate systems in corners of Fig. 3.1 (schematic overview), Fig. 3.3 (drawing of the vacuum assembly), Fig. 3.4 (photograph) as well as Fig. 4.2 (detailed drawing of the active fiber-based retroreflector) for comparison between the figures.

The cylindrical vacuum chamber has a diameter of 50 cm and a usable height of 33 cm, and is pumped with a turbo pump[1] to achieve a pressure of typically 10^{-6} mbar. The bottom part of the chamber, separated from the upper part by the chamber floor (FL), bears a cryopump[2] (CP) which continuously cycles helium with an external compressor to cool the charcoal-coated layers to the temperature of 19 K and thereby freeze common residual gases or remove hydrogen and deuterium gas by cryosorption [155]. These compressing cycles occur on a timescale of 1 s and lead to large vibrations on the whole setup. Therefore, the cryopump needs to be periodically switched on and off on a timescale of ∼5 min during spectroscopy measurements, such that data is only taken when the cryopump is off. The cryopump pumps the high-vacuum region enclosed by the high-vacuum enclosure (HV). This region is separated from the main chamber vacuum by the circular entrance aperture (EA) of 2.4 mm diameter and 1.0 mm length, as well as the output aperture (OA) of 7 mm diameter and 13 mm length. However, to reduce the pressure in the main chamber before the start of experiment, as well as to efficiently pump out the accumulated hydrogen or deuterium in the cryopump after the operation of the experiment, the cryopump (high-vacuum) region is connected with the main

[1] Magnetically levitated turbo-pump, Pfeiffer HiPace 700 M, SN 16341623, with pumping speed / compression ratio of 685 l/s / $> 10^{11}$ for nitrogen and 480 l/s / 2×10^5 for hydrogen. This pump was installed on 23.01.2020 to replace the similar hybrid bearing version (Pfeiffer HiPace 700, SN 1440995). The turbo pump is connected to the Pfeiffer ACP40 multi-stage roots pump with 37 m^3/h peak pumping speed at 1 mbar (also the Edwards XDS35i scroll pump was used during the maintenance of ACP40).

[2] Leybold RPK 10000 with a pumping speed of 10^4 l/s for hydrogen and nitrogen, and 29×10^3 l/s for water.

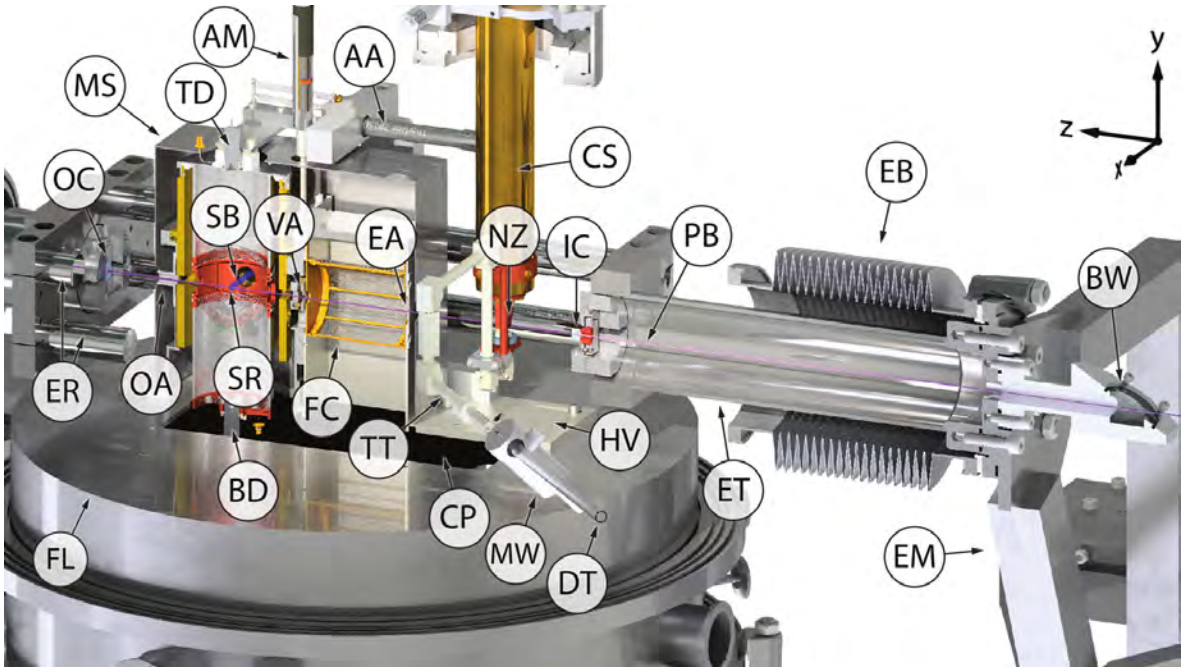

Figure 3.3: 3D engineering drawing of the hydrogen and deuterium spectrometer apparatus, see text for description. The cylindrical vacuum chamber has a diameter of 50 cm. Note the coordinate system in the upper right corner of the figure for comparison with Fig. 3.1 for a schematic overview, Fig. 3.4 for the photograph of the vacuum assembly as well as Fig. 4.2 for a detailed drawing of the active fiber-based retroreflector. For even more details of the vacuum assembly, see Sec. 4.2 and Figs. 4.1 and 4.2 of [71]. (AA) α alignment actuator, (AM) variable aperture actuator, (BD) bottom detector, (BW) 243 nm Brewster's window, (CP) cryopump, (CS) cryostat, (DT) dissociator discharge tube, (EA) high-vacuum entrance aperture, (EB) spacer bellows for the 243 nm enhancement cavity (EC), (EM) EC mounting brackets to the optical table, (ER) EC spacer Invar rods, (ET) EC spacer tubes, (FC) 1S-2S Faraday cage, (FL) cylindrical vacuum chamber floor, (HV) high-vacuum enclosure, (IC) piezo-actuated 243 nm incoupling mirror, (MS) magnetic shield, (MW) dissociator microwave cavity, (NZ) copper nozzle, (OA) high-vacuum output aperture, (OC) 243 nm outcoupling mirror, (PB) atomic beam and 1S-2S preparation laser beam, (SB) 2S-6P spectroscopy 410 nm laser beam, (SR) 2S-6P spectroscopy region, (TD) top detector, (TT) polytetrafluoroethylene (PTFE or 'Teflon') tubing, (VA) variable aperture.

region via an additional bypass tube (seen in the lower right corner of Fig. 3.4) which can be opened with a dedicated valve. When no hydrogen or deuterium is injected in the chamber, the cryopump typically reduces the pressure in the high-vacuum region to $\sim 5 \times 10^{-8}$ mbar, while with[1] a hydrogen or deuterium flow[2] of 0.35 mln/min the pressure is typically $\sim 2 \times 10^{-7}$ mbar. In the cryopump region, the hot cathode ion pressure gauge which is directly attached to the chamber produces ~100 cts/s background at the bottom detector and is therefore switched

[1]For the used hot cathode pressure gauges (Leybold ITR 200, ITR 90) there is a calibration factor of 2.4 between nitrogen and hydrogen. Therefore, with no hydrogen the value for nitrogen is most applicable, while with hydrogen-dominated pressure the value is $\sim 2.4 \times 8 \times 10^{-8}$ mbar. Though there are differences in the behavior of hot cathode gauges between hydrogen and deuterium [156], the relative factor between the actual and measured pressure values is on the order of few percent [157], and therefore within the ±15% accuracy of our pressure gauges.

[2]The unit mln/min gives the volumetric flow in ml/min referenced to normalized conditions defined to be at a temperature of 0°C and pressure of 1013.25 mbar. This is close to the conditions before the gas dosing valve to the discharge, where the flow is measured.

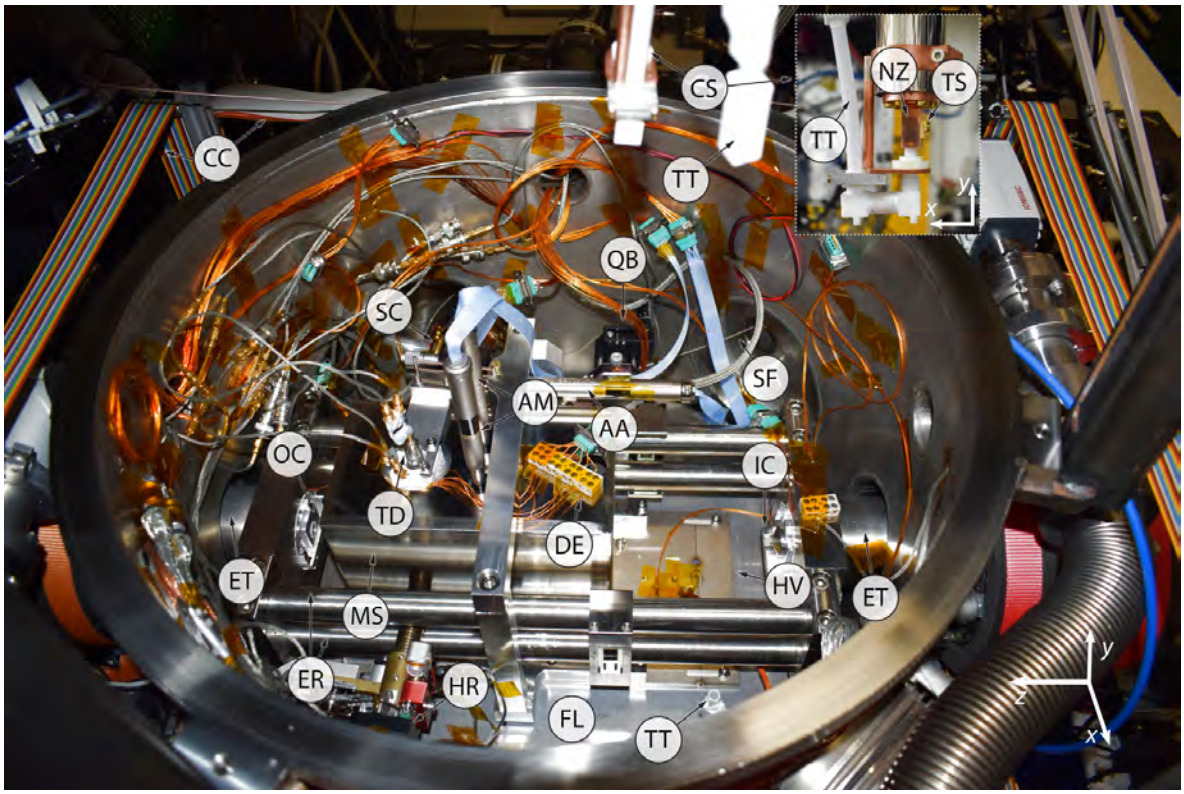

Figure 3.4: Hydrogen and deuterium spectrometer vacuum assembly photograph, see text for description. Note the coordinate system in the lower right corner of the figure as well as in the upper photograph of the cryostat cold head for comparison with Fig. 3.1 for a schematic overview, Fig. 3.3 for the drawing of the vacuum assembly as well as Fig. 4.2 for a detailed drawing of the active fiber-based retroreflector. (AA) α alignment actuator, (AM) variable aperture actuator, (CC) magnetic field compensation coils, (CS) cryostat, (DE) detector electrodes connections, (ER) spacer Invar rods of the 243 nm enhancement cavity (EC), (ET) EC spacer tubes, (FL) cylindrical vacuum chamber floor, (HR) high-reflectivity mirror of the active fiber-based retroreflector (AFR), (HV) high-vacuum enclosure, (IC) piezo-actuated 243 nm incoupling mirror, (MS) magnetic shield, (NZ) copper nozzle, (OC) 243 nm outcoupling mirror, (SC) four-lens fiber collimator of the AFR, (SF) polarization-maintaining fiber of the AFR, (TD) top detector, (TT) polytetrafluoroethylene (PTFE or 'Teflon') tubing, (TS) nozzle temperature sensor, (QB) 2S-4P quench laser blade (for a possible future hydrogen/deuterium 1S-2S as well as 2S-6P deuterium initial state asymmetry measurements).

off during the measurement. Therefore, a second similar pressure gauge is attached via two right-angle bends which produces a negligible background of < 1 cts/s and is kept on during the measurement[1].

The high-vacuum region is magnetically shielded with a high-permeability (mu-metal) magnetic shield (MS) of 1 mm thickness[2]. Furthermore, the magnetic field compensation coils (CC) placed outside the vacuum chamber (only shown in Fig. 3.4) reduce the magnetic field

[1]For typical measurement conditions, i.e. with operating cryopump, cold nozzle, and hydrogen/deuterium flow of 0.35 mln/min, the directly attached pressure gauge measures a factor of $0.6 - 0.7$ lower pressure than the one connected over two right-angles.

[2]Custom manufacturing by Meca Magnetic. The mumetal has a permeability of $3 - 4 \times 10^5$ (for a continuous field) and consists of 80% nickel, 15% iron, and 5% molybdenum (with $< 1\%$ traces of carbon, silicon and manganese).

inside the 2S-6P spectroscopy region (SR) to below 1 mG for the most critical x direction and below 2 mG for other directions, as described in Section 3.4 and shown in Fig. 3.13. There are two coils, which are arranged approximately in the Helmholtz configuration, for each of the three directions (in Fig. 3.4 only the coils for the x and z directions are visible, since the coil wires for the y direction are wrapped around the cylindrical vacuum chamber).

The hydrogen or deuterium molecules are supplied from gas cylinders[1] connected through pressure regulators[2], safety devices[3], leak-tight connections and valves[4], a flowmeter[5] , and a gas dosing valve[6] to the microwave dissociator discharge tube[7] (DT). The atoms are generated by splitting the molecules in the dissociator microwave cavity (MW) (see [158] for a similar design). The discharge is ignited using a high-voltage high-frequency pulse with a small Tesla coil[8], which is held near the discharge tube. The microwave radiation at 2.45 GHz is supplied by a solid-state microwave generator[9], which produces 40 W of power and monitors the reflection (optimized to < 1 W by adjusting the microwave cavity). The microwave cavity is constantly cooled to $-30 \cdots -10\,^{\circ}$C with cold nitrogen gas. At the end of the discharge tube, a polytetrafluoroethylene (PTFE or 'Teflon') tube is inserted which has an orifice of 0.3 mm diameter and 2.1 mm length. With the typical deuterium gas flow of 0.35 mln/min,

[1]Hydrogen: 6.0 purity ($> 99.9999\%$ purity with ≤ 0.5 ppm N_2, ≤ 0.5 ppm O_2, ≤ 0.5 ppm H_2O, ≤ 0.1 ppm Hydrocarbons, ≤ 0.1 ppm CO, ≤ 0.1 ppm CO_2), 2 l / 200 bar (0.356 m^3 filling volume) bottle by Linde (10100419). Deuterium: 99.96% purity (according to test sheet around $\sim$0.03% hydrogen impurities from residual H_2 and HD molecules and < 10 ppm other impurities: 99.97 atom % D from mass spectrometry, chemical purity 99.999%, < 0.6 ppm Ar/O_2, 0.7 ppm N_2, < 0.1 ppm CO, 0.9 ppm CO_2, 0.2 ppm CH_4+C_2H_6, 0.7 ppm H_2O), 0.5 l / 20 bar bottle (10 l filling volume) by Sigma Aldrich (368407-25L-EU),

[2]Spectron Gas Control Systems two-stage pressure regulator FM53-L-200-1,5-DIN1-M-M-O-A-B-H2 with the valve DV-V6M-3-A for hydrogen, and Sigma Aldrich single-stage (0-22 psig delivery pressure, CGA 180 inlet size, Z512958-1EA) for deuterium (in the future it can be replaced by the two-stage regulator FM53-L-200-1,5-CGA180-M-M-DVV6MAV-A-B-D2).

[3]Spectron Gas Control Systems (Model DG91NH) according to the EN 730-1, ISO 5175, AS 4603 norms, opening pressure 10 mbar. These safety devices are mounted after the deuterium and hydrogen pressure regulators and protect against sudden and creeping gas return (NV), flashback (flame arrestor, FA) and burnback (temperature controlled cutoff-valve, TV).

[4]The leak rate substantially improved from $\sim 10^{-5}$ l/s to be $\sim 10^{-7}$ l/s after replacing all stainless steel integral nonnet needle valves (Swagelok SS-1RS4) by stainless steel bellows sealed valves (Swagelok SS-4H2). Before opening the hydrogen or deuterium valves, the whole connection line is pumped out using a separate turbo pump (Leybold TURBOVAC 90 iX) to a pressure $< 10^{-5}$ mbar monitored with a Leybold TTR 101 N pressure gauge. With hydrogen or deuterium in the line the pressure regulators are adjusted such that this pressure gauge shows around 0.9-1.1 bar.

[5]Bronkhorst F-110C-005-AAD-33-V, accuracy ± 0.01 mln/min. The calibration factor of 1.006 between hydrogen and deuterium is close to 1 since only the product of density and heat capacity enters the measurement principle: deuterium has a factor of $\sim$2 higher density but also a factor of $\sim$2 lower heat capacity than hydrogen.

[6]Pfeiffer Vacuum EVN 116.

[7]Inner diameter of 7.25 mm, outer diameter 9.3 mm, length 250 mm, made from crystalline sapphire (Al_2O_3) which has a better thermal conductivity compared to fused quartz used in [158]. A metallic layer may build up in the tube over time depending on the operation conditions of the discharge. Then the tube can be cleaned with 5% NaOH in deionized water.

[8]Electro-Technic Products BD-10ASV high-frequency generator: 20-50 kV ouput voltage, 500 kHz output frequency, max 0.1 mA output current.

[9]SAIREM GMS 200.

a pressure around 3 mbar is measured in the discharge region[1]. The atoms are then guided through teflon tubings (TT) to the T-shaped copper nozzle (NZ) (through-hole with diameter of 2.0 mm and length 8.0 mm, and a blind hole of 4.0 mm diameter in the bottom). A short teflon spacing tube with 0.45 mm wall thickness forms a 0.2 mm gap to thermally isolate the nozzle.

The copper nozzle is attached with brass screws and a thin layer of thermal grease[2] to the cold head of the liquid-helium flow cryostat[3] (CS). The cryostat is mounted on the chamber lid which is lifted up in Fig. 3.4, and is therefore only visible out of focus in the top of Fig. 3.4 with disconnected teflon tubings. A photograph of the cold head of the cryostat from the different perspective is inserted, showing the nozzle with the attached temperature sensor[4] (TS). Another temperature sensor[5] monitors the temperature inside the cryostat. The cryostat is mounted on a manipulator[6] providing ±15 mm motion in the x and z directions and 50 mm in the y direction, which enables to align the nozzle with the 243 nm (1S-2S) preparation laser beam (PB) parallel to the atomic beam.

The 243 nm beam enters the vacuum chamber through the 243 nm Brewster's window (BW). The laser beam is then guided into the 243 nm enhancement cavity (EC), formed by the piezo-actuated[7] 243 nm incoupling mirror[8] (IC) and the outcoupling mirror[9] (OC), see Section 3.2.1. Both mirrors are mounted on remotely controlled mirror mounts[10]. The important property of the vacuum assembly is that the EC is attached to the optical table via mounting brackets (EM), while the rest of the setup (including the active fiber-based retroreflector) sits on the laboratory floor and is therefore subject to more mechanical noise. The whole EC setup is held together by spacer tubes (ET) and Invar rods (ER) attached to the two mounting brackets

[1] This is the reading value of the Leybold TTR 101 N pressure gauge which has a calibration factor depending on the gas and the pressure (below 10 mbar the measurement is performed with the Pirani sensor). Between 1 . . . 3 mbar reading value the calibration factor for hydrogen is 0.7 . . . 0.5 (the actual pressure is lower than the reading value). The thermal conductivity of the deuterium gas is $\sim\sqrt{2}$ lower due to the mass difference [159, 160], such that the reading value is a factor of $\sim\sqrt{2}$ higher and the correction factor for the reading value in this pressure range is close to unity, 1.0 . . . 0.7. This agrees with the observation that for 0.35 mln/min of hydrogen the reading value is around 2 mbar (together with the correction factor leading to the same actual pressure of ∼3 mbar). In the future, this pressure gauge can be replaced by the more accurate gauge based on the capacitative pressure measurement independent of the gas species (e.g. Leybold CTR 100 N).

[2] Apiezon N.

[3] Advanced Research Systems ARS LT3-B, customized design.

[4] LakeShore DT-670-BO-1.4L, SN D6076038, accuracy ±12 mK in the range 1 . . . 10 K. Four Manganin 36 AWG are soldered to the sensor to provide the electrical connection. Special care needs to be taken to wrap the wires the cryostat cold head to reduce Joule heating depositing through the sensor. The wrapped wires need to touch the cold cryostat head which is achieved by fixing the wire with dental floss (Oral-B EssentialFloss).

[5] LakeShore DT-670B-SD.

[6] UHV Design TTX63-63-50-H.

[7] For the 2S-6P deuterium measurement, the piezo-mirror design was modified to achieve higher bandwidth, see Appendix A.5, for a possible future upgrade of the apparatus which requires to increase the cavity length.

[8] Custom order by Layertec: substrate SQ1-E248, plane/plane, diameter 7.75(-0.10) mm, thickness 4.0(±0.1) mm, wedge=30(±10)′, surface form tolerance according to the ISO 10110 on both sides 3/0.2(0.2) (λ/10 power and λ/10 irregularity with λ = 546 nm), side 1 (wedged side): AR(0°, 243 nm)<0.3% (target <0.2%); side 2 (ˆ): PR(0°, 243 nm) =98.3(±0.5)%, T(0°,243 nm)∼1.5(±0.5)%. Coating material: AlO_2+SiO_2, top layer of coating SiO_2, coating process: ion beam sputtering (IBS).

[9] Custom order by Layertec: substrate SQ1-E248, plane/curved, diameter 12.7(-0.1) mm, thickness 6.35(±0.1) mm, wedge=30(±10)′, surface imperfection tolerance 5/1x0.025 L1x0.001, surface form tolerances 3/0.2(0.2) and 3/-(0.2) (λ/10 reg.), side 1: AR(0°, 243 nm)<0.3%, side 2 (ˆ): radius 4 m(±5%) CC, HR(0°, 243 nm) >99.5%, T(0°,243 nm)= 0.01 − 0.001%. Same coating material and process as for input coupler.

[10] Newport Picomotor Actuator Piezo Mirror Mount, Pint-Sized, Center Mount, 0.5 inch diameter, UHV compatible, Model 8885-UHV.

(only one side is shown in Fig. 3.3). The spacer bellows (EB) suppress the mechanical noise coupling between the EC and the rest of the vacuum setup. In the future, the part of the setup mounted on the high-vacuum enclosure may be also attached to these rods such that the sensitive active fiber-based retroreflector is subject to less vibrations. However, this may influence the stability of the EC which needs to be tested.

After the atoms enter the magnetically shielded high-vacuum region, they pass the 1S-2S Faraday cage (FC). This is especially important if the apparatus is used to measure the 1S-2S transition. In this case, a 2S-4P laser blade (QB) (shown only in Fig. 3.4) quenches the atoms from the 2S state to the ground state right before they enter the Faraday cage, such that the 2S atoms are only generated in the electrically and magnetically shielded region. For the 2S-6P measurement, this quench laser blade is not operated. However, the 2S-4P blade may also be used with circular polarized light for possible future deuterium initial state asymmetry measurements, as described in Appendix A.2.

After the 1S-2S Faraday cage, the atomic beam is constrained using the variable aperture (VA), which has a fixed height of 2.0 mm and a variable width (typically set to 1.2 mm) as well as adjustable horizontal centering. The two slits of this aperture are controlled using two remotely controlled variable aperture actuators[1] (AM) (only one is shown in Fig. 3.3). The position of the apertures is calibrated on each day using an auxiliary laser beam (from a Helium-Neon-Laser[2]), which propagates in the opposite direction of the 243 nm and atomic beams (see Sec. 4.5.3 of [71] and Clarissa Kroll's Bachelor's thesis [161] for more details). This auxiliary laser beam is aligned with the 243 nm laser beam using two circular apertures placed outside of the vacuum chamber before each of the two Brewster's windows. The same auxiliary laser beam is also used for nozzle imaging purposes (see Sec. 4.5.2.5 of [71])[3].

After having passed the variable aperture, the atoms enter the cylindrical 2S-6P fluorescence detector, which is not only used to detect the fluorescence signal, but also to apply electric field inside the detection region (the voltage is supplied by the detector electrodes connections (DE)). Applying and reversing the electric fields in each of the three spatial directions allows for an in-situ determination of the electric field, see Section 3.5 and Fig. 3.14. The photoelectrons are collected at the top and bottom channeltron electron multipliers (CEMs), also denoted as 'top detector' (TD) and 'bottom detector' (BD) throughout this thesis. Inside the detector, the atomic beam crosses the 2S-6P spectroscopy laser beam (SB), which emerges from the polarization-maintaining fiber (SF), is collimated by the four-lens fiber collimator (SC), and retroreflected by the high-reflectivity mirror (HR). These are the main parts of the active fiber-based retroreflector (AFR) for the suppression of the first-order Doppler shift, treated in detail in Chapter 4 (see Fig. 4.2 for the detailed vacuum assembly drawing of the AFR). The whole AFR setup including the fluorescence detector can be rotated against the

[1] Thorlabs Z 806 V, absolute on-axis accuracy 42 µm, bi-directional repeatability 1.5 µm. The conversion factor between the horizontal position of the blade and the motor position was determined to be 2.61(1), i.e. the absolute horizontal blade position accuracy is $\sim 2.6 \times 42\,\mu\text{m} \simeq 110\,\mu\text{m}$. However, the absolute position is anyway calibrated on each measurement day using an auxiliary laser beam. Typically, the scatter of the determined blade position from calibration is $\sim 20\,\mu\text{m}$.

[2] Thorlabs HNLS008L-EC.

[3] Fot the 2S-6P hydrogen measurement, the nozzle imaging was also used for the alignemnt of the nozzle relative to the 243 nm beam. However, for the 2S-6P deuterium measurement, the new ARS LT3-B cryostat on an accurate UHV Design manipulator was installed. The nozzle was then aligned using the scaling on the cryostat manipulator.

atomic beam by the α alignment actuator[1] (AA) to adjust the angle between the atomic beam and 2S-6P laser beam close to 90° such that $\alpha = 90° + \delta\alpha$ with $\delta\alpha \ll 1°$ (see Section 5.3).

Since the 243 nm cavity is mounted to the optical table, whereas the rest of the setup, including the AFR setup, sits on the laboratory floor, the alignment of chamber w.r.t. the 243 nm cavity is necessary. This is achieved by adjusting the feet of the vacuum chamber, while placing a lens cleaning tissue and a beam camera on a specially designed mount at two points: first, the lens cleaning tissue is placed directly after the incoupler mirror (IC) with the beam camera put between the entrance aperture (EA) and the variable aperture (VA) (with the 1S-2S Faraday cage being removed), and second, the lens cleaning tissue is placed directly before the entrance aperture while the beam camera is placed between the high-vacuum output aperture (OA) and the outcoupler mirror (OC). The lens cleaning tissue scatters the laser light such that the boundaries of the apertures are visible on the beam camera. On the other hand, with the lens cleaning tissue being removed, the position of the 243 nm beam is determined. By iteratively adjusting the alignment at the two points, the 243 nm beam is finally aligned to the apertures and thus to the whole apparatus. During the measurement, the nozzle is aligned with the 243 nm beam by measuring the 243 nm cavity transmission signal while adjusting the manipulator of the cryostat[2].

3.2 1S-2S/2S-6P laser systems and frequency comb

An important ingredient for precision laser spectroscopy is a stable laser, preferrably with a linewidth much smaller than the uncertainty goal. Furthermore, the laser frequency needs to be accurately measured. For the 2S-6P measurement in deuterium, two lasers are required: one laser at 243 nm which drives the two-photon 1S-2S transition (Section 3.2.1), and the other at 410 nm which drives the 2S-6P transition (Section 3.2.2). Both laser systems are very similar: the master lasers are external cavity semiconductor diode lasers (ECDL) in the infrared (at 972 nm and at 820 nm), which are stabilized to ultra low expansion glass (ULE) Fabry-Pérot cavities for achieving a sub-hertz linewidth. The laser frequency is doubled once (for 410 nm) or twice (for 243 nm) using non-linear crystals in second harmonic generation (SHG) cavities. The power of the 243 nm laser is enhanced in the in-vacuum enhacement cavity where the 1S-2S excitation takes place. This cavity also provides counter-propagating beams for the first-order Doppler-free two-photon excitation of the 1S-2S transition. The 410 nm laser serves for the active fiber-based retroreflector covered in Chapter 4. The infrared laser frequency is measured with an ultra-low noise frequency comb, provided with a frequency standard from a passive hydrogen maser. The maser is continuously compared to the Coordinated Universal Time (UTC), which is based on the International Atomic Time (TAI), using the Global Positioning System (GPS), see Section 3.2.3.

The research on our narrow linewidth lasers has been reported in [162, 163, 164]. Many details on the 243 nm enhancement cavity, including the discussion on mirror degradation and the chopper-triggered stabilization of cavity length and intracavity power, are treated in

[1] Thorlabs Z825BV with following key specifications: absolute on-axis accuracy 130 µm, bi-directional repeatability <1.5 µm, backlash <8 µm, home location repeatability <2 µm, min. repeatable incremental movement 0.2 µm. The actuator rotates the AFR by 16.7 mrad $\simeq 0.96°$ per 1 mm linear movement (for approximately orthogonal angle $\alpha \approx 90°$ between the atomic beam and the 2S-6P laser beam).

[2] For the 2S-6P hydrogen measurement with the old cryostat, the nozzle was aligned using the nozzle imaging from the auxiliary alignment laser (see Sec. 4.5.2.5 of [71]), since the cryostat was not mounted on an accurate manipulator.

the thesis by Lothar Maisenbacher, see Sec. 4.3 in [71]. The optical setup of the 410 nm laser system is largely part of the active fiber-based retroreflector, see Chapter 4 for details. Here, only an overview of the laser systems is given, with a focus on the differences between the hydrogen and deuterium setups.

3.2.1 243 nm laser system for 1S-2S excitation

The scheme of the 243 nm laser system (called 'FP1' in our laboratory) is shown in Fig. 3.5. The master laser is an extended cavity diode laser (ECDL), producing 32 mW of laser power at a wavelength of $\lambda = 972.274\,\text{nm}$ for deuterium spectroscopy. The laser cavity of 23 cm length consists of a grating and a laser diode in the Littrow configuration [162], with an electro-optical modulator (EOM)[1] placed inside the laser cavity (intra-cavity EOM). The infrared light is amplified by the tapered amplifier (TA)[2] to 2.7 W (for 4.0 A TA current). Optical isolators are placed before and after the TA to avoid reflections back into the TA and the master laser. Around 80 mW are split off for the frequency stabilization and determination unit, see dashed box in Fig. 3.5.

The two electrodes of the intra-cavity EOM as well as a piezoelectric element of the grating mount are used to stabilize the master laser to the ultra low expansion glass (ULE) Fabry-Pérot (FP) reference cavity (finesse $\mathcal{F}_{\text{FP1}} \sim 400\,000$, free spectral range $\text{FSR}_{\text{FP1}} \simeq 1.9326\,\text{GHz}$) [163]. This stabilization is achieved through the Pound-Drever-Hall technique [165, 166], with a modulation EOM and a reflection photodetector placed before the cavity (not shown in Fig. 3.5), producing the error signal used for 'locking' (stabilizing) the master laser[3].

The light is sent to the FP reference cavity setup through a polarization-maintaining (PM) fiber, which is subject to acoustic and thermal noise. This noise is compensated by the 'Fiber noise AOM' using a similar[4] scheme as in [167]. This AOM is operated in the -1^{st} diffraction order, resulting in a frequency change of $\Delta\nu = -f_{\text{fiber}} = 39\,337\,184\,\text{Hz}$. Another AOM is placed in the setup ("Scan AOM") for two reasons: first, the master laser frequency required for the 1S-2S transition needs to match one of the ULE FP reference

[1] Gsänger Optoelektronik GmbH, PM 25, potassium dideuterium phosphate (KD*P) crystal. The company Gsänger was first bought by Linos AG, which in turn was integrated into Qioptiq Photonics GmbH, where now the PM 25 phase modulator is available.

[2] Toptica TA unit (as part of the TA-FHG pro 15025 system), article number TA-0970-3000-1, serial number 212207, production date 09.12.2019, polarization type TE. The TA was replaced in December 2019 (as part of the overall upgrade of the Toptica 243 nm system), including an upgrade of power supply for up to 5 A, and new mechanics for better longtime stability.

[3] The Fabry-Pérot cavity EOM and photodetector signals for Pound-Drever-Hall locking are connected via RF transformers (Mini-Circuits FTB-1-1*A15+) to the phase detector (Mini Circuits ZRPD-1, 1-100 MHz), whose output is fed into the Toptica Fast Analog Linewidth Control (FALC 110) module. The main output of this 'lockbox' provides feedback to the first electrode (bandwidth $\sim 1\,\text{MHz}$) of the intra-cavity master laser EOM, while a separate lockbox (MPQ-made by H. Brückner) can be used to provide a lower-frequency feedback (bandwidth $\sim 100\,\text{kHz}$). The slow drifts of the laser cavity length are compensated by the feedback to the piezoelectric element of the grating (either by the unlimited intergrator of the FALC 110 module or by an additional MPQ-made 'lockbox')

[4] In contrast to [167], the same AOM is used for detecting and correcting the phase noise. To this end, a beamsplitter is placed after the 'Fiber noise AOM', such that one part of the diffracted light is retroreflected and passes this AOM a second time on the returning path. After the backpropagation through the fiber, the light (whose frequency is shifted by $-2 \times f_{\text{fiber}}$) is superimposed with the reflection of the fiber tip before the propagation through the fiber. From this beat note the error signal is derived for the feedback loop, which compensates the noise on a single pass through the 'Fiber noise AOM' (whose frequency is controlled with a voltage controlled oscillator supplied by the output signal of the lockbox).

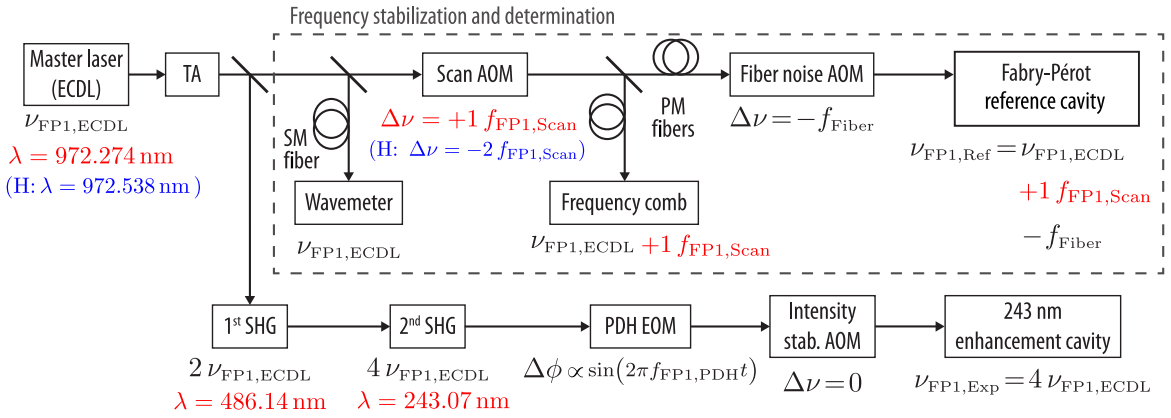

Figure 3.5: Laser system scheme for driving the $1S_{1/2}^{F=1/2} - 2S_{1/2}^{F=1/2}$ transition in deuterium at 243 nm ('FP1' laser system). The extended cavity diode laser (ECDL) serves as the master laser for the system and is amplified by a tapered amplifier (TA). Most of the light is guided to the two second harmonic generation (SHG) units, which double the frequency twice to produce 243 nm light. The 243 nm light is guided to the 243 nm enhancement cavity in vacuum, whose intensity is stabilized with the dedicated acousto-optic modulator (AOM), whereas for the length stabilization the Pound-Drever-Hall (PDH) technique with an electro-optic modulator (EOM) is used. A small fraction of the infrared light is split off for frequency stabilization to the Fabry-Pérot (FP) reference cavity, and for the frequency determination with a wavemeter and a frequency comb, where the light is guided through single-mode (SM) or polarization-maintaining (PM) fibers. The frequency of the laser is matched to the resonance of the FP reference cavity with the "Scan AOM", which is also used to scan the laser frequency over the 1S-2S resonance. Another AOM is used for cancellation of the fiber noise. The differences to hydrogen are marked in red, with the configuration for hydrogen ('H') written in parantheses in blue. The master laser is at the lower wavelength for deuterium compared to hydrogen, which requires a different "Scan AOM" configuration to match the laser frequency to the FP reference cavity resonance.

cavity resonances (separated by $\mathrm{FSR_{FP1}} \simeq 1.9326\,\mathrm{GHz}$). This AOM shifts the laser frequency accordingly. Second, this AOM is used to scan the frequency over the 1S-2S resonance, which is here possible due to the small scan range within the tuning range of the master laser (the typical linewidth of the 1S-2S transition is around 5 kHz which translates into $5/8 \sim 0.6$ kHz for the infrared light due to the two-photon excitation plus two SHG units).

The differences to hydrogen are marked in red in Fig. 3.5, with the configuration for hydrogen ('H') written in parantheses in blue. The master laser needs to be at the longer wavelength for hydrogen, separated from deuterium by ~ 0.264 nm or 83.78 GHz $\simeq 43.35 \times \mathrm{FSR_{FP1}}$. Therefore, to match the laser frequency to the FP reference cavity resonance, a different "'Scan AOM" configuration is required for deuterium compared to hydrogen. While for deuterium the "Scan AOM" is operated in the single-pass configuration in the $+1^{\mathrm{st}}$ diffraction order (at $f^{\mathrm{D}}_{\mathrm{FP1,Scan}} \simeq 383\,\mathrm{MHz}$), for hydrogen the same AOM is operated in the double-pass configuration in the -1^{st} diffraction order (at $f^{\mathrm{H}}_{\mathrm{FP1,Scan}} \simeq 434\,\mathrm{MHz}$), such that the difference is $f^{\mathrm{D}}_{\mathrm{FP1,Scan}} + 2 \times f^{\mathrm{H}}_{\mathrm{FP1,Scan}} \simeq 0.65\,\mathrm{FSR_{FP1}}$ and a $44 \times \mathrm{FSR_{FP1}}$ larger resonance frequency of the ULE FP reference cavity is used for deuterium compared to hydrogen.

Before the "Scan AOM", a fraction of light is guided via a single-mode fiber to the wavemeter[1] for a coarse wavelength measurement to match the correct resonance of the ULE FP

[1] HighFinesse WS7-60 wavelength meter, absolute accuracy ±60 MHz (for 420-1100 nm) solid state, super precision, USB version, with the MC4-780P multichannel option (single-mode, four inputs) such that the same wavelength meter can be used simultaneously for up to four different lasers.

reference cavity. After the "Scan AOM", around 1 mW of laser light is guided to the beat detection unit of the frequency comb for a precise frequency measurement (see Section 3.2.3).

Most of the infrared laser light after the TA is guided to the two second harmic generation (SHG) units (part of the commercial system[1]) for the production of 243 nm laser light. The first SHG uses a lithium triborate (LBO) crystal for frequency conversion, and is locked using the PDH technique with a modulation of the master laser current[2]. The second SHG uses a β-barium borate (BBO) crystal, and is also locked using the PDH technique, but with the modulation signal (at 5 MHz) from a dedicated EOM placed after the first SHG cavity. Two pairs of cylindrical lenses after each SHG collimate the laser beam. The output 243 nm laser beam of up to 120 mW power is slightly elliptical with major and minor beam waists ($1/e^2$ intensity radius) of 121 µm and 134 µm with waist positions around 20 cm before the output of the laser system enclosure.

3.2.1.1 243 nm enhancement cavity in vacuum

Since the 243 nm laser power is not sufficient to excite enough atoms into the metastable 2S state, the power is enhanced in the 243 nm enhancement cavity. Furthermore, the counter-propagating beams in the cavity automatically provide the setup for the first-order Doppler-free two-photon excitation of the 1S-2S transition.

The optical setup for the 243 nm enhancement cavity in the spectroscopy apparatus is shown in Fig. 3.6. The 120 mW output beam power from the laser system can be reduced with a half-waveplate in combination with a Glan-Laser polarizer[3] and a beam dump[4]. Then the light is modulated by the electro-optical modulator[5] (EOM) for the Pound-Drever-Hall stabilization of the 243 nm cavity. Thereafter, the beam is guided through a pair of lenses, first with $f = 75$ mm and then with $f = 100$ mm focal lengths, for two reasons. First, this telescope enables to adjust the mode matching to the 243 nm cavity[6]. Second, the intermediate focus

[1] Toptica TA-FHG pro 15025 system. This system was upgraded in December 2019, where the second SHG unit for the UV light production was entirely replaced by the new model, which is more stable and can provide more 243 nm laser power. In order for this new SHG unit to meet the requirements, the TA was replaced to garantee up to 3 W of 972 nm light (for max. TA current of 4.26 A), such that up to 1.5 W of 486 nm light can be produced after the first SHG unit. Furthermore, the EOM for Pound-Drever-Hall locking of the second SHG was replaced by a new model which can sustain high powers at 486 nm.

[2] The internal oscillator of the Pound-Drever-Hall PDD 110 module of the Topica system modulates the seed laser current at 19.66 MHz, and receives the reflection photodiode signal to produce an error signal. This error signal is guided to two control modules (FALC 110 and PID 110) to stabilizy the first SHG cavity length (a fast and a slow piezo).

[3] Thorlabs GLB10 Glan-Laser alpha-BBO Polarizer with MgF_2 anti-reflection coating, providing up to 80% transmission at 243 nm.

[4] Thorlabs BT600/M, 200 nm-3 µm, 80 W max average power (CW only).

[5] Qubig PM8-UV-45F, resonant high-Q electro-optic phase modulator, reflection and transmission at 235 nm $R < 0.5\%$ and $T > 90\%$, laser intensity $< 0.5\,\mathrm{W/mm^2}$ (at 223 nm), required RF power for full modulation 27 dBm (at 235 nm). fixed resonance frequency $f_{\mathrm{FP1,PDH}} = 45$ MHz. The EOM is driven by 10 dBm RF power produced by the Rigol DG 1032 Z function generator.

[6] For an estimation of the required lenses and distanced for mode-matching, the online 'Mode Matching Calculator' from Peter Beyersdorf's Laboratory Optics site (laboratoryoptics.com) is useful. Further calculations can then performed for example with the 'reZonator' software (rezonator.orion-project.org). With an input beam of 125 µm beam waist radius, with a 74 cm distance from the waist position to the $f = 75$ mm lens, which is separated by 187 mm from the subsequent $f = 100$ mm lens, the beam waist after the telescope lies 163 cm after the second lens (position of the input coupler for the 243 nm cavity) with a $1/e^2$ intensity waist radius of ~ 300 µm matching the TEM_{00} mode of the cavity.

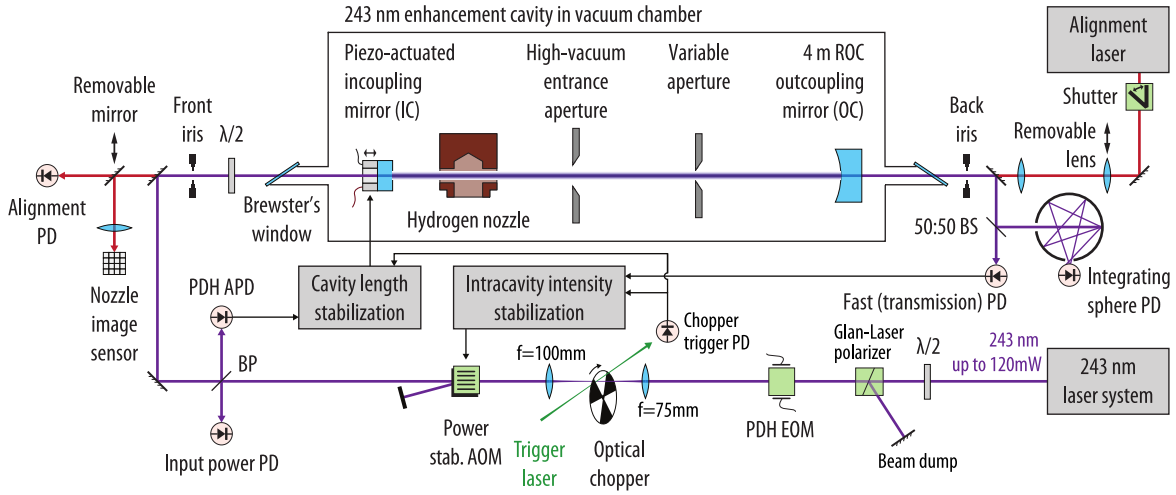

Figure 3.6: Optical setup for the 243 nm enhancement cavity in vacuum (not to scale), see main text for description. $\lambda/2$: half-waveplate, AOM: acousto-optic modulator, APD: avalanche photodiode detector, BP: beam sampler, BS: beamsplitter, EOM: electro-optic modulator, PD: photodetector, PDH: Pound-Drever-Hall rechnique, ROC: radius of curvature.

allows to precisely overlap an auxiliary trigger laser[1] at the optical chopper[2]. Since various feedback loops are triggered to the chopper, the trigger laser continously provides the trigger signal independent of the 243 nm laser which occasionally 'falls out of lock'. The trigger signal is distributed to various devices, e.g. for the intracavity intensity and cavity length stabilizations (see [71] for details).

The intracavity intensity stabilization is achieved using the cavity transmission signal (from the 'Fast (transmission) PD' in Fig. 3.6) for generating the error signal, with the feedback applied[3] to the power produced by the signal generator[4] to drive the AOM[5] serving here as an actuator: the diffracted laser beams are blocked, while the non-diffracted beam is transmitted. The RF power delivered to the AOM actively changes the power ratio between the diffracted and non-diffracted beams such that the power in the 243 nm cavity is kept stable.

The cavity length is stabilized using the Pound-Drever-Hall technique with an avalanche photodiode detector[6] ('PDH APD' in Fig. 3.6) measuring the reflection from a beam sampler. On the forward propagating path, the reflection from this beam sampler is used to monitor the incoming 243 nm power ('Input power PD' in Fig. 3.6). The feedback for length stabilization

[1]Thorlabs CPS 405 (wavelength 405 nm with 4.5 mW laser power).

[2]Stanford Research Systems SR 540 (O 540 RCH head and O 5402530 blade), with New Focus 3501 controller set to 160 Hz. The rise and fall times due to finite focus size and slot width are ∼3 µs, which is the same order of the jitter of switching time of the laser beams. The imperfections of the chopper lead to a ∼5 µs variation of the 3125 µs long chopper cycles.

[3]Vescent Photonics D2-125 Laser Servo is used as the 'lockbox'.

[4]Rohde und Schwarz GmbH, SMC 100 A signal generator, where the amplitude modulation feature (3 dB bandwidth of 50 kHz) is employed in a feedback loop. The output of the signal generator is amplified by the Mini-Circuits Model ZHL-1-2W+ radio frequency amplifier.

[5]IntraAction ASM-1101M3 AOM, 110 MHz center frequency, active medium: UV-grade fused silica, broadband UV AR coating, transmission of 98% at 243 nm.

[6]Thorlabs APD430A2/M.

is provided[1] to the piezo-actuated incoupling mirror (IC). To increase the feedback bandwidth for a possible future upgrade to the longer cavity, the design of the mirror mount was modified, see Appendix A.5.

An auxiliarly alignment laser[2] is aligned with the 243 nm laser beam using the front and back irises before the vacuum chamber. For the alignment of the variable aperture, the 'Alignment PD' measures the transmitted laser power while scanning the aperture distances. The alignment laser serves also for the purpose of nozzle imaging. In this case, an additional lens is placed in the beam path ('Removable lens' in Fig. 3.6), and an additional mirror ('Removable mirror') guides the transmitted light to the nozzle image sensor[3]. During the spectroscopy measurement, the alignment laser is blocked with a shutter.

The power $P_{\text{1S-2S}}$ (per direction) circulating in the 243 nm cavity is monitored by the transmission signal from the 'integrating sphere PD', which captures approximately half of the transmission after a 50:50 beamsplitter (while the other half is detected by the 'Fast transmission PD' for cavity length stabilization). The voltage on the photodetectors is calibrated for conversion to optical power with a separate measurement of the transmitted power. This measurement is typically performed several times during the measurement campaign. The power inside the cavity is then calculated using the separately characterized transmittance of the outcoupling mirror, the Brewster's window and the steering mirror. For this measurement, the powermeter[4] is placed right before the beamsplitter, but after an additional steering mirror. The total transmittance was determined by measuring the power before the outcoupler mirror (in the opened vacuum chamber with the incoupler mirror being removed) and the transmitted power through the outcoupler mirror, the Brewster's window and the steering mirror. This measurement was performed with 35.5 mW before the outcoupler mirror, and the transmission was measured to 2.0 µW, which yields $T_{\text{OC}}T_{\text{path}} = 5.6(5) \times 10^{-5}$, where T_{OC} is the transmission of the outcoupler mirror[5] and T_{path} the combined coefficient of the transmission of the Brewster's window and the reflection of the steering mirror. During the spectroscopy measurement, this transmission coefficient can then be used to deduce the intra-cavity power while the cavity is locked. Note that a factor of two needs to be taken into account due to the duty cycle of the chopper, e.g. for $P_{\text{tr,meas}} = 40\,\mu\text{W}$ measured transmitted average power, the deduced power circulating in the 243 nm cavity during the bright phase is $P_{\text{1S-2S}} = 2 \times P_{\text{tr,meas}}/(T_{\text{OC}}T_{\text{path}}) \simeq 1.4(1)\,\text{W}$. The intra-cavity power can also be deduced from the measured input power combined with the power enhancement from the measured finesse together with the incoupler transmission. However, the finesse measurement may be affected by the rapid degradation of the mirrors when the cavity is locked, and recovery thereafter, as discussed below.

[1] Using a Vescent Photonics D2-125 Laser Servo 'lockbox'.

[2] Thorlabs Helium-Neon laser, HNLS008L-EC, 0.8 mW at 633 nm, polarized.

[3] UI-3380CP-M-Gl by IDS Imaging Development Systems, with cover glass removed by Eureca Messtechnik.

[4] Newport 843-R Power Meter with Newport 818-UV/DB UV Enhanced Silicon Diode Sensor (calibrated March 2022), calibration uncertainty ±2% at 243 nm, uniformity over the sensor area ±2%, linearity ±0.5%, minimum measurable power 20 pW, maximum measurable power 1500 mW (with attenutator) and 5 mW (without attenutator in the wavelength range 200-400 nm). According to the manual, especially for UV measurements, the power meter and the sensor need to be calibrated annually to achieve the specified uncertainty.

[5] The separately characterized transmittance of the outcoupling mirrors from the same order was measured to $T_{\text{OC}} \sim 9.5 \times 10^{-5}$, with an uncertainty of ∼10% depending of the mirror position. This measurement was performed with the Newport 843-R Power Meter with Newport 918D-UV-OD3R UV sensor (without attenuator), which was not calibrated since 2017. However, comparison to the newly calibrated sensor and other power meters agreed with the 918D-UV-OD3R UV sensor (without attenuator) within 5%, which is lower than the uncertainty depending on the mirror position.

The 243 nm enhancement cavity is formed by a flat[1] ($r_{\mathrm{IC}} = \infty$) incoupling mirror (IC) and a concave outcoupling mirror with a radius of $r_{\mathrm{OC}} \simeq 4\,\mathrm{m}$. The cavity length is $L_{\mathrm{EC}} = 358\,\mathrm{mm}$, leading to a free spectral range of $\mathrm{FSR} = c/(2\,L_{\mathrm{EC}}) = 419\,\mathrm{MHz}$. The waist size is given by [168]:

$$w_0 = \sqrt{\frac{\lambda\, L_{\mathrm{EC}}}{\pi}\sqrt{r_{\mathrm{OC}}/L_{\mathrm{EC}} - 1}} \simeq 297(10)\,\mu\mathrm{m}. \tag{3.1}$$

The ±5% uncertainty in the curvature radius results in an uncertainty of ±10 µm on w_0.

The resonant frequencies $\nu_{q,nm}$ of the $\mathrm{TEM}_{q,nm}$ Hermite-Gaussian modes [169] are given by [168]:

$$\nu_{q,nm} = \left(q + (n+m+1)\frac{\arccos\sqrt{1 - L_{\mathrm{EC}}/r_{\mathrm{OC}}}}{\pi}\right)\mathrm{FSR}, \tag{3.2}$$

where q, n, m are the integer mode numbers. The cavity is operated on the fundamental $\mathrm{TEM}_{q,00}$ mode. The higher-order modes are separated by $(\arccos\sqrt{1 - L_{\mathrm{EC}}/r_{\mathrm{OC}}})/\pi \simeq 0.097(2)\,\mathrm{FSR}$ (with uncertainty due to the 5% tolerance of r_{OC}), such that the number of the first transverse modes per FSR is 10.3(2) and the $\mathrm{TEM}_{q,nm}$ modes with $n + m = 10$ and $n + m = 11$ are out of resonance with the $\mathrm{TEM}_{q,00}$ mode.

The finesse of the cavity, $\mathcal{F} = \mathrm{FSR}/\delta\nu_{\mathrm{FWHM}}$ where $\delta\nu_{\mathrm{FWHM}}$ is the full width at half maximum of the circulating intensity at resonance, can be calculated from the reflectances of the incoupling and outcoupling mirrors, R_{IC} and R_{OC} respectively, as [168]:

$$\mathcal{F} = \frac{\pi\sqrt{\sqrt{R_{\mathrm{IC}}R_{\mathrm{OC}}}T_{\mathrm{EC}}}}{1 - \sqrt{R_{\mathrm{IC}}R_{\mathrm{OC}}}T_{\mathrm{EC}}}, \tag{3.3}$$

where we took into account the single-path intensity transmission (round-trip field transmission) of the medium T_{EC} into account. In the following we set $T_{\mathrm{EC}} = 1$, but note that for instance misalignment of the apparatus could lead to clipping losses on apertures or the nozzle through-hole such that $T_{\mathrm{EC}} < 1$. In the case of ideal alignment of the apparatus, the rectangular aperture of 1.2 mm × 2.0 mm (which is the size of the variable aperture) results in $T_{\mathrm{EC}} \simeq 10^{-4}$ (see Fig. 4.13 of [71]).

For the given mode-matching η_{mode}, the power enhancement $\mathrm{PE} = P_{\mathrm{in}}/P_{\mathrm{circ}}$, where P_{in} is the power before the cavity and P_{circ} the circulating power inside the cavity, is given by [168]:

$$\mathrm{PE} = \frac{P_{\mathrm{in}}}{P_{\mathrm{circ}}} = \frac{\eta_{\mathrm{mode}}\,T_{\mathrm{IC}}}{(1 - \sqrt{R_{\mathrm{IC}}R_{\mathrm{OC}}}T_{\mathrm{EC}})^2} = \eta_{\mathrm{mode}}T_{\mathrm{IC}}\frac{4\mathcal{F}^4}{\pi^2\left(\pi - \sqrt{4\mathcal{F}^2 + \pi^2}\right)^2}, \tag{3.4}$$

where in the last step the factor $\sqrt{R_{\mathrm{IC}}R_{\mathrm{OC}}}T_{\mathrm{EC}}$ was expressed through the finesse $\mathcal{F}$ using Eq. (3.3). For optimal mode-matching, the power enhancement and finesse are therefore linked only through the transmission of the input coupler T_{IC}. The measurement of the finesse, T_{IC} and η_{mode} thus gives the value for the power enhancement.

For the UV mirrors, typically a significant fraction of light is absorbed and scattered in the mirror. Therefore, the reflectance and transmittance coefficients are related by

$$R_{\mathrm{IC}} + T_{\mathrm{IC}} + A_{\mathrm{IC}} = 1 \quad \text{and} \quad R_{\mathrm{OC}} + T_{\mathrm{OC}} + A_{\mathrm{OC}} = 1, \tag{3.5}$$

[1] It was found that the used ring piezo (PI Ceramic GmbH, PD080.31, 2 µm range, thickness 2.5 mm, inner diameter 4.5 mm, outer diameter 8.0 mm) can distort the flat mirror curvature to a radius of up to $r_{\mathrm{IC}} \simeq -50\,\mathrm{m}$ for 60 V applied voltage. For our cavity geometry, assuming a flat incoupling mirror translates in this case into an effective change of the outcoupling mirror radius from $r_{\mathrm{OC}} \simeq 4.0\,\mathrm{m}$ to $r_{\mathrm{OC}} \simeq 4.35\,\mathrm{m}$.

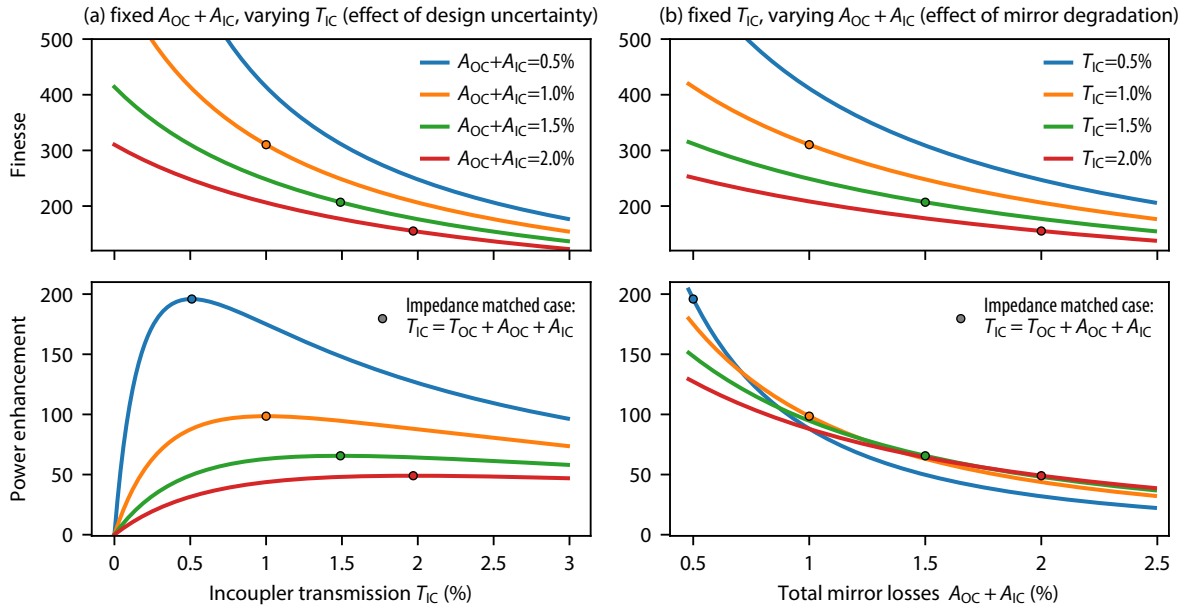

Figure 3.7: Finesse and power enhancement for the 243 nm enhancement cavity, according to Eq. (3.4) and Eq. (3.3) with approximation Eq. (3.6), such that only the total absorbance $A_{OC}+A_{IC}$ is relevant. The outcoupler transmittance is set to $T_{OC} = 0.01\%$ (which is negligible compared to T_{IC} such that the results do not change significantly with zero T_{OC}). For all the plots, the impedance matched case $T_{IC} = T_{OC} + A_{IC} + A_{IC}$ is marked with corresponding colored points for each scenario. (a) For different values of $A_{OC} + A_{IC}$ the finesse and power enhancement are plotted in dependence on T_{IC}, thereby visualizing the effects of mirror design uncertainty in T_{IC}: especially for lower absorbance of $A_{OC} + A_{IC} = 0.5\%$ (blue curve), a lower T_{IC} than designed for the impedance matched case (blue marker) would result in a sharp drop of the power enhancement. (b) For different values of T_{IC}, the finesse and power enhancement are plotted in dependence on $A_{OC} + A_{IC}$, thereby visualizing the effect of mirror degradation (increasing losses over time). Given the design uncertainty in T_{IC} and $A_{OC} + A_{IC}$, as well as increasing $A_{OC} + A_{IC}$ over time, it is advantageous to choose the overcoupled case $T_{IC} > T_{OC} + A_{OC} + A_{IC}$.

where A_{IC} and A_{OC} are the fractions of absorbed or scattered intensity in the incoupling and outcoupling mirrors, respectively. Since $T_{IC}, T_{OC}, A_{IC}, A_{OC} \ll 1$, the factor $\sqrt{R_{IC}R_{OC}}T_{EC}$, which enters the finesse and the power enhancement, can be approximated as:

$$\sqrt{R_{IC}R_{OC}}T_{EC} \simeq T_{EC}\left(1 - \frac{A_{IC} + A_{OC}}{2} - \frac{T_{IC} + T_{OC}}{2}\right). \tag{3.6}$$

Therefore, in the leading order, both the finesse and power enhancement depend only on the sum of the absorption coefficients $A_{IC} + A_{OC}$, but not on how the total absorbance is distributed among the two mirrors. The measurement of finesse and power enhancement can thus not distinguish between incoupler and outcoupler losses. The finesse measurement can also not distinguish between the individual transmittances, while the power enhancement depends on T_{IC} which enters Eq. (3.4) in addition to the above factor.

For the design of the mirrors, two challenges are important to consider: first, the design uncertainty in the coefficients, and second, the degradation of mirrors, i.e. the increase of coefficients $A_{IC} + A_{OC}$ over time. If the coefficients are exactly known and would not change over time, the optimal design leading to maximum power enhancement is achieved for an

impedance matched cavity. In this case, the intensity transmission coefficient of the incouping mirror is equal to the sum of all of the other losses, excluding the input coupling [168]: $T_{\mathrm{IC}} = T_{\mathrm{OC}} + A_{\mathrm{OC}} + A_{\mathrm{IC}}$, assuming no intra-cavity losses (medium losses), i.e. for $T_{\mathrm{EC}} = 1$. However, due to the uncertainty in the coefficients and the mirror degradation, it is advantageous to aim for an overcoupled cavity, i.e. $T_{\mathrm{IC}} > T_{\mathrm{OC}} + A_{\mathrm{OC}} + A_{\mathrm{IC}}$. If the T_{IC} turns out to be smaller than expected, and the absorption coefficients are underestimated and/or increase over time, the power enhancement is lower initially than in the ideal impedance-matched case, but higher for increasing losses and/or lower T_{IC}. This is illustrated in Fig. 3.7, where in (a) the finesse and power enhancement are shown for various values for $A_{\mathrm{IC}} + A_{\mathrm{OC}}$ as a function of T_{IC} (visualizing the effect of design uncertainty), and in (b) for various T_{IC} as a function of total mirror losses $A_{\mathrm{IC}} + A_{\mathrm{OC}}$ (visualizing the effect of mirror degradation). The impedance matched case is marked with points in each graph. For a detailed discussion of mirror degradation, see Sec. 4.3.3 of [71].

The finesse $\mathcal{F}$ can be measured by scanning the cavity length with the piezo of the incoupling mirror while recording the transmission and the Pound-Drever-Hall (PDH) error signals, which is demostrated in Fig. 3.8. The transmission $T_{q,nm}$ of the cavity resonances is fitted with a Lorentzian:

$$T_{q,nm} \propto \frac{(\delta\nu_{\mathrm{FWHM}}/2)^2}{\Delta\nu^2 + (\delta\nu_{\mathrm{FWHM}}/2)^2}, \tag{3.7}$$

where $\delta\nu_{\mathrm{FWHM}}$ is the full width half maximum of the resonance and $\Delta\nu = \nu - \nu_0$ is the detuning from the resonance at the frequency ν_0 with the laser frequency ν. Scanning the cavity length can here be considered equivalent to detuning the laser frequency. The comparison of amplitudes for higher order modes to the fundamental mode in Fig. 3.8(a) yields the mode-matching of $\eta_{\mathrm{mode}} \simeq 0.95$. The fit for two neighboring $\mathrm{TEM}_{q,00}$ and $\mathrm{TEM}_{q+1,00}$ resonances (see Fig. 3.8(a)) yields the separation in the resonance frequencies ν_0, determining the free spectral range to $\mathrm{FSR} \simeq 11.37\,\mathrm{V}$ (in units of piezo voltage[1]), which along with the full width half maximum $\delta\nu_{\mathrm{FWHM}} \simeq 0.075(4)\,\mathrm{V}$ yields $\mathcal{F} = \mathrm{FSR}/\delta\nu_{\mathrm{FWHM}} \simeq 152(8)$. The accuracy this finesse measurement is limited by the non-linearity of the piezo on the order of 20%.

A more accurate way to determine the finesse can be to fit the PDH error signal, which is given by [168]:

$$V_{\mathrm{PDH}} \propto J_0(\beta)J_1(\beta)\frac{\nu_m^2}{\delta\nu_{\mathrm{FWHM}}^3} \times \frac{\Delta\nu - 4\frac{\Delta\nu(\Delta\nu+\nu_m)(\Delta\nu-\nu_m)}{\delta\nu_{\mathrm{FWHM}}^2}}{\left(1+4\frac{\Delta\nu^2}{\delta\nu_{\mathrm{FWHM}}^2}\right)\left(1+4\frac{(\Delta\nu+\nu_m)^2}{\delta\nu_{\mathrm{FWHM}}^2}\right)\left(1+4\frac{(\Delta\nu-\nu_m)^2}{\delta\nu_{\mathrm{FWHM}}^2}\right)}, \tag{3.8}$$

where J_0 and J_1 are the Bessels functions of the first kind of order 0 and 1 with an input parameter β (modulation index), and $\nu_m = 45\,\mathrm{MHz}$ the known modulation frequency. The fit yields ν_m in units of applied piezo voltage, which can be used to convert the piezo voltage to frequency. Along with $\mathrm{FSR} = c/(2\,L_{\mathrm{EC}}) = 419\,\mathrm{MHz}$ from the known cavity length $L_{\mathrm{EC}} = 358\,\mathrm{mm}$, the value for the finesse is then determined from the data in Fig. 3.8(a) to $\mathcal{F} \simeq 143(2)$. Yet another way is to use the mode spacing from Eq. (3.2) of $0.097(2) \times \mathrm{FSR}$ with the given cavity length and curvature radius (with the uncertainty dominated by the curvature radius tolerance). The mode separation is best measured with misaligned coupling into the cavity, where the higher-order modes are more pronounced, as shown in Fig. 3.8(b). For lower piezo voltages, the spacing between the $\mathrm{TEM}_{q,00}$ and the $\mathrm{TEM}_{q,01}$ (degenerate with $\mathrm{TEM}_{q,10}$) modes

[1]The 11.37 V separation of the $\mathrm{TEM}_{q,00}$ and $\mathrm{TEM}_{q+1,00}$ is equal to the wavelength $\lambda = 243\,\mathrm{nm}$, which approximately agrees with the 2 µm travelling range of the piezo for 100 V applied voltage.

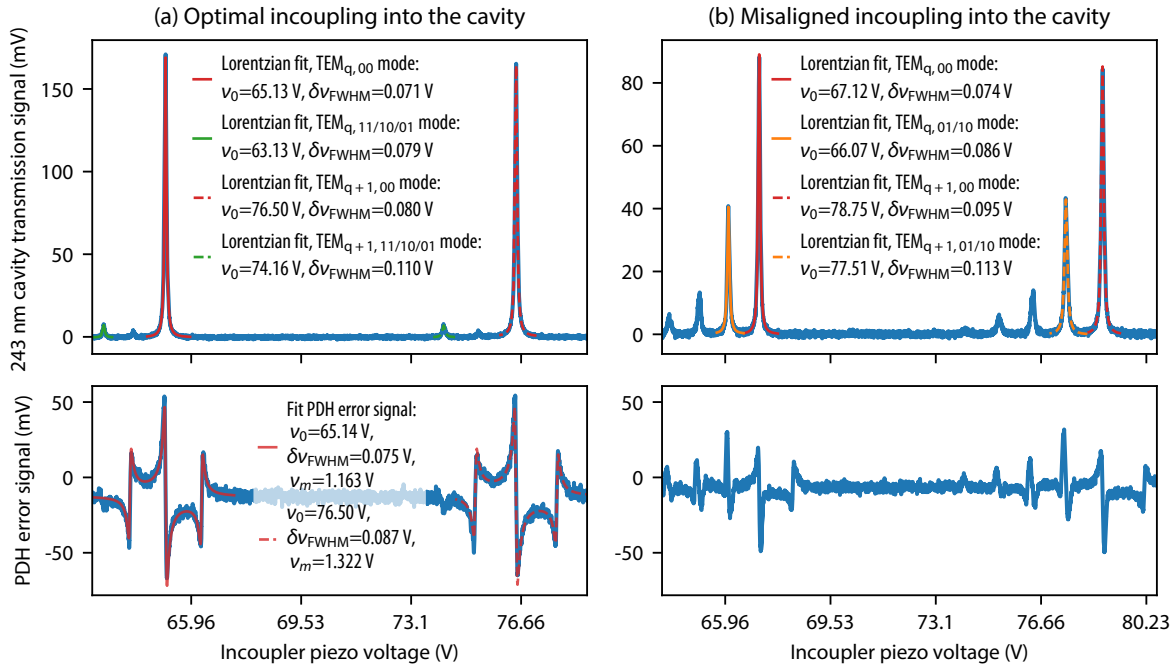

Figure 3.8: Finesse measurement of the 243 nm enhancement cavity: the cavity transmission signal (from the 'Fast transmission PD' in Fig. 3.6) and the Pound-Drever-Hall (PDH) error signal (from the 'PDH APD' signal mixed with the 'PDH EOM' signal) are measured while scanning the cavity length with the piezo of the incoupling mirror. In (a) the cavity is optimally aligned such that the higher-order modes are suppressed. The finesse can be determined from the Lorentzian fits of the $\mathrm{TEM}_{\mathrm{q},00}$ and $\mathrm{TEM}_{\mathrm{q}+1,00}$ resonances: the separation in the resonance frequencies ν_0 approximately yields the free spectral range $\mathrm{FSR} \simeq 11.37\,\mathrm{V}$ (in units of piezo voltage), which along with the full width half maximum $\delta\nu_{\mathrm{FWHM}} \simeq 0.075(4)\,\mathrm{V}$ yields $\mathcal{F} = \mathrm{FSR}/\delta\nu_{\mathrm{FWHM}} \simeq 152(8)$, with limiting uncertainty from the non-linearity of the piezo. Alternatively, the piezo voltage scale can be converted to frequency from the fit of the PDH error signal according to Eq. (3.8), which yields the known modulation frequency $\nu_m = 45\,\mathrm{MHz}$ to obtain $\delta\nu_{\mathrm{FWHM}} \simeq 2.93(3)\,\mathrm{MHz}$. Along with $\mathrm{FSR} = c/(2\,L_{\mathrm{EC}}) = 419\,\mathrm{MHz}$ from the known cavity length $L_{\mathrm{EC}} = 358\,\mathrm{mm}$, the value for the finesse is $\mathcal{F} \simeq 143(2)$. Yet another way to determine the finesse is from the spacing of higher-order modes, which is calculated from the cavity length and the curvature radius to $\sim 0.097(2)\,\mathrm{FSR}$ (see Eq. (3.2)). The finesse measurement is then performed with the misaligned cavity incoupling shown in (b), where the higher-order modes are more pronounced. The spacing between the $\mathrm{TEM}_{q,00}$ and the $\mathrm{TEM}_{\mathrm{q},01}$ (degenerate with $\mathrm{TEM}_{q,10}$) modes is 1.05 V which yields $\mathcal{F} \simeq 146(3)$, in agreement with the other methods.

is 1.05 V which yields $\mathcal{F} \simeq 146(3)$, in agreement with the other methods. For higher voltages this finesse measurement method might also be affected by the curvature distortion of the piezo mirror[1].

For the deuterium 2S-6P measurement, mirrors coated with aluminum oxide ($AlO_2 + SiO_2$ coating layers) were used, in the hope that these coatings perform better than those with hafnium oxide ($HfO_2 + SiO_2$ coating layers) used previously. The mirrors are specified for

[1]It was found that the ring piezo (PI Ceramic GmbH, PD080.31, 2 µm range (for 0-100 V applied voltage), thickness 2.5 mm, inner diameter 4.5 mm, outer diameter 8.0 mm, 300 nF capacity) can distort the flat mirror curvature to a radius of up to $r_{\mathrm{IC}} \simeq -50\,\mathrm{m}$ for 60 V applied voltage. For our cavity geometry, assuming a flat incoupling mirror translates in this case into an effective change of the outcoupling mirror radius from $r_{\mathrm{OC}} \simeq 4.0\,\mathrm{m}$ to $r_{\mathrm{OC}} \simeq 4.35\,\mathrm{m}$.

$T_{IC} = 1.5 \pm 0.5\%$, $R_{IC} = 98.3 \pm 0.5\%$, $T_{OC} \sim 0.01\%$ and $R_{OC} > 99.5\%$. The transmittances of the mirrors were measured to be $T_{IC} = 1.7(1)\%$ and $T_{OC} = 9.5(1.0) \times 10^{-5}$. However, the measured finesse and power enhancement were lower than the expected values from the calculations based on mirror specifications. In the beginning of the deuterium measurement campaign, the finesse was $\mathcal{F} \sim 165$ and dropped to $\mathcal{F} \sim 145$ after seven measurement days, corresponding to $\sqrt{R_{IC}R_{OC}}T_{EC} = 0.9786 \ldots 0.9811$ and an increase in the total mirror losses from $A_{IC} + A_{OC} \simeq 2.1\%$ to 2.6% according to Eq. (3.6) (assuming no intra-cavity losses, i.e. $T_{EC} = 1$, and with $T_{IC} = 1.7\%$ and $T_{OC} = 0.01\%$). When the cavity mirrors were just installed, a finesse of $\mathcal{F} \sim 190$ was observed which results in $A_{IC} + A_{OC} \simeq 1.6\%$. The total absorption of $A_{IC} + A_{OC} \sim 2\%$ is higher than expected. Assuming that the absorption coefficients are equal for both mirrors, the reflectance of the outcoupler mirror is only $R_{OC} \sim 99.0\%$ which is lower than the specified $R_{OC} > 99.5\%$. For the hafnium oxide coated mirrors used for the hydrogen 2S-6P campaign, the total absorption was initially only $A_{IC} + A_{OC} \sim 0.5\%$, with a similar total degradation by $1 - 2\%$. The outcoupling mirror was specified to $R_{OC} > 99.9\%$ such that the deduced $R_{OC} \simeq 99.7\%$ (before degradation) also did not meet the specification.

Along with measured $T_{IC} = 1.7(1)\%$ and $\eta_{mode} \simeq 0.95$, using Eq. (3.4), the finesse values $\mathcal{F} \sim 145 \ldots 165$ yield a power enhancement of $35(2) \ldots 45(2)$. However, the power enhacement determined from the input power and the transmitted power was measured to be lower at PE $\sim 26(5) \ldots 31(5)$. A similar discrepancy was also observed during the second run of the hydrogen 2S-6P measurement campaign (see Fig. 4.9 in [71]). This discrepancy could originate from the rapid degradation of the cavity when it is locked, and a recovery when the cavity is unlocked or scanned during finesse measurements. The more direct intra-cavity power measurement from the transmitted power (when the cavity is locked) seems more reliable. However, effects like power-dependent absorption in the coating of the outcoupler mirror, or thermal-induced birefringence in the mirror, which may lead to higher reflection losses at the Brewster's window, could in principle also disturb the power measurement from the cavity transmission. Further characterization is needed to resolve this discrepancy.

In the future, the degradation of mirrors can be prevented by upgrading the apparatus with differential pumping to flush the mirrors with oxygen. Furthermore, recently it was reported that mirrors with fluoride coatings instead of oxide coatings are much more robust against mirror degradation [170]. The order for fluoride coated mirrors for our experiment is currently in progress.

3.2.2 410 nm laser system for 2S-6P excitation

The laser system for the 410 nm wavelength of the 2S-6P excitation (called 'FP3' in our laboratory) is very similar to the 1S-2S laser system, see Fig. 3.9 for the setup. The master laser is also an external cavity diode laser (ECDL) in the Littrow configuration as described in [164], with a 20 cm cavity length between the grating and the diode. The output light of 820 nm wavelength is amplified using a commercial tapered amplifier[1] (TA) to 1.1 W (for 2.2 A TA current). Most of the infrared light is sent to the second harmonic generation (SHG) cavity, which produces up to 150 mW of 410 nm light in a lithium triborate (LBO) crystal. The cavity is constantly flushed with oxygen to reduce humidity and prevent the degradation

[1] Toptica TA-0808-2000-1, operating current up to 3050 mA, polatization type TE (horizontal), negative polarity, output power up to 2 W, center wavelength 805 nm with 26 nm gain width (10 dB below peak), with two collimating lenses Thorlabs C230TME-B.

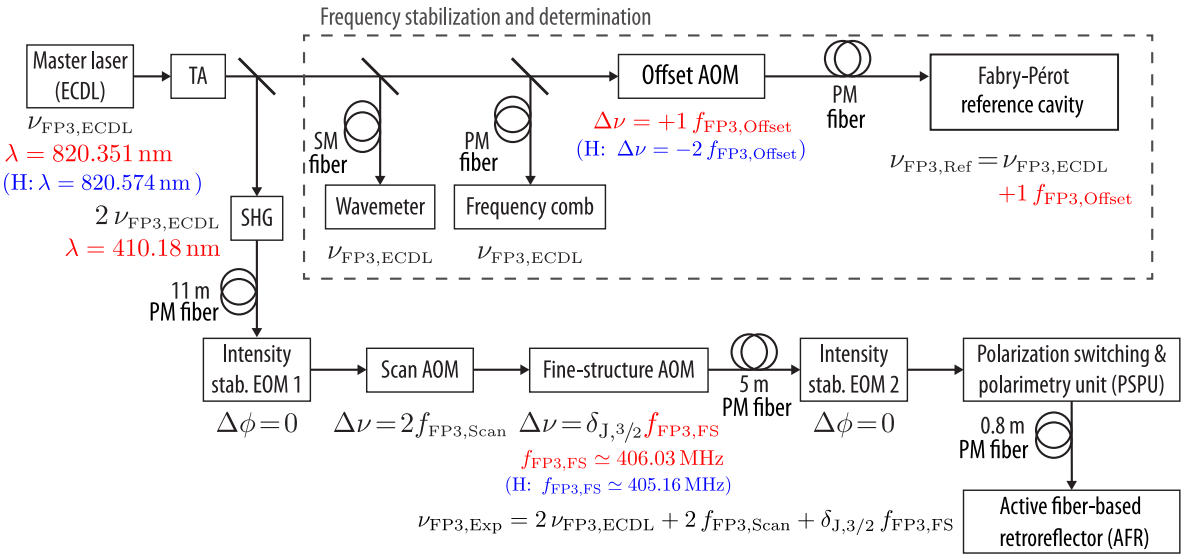

Figure 3.9: Laser system scheme for driving the $2S_{1/2}^{F=1/2} - 6P_{1/2}^{F=1/2,3/2}$ and $2S_{1/2}^{F=1/2} - 6P_{3/2}^{F=1/2,3/2}$ transitions in deuterium at 410 nm ('FP3' laser system). Similar to the 243 nm laser system from Fig. 3.5, the extended cavity diode laser (ECDL) serves as the master laser for the system and is amplified by a tapered amplifier (TA). Most of the light is guided to the second harmonic generation (SHG) unit for producing 410 nm light, which is used for 2S-6P spectroscopy with the active fiber-based retroreflector (AFR), see Fig. 4.1 and Chapter 4 for details. Two electro-optic modulators (EOM) serve as actuators for the two intensity stabilizations, see Section 4.5. In contrast to the 243 nm laser system, because of the much larger required scanning range, the frequency is scanned with a separate acousto-optic modulator (AOM) at 410 nm. Spectrocopy light can also be guided through an additional AOM to address the $J = 3/2$ ($6P_{3/2}$) fine-structure state manifold ($\delta_{J,3/2} = 1$). If the $J = 1/2$ ($6P_{1/2}$) fine-structure state manifold is addressed, this AOM is bypassed ($\delta_{J,3/2} = 0$). The frequency stabilization and determination unit is similar to Fig. 3.5, with two differences: first, no fiber noise cancellation is applied (due to the lower requirements on the laser spectrum), and second, to match the frequency of the laser to the Fabry-Pérot reference cavity resonance, an 'Offset AOM' with a fixed frequency is placed after some part of the light is split for the frequency comb. The differences to hydrogen are marked in red, with the configuration for hydrogen ('H') written in parantheses in blue. Due to the lower wavelength for deuterium compared to hydrogen, a different 'Offset AOM' configuration is required to match the Fabry-Pérot reference cavity resonance.

of the crystal (as opposed to the commercial SHG cavities of the 243 nm laser system which are sealed and contain desiccants). The cavity length is stabilized by the Hänsch-Couillaud technique [171, 166], which makes use of the polarization-sensitivity of the cavity reflection.

The frequency stabilization and determination unit of the 2S-6P laser system (dashed box in Fig. 3.9) differs from the 1S-2S laser system (recall Fig. 3.5) in two points. First, the laser frequency is matched to the resonance of the ultra low expansion glass Fabry-Pérot (ULE FP) reference cavity by the "Offset AOM" (operated at a fixed frequency) after some light is split for the frequency comb. In constrast to the narrow 1S-2S transition, the much larger scan range for the broader 2S-6P transition (typical linewidth ~ 10 MHz which translates into 5 MHz for the infrared light before the SHG unit) exeeds the tuning range of the master laser such that a separate "Scan AOM" is required. Second, no fiber noise cancellation is implemented due to the lower requirements on the laser spectrum.

The differences to hydrogen are marked in red in Fig. 3.9, with the configuration for

hydrogen ($2S^{F=0}_{1/2} - 6P^{F=1}_{1/2}$ and $2S^{F=0}_{1/2} - 6P^{F=1}_{3/2}$ transitions) written in parantheses in blue. The master laser needs to be at the longer wavelength for hydrogen, separated from deuterium by $\sim 0.223\,\text{nm}$ or $99.36\,\text{GHz} \simeq 51.4 \times \text{FSR}_{\text{FP3}}$, where $\text{FSR}_{\text{FP3}} \simeq 1.9321\,\text{GHz}$ is the free spectral range of the ULE FP reference cavity. Therefore, to match the laser frequency to the FP reference cavity resonance, a different 'Offset AOM' configuration is required for deuterium compared to hydrogen. While for deuterium the 'Offset AOM' is operated in the single-pass configuration in the $+1^{\text{st}}$ diffraction order (at $f^{\text{D}}_{\text{FP3,Offset}} = 296.6\,\text{MHz}$), for hydrogen the same AOM can be operated in the double-pass configuration in the -1^{st} diffraction order (at $f^{\text{H}}_{\text{FP3,Offset}} = 410\,\text{MHz}$), such that the difference is $f^{\text{D}}_{\text{FP3,Offset}} + 2 \times f^{\text{H}}_{\text{FP3,Offset}} \simeq 0.6\,\text{FSR}_{\text{FP3}}$ and a $51 \times \text{FSR}_{\text{FP3}}$ higher resonance frequency of the ULE FP reference cavity is used for deuterium compared to hydrogen. Alternatively, the deuterium laser frequency can be achieved with the double-pass configuration using the $+1^{\text{st}}$ diffraction order, but replacing the AOM by a different model[1] such that it operates at $f^{\text{D}}_{\text{FP3,Offset}} \simeq 148.3\,\text{MHz}$.

After the SHG unit, the 410 nm light is sent via 11 m long polarization-maintaining (PM) fiber to the optical setup which is shown in Fig. 4.1 of Chapter 4 in more detail. Two electro-optic modulators (EOM 1 and 2) are used for the intensity stabilization discussed in Section 4.5. The laser frequency is scanned in the $\pm 50\,\text{MHz}$ range with the "Scan AOM"[2], which is operated at the center frequency 350 MHz in the double-pass configuration (such that the scan range is $\pm 25\,\text{MHz}$ for the AOM frequeny). An additional AOM ("Fine-structure AOM", only shown in Fig. 3.9, but not in Fig. 4.1) can shift the frequency by 406 MHz (which differs between hydrogen and deuterium by $\sim 1\,\text{MHz}$, see Table 2.5) to address the $J = 3/2$ ($6P_{3/2}$) fine-structure state manifold. If the $J = 1/2$ ($6P_{1/2}$) state manifold is addressed, this AOM is bypassed. The polarization switching and polarimetry unit (PSPU) enables to switch the linear polarization (rotate the linear polarization rotation angle by 90°) as well as to deduce the circular polarization fraction of light in the spectroscopy region. The 410 nm light is guided via the 0.8 m long PM fiber to the active fiber-based retroreflector vacuum setup, which is treated in Chapter 4.

Due to the n^{-2}-scaling of the gross energy level structure in hydrogen and deuterium, the 1S-3S transition frequency is approximately equal to four times the 2S-6P transition frequency. Therefore, the laser system described above is also used as a reference for the 1S-3S hydrogen experiment [12]. For this purpose, a fraction of 820 nm light is splitted via a fused fiber splitter before guiding the light to the frequency comb (not shown in Fig. 3.9), and transferred to the neighboring 1S-3S laboratory.

[1] For the single-pass configuration, the following AOM was used: IntraAction, ATM-3501A2, S/N 441235, center frequency $f_0 = 350\,\text{MHz}$, frequency shifting bandwidth $f_0/2 = 175\,\text{MHz}$, acousto-optical material: tellurium dioxide TeO_2, sound velocity $V = 4260\,\text{m/s}$ (longitudinal), beam separation $\lambda \times f_0/V = 67\,\text{mrad}$ (for $\lambda = 820\,\text{nm}$). It was suspected that etalon effects lead to increased noise of the laser in the single-pass configuration (which later turned out to be due to the non-optimal master laser parameters for the desired wavelength, though). The AOM was replaced for the double-pass configuration using the following model: Gooch and Housego, Model 3200-1214, S/N 176327, center frequency 200 MHz, bandwidth 100 MHz, tellurium dioxide TeO_2.

[2] Brimrose TEF-350-100-400, center frequency 350 MHz, bandwidth 100 MHz.

3.2.3 Laser frequency determination with a frequency comb

The laser frequencies are determined using the optical frequency comb metrology [10, 172, 173]. The commercial frequency comb[1] used in our apparatus is based on the figure 9® mode locked femtosecond erbium-doped fiber laser (1560 ± 20 nm center wavelength) [174, 175] with an erbium doped fiber amplifier (EDFA) and two high bandwidth electro-optic modulators [176] for controlling the repetition rate f_{RRE} and carrier envelope offset f_{CEO}. An integrated stepper motor and a piezo transducer allow to change the laser cavity length for modifying the repetition rate in the 4 MHz range around $f_{\mathrm{RRE}} \simeq 250$ MHz, while an integrated actuator enables to tune f_{CEO} within ± 250 MHz.

Extension modules spectrally broaden the light and double the frequency in all-fiber-coupled second harmonic generation units to reach the 972 nm and 820 nm wavelength of the 1S-2S and 2S-6P laser systems. Fiber-based beat detection units (BDUs) spectrally filter the frequency comb light and superimpose it with the laser light from the 1S-2S or 2S-6P laser systems. Unfortunately, the fiber bragg grating filter of these BDUs can only be tuned in the range 820.5 nm ... 820.8 nm and 972.4 nm ... 972.7 nm which does not cover the deuterium wavelengths. Therefore, a free-space beat detection setup was built for the deuterium measurement.

The 10 MHz frequency reference is provided by the passive hydrogen maser[2], which is distributed[3] to all frequency synthesizers (e.g. those for driving AOMs which change the laser frequency) and the frequency comb. The maser frequency is continuously compared against the Coordinated Universal Time (UTC), which is based[4] on the International Atomic Time (TAI[5]), with a Global Positioning System (GPS) receiver. Since the atomic time is defined at sea level, the fractional frequency offset relative to UTC, $\Delta f/f(\mathrm{UTC})$, is linked to the shift relative to the caesium standard of the International System of Units (SI), $\Delta f/f(\mathrm{Cs})$, with the gravitational redshift at the height of $h \simeq 482$ m above sea level at MPQ in Garching, the gravity of Earth $g \simeq 9.8\,\mathrm{m/s^2}$ and the speed of light c as:

$$\Delta f/f(\mathrm{Cs}) = \Delta f/f(\mathrm{UTC}) - h\frac{g}{c^2} \simeq \Delta f/f(\mathrm{UTC}) - 5.3 \times 10^{-14}. \tag{3.9}$$

The fractional frequency offset of the maser is steered relative to the caesium standard, such that $\Delta f/f(\mathrm{Cs})$ is kept below 10^{-13}, which translates into the uncertainty of ~ 70 Hz for the 2S-6P transition frequency and ~ 250 Hz for the 1S-2S transition frequency. This uncertainty

[1] Menlo Systems FC1500-250-ULN Optical Frequency Comb with ultra-low-noise peformance, with following key specifications: comb spacing 250 MHz (4 MHz tuning range), stability: 2×10^{-16} in 1 s, 3×10^{-18} in 1000 s (or same as reference, whichever applies first), phase noise on both the carrier envelope offset and repetition rate (for optical lock) below 100 mrad (integrated 2 MHz ... 100 Hz). Additional ports: 2x HMP-VIS high power measuring port at 972 nm and at 820 nm (> 3mW in 3 nm, fiber-coupled), HMP-NIR high power measuring port at 1029-1033 nm (> 3mW in 4 nm, fiber-coupled), M-VIS supercontinuum port from 600-973 nm (free space), up to 3 measuring ports at 1560 nm for future upgrades.

[2] Passive Hydrogen Maser Clock T4Science pHMaser 1008, Allan deviation (1 Hz bandwidth): 5×10^{-13} (at 1 s), 9×10^{-15} (at 1 h), 4×10^{-15} (at 1 day).

[3] The 10 MHz signal is guided from the maser room to the experiment laboratory using M17/75-RG 214 cables to frequency distribution amplifiers, e.g. TimeTech High Performance Frequency Distribution Amplifier 5 to 100 MHz.

[4] Due to leap seconds, the UTC time is at the time of thesis writing (year 2022) exactly 37 seconds behind TAI, with the last leap second applied in 2017.

[5] Temps Atomique International (french). The TAI is based on the network of hundreds of caesium atomic clocks worldwide.

can be further reduced with GPS corrections within the appropriately chosen time window[1].

The frequencies $f_{\mathrm{FP1,ECDL}}$ and $f_{\mathrm{FP3,ECDL}}$ of the 1S-2S and 2S-6P master lasers, respectively, are given by:

$$f_{\mathrm{FP1,ECDL}} = 2\, f_{\mathrm{CEO}} + N_{\mathrm{FP1}} \times f_{\mathrm{RRE}} + f_{\mathrm{FP1,beat}} - f_{\mathrm{FP1,Scan}}, \tag{3.10}$$

$$f_{\mathrm{FP3,ECDL}} = 2\, f_{\mathrm{CEO}} + N_{\mathrm{FP3}} \times f_{\mathrm{RRE}} + f_{\mathrm{FP3,beat}}, \tag{3.11}$$

where $f_{\mathrm{FP1,beat}}$ and $f_{\mathrm{FP3,beat}}$ are the beat note frequencies between the frequency comb and the laser light, $f_{\mathrm{FP1,Scan}}$ is the "Scan AOM" frequency (see Fig. 3.5, defined to be always positive, i.e. the sign from the AOM configuration is taken into account in the above equation but not in $f_{\mathrm{FP1,Scan}}$) which shifts the frequency of the master laser before it is sent to the frequency comb (contrary to the 2S-6P master laser which is probed directly by the frequency comb, see Fig. 3.9). $N_{\mathrm{FP1}} = 1\,233\,368$ and $N_{\mathrm{FP3}} = 1\,461\,777$ are the comb mode numbers next to the two laser frequencies, which can be determined by the wavemeter. Note that there is a factor of two in f_{CEO} due to the second harmonic generation of the frequency comb light.

The carrier-envelope offset frequency f_{CEO} is stabilized to $f_{\mathrm{CEO}} = -45\,\mathrm{MHz}$. The repetition rate f_{RRE} can also be stabilized to $f_{\mathrm{RRE}} = 250\,\mathrm{MHz}$, which is denoted as the 'radio frequency (RF) lock' of the frequency comb. Alternatively, one of the comb lines can be stabilized to one of the narrow linewidth lasers, while the repetition rate needs then to be measured. This approach is called 'optical lock' of the frequency comb. The accuracy of the absolute frequency determination is the same for both methods, limited by the accuracy of the 10 MHz maser reference. However, the advantage of the optical lock is that the comb lines will have the same linewidth as the narrow linewidth laser, for our lasers around 1 Hz (while for the RF lock the comb lines have typically a linewidth of hundreds of kHz). Our ultra-low-noise frequency comb transfers the comb linewidth over a spectral range larger than 200 nm: if the frequency comb is optically locked to a narrow linewidth laser at 1033 nm (from the neighboring He^+ spectroscopy laboratory), the comb lines for the beat notes with the 1S-2S and 2S-6P lasers at 820 nm and 972 nm have also a narrow linewidth around 1 Hz. This allows to optimize the feedback loops for the laser stabilizations by observing the noise on the beat notes with the frequency comb. During the deuterium 2S-6P measurement campaign in July 2021, the frequency comb was optically locked to the narrow linewidth laser from the helium laboratory at 1032.87 nm (beat note with the frequency comb at $f_{\mathrm{He,beat}} = +19.737\,\mathrm{MHz}$, mode number $N_{\mathrm{He}} = 1\,161\,003$). The spectrum of the beat notes $f_{\mathrm{FP1,beat}}$ and $f_{\mathrm{FP3,beat}}$ is similar to [162, 163]: at 30 kHz resolution bandwidth, the carrier frequency is superimposed on the ~ 5 MHz noise pedestal with a signal-to-noise ratio of ~ 40 dB. Outside this noise pedestal the signal-to-noise ratio improves by ~ 15 dB (to ~ 55 dB).

The radio frequencies f_{CEO}, f_{RRE}, $f_{\mathrm{FP1,beat}}$, $f_{\mathrm{FP3,beat}}$ are redundantly measured with commercial high precision counters[2] [177]. The CEO frequency $f_{\mathrm{CEO}} = -45\,\mathrm{MHz}$ is stabilized but also measured for redundancy. The repetition rate of $f_{\mathrm{RRE}} \simeq 250\,\mathrm{MHz}$ is measured in two redundant ways: first, the 4th harmonic of f_{RRE} at around 1 GHz is mixed with 980 MHz, such

[1] If the maser counts a too large (small) frequency, the measured hydrogen transition frequency needs to be increased (decreased) by the same relative factor, which may seem counter-intuitive.

[2] K+K Messtechnik FX 80 (input frequency range up to 55 MHz) and FXE (input frequency range up to 130 MHz) frequency counters. These counters require a square wave signal with $1 - 5$ V level (TTL signal) as input signals. Therefore, the RF signal from the beat notes is converted to the TTL signal using a circuit based on the Philips SA5214 postamplifier with link status indicator (minimum input signal peak-to-peak voltage 12 mV, maximum operating frequency 75 MHz). We typically denote the latter component as the "comparator".

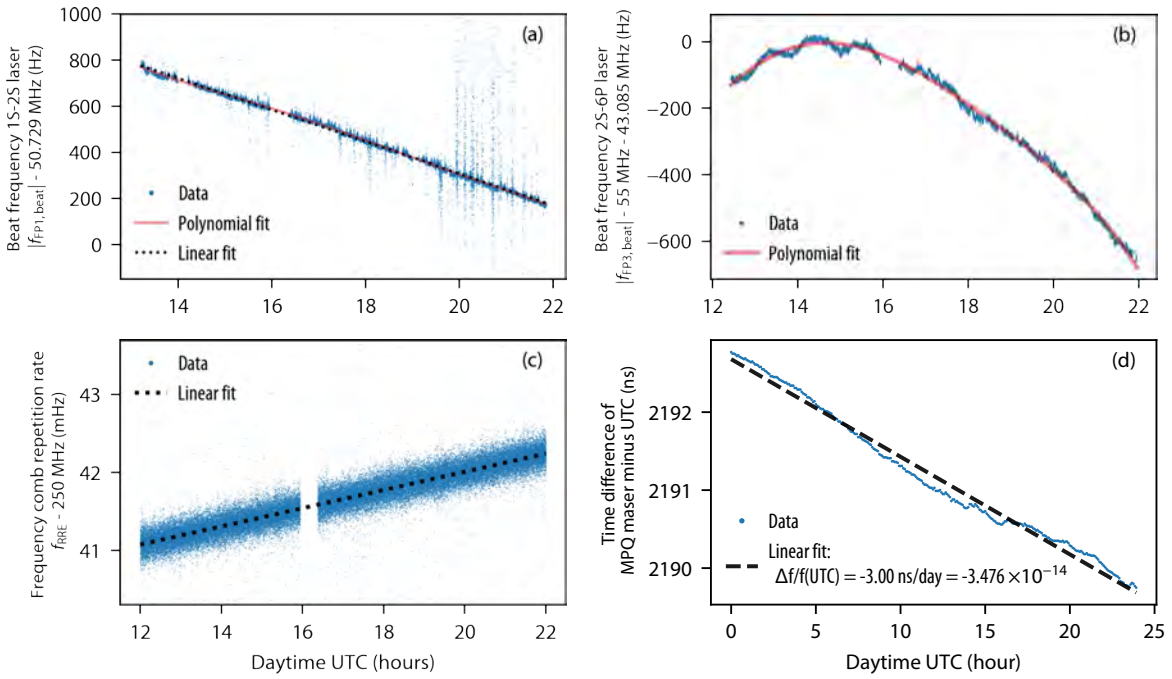

Figure 3.10: Determination of laser frequencies with a frequency comb (July 22, 2021). (a) Measurement of the beat note of the 1S-2S laser at 972 nm with the frequency comb at $f_{\mathrm{FP1,beat}} \simeq 50.7\,\mathrm{MHz}$ (note the axis offset of 50.729 MHz). (b) Measurement of the beat note of the 2S-6P laser at 820 nm with the frequency comb at $f_{\mathrm{FP3,beat}} \simeq -98.7\,\mathrm{MHz}$, which is mixed with 55 MHz to count the frequency around 43.7 MHz (note the axis offset of 55+43.085 MHz). (c) Measurement of the frequency comb repetition rate $f_{\mathrm{RRE}} \simeq 250\,\mathrm{MHz}$ (note the axis offset of 250 MHz). The shown value for f_{RRE} has been deduced from the 40th harmonic of f_{RRE} at $\sim 10\,\mathrm{GHz}$, which is mixed with 9.980 121 089 GHz such that a frequency $\sim 19.88\,\mathrm{MHz}$ is counted. (d) Time difference of the passive hydrogen maser (providing the frequency reference for all devices including the frequency comb) against the Coordinated Universal Time (UTC) from a comparison with a Global Positioning System (GPS) receiver. The linear fit yields a fractional frequency offset of $\Delta f/f(\mathrm{UTC}) \sim -3.5 \times 10^{-14}$, which translates into the fractional frequency offset to the caesium standard of the International System of Units (SI) of $\Delta f/f(\mathrm{Cs}) \sim -8.8 \times 10^{-14}$ according to Eq. (3.9).

that the frequency around 20 MHz is measured. Second, the 40th harmonic of f_{RRE} at around 10 GHz is mixed with 9.980 121 089 GHz (this crooked number is chosen to avoid noise from interference of signals) supplied by an auxiliary signal generator[1] to measure the frequency around 19.88 MHz. The sign of the beat notes $f_{\mathrm{FP1,beat}}$ and $f_{\mathrm{FP3,beat}}$ can be determined by slightly changing f_{RRE} while observing the effect on the beat note frequency: for increasing f_{RRE} the absolute value of the beat note frequency decreases if the sign of the beat note is positive, and increases if the sign of the beat note is negative. The beat note with the 2S-6P laser is at around $f_{\mathrm{FP3,beat}} \simeq -98.1\,\mathrm{MHz}$ which is too high to be measured directly with our counters. Therefore, the signal is mixed with 55 MHz such that a beat frequency around 43.1 MHz is counted. The beatnote with the 1S-2S laser is around $f_{\mathrm{FP1,beat}} \simeq 50.7\,\mathrm{MHz}$ and is counted directly.

Fig. 3.10 exemplarily shows the measurement of the radiofrequencies needed to determine the master laser frequencies of the 1S-2S (at 972 nm) and 2S-6P (at 820 nm) lasers according

[1] Agilent E 8257 D, Analog Signal Generator, 250 kHz-20 GHz.

to Eq. (3.10) and Eq. (3.11). Fig. 3.10(a) and (b) show the measurement of $f_{\mathrm{FP1,beat}}$ and $f_{\mathrm{FP3,beat}}$, and (c) the deduced f_{RRE} from the 40th harmonic of the repetition rate mixed with $\sim 10\,\mathrm{GHz}$. Note that an increase in noise is visible in Fig. 3.10(a) in the last two hours of the data, which is attributed to polarization drifts in the fiber resulting in drifts of the signal-to-noise ratio of the beat signal. This can be improved in the future with a modified beat detection setup of the 1S-2S laser, which has a better signal-to-noise ratio of the beat note and which is less sensitive to polarization drifts. The laser frequency of both master lasers drifts within the shown measurement day on the order of $\sim 1\,\mathrm{kHz}/10\,\mathrm{h}$. While it is typically observed that the 1S-2S laser drifts almost linearly, the 2S-6P laser shows a non-linear drift, which remains to be investigated[1]. The repetition rate drifts by $\sim 1\,\mathrm{mHz}/10\,\mathrm{h}$ due to the $\sim 3\,\mathrm{kHz/day}$ drift of the 1033 nm laser to which the frequency comb is optically locked. Fig. 3.10(d) shows the time difference between the maser and UTC from the GPS receiver data. The absolute offset of $\sim 2\,\mathrm{ms}$ is irrelevant since only the slope matters for the fractional frequency offset. For this data, the linear fit yields a fractional frequency offset of $\Delta f/f(\mathrm{UTC}) \sim -3.5 \times 10^{-14}$, which translates into $\Delta f/f(\mathrm{Cs}) \sim -8.8 \times 10^{-14}$ according to Eq. (3.9).

From the laser frequency measurement of the infrared 1S-2S and 2S-6P master lasers, the 1S-2S and 2S-6P frequency as seen by atoms is given by:

$$f_{\text{1S-2S}} = 2 \times 2 \times 2 \times f_{\mathrm{FP1,ECDL}} = 8 \times f_{\mathrm{FP1,ECDL}}, \tag{3.12}$$

$$f_{\text{2S-6P}} = 2 \times f_{\mathrm{FP3,ECDL}} + 2 \times f_{\mathrm{FP3,Scan}} + \delta_{J,3/2} f_{\mathrm{FP3,FS}}, \tag{3.13}$$

where for the 1S-2S frequency we accounted for two SHG units (doubling the laser frequency twice) to reach 243 nm and an additional factor of two due to the two-photon transition. For the frequency of the one-photon 2S-6P transition, only one SHG unit is present. The two additional terms account for the frequencies of the double-passed "Scan AOM" and the "Fine-structure AOM" ($\delta_{J,3/2} = 0$ if the $2\mathrm{S}_{1/2}$-$6\mathrm{P}_{1/2}$ transition is probed and $\delta_{J,3/2} = 1$ if the $2\mathrm{S}_{1/2}$-$6\mathrm{P}_{3/2}$ transition is probed), see Fig. 3.9.

3.3 Numerical modeling of the time-resolved signal

Numerical modeling is an important part of the experiment for various reasons. One major reason for the necessity of simulations is the determination of the different mean velocities of atoms for the different delays from the time-resolved detection (see Section 3.1.1). Other reasons involve the study of systematic effects such as quantum interference. The simulations of the 2S-6P deuterium signals are composed of several steps: first, from the geometry constraints of the apparatus, random trajectories of atoms are generated. Along with these Monte-Carlo trajectory simulations, the 1S-2S excitation is simulated, as described in Section 3.3.1. Next, the 2S-6P excitation is simulated with the so-called "Big Model" which involves all possible (intermediate) states, decays and excitations (see Section 3.3.2). Finally, as demonstrated in Section 3.3.3, the 1S-2S simulations for a given trajectory set are combined with the 2S-6P "Big model" simulations, leading to the experimental 2S-6P signal with the expected speed distribution of the flux and the mean velocity for each delay.

[1] This could be related to temperature drifts in the cavity after the laser is switched on together with the non-optimal cavity temperature where the linear expansion coefficient does not vanish.

Table 3.1: Range of parameters used for the Monte Carlo simulation of the trajectories of metastable 2S deuterium atoms. The parameters are classified into three groups: the geometry of the apparatus, the speed distribution of the flux of ground state (1S) atoms where the atomic mass includes the information on the isotope, and the properties of the 1S-2S preparation laser beam. Typically, 10^6 trajectories are simulated ('trajectory set'), with single values for each parameter. Various trajectory sets with different parameter sets according to the given experimental range are simulated to match the different experimental conditions during the measurement campaign. For comparison to hydrogen 2S-6P, see Table 5.3 in [71].

Parameter	Value
Geometry	
Nozzle orifice radius r_1	1.0 mm
Distance L_1 from nozzle orifice to variable aperture	153.6 mm
Width $d_2 = 2r_2$ of variable aperture along x-axis	1.2 mm
Height $d_{2,y} = 2r_{2,y}$ of variable aperture along y-axis	2.0 mm
Distance L from nozzle orifice to 2S-6P spectroscopy laser beam	204.0 mm
Speed distribution of the flux of ground state (1S) atoms	
Speed distribution of the flux $p(v)\,\mathrm{d}v$	$\propto v^3 e^{-\frac{m_\mathrm{D} v^2}{2k_\mathrm{B}T_\mathrm{N}}} e^{-\frac{v_\mathrm{cutoff}}{v}}\,\mathrm{d}v$
Angular distribution $p(\theta)\,\mathrm{d}\Omega$	$\propto \cos(\theta)\,\mathrm{d}\Omega$
Nozzle temperature T_N	7.1 K... 7.4 K
Cutoff speed v_cutoff	60 m/s... 150 m/s
1S-2S preparation laser	
Beam waist radius $w_{\mathrm{1S\text{-}2S}}$ ($1/e^2$ intensity radius)	297 µm
Distance of waist to nozzle orifice	0.0 mm
Intracavity power $P_{\mathrm{1S\text{-}2S}}$ (per direction)	0.9 W... 1.5 W
Detuning from $1\mathrm{S}_{1/2}^{F=1/2} - 2\mathrm{S}_{1/2}^{F=1/2}$ resonance $\Delta\nu_{\mathrm{1S\text{-}2S}}$	0.3 kHz... 2.0 kHz
Chopper frequency f_chop (equal slit width)	160 Hz

The numerical modeling procedure is the same as for hydrogen and is treated in detail in Ch. 5 of [71]. Here, many details are left out and only a brief overview with exemplary simulations for the deuterium 2S-6P measurement is given.

3.3.1 Simulations of metastable atomic beam trajectories

The numerical modeling starts with Monte-Carlo simulations of atomic trajectories along with the simulation of the 1S-2S excitation, thus simulating the atomic beam in the metastable 2S state. The parameters for these simulations are summarized in Table 3.1. The parameters are grouped into three categories: the geometry of the apparatus, the speed distribution of the flux of the ground state (1S) atoms, and the 1S-2S preparation laser properties.

The geometry of the apparatus is given by the nozzle orifice radius $r_1 = 1.0\,\mathrm{mm}$, the distance $L_1 = 153.6\,\mathrm{mm}$ from the nozzle orifice to the variable aperture, along with its variable width set to $d_2 = 1.2\,\mathrm{mm}$ (in the experiment routinely aligned to this optimal value) and fixed height $d_{2,y} = 2.0\,\mathrm{mm}$, as well as the distance $L = 204\,\mathrm{mm}$ from the nozzle orifice to the 2S-6P spectroscopy region. Note that the circular high-vacuum entrance aperture (EA in Fig. 3.1, Fig. 3.3, Fig. 3.4) placed at 69 mm after the nozzle orifice does not matter here because its diameter of 2.4 mm is larger than the dimensions of the variable aperture.

The next category of parameters describes the speed distribution of the flux of ground state (1S) atoms emerging from the nozzle. In our apparatus, the atoms are generated in the copper nozzle, which is cooled for deuterium spectroscopy to $T_\mathrm{N} \sim 7\,\mathrm{K}$ using a liquid-helium flow cryostat. The speed and angular distribution is assumed to be the same over the whole area of the nozzle. The geometrical T-shaped nozzle design[1] is inevitable in our setup where the atomic beam needs to be collinear with the 1S-2S preparation beam. However, the speed distribution of the flux of atoms emerging from such a nozzle is distorted from the Maxwell-Boltzmann distibution, particularly for slow atoms as has been studied in [178]. Furthermore, other effects such as the "Zacharias effect" from intra-beam collisions, where fast atoms "kick out" slow atoms from the beam, lead to the depletion of slow atoms [179, 180]. For a discussion of the cryogenic deuterium atomic beam formation, see Section 3.6.1. Here, these effects are taken into account with an effective model, where the speed distribution of the flux for an effusive beam [181, 182] is multiplied with an exponential cutoff factor [180]. The probability $p(v)$ of a flux of atoms with the speed interval between v and $v + \mathrm{d}v$ (which is proportional to the number of atoms that pass through the cross section of the atomic beam with these speeds per unit of time) is then assumed to be

$$p(v)\,\mathrm{d}v \propto v^3 e^{-\frac{m_\mathrm{D} v^2}{2 k_\mathrm{B} T_\mathrm{N}}} e^{-v_\mathrm{cutoff}/v}\,\mathrm{d}v, \tag{3.14}$$

where v_cutoff is a parameter characterizing the bottleneck of slow atoms, k_B the Boltzmann constant, T_N the nozzle temperature, and m_D the mass of deuterium atoms. The probability distribution from Eq. (3.14) can be normalized, here we show the proportionality dependence only. For atomic beam modelling, the joint spatial, angular and speed distribution of the flux is required. For an effusive beam such as here, the relation

$$p(\theta)\,\mathrm{d}\Omega \propto \cos\theta\,\mathrm{d}\Omega = \cos\theta \times 2\pi \sin\theta\,\mathrm{d}\theta \tag{3.15}$$

can be assumed [181, 182], where $\mathrm{d}\Omega = 2\pi \sin\theta\,\mathrm{d}\theta$ is the surface element of a unit sphere, and $p(\theta)$ is the probability to find the atom between the angle θ (w.r.t. the normal of the plane of the orifice) and $\theta + \mathrm{d}\theta$.

For each trajectory, the simulation of the 1S-2S excitation is performed by numerically solving the Optical Bloch Equations, including the ac-Stark shift and the second-order Doppler shift of the transition frequency. The parameters for this simulation are the beam waist radius ($1/e^2$ intensity radius) $w_\mathrm{1S-2S} = 297\,\mu\mathrm{m}$, the zero distance of the waist to the nozzle orifice, the intracavity power $P_\mathrm{1S-2S}$ (per direction, i.e. the total power from both counter-propagating beams in the cavity is $2 \times P_\mathrm{1S-2S}$), and the detuning from the $1\mathrm{S}_{1/2}^{F=1/2} - 2\mathrm{S}_{1/2}^{F=1/2}$ resonance $\Delta\nu_\mathrm{1S\text{-}2S}$. The latter two parameters are varied within the typical experimental conditions. Furthermore, the chopper frequency $f_\mathrm{chop} = 160\,\mathrm{Hz}$ is an input parameter along with an assumption of equal slit width of the chopper wheel slits.

As an example, the analysis of 10^7 trajectories for a given set of parameters ($T_\mathrm{N} = 7.2\,\mathrm{K}$, $v_\mathrm{cutoff} = 65\,\mathrm{m/s}$, $P_\mathrm{1S\text{-}2S} = 0.9\,\mathrm{W}$, $\Delta\nu_\mathrm{1S\text{-}2S} = 0.3\,\mathrm{kHz}$, along with the other fixed parameters from Table 3.1) is shown in Fig. 3.11. All three figures show the resulting number of 2S atoms (solid lines), with the underlying distribution of ground state (1S) atoms shown in dashed lines (scaled to envelope the 2S distribution). Each distribution is exemplarily shown for 6 out of 16 different delays in a separate color for each delay. For each delay i, the delay times τ_i

[1] 2.0 mm diameter through-hole combined with a 4.0 mm diameter blind hole in a 10.0 mm × 8.0 mm rectangular block of copper. See [71] for a technical drawing and details.

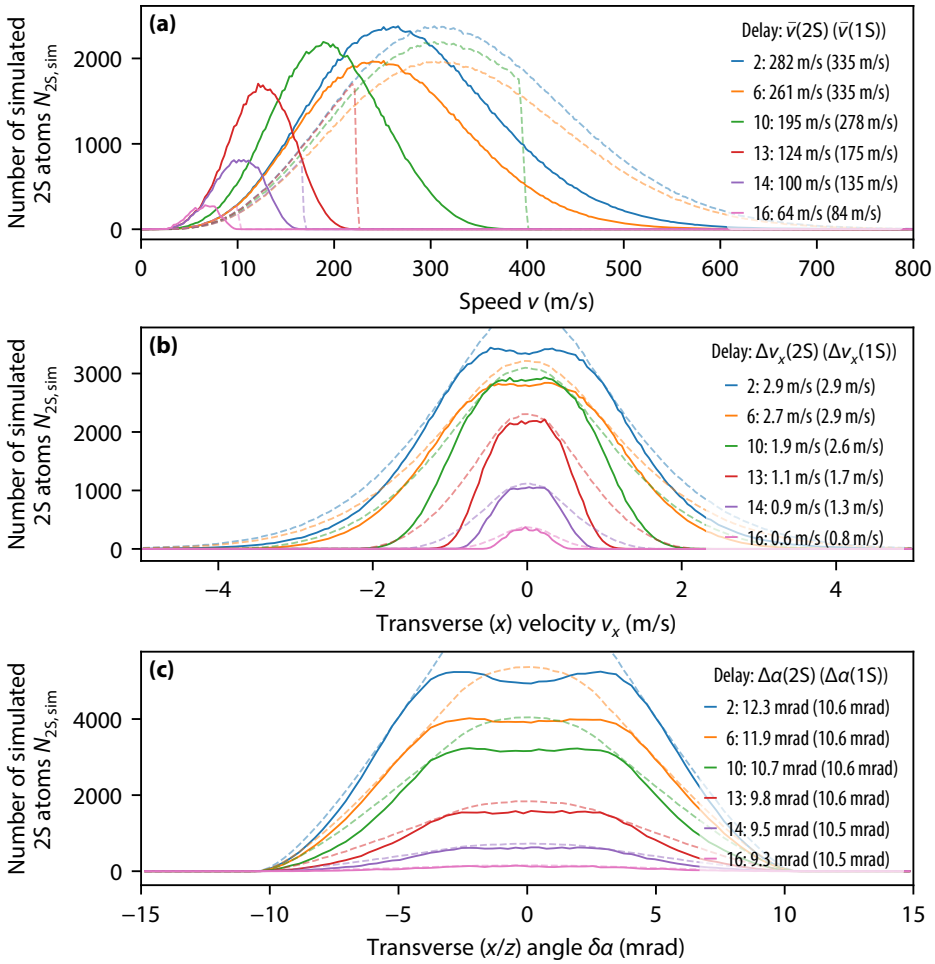

Figure 3.11: Monte Carlo simulation of the trajectories of 2S metastable deuterium atoms, based on the work described in Sec. 5.2 of [71]. For comparison to hydrogen, see Fig. 5.4 in [71]. The parameters are $T_N = 7.2\,\mathrm{K}$, $v_{\mathrm{cutoff}} = 65\,\mathrm{m/s}$, $P_{1S\text{-}2S} = 0.9\,\mathrm{W}$, $\Delta\nu_{1S\text{-}2S} = 0.3\,\mathrm{kHz}$, along with the fixed parameters from Table 3.1. All results are exemplarily shown with different colors for 6 out of 16 delays (see Table 3.2 for the delay times). All figures show the resulting simulated number of 2S atoms in solid lines, while the distribution of ground state (1S) atoms is shown in dashed lines (scaled to envelope the 2S distribution). The total number of simulated trajectories is 10^7. (a) Distribution of the atomic speed v for the 1S and 2S atoms, with the mean speed $\bar{v}$ written in the legend (see also Table 3.2). For longer delays, the maximum velocity $v_{\mathrm{max}} \simeq L/\tau$ is visible for the 1S atoms (dashed lines), where $L = 204\,\mathrm{mm}$ is the distance from the nozzle to the 2S-6P spectroscopy region and τ the delay time. (b) Distribution of the transverse velocity v_x along the 2S-6P spectroscopy laser beams (x direction), with the full width half maximum (FWHM) of the 2S atoms distributions $\Delta v_x(2S)$ written first in the legend, and the FWHM of the 1S atoms distributions $\Delta v_x(1S)$ written in the parantheses in the legend. (c) Distribution of the transverse angle $\delta\alpha$ from the z axis to the x axis. The distribution for the ground state (1S) atoms is given only by the geometry and thus identical for all delays up to the scale factor, which has been here adjusted to envelope the 2S distribution. See main text for the explanation of the dip for v_x and $\delta\alpha$ around zero in (b) and (c).

(with the corresponding delay durations $\Delta\tau_i$) including the main results of the simulation are summarized in the first columns of Table 3.2. For a given delay, there is a maximum velocity $v_{\mathrm{max}} \simeq L/\tau$ of atoms which can contribute to the signal. This is visible in Fig. 3.11(a),

which shows the speed distribution of the flux of ground state (1S) and 2S atoms: for ground state atoms, a sharp drop is visible at $v_{\max}$ for longer delays. This drop is not visible in the speed distribution of the flux of 2S atoms, where the number of atoms is almost zero for even lower velocities than $v_{\max}$. The mean velocity of 1S atoms, $\overline{v}(1S)$, is higher than that of 2S atoms, $\overline{v}(2S)$, with corresponding values written in the legend of Fig. 3.11(a) and in Table 3.2. Fig. 3.11(b) shows the distribution of the transverse velocity along the 2S-6P spectroscopy laser beams (x direction), with the full width half maximum (FWHM) of the 2S atoms distributions $\Delta v_x(2S)$ written first in the legend (see also Table 3.2), and the FWHM of the 1S atoms distributions $\Delta v_x(1S)$ written in the parantheses in the legend. The distribution of the transverse angle $\delta\alpha$ from the z axis to the x axis (given by $\delta\alpha = \arctan(v_x/v_z) \simeq v_x/\overline{v}$) is shown in Fig. 3.11(c). Note that the distribution for the ground state (1S) atoms is given only by the geometry and thus identical for all delays up to the scale factor, which has been here adjusted to envelope the 2S distribution.

In Fig. 3.11(b) and (c), the dip in the number of 2S atoms for v_x and $\delta\alpha$ around zero is due to the circumstance that atoms with trajectories parallel to the 1S-2S laser beam have a smaller probability to be excited (if close to the edge or outside of the 1S-2S laser beam) or a larger probability to be ionized (if close to the center of the 1S-2S laser beam) as compared to atoms crossing the 1S-2S laser beam at an angle. Note also that this mechanism depends on the mean speed of atoms and is more pronounced for fast atoms (smaller delays). This phenomenon is related to the discussion in Section 5.3 (see Fig. 5.7).

3.3.2 Simulations of the 2S-6P fluoresence ("Big Model" simulations)

We call the 2S-6P excitation simulations "Big Model" simulations since they include all possible intermediate states with all excitation and decay paths. These simulations are based on Arthur Matveev's so far unpublished work, which has also been used in Section 2.5.3 to verify the results of the perturbative quantum mechanical model for the effect of quantum interference between unresolved hyperfine components. The fluorescence from the $2S_{1/2}$-$6P_{1/2}$ (or $6P_{3/2}$) excitation involves 234 sub-levels, which generally results in $234^2 = 54756$ coupled differential equations (Optical Bloch Equations or "Master Equations") for calculating the time evolution of the system. However, many of the possible excitation and decay paths do not contribute and the number of equations can be greatly reduced to those which result in a non-zero time evolution. Here, the simulations are performed with linear polarization only, and with no asymmetry between the $m_F = \pm 1/2$ initial sub-states of the $2S_{1/2}$ initial state manifold, such that the number of equations reduces to 1442. Still the simulations remain numerically extensive and are performed on the supercomputer Raven[1] of the Max Planck Computing and Data Facility. The code is written in C++ with the routine using the eight-order Dormand-Prince method for solving the equations (Dopr853 from [183]).

For a Gaussian laser beam of certain power, each atomic trajectory through the laser beam can be transformed into an equivalent trajectory crossing the center of the laser beam

[1]The supercomputer Raven (in operation since June 2021) has the following key performance properties: 1592 CPU compute nodes, processor type: Intel Xeon IceLake-SP (Platinum 8360Y), processor base frequency: 2.4 GHz, 72 cores per node (each with 2 hyperthreads, thus 144 logical CPUs per node), main memory (RAM) per node: 256 GB (1524 nodes), 512 GB (64 nodes), 2048 GB (4 nodes), theoretical peak performance per node (FP64, 'double precision' (DP)): 2.4 GHz × 32 DP Flops/cycle × 72 = 5530 GFlop/s, total theoretical peak performance (FP64): 5530 GFlop/s × 1592 = 8.8 PFlop/s, CPU nodes interconnected with a Mellanox HDR InfiniBand network (100 Gbit/s) using a pruned fat-tree topology with four non-blocking islands. In addition, 192 GPU-accelerated nodes are available.

under a certain angle with possibly lower laser power. Therefore, the simulation of the 2S-6P fluorescence for a given set of atomic trajectories requires to vary only three parameters: the speed of the atom, the 2S-6P excitation laser power (the laser beam radius $W_0 \simeq 2.2\,\mathrm{mm}$ is a fixed input parameter), and the crossing angle. The simulations are performed for the following ranges of these parameters, respectively: $25 \ldots 1000\,\mathrm{m/s}$ in $25\,\mathrm{m/s}$ steps, $5 \ldots 50\,\mu\mathrm{W}$ in $5\,\mu\mathrm{W}$ steps, and $0.5 \ldots 15.5\,\mathrm{mrad}$ in $1\,\mathrm{mrad}$ steps. This "simulation grid" thus consists of $40 \times 10 \times 16 = 6400$ parameter sets or resonance lines which need to be simulated. Since the supercomputer Raven has 72 cores per node, it is advantageous to parallelize the computation for a multiple of 72 frequency points. For 72 frequency points the parallelized simulation (on one CPU node with 72 cores) takes $\sim 7.5\,\mathrm{h} = 540\,\mathrm{coreh}$ for the whole range of velocities with a given laser power and crossing angle. As expected from the velocity-dependent integration time, the computation time for each individual resonance line strongly depends on the velocity: for $25\,\mathrm{m/s}$ atoms the single resonance line is calculated in $\sim 100\,\mathrm{min}$, for $50\,\mathrm{m/s}$ atoms in $\sim 50\,\mathrm{min}$, and for $1000\,\mathrm{m/s}$ atoms in only $\sim 3\,\mathrm{min}$. The total computation time for 160 parameter sets of laser powers and crossing angles is $\sim 7.5\,\mathrm{h} \times 160 = 1200\,\mathrm{h} = 86.4\,\mathrm{kcoreh}$. With 16 CPU nodes simultaneously, the computation time on Raven reduces to $\sim 75\,\mathrm{h}$. After the simulation grid has been calculated, for each decay channel, the results are interpolated to create a "dense grid", for instance with 101 laser power points, 64 crossing angle points, and 196 velocity points.

3.3.3 Simulation of the time-resolved experimental 2S-6P signal

To simulate the experimental time-resolved 2S-6P fluorescence signal, the 2S trajectory simulations from Section 3.3.1 are combined with the 2S-6P simulation grid from Section 3.3.2. The trajectories are first grouped for each delay into 200 speed bins of $5\,\mathrm{m/s}$ width from $0 \ldots 1000\,\mathrm{m/s}$. For a given trajectory set, each speed bin in each delay contains the corresponding number of 2S atoms. Using the results of the 2S-6P simulation dense grid, for each 2S-6P frequency detuning, in each speed bin for each delay the fluoresence signal is then calculated, thereby yielding the interpolated grid connected to a certain trajectory set. Since the 2S-6P simulations from Section 3.3.2 are performed for each decay channel separately, for the given linear polarization angle of the 2S-6P laser beam, the detection efficiency can be included in this calculation (see Secs. 4.6 and 5.3 of [71]). In the next step, the resonance lines are fitted with a given line shape function to determine the amplitude in each speed bin for each delay. Therefore, the end result for the mean velocity in each delay depends on the fit function and the frequency sampling, though this dependence is typically negligible compared to the sensitivity on other input parameters[1]. For each delay, the resonance line amplitudes in each speed bin give the speed distribution of the flux.

Fig. 3.12(a) exemplarily shows the resulting speed distribution of the flux of atoms contributing to the 2S-6P signal for the same trajectory set as in Fig. 3.11 (parameters $T_\mathrm{N} = 7.2\,\mathrm{K}$, $v_\mathrm{cutoff} = 65\,\mathrm{m/s}$, $P_\mathrm{1S\text{-}2S} = 0.9\,\mathrm{W}$, $\Delta\nu_\mathrm{1S\text{-}2S} = 0.3\,\mathrm{kHz}$, along with the fixed parameters from Table 3.1). Only the dominant Lyman-ϵ signals are taken into account here, with equal weights of the three spherical components (which corresponds to a detector measuring the fluoresence into the whole solid angle ("4π detector") with equally distributed detection efficiency). The calculation is performed for the 2S-6P laser power of $30\,\mu\mathrm{W}$. The speed distribution of the

[1] Using a Lorentzian function instead of the Voigt function typically results in mean velocity changes on the order of $\sim 1\,\mathrm{m/s}$. Sampling the line not around the center, but shifted by $\sim 0.5\,\mathrm{MHz}$ (on the order of the recoil shift), results in a mean velocity change on the order of $\sim 0.1\,\mathrm{m/s}$.

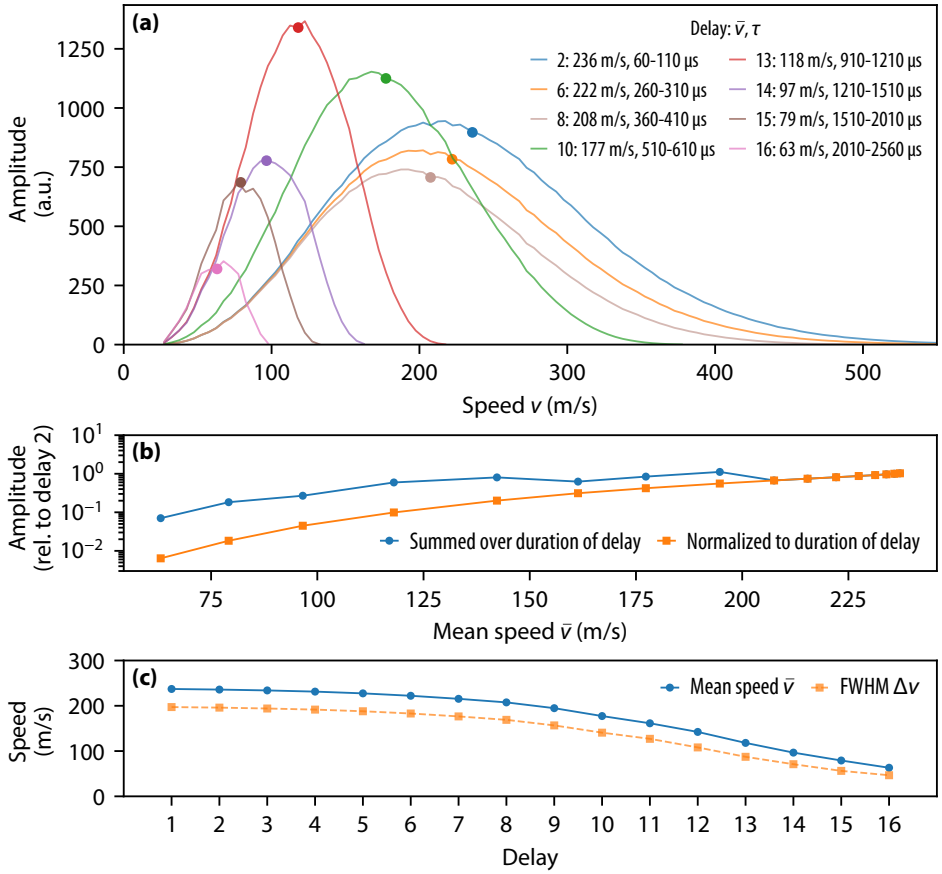

Figure 3.12: Simulation of the 6P speed distribution of the flux, which is the distribution of atoms contributing to the 2S-6P fluorescence signal. This simulation has been obtained from the 2S trajectory set simulation shown in Fig. 3.11 combined with the 2S-6P 'Big Model' simulations for the 2S-6P laser power of 30 µW. For each delay, the number of 2S atoms from a given trajectory set simulation is grouped into 200 speed bins with 5 m/s width. The resulting resonance lines from the combination with 2S-6P simulations are then fitted with a Voigt line shape function, which yields the shown amplitudes for each speed bin and delay. Only the dominant Lyman-ϵ signals (all three spherical components) have been taken into account here. For comparison to hydrogen 2S-6P and more details on the simulation procedure, see Sec. 5.5 and Fig. 5.5 in [71]. (a) The speed distribution of the flux of 6P atoms is exemplarily shown for 8 out of 16 delays, each with its own color. The points mark the mean speed, which is also written in the legend along with the delay times (see also Table 3.2). (b) The relative amplitude to delay 2 is shown as a function of the mean speed $\overline{v}$ in each delay, either summed over the whole duration of delay (A_i/A_2, blue circular markers), or normalized to the duration of delay $\Delta\tau_i$ ($A_i\Delta\tau_2/(A_2\Delta\tau_i)$, orange square markers), see also the two last columns in Table 3.2. (c) The mean speed $\overline{v}$ (blue circular markers) and the full width half maximum (FWHM) of the speed Δv (orange square markers) is plotted versus the delay number.

flux is exemplarily shown for 8 out of 16 delays, each in its own color. The points mark the mean speed $\overline{v}$, which is also written in the legend along with the corresponding delay times τ. Fig. 3.12(b) shows the relative signal amplitude for each delay as a function of the mean speed, either summed over the whole duration of the delay, or normalized to the duration of the delay. Fig. 3.12(c) shows the mean speed $\overline{v}$ (blue circled markers) and the full width half maximum (FWHM) of the speed, Δv, as a function of the delay number.

Table 3.2: Speed distribution of the flux for the 16 delays i with delay times τ_i and durations $\Delta\tau_i$, for following parameters: $T_\mathrm{N} = 7.2\,\mathrm{K}$, $v_\mathrm{cutoff} = 65\,\mathrm{m/s}$, $P_\mathrm{1S\text{-}2S} = 0.9\,\mathrm{W}$, $\Delta\nu_\mathrm{1S\text{-}2S} = 0.3\,\mathrm{kHz}$, along with the other fixed parameters from Table 3.1. Together with the distance L from the nozzle orifice to the 2S-6P spectroscopy region, the delay time determines the maximum speed $v_\mathrm{max} \approx L/\tau$ of atoms that can contribute to the signal. The mean speed is different for the ground state atoms, $\overline{v}(1\mathrm{S})$, for atoms in the 2S excited state, $\overline{v}(2\mathrm{S})$, and for atoms contributing to the 2S-6P fluoresence signal, $\overline{v}(6\mathrm{P}) \equiv \overline{v}$ (where the 1S-2S and 2S-6P excitations are combined). See Fig. 3.11(a) for visualizations of $v(1\mathrm{S})$ and $v(2\mathrm{S})$, and Fig. 3.12(a) and (c) for visualizations of $v(6\mathrm{P}) \equiv v$. Furthermore, the transverse velocity full width half maximum (FWHM) of 2S atoms, $\Delta\overline{v}_x(2\mathrm{S})$, is given (see Fig. 3.11(b)). The last two columns give the relative signal amplitudes, either summed over the whole duration of delays, or normalized to the duration of delays, see Fig. 3.12(b) for visualization. For comparison to hydrogen 2S-6P and more details, see Tables 5.1, 5.4 and 5.5 in [71].

Delay i	τ_i (µs)	$\Delta\tau_i$ (µs)	v_max (m/s)	$\overline{v}(1\mathrm{S})$ (m/s)	$\overline{v}(2\mathrm{S})$ (m/s)	$\Delta v_x(2\mathrm{S})$ (m/s)	$\overline{v}$ (m/s)	$\frac{A_i}{A_2}$	$\frac{A_i \Delta\tau_2}{A_2 \Delta\tau_i}$
1	10…60	50	>1000	334.8	282.5	2.90	237.1	1.03	1.03
2	60…110	50	>1000	334.8	281.5	2.89	235.8	1.00	1.00
3	110…160	50	>1000	334.8	279.6	2.87	233.9	0.97	0.97
4	160…210	50	>1000	334.8	276.1	2.84	231.3	0.92	0.92
5	210…260	50	971	334.8	269.9	2.78	227.4	0.87	0.87
6	260…310	50	785	334.5	260,7	2.69	222.1	0.81	0.81
7	310…360	50	658	331.9	249.3	2.56	215.4	0.74	0.74
8	360…410	50	567	324.0	236.7	2.41	207.5	0.67	0.67
9	410…510	100	498	310.9	218.4	2.19	194.7	1.11	0.56
10	510…610	100	400	277.6	195.0	1.92	177.3	0.84	0.42
11	610…710	100	334	245.0	174.8	1.69	161.4	0.63	0.31
12	710…910	200	287	217.3	152.2	1.44	142.3	0.80	0.20
13	910…1210	300	224	175.5	124.5	1.15	118.0	0.59	0.10
14	1210…1510	300	169	135.2	100.5	0.91	96.6	0.27	0.04
15	1510…2010	500	135	109.9	81.6	0.73	79.1	0.18	0.02
16	2010…2560	550	101	83.7	64.3	0.57	63.1	0.07	0.01

Table 3.2 gives the delay times and durations along with 1S-2S trajectory simulation results (visualized in Fig. 3.11), the mean speed $\overline{v}$ of atoms contributing to the 2S-6P signal (visualized in Fig. 3.12(a) and (c)), as well as the relative amplitudes (normalized to delay 2) in each delay (visualized in Fig. 3.12(b)). The mean speed of ground state atoms $\overline{v}(1\mathrm{S})$ is higher than the mean speed of 2S atoms $\overline{v}(2\mathrm{S})$: for slower atoms, the longer interaction time with the 1S-2S laser increases the excitation probability, thus shifting the speed distribution of the flux to lower speeds. Similarly, the mean speed of 6P atoms $\overline{v}(6\mathrm{P}) \equiv \overline{v}$ is lower than $\overline{v}(2\mathrm{S})$.

Note that Fig. 3.11, Fig. 3.12 and Table 3.2 present only an example for a certain parameter set. For the analyis of the experiment, the parameters need to be chosen such that they closely match the experimental conditions. The mean speed $\overline{v}$, which is decisive for the 2S-6P spectroscopy analysis, varies depending on the experimental conditions during the measurement. Apart from obvious conditions, such as different 1S-2S and 2S-6P laser powers, also the speed distribution of the flux may change over time. The comparison of the simulated and measured relative signal amplitudes in the different delays allows to obtain some information on the velocity distribtion, specifically the cutoff-speed v_cutoff, as discussed in Section 3.6.2

and visualized in Fig. 3.22 and Fig. 3.23.

Compared to the hydrogen 2S-6P spectroscopy, the simulations yield very similar results (see Fig. 5.5 in [71]). This is mainly due to the fact that for hydrogen the optimal nozzle temperature is around $T_N \simeq 5\,K$, while for deuterium the temperature is higher at $T_N \simeq 7\,K$, as discussed in Section 3.6.1. Therefore, the effect of higher mass for deuterium is compensated by the higher temperature.

3.4 Magnetic field suppression and measurement

Minimizing the magnetic field in the 2S-6P interaction region is crucial for suppressing the Zeeman shift, with the x direction along the 2S-6P spectroscopy laser beam being most decisive. Therefore, the high-vacuum region is magnetically shielded with a high-permeability (mu-metal) magnetic shield (MS) of 1 mm thickness[1]. To further minimize the magnetic field, the vacuum chamber is surrounded by three pairs of coils in the approximate Helmholtz configuration (one pair for each of the three spatial directions). In Fig. 3.4, part of the compensation coils (CC) is visible for the x and z direction, which are made of ribbon cables. The compensation coils for the y direction are wrapped around the cylindrical vacuum chamber.

Without the magnetic shield and with compensation coils switched off, the magnetic field in the interaction point is $(B_x, B_y, B_z) = (-508.6(3), -707.1(3), -11.1(3))\,mG$. With the magnetic shield, but with compensation coils switched off, the magnetic field in the interaction point was measured to be $(B_x, B_y, B_z) = (-12.5(3), -111.0(3), -38.4(3))\,mG$. The magnetic shield is therefore most effective in the most important x direction, while the suppresion in the y direction suffers from the $\sim$7 cm hole needed for the detector, whereas in the z direction no large magnetic field is present (such that the value in this direction is even increased due to the overall change in the magnetic field vector). With magnetic shield and compensation coils switched on (in the optimized configuration) the magnetic field in the interaction point is reduced to $(B_x, B_y, B_z) = (+0.1(3), +1.0(3), -1.8(3))\,mG$. The results of the magnetic field measurements in the interaction region within ± 1.5 cm distance from the interaction point are shown in Fig. 3.13, with the magnetic shield and with the optimized coil compensation configuration. For this configuration, the currents on the three pairs of (x, y, z) coils are kept at $(-1.200, -0.610, 0.414)\,A$, while the supplied voltages of around $(14.1, 4.4, 11.2)\,V$ may slightly vary depending on the temperature. Fig. 3.13 demonstates that the magnetic field values for the x direction (B_x), which is most important for the Zeeman shift of the 2S-6P spectroscopy measurement, are below 1 mG within three times the $1/e^2$ beam diameter (beam radius $W_0 = 2.2\,mm$) of the 410 nm spectroscopy laser beam (± 0.7 cm around the interaction point).

The magnetic field inside the detection region is measured with a fluxgate magnetometer probe[2], with the cylindrical detector (shown in Fig. 3.14) being removed. All other com-

[1] Custom manufacturing by Meca Magnetic. The mu-metal has a permeability of $3-4\times10^5$ (for a continuous field) and consists of 80% nickel, 15% iron, and 5% molybdenum (with $< 1\%$ traces of carbon, silicon and manganese).

[2] Bartingtom Magnetometer Mag13MC60, conversion factor 60.24 mG/mV, absolute accuracy with various crosschecks (e.g. rotation) was found to be ~ 0.3 mG. In the future, the Stefan Mayer Instruments FLUXMASTER probe can be used in addition to probe the magnetic field with a similar accuracy along the x direction with the detector being in place. This probe is small anough to be inserted into the 15 mm diameter tube (from the side where the HR mirror and the PMT of the AFR are mounted), but measures in one direction only.

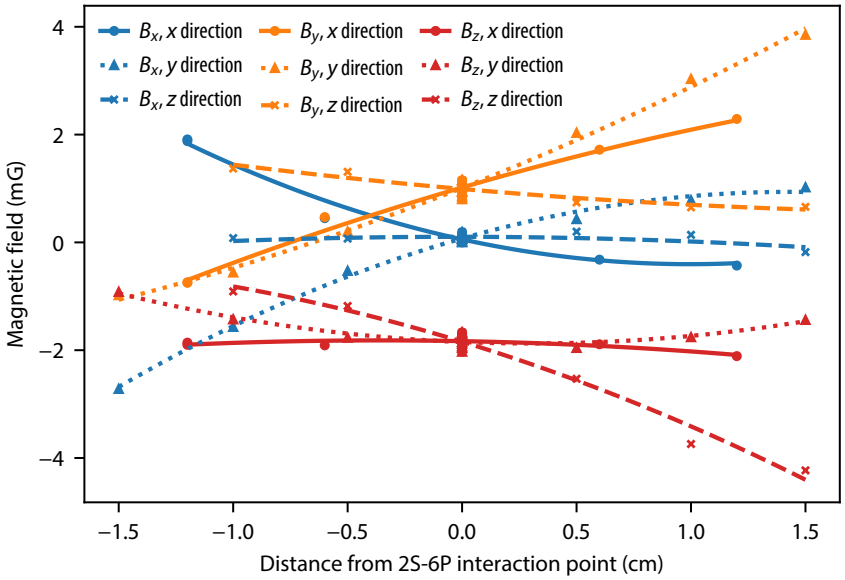

Figure 3.13: Measurement of the magnetic field in the ±1.5 cm region around the 2S-6P interaction point. Data points show the values for the magnetic field values B_x, B_y, B_z in the direction along the 2S-6P spectroscopy beam x (blue), vertical direction y (orange), and atomic beam direction z (red), respectively, according to the coordinate system definition as shown e.g. in Figs. 3.1, 3.3, 3.4, or 4.2. The different markers and lines (quadratic fit to the data) signify the directional distance from the interaction point: x (circular markers, solid lines), y (triangular markers, dotted lines), and z (cross markers, dashed lines). The absolute accuracy on each data point is ∼0.3 mG. The values for B_x (most important for the Zeeman shift of the 2S-6P spectroscopy measurement) are below 1 mG within three times the $1/e^2$ beam diameter of the 410 nm spectroscopy laser beam (±0.7 cm).

ponents in the vacuum assembly are mounted in place. Closing the vacuum chamber lid or moving the illumination lamp near the chamber changes the values in each of the three directions by < 0.4 mG. All components in the high-vacuum region as well as all possible other components are made from non-magnetic materials such as titanium screws. No magnetic materials are used in the detector (also the small M1×15 screws holding the detector together are made from titanium).

The compensation coils can also be used to apply a larger magnetic field for systematic uncertainty checks. However, due to the magnetic shield, the maximum amplitude is significantly smaller than the earth's magnetic field. Along the x direction, with a maximum achievable current through the x-coils between −3 A and 3 A, the magnetic field B_x was measured to vary between −20 mG and 50 mG.

Though the magnetic field is not measured in-situ during the measurement, another probe[1] is mounted on the outside wall of the vacuum chamber (at ∼20 cm distance from the 2S-6P spectroscopy region), which monitors the magnetic field inside the magnetically compensated region. Therefore, any magnetic field changes, i.e. due to a current change in the compensation coils, are immediately noticed. With the compensation coils switched off, this probe mea-

[1] LakeShore FP-2X-250-ZS05M Hall probe, accuracy ∼5 mG.

sures[1] the magnetic fields $(B_x, B_y, B_z) = (-386(5), -965(5), +257(5))$ mG, while with compensation coils switched on the values are $(B_x, B_y, B_z) = (+262(5), -760(5), +685(5))$ mG. These values varied by less than 30 mG over the time period of more than two years.

3.5 Fluorescence detector and in-situ stray electric field measurement

The fluorescene detector serves not only the purpose of detecting the 2S-6P fluorescence photons, but also for an in-situ stray electric field measurement which is crucial to place a limit on the quadratic dc-Stark shift for the precision spectroscopy. The quadratic dc-Stark shift of 2S-nP transitions scales approximately as $\propto n^7$ (see discussion in the beginning of Section 2.2.1). For the 2S-4P measurement, an estimate of the dc-Stark shift was made without an in-situ measurement, while for the 2S-6P transition measurement, such an estimate is not sufficient.

The stray electric field in the interaction region is determined from the varying quadratic dc-Stark shift of the 2S-6P resonance with exactly reversed applied electric fields in the interaction region. Therefore, first the fluorescence detector assembly along with the possibility to apply electric fields is described. Second, the procedure to measure the stray electric fields is given, along with an example measurement.

Much more details on the detector are found in Sec. 4.6 of [71], while here only an overview is presented. More specifically, [71] covers also the details for the operation of the channeltron electron multipliers (CEMs), the saturation of CEMs due to photoionization of 2S atoms in the bright phase, the high-voltage gain switching of CEMs, as well as simulations of detection efficiencies.

3.5.1 Fluorescence detector assembly

Fig. 3.14(a) shows the photograph of the whole assembled detector lying on the table. The detector consists of two aluminum cylinders (each with inner radius of 28 mm and ∼85 mm length) and an electrode section in the center. The cylinders serve the purpose of emitting photoelectrons from 94 nm fluorescence photons hitting their inner walls. While for the previous 2S-4P measurement graphite coated copper cylinders were used, for the 2S-6P measurement the material was replaced by aluminum which has a substantially higher yield for 94 nm photons. The top part of the detector is enclosed with an aluminum cap, see left of Fig. 3.14(a), with a hole for the top channeltron electron multiplier[2] (CEM) (TD). The bottom part of the detector, shown in Fig. 3.14(b), is enclosed by a graphite-coated mesh on a copper

[1] The apparatus in the lab is oriented such that the z axis as defined e.g. in Fig. 3.4 points in the north-north-east direction, the x axis in the west-west-north direction, and the y axis to the top. The magnetic field in the lab usually points towards the bottom north-east direction: negative sign for the x and y directions, and positive sign for the z direction. Outside the MPQ building, the values in the same coordinate system are approximately $(B_x, B_y, B_z) = (+0.18(5), -0.44(5), +0.12(5))$ G, which corresponds to the bottom north direction (positive sign for x in contrast to the lab). Therefore, the building or the surroundings of the lab significantly change the earth's magnetic field direction. However, the magnetic field in the lab stays stable within 30 mG over more than two years.

[2] Photonis MAGNUM Channeltron Model 5901 Extended Dynamic Range (EDR) version. For the preliminary 2S-6P deuterium in July 2021, the top CEM was Serial No. CEM3Y6N0-02, date 02-Apr-19, voltage 2232 V, bias current 181 µA, gain 6.4×10^7, dark count 0 cts/min@3kV, FWHM/V_0 47%. Bottom CEM: CEM3Y6N0-03, 21-Mar-19, 2360 V, 290 µA, 6.4×10^7, 59 cts/min@3kV, FWHM/V_0 89%.

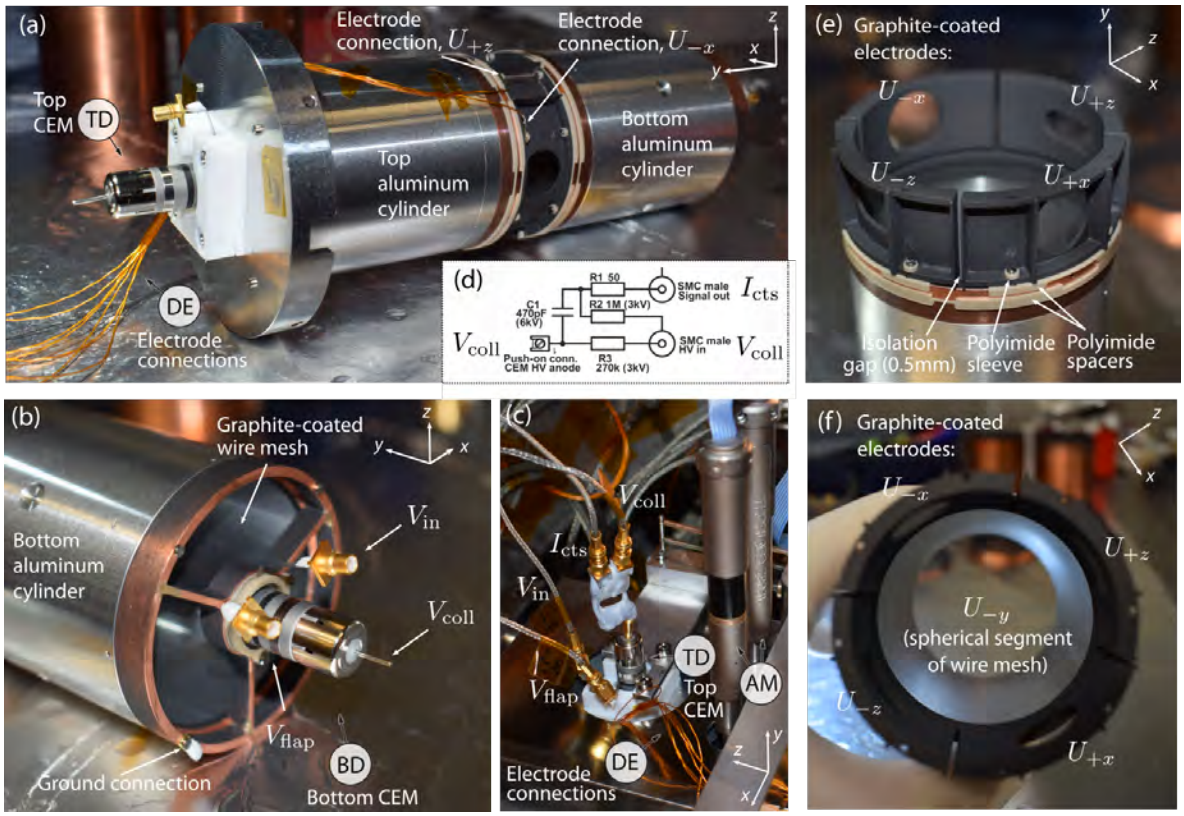

Figure 3.14: Fluorescence detector assembly. (a) The assembled detector lying on the table, along with the top channeltron electron muliplier (CEM) (TD). The detector consists of the top and bottom aluminum cylinders with an electrode section in the center. Visible are two electrodes and the corresponding connections for applying the voltages U_{+z} and U_{-x}, as well as the cable bundle of all the seven ($\pm x$, $\pm y$, $\pm z$, ground) electrode connections (DE). (b) Details of the bottom part of the detector. The graphite-coated wire mesh enables pumping through the bottom part of the cylinder. This mesh is attached to a copper mount to which the ground is connected. The bottom CEM (BD) is shown with the three connections required for the operation: input V_{in}, flap V_{flap} and collector V_{coll} voltages (see text for details). Photograph (c) shows how the top detector is connected in the vacuum setup (variable aperture motors (AM) are labelled for comparison to Fig. 3.4). Figure part (d) gives the circuit for the collector, which is put at a high voltage V_{coll} and at the same time captures the signal pulses (counts) current I_{cts} (see text for details). Photographs (e) and (f) show the half-assembled detector in two perspectives. In (e) the four graphite-coated ring electrodes (quarter segments of a ring) for applying voltages along the 2S-6P spectroscopy laser beam ($U_{\pm x}$) and along the atomic beam ($U_{\pm z}$) are shown in detail, with an isolation gap in between, polyimide sleeves for the screws, and polyimide spacers for isolating the bottom electrode. (f) The bottom electrode (applied voltage U_{-y}) is made of the spherical segment of a graphite-coated wire mesh.

mount to ensure the pumping of the detection region. The detector ground is connected to the bottom copper mount shown in Fig. 3.14(b).

In Fig. 3.14(b), the bottom CEM (BD) is labelled with the three connections (same for the top CEM) to show how the CEM is connected. The part of the CEM facing the inner detector region is put under the input voltage $V_{\text{in}} = 270\,\text{V}$ to create electric fields which collect the electrons. A significantly higher output voltage V_{out} is needed to produce secondary electrons, thereby multiplying the primary electrons by a gain of $G_{\text{CEM}} \sim 5 \times 10^7$ for the CEMs used

here. What matters for the multiplication is then the bias voltage $V_{\text{bias}} \simeq V_{\text{out}} - V_{\text{in}}$. Between V_{in} and V_{out} there is a resistance R_{chan}. The output voltage is supplied via the flap voltage V_{flap} connection, with a resistance R_{bias} between V_{flap} and V_{out}. This resistance is specified to be $10-20\%$ of the total CEM resistance $R_{\text{CEM}} = R_{\text{bias}} + R_{\text{chan}} \sim 15-20\,\text{M}\Omega$. Here, we assume $R_{\text{bias}} \simeq 0.15 R_{\text{CEM}}$ which leads to $V_{\text{bias}} = 0.85(V_{\text{flap}} - V_{\text{in}})$. For the top CEM, the applied flap voltage during the preliminary 2S-6P deuterium measurement was $V_{\text{flap}} = 2.20 - 2.25\,\text{kV}$, and for the bottom CEM $V_{\text{flap}} = 2.4 - 2.7\,\text{kV}$. The CEMs are tested each time before the experiment is started by measuring the pulse height distribution. Depending on the specific CEM and the day, the applied voltage may vary. Sometimes, it was observed that 'spiking' of the bottom CEM occurs, i.e. occasional bursts of much higher count rate. In this case, lowering the voltage usually solves the problem. The bottom CEM is also affected by the cryopump which cools the CEM and affects the resistance R_{CEM}. For more details on the operation of the CEMs, see Sec. 4.6.2. of [71].

The pulses emerging from the CEM are collected on an electrically isolated collector, which is placed under the voltage V_{coll} (the electrons flow over a short gap which corresponds to a capacitor between V_{coll} and V_{out}). V_{coll} is 200 V higher than V_{flap} such that $V_{\text{coll}} = V_{\text{flap}} + 0.2\,\text{kV}$ This voltage is applied via a current-limiting $270\,\text{k}\Omega$ resistor. The pulse current $I_{\text{cts}} = N\,e\,G_{\text{GEM}}$, where N is the number of pulses per second and e is the electron charge, is split off with a 470 pF capacitor and transmitted through a $50\,\Omega$ resistor to match the output impedance to the coaxial signal cable (thereby avoiding reflections). Furthermore, the capacitor is connected to the grounded shield of the V_{coll} cable through a $1\,\text{M}\Omega$ resistor to discharge leakage currents through the capacitor which may lead to a high-voltage on the signal connection. This circuit is shown in Fig. 3.14(d), while Fig. 3.14(c) shows how this circuit is built into a vacuum-compatiple epoxy to connect the top CEM using a push-on connector[1] in the vacuum assembly.

Fig. 3.14(e) and (f) show the center electrode section of the half-assembled detector in more detail. The four ring electrodes (quarter segments of a ring) make it possible to apply the voltage along the 2S-6P spectroscopy beam ($U_{\pm x}$) and the atomic beam ($U_{\pm z}$). The circular apertures for the 2S-6P spectroscopy beam have a diameter of 15 mm, while rectangular apertures with dimensions 16.5 mm × 7.0 mm clear the way for the atomic beam and the 1S-2S preparation laser beam. The ring electrodes are isolated between each other with a 0.5 mm gap, and with polyimide spacers[2] from the top and bottom electrodes (the top part is disassembled). The electrodes are held together with the rest of the detector by M1×15 titanium screws with polyimide sleeves for isolation[3].

Fig. 3.14(f) shows the bottom wire mesh[4] made from 30.5 µm-diameter stainless steel

[1] Allectra, part no. 360-PPO-1.0.

[2] DuPont Vespel polyimide-based plastic. The spacers are 0.5 mm thick and hidden from the inner region, i.e. recessed from inner walls by 3 mm. More details along with a technical drawing of the detector are found in Sec. 4.6.1 of [71].

[3] The cylindrical 5 mm copper rings separating the electrode section from the aluminum cylinders (visible between the polyimide spacers and the aluminum cylinders in Fig. 3.14(a) and (e)) are in place for historical reasons. For some 2S-6P hydrogen measurements, additional blocking meshes were installed to prevent charged particles to enter the top and bottom regions of the detector by applying corresponding voltages [71]. These blocking meshes were then removed, but the aluminum cylinders were kept the same such that the 5 mm copper rings were needed to keep the same height of the detector. In principle, they can be removed by making each of the two aluminum cylinders 5 mm longer.

[4] TWP Inc., 50 Mesh T316 Stainless High Transparency, 0.0012" (30.48 µm) wire diameter, opening 477.52 µm (88%), part number 050X050T0012.

wires spaced 508 µm apart, which is initially flat and bent into the shape of a spherical segment. (Only one wire mesh is visible in Fig. 3.14(f) since the other one is not mounted in the half-assembled detector.) Altogether the electrodes form a Faraday cage for shielding the spectroscopy region from electric fields, for instance from the field created by the input voltages of the CEMs. The coating with colloidal graphite[1] suppresses stray electric fields due to accumulating charges on isolating oxide layers on metals, contact potentials, or surface contaminations. The graphite coating reduces the mesh transparency from 88% to 70% − 80%.

Unfortunately, the graphite coating of the electrodes makes the assembly of the detector very sensitive to accidential shorts between the electrodes. Furthermore, some graphite could fall in between the gaps and short some electrodes even during the operation of the experiment (e.g. due to strong cryopump vibrations). Therefore, the resistance between all electrodes is checked each time before the spectroscopy measurement. Typically, the resistances between the individual electrodes or between each electrode and the ground are $> 100\,\mathrm{M\Omega}$. The resistance between the vacuum feedthrough cable shield and the ground is typically $\sim 0.5\,\Omega$. During the preliminary 2S-6P deuterium measurement in July 2021, the connection between the bottom electrode and the side electrode towards the fiber collimator (i.e. between the electrodes for applying U_{-x} and U_{-y}) was measured to be between $2 - 4\,\mathrm{M\Omega}$, which is still not considered as a short, but is an indication of a short-circuit risk. However, any short between the electrodes would also be observed in the in-situ electric field measurement which is performed during a measurement day several times.

3.5.2 In-situ stray electric field measurement

The six electrodes of the fluorescence detector give the possibility to apply[2] approximately uniform electric fields in each of the three spatial directions. When applying opposite voltages of the same magnitude to two corresponding electrodes, the electric field in the 5 mm radius sphere centered at the 2S-6P interaction point was simulated to have $< 10\%$ deviations from the mean electric field in this region for each of the three spatial directions [71].

Applying an electric field F leads to the quadratic dc-Stark shift of the resonance frequency as:

$$\nu_0(F) = \tilde{\beta}_{\mathrm{dc}}(F - \Delta F)^2 + \nu_0(F = 0\,\mathrm{V/m}), \tag{3.16}$$

where $\nu_0(F)$ is the resonance frequency with the applied electric field F, ΔF is the stray electric field which we wish to measure, $\nu_0(F = 0\,\mathrm{V/m})$ the resonance frequency with zero applied field, and $\tilde{\beta}_{\mathrm{dc}}$ the effective quadratic dc-Stark coefficient. Measuring the resonance frequency as a function of the applied electric field determines $\tilde{\beta}_{\mathrm{dc}}$ and ΔF, from which the dc-Stark shift $\Delta\nu_{\mathrm{dc,2S\text{-}6P}}$ due to the stray electric field ΔF in the corresponding direction is

[1] Spray can by Kontakt Chemie Graphit 33 (part no. 76009-AC)

[2] For $\pm 1\,\mathrm{V}$ applied to one of the pairs of (x,y,z) electrodes (e.g. for x direction: $U_{\pm x} = \pm 1\,\mathrm{V}$, $U_{\pm y} = U_{\pm z} = 0\,\mathrm{V}$), the electric field at the center was simulated [71] to be $(F_{x,0}, F_{y,0}, F_{z,0}) = (18.99, 43.47, 19.65)\,\mathrm{V/m}$ (e.g. for the x direction with $U_{\pm x} = \pm 1\,\mathrm{V}$, $U_{\pm y} = U_{\pm z} = 0\,\mathrm{V}$: $F_{x,0} = 18.99\,\mathrm{V/m}$, $F_{y,0} = F_{z,0} = 0$). The voltages are applied by the National Instruments NI-9264 Analog Output Module with cDAQ-9181 chassis, which provides max. output of $\pm 10\,\mathrm{V}$. To adjust the desired maximum resulting electric field approximately according to the full range for each direction, the voltage is applied through different voltage dividers ($500\,\mathrm{k\Omega}/50\,\mathrm{k\Omega}$ divider providing a ratio around 1:0.09 for the y direction, and $500\,\mathrm{k\Omega}/150\,\mathrm{k\Omega}$ divider providing a ratio around 1:0.23 for the x and z directions), resulting in the electric fields $(F_{x,0}, F_{y,0}, F_{z,0}) = (4.332, 3.934, 4.483)\,\mathrm{V/m}$ (values from measured resistance ratios combined with simulations for the resulting center field from the electrodes) for applied voltages $\pm 1\,\mathrm{V}$ from the analog output module.

given as:

$$\Delta\nu_{\mathrm{dc,2S\text{-}6P}} = \tilde{\beta}_{\mathrm{dc}}\,\Delta F^2. \tag{3.17}$$

For details and corresponding theory, see Sec. 2.4 of [71]. For the discussion here, it is important to note that in general the dc-Stark shift depends on the state structure (i.e. how the electric field couples different levels), as well as on how the signal is detected and the resonance frequency is determined. The observed shift of the transition may not correspond to the combined shift of the involved energy levels. For example, for the $2S_{1/2}$-$6P_{3/2}$ transition, the dc-Stark shift results mostly from the coupling of the $6P_{3/2}$ level with the $6D_{3/2}$ levels. Since the $6P_{3/2}$ and $6D_{3/2}$ levels are separated by less than the linewidth of the 2S-$6P_{3/2}$ transition, the observed resonance splits into several components. However, for the $2S_{1/2}$-$6P_{1/2}$ transition, the situation is much simpler since the dc-Stark shift of the $6P_{1/2}$ level results mostly from coupling to the $6S_{1/2}$ levels which are separated by multiple linewidths of the $2S_{1/2}$-$6P_{1/2}$ transition. To a good approximation, the observed dc-Stark shift of the single $2S_{1/2}$-$6P_{1/2}$ resonance is then equal to the dc-Stark shift of the $6P_{1/2}$ level minus the (more than three orders of magnitude smaller) dc-Stark shift of the inital $2S_{1/2}$ level. For the sake of simplicity, the discussion here is limited to the case of the $2S_{1/2}$-$6P_{1/2}$ transition only.

Fig. 3.15 shows the stray electric field measurements in each of the three spatial directions: (a) and (b) show the measurements in the x direction, (c) and (d) in the y direction, (e) and (f) in the z direction. On the left, the resonance line scans of the $2S_{1/2}$-$6P_{1/2}$ transition in deuterium are shown for the case of no applied field (in blue, same data for all directions), as well as for maximum positive (orange) and negative (red) applied field. Each resonance line is fitted with a Voigt fit function (see Eq. (2.73)) to determine the center frequency ν_0, which is shifted on the order of $1 - 3\,\mathrm{MHz}$ with maximally applied field. Only the data for the first delay is shown here as an example. For the analysis on the right, the Doppler-extrapolated frequency $\nu_{0,e}$ is used, which is determined from the center frequency $\nu_0(\overline{v})$ together with the mean velocity $\overline{v}$ of each delay (see Table 3.2), assuming linear velocity dependence: $\nu_0(\overline{v}) = \nu_{0,e} + \kappa\,\overline{v}$. This frequency determination is shown in Chapter 5, Fig. 5.2. Even though the velocity-dependent shifts (e.g. Doppler-shift or light force shift) in the apparatus are typically on the kHz-level compared to the MHz-shifts with applied electric field, this procedure makes the measurement of stray electric fields independent of possible velocity-dependent shifts.

To determine the stray electric field ΔF, the center frequencies $\nu_{0,\mathrm{e}}$ are plotted against the applied electric field and fitted with a quadratic function, from which according to Eq. (3.16) the values for $\tilde{\beta}_{\mathrm{dc}}$ and ΔF are determined (see the legend of the right plots). For the measurements shown here, the stray electric fields are compatible with zero within the uncertainty of $\sim 0.1\,\mathrm{V/m}$. During the hydrogen 2S-6P measurement campaign, on some days it was observed that a stray electric field in the y direction on the order of $\sim 0.5\,\mathrm{V/m}$ is present. Such an electric field is suspected to originate from the temperature gradient along the detector, leading to a thermoelectric voltage through the Seebeck effect[1]. The data for the whole deuterium 2S-6P measurement campaign from July 2021 is shown in Fig. 5.8 and discussed in Section 5.4. Also in this data set, stray electric fields, which are not compatible with zero, mostly occur only in the y direction and are on the same order of $\sim 0.5\,\mathrm{V/m}$.

[1] Note that the Seebeck effect is only present with dissimilar materials, which can be viewed as a temperature-dependent contact potentials. The contact potentials of the electrodes are suppressed with a colloidal graphite coating (which may be imperfect), while the aluminum is left uncoated as explained in Section 3.5.1. The aluminum walls can be assumed to have an oxidized layer. It remains to be investigated how exactly the Seebeck effect and contact potentials may be manifested in our detector.

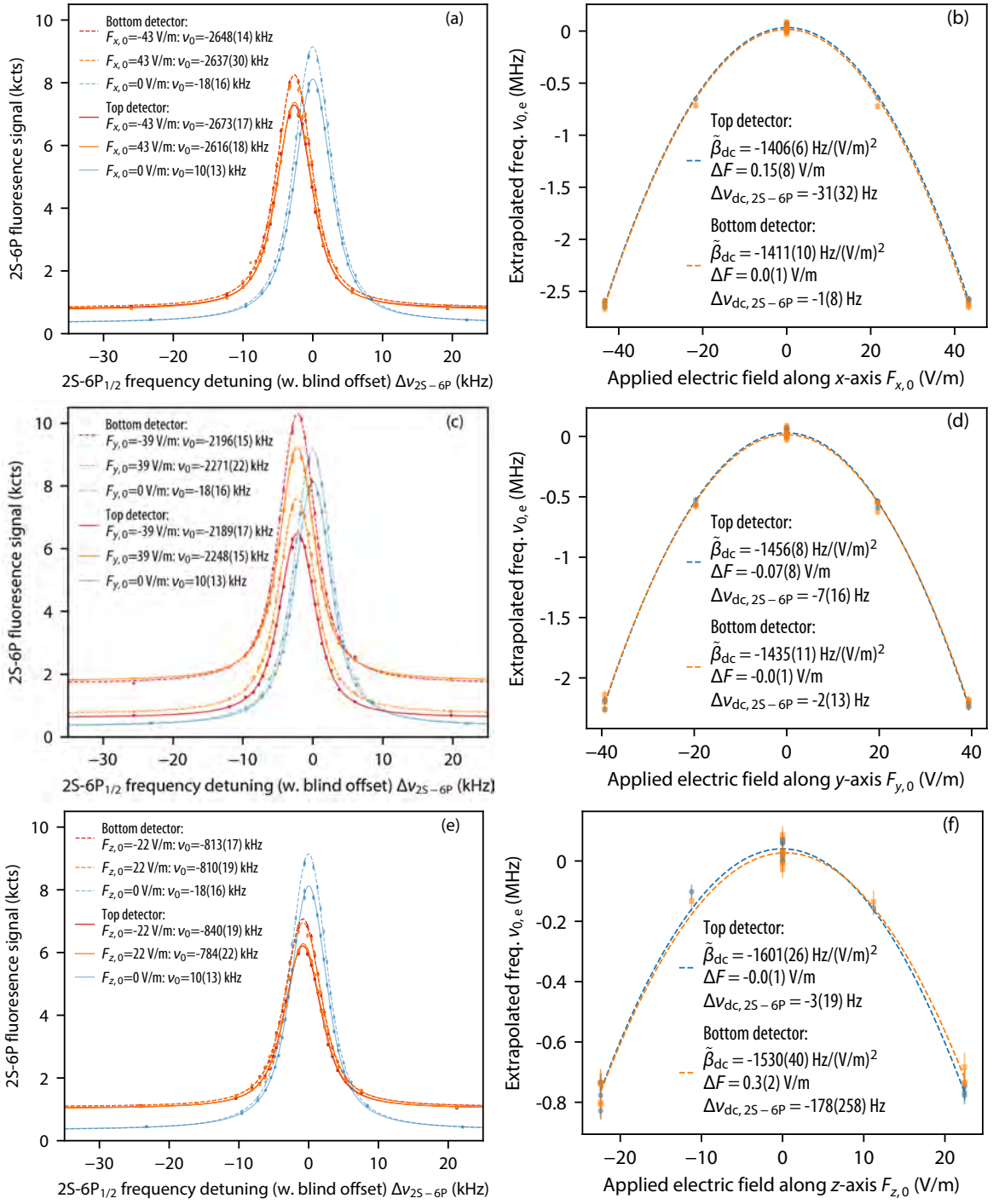

Figure 3.15: Example of in-situ stray electric field measurements in the x (figs. (a) and (b)), y (figs. (c) and (d)), and z (figs. (e)-(f)) directions. The left plots exemplarily show the $2S_{1/2}$-$6P_{1/2}$ deuterium resonance line scans (delay 1) with no applied electric field (faint blue, same data for all directions), and with negative (red) or positive (orange) applied electric field given in the legend along with the Voigt fit result for the center frequency ν_0. The right plots show the Doppler-extrapolated frequency $\nu_{0,e}$ versus the applied electric field, along with quadratic fits to the data from the top and bottom detectors. The fit results for the effective dc-Stark coefficient $\tilde{\beta}_{dc}$, the deduced stray electric field ΔF as well as the dc-Stark shift with no applied electric field $\Delta\nu_{dc,2S\text{-}6P}$ are given in the legend.

The background mainly[1] originates from the 2S atoms, which are quenched into the ground state, emitting a Lyman-α photon at a wavelength of 121 nm. Though with a lower efficiency, these photons also produce photoelectrons in the aluminum walls of the detector. The 2S atoms can be for instance quenched by intra-beam collisions, hitting the atomic beam aperture edges, as well as by electric fields. The latter reason is responsible for the fact that the background increases while the signal decreases when applying an electric field. This effect is more pronounced for the z direction along the atomic beam, where the atoms are subject to the higher electric field as soon as they enter the detector region. Therefore, even for the factor of two smaller applied electric field in the z direction, see Fig. 3.15(e), the signal is smaller and the background is larger compared to the x direction, see Fig. 3.15(a).

It is instructive to compare the signal and background between the top detector (solid curves) and bottom detector (dashed curved) in the left plots in Fig. 3.15. There is an overall $\sim$10% difference in the count rate for the top and bottom detectors due to the slightly different properties of the detectors, which is not of interest here. However, comparing the signal and background values for the opposite applied electric field between the top and bottom detectors, their values are the same for x and z directions, but different for the y direction. Both the signal and background decrease or increase by approximately the same amount depending on the direction of the field. This is attributed to the fact that an applied vertical field accelerates photolectrons from within the inner regions towards the top or bottom detector (depending on the direction of the electric field). Thereby, the count rate is increased on one detector while decreased on the other detector, with the behavior being reversed for the opposite electric field.

While the right plots in Fig. 3.15 show the stray electric field with five applied electric field values, typically only line scans with the two highest applied electric fields are measured (with three resonance line scans for each sign of the applied electric field). This procedure optimizes the trade-off between the overall uncertainty in the determination of electric fields and the required measurement time. The line scans for zero applied electric field are typically taken from previously measured precision line scans.

3.5.3 Non-linearity of the channeltron electron multipliers (CEMs)

Here we consider the non-linearity of the channeltron electron multipliers (CEMs), which give rise to the signal in our fluorescence detector. This non-linearity is revealed in the measurement of the fluorescence signal in dependence on the 2S-6P laser power $P_{\text{2S-6P}}$. Note that here we do not consider the non-linearity in the measurement $P_{\text{2S-6P}}$, which is assumed to be linear (justified by the specifications of the photodetectors having <2% non-linearity, which is smaller than the non-linearity the CEMs discussed here). However, the signal scales non-linearly with $P_{\text{2S-6P}}$ due to the saturation of the 2S-6P resonance, which complicates the

[1]For the experimental conditions here (2S-6P spectroscopy laser power of $P_{\text{2S-6P}} \simeq 30\,\mu\text{W}$, 1S-2S laser power $P_{\text{1S-2S}} \simeq 1.5\,\text{W}$, nozzle temperature 7.1 K, variable aperture set to 1.2 mm), the total background (for all delays) with no applied electric field is $\sim$4% of the total signal (5.8(1) kcts for the top detector (TD) and 5.5(1) kcts for the bottom detector (BD) for all delays in 1 s or 160 chopper cycles), of which $\sim$90% originates from 2S atoms, while $\sim$10% is due to scattering of 243 nm photons. This was checked by detuning the 1S-2S (243 nm) laser out of resonance (which removed $\sim$90% background, leaving 0.5(1) kcts at TD and 0.6(1) kcts at BD) and blocking the 1S-2S (243 nm) laser light (which removes the remaining $\sim$10% of the background, leaving only 3 ± 2 cts at TD and 10 ± 5 cts at the BD). The background significantly increases with larger atom flows, suggesting that intra-beam collisions and collision with the residual gas in the chamber are important (see Sec. 4.5.2.4. in [71]).

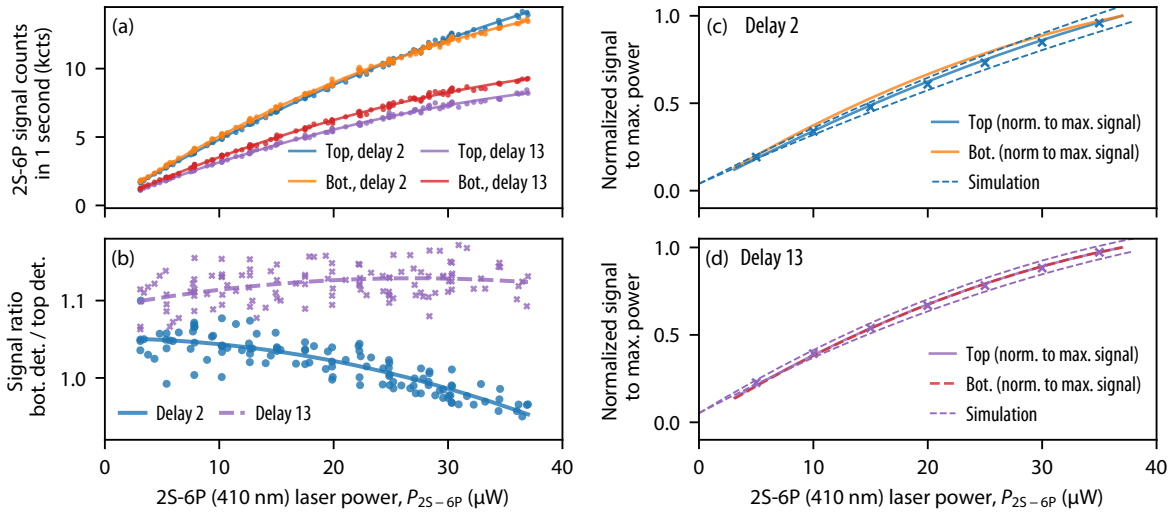

Figure 3.16: Deuterium 2S-6P fluorescence signal counts in dependence on the 2S-6P laser power for delay 2 and 13 as well as for the top and bottom detector. This measurement reveals the (relative) non-linearity of the detectors. (a) The signal counts from 160 chopper cycles (equal to 1 second) are shown as a function of the 2S-6P laser power for delay 2 (top detector in blue, bottom detector in orange) and 13 (top detector in purple, bottom detector in red). (b) The signal ratio of the bottom detector divided by the top detector reveals their relative non-linearity: for linear (or exactly the same non-linear) behavior of the detectors, the signal ratio should be independent of the count rate or the 2S-6P laser power, which is not the case here. As expected, the relative non-linearity is more pronounced for the delay 2 (blue circled markers, solid line) with higher count rate as compared to delay 13 (purple crossed markers, dashed line) with lower count rate. In (c) and (d) the signal for each detector is normalized to the signal at highest laser power, with the data from delay 2 shown in (c) and delay 13 shown in (d). Only the interpolation for the data from (a) is shown for clarity. The crossed markers show the simulation points of the signal dependence on the laser power (normalized to the highest power in each delay), performed with the procedure described in Section 3.3. The comparison between measurement and simulations places a limit on the absolute non-linearity for each detector. Dashed blue lines show the interpolation of the simulation result within the ±7% uncertainty of the laser power calibration, which is in excellent agreement for both detectors for delay 13. For delay 2, the bottom detector is slightly outside the expected curve, which demonstrates the non-linearity of ∼10% of the bottom detector already anticipated from the relative non-linearity in (b). The top detector can only be confirmed to be linear within the ±7% power calibration uncertainty.

discussion on the non-linearity of the CEMs. Therefore, simulations of the 2S-6P signal as a function of $P_{\text{2S-6P}}$ (which include saturation effects of the 2S-6P resonance) are compared to the measured signal, thereby allowing to extract some information on the non-linearity of CEMs. Furthermore, the non-linearity of the CEMs can be examined by comparing the signal ratio of the top to bottom CEMs of the fluorescence detector in the different delays. This is because the non-linearity of the CEMs depends on the signal amplitude, which is different between the delays (fast atoms, i.e. small delays, give rise to higher signal than slow atoms, i.e. large delays).

Let us first consider the origin of the possible non-linearity of CEMs. The electron pulses from the CEM give rise to the average signal current $I_{\text{cts}} = N\, e\, G_{\text{CEM}}$, where N is the number of pulses per second, e the electron charge, and G_{CEM} the gain of the CEM. The bias current $I_{\text{bias}} = V_{\text{bias}}/R_{\text{chan}}$ (where $V_{\text{bias}} = V_{\text{out}} - V_{\text{in}}$ is the bias voltage and R_{chan} the resistance

between V_{out} and V_{in}) flows in the same direction[1]. Since the electrons need to be supplied by the bias current, the signal current cannot exceed the bias current, and the gain starts to decrease at $I_{\text{cts}} \sim 0.1\, I_{\text{bias}}$ [184], which corresponds to a certain count rate N_{sat} where the CEM begins to saturate. For count rates close to N_{sat}, the CEM is thus expected to be non-linear. In our case $I_{\text{bias}} \sim 0.1\,\text{mA}$ (with $R_{\text{CEM}} \sim 20\,\text{M}\Omega$, $V_{\text{bias}} \sim 0.85(V_{\text{flap}} - V_{\text{in}}) \sim 2\,\text{kV}$), such that $N_{\text{sat}} \sim 2\,\text{Mcts/s}$ (with $G_{\text{CEM}} \sim 5 \times 10^7$). Indeed, this value corresponds to the highest observed count rate: we observe $\sim 15\,\text{kcts}$ in delay 2 (with a duration of $\Delta\tau = 50\,\mu\text{s}$) for 160 chopper cycles corresponding to 1 second, such that the count rate is $\sim 15\,\text{kcts}/\Delta\tau/160 \sim 2\,\text{Mcts/s}$.

The non-linearity of the CEMs of our fluorescence detector is visible in Fig. 3.16, where the 2S-6P fluorescence signal is measured versus the 2S-6P (410 nm) laser power $P_{\text{2S-6P}}$. The measurement of $P_{\text{2S-6P}}$ is assumed to be linear. Fig. 3.16(a) shows the signal counts for the delay 2 and 13 (in 1 s or 160 chopper cycles) for the top (blue and purple) and bottom CEM (orange and red). The ratio between the bottom and the top CEM is plotted in Fig. 3.16(b), in blue for delay 2 (circled markers, solid interpolation line) and in purple for delay 13 (squared markers, dashed interpolation line). If the CEMs are both linear (or both have exactly the same non-linearity), the ratio should be independent of the laser power and the same for all delays, solely given by the relative constant gain ratio of the CEMs. However, this is not the case, meaning that the relative non-linearity between the CEMs is present (either both CEMs have a different non-linearity, or one of the CEMs is linear while the other is not). As expected, the non-linearity is more pronouced for the higher count rate in delay 2, where the ratio changes by $\sim 10\%$ between high and low laser powers.

While Fig. 3.16(a) and (b) only demonstrates the relative non-linearity between the CEMs, Fig. 3.16(c) and (d) explores the absolute non-linearity for each of the CEMs. The non-linearity would be most easily characterized with a known linear signal source, which is here not easily available. Despite the assumption of the linearity in the measurement of $P_{\text{2S-6P}}$, the signal is expected to scale non-linearly with $P_{\text{2S-6P}}$ due to saturation of the 2S-6P resonance. Therefore, only the comparison between the simulated signal, which includes the saturation, and observed signal can give evidence on the absolute non-linearity of each CEM. For this comparison, the experimental data from Fig. 3.16(a) is normalized to the highest power in each delay (Fig. 3.16(c) for delay 2 and Fig. 3.16(d) for delay 13). Only the interpolated data curves but not the data points are shown for clarity. The simulation is performed with the procedure described in Section 3.3, with parameters $P_{\text{1S-2S}} = 1.0\,\text{W}$, $\Delta\nu_{\text{1S-2S}} = 0.75\,\text{kHz}$, $T_{\text{N}} = 7.1\,\text{K}$, $v_{\text{cutoff}} = 120\,\text{m/s}$ and other fixed parameters from Table 3.1 for seven 410 nm laser power values between $5 \ldots 35\,\mu\text{W}$ (crossed markers). The observed experimental background of $\sim 4\%$ is added on top of the background-free simulation results. The simulation results are then interpolated and normalized in each delay to the signal at the highest experimental laser power at $37\,\mu\text{W}$. The interpolated curves at $\pm 7\%$ laser power calibration uncertainty are shown as dashed blue curves. For both delays, the simulation is in agreement for the top CEM, and for delay 13 (with lower count rate) the normalized signal for both CEMs is also in agreement with the simulation as well as with each other (the data for the bottom CEM is shown as dashed red curve to make the overlap with the top CEM data visible). Therefore, the top CEM for both delays as well as the bottom CEM for delay 13 can be judged to be linear within the $\pm 7\%$ laser power calibration uncertainty. However, for the delay 2 with higher count rate, the bottom CEM disagrees with the top CEM and the data is outside the

[1] Note that the electrons flow in the opposite direction since the technical flow direction of the current is defined to be in the direction of positive charges.

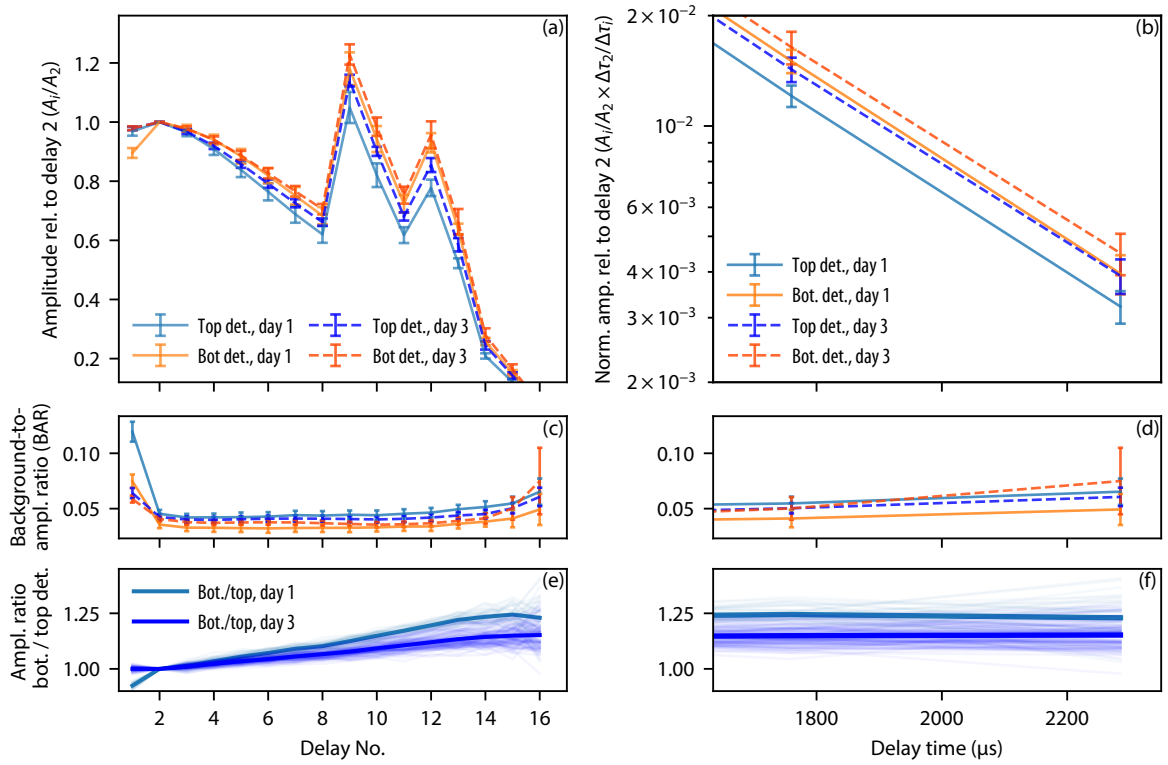

Figure 3.17: Variation of the relative signal amplitude between the top and bottom detector (CEM) within a measurement day as well as between two measurements days. (a) Measured signal amplitude relative to delay 2 (A_i/A_2, see blue points in Fig. 3.12(b) for an exemplary simulation) as a function of the delay number (see Table 3.2 for the definition of delays), with the same legend as in (b) where the relative amplitude is normalized to the duration of the delay ($A_i\Delta\tau_2/(A_2\Delta\tau_i)$, see orange points in Fig. 3.12(b) for an exemplary simulation) is shown for the last two delays (No. 15 and 16) as a function of the delay time. The error bars show the variation within a measurement day (also discussed in Fig. 3.23), whereas the solid and dashed lines with different colors compare two measurement days. (c) and (d) show the background-to-amplitude ratio (BAR). In (e) and (f) the relative amplitude ratio between the bottom and top CEMs is shown, with a clear light blue line for the average of measurement day 1 and a clear bright blue line for the average of the measurement day 3. Faint lines show the data for each resonance line scan within a measurement day. The changing amplitude ratios between the bottom and top CEM for different delays reveal their relative non-linearity (similar to Fig. 3.16(b)), while the difference between the two measurement days demonstrates that this non-linearity is not the same for each day.

simulation curve. This confirms the $\sim 10\%$ relative non-linearity in Fig. 3.16(b), and suggests that the non-linearity of the bottom CEM is mainly responsible for the observed relative non-linearity.

The non-linearity of the CEMs may change between the measurement days as well as within a measurement day, which is demonstrated in Fig. 3.17. In Fig. 3.17(a), the signal amplitude A_i/A_2 relative to delay 2 is shown versus the delay number for the top and bottom CEMs and two measurement days (day 1 and day 3), with the same legend as in Fig. 3.17(b) and (c). This relative amplitude is important for the comparison between simulations and measurements to gain insight on the speed distribution of the flux, as discussed in Section 3.6.2 and Fig. 3.22. In Fig. 3.17(b), the relative signal amplitude is normalized to the duration

of the delay, $A_i\Delta\tau_2/(A_2\Delta\tau_i)$, and is plotted as a function of delay time for the last two delays, which are most significant for the determination of the cutoff-velocity v_{cutoff} from the comparison to simulations. The difference between the top and bottom CEMs illustrates the effect of the non-linearity on A_i/A_2, which also manifests in the background-to-amplitude ratio (BAR) shown in Fig. 3.17(c) and (d). Especially for the first delay, the BAR is affected by the stronger non-linearity on day 1. Fig. 3.17(e) and (f) show the amplitude ratio relative to delay 2 between the bottom and top CEMs for measurement day 1 and 3, which gives the relative non-linearity between the CEMs similar to Fig. 3.16(b) (note that here the ratio is normalized to delay 2 as compared to Fig. 3.16(b) where the ratio is not normalized). If the CEMs were linear (or had exactly the same non-linearity), this ratio would be one for all delays. The increase of the ratio by $10-20\%$ to longer delays thus shows the relative non-linearity between the CEMs. Faint lines show the data for each resonance line scan within a measurement day, and thus demonstrate how the non-linearity varies within a measurement day. Clear light blue lines (day 1) bright blue lines (day 3) show the average of each measurement day. On day 1, the average relative non-linearity is $\sim 20\%$, whereas on day 3 it is lower at $\sim 10\%$ (in agreement with Fig. 3.16 where the data is also from day 3).

The difference in the CEM behavior mainly originates from different operation voltages, which are optimized on each measurement day. However, the operation voltages are typically not changed within a measurement day (only if the 'spiking' behavior is observed which requires to reduce the voltages). The variation in the non-linearity is then attributed to changing R_{CEM} over time due to the temperature change (particularly for the bottom CEM which is close to the cryopump). The data from Fig. 3.17 demonstrates that an uncertainty of $10-20\%$ from the non-linearity of the CEMs has to be taken into account when comparing the measured and simulated amplitude ratios, as for instance to deduce the cutoff-velocity, which is treated in Section 3.6.2.

3.6 Cryogenic deuterium atomic beam

The first ingredient to suppress velocity-dependent effects, such as the first-order Doppler shift for measuring the 2S-6P transition frequency in deuterium, is to reduce the velocity of atoms. At room temperature ($T \sim 300\,\mathrm{K}$) the mean velocity[1] of deuterium atoms in thermal equilibrium (following the Maxwell-Boltzmann distribution) is around $v_{\mathrm{th}} = \sqrt{8\,k_{\mathrm{B}}\,T/(\pi\,m_{\mathrm{D}})} \sim 1.8\,\mathrm{km/s}$, where k_{B} is the Boltzmann constant and m_{D} the mass of a deuterium atom. Reducing the temperature to $T \sim 7\,\mathrm{K}$ results in $v_{\mathrm{th}} \sim 270\,\mathrm{m/s}$.

The cryogenic atomic beam formation in our apparatus is thoroughly covered in Sec. 4.5 of [71], including details on the dissociation fraction, the nozzle design, and various effects playing a role in the atomic beam formation. Here, only an overview is given, and the differences to deuterium are added. More specifically, the optimal temperature point for generating the maximum number of cryogenic deuterium atoms is shifted to higher temperatures around the nozzle temperature $T_{\mathrm{N}} \sim 7\,\mathrm{K}$ as opposed to hydrogen where $T_{\mathrm{N}} \sim 5\,\mathrm{K}$ is optimal. As shown in Section 3.6.1, this is mainly due to the freezing of deuterium, which is necessary to suppress recombination and occurs at higher temperatures compared to hydrogen. This

[1] For the Maxwell-Boltzmann distribution, the root mean square velocity is a factor of $\sqrt{3/(8\pi)} \simeq 1.09$ higher than the mean velocity. For an effusive beam emerging from a small hole in the thermal container, the speed distribution of the flux is obtained from multiplication with a factor v (arising from the fact that the probability for an atom to escape through the hole scales with v) such that the mean speed is a factor of $3\pi/8 \simeq 1.18$ higher than that of an atom following the Maxwell-Boltzmann distribution [182].

difference is predicted by the model and is experimentally confirmed, where hydrogen and deuterium freezing is observed by the drop of pressure for a constant flow. Section 3.6.2 studies the temperature dependence of the deuterium 2S-6P spectroscopy signal, demonstating the optimal temperature region for maximizing the deuterium spectroscopy signal in our apparatus. Furthermore, the comparison of measured and simulated relative amplitudes for different delays is presented, which gives some information about the speed distribution of the flux, specifically the cutoff-velocity v_{cutoff} from Section 3.3.

From the following discussion in Secs. 3.6.1-3.6.2, it becomes clear that the deuterium 2S-6P signal is highly sensitive to temperature. Temperature fluctuations on the nozzle lead to atomic flux fluctuations, which results in excess scatter of the count rate for resonance line scans during spectroscopy measurements. Therefore, the high tempereature sensitivity of the atomic beam formation requires the best possible temperature stability of the cryostat. To this end, a high performance liquid-helium flow cryostat with a specified temperature stability $< 2\,\mathrm{mK}$ has been installed in February 2020, described in Section 3.6.3. However, achieving such high temperature stability above the base point of around 4.5 K turned out to be more challenging since the cryostat did not perform as expected. Nevertheless, the preliminary deuterium 2S-6P measurement could be carried out with an acceptable temperature stability around 10 mK similar to the hydrogen 2S-6P measurement campaign.

3.6.1 Cryogenic atomic beam generation: differences between hydrogen and deuterium

In addition to the complex dynamics of the atomic beam generation in a T-shaped nozzle, the generation of hydrogen H or deuterium D atoms is complicated by the fact that these atoms prefer the energetically favorable molecule state, H_2 or D_2 (or HD for a mixture or isotopic impurities). The recombination probability for hydrogen on copper, $\gamma_{\mathrm{H}}^{\mathrm{Cu}}$, increases strongly below 20 K, reaching up to $\gamma_{\mathrm{H}}^{\mathrm{Cu}} \sim 20\%$ per collision for a temperature around 5-10 K [185]. For deuterium, one might expect a similar recombination rate on copper from the underlying models [186, 187] (measurements seem to be available only at temperatures above room temperature [188, 189]). Even though the emerging atoms from the T-shaped nozzle undergo only a few collisions with the walls, such a high recombination rate significantly reduces the number of atoms. On the other hand, the recombination rate on solid H_2 or D_2 is lower than for copper, though the values also increase with decreasing temperature. The recombination rate decreases as soon as the copper walls are covered with solid H_2 or D_2, such that the number of emerging atoms is expected to rise as soon as hydrogen or deuterium begins to freeze on the nozzle. Below a certain optimal temperature, the signal is then again expected to decrease because of the increase in the recombination rate on solid H_2 or D_2.

In Fig. 3.18 the vapor pressure of solid H_2 or D_2 is shown (blue curves, left scale), based on the data from [190]. The vapor pressure for deuterium (dashed curve) is shifted to higher temperatures by $\sim$2 K compared to hydrogen (solid curve). The pressure in the nozzle was

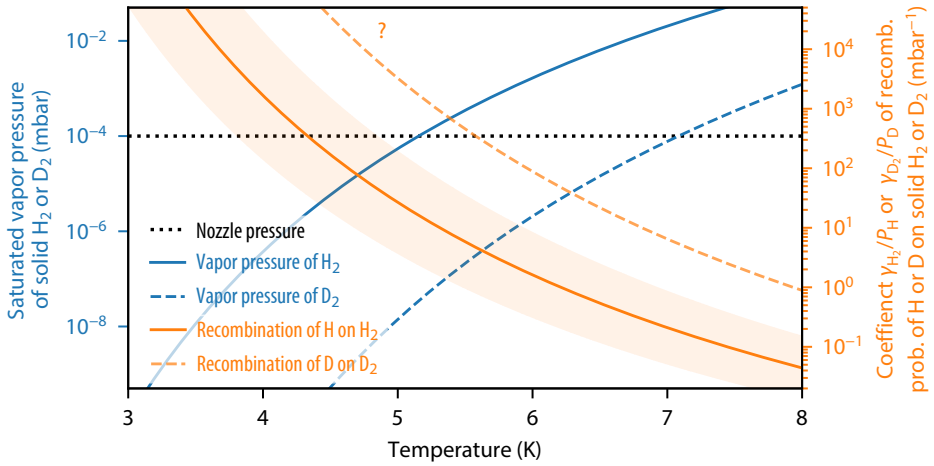

Figure 3.18: The saturated vapor pressure (blue curves, left scale, data from [190]) of solid H_2 (solid curve) and D_2 (dashed curve) drops below the nozzle pressure (dotted line, in our nozzle estimated to be around 10^{-4} mbar for the flow of 0.35 ml/min) at ∼5 K for hydrogen and at ∼7 K for deuterium. These temperatures are approximately optimal for the production of H or D atoms, because a solid H_2 or D_2 layer can then form to suppress the higher recombination on the copper walls. At lower temperatures, the recombination of H or D atoms on solid H_2 or D_2 (right scale, orange solid or dashed curves, respectively) exponentially increases with lower temperature such that less atoms become available. The recombination coefficients γ_{H_2} and γ_{D_2} are given per partial pressure of hydrogen P_H or deuterium P_D, estimated to be roughly around 10^{-5} mbar inside the nozzle. The recombination curve for hydrogen using Eq. (3.18) is based on the adsorption energy $\epsilon_a/k_B = 38 \pm 5$ K from [158, 191] with the resulting uncertainty shown as the faint region, whereas no data is available for deuterium. However, [158, 191] qualitatively suggest a larger adsorption energy of D on D_2 which shifts the hydrogen curve to higher temperatures. The question mark indicates that the recombination curve for deuterium is speculative.

simulated[1] to be around $10^{-5} \ldots 10^{-4}$ mbar. When the vapor pressure drops below the nozzle pressure, a solid H_2 or D_2 layer forms on the nozzle walls. According to Fig. 3.18, this occurs at ∼5 K for hydrogen and at ∼7 K for deuterium. These temperatures approximately correspond to the optimal temperatures for the number of atoms leaving the nozzle: above this temperature, no solid H_2 or D_2 layer is formed, such that the atoms recombine on copper nozzle walls. Below this temperature, also the recombination on solid H_2 or D_2 increases, thereby diminishing the number of atoms.

The recombination coefficient γ is shown in Fig. 3.18 with the orange curves using the right scale. This coefficient is given by [158]

$$\gamma = 4\, K_{S2}\, n/v_{th} \quad \text{with} \quad K_{S2} = K_{S2}^0\, T^{-1/2}\, e^{-2\epsilon_a/(k_B T)}, \tag{3.18}$$

where n is the number density of atoms, $v_{th} = \sqrt{8\, k_B\, T/(\pi\, m)}$ is the thermal mean speed of atoms with mass m. K_{S2} is the temperature-dependent surface recombination rate of second

[1] Simulations performed with COMSOL Multphysics 5.5.0.036. For the simulation, a certain nozzle temperature T_N, volume flow Q of H_2 or D_2, vacuum chamber pressure outside the nozzle $P_{chamber}$, and dissociation fraction $\alpha_{dis} = N_H/(N_H + 2N_{H_2})$ (where N_H is the number of H or D atoms and N_{H_2} the number of H_2 or D_2 molecules) are assumed. For example, for $T_N = 8$ K, $Q_{D_2} = 0.35$ ml/min, $P_{chamber} = 2.3 \times 10^{-6}$ mbar and $\alpha_{dis} = 0.1$, the partial pressure of D atoms is simulated to be $P_D \sim 4 \times 10^{-6}$ mbar and of D_2 molecules $P_{D_2} \sim 3 \times 10^{-5}$ mbar. The poorely known α_{dis} makes the simulation of partial pressures uncertain up to a factor of ∼5 (see [71] for a discussion of α_{dis}). Furthermore, the simulation does neither include the adsorption on the walls, nor the recombination. However, the simulation can still provide an order of magnitude estimate.

order and ϵ_a the adsorption energy of atoms on the surface. For recombination of H atoms on solid H_2, $K_{S2}^0 \simeq 8.4 \times 10^{-28}\,\mathrm{m^4\,K^{1/2}\,s^{-1}}$ and $\epsilon_a/k_B = 38 \pm 5\,\mathrm{K}$ [158, 191]. Using the ideal gas law, the number density is related to the partial pressure of the corresponding atomic species as $n = P/(k_B\,T)$. For example, using the above relations for hydrogen at $T = 5\,\mathrm{K}$, one finds $\gamma_{H_2} \simeq n_H \times 2 \times 10^{-23}\,\mathrm{m^3} \simeq P_H \times 30\,\mathrm{mbar^{-1}}$. The temperature dependence of the recombination coefficient per partial pressure γ_{H_2}/P_H for H atoms on solid H_2 is shown as a solid orange curve (right scale) in Fig. 3.18. Note that due to the exponential dependence on the adsorption energy ϵ_a, its uncertainty of $\pm 5\,\mathrm{K}$ results in an order of magnitude uncertainty on γ_{H_2}, marked as faint region in Fig. 3.18. No data of recombination coefficients of D on D_2 is available to the knowledge of the thesis author. However, [158, 191] qualitatively suggest a larger adsorption energy of D on D_2. Assuming the same value for K_{S2}^0, a larger value for ϵ_a shifts the hydrogen curve to higher temperatures, which is exemplarily shown as dashed curve for $\epsilon_a = 50\,\mathrm{K}$ along with the question mark indicating that this curve is speculative. Given the approximately simulated partial pressure of deuterium atoms of $P_D \sim 10^{-5} \ldots 10^{-6}\,\mathrm{mbar}$, the recombination coefficient rises to the percent level ($\gamma_{D_2} \sim 10^{-2}$) around 5 K.

The freezing of hydrogen or deuterium on the nozzle walls also leads to clogging of the nozzle over time such that the 1S-2S preparation laser beam is clipped after a certain operation time. Therefore, after a certain time, this requires to 'unfreeze' the nozzle by heating. Typically, the cryostat is heated up to room temperature since we also regularly observe that impurities freeze on the nozzle[1], where some of them unfreeze only between 200 K and 300 K. We refer to the time duration between the start of the hydrogen or deuterium gas flow with a cold nozzle and heating up the nozzle (when the nozzle begins to clip the 1S-2S laser beam) as a "freezing cycle". Note that the clogging of the nozzle also changes the pressure inside the nozzle, which in turn changes the nozzle dynamics. Therefore, also the spectroscopy signal slowly changes over the time of the freezing cycle. For hydrogen, the freezing cycle was typically 2 hours long (at a nozzle temperature of $T_N = 4.8\,\mathrm{K}$ with a flow of 0.35 mln/min, 2.0 mm × 4.0 mm T-shaped nozzle, 300 µm diameter orifice after the discharge). For deuterium, the freezing cycle was observed to be much longer, around 7 hours (nozzle temperature $T_N = 7.0 - 7.2\,\mathrm{K}$, all other parameters were the same). Since the vapor pressure curves in Fig. 3.18 differ by the same $\sim 2\,\mathrm{K}$ difference as the optimal nozzle temperature difference ($T_N \simeq 5\,\mathrm{K}$ for hydrogen vs $T_N \simeq 7\,\mathrm{K}$ for deuterium), this suggests that the recombination curve for deuterium is shifted by less than 2 K. For the same vapor pressure of D_2 as for H_2, the recombination rate would then be lower, which could explain the slower accumulation of solid D_2 on the nozzle walls. However, this reasoning assumes the same nozzle pressure and dissociation fraction from the discharge to the nozzle, which could differ for hydrogen and deuterium. Furthermore, the dissociation fraction at the nozzle is probably only around 10% (see Sec. 4.5.2. of [71] for discussion), such that there are much more molecules than atoms in the nozzle already without the recombination on the nozzle walls.

The freezing of hydrogen and deuterium is also observed by measuring the pressure in the vacuum chamber for a constant flow, while cooling down the nozzle. Fig. 3.19(a) shows the cooldown with hydrogen, and Fig. 3.19(b) the cooldown with deuterium. The upper

[1] Note that due to these impurities, the nozzle may not be entirely covered with a solid layer of hydrogen or deuterium snow during the operation of the experiment. It remains to be investigated how these impurities may affect the generation of the atomic beam.

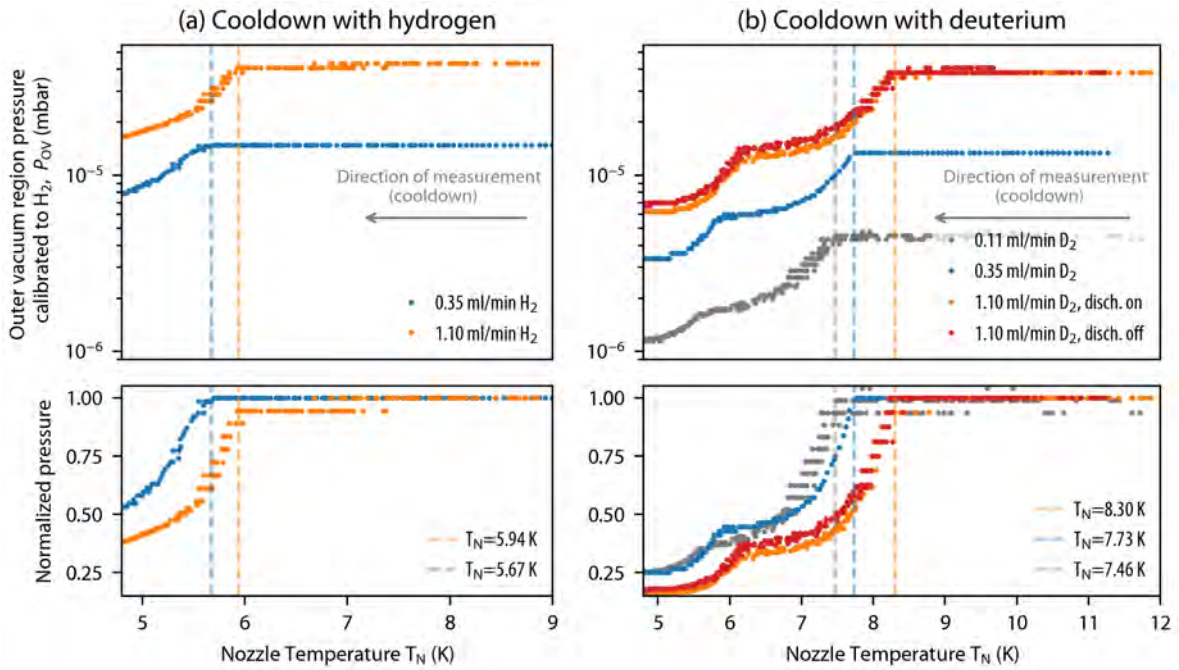

Figure 3.19: Observation of hydrogen and deuterium freezing during the cooldown of the nozzle by measuring the pressure in the outer vacuum region P_{OV}, which is plotted versus the nozzle temperature T_{N}. Below a certain temperature, the vapor pressure drops below the nozzle pressure (see Fig. 3.18) such that some fraction of incoming hydrogen or deuterium gas freezes on the nozzle, resulting in the reduced pressure in the vacuum chamber. (a) Cooldown with hydrogen for a flow of 0.35 ml/min (orange data points) and 1.1 ml/min (blue data points). For the smaller flow, hydrogen freezes below $T_{\mathrm{N}} \simeq 5.7\,\mathrm{K}$, while for the larger flow the transition is shifted to higher temperatures due to the higher nozzle pressure, as expected from Fig. 3.18. (b) Cooldown with deuterium: the freezing occurs at a $\sim 2\,\mathrm{K}$ higher temperature compared to hydrogen, in agreement with Fig. 3.18. As for hydrogen, the transition temperature is higher for higher flows. The second transition, which occurs at lower temperatures around $T_{\mathrm{N}} \sim 6\,\mathrm{K}$, originates from deuterium freezing on the outside of the cryostat cold finger and the outside of the nozzle, where the pressure is approximately an order of magnitude lower than inside the nozzle such that the freezing point is shifted to lower temperatures. No significant difference is observed between the discharge being switched on (orange points) or off (red points) for the flow of 1.1 ml/min (the discharge is off for the other flows).

plots show the outer vacuum region pressure P_{OV} (calibrated to hydrogen[1]) with a constant hydrogen or deuterium gas flow as a function of nozzle temperature T_{N}. Without any gas flow, the pressure is $P_{\mathrm{OV}} \sim 10^{-6}\,\mathrm{mbar}$ (not shown in the figure). With the gas flow, the pressure stays at a certain constant value (depending on the flow) above the freezing point of hydrogen or deuterium. Below a certain temperature, the vapor pressure drops below the pressure in the nozzle, such that some fraction of hydrogen or deuterium freezes on the nozzle walls. For hydrogen, the pressure in the chamber starts to decreases below $T_{\mathrm{N}} \simeq 5.7\,\mathrm{K}$ (vertical dashed

[1]For the used hot cathode pressure gauge (Leybold ITR 200) there is a calibration factor of 2.4 between nitrogen and hydrogen. Therefore, with no hydrogen the value for nitrogen is most applicable, while with hydrogen-dominated pressure the value is $\sim 2.4 \times 8 \times 10^{-8}\,\mathrm{mbar}$. Even though there are differences in the behavior of hot cathode gauges between hydrogen and deuterium [156], the relative factor between the actual and measured pressure values is on the order of few percent [157], and therefore within the $\pm 15\%$ accuracy of our pressure gauges.

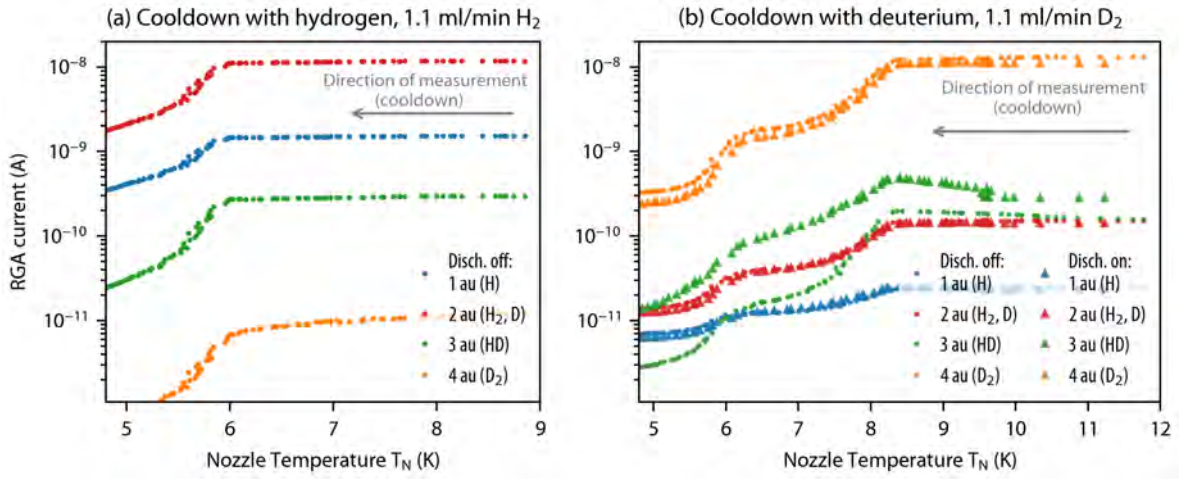

Figure 3.20: Observation of hydrogen and deuterium freezing with a Residual Gas Analyzer (RGA), which ionizes the atoms coming from the residual gas of the vacuum chamber and performs a mass spectrometer measurement. The signal current from the different species of ions is grouped by the atomic mass unit (a.u.), here shown are 1 a.u. (blue, attributed to atomic hydrogen, H), 2 a.u. (red, attributed to molecular hydrogen or atomic deuterium, H_2 or D), 3 a.u. (green, attributed to hydrogen deuteride, HD), and 4 a.u. (orange, attributed to molecular deuterium, D_2). However, the crosstalk between neighboring channels challenges the distinction between neighboring mass species. (a) For the cooldown with hydrogen, the most prominent 2 a.u. signal (red) shows the same freezing behavior as in Fig. 3.19(a) for the overall pressure. The signal for the other mass species with the same freezing pattern is mainly attributed to the crosstalk between the neighboring mass channels. (b) For the cooldown with deuterium, the 4 a.u. signal (orange) is most prominent and shows the same freezing behavior as Fig. 3.19(b), confirming that the freezing of molecular deuterium is responsible for the pressure drop. The data was also taken with discharge switched on (triangle data points), showing no significant difference to the measurement with the discharge switched off (circle data points), except for the 3 a.u. signal, indicating the increased formation of HD molecules with the discharge. The RGA is mounted such that gas particles need to collide with the vacuum chamber walls many times before reaching the RGA. The deuterium atoms could then easily recombine on the way to the RGA, such that no conclusion can be made regarding the dissociation fraction from this measurement.

blue line) for the flow of 0.35 ml/min (blue data points). For the higher flow of 1.1 ml/min (orange data points), this transition temperature is higher at $T_N \simeq 5.9\,K$ (vertical dashed orange line). This is in agreement with the expectation from Fig. 3.18: for a higher nozzle pressure, the point at which the vapor pressure starts to be below the nozzle pressure is shifted to higher temperatures. For the same flow of deuterium instead of hydrogen, the freezing occurs at a $\sim 2\,K$ higher temperature, as expected from Fig. 3.18. The bottom plots show the normalized pressure to the value above the freezing point, such that the shift in the transition point is clearly visible. For a flow of 1.1 ml/min, the freezing behavior was also compared between the setting with the discharge on (orange data points) and off (red data points), where no significant difference was observed (for the other flow values, the discharge was kept off).

For deuterium, a second drop in pressure is observed at around $\sim$6 K. This second pressure drop originates from freezing of deuterium on the outside of the cryostat cold finger and the outside of the nozzle. The pressure in the outer vacuum region is approximately an order of magnitude lower than inside the nozzle, such that deuterium begins to freeze at lower

temperatures than inside the nozzle. This was verified with a cooldown without the teflon tubing connected to the nozzle, such that deuterium does not enter the vacuum region through the nozzle. In this case, only one transition at lower temperatures was observed. In the utilized cryostat configuration (without pumping on the helium exhaust port), it was not possible to cool below 4.7 K where a similar transition for hydrogen is expected. However, this can be done in the future.

The freezing behavior was also measured with a Residual Gas Analyzer (RGA)[1] for the same flow of 1.1 ml/min of hydrogen or deuterium gas, see Fig. 3.20. The RGA distinguishes between different species in the residual gas by ionizing the atoms and performing a mass spectrometer measurement. The strength of signal is given by the current from the corresponding ion species grouped by the atomic unit (a.u.) mass. However, the cross-talk between the neighboring channels limits the measurement of neighboring mass species[2]. For hydrogen, see Fig. 3.20(a), the RGA current is highest for 2 a.u. mass and shows the same freezing behavior as on the overall pressure signal in Fig. 3.19(a). For deuterium, see Fig. 3.20(b), the 4 a.u. signal shows the same freezing behavior as in Fig. 3.19(b), confirming that indeed molecular deuterium is responsible for this freezing pattern. With the discharge switched on (faint triangle data points), no significant difference in the RGA signals is observed except for the 3 a.u. signal, attributed to hydrogen deuteride molecules (HD), which could be formed in the discharge or on the way to or inside in the RGA. The RGA is mounted through a right-angle bend in the high-vacuum region pressure monitor port of the vacuum chamber. Therefore, in order to make the way from the nozzle to the RGA, the atoms need to pass through several obstacles where they could recombine. Therefore, in this setting, the 2 a.u. signal is not reliable. For a reliable measurement of the dissociation fraction, the RGA would need to be placed right in the way of the atomic beam. Even though the 2 a.u. signal would probably still be unreliable due to the crosstalk with the neighboring channels, the reduction of the 4 a.u. signal when the discharge is switched on could provide a reliable measurement of the dissociation fraction.

3.6.2 Temperature dependence of the deuterium 2S-6P spectroscopy signal

The discussion in the previous section considers only the production of ground state deuterium atoms. As has been discussed, the complex dynamics of the atomic beam production in the T-shaped nozzle is further complicated by the balance between freezing of molecular deuterium on the nozzle walls and the recombination on the solid layer of deuterium. Moreover, the latter effect is velocity-dependent, as evident from Eq. (3.18), which suggests a different behavior for different velocity groups of atoms. On top of the ground state atomic beam formation, the situation complicates even further when considering 2S atoms formed in the atomic beam after the nozzle. These metastable 2S atoms are very sensitive due to the perturbative mixing with the 2P state which quenches the atoms into the ground state. For example, this quenching is triggered by the intra-beam collisions of atoms and collisions with the background gas molecules. The overall temperature-dependent behavior of the metastable

[1] Pfeiffer Vacuum PrismaPlus QMG 220 F1, detection limit 10^{-12} mbar, operating pressure max. 10^{-4} mbar, sensitivity for Ar 10^{-3} A/mbar, resolution $0.5 - 2.5$ a.u..

[2] If no hydrogen or deuterium gas is guided into the vacuum chamber, at a pressure of $\sim 10^{-6}$ mbar, the current for zero mass species (0 a.u.) is around 10^{-12} A, resulting from the signal for 1 a.u. and 2 a.u. species around 2×10^{-11} A. For 3 a.u. species the signal is 10^{-12} A, and for 4 a.u. 10^{-13} A. These background measurements indicate the cross-talk signal to be a factor of $10 - 100$ of the neighboring mass signal.

deuterium atomic beam production is difficult to predict quantitatively, and only rough qualitative arguments can be made to explain some dependencies. Therefore, to find the optimal nozzle temperature, the temperature dependence of the deuterium 2S-6P signal has been characterized experimentally.

Fig. 3.21 shows the measured temperature dependence of the deuterium 2S-6P spectroscopy signal. For this measurement, deuterium 2S-6P resonance line scans were performed for different temperatures to extract the signal amplitude (left plots (a) and (b)) and the background (right plots (c) and (d)). Fig. 3.21(a) shows the deuterium 2S-6P signal amplitude on resonance for delay 2 (blue), delay 13 (orange) and delay 16 (red), also applicable to other plots. Circular markers with solid curves (to guide the eye) show the data as the nozzle temperature was decreased from $T_N = 7.8\,K$ to $T_N = 6.3\,K$ (in total $\sim 40\,min$ measurement time), indicated by solid arrows in Fig. 3.21(a). A few minutes after the lowest temperature point, the nozzle temperature was gradually increased: crossed markers with dashed curves show the corresponding data (in total $\sim 50\,min$ measurement time) and the dashed arrows in Fig. 3.21(a) indicate the direction of temperature change. The signal amplitude is maximal for the temperature between $T_N \simeq 6.8\,K$ (slowest atoms, delay 16) and $T_N \simeq 7.5\,K$ (fast atoms, delay 2) depending on the delay. The observed approximate optimal nozzle temperature $T_N \sim 7\,K$ for maximum signal confirms the prediction from Fig. 3.18. However, the exact value of the optimal temperature for maximum signal is different depending on the velocity group which demonstrates the complicated beam formation dynamics.

Fig. 3.21(b) shows the same data as in Fig. 3.21(a), which has been normalized to the maximum signal amplitude for decreasing temperature (for each delay separately). After the nozzle has been exposed to lower temperatures, the signal amplitude increases by up to 45% when increasing the temperature back to the optimal point. This can be explained by the fact that the solid deuterium layer is more efficiently formed on the nozzle at lower temperatures and also reduces the recombination at higher temperatures. It has been regularly observed that if the nozzle temperature is increased further above the freezing point[1], the solid deuterium layer evaporates such that the signal amplitude is lower at the optimal temperature[2].

The temperature dependence of the background is shown in Fig. 3.21(c). Most of the background (∼90%) originates from the 2S atoms, that are quenched to the ground state, emitting a Lyman-α photon at a wavelength of 121 nm. This quenching can be for instance triggered by the electric field (see discussion in Section 3.5.2), by collisions with the residual background gas, and by collisions within the atomic beam. Since the background scales with the number of 2S atoms, a similar tendency of the temperature dependence is observed for the background as for the 2S-6P signal. However, the temperature for the maximum background is different from the temperature for the maximum signal. The overall behavior is complicated since the quenching also depends on the fraction of atoms and molecules in the atomic beam. Fig. 3.21(d) shows the background-to-amplitude ratio (BAR). For fast atoms (delay 2, blue),

[1] This can for instance occur later during the measurement day, when a large solid layer of deuterium is formed on the nozzle and some solid deuterium 'snow' drops off the nozzle. This typically leads to a temperature and pressure spike (lasting only for a few seconds or less). Sometimes, this is also observed on the nozzle imaging camera. This temperature spike can be as high as $T_N \sim 10\,K$ which quickly evaporates more of the solid deuterium such that the spectroscopy signal amplitude is decreased afterwards.

[2] The nozzle can then again be exposed to lower temperatures for a few minutes to build up the solid deuterium layer. However, during the 2S-6P deuterium measurement campaign in July 2021, this was not always possible since the base temperature of the cryostat increased over the course of the measurement day (and also increased for each following measurement day).

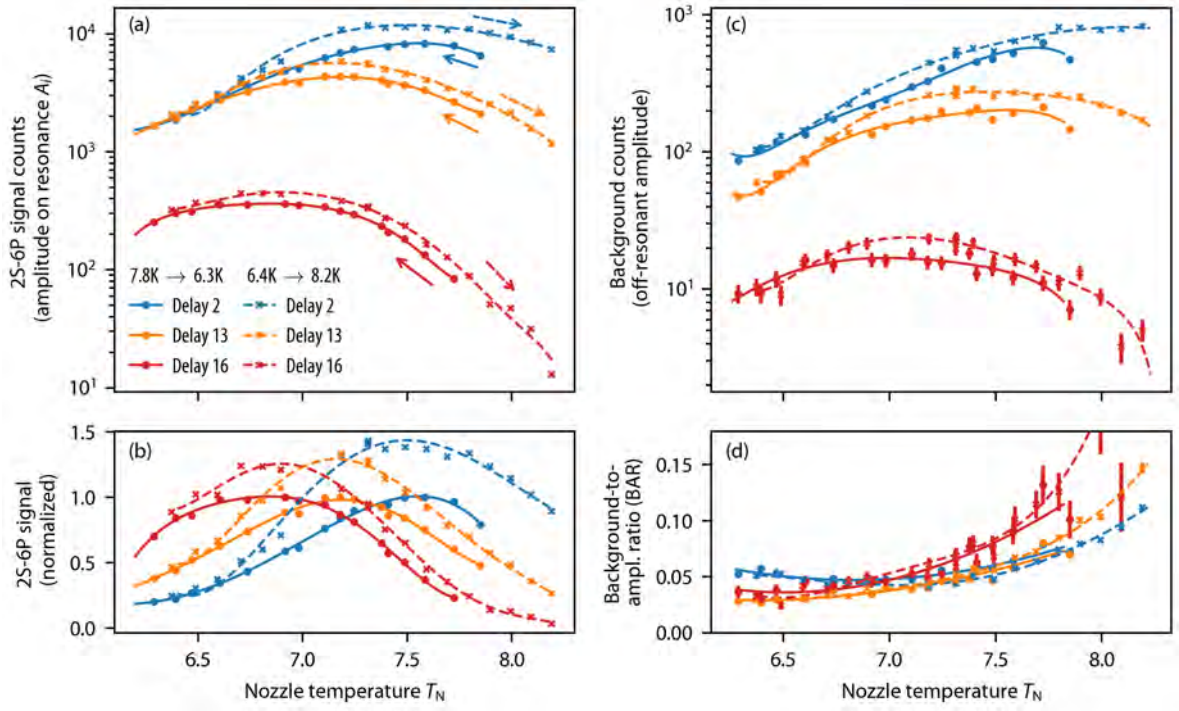

Figure 3.21: Temperature dependence of the deuterium 2S-6P signal, where from deuterium 2S-6P resonance line scans the signal amplitudes (left) and the background levels (right) are extracted for different nozzle temperatures T_N (laser powers: $P_{2S-6P} \simeq 30\,\mu W$, $P_{1S-2S} \simeq 1.4\,W$). Both signal and background levels are shown for delay 2 (blue), delay 13 (orange) and delay 16 (red). Circular markers with solid curves (to guide the eye) show the data when the nozzle temperature is gradually decreased from $T_N = 7.8\,K$ to $T_N = 6.3\,K$ (indicated by solid arrows), whereas crossed markers with dashed curves show the subsequent measurement after the nozzle has been cooled down to $T_N = 6.3\,K$ for a few minutes and the temperature is increased to $T_N = 8.2\,K$ (indicated by dashed arrows). (a) The signal is maximized between $T_N \simeq 6.8\,K$ (slowest atoms, delay 16) and $T_N \simeq 7.5\,K$ (fast atoms, delay 2). (b) For each delay, the data from (a) is normalized to the maximum signal for the decreasing temperature. After the nozzle has been exposed to lower temperatures, the signal at the optimal temperature is higher, which is attributed to the formation of the solid layer of deuterium reducing the recombination. (c) The background, which mainly originates from collisional quenching of metastable 2S atoms to the ground state, has a different dependence on temperature. (d) Consequently, the background-to-amplitude ratio (BAR) also depends on temperature. No significant difference between decreasing and increasing temperature is observed. The BAR is minimized for fast atoms (delay 2, blue) around $T_N \simeq 7\,K$, whereas for slow atoms (delays 13 and 16, orange and red) the BAR continues to drop for even lower temperatures.

the BAR is minimized to ∼4% for a temperature around $T_N \simeq 7\,K$, while for slow atoms (delays 13 and 16, orange and red) the BAR slightly decreases further at lower temperatures. Above $T_N \simeq 7.5\,K$ the BAR strongly increases both for slow and fast atoms. Note that there is no significant difference between decreasing (circular markers, solid curves) and increasing temperature (crossed markers, dashed curves).

Fig. 3.21 clearly shows that the temperature dependence of the signal varies for the different delay: the signal is maximized for fast atoms (first delays) at higher temperatures compared slow atoms (last delays). Therefore, also the speed distribution of the flux depends on temperature. This is visualized in Fig. 3.22(a) and (b), which compares the observed (cir-

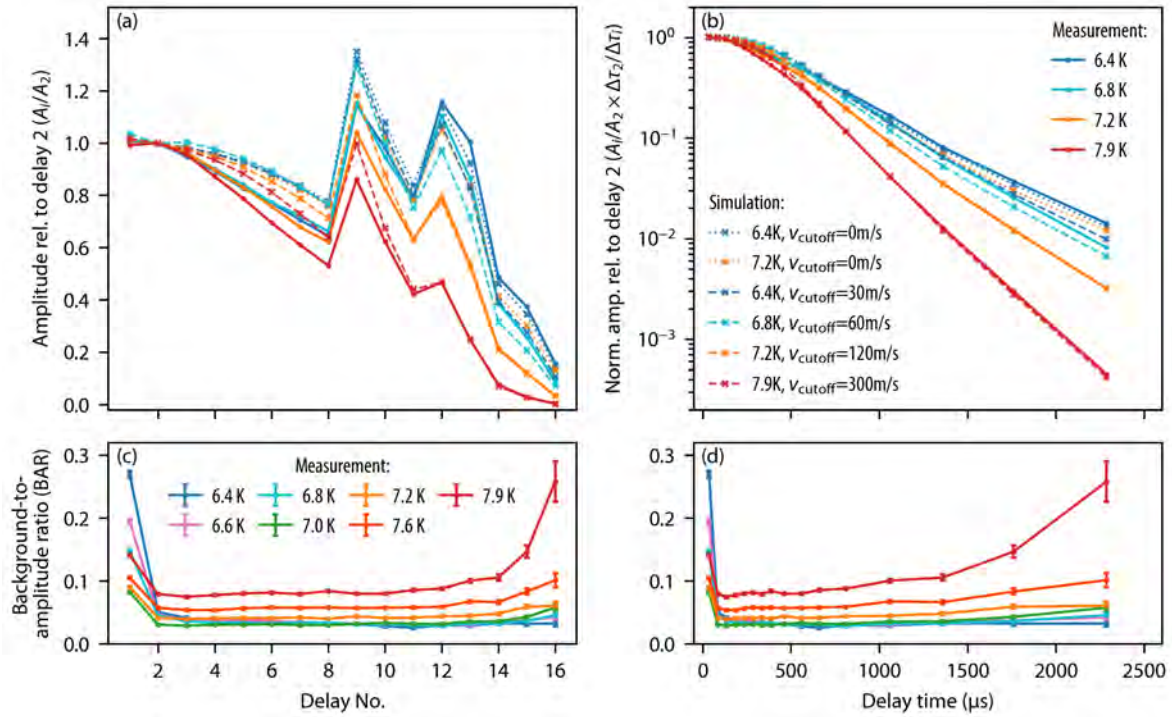

Figure 3.22: The observed time-resolved relative amplitude normalized to delay 2 (circular markers, solid curves) for selected data from Fig. 3.21 is compared with simulations (crossed markers, dashed lines) for different temperatures, which gives information about the temperature dependence of the speed distribution of the flux. (a) The observed and simulated relative amplitude of each delay, A_i/A_2 (see exemplary blue curve in Fig. 3.12(b), second last column in Table 3.2) is shown with the same legend as in (b) where the relative amplitude normalized to $\Delta\tau_i$ (duration of delay which is different for some delays), $A_i/A_2 \times \Delta\tau_2/\Delta\tau_i$ (orange in Fig. 3.12(b), last column in Table 3.2) is plotted. The measurement (circular markers connected by solid lines) is shown for four nozzle temperatures: $T_N = 6.4\,K$ (blue), 6.8 K (cyan), 7.2 K (orange) and 7.9 K (red). Simulations for the same temperatures with a different non-zero cutoff-velocity v_{cutoff} from Eq. (3.14) is shown with crossed markers connected by dashed lines (in (b) the red and orange dashed lines almost overlap with the solid lines). This cutoff-velocity increases by an order of magnitude from $v_{cutoff} \sim 30\,m/s$ to $v_{cutoff} \sim 300\,m/s$ within a temperature change of only 1.5 K. For reference, the simulations with $v_{cutoff} = 0\,m/s$ (velocity-weighted Maxwellian distribution of an atomic beam [182]) are shown with dotted curves for $T_N = 6.4\,K$ (blue) and 7.2 K (orange) to visualize that the change in the number of slow atoms due to the slightly different thermal velocity in negligible. The discrepancy between simulation and experiment for the first delays is mainly attributed to the non-linearity of detectors (see main text for discussion). (c) and (d) show the measurement of the background-to-amplitude ratio (BAR) for temperatures in (a) and (b) along with the data for more temperature values. The BAR decreases for lower temperatures and is approximately constant over the delays, except the first delay and the last delays (see main text for discussion).

cular markers, solid lines) and simulated (crossed markers, dashed and dotted lines) relative amplitudes for four different nozzle temperatures (same data as in Fig. 3.21): $T_N = 6.4\,K$ (blue), 6.8 K (cyan), 7.2 K (orange) and 7.9 K (red). In Fig. 3.22(a), the amplitude relative to delay 2 summed over the duration of the delay, A_i/A_2, is plotted (for an exemplary parameter set, see blue curve in Fig. 3.12(b) and second last column in Table 3.2). In Fig. 3.22(b), the relative amplitude is weighted with the delay duration, $A_i/A_2 \times \Delta\tau_2/\Delta\tau_i$ (orange in Fig. 3.12(b),

last column in Table 3.2). The dashed lines show the simulation results with each measured temperature as an input parameter along with a different non-zero cutoff velocity v_{cutoff} (see Eq. (3.14)), which was chosen such that the simulated relative amplitude matches the measured relative amplitude for slow atoms (last delays). This cutoff velocity changes by an order of magnitude from $v_{\mathrm{cutoff}} \sim 30\,\mathrm{m/s}$ to $v_{\mathrm{cutoff}} \sim 300\,\mathrm{m/s}$ within a temperature change of only 1.5 K. To visualize that within a small temperature change, the speed distribution of the flux changes insignificantly due to the different thermal speed, dotted lines compare the simulated amplitude for zero v_{cutoff} (velocity-weighted Maxwellian distribution of an atomic beam [182]) between $T_{\mathrm{N}} = 6.4\,\mathrm{K}$ (blue) and 7.2 K (orange).

Even though the simulation (with a corresponding v_{cutoff}) agrees with the measured relative signal amplitudes for slow atoms (last delays) in Fig. 3.22(b), for the first ∼10 delays there is a $10 - 20\%$ discrepancy in the relative ampltide as visible in Fig. 3.22(a). This is mainly attributed to the non-linearity of the CEMs as discussed in Section 3.5.3. The discrepancy for first delays (fast atoms) does not significantly influence the determination of v_{cutoff} from the comparison of the simulations with the measurement, since for the last delays (slow atoms) the relative amplitude changes by more than an order of magnitude where a 20% error does not make a big difference.

Fig. 3.22(c) and (d) show the measured background-to-amplitude ratio (BAR) for different temperatures versus the delay number or delay time. In addition to the temperature values from (a) and (b), more data is added here. For most delays, the BAR is approximately equal and decreases by a factor of two from ∼8% at $T_{\mathrm{N}} = 7.9\,\mathrm{K}$ to ∼4% at $T_{\mathrm{N}} = 7.0\,\mathrm{K}$, with no further decrease for lower temperatures. However, the first and last delays are an exception. For very fast atoms, the BAR is larger and increases again at lower temperatures reaching more than 15% at $T_{\mathrm{N}} = 6.4\,\mathrm{K}$. One hypothesis is that these fast atoms originate from atoms which did not thermalize with the nozzle temperature (see also discussion in Sec. 4.5.2.4. of [71]). The slight increase of BAR for slower atoms in the last delays is expected: the velocity of 2S atoms decreases for larger delays, while the speed distribution of the flux of ground state atoms and molecules in the atomic beam as well as background gas particles, which are all responsible for quenching the 2S atoms, stays the same. Therefore, the probability for quenching the 2S atoms increases for larger delays and leads to a larger background.

The speed distribution of the flux also changes over the measurement day, as demonstrated in Fig. 3.23. The relative amplitude is here shown for two times over the course of the measurement day: around 1 h after the nozzle cooldown to $T_{\mathrm{N}} = 7.1\,\mathrm{K}$ (at 11:34, dark blue), and 4 h later without any warm-up in between (at 15:36, light blue). The data is shown for both the top detector (circular markers, solid lines) and bottom detector (triangular markers, dashed-dotted lines), revealing a $10 - 20\%$ discrepancy in the relative amplitude originating from the non-linearity discussed in Section 3.5.3. Fig. 3.23(e) and (f) show the amplitude ratio (relative to delay 2) of the top and bottom detectors, which increases for larger delay times (also observed in Fig. 3.16(b) and Fig. 3.17(e) and (f)). The ratio dependence on the delay differs for the two times, indicating that the non-linearity varies over the measurement day (this is attributed to changing R_{CEM} due to temperature, since the detector voltages V_{in}, V_{flap} and V_{coll} were kept the same, see Section 3.5.3). Despite the non-linearity, which limits the determitation of v_{cutoff} to around $\pm 10\,\mathrm{m/s}$, the observed drop of relative amplitude for slow atoms in Fig. 3.23(b) indicates the increase in the cutoff-velocity over the course of the measurement day, from $v_{\mathrm{cutoff}} \sim 80\,\mathrm{m/s}$ (orange dotted line) to $v_{\mathrm{cutoff}} \sim 110\,\mathrm{m/s}$ (red dotted line) according to simulations. This change in the speed distribution of the flux originates from the continuous nozzle freezing, which rises the nozzle pressure, thereby modifying the

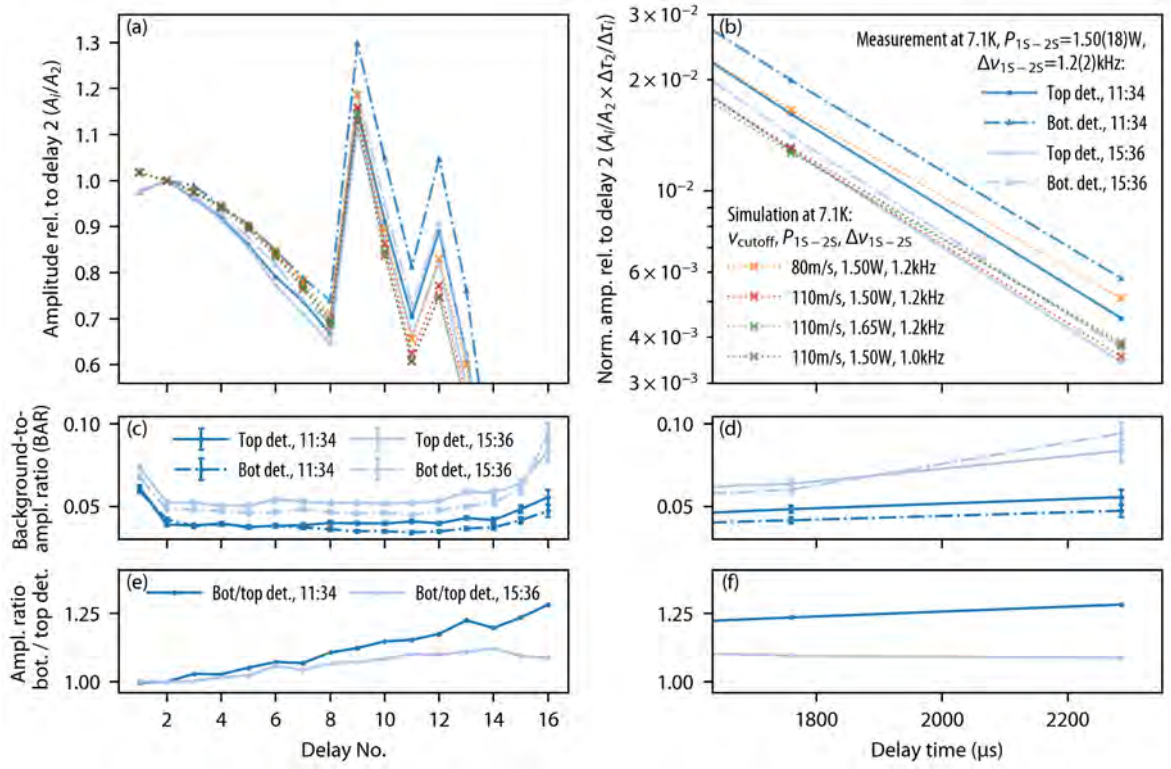

Figure 3.23: Similar to Fig. 3.22, here showing the observed variation of the relative amplitude over the measurement day as well as simulations (crossed markers, dotted lines) for different v_{cutoff} and 1S-2S laser parameters (power P_{1S-2S} and detuning ν_{1S-2S}). The measured data is shown for two times: in dark blue at 11:34 ($\sim$1 h after the nozzle is cooled down to $T_N = 7.1$ K) and in light blue at 15:36 ($\sim$5 h after the nozzle is cooled down, without any warm-up in between). Furthermore, the measurement is compared between the top (solid lines) and bottom detectors (dashed-dotted lines), revealing a $10-20\%$ discrepancy in the relative amplitude due to the non-linearity of the detectors discussed in Section 3.5.3. The bottom plots (e) and (f) compare the amplitude ratio (relative to delay 2) between the bottom and top detectors (as in Fig. 3.17), showing that the non-linearity also varies over the measurement day. The non-linearity limits the determination of v_{cutoff} from the comparison between simulations and measurements to around ± 10 m/s. However, as shown in (b), the drop in the relative amplitude for the last delays over time for each detector indicates an increase in v_{cutoff} over time, here from $v_{\mathrm{cutoff}} \sim 80$ m/s (orange dotted line) to $v_{\mathrm{cutoff}} \sim 110$ m/s (red dotted line). This is attributed to the nozzle freezing over time, which leads to an increased nozzle pressure and thus changes the atomic beam formation dynamics. The green ($P_{1S-2S} = 1.65$ W, $\Delta\nu_{1S-2S} = 1.2$ kHz) and gray ($P_{1S-2S} = 1.5$ W, $\Delta\nu_{1S-2S} = 1.0$ kHz) dotted lines show the sensitivity of simulations to the 1S-2S laser parameters P_{1S-2S} and $\Delta\nu_{1S-2S}$, each varied on the order of the experimental uncertainty of these parameters ($P_{1S-2S} = 1.50(18)$ W, $\Delta\nu_{1S-2S} = 1.2(2)$ kHz). Other experimental parameters are: deuterium flow 0.35 ml/min, $T_N = 7.1$ K, $P_{2S-6P} \simeq 30$ μW, variable aperture width 1.2 mm.

beam formation dynamics. Consequently, also the background-to-amplitude ratio (BAR), which is plotted in Fig. 3.23(c) and (d) increases by $1-2\%$ (for most delays from $\sim$4% to $\sim$5%). A similar behavior was observed in the hydrogen 2S-6P measurement campaign, where v_{cutoff} typically changes by $30-50$ m/s over the freezing cycle (see Fig. 6.1 of [71]).

Apart from the non-linearity, the comparison between the simulated and observed relative amplitudes depends on the input simulation parameters (see Table 3.1). Comparing the

simulated relative amplitudes to the measurement gives some information about v_{cutoff} as discussed above, which however assumes certain values of other parameters. From the other parameters, the 1S-2S laser power P_{1S-2S} and the detuning $\Delta\nu_{1S-2S}$ have the most influence. The power measurement accuracy is limited by calibration which allows to determine P_{1S-2S} only to 12%, while the measurement of ν_{1S-2S} is limited to $\sim$0.2 kHz by the frequency reference. To illustrate the dependency on these two parameters, Fig. 3.23(a) and (b) show two more simulations, where P_{1S-2S} and $\Delta\nu_{1S-2S}$ have been varied on the order of the uncertainty in these parameters, while v_{cutoff} is kept the same: $P_{1S-2S} = 1.65\,\mathrm{W}$ and $\Delta\nu_{1S-2S} = 1.2\,\mathrm{kHz}$ (green dotted line) as well as $P_{1S-2S} = 1.65\,\mathrm{W}$ and $\Delta\nu_{1S-2S} = 1.0\,\mathrm{kHz}$ (gray dotted line). For these input parameter deviations, the relative amplitude varies around 10%, which is on the same order as the non-linearity of the detectors. Therefore, the determination of v_{cutoff} is similarly affected on the order of 10 m/s by the uncertainty in P_{1S-2S} and $\Delta\nu_{1S-2S}$, with the larger influence of the latter.

3.6.3 High performance cryostat

The high sensitivity of the deuterium 2S-6P spectroscopy signal on the temperature requires the best possible temperature stability of the cryostat. Furthermore, the cryostat should have a low level of vibrations in order to not disturb the sensitive active fiber-based retroreflector as well as the 1S-2S enhancement cavity. Therefore, a high performance cryostat[1] by Advanced Research Systems (ARS) was installed in the apparatus in February 2020. Two main points affect the vibration level and temperature stability of the cryostat: first, the stable liquid helium flow while it is transferred from the dewar to the cryostat, and second, the efficient and smooth heat transfer to the cold finger. ARS developed the so-called Helitran® technology which adresses both points with a matrix heat exchanger and a coaxial transfer line [192].

Conventional helium flow cryostats have a reservoir at the cold finger which transfers the heat from the cold finger tip to the refrigerant. The liquid helium boils in the reservoir and the exhaust helium gas temperature is at $\sim$4.2 K independent of the cold finger tip temperature. Only the latent heat of vaporization is then used for cooling, but not the substantial enthalpy ($\sim$1.5 J/kg) of the helium gas. Furthermore, helium bubbles may form an insulating layer between the cup and the liquid helium (Leidenfrost effect), which disturbs the heat transfer and leads to temperature fluctuations. When the sample is heated above the base temperature, the sharp transition between nucleate boiling and film boiling, which is typified by a sharp change in the heat transfer coefficient, influences the temperature stability [193]. For liquid helium, this transition occurs at a temperature difference of $\sim$1 K between the heated surface and the bath [194, 195], which is unfortunately in the desired regime for deuterium spectrocopy with the nozzle temperature $T_{\mathrm{N}} \simeq 7\,\mathrm{K}$. The ARS cryostat replaces the reservoir by a matrix heat exchanger. First, the matrix heat exchanger greatly increases the area, which improves the heat transfer, and prevents larger helium bubbles from forming

[1] Advanced Research Systems ARS LT3-B high performance liquid helium flow cryostat, angstrom level vibrations, high efficiency matrix heat exchanger, coaxial shield flow transfer line, orientation free, <2 K base temperature with exhaust port pumping, 4.2 K base temperature without pumping, temperature stability $<$2 mK (with properly tuned flow), cooling power 1.5 W at 4.2 K, cooldown time 30 min, liquid helium consumption rate 0.75 l/hr at 4.2 K, thermofoil heater for max. 36 W, LakeShore DT-670B-SD inner temperature silicon diode sensor, custom disconnect plug for a second temperature sensor (LakeShore DT-670B-1.4L temperature silicon diode sensor with 4" free length was supplied by ARS, and replaced by DT-670-BO-1.4L (SN D6076038) which has a suitable mount for the nozzle.). The cryostat was customized for our apparatus with a 269 mm length from the flange to the tip, custom cold tip, and a transfer line with 8 ft $\simeq$ 2.4 m flexible section.

due to the restricted volume. Second, the exhaust helium gas passes through the exchanger, which captures the enthalpy of the helium gas for additional cooling. For optimized flow, the exhaust helium gas temperature corresponds to the cold finger temperature, which also reduces the helium consumption.

To transfer the liquid helium from the dewar to the cryostat, conventional cryostats use a superinsulated (e.g. with aluminized mylar) vacuum-jacket transfer line. However, even with a perfect vacuum in the transfer line, the stability of the helium tip flow is limited by the heat transferred through blackbody radiation from the environment to the core part of the transfer line. This results in a boiling of helium, which disturbs the stable flow due to the vapor lock effect: since the liquid helium moves through compressible pressure pockets of gas, the flow is uneven (two-phase flow). The specially designed 'coaxial flow' transfer line of the ARS cryostat addresses this problem by surrounding the core part of the transfer line (where the tip flow is transferred) by helium with a temperature smaller than the boiling temperature of liquid helium at 4.2 K. This is achieved by introducing a coaxial shield flow (separated from the tip flow) with a temperature less than 4.2 K. The temperatue of the shield flow is reduced with the help of an expansion nozzle, where a pressure differential is created by a flow restriction. Thereby, the shield flow helium gas passing through this nozzle is cooled via the Joule-Thompson expansion to below the boiling temperature.

The main parts of the ARS cryostat system are shown in Fig. 3.24. The liquid helium is supplied by a liquid helium dewar[1], see Fig. 3.24(a). The dewar is typically[2] pressurized to $0.2 - 0.6$ bar above the atmospheric pressure to push the liquid helium into the transfer line. This is achieved by a warm helium supply sent into the dewar (white dashed arrow). An analogue pressure sensor on the dewar monitors the overpressure. Typically, the dewar pressure drops by ~ 0.1 bar on a timescale of $30-60$ min, such that the dewar pressure needs to be regularly adjusted. Liquid helium is guided into the transfer line in two separate regions, one for the tip flow (blue arrow) and the other for the shield flow (orange arrow). Fig. 3.24(c) shows the details of the transfer line end on the dewar side, where the tip flow input tube and the smaller shield flow input tube are visible. The filter prevents dirt particles to block these tubes[3]. The dewar side of the transfer line has the exhaust port for the returning shield flow. After the shield flow circulated around the whole transfer line, the returning gas is captured and guided to the flowmeter (dashed orange arrow). Furthermore, the dewar side of the transfer line has a vacuum isolation pumping port, through which the vacuum isolation

[1] Cryo Anlagenbau GmbH, type CS 230 HDS, No. 8400, year 2002, filling volume 230 l, operating overpressure max. 1.2 bar, test overpressure 3.3 bar. With this dewar, around 3.1 l liquid helium per day evaporate into the helium recovery system.

[2] If the cryostat is operated with pumping the helium exhaust tip flow, the dewar also needed to be pressurized to 0.15 bar to achieve the tested lowest possible nozzle temperature of $T_N \simeq 2.9$ K. Pumping is only necessary to achieve nozzle temperatures below 4.4 K with this cryostat.

[3] Even with the filter, the transfer line should always be put at least a few cm above the dewar floor to prevent capturing dirt particles. Our transfer line has a 20 cm extension, which is screwed onto the transfer line end, sealed with an indium wire. The filter is then screwed onto the extension tube (also sealed with an indium wire). The length of the dewar transfer line bayonet with extension is 139 cm, but 8.5 cm need to be substracted for the dewar adapter which is inserted into the dewar to match the diameter of the transfer line (the dewar adapter has also the overpressure control function with two popoff valves, one which opens at 2.5 psi $\simeq$ 0.17 bar but can be closed for cooldown, and another at 5 psi $\simeq$ 0.34 bar, which we modified to ~ 9 psi ~ 0.6 bar to operate the cryostat with higher dewar overpressure). The dewar has a depth of 140 cm, such that with the extension and the dewar adapter, the transfer line sits around 10 cm above the dewar floor (corresponding to ~ 25 l of liquid helium left in the dewar when no more liquid helium can be captured by the transfer line).

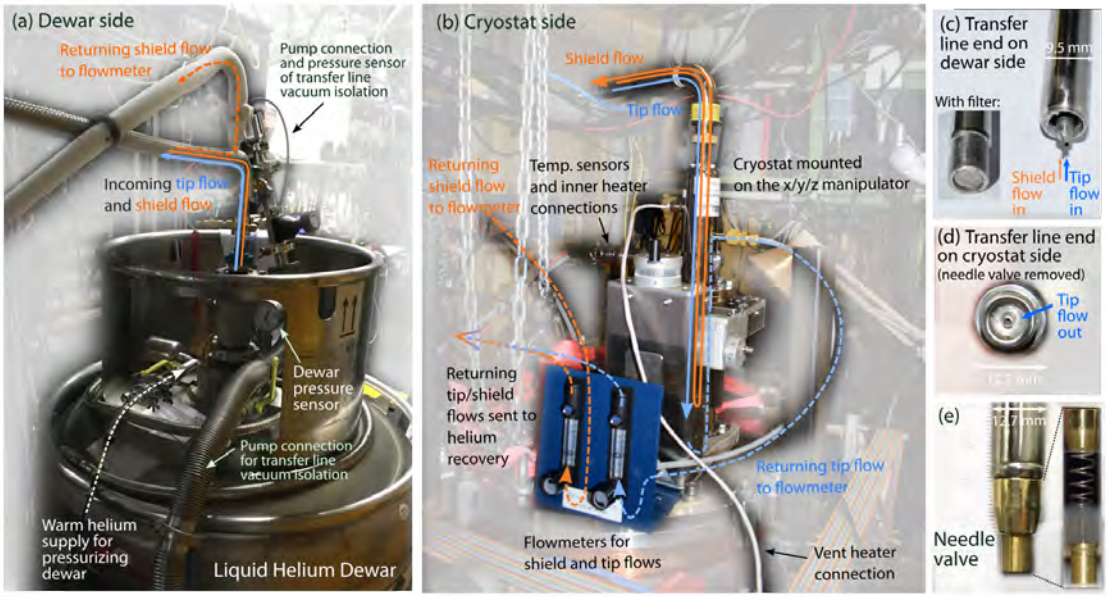

Figure 3.24: Main components of the high performance liquid helium flow cryostat. (a) Dewar side of the cryostat system. The liquid helium is supplied from the helium dewar which is pressurized to 0.2−0.6 bar above the atmospheric pressure using a separate warm helium supply (dashed white arrow). The dewar pressure is monitored with an analogue pressure sensor. The transfer line is inserted into the dewar, where liquid helium is guided into two separate regions, one for the tip flow (blue arrow) and the other for the shield flow (orange arrow). While the tip flow is transferred to the cryostat cold finger, the shield flow coaxially embraces the whole transfer line, and the returning shield flow is output on the dewar side (dashed orange arrow). Furthermore, the vacuum isolation of the transfer line is pumped and the pressure is monitored. (b) Cryostat side of the cryostat system. The cryostat is mounted on the x/y/z manipulator which sits on the vacuum chamber lid. The transfer line brings the tip flow of liquid helium (blue arrow) to the cold finger. Having passed through the matrix heat exchanger, the returning tip flow is guided to the flowmeter panel (dashed blue arrow). The shield flow passes through the whole transfer line (orange arrows). The returning shield flow (captured from the dewar side end of the transfer line) is also guided to the flowmeter. After the flowmeters, both returning flows are connected to guide all the helium exhaust gas to the helium recovery system. Furthermore, the connections for the outer vent heater (white cable) as well as the 10 pin feedthrough connection to the two temperature sensors and the inner heater are labelled. (c) Detail of the transfer line end on the dewar side. When the filter is removed (right picture), the separate input tubes for the shield and tip flows are visible. (d) and (e) show the cryostat side of the transfer line. In (d) the needle valve has been removed and the transfer line end is viewed from the bottom, where the tip flow output is visible. In (e) the needle valve is in place and the transfer line is viewed from the side. The right pictures show the three parts of the needle valve assembly: the retaining cap, the spring, and the needle itself.

pressure below 5×10^{-5} mbar is maintained. The pumping is performed with a small turbo pumping station[1], while a sensor[2] monitors the pressure.

[1]Pfeiffer Vacuum, HiCube 80 Eco/MVP 0.15-4 with a HiPace turbo pump (67 l/s pumping speed) and MVP 015-4 diaphragm pre-pump (0.75 m^3/s pumping speed).

[2]Leybold TTR 101 N.

Fig. 3.24(b) shows the cryostat side of the system. The cryostat is mounted on a manipulator[1], which is attached to the vacuum chamber lid. The transfer line provides the tip flow via the matrix heat exchanger to the cold finger as indicated by the blue arrow. Fig. 3.24(d) and (e) show the details of the transfer line end which supplies the matrix heat exchanger with liquid helium. The view from the bottom in Fig. 3.24(d) shows the ~ 0.5 mm opening for the output of the tip flow. A needle valve can be screwed onto this transfer line end, as shown in Fig. 3.24(e). The needle valve is composed of the needle on a copper mount, the spring and the retaining cap (right pictures). It can be used for flow control in addition to the valve on the tip flowmeter. If the cryostat is operated in the pumping mode (where an additional pump is attached to the tip flow exhaust to pump the tip flow, thereby achieving lower temperatures than 4.2 K), the tip flow can only be controlled with the needle valve since the flowmeter connection is replaced by the pump. However, in our typical operation mode of the cryostat without pumping, the tip flow can be controlled with the flowmeter and the needle valve has been removed to reduce the risk of blocking the tip flow output[2].

After the matrix heat exchanger, the returning flow is guided to the flowmeter panel, see the dashed blue arrow in Fig. 3.24(b). The shield flow is coaxially guided through the whole transfer line (orange arrow). The returning shield flow from the dewar side end of the transfer line is guided to the second flowmeter (dashed orange arrow). Both flowmeters have a valve which enables to control and adjust the shield and tip flows for optimal operation of the cryostat. During the operation of the cryostat, to prevent snow and ice accumulation on the outside, the top part of the cryostat needs to be heated with a vent heater (white labelled cable). Typically, the returning tip flow tube from the cryostat to the flowmeter is also heated[3] to prevent accumulation of snow and ice (not shown in Fig. 3.24(b)).

The temperature of the nozzle is controlled with a temperature controller[4] which reads out the two temperature sensors (inner cryostat sensor and the nozzle sensor) and provides a current source for the inner heater of the cryostat[5]. This device has a built-in PID controller[6] to provide active feedback for a given set temperature of one of the sensors, with the bandwith limited by the 10 Hz controller update rate. The 10 pin feedthrough connection for the inner heater and the two temperature sensors, which connects the cryostat with the temperature controller, is labelled in Fig. 3.24(b).

The intended operation of the cryostat is the following: the dewar overpressure should be kept at 5 psi for the cooldown and then reduced to 2.5 psi when the cryostat is cold. Tip and shield flows should then be adjusted for the desired temperature. The tip flow should be optimized to achieve the desired stable temperature, e.g. higher temperatures require to reduce the tip flow with the help of the needle valve or the flowmeter. The tip flow should be adjusted such that without heating almost the desired temperature is reached. To stabilize

[1] UHV Design TTX63-63-50-H, providing $\pm$15mm motion in the x and z directions and 50mm in the y direction (in the coordinate system of our experiment).

[2] Great care has to be taken when working with the needle valve: since the needle is very thin, it can easily bend if too much pressure is applied on the needle valve, and thereby block the tip flow.

[3] Hemi Heating (distributed by Tectra GmbH), metal braided heating tape, MB015, 200 W. This tape is wrapped around the returning tip flow tube (which has been replaced by stainless tubes in contrast to plastic tubes shown in Fig. 3.24(b)).

[4] CryoCon 32 B.

[5] The inner heater cable is wrapped around the copper cold tip of the cryostat and has a resistance of 36 Ω. The current through this heater should not exceed 1 A, limiting the heating power to 36 W.

[6] Typically, the internal PID parameters are set to (1-10,100,0), i.e. the integrator gain is a factor of 10-100 higher than the proportional gain, and the differential gain is zero (switched off).

the temperature, only a minimal amount of heating power should then be used. The shield flow can also be reduced to the point where the stable tip flow can still be maintained without introducing instabilities. However, a higher shield flow is not disadvantagous (except for the higher helium consumption), since only a minimum amount of shield flow is needed to ensure the stable tip flow transfer.

Unfortunately, our cryostat did not behave as intended for a so far unknown reason. Reducing the tip flow with the flowmeter or the needle valve could not produce stable temperatures above the $\sim 4.5\,\mathrm{K}$ base temperature at the nozzle, but resulted in slow oscillations on a timescale of minutes with an amplitude of few Kelvin. Many different combinations of tip and shield flows as well as the needle valve tip flow adjustment were tested, but the behavior remained the same. It was also checked that the temperature controller does not influence this behavior (e.g. due to non-optimal PID parameter settings). However, with a higher dewar overpressure around $0.3 - 0.6\,\mathrm{bar}$ excellent temperature stability could be reached below $T_\mathrm{N} \sim 5\,\mathrm{K}$, with fluctuations even below 1 mK for $T_\mathrm{N} \sim 4.6 - 4.9\,\mathrm{K}$. Lower dewar pressure decreases the highest possible temperature with this temperature stability. Higher temperatures could still be reached with more heating power, but with increased temperature fluctuations. Many tests were performed with the cryostat and the above behavior could always be reproduced, with the last test in March 2021 before the deuterium 2S-6P measurement campaign in July 2021. It could be that the increased custom length of the cryostat and the longer transfer line affect the behavior of the cryostat. Nevertheless, the cryostat performs with the desired temperature stability below 1 mK around $\sim 4.8\,\mathrm{K}$ which is the required temperature for hydrogen. For deuterium, it was planned to install stainless steel shims[1] between the cold finger of the cryostat and the nozzle to increase the nozzle temperature without increasing the croystat temperature, and thereby ensure the temperature stability below 1 mK for the desired temperature $T_\mathrm{N} \sim 7\,\mathrm{K}$ for the deuterium spectroscopy.

However, when the deuterium 2S-6P measurement campaign started in July 2021, the cryostat behaved very different than before. The cooldown time was longer ($\sim 1.5\,\mathrm{h}$ in July 2021 compared to $\sim 45\,\mathrm{min}$ in March 2021), and the nozzle could not be cooled below $T_\mathrm{N} \sim 6.3\,\mathrm{K}$, even though nothing obvious was intentionally changed in the apparatus compared to March 2021. One possible explanation was the partial blocking of the tip flow in the transfer line, which could originate from dirt in the filter[2]. This was confirmed in August 2022, when the cryostat was tested with the new transfer line filter supplied by the manufacturing company. The cryostat could then again cool down the nozzle down to $T_\mathrm{N} \sim 4.6\,\mathrm{K}$ and behaved as in March 2021. However, in July 2021, the partial blocking of the filter lead to the better temperature stability in the desired temperature range around $T_\mathrm{N} \sim 7\,\mathrm{K}$ for deuterium spectroscopy. This could point to a possible solution for better cryostat temperature stability in the normal operation: it may be advantageous to reduce the tip flow on the dewar side rather than on the cryostat side. However, this requires a substantional modification of the

[1] In 2019 with another cryostat, it was tested than thin stainless steel shims ($50 - 200\,\mu\mathrm{m}$ thickness), placed between the nozzle and the cold finger of the cryostat, could increase the nozzle temperature while maintaining the same cryostat temperature. These stainless steel shims need to be annealed to reduce the magnetisation and prevent magnetic field distortions near the nozzle.

[2] Sometimes, air freezes in the transfer line which blocks the tip and/or shield flows. Then the transfer line needs to be warmed up and flushed with warm helium (which also should be done right before the transfer line is put into the dewar). However, here the behavior was different. Several attempts were made to flush the transfer line with warm helium from both sides, and re-insert the transfer line into the dewar. If the flow is blocked by frozen air in the transfer line, some change in the behavior would be expected after the warm-up, which did not occur. Therefore, most likely some dirt particles blocked the flow in the filter.

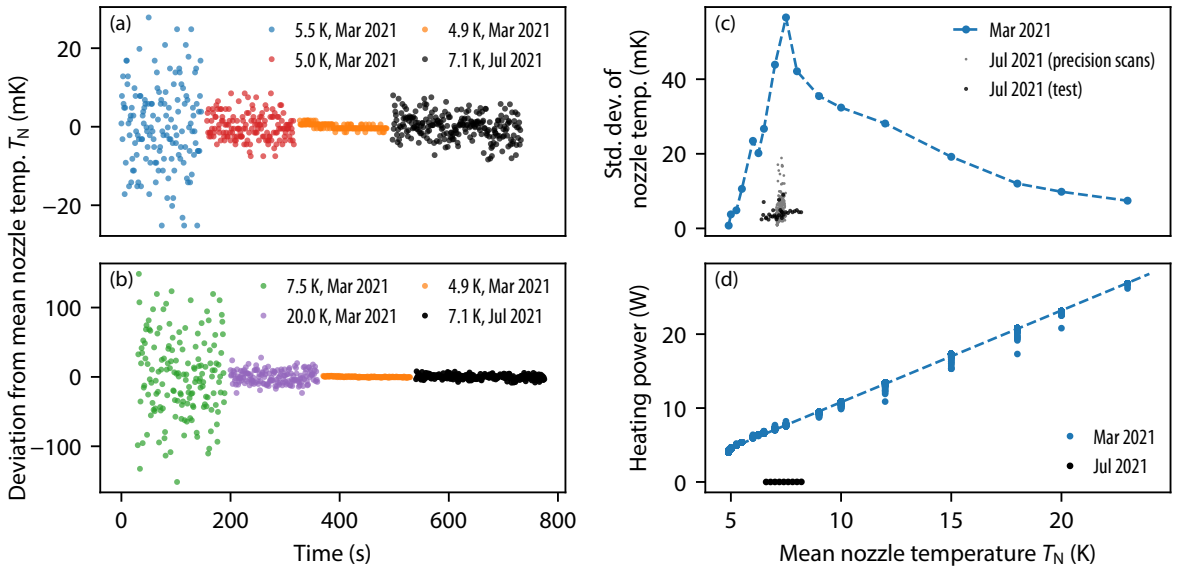

Figure 3.25: Temperature stability of the cryostat depending on the mean nozzle temperature. (a) and (b) show the temperature deviation from the mean nozzle temperature T_N over time for different temperatures. From the installation of the cryostat in February 2020 to the cooldown tests in March 2021 (last test before July 2021), the cryostat showed a temperature stability of below 2 mK for nozzle temperatures below $T_N \leq 4.9\,K$, see orange points in (a) and (b) (same data). The temperature instability increased for higher temperatures, reaching highest fluctuations within ±100 mK (standard deviation ∼50 mK) for $T_N \simeq 7.5\,K$ (green points in (b)). For higher temperatures, the fluctuations decreased again down to ±20 mK (standard deviation ∼10 mK) for $T_N \simeq 20\,K$ (purple points in (b)). During the July 2021 deuterium 2S-6P measurement campaign, the cryostat behaved very differently (most likely due to partial blockade of tip flow in the transfer line), such that nozzle temperatures below $T_N \sim 6.3\,K$ could not be reached. However, this resulted in much better temperature stability of $\pm 6 - 8\,mK$ (standard deviation $3 - 4\,mK$) for the desired temperature $T_N \sim 7\,K$ for the deuterium 2S-6P spectroscopy, see black data in (a) and (b). (c) shows the standard deviation from the mean temperature T_N as a function of T_N for the March 2021 data (blue points) and July 2021 data (black points for test data at different temperatures and gray points for precision line scans data shown below in Fig. 3.26). In (d) the corresponding heating power needed to stabilize for a certain nozzle temperature is shown. In March 2021 no stable temperature could be reached by adjusting the tip and shield flows on the flowmeters, such that higher temperatures could only be achieved with higher heating power, e.g. ∼6 W at ∼7 K. On the contrary, in July 2021 the heating power was around three orders of magnitude lower at only $5 - 10\,mW$.

transfer line. Therefore, steel shims placed between the cryostat cold finger and the nozzle seem to be a better solution.

The temperature stability for different temperatures is shown in Fig. 3.25 and compared between March and July 2021 to show the different cryostat behavior described above. In (a) and (b) the temperature deviation from the mean temperature is plotted over time, where black data points show the temperature in July 2021 for $T_N \simeq 7.1\,K$, having a stability of ±6−8 mK (standard deviation 3−4 mK). On the contrary, in March 2021, the temperature stability of ±100 mK (standard deviation 50 mK) was observed in this temperature range (green data points in (b)). The temperature stability for $T_N \leq 4.9\,K$ was below 2 mK (standard deviation $< 0.5\,mK$), see orange data points. Interestingly, the temperature stability improves for higher temperatures ±20 mK (standard deviation ∼10 mK) for $T_N \simeq 20\,K$ (pur-

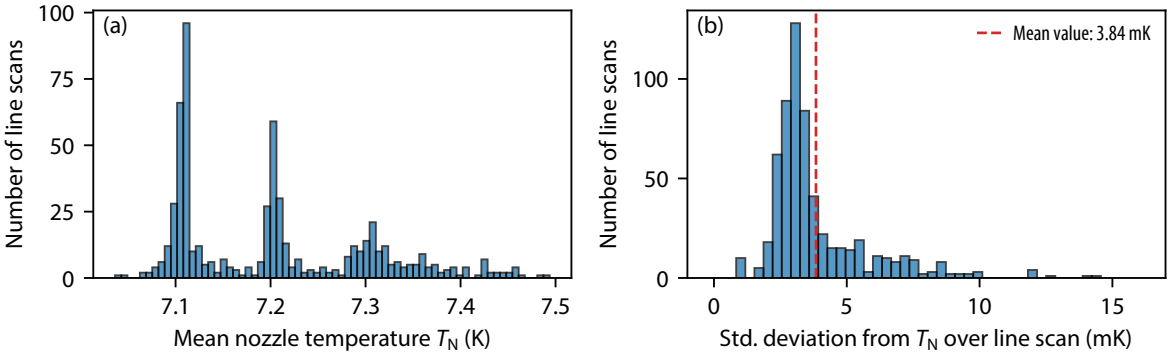

Figure 3.26: Mean nozzle temperature and temperature stability for deuterium 2S-6P precision scans during the July 2021 measurement campaign (in total 603 line scans). The histogram in (a) shows the mean nozzle temperature T_N within minute-long line scans. Most line scans were performed with a nozzle temperature stabilized to $T_N \simeq 7.1\,K$. However, over the course of each measurement day, the lowest possible stable temperature which could be achieved without too much dewar overpressure shifted from $\sim 7.1\,K$ to $\sim 7.4\,K$. Therefore, the set point for the nozzle temperature was varied over this temperature range depending on the cryostat performance. The standard deviation from the mean nozzle temperature within the line scans is shown in (b). The mean value for this standard deviation (vertical red line) for all line scans is 3.8 mK.

ple points in (b)). A possible origin of this behavior is the transition between nucleate and film boiling. The temperature fluctuations are on a timescale $< 1\,s$ and cannot be further resolved due to the limitations of the temperature controller. Most likely, the fluctuations are on an even faster timescale, similar to the instabilities arising from the transition between the nucleate and film boiling, which are on the timescale of tens of milliseconds [196]. Fig. 3.25(c) compares the standard deviation from the mean nozzle temperature T_N as a function of T_N. For the March 2021 data (in blue), the standard deviation reaches its maximum for $T_N \simeq 7.5\,K$, whereas for July 2021 data the fluctuations are reduced to a standard deviation of $3-4\,mK$ (in black: test data at different temepratures, in gray: precision line scans data discuseed below in Fig. 3.26). The heating power at $\sim 7\,K$, see Fig. 3.25(d), is reduced from $\sim 6\,W$ in March 2021 to only $5-10\,mW$ in July 2021.

Fig. 3.26 shows the mean nozzle temperature and the temperature stability for 603 precision line scans in the July 2021 deuterium 2S-6P measurement campaign. Over the course of the measurement day, the lowest possible temperature, which could be reached without too much overpressure in the dewar, increased from $\sim 7.1\,K$ to $\sim 7.4\,K$, such that towards the end of the measurement day the nozzle was stabilized to higher temperatures. This behavior also changed over the course of the whole measurement campaign, such that the time duration where the nozzle could be operated at $\sim 7.1\,K$ decreased with each following day, and the dewar pressure needed to be increased more regularly as well as to higher overpressures up to 0.6 bar. The temperature stability within the minute-long line scans is shown in Fig. 3.26 (b). The mean standard deviation is 3.8 mK, which is approximately a factor of two lower than for the hydrogen 2S-6P measurement campaign with the previous cryostat (see Fig. 4.26 in [71]). Most line scans have a standard deviation of 3.0 mK or even less. In the future, with the help of suitable stainless steel shims placed between the cold finger and the nozzle, it is hoped that a temperature stability $< 1\,mK$ can be reached.

Chapter 4

Improved Active Fiber-Based Retroreflector (AFR)

This chapter presents an improved active fiber-based retroreflector (AFR) providing high-quality wavefront-retracing anti-parallel laser beams in the near UV, specifically for the 410 nm wavelength of the 2S-6P transition in atomic hydrogen and deuterium. The key principle is to accurately collimate the beam from the fiber with a low-aberration collimator and to precisely control as well as to actively stabilize the retroreflection from the high-reflectivity (HR) mirror placed after the collimator using the signal of backcoupled light through the fiber. The AFR is crucial for the first-order Doppler-shift suppression in the precision spectroscopy of one-photon transitions such as the 2S-6P transition. Improving the AFR and rebuilding the setup for the near UV is one of the major contributions of this thesis, summarized in a corresponding publication [110]. Therefore, parts of this chapter are identical to [110]. Some topics were not treated or shortened for [110]. Where this is the case, the corresponding sections are added or expanded compared to [110].

The AFR was initially used for the precision spectroscopy of the 2S-4P transition in atomic hydrogen at a wavelength of 486 nm [197, 198, 14]. It turned out that rebuilding this setup for the 2S-6P transition measurement at a shorter wavelength of 410 nm required much more effort than anticipated, as outlined in Section 4.1, which gives an overview of the improved AFR setup. More specifically, it was found that designing and producing a low-aberration fiber collimator for the near UV is much more challenging than for 486 nm. The first attempt was a three-lens collimator, but weak aberrations produced by this collimator limited the performance of the AFR, though they remained unobserved in the intensity distribution of the collimated beam. The general results on characterizing these aberrations with a caustic measurement are described in Section 4.2 and can be applied to any system where a collimated high-quality laser beam is required. This section also reports on how the collimator design process was extended by wave optics propagation tools, and how a four-lens collimator design was developed for the wavelength range 380–486 nm suitable for all 2S-nP transitions in hydrogen and deuterium with $4 \leq n \leq 10$. The beam quality factor of $M^2 \simeq 1.02$ produced by this four-lens collimator is limited only by the not exactly Gaussian beam profile from the single-mode fiber.

In addition to the careful study of aberrations along with a novel collimator for the near UV, other significant improvements in the AFR are presented. A more accurate adjustment of the distance between the fiber tip and the collimator, which is crucial to optimize the

retroreflection, is made possible by adding a piezo actuator, as detailed in Section 4.3. This piezo actuator also allows to characterize the AFR for optical etalons. Surprisingly, we found that Rayleigh scattering in the fiber leads to an etalon effect as described in Section 4.4. To suppress the intensity variation arising from this effect as well as intenstity fluctuations from other sources, an intensity stabilization of the wavefront-retracing beams in the AFR was implemented, discussed in Section 4.5. Moreover, to deduce the in-situ polarization in the AFR which is especially important for precision spectroscopy of the 2S-6P transition in deuterium, the polarization of the backcoupled light is continuously monitored, see Section 4.6.

4.1 Overview of the improved AFR setup

In the field of atomic, molecular and optical physics, different applications may require a high-quality laser beam, for instance fluorescence microscopy [199], single atom imaging [200], cold atom experiments [201], and quantum information research [202]. Some experiments, for instance in atom interferometry [29, 203, 204] or the precision spectroscopy experiment described in this thesis and others [205, 206], depend upon a retroreflection of high-quality beams to create wavefront-retracing beams (which has also been called phase-retracing beams in previous works [197, 198]). For this purpose, we have constructed an active fiber-based retroreflector (AFR) that employs a beam emerging from a single-mode fiber that is collimated and coupled back into the same fiber with a highly reflective mirror. By maximizing the backcoupled light fraction, a wavefront-retracing standing wave of high quality is obtained whose performance critically depends on minimizing aberrations as has already been demonstrated for the 2S-4P hydrogen measurement [197]. Creating such a beam is especially challenging in the far blue and near UV regions, owing to the increased sensitivity to lens surface imperfections as well as a limited number of suitable glasses and therefore lack of aberration-reduced composite elements such as achromatic doublets [207].

As an alternative approach to the AFR, optical cavities may provide wavefront-retracing beams, acting naturally as a filter of beam imperfections [208, 209]. Our experiment would require a relatively low intra-cavity power of $< 30\,\mu\mathrm{W}$ to keep the power-dependent systematic uncertainty sources (e.g. light force shift) small. This implies a very low impinging power for a high finesse cavity. The small impinging power would yield a noisy error signal for stabilizing the cavity length. Moreover, we need a large beam radius of $W_0 \sim 2\,\mathrm{mm}$, which may require to operate the cavity close to the stability edge or to use special cavity geometries [210, 211]. Therefore, we rather chose to improve our existing AFR setup.

As already outlined in Ch. 3, we use our AFR to suppress the first-order Doppler shift of one-photon transitions in atomic hydrogen and deuterium from the metastable 2S level to nP levels. Recalling Eq. (2.28), the first-order Doppler shift $\Delta\nu_\mathrm{D}$ of a single atom with velocity $\vec{v}$ interacting with a wave described by a local wave vector $\vec{k}$ is given by

$$\Delta\nu_\mathrm{D} = \vec{k}\cdot\vec{v}/2\pi = v\cos(\alpha)/\lambda, \tag{4.1}$$

where λ denotes the wavelength, v the magnitude of the atom's velocity vector, and α its angle with respect to the wave vector. Cooling the atoms and aligning the angle α as close as possible to 90° reduces the Doppler shift. In our setup, for liquid-helium cooled atoms and our accuracy goal of $\lesssim 1\,\mathrm{kHz}$, the angle deviation $\delta\alpha$ from the perpendicular case ($\alpha = 90° + \delta\alpha$) would have to be less than $\delta\alpha < 1\,\mu\mathrm{rad}$. Apart from being mechanically challenging, in our setup such an alignment cannot be achieved due to the much larger laser and atomic beam

divergence angles. Therefore, we further suppress the Doppler shift using two locally counter-propagating waves with wave vectors $+\vec{k}$ and $-\vec{k}$. The two beams need to fulfill this wavefront-retracing condition everywhere along the atomic beam trajectory, and the intensities of both beams have to be equal everywhere. The AFR helps to satisfy both conditions.

The previous setup [197] was successfully used to measure the 2S-4P transition in hydrogen at a wavelength of 486 nm. 2S-nP transitions in hydrogen and deuterium with $n > 4$ bear the potential for an even higher precision and an improved determination of the Rydberg constant and proton/deuteron radius due to their narrower natural linewidth [120]. To this end, we rebuilt our apparatus for the shorter wavelength of 410 nm (2S-6P transition) and have a laser system for 380–390 nm (2S-8P, 2S-9P and 2S-10P transitions) ready to be integrated into the apparatus for future measurements.

The general concept of an active fiber-based retroreflector (AFR) is discussed in detail in a previous publication and thesis by Axel Beyer [197, 198]. The main idea is to collimate a laser beam from a single-mode fiber and to use a highly reflective (HR) mirror to couple the light back through the collimator into the same fiber. Using a beamsplitter before the fiber, the backcoupled light fraction can be monitored and maximized by adjusting the distance between the collimator and the fiber, as well as the tip-tilt alignment of the HR mirror. This tip-tilt alignment is actively stabilized with piezoelectric actuators on the mirror mount[1]. Maximizing the backcoupled light fraction corresponds to optimizing the wavefront-retracing property of the beam: for a perfectly flat, fully reflective HR mirror and an aberration-free beam, the wavefront-retracing and amplitude matching conditions are satisfied if the waist of the collimated beam is located on the mirror, resulting in all of the optical power being coupled back into the fiber.

The optical setup of our hydrogen spectrometer relevant to the AFR is shown in Fig. 4.1. We start with around 100 mW of 410 nm laser light which is sent to the experiment through an 11 m-long polarization-maintaining (PM) fiber. An acousto-optic modulator (AOM) is used to scan the optical frequency across the atomic resonance. An electro-optic modulator (EOM 1), in sequence with a polarizing beamsplitter (PBS) and half-waveplates, is used for intensity control. The light is transferred via another 5 m-long PM fiber to a polarization switching and polarimetry unit (PSPU). The intensity after this fiber is stabilized using the signal of photodetector PD 1 in combination with EOM 1 as an actuator (1^{st} intensity stabilization). Additional photodetectors (PD 2, PD 3 and PD 4) monitor the intensity out-of-loop. In the PSPU, Glan-Thompson polarizers providing PER > 50 dB improve the polarization extinction ratio PER $= P_{\max}/P_{\min}$ of light coupled into the last fiber, where $P_{\max}$ and $P_{\min}$ are the maximal and minimal transmitted optical powers in the two orthogonal polarization directions. Isolators in each arm suppress optical etalons, with a minimal number of optical surfaces being placed after the isolators. The beam path of the unused polarization is blocked by the polarimeter which is used to measure the polarization of the returning light. In order to switch between horizontal and vertical linear polarizations, this polarimeter is manually moved to the other arm of the PSPU. After the PSPU, the light passes through non-polarizing beamsplitters BS 2 and BS 3.

Finally, the laser light (5–30 µW laser power) reaches the in-vacuum AFR setup via the last 80 cm-long polarization-maintaining (PM) fiber[2] (SF), see Fig. 4.2 for an engineering drawing.

[1] Radiant Dyes MDI-H with Piezo Drive. Two Newport 8301-UHV Picomotor actuators have been added for coarse alignment.

[2] Vacuum-compatible Nufern PM-S405-XP fiber in a 900 µm-diameter PEEK jacket, produced and AR-coated by Diamond GmbH.

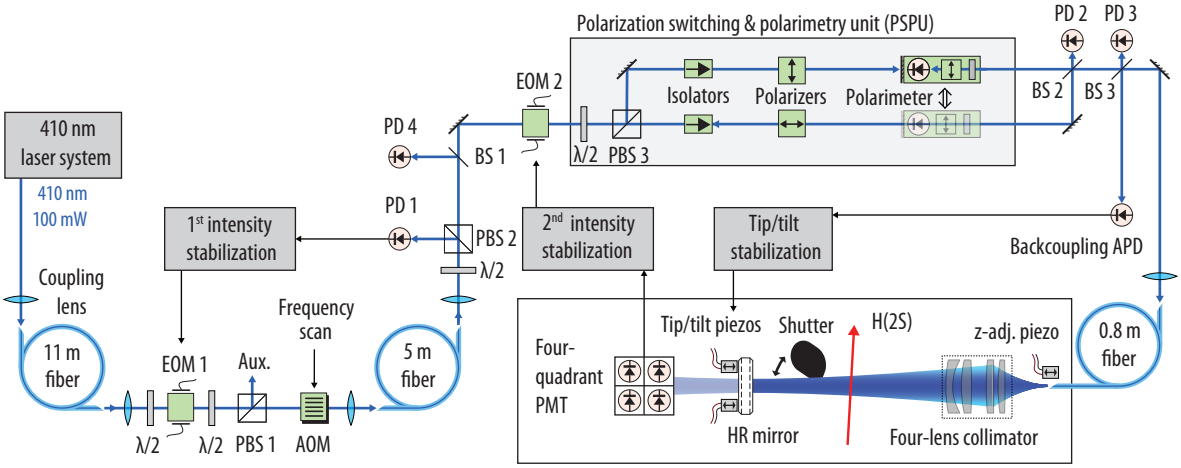

Figure 4.1: Optical setup of the 2S-nP hydrogen apparatus relevant to the AFR. EOM: electro-optic modulator, λ/2: half-waveplate, PBS: polarizing beamsplitter, BS: non-polarizing 50:50 beamsplitter, AOM: acousto-optic modulator, PD: photodetector, APD: avalanche photodiode, H(2S): metastable hydrogen atoms in the 2S level, PMT: photomultiplier tube, z-adj. piezo: adjustment of the fiber-collimator distance, HR mirror: highly reflective mirror. A polarimeter is placed into the unused arm of the PSPU to analyze the polarization of the returning light, whereas the part of the returning light in the used arm of the PSPU is blocked by the isolator.

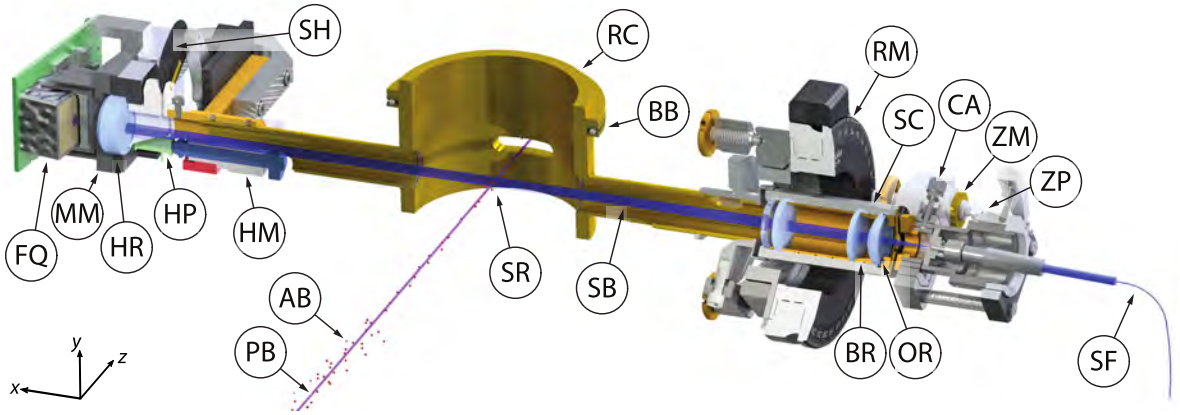

Figure 4.2: 3D engineering drawing of the AFR assembly in vacuum for the 2S-6P hydrogen and deuterium experiment. Note the coordinate system in the lower left corner of the figure for comparison with Fig. 3.1 for a schematic overview of the experiment, Fig. 3.3 for a drawing of the vacuum assembly of the whole experiment as well as Fig. 3.4 for the photograph of the vacuum assembly. (AB) hydrogen atomic beam, (BB) base cylinder ball bearing, (BR) brass ring spacer between collimator lenses, (CA) collimator-fiber alignment, (FQ) four-quadrant photomultiplier, (HM) horizontal (tip) precision motor with (HP) piezo actuator of the (HR) highly reflective (MM) mirror mount, (OR) retainer with O-ring holding collimator lens system in place, (PB) 1S-2S preparation laser beam, (RC) rotatable base cylinder, (RM) collimator rotation mount, (SB) 410 nm spectroscopy laser beam, (SC) four-lens collimator, (SF) polarization-maintaining fiber, (SH) shutter, (SR) hydrogen 2S-6P transition spectroscopy region, (ZM) precision motor and (ZP) piezo actuator for fiber-collimator distance adjustment.

The whole in-vacuum AFR setup is mounted on a rotatable cylinder (RC), which sits on ball bearings (BB) such that the angle between the spectroscopy laser beam (SB) and the metastable atomic hydrogen beam (H(2S), (AB)) collinear to the 1S-2S preparation laser beam (PB) can be aligned close to 90°. The four-lens collimator (SC) is mounted onto a mirror mount combined with a manual precision rotation stage[1] (RM). The collimation is adjusted with the help of a commercial fiber translation mount[2] which we rebuilt for accurate distance control using a precision motor[3] (ZM) combined with a piezo actuator[4] (z-adj. piezo / (ZP)). This part is placed onto a cage system mounted to a flexure adjustment plate[5] (CA) needed for precise centering between the fiber and the collimator, see Section 4.2.4. The light is retro-reflected by the HR mirror[6] (HR) and passes back through the fiber, where approximately one-half of the backcoupled light is detected after BS 3 on the avalanche photodiode (backcoupling APD) whose signal is used for the tip-tilt stabilization using piezo actuators (only the horizontal piezo actuator (HP) is shown in Fig. 4.2). Another fraction of the backcoupled light is split by BS 2, with the light then terminating either in the polarimeter or the isolator. The home-built remotely controlled shutter (SH) makes it possible to block the reflected beam for a measurement of the Doppler shifted spectroscopy signal.

The sum signal of the four-quadrant photomultiplier[7] (PMT) (FQ) after the HR mirror is used for intensity stabilization of the wavefront-retracing beam, with EOM 2 serving as the actuator (2^{nd} intensity stabilization). The PMT is mounted under an angle of $\sim 10°$ (in order to suppress optical etalons) with an interference bandpass filter[8] and scattering disk[9]. The use of a position-sensitive PMT has the practical advantage of misalignment monitoring. An angular misalignment of the HR mirror or the collimator-fiber system by 200 µrad leads to a complete loss of the backcoupled signal [197]. If the optimal orientation of AFR is lost (e.g. during work on the apparatus), the horizontal and vertical position signals of the PMT help to retrieve the alignment.

4.2 Fiber collimator with minimized aberrations in the near UV

In the AFR, the collimator plays a central role since aberrations may be imprinted on the wavefronts of the spectroscopy laser beams. These aberrations distort the wavefronts such that there may be no position in the collimated beam with a plane wavefront, and thus the backward-traveling beam will not retrace the wavefronts of the forward-traveling beam. The backcoupled light fraction is a quantity which characterizes how well the wavefront-retracing property is maintained, because this quantity is directly linked to the overlap integral of the forward- and backward-traveling beams. In our previous setup of the AFR at 486 nm, a collimator design based on two achromatic lens doublets was used to minimize aberrations and

[1] Thorlabs POLARIS-K2S3, PRM2/M.
[2] Thorlabs SM1Z.
[3] Newport 8301-V.
[4] Thorlabs PK4FQP2.
[5] Thorlabs CP1XY.
[6] Custom-order from Layertec, reflectivity $R_{\text{HR}} > 99.995\,\%$, transmission $T \simeq 2 \times 10^{-5}$, substrate with $\lambda/30$ @ 633 nm irregularity and < 1.5 Å RMS roughness.
[7] Hamamatsu R11265-200-M4.
[8] Edmund Optics 34-494, 10 nm-wide passband (FWHM), centered at 413 nm.
[9] Thorlabs DG10-1500-A.

achieve a backcoupled fraction consistent with 100 % within 1 % [197]. Apart from correcting chromatic aberrations, which are irrelevant for our single-wavelength application, achromatic lens doublets have the advantage of reducing spherical aberration compared to a single lens, due to the fact that there are more refractive surfaces.

With shorter wavelengths, designing and manufacturing suitable optics becomes more challenging since fewer glass types are sufficiently transparent. We chose to work with fused silica which has a high UV transmission down to 180 nm. In theory, aberration-free collimation can be achieved with a single aspheric lens of the desired shape. To this end, we tested custom-made aspheres [1] machined with the advanced technique of magnetorheological finishing (MRF) [212, 213, 214]. Unfortunately, imperfections due to mid-spatial frequency errors were still clearly visible on the collimated beam and only around 80 % of backcoupled light fraction could be achieved. Therefore, we chose to only work with spherical lenses which are available with smaller surface roughness.

First, at 410 nm we tested a three-lens collimator based on spherical lenses. A design with minimized aberrations was found by following conventional ray-tracing techniques such as optimizing the point-spread function and minimizing the optical path difference of rays, similar to the previous two-achromats design at 486 nm [197]. However, when testing the assembled custom-made collimator we found that residual spherical aberrations limit the backcoupled fraction to 94.0(1.2) %. Contrary to our previous experience where collimator imperfections were clearly visible as distortions in the collimated beam [197], aberrations of the three-lens collimator were not visible in the intensity profiles of the collimated beam and were revealed only by a caustic measurement, i.e. beam profile measurements at different position within a caustic. For our application, the usual ray tracing design process was extended by wave optics propagation tools. Finally, together with the manufacturing company[2] we arrived at a four-lens design whose optical performance was confirmed with a caustic measurement and showed no aberrations above our detection limit. With this collimator, we achieved a measured backcoupled light fraction of 99.3(1.2) %, consistent with 100 %. In the following the design and characterization processes are described.

4.2.1 Characterization of aberrations: caustic measurement

In the previous setup at 486 nm, imperfections of various collimators were identified by observing distortions in the intensity profiles of the collimated beams [197]. With the three-lens collimator designed for 410 nm, we do not observe any distortions in the collimated beam even after propagation of several meters. However, because of the 6 % missing backcoupled light fraction we know that the forward- and backward-traveling beams are not fully wavefront-retracing. Aberrations may solely be imprinted on the phase of electric field and remain imperceptible in the intensity profile within a certain propagation range. When inspecting only the collimated beam after the collimator even up to arbitrarily large propagation distances, the corresponding aberrations may not appear as intensity distortions because only half of the caustic is accessible. Hence, aberrations present in the phase need to be transformed into distinct intensity distortions by propagation through the full caustic [215]. In principle, one could reveal the same information from wavefront sensors. Though more so-

[1] Thorlabs MRF-polished diffraction-limited, high-precision aspheres AL1225H (stock item) and AL1225H-50URAD-SP (custom order, best possible surface quality with 50 µrad peak-valley slope, optimized for performance between 380-410nm).

[2] B. Halle Nachfl. GmbH, Berlin, Germany.

phisticated wavefront measurement techniques are available [216, 217, 218], the commercial Shack-Hartmann wavefront sensor available to us was not accurate enough for this purpose (specified wavefront measurement accuracy of $\lambda/60$ RMS at 633 nm).

The electric field $E_{\text{coll.}}$ immediately after the collimator (axial coordinate $z = 0$) can be modeled with an incoming field E_0, aberration-free focusing phase $\phi_{\text{foc}}(r)$, and aberrations imprinted by the collimator summarized in the phase term $\phi_{\text{ab}}(r)$, where r denotes the radial coordinate, as

$$E_{\text{coll.}}(z=0,r) = E_0 \exp\big(\mathrm{i}(\phi_{\text{foc}}(r) + \phi_{\text{ab}}(r)\big) = \sum_{p=0}^{\infty} c_p \,\mathrm{LG}_p^0(z=0,r;q_0). \tag{4.2}$$

In the above equation, the aberrated field has been decomposed with complex coefficients c_p in the complete basis of Laguerre-Gaussian modes LG_p^l [169] with radial index p, azimuthal index l and common complex beam parameter $q_0 = -z_0 + iz_R$ with waist position z_0 and Rayleigh length $z_R = \pi w_0^2/\lambda$ where w_0 is the waist radius of the LG_0^0 mode. Here we consider for simplicity fully stigmatic (i.e. axially symmetric) beams such that $l = 0$ due to the cylindrical symmetry of the problem. The z-dependent expression of Laguerre-Gaussian modes LG_p^0 is given (up to a mode-dependent normalization constant) with $q(z) = q_0 + z$ and $w(z) = w_0\sqrt{1 + (z-z_0)^2/z_R^2}$ by

$$\begin{aligned}\mathrm{LG}_p^0(z,r;q) \propto& \frac{1}{w(z)} L_p\left(\frac{2r^2}{w(z)^2}\right) \exp\left(\mathrm{i}kz - \mathrm{i}k\frac{r^2}{2q(z)} + \mathrm{i}\varphi_p(z)\right)\\ =& \frac{1}{w(z)} L_p\left(\frac{2r^2}{w(z)^2}\right) \exp\left(-\frac{r^2}{w(z)^2}\right) \exp\left(\mathrm{i}kz - \mathrm{i}k\frac{r^2}{2R(z)} + \mathrm{i}\varphi_p(z)\right),\end{aligned} \tag{4.3}$$

where L_p are the Laguerre polynomials[1]. The mode-dependent phase φ_p of LG_p^0 modes is discussed below, see Eq. (4.9). In the last step we made use of the relation

$$\frac{1}{q(z)} = \frac{1}{R(z)} - \mathrm{i}\frac{2}{kw(z)^2} \quad \text{with} \quad R(z) = (z-z_0) + \frac{z_R^2}{z-z_0}, \tag{4.4}$$

where $R(z)$ is the mode-independent wavefront curvature radius. Since $w(z)$ can be expressed in terms of the real and imaginary parts of $q(z)$ or simply the imaginary part of $1/q(z)$, all the information about the z- and r-dependence of a given mode LG_p^0 is contained in this (inverse) complex beam parameter, illustrating its prominent role for the common description of the modes. Note that even though q_0 and hence z_R are the same for all modes, the actual waist radius $W_0 = M\, w_0$ of higher-order modes is larger, where M is the factor defined below.

The expansion in Eq. 4.2 can be in principle performed for any q-parameter (any choice of z_0 and z_R or w_0). However, it is advantageous for the discussion here to set the q-parameter such that z_0 and z_R have the following physical meaning: If the radius $W(z)$ of a beam with an arbitrary mode decomposition is defined through second moments of the transverse intensity distribution ('D4σ-method' according to the ISO standard [219]), any beam radius $W(z)$ follows the hyperbolic propagation law [220, 169, 221],

$$W(z) = W_0\sqrt{1 + (z-z_0)^2/z_R^2}, \quad \text{with} \quad z_R = \frac{\pi w_0^2}{\lambda} = \frac{\pi W_0^2}{M^2\lambda}, \tag{4.5}$$

[1]The Laguerre polynomials are defined as $L_p(x) = \sum_{k=0}^{\infty} \binom{p}{k} \frac{(-1)^k}{k!} x^k$.

such that z_0 and z_R (or $w_0 = W_0/M$) correspond to measurable quantities, with the factor M entering the above equation in z_R as M^2 denoted as beam quality factor.

The aberration-free focusing phase and the leading spherical aberration term can be written as

$$\phi_{\text{foc}}(r) = -\frac{k\,r^2}{2\,f}, \quad \phi_{\text{ab}}(r) \simeq S\left(\frac{r^4}{W^4} - 2\frac{r^2}{W^2}\right), \tag{4.6}$$

with f being the focal distance, k the wavenumber, and W the beam radius at the position where the aberration is imprinted. The focusing effect of the r^4-term in $\phi_{\text{ab}}(r)$ is compensated by the r^2-term to isolate the contribution of the aberration. Hence the parameter S characterizes the strength of spherical aberration. For a thin spherical lens, a following expression can be derived [222]:

$$S_{\text{thin lens}} = \frac{2\pi W^4}{\lambda\,f^3} \times \frac{n^3 + (3n+2)(n-1)^2p^2 + (n+2)q^2 + 4(n^2-1)p\,q}{32\,n\,(n-1)^2}, \tag{4.7}$$

where n is the refractive index of the lens, q is the shape factor of the lens ($q = 0$ for the curved-curved spherical lens, and $q = \pm 1$ for the plano-curved or curved-plano spherical lenses), and p is the dimensionless measure of the input and output radii of curvature of the beam relative to the lens focal length, see [222] for details. If in our case ($\lambda \simeq 410\,\text{nm}$, $f \simeq 30\,\text{mm}$, $W \simeq 2.2\,\text{mm}$, $n \simeq 1.5$) we used a single thin plano-convex collimating lens oriented the right way (flat surface facing the fiber, $p = \pm 1$ and $q = \mp 1$), spherical aberrations would be as large as $S \simeq 4$ following the analytical expression of the above equation. A plano-convex collimating lens oriented the wrong way (curved surface facing the fiber, $p = q = \pm 1$) would result in $S \simeq 16$, whereas a curved-curved lens would result in $S \simeq 6$.

For an impinging beam with beam quality factor M_0^2 passing through optics with spherical aberrations of strength S as defined in Eq. 4.6, the beam quality factor is modified by an additional contribution $M_S^2 \simeq \sqrt{2}S$ as [222]

$$M^2 = \sqrt{\left(M_0^2\right)^2 + \left(M_S^2\right)^2}. \tag{4.8}$$

In order to understand how aberrations affect the intensity profile of the propagated beam, consider the mode-dependent phase φ_p of LG_p^0 modes, which corresponds to the accumulated phase on the beam axis relative to the plane wave,

$$\varphi_p(z) = (2p+1)\,\psi(z), \quad \psi(z) = \arctan\left((z - z_0)/z_R\right), \tag{4.9}$$

where ψ is the Gouy phase. Because φ_p is the only mode-dependent phase term, the Gouy phase plays an essential role in the description of beam propagation [223, 224]. The electric field after the collimator at a certain distance z can either be expressed by the diffraction integral or equivalently, once written in form of the mode expansion from Eq. 4.2, directly calculated from propagation-independent coefficients c_p with $q = z + q_0$ as

$$E_{\text{coll.}}(z, r) = \sum_{p=0}^{\infty} c_p\,\text{LG}_p^0(z, r; q). \tag{4.10}$$

Aberrations imprinted in the phase remain unobservable in the intensity unless propagation changes the phase relationship between different contributing modes according to Eq. 4.9. Since the Gouy phase ψ is the only position-dependent parameter which affects the phase

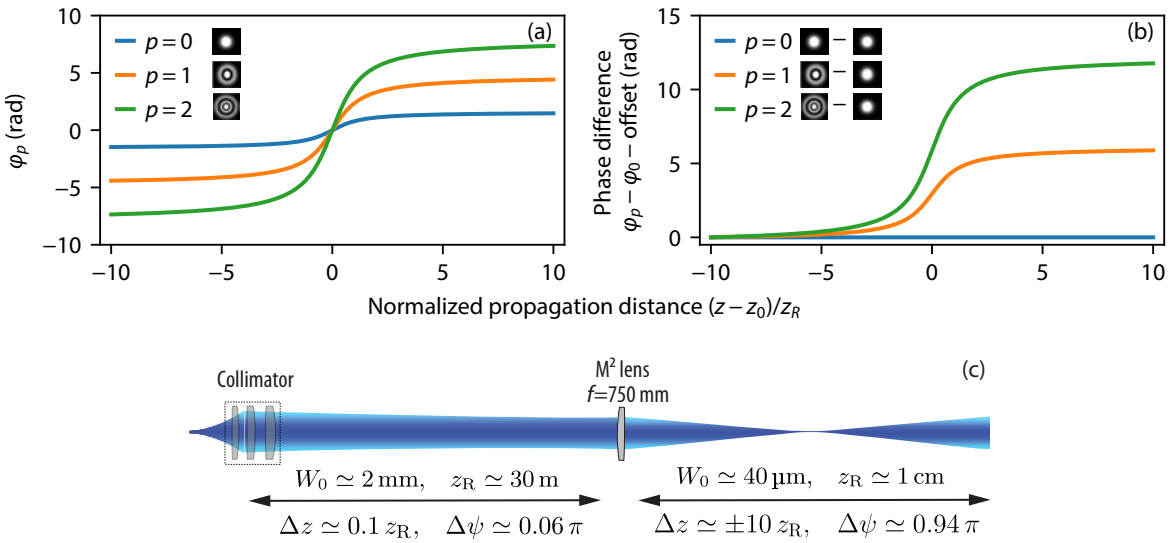

Figure 4.3: (a) Mode-dependent phase φ_p according to Eq. 4.9 for the first three LG_p^0 modes with $p = 0, 1, 2$ over the normalized propagation distance $(z - z_0)/z_R$. (b) The phase difference between the modes is given by the Gouy phase, $\varphi_p - \varphi_0 = 2p\,\psi$, and determines how aberrations present in the phase transform into intensity. The constant phase offset between the modes has been subtracted such that at the point where aberrations are imprinted ($\simeq -10\,z_R$ from the waist position) the difference is zero. Propagation must cover a substantial fraction of the complete range of the Gouy phase, $\Delta\psi \approx \pi$, to obtain the full information about aberrations from the evaluation of intensity profiles. (c) Gouy phase change when inspecting the collimator for aberrations: in the collimated beam only a small fraction of Gouy phase change is covered, i.e. $\Delta\psi \ll \pi$, due to the large Rayleigh length of $z_R \simeq 30\,\mathrm{m}$. With a focusing lens ("M^2 lens") the beam is transformed such that a propagation of $\pm 10 z_R$ around the waist position becomes possible, $\Delta\psi \approx \pi$, and the manifestation of aberrations is observed in the intensity profiles of a caustic measurement.

change between the LG_p^0 modes, we can use ψ or $\tan\psi$ (see Eq. 4.9) as a parameter to determine where aberrations present in the phase transform to intensity distortions [223]. Fig. 4.3 (a) shows the mode-dependent phase φ_p for the first three modes and Fig. 4.3 (b) the phase difference relative to the fundamental Gaussian (LG_0^0) mode, which is proportional to the Gouy phase ψ. From Eq. (4.9) it is clear that the dimensionless distance $(z - z_0)/z_R = \tan\psi$ governs the propagation. The Gouy phase changes mostly within a few Rayleigh lengths around the waist position (focus) z_0. Within $\pm 10\,z_R$, almost the full range of phase change ($\Delta\psi \simeq 0.94\,\pi$) between different modes is covered.

In our case the collimated beam has a waist radius of $W_0 \simeq 2.2\,\mathrm{mm}$ corresponding to $z_R \simeq 37\,\mathrm{m}$ with a waist position $z_0 \simeq 29\,\mathrm{cm} \ll z_R$ lying at the HR mirror. Therefore, even if it was possible to observe propagated beam profiles up to an arbitrary large distance after the collimator, only half of the possible phase change would be covered, $\Delta\psi \approx \pi/2$. With practically accessible propagation distances of up to few meters, i.e. $\Delta z \simeq 0.1\,z_R$, only a small range of Gouy phase change is covered, $\Delta\psi \simeq 0.06\,\pi$. It can be computed that spherical aberrations with $S \simeq -0.3$ appear as clear distortions in intensity, e.g. visible as a dip in the center of the intensity profile, after a propagation corresponding to a change in Gouy phase by $\Delta\psi \approx 0.85\,\pi$ [225]. In order to observe these aberrations it is necessary to transform the beam with a dedicated lens ("M^2 lens") such that the full range of propagated beam profiles

becomes accessible. This procedure corresponds to the commonly used M^2 measurement setup. By observing intensity profiles around the focus, all information about the beam mode decomposition can be extracted since the complete range of the Gouy phase propagation of $\Delta\psi \approx \pi$ is covered. The focal distance f of the M^2-lens has to be large enough for the used beam camera to resolve beam profiles around the focus created by the M^2-lens, and to avoid imprinting additional aberrations on the beam proportional to $S \propto k\,W^4/f^3$ as evident from Eq. 4.7 [222, 226]. Fig. 4.3(c) illustrates the situation in our case: for an M^2-lens of $f = 750\,\mathrm{mm}$ ($S \sim 10^{-4}$ for a plano-convex lens) propagation of $\Delta z \simeq \pm 10\, z_R$ is achieved such that $\Delta\psi \simeq 0.94\,\pi$.

4.2.2 Influence of the single-mode fiber profile

When discussing possible mode contributions from aberrations the question arises of how the fiber mode may affect imperfections in the AFR. We use a polarization-maintaining step-index single-mode fiber[1] where the polarization-maintaining property is achieved through stress-induced birefringence. The stress-inducing rods used for this purpose make the mode slightly elliptical, for our fiber resulting in the ellipticity[2] of $\varepsilon \simeq 1.02(1)$. Since in our configuration the retroreflection preserves ellipticity, we assume for simplicity fully circular symmetric fiber modes.

For an ideal circularly symmetric weakly-guiding step-index fiber, three parameters determine the linear polarization modes: wavelength λ, core radius a and numerical aperture $\mathrm{NA} = \sqrt{n_{\mathrm{clad}}^2 - n_{\mathrm{core}}^2}$ with refractive indices of the cladding, n_{clad}, and the core, n_{core} [227]. The electric field is readily calculated from the paraxial wave equation, and the V-number $V = \mathrm{NA} \times 2\,\pi\, a/\lambda$ determines the number of possible solutions. For $V < 2.405$ only a single solution exists such that the fiber is said to be single-mode. The electric field of this mode is piecewise given by two Bessel functions [227, 228], the Bessel function of the first kind of order 0 and 1, J_0 and J_1, respectively, and the modified Bessel function of the second kind of order 0 and 1, K_0 and K_1, respectively:

$$|\vec{E}_{\mathrm{fiber}}(r)| \propto \begin{cases} J_0(k_T\, r) & \text{for} \quad r \le a \quad (\text{core with } n_{\mathrm{core}}) \\ K_0(\gamma\, r) & \text{for} \quad r \ge a \quad (\text{cladding with } n_{\mathrm{clad}}), \end{cases} \tag{4.11}$$

where the two constants k_T and γ are given through the equation obtained from the boundary condition at $r = a$:

$$X \frac{J_1(X)}{J_0(X)} = Y \frac{K_1(Y)}{K_0(Y)}, \tag{4.12}$$

where $X = a\,k_T$, $Y = \sqrt{V^2 - X^2} = a\,\gamma$. The electric field inside the fiber from Eq. 4.11 can be approximated by a Gaussian. However, in the expansion of this fiber mode also higher-order Laguerre-Gaussian modes contribute.

Figs. 4.4(a) and (b) show the calculated and measured intensity profiles from our fiber after a propagation distance of around $z \simeq 30\,\mathrm{mm}$ (corresponding to the beam profile at the collimator with $W \simeq 2\,\mathrm{mm}$) on linear and logarithmic scales, along with a Gaussian fit to the data. The calculated intensity profile (orange curve) is obtained using Eq. 4.11 along with

[1] Nufern PM-S405-XP.

[2] We define the ellipticity $\varepsilon \ge 1$ to be the ratio between the major and minor beam widths, i.e. $\varepsilon = 1$ corresponds to the fully circularly symmetric case (no ellipticity).

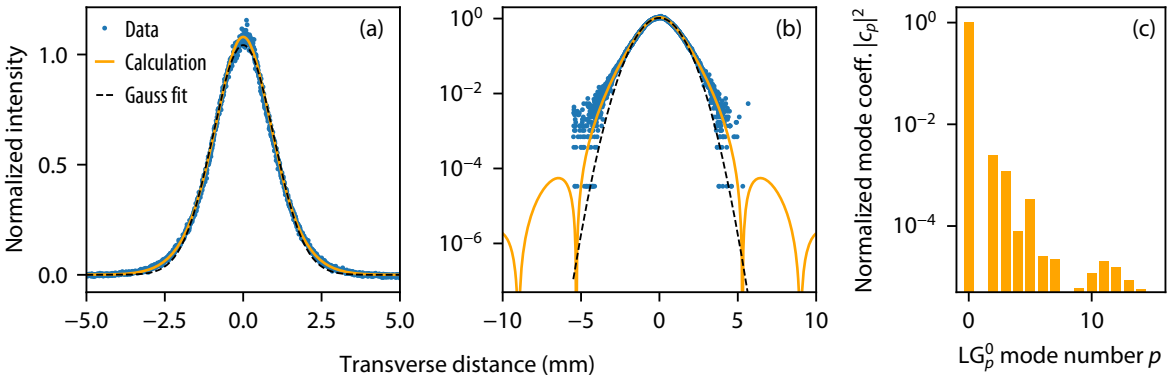

Figure 4.4: Measured and calculated intensity profiles from the single-mode fiber used in the AFR at a propagation distance of 30 mm ($\simeq 1000\, z_R$) after the fiber tip, corresponding to the position of the collimator. Data (blue points) is depicted together with a calculation using the specified core radius and measured NA (orange line) and a Gaussian fit (black dashed line) on a linear and logarithmic scale in (a) and (b), respectively. The right plot (c) shows squared normalized mode coefficients $|c_p|^2$ of the calculated fiber mode corresponding to the overlap with LG_p^0 modes with a q-parameter that cancels $|c_1|^2$. The overlap with the Gaussian is $|c_0|^2 \simeq 0.9958$.

the diffraction integral [169]:

$$|\vec{E}_{\mathrm{diffr.}}(r)| = \frac{2\pi \mathrm{i}}{\lambda\, z}\, \exp\left(-\mathrm{i}k\frac{r^2}{2z}\right) \int_0^\infty \mathrm{d}\rho\, |\vec{E}_{\mathrm{fiber}}(\rho)|\ \ \rho\, J_0(k\rho r/z)\, \exp\left(-\mathrm{i}k\frac{\rho^2}{2z}\right). \tag{4.13}$$

Equivalently, one can decompose $|\vec{E}_{\mathrm{fiber}}|$ into the Laguere-Gaussian mode coefficients c_p and propagate the beam using an analogous expression as in Eq. 4.10. For the calculation of the fiber mode from Eq. 4.11 with $\lambda = 410\,\mathrm{nm}$, the specified core radius of $a = 1.5\,\mu\mathrm{m}$ was used along with a measured NA of the fiber[1].

On the logarithmic scale in Fig. 4.4(b) one can see that the fiber mode has larger intensity on the wings of the beam as compared to the Gaussian. Diffraction rings are expected from the calculation for radial distances $r > 2.5\,W$ and with a relative intensity below 10^{-4}, which is not resolved by the data and outside the detector area. Nevertheless, the question arises whether these rings may be relevant for the wavefront-retracing condition in the AFR. In Fig. 4.4(c) the calculated mode composition for our fiber with $a = 1.5\,\mu\mathrm{m}$, NA $= 0.10$ and $\lambda = 410\,\mathrm{nm}$ is shown. The q-parameter for expansion was chosen such that the contribution of LG_1^0 mode vanishes and the overlap of the LG_0^0 mode is maximized resulting in 99.58 % overlap.

Once a circular symmetric beam (such that $l = 0$ for the Laguerre-Gaussian modes) is expanded in terms of normalized mode coefficients c_p, one can calculate its M^2 value with

[1]Note that $\mathrm{NA} = \sqrt{n_{\mathrm{clad}}^2 - n_{\mathrm{core}}^2}$ does not exactly correspond to the numerical aperture of the Gaussian beam $\mathrm{NA_G} = n \sin\theta$ by which the emerging beam from the fiber is best approximated (where $n \simeq 1$ is the refractive index of the medium and $\theta = \lambda/(\pi\, n\, w_0)$ is the divergence angle with wavelength λ and waist radius w_0, where we assumed the beam quality factor $M^2 = 1$). Here, for the measurement of the NA parameter of the fiber at $\lambda = 410\,\mathrm{nm}$, the theoretical diffracted fiber profiles were evaluated for different NA values (and a specified fiber core $a = 1.5\,\mu\mathrm{m}$) at various distances after the fiber and compared to the corresponding measured profiles. From this comparison, the measured NA $\simeq 0.100(2)$ value of the fiber is obtained, whereas the emerging beam from the fiber is best approximated by the Gaussian beam with $w_0 \simeq 1.89(2)\,\mu\mathrm{m}$ yielding $\mathrm{NA_G} \simeq 0.068(1)$.

the following expression [215]

$$M^2 = \sum_{p=0}^{\infty} (2p+1)|c_p|^2. \tag{4.14}$$

The above equation with the coefficients from Fig. 4.4(c) leads to a theoretical fiber-mode beam quality factor of $M^2_{0,F_s=\infty} \simeq 1.024$. However, note that for this number we integrated the beam to infinity which does not correspond to the experimental situation. Using a self-convergent-width factor of $F_s = 3$ as later used in the measurement, i.e. integration area within $\pm 3\,W$ for second-moments determination as is usually recommended [219, 229], the contribution of higher-order modes leads to the fiber-mode beam quality of $M^2_{0,F_s=3} \simeq 1.017$.

Since the wavefront of the beam at the fiber tip is plane, all the coefficients c_p in the mode expansion are real. Propagation to the collimator corresponds almost to the far-field ($\simeq 1000\,z_R$) with a Gouy phase change of $\Delta\psi \simeq \pi/2$. The phase shift of the LG^0_p modes relative to the LG^0_0 is then $\Delta\varphi \simeq p\pi$ which leads to a sign flip of all uneven mode coefficients. After the backpropagation the phase differences are a multiple of almost 2π with a common propagation phase for all modes. Therefore, the wavefront-retracing property of the AFR is mostly not affected by contributions of higher-order LG^0_p modes from the fiber mode. The small residual effect from the fact that the propagation from the fiber tip to the collimator does not exactly correspond to the far-field is shown later in Fig. 4.6. Apart from this effect, due to the higher intensity at the wings of the beam, the fiber mode is more sensitive to possible aberrations from the collimator as compared to the Gaussian beam.

4.2.3 Collimator design process

For our previous collimator at 486 nm, each of the commercial achromatic doublets exhibited little spherical aberrations by itself, and the combination of two doublets found by ray tracing turned out to satisfy the requirements of the AFR without further investigation. For shorter wavelengths, we found that the three-lens collimator designed by ray tracing optics alone showed residual aberrations revealed through the caustic measurement (see Fig. 4.11 introduced below). Therefore, the design process was extended by wave optic propagation tools of the optics design software[1]. Ray tracing allows minimization of wavefront aberrations within a given aperture width, with the Gaussian beam profile not easily accounted for. For a given number of lenses a compromise has to be made between the width of the aperture employed for minimizing the wavefront deviations and the magnitude of acceptable deviations from the aberration-free wavefront. In the case of spherical aberrations, recalling Eq. 4.6, deviations from the aberration-free wavefront increase as $\propto r^4$ such that for larger radial distances r it becomes progressively more difficult to meet this compromise, especially at shorter wavelength. Because the wings of a laser beam extend to large r, it is a priori unclear which ray tracing criteria should be used.

Therefore, we followed an iterative design procedure together with the manufacturing company[2]. Ray tracing was used as a guidance based on the manufacturability of lenses and the requirement of effective focal length of $f \simeq 30$ mm. Using wave optics propagation, the designs found in this way were evaluated with simulated intensity profiles in the caustic measurement simulation. Furthermore, the electric field phase and amplitude were extracted for simulations of residual Doppler shift with optical Bloch equations. Another important

[1] Zemax OpticStudio 15.5, Professional Edition with Physical Optics Propagation (POP) option.
[2] Bernhard Halle Nachfl. GmbH, Germany.

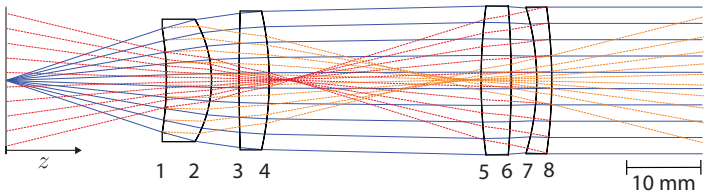

Figure 4.5: Four-lens collimator design with blue solid rays illustrating the collimated beam from the fiber and numbered lens surfaces from table below. Dashed rays exemplary show reflections from the last surface (8) back into the fiber (red) and from the first surface (1) back to the HR mirror (orange). The shown lens radii correspond to the open lens apertures.

Table 4.1: Lens surface data of the fused silica four-lens collimator design, along with the first-order reflection analysis. For each of the surfaces the distance z from the fiber tip, the distance d to the previous surface, and the curvature radius R are listed. The next two columns give the spatial overlap values of first-order reflection beams with the fiber mode ($z = 0$), η_{fiber}, and with the collimated beam η_{coll}. The last column lists the beam radius W_{refl} of reflections towards the HR mirror at the spectroscopy region.

Lens surface	z (mm)	d (mm)	R (mm)	η_{fiber}	η_{coll}	W_{refl} (mm)
1	21.32	–	43.89	4.0×10^{-6}	8.2×10^{-6}	21
2	27.32	6.00	16.11	0.6×10^{-6}	1.0×10^{-6}	66
3	30.99	3.67	−300.00	3.5×10^{-6}	4.1×10^{-6}	30
4	34.99	4.00	42.14	2.8×10^{-6}	3.2×10^{-6}	37
5	63.16	28.17	−75.91	2.7×10^{-6}	3.7×10^{-6}	29
6	67.16	4.00	126.05	3.2×10^{-6}	4.5×10^{-6}	30
7	70.55	3.39	33.64	0.8×10^{-6}	0.8×10^{-6}	67
8	72.55	2.00	70.10	6.4×10^{-6}	5.2×10^{-6}	28

design criterion explained below is the consideration of residual reflections from lens surfaces back to the fiber and to the spectroscopy region. After several iterations we found that three lenses are not enough to meet our requirements and a four-lens design was needed. In order to be able to use the same collimator for spectroscopy of all 2S-nP transitions with $n \geq 4$, the collimator was designed for wavelengths from 380 nm to 486 nm. The final collimator design with an effective focal length of $f = 31.02$ mm is shown in Fig. 4.5, and Table 4.1 lists the surface data, along with the first-order reflection analysis (see next section).

4.2.3.1 Residual reflections from lens surfaces

Even though all the collimator lenses are AR-coated for the desired wavelength[1], residual reflections can lead to performance loss of the AFR. Here, we only consider single reflections from lens surfaces, since multiple reflections are strongly suppressed through the AR coatings. Then, two types of reflections need to be considered. First, reflections of the forward-traveling wave on lens surfaces back towards the fiber. The part of these reflections that is coupled back into the fiber can disturb the tip-tilt stabilization. To reduce the influence of these reflections, efficient coupling into the fiber needs to be avoided. This can be evaluated by calculating the spatial overlap integral

$$\eta_{\text{fiber}} = \frac{\left|\int E_1^* E_2 \mathrm{d}A\right|^2}{\int |E_1|^2 \mathrm{d}A \int |E_2|^2 \mathrm{d}A}, \tag{4.15}$$

[1]Coating provided by Layertec, reflectivity $R_{\text{AR}} < 0.15\%$ for 0–10° angle of incidence.

where E_1 and E_2 are the electric fields of the reflected beam and the fiber mode.

The second type of reflections are reflections of the backward-traveling beam back toward the atomic spectroscopy region and the HR mirror. These reflections can influence the spectroscopy in two ways. Just like the reflection toward the fiber, an optical etalon is formed with the collimated beam, with the spatial overlap integral given by η_{coll} analogous to Eq. 4.15. This etalon with reflectivities $R_{\mathrm{HR}} \sim 100\,\%$ and $\sim R_{\mathrm{AR}} \times \eta_{\mathrm{coll}}$ will lead to intensity variations in the spectroscopy region that depend on length and the laser frequency, which can give rise to systematic line shifts. However, since the laser intensity is stabilized to the signal of the PMT behind the HR mirror, these intensity modulations are suppressed and will instead influence the backcoupled light, possibly disturbing the tip-tilt stabilization. The reflections can also give rise to a residual Doppler effect. The more the reflections are focused near the spectroscopy region, either before or after the reflection of the HR mirror, the greater the intensity imbalance between the beams as seen by the atoms. To minimize the influence of these reflections, the design was chosen such that all reflections are diverging with a beam radius $W_{\mathrm{refl}} \gg W_0$ at the first pass through the spectroscopy region.

The last three columns in Table 4.1 give the values of the spatial overlaps η_{fiber} and η_{coll} as well as the beam radius W_{refl} of the second type of reflections at the spectroscopy region for all surfaces of the collimator design. All values are smaller than $\eta < 10^{-5}$ such that with an additional suppression from the AR coating the overlaps are $< 10^{-8}$. An example of a reflection back to the fiber from the last collimator surface is illustrated with red dashed rays in Fig. 4.5. Orange dashed rays illustrate the reflection back to the HR mirror and the spectroscopy region (located at $z_{\mathrm{HR}} \simeq 36\,\mathrm{cm}$ and $z_{\mathrm{atom}} \simeq 20\,\mathrm{cm}$) from the first surface, demonstrating that not only surfaces with negative curvature radii may focus the reflected beam towards the atoms. In total, three surfaces focus the second type of reflections: surfaces 1 and 3 with foci around 1 cm before the collimator end surface, and surface 5 with focus at 2 cm after the collimator but still well before the spectroscopy region. Additionally, the highly suppressed 28 combinations of reflections on two lens surfaces of the forward-traveling beam lead to 26 strongly diverging and two nearly-collimated reflected beams at the spectroscopy region.

4.2.3.2 Doppler shift simulations with optical Bloch equations

The collimator designs were evaluated using the wave optics propagation tool of our optics design software with the fiber mode or a Gaussian beam profile as an input beam. We extracted the electric field amplitude and phase after the collimator to perform simulations of the residual Doppler shift in the AFR. For this purpose, optical Bloch equations were numerically solved for our configuration of the experiment, using the atomic system for the 2S-6P transitions in hydrogen with 10 µW of laser power. We simulated individual trajectories of atoms moving through the center of the laser beam at different angles $\alpha = 90° + \delta\alpha$, and determine the Doppler shift $\Delta\nu_{\mathrm{D}}$ by fitting a Voigt function to the resulting fluorescence line shape. The atomic velocity is set to $v = 200\,\mathrm{m/s}$ which, according to Eq. (4.1), would result in an unsuppressed collinear ($\alpha = 0°$) Doppler shift of $\Delta\nu_{\mathrm{D}} = 490\,\mathrm{MHz}$ and $\Delta\nu_{\mathrm{D}} = 2\,\mathrm{MHz}$ for $\delta\alpha = 4\,\mathrm{mrad}$. In the simulations, we evaluate the Doppler shift as a function of the fiber-collimator displacement δd_{fc} defined such that zero δd_{fc} corresponds to the collimation with maximized backcoupled light fraction. Because in the experimental situation the collimation is adjusted such that the backcoupled light fraction is maximized, the Doppler shift at zero δd_{fc} is an important figure of merit for the AFR. No tip-tilt misalignment of the reflected

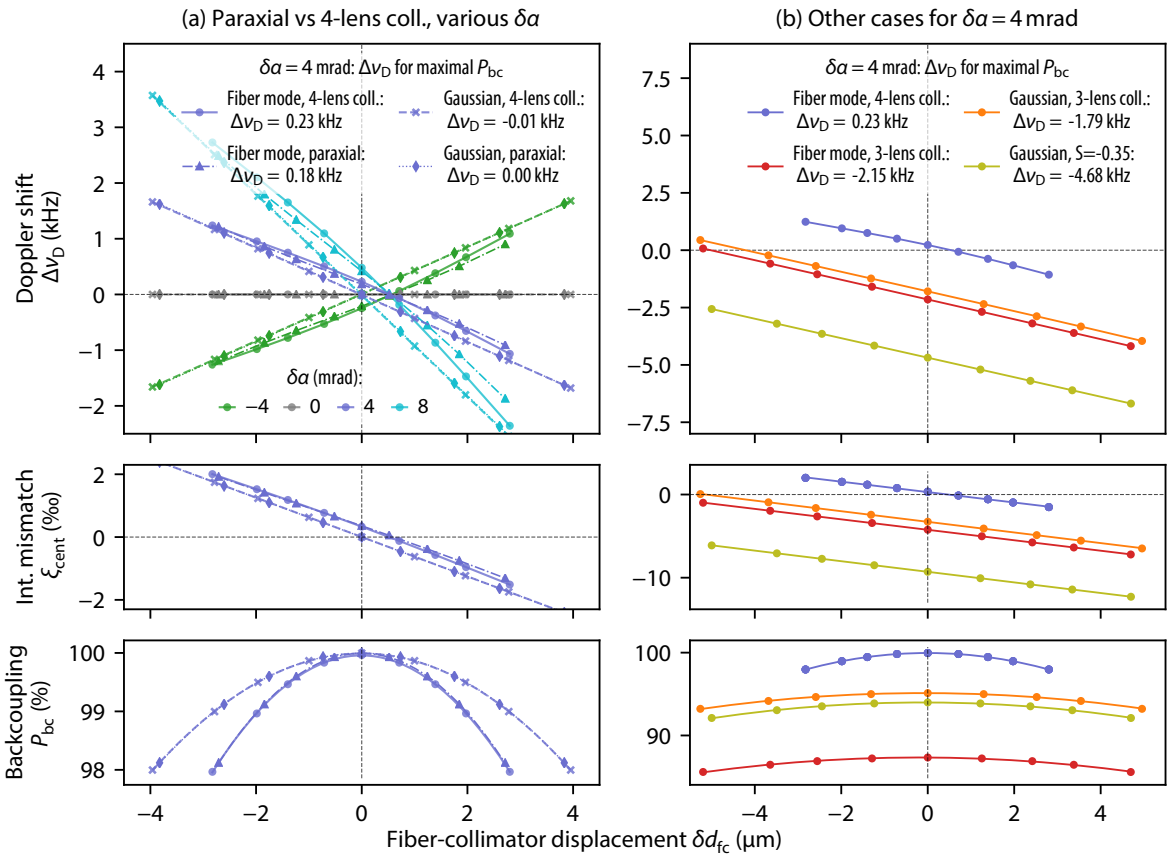

Figure 4.6: The top graphs show the simulated Doppler shift $\Delta\nu_\mathrm{D}$ for the 2S-6P transition for different AFR configurations versus the fiber-collimator displacement δd_fc. The bottom graphs show the intensity mismatch ξ_cent of forward- and backward-traveling beams at their beam centers and the backcoupled light fraction P_bc, also versus δd_fc. (a) Aberration-free paraxial collimation compared to the four-lens collimator for different angles $\delta\alpha$. Either a Gaussian beam (dashed and dotted lines) or the fiber mode (solid and dash-dotted lines) are used as the input beam for simulations. As a figure of merit, the Doppler shift is evaluated at the maximal backcoupling (zero δd_fc) for $\delta\alpha = 4\,\mathrm{mrad}$ (blue points and curves), demonstrating that the four-lens collimator performs almost as well as the aberration-free collimation. With the Gaussian beam as an input, no substantial difference is observed in the simulations. On the other hand, with the fiber mode as an input, the residual shift of $\Delta\nu_\mathrm{D} \simeq 0.2\,\mathrm{kHz}$ is dominated by the fiber mode and not the aberrations from the collimator. (b) Simulations for $\delta\alpha = 4\,\mathrm{mrad}$. The four-lens collimator with the fiber mode (blue) is shown as a reference to (a). The three-lens collimator as well as a Gaussian beam with spherical aberrations show a residual Doppler shift of $\Delta\nu_\mathrm{D} \simeq 2$–$5\,\mathrm{kHz}$, thereby limiting the performance of the AFR. This residual Doppler shift is mainly caused by the intensity mismatch at the beam center ξ_cent (despite the same power of forward- and backward-traveling beams), which vanishes for approximately the same value of δd_fc as the Doppler shift.

beam from the HR mirror is assumed here.

Fig. 4.6 (a) compares simulations of perfect paraxial collimation (described by the phase $\phi_\mathrm{foc}(r)$ from Eq. 4.6) to the four-lens collimator. Both cases are evaluated with the Gaussian beam and the fiber mode as input beams for different angles $\delta\alpha$. The top graph shows the resulting Doppler shift $\Delta\nu_\mathrm{D}$. The bottom graphs show two AFR beam properties: the

intensity mismatch of forward- and backward-traveling beams at their beam centers, ξ_{cent}, and the backcoupled light fraction P_{bc}. In the perfectly orthogonal case (zero $\delta\alpha$, gray points and curves), the Doppler shift is strongly suppressed and found to be zero within the numerical uncertainty independent of δd_{fc}. For $\delta\alpha \neq 0$, there is one value of δd_{fc} where the Doppler shift vanishes independent of $\delta\alpha$ for each laser beam configuration. For an aberration-free Gaussian beam ("Gaussian, paraxial"), this value corresponds to the maximum backcoupled light fraction (zero δd_{fc}). As discussed in Section 4.2.2, the fiber mode mostly does not affect the wavefront-retracing property. However, since the propagation from the fiber to the collimator does not exactly correspond to the far field, the value of δd_{fc} where the Doppler shift vanishes does not exactly correspond to the point of maximal backcoupled light fraction.

Here, only single atomic trajectories are evaluated, though in the experiment a finite atomic beam divergence of 8–10 mrad (FWHM) is present. However, as Fig. 4.6 (a) demonstrates, the Doppler shift is approximately linear in $\delta\alpha$ within the range of interest. For a symmetric atomic beam which is aligned such that, on average, the atoms cross the laser beams at an offset angle $\delta\alpha$ from the orthogonal, there is for each atom with a crossing angle of $\delta\alpha + \delta\tilde{\alpha}$ another atom with a crossing angle $\delta\alpha - \delta\tilde{\alpha}$, where $\delta\tilde{\alpha}$ is an angle within the beam divergence. This results in a partial cancellation of the overall Doppler shift, with the remaining residual Doppler shift corresponding to that of a single trajectory with angle $\delta\alpha$. As a figure of merit for the AFR performance, we evaluate the Doppler shift at the point of maximum backcoupling (zero δd_{fc}) for an angular displacement of $\delta\alpha = 4\,\mathrm{mrad}$, corresponding to the typical alignment accuracy in the experiment (see blue points and lines in Fig. 4.6 (a)). The residual Doppler shift for the aberration-free collimation with the fiber mode is $\Delta\nu_{\mathrm{D}} = 0.18\,\mathrm{kHz}$, while for the Gaussian beam the value is exactly zero. For the four-lens collimator with the Gaussian beam as the input beam, we find almost no difference to the aberration-free Gaussian beam such that $\Delta\nu_{\mathrm{D}} = -0.01\,\mathrm{kHz}$. With the fiber mode, the difference to aberration-free collimation is slightly larger but small enough such that the overall effect of the fiber mode dominates the residual Doppler shift of $\Delta\nu_{\mathrm{D}} = 0.23\,\mathrm{kHz}$. Comparing the Doppler shift with the intensity mismatch for different values of δd_{fc}, we find that the residual Doppler shift from the fiber mode is dominated by the induced intensity mismatch ξ_{cent} which becomes zero for the same value of δd_{fc} as the Doppler shift.

In Fig. 4.6 (b) several simulations are shown for $\delta\alpha = 4\,\mathrm{mrad}$. The Gaussian beam with spherical aberrations of $S \simeq -0.35$ (an approximate value from Eq. 4.8 according to the measured beam quality factor shown later in Fig. 4.11) results in $\Delta\nu_{\mathrm{D}} = -4.68\,\mathrm{kHz}$ (green line). We find again that the residual Doppler shift is mainly caused by the intensity mismatch which vanishes approximately for the same value of δd_{fc}. Therefore, in principle, for an aberrated beam in the AFR one could adjust δd_{fc} such that the Doppler shift vanishes. However, in practice, reliable identification and adjustment of this position is challenging unless it is the point of maximized backcoupled light fraction. For the three-lens collimator with the Gaussian beam as input (orange line) we find $\Delta\nu_{\mathrm{D}} = -1.79\,\mathrm{kHz}$, and with the fiber mode as input (red line) we find $\Delta\nu_{\mathrm{D}} = -2.15\,\mathrm{kHz}$. Though this residual Doppler shift still corresponds to a suppression factor $> 10^5$ of the full collinear shift, its value is comparable to the uncertainty of the previous 2S-4P result [14]. Looking at the calculated backcoupled light fraction, we find $P_{\mathrm{bc}} \simeq 88\,\%$ for the three-lens collimator with the fiber mode which is lower than the measured value of 94.0(1.2)%. We attribute this discrepancy to the not exactly known fiber parameters, as well as to the approximation that the fiber has a perfect step-index profile. Note that this may also indicate that the residual Doppler shift with the four-lens collimator using our fiber may deviate from the simulated $\Delta\nu_{\mathrm{D}} = 0.23\,\mathrm{kHz}$, though

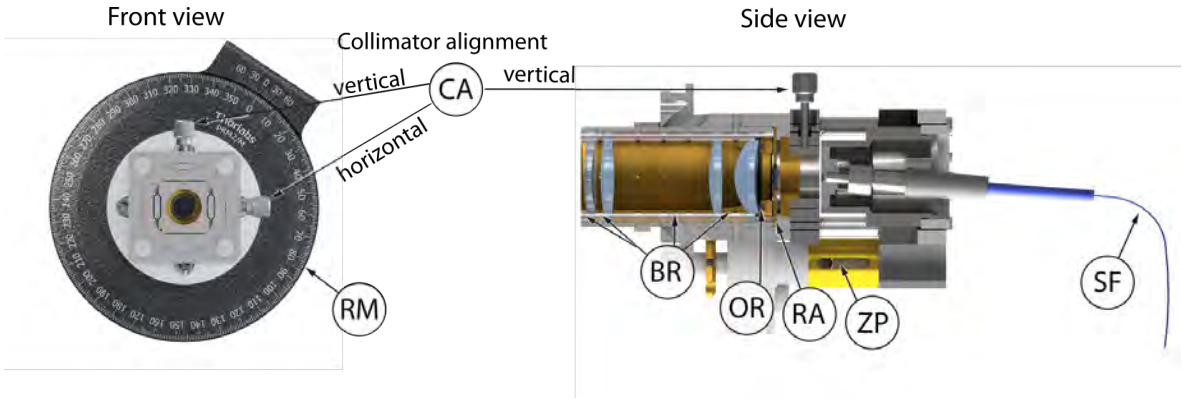

Figure 4.7: Front and side views of the collimator-fiber system assembly showing how the collimator alignment (CA) w.r.t. the fiber is made possible. The front view is cut along the flexure translation mount to show how the collimator (attached through the collimator mount, which is threaded into the adjustable center bore) can be aligned relative to the polarization-maintaining fiber (SF) (attached through the fixed cage system) in both the horizontal and vertical orientation using the two corresponding fine pitch adjustment screws. Furthermore, the front view shows the rotation mount (RM) which rotates the whole fiber-collimator system assembly shown in the side view. The brass ring spacers (BR) between the collimator lenses ensure the accurate centering of lenses inside the collimator. The retainer with an O-ring (OR) holds the collimator lens system in place without applying too much stress on the lenses. The aperture (RA) blocks the reflection of the backward-travelling beam reflected from the angle-cleaved fiber tip. Furthermore, the piezo actuator (ZP) for the accurate fiber-collimator distance adjustment is labelled.

one would expect it to be smaller due to the higher observed backcoupled light fraction within the discrepancy from the three-lens collimator. In reality, other imperfections such as the mid-spatial frequency errors from imperfect lens polishing ('orange-peel' structure, see Fig. 4.12) or residual astigmatism (see Fig. 4.9) may limit the Doppler shift suppression in the AFR, rather than the not exactly Gaussian beam profile from the fiber. In the future, these imperfections may also be included in the Doppler shift simulations.

Recalling Section 4.1, two effects may lead to a residual Doppler shift in the AFR: first, non-matching wavefronts of the forward- and backward-traveling beams, and second, imbalances of their intensities. Surprisingly, we find in our simulations, that the second effect dominates the induced Doppler shift for imperfections caused by aberrations. We do not observe significant deviations from our simulation results if, after propagation of forward- and backward-traveling beam, the wavefront mismatch but not the intensity mismatch of both beams is fully neglected in the spectroscopy region. Therefore, though aberrations are initially imprinted in the wavefront of the beam, after propagation, they are effectively manifested in an intensity mismatch (despite equal powers of forward- and backward-traveling beams) in terms of their influence on the Doppler shift. For an aberration-free beam, the fiber-collimator distance with optimal backcoupled fraction (zero δd_{fc}) corresponds to the same distance with balanced intensities of forward- and backward-traveling beams. In the presence of aberrations, those distances are not the same, such that for zero δd_{fc} there is a residual Doppler-shift mainly due to the intensity imbalance.

4.2.4 Collimator-fiber system assembly and alignment

Aligning and mounting the collimator w.r.t. the fiber is important because any asymmetry present in the fiber–collimator system results in an astigmatism which distorts the wavefront-retracing condition. Correspondingly, the lenses of the collimator need to be precisely mounted without applying too much mechanical stress leading to deformation and stress-induced birefringence. The front and side views of the collimator-fiber system assembly are shown in Fig. 4.7. The assembly of lenses was designed by the manufacturing company such that the lens decenter w.r.t. the optical axis is $< 30\,\mu m$, achieved with brass rings (BR in Fig. 4.7) matching the lens curvatures. A retainer with a single O-ring holds the lens system in place without introducing too much deformation and birefringence (OR in Fig. 4.7). The fiber and collimator mounting parts are aligned w.r.t. each other using the two fine pitch adjusters (CA in Fig. 4.2) from a commercial flexure translation mount[1]. This allows to center the fiber w.r.t. the collimator to better than 40 µm. Even though we observe tip-tilt misalignment of the fiber-collimator assembly (see Sec. 4.3), in simulations we find that tip-tilt misalignment does not introduce significant astigmatism as compared to decenter, so that we restrict the alignment to the dominant case of centering only.

The backward-travelling beam in the AFR is reflected by the fiber tip. This reflection is directed towards the atoms and could potentially affect the precision spectroscopy measurement. To suppress this effect, the fiber tip is cleaved under an angle of 8° which results in the relative angle of 23.6° between the forward propagating beam from the fiber and the reflected beam. Furthermore, the fiber tip surface is AR-coated ($R < 0.1\%$ for 405-490 nm). In addition, an aperture is placed before the collimator, see RA in Fig. 4.2, which blocks most of the power of this reflection. This aperture with a thickness of 1 mm has a radius of 3.6 mm and is placed at a distance of 14.5 mm after the fiber tip, corresponding to an aperture of ∼4 times the beam diameter of the forward travelling beam at this position.

In order to perform the collimator–fiber alignment, the astigmatism (a in Eq. (4.16)) is measured through the caustic measurement setup (as shown below in Fig. 4.11). The astigmatism is defined to be the difference in the waist positions in units of the Rayleigh length. Note that the astigmatism is different from the ellipticity (ratio of waist radii, see ε in Eq. (4.16)): the beam can be elliptic everywhere without being astigmatic. Here, the astigmatism values are given as measured in the caustic measurement setup, i.e. the difference in the waist positions after the additional focusing lens (M^2-lens). Combining a linear stage[2] with a beam camera[3], we built a caustic measurement device without additional mirrors in the setup and capable of performing a caustic measurement within one minute for the typical amount of ∼60 different beam positions required for our astigmatism measurement. This is described in more detail in the Bachelor thesis by Alexander Hertlein [230].

Fig. 4.8 shows the results of the four-lens collimator alignment. We have two copies of the four-lens collimator which we named A and B, here the results of the collimator A are shown. Fig. 4.8(a) shows two examplary alignment measurements in both horizontal (orange) and

[1] In the final setup Thorlabs CP1XY was used giving a range of 0.5 mm in both horizontal and vertical alignment (decenter w.r.t. the fiber). Initially, we tried the Thorlabs CXY1 mount, having a two times larger travel of 1 mm in both directions. However, the Thorlabs CXY1 mount turned out to be not very stable and reliable, especially since the amount of oil needed to be reduced to make this mount (more) vacuum compatible. The Thorlabs CP1XY mount is vacuum compatible by design and proved to be much more stable and reliable, and the travel range of 0.5 mm is sufficient.

[2] Thorlabs LTS300/M.

[3] UI-3380CP-M-Gl by IDS Imaging Development Systems, cover glass removed by Eureca Messtechnik.

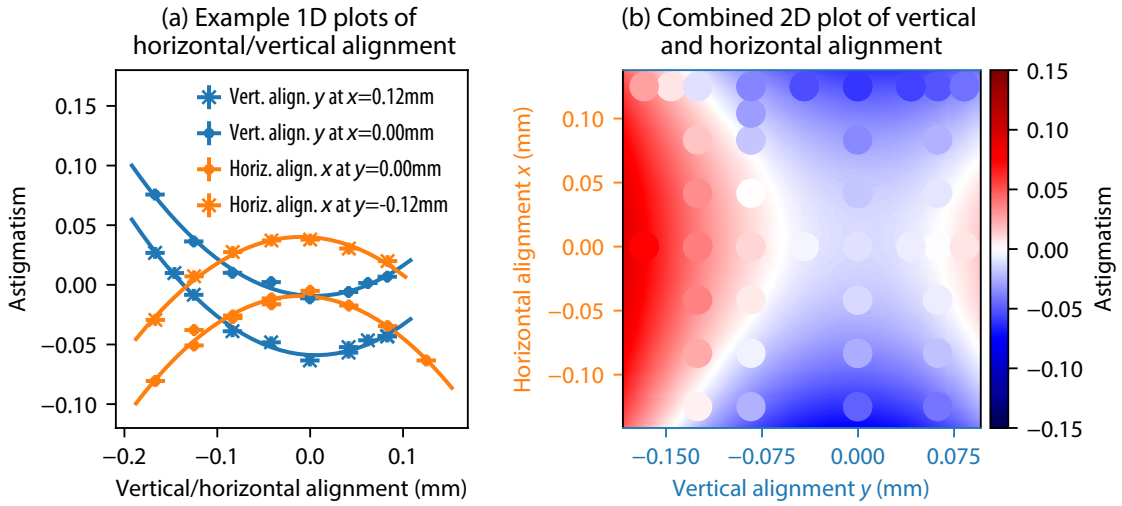

Figure 4.8: Alignment of the four-lens collimator A. In (a) two exemplary alignment scans are shown for each of the two directions, where for each alignment position (incrementally adjusted by the pitch screws marked as (CA) in Fig. 4.7) the astigmatism (difference in the waist positions in units of the Rayleigh length, see a in Eq. (4.16)) is measured by a caustic measurement (as shown below in Fig. 4.11). The data is fitted with a quadratic function. In (b) all the data is shown as circles with the radius giving the positional uncertainty and the color of the measured astigmatism value according to the color bar on the right. The background image between the data points is obtained from the fits to the data. The symmetry point (optimal alignment) is not known initially, and the offset in both directions has been adjusted after the measurement for presentation purposes such that x and y are zero for the optimal alignment. Note that the measured astigmatism depends on the coordinate frame of the measured beam widths in the caustic measurement and hence its absolute value at the symmetry point does not yield the information about the internal asymmetry of the collimator (Fig. 4.9 below analyses the astigmatism independent of the coordinate frame).

vertical (blue) directions, x and y, respectively. The corresponding fine pitch adjustment screw is rotated in incremental steps of 1/8 or 1/4 of a full revolution, where one full revolution of the adjustment screw corresponds to a vertical or horizontal decenter of 0.167 mm (calibrated in a separate measurement). For each position of the adjustment screw a caustic measurement (as shown below in Fig. 4.11) is performed, yielding an astigmatism value for each alignment position. Since the collimator is already approximately centered through the mechanics of the whole assembly, only small values of the measured astigmatism[1] in the range of ± 0.15 are observed, and the data can be fitted by a quadratic function around the optimal alignment. For clarity, the offset in the horizontal and vertical alignment axes of Fig. 4.8 was chosen such that the optimally centered alignment corresponds to x and y being zero. Initially, this optimal position is unknown such that the astigmatism needs to be measured across different values of x and y. All the data points are shown as circles in Fig. 4.8(b) on a two-dimensional plot, with the color of a measured astigmatism value and the circle radius of the position uncertainty (1/16 of a full revolution of the adjustment screw corresponding to 0.01 mm). As

[1]Note that the measured astigmatism values give the astigmatism of the beam after the M^2-lens. Using the focal length of the M^2-lens ($f = 750$ mm), one could calculate the astigmatism of the collimated beam before the M^2-lens.

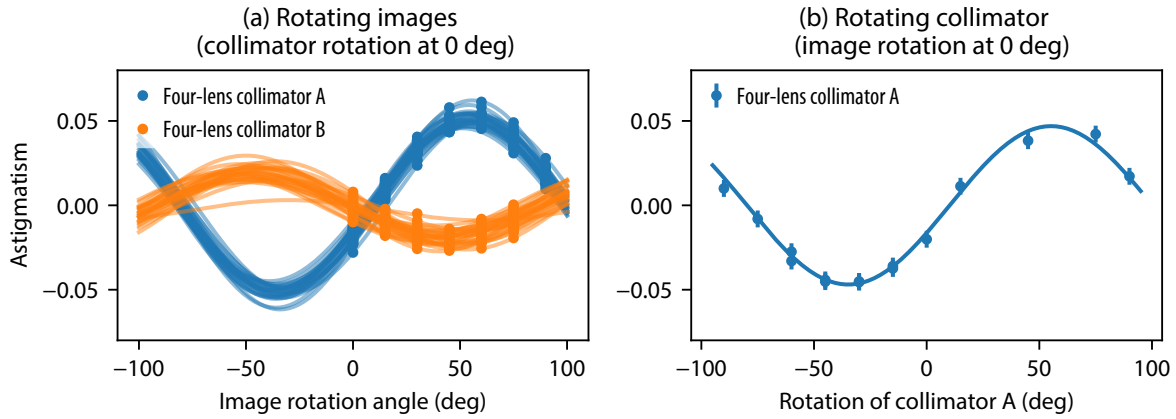

Figure 4.9: Astigmatism of the four-lens collimators A and B for optimal alignment. In (a) the astigmatism is plotted as a function of the image rotation angle for the beam width determination in the caustic measurement from which the astigmatism is extracted (i.e. rotation of the x/y coordinate frame). Data for 30 consecutive measurements for the four-lens collimator A (blue) and B (orange) are shown as points for several values of the rotation angle, where for each measurement the data is fitted with a sine function (faint curves). In (b) the four-lens collimator A has been physically rotated using the rotation mount (RM) in Figs. 4.7 and 4.2 to confirm the analysis presented in (a). For the rotation of 0° the astigmatism value of around −0.02 for the collimator A corresponds to the value at the symmetry point from Fig. 4.8. The maximal absolute value of astigmatism for the collimator A is 0.051(4) which is higher than 0.019(4) for the collimator B, indicating a larger stress-induced deformation of the lenses as discussed below.

Fig. 4.8(a) demonstrates, in both directions the measured astigmatism is well approximated by a quadratic function, such that the background image Fig. 4.8(b) can be accurately obtained from the quadratic fits to the data.

The symmetry point in Fig. 4.8(b) corresponds to the optimal alignment of the collimator. However, note that the astigmatism is not zero at this point (see discussion below for the possible origin of the residual astigmatism due to the stress-induced deformation of the collimator lenses). There are infinitely many alignment positions where the measured astigmatism is zero (white region in Fig. 4.8(b)) outside the optimal alignment. This is due to the fact that the astigmatism obtained from the caustic measurement (as shown below in Fig. 4.11) is linked to beam width measurements along the caustic which are calculated in a fixed coordinate system (x and y). For a beam asymmetry exactly under 45° to the x and y axes, the astigmatism as obtained from the beam widths measurements along x and y is zero no matter how large this asymmetry is. However, note that the symmetry point is independent of the coordinate system such that the alignment of the collimator-fiber system can be performed in any coordinate system and thus for all possible asymmetries.

Though the symmetry point of optimal alignment (where x and y are both zero in Fig. 4.8(b)) is independent of the coordinate system, the absolute value of the astigmatism at this point depends on the coordinate system. Therefore, to characterize the internal asymmetry of the collimator (e.g. due to possible misalignment of lenses w.r.t. each other) it is instructive to determine an astigmatism value independent of the coordinate system. This analysis is presented Fig. 4.9. In Fig. 4.9(a) the beam camera images used to determine the beam widths in the caustic measurement are rotated (corresponding to a rotation of the x/y coordinate system). The data is shown for the four-lens collimator A (blue) and B (orange),

each for 30 consecutive caustic measurements. For each caustic measurement, the images have been rotated in the range between 0° and 90°, and the extracted astigmatism value as a function of the rotation angle is fitted with a sine. This analysis has been confirmed by a physical rotation of the whole fiber-collimator assembly with collimator A as shown in Fig. 4.9(b) using the rotation mount (RM) in Figs. 4.7 and 4.2, yielding as expected the same results as rotating the coordinate frame of the images. The maximal absolute value of the astigmatism is independent of the coordinate system and yields 0.051(4) for the collimator A and 0.019(5) for the collimator B, at 55(2)° and 44(7)°, respectively. As discussed below, this indicates a larger stress-induced deformation of the lenses for the collimator A compared to the collimator B.

The astigmatism can be simulated using the optics design software for different misalignments of the lenses or tilt of the collimator. We found that the astigmatism produced by tilting the collimator even as large as by 10° could always be compensated to < 0.005 by centering, such that we decided to limit the alignment of the collimator to the dominant case of centering only. From the simulations it was found that the astimatism is most senstive to the centering of the last lens in the collimator (formed by surfaces 7-8 in Table 4.1). The observed astigmatism of $\sim$0.05 would be produced by decentering this lens by 300 µm, which is an order of magnitude larger than the specified centering within 30 µm. However, stress-induced birefringence measurements indicate that, for optimal alignment, the residual (coordinate frame independent) astigmatism is caused by the stress-induced deformation of the lenses.

Fig. 4.10 shows a measurement of the stress-induced birefringence of the four-lens collimator B (the one which produces less astigmatism). For this measurement, the PM fiber has been rotated w.r.t. the collimator. At each rotation angle γ, the circular polarized fraction S_3/S_0 of laser light after the collimator has been measured for both the vertical (blue) and horizontal (orange) input polarization into fiber (slow and fast polarization-maintaining axes of the PM fiber). The birefringence of the collimator δ produces a modulation $S_3/S_0 = \sin\delta \sin(2\gamma - 2\gamma_0) + o$, where γ_0 gives the orientation of the birefringence axis of the collimator and o is an offset originating from the fiber (e.g. due to stress-induced birefringence of the connector) or polarization gradients across the lens system. The fit to the data gives a retardance of $\delta_{\text{Coll. B}} \sim 0.07\,\text{rad}$.

For the collimator A, such a birefringence measurement was not performed for the following reason. After the collimator A has been installed into the setup, we observed that during the work on apparatus dust particles can be accumulated on the lens surfaces of the collimator. In particular, dust particles can also enter the volume between the lenses through holes needed for pumping out the inner region of the collimator. Unfortunately, the dust particles could then not be removed, and the collimator A was sent to the company to clean the lenses of the disassembled collimator individually. Therefore, collimator B was installed into the vacuum setup and special care was taken to minimize the risk of accumulating dust particles on the collimator. The time when the collimator is exposed to air outside vacuum was kept as short as possible and a birefringence measurement was not performed. However, when first mounting the collimator, a large circular polarized fraction of $S_3/S_0 \sim 0.3$ (for vertical polarization) and $S_3/S_0 \sim -0.3$ (for horizontal polarization) was observed. Comparing to Fig. 4.10, that means that the stress-induced birefringence of collimator A is $\delta_{\text{Coll. A}} \gtrsim 0.15\,\text{rad}$, at least twice as large as for collimator B. This observation matches the data for the larger astigmatism of collimator B and supports the hypothesis that the residual astigmatism is mainly caused by stress-induced deformation of the lenses. In the future, one could use a softer O-ring (OR in

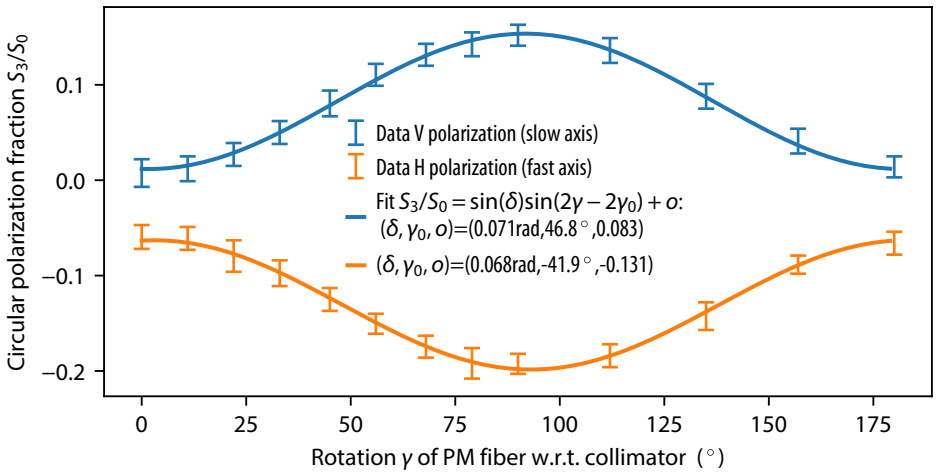

Figure 4.10: Birefringence measurement of the four-lens collimator B. As the PM fiber is rotated against the collimator, the circular polarized fraction S_3/S_0 is measured after the collimator for both vertical (blue) and horizontal (orange) input polarization before the fiber. The data is fitted with $S_3/S_0 = \sin\delta\sin(2\gamma - 2\gamma_0) + o$, where δ is the collimator retardance, γ the rotation of the PM fiber w.r.t. the collimator, γ_0 the orientation of the birefringence axis of the collimator and o is an offset originating from the fiber. The fit yields a retardance of $\delta_{\text{Coll. B}} \sim 0.07\,\text{rad}$ for the four-lens collimator B.

Fig. 4.7) and/or slightly untighten the lens system while measuring the residual astigmatism. The collimator A was then rotated by 90° w.r.t the fiber, which reduced the circular polarized fraction to $|S_3/S_0| \lesssim 0.1$. This rotation could be done quickly, since the cage system of the fiber mount assembly (see Fig. 4.7) can be easily rotated in steps of 90°.

4.2.5 Measurement of collimator performance

We measured the collimator performance at 410 nm by analyzing intensity profiles in the caustic measurement shown in Fig. 4.11. The beam radius $W(z)$ is determined for the orthogonal x and y transverse directions according to the second-moment definition [219] with a self-convergent-width factor [229] of $F_s = 3$. This beam radius determination is performed at different positions around the focus of the M^2 lens ($f = 750\,\text{mm}$), corresponding to propagation distances from $-10\,z_R$ to $+10\,z_R$ around the waist position. From the fit according to Eq. 4.5 the beam waist radii $W_{0,x}$ and $W_{0,y}$, waist positions $z_{0,x}$ and $z_{0,y}$, and beam quality values M_x^2 and M_y^2 are extracted. These values determine the ellipticity ε, astigmatism a, and combined beam quality M^2 as

$$\varepsilon = \max\left(\frac{W_{0,x}}{W_{0,y}}, \frac{W_{0,y}}{W_{0,x}}\right), \quad a = \frac{z_{0,x} - z_{0,y}}{(z_{R,x} + z_{R,y})/2}, \quad M^2 = \sqrt{M_x^2\, M_y^2}. \tag{4.16}$$

The fits and the determined parameters are shown at the upper part of Fig. 4.11. The measured ellipticity of a few percent is in agreement with the slightly elliptical beam from our polarization-maintaining fiber, see Section 4.2.2. The reduced astigmatism of the four-lens collimator, $a = 0.014(4)$, was achieved with the help of alignment described in Section 4.2.4 compared to the three-lens collimator with $a = 0.216(5)$ where the collimator was aligned with the help of centering the observed distortions in the intensity profiles. For the three-lens

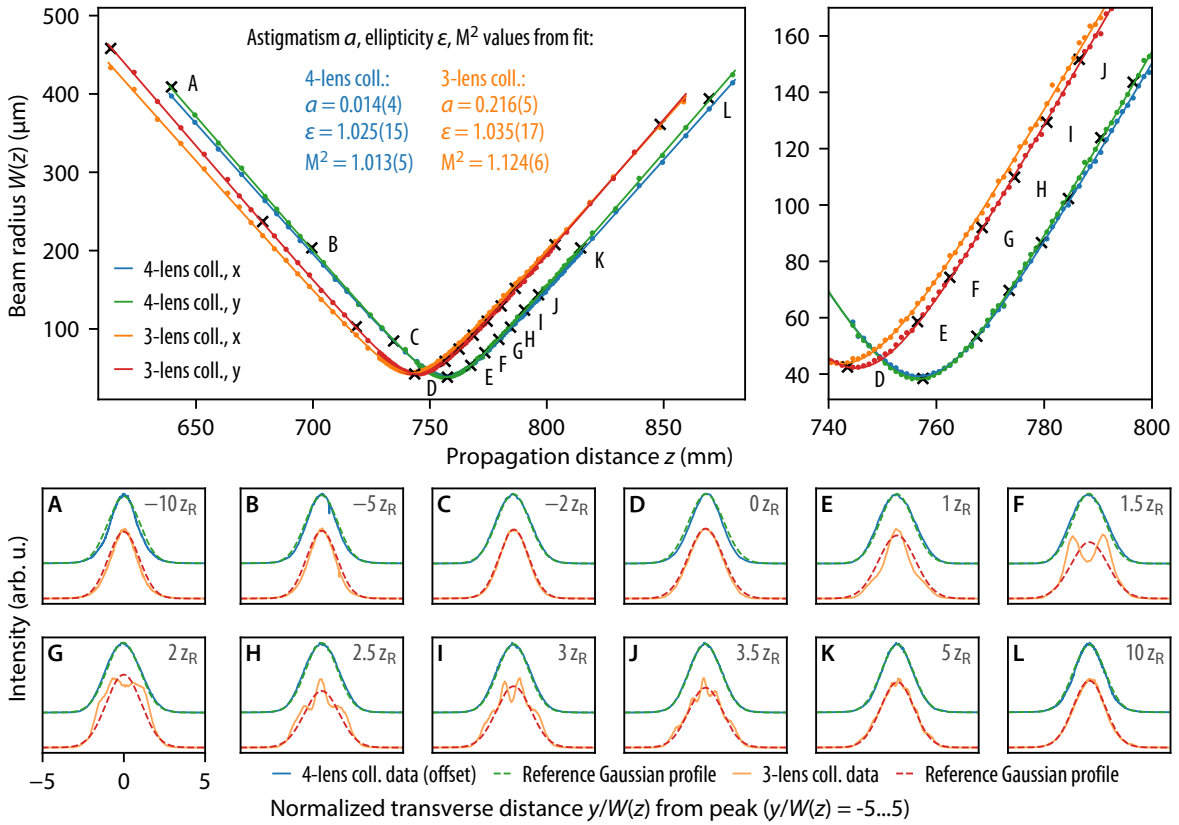

Figure 4.11: Caustic measurement of the three-lens and four-lens collimators at 410 nm. At the top, the beam radius $W(z)$, obtained from second-order moments in the x and y directions, is plotted against the propagation distance z (with different offset for the two collimators) after the $f = 750\,\mathrm{mm}$ focusing lens, with a zoomed region of up to four Rayleigh lengths after the focus where distortions due to spherical aberrations are expected. The fitted beam quality value for the three-lens collimator is $M^2 = 1.124(6)$ due to spherical aberrations with $|S| \simeq 0.34$, whereas for the four-lens collimator the beam quality of $M^2 = 1.013(5)$ is not limited by spherical aberrations but by the fiber mode profile described in Section 4.2.2. At the bottom, normalized intensity profiles at selected propagation distances A to L (from $-10\,z_R$ to $+10\,z_R$, marked on the top plot) are depicted, along with reference Gaussian beams of $1/e^2$ intensity radius $W(z)$.

collimator we find $M^2 = 1.124(6)$ which corresponds to $|S| = 0.33(1)$ according to Eq. 4.8. Aberrations are also revealed as distortions in intensity around the focus after the M^2 lens, see bottom of Fig. 4.11 where the intensity profiles at selected positions A to L marked on the top are shown. For the three-lens collimator we observe the characteristic intensity profiles for a beam with spherical aberrations [225]. Note that distortions in intensity appear only in the region between z_R and $4\,z_R$ after the focus, which demonstrates that the manifestation of aberrations cannot be readily observed in intensity of collimated beam without the caustic measurement. In the simulations of caustic intensity profiles for the given three-lens collimator design, we find a larger dip depth and more distorted intensity profiles than observed, which we attribute to high sensitivity to single-mode fiber input parameters and/or the limitation of the step-index approximation of the fiber. For the four-lens collimator, no beam profile distortions are observed in agreement with simulations using the given lens design, and the beam quality factor $M^2 = 1.013(5)$ is limited by the fiber profile as calculated in Section 4.2.2.

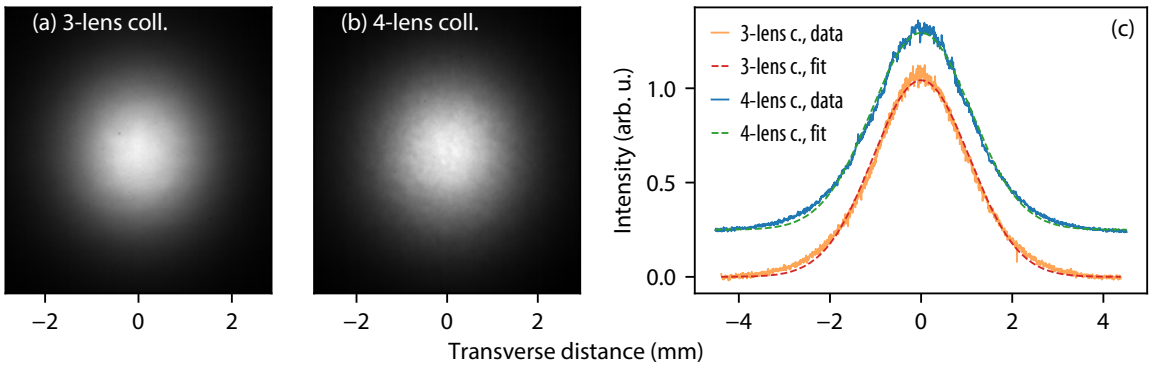

Figure 4.12: Measured beam profile of the collimated beam in the spectroscopy region of the AFR (12 cm after the collimator) for: (a) 3-lens collimator, (b) 4-lens collimator. A weak 'orange-peel' structure is visible in both beam profiles, but more pronounced on the 4-lens collimator beam profile (note that this is only visible in the digital version of the document, but not in the printed version). Cuts through the beam profiles are shown in (c) along with a Gaussian fit to the data (offset for 4-lens collimator). Note that aberrations present in the phase at this position are not observed in the shown intensity profile, but are revealed through the caustic measurement as demonstrated in Fig. 4.11.

The collimated beam intensity profiles in the spectroscopy region (corresponding to 12 cm propagation distance after the collimator) are shown in Fig. 4.12 (a) and (b) for the three-lens and four-lens collimator, respectively. Though no performance shortcomings of the four-lens collimator are observed in the caustic measurement, a weak residual "orange-peel" structure is observed on the collimated beam of both collimators, which is more pronounced for the four-lens collimator. This structure is barely observed on cuts through intensity profiles as shown in Fig. 4.12(c). We observed similar but much stronger deviations in beam profiles from aspheric lenses where these mid-spatial frequency errors are more pronounced, as well as for some other collimators[1]. It is important to note that these lens imperfections imprint phase distortions which may disturb the wavefront-retracing property of the AFR. After propagation, these phase distortions transform into intensity distortions and may introduce a residual Doppler shift. Therefore, it is important to ensure best possible lens polishing quality, minimizing mid-spatial frequency errors. In our case, the lens surfaces and polishing processes responsible for deviations observed in Fig. 4.12 (b) could not yet be identified and remain under investigation together with the manufacturer. We believe that the observed orange-peel structure originates from residual grinding structures on some lens surface which are not fully removed by polishing. Such beam profile distortions also play an important role in atom interferometry [231, 30]. In these experiments, it was found that systematic errors arising from a similar "orange-peel" structure of the beam (called "beam speckle") could be suppressed when the beam is propagated for a few meters which "washes out" this structure.

As discussed at the beginning of this section, the backcoupled light fraction gives an important figure of merit of the collimator performance. Compared to the three-lens collimator with a backcoupled fraction of 94.0(1.2) %, the backcoupled light fraction of the four-lens collimator is measured to be 99.3(1.2) %. Note that this number gives the spatial overlap of

[1]In particular, we have three copies of the three-lens collimator where one of the three-lens collimators showed an even stronger "orange-peel" structure than the four-lens collimator. Here we show the profile of our best three-lens collimator. Both four-lens collimators A and B show the same magnitude of the "orange-peel" structure.

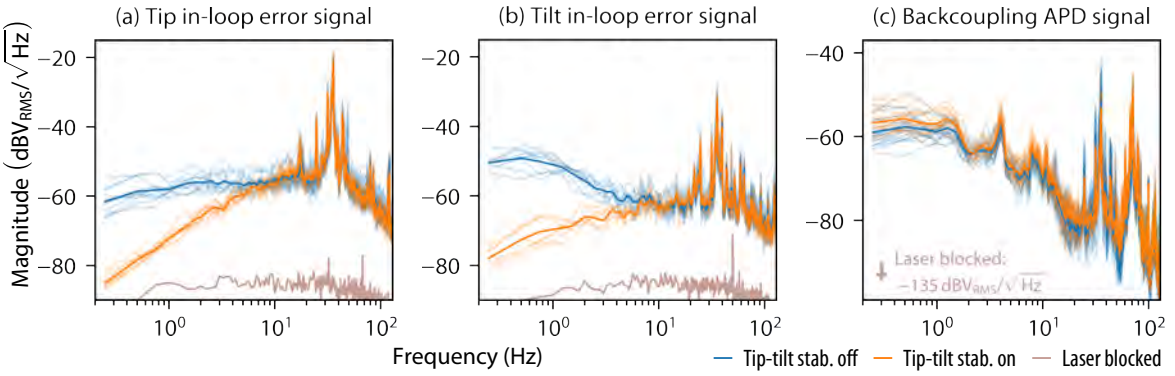

Figure 4.13: Performance of the tip-tilt stabilization of the AFR (with 2nd intensity stabilization switched on). Spectra of the in-loop error signals produced by the lock-in amplifiers (1 ms time constant) for the horizontal and vertical (tip and tilt) feedbacks of the HR mirror are shown in (a) and (b). The power spectrum of the backcoupled light on the 'Backcoupling APD' (see Fig. 4.1) is shown in (c). All spectra are shown with tip-tilt stabilization switched on (orange line), off (blue line) and with the laser blocked (gray line). Each faint line is a 15 s average with a resolution bandwidth of 0.25 Hz, whereas heavy lines are the average of all data. Large resonances around 30 Hz are observed on all signals, limiting the feedback bandwidth to around 10 Hz as deduced from the in-loop error signals.

the forward- and backward-traveling beams in the AFR, with the known transmission losses of the beam path from the spectroscopy region to the backcoupling APD taken into account. The uncertainty of 1.2 % is deduced from the quadrature sum of uncertainties for position-dependent photodiode sensitivity, beamsplitter transmission, fiber attenuation, as well as AR coating uncertainties of the fiber coupling lens, fiber tips, and collimator lenses.

Ultimately, for our experiment only the velocity-resolved spectroscopy measurement provides certainty on the suppression factor of the Doppler shift. In the preliminary analysis of our recent precision measurement of the 2S-6P transition in hydrogen (see thesis by Lothar Maisenbacher for details [71]) using the four-lens collimator discussed here, the Doppler shift is consistent with zero within the uncertainty of the measurement (∼3 Hz/(m/s)). The four-lens collimator performed also well for the preliminary measurements of the 2S-6P transition in deuterium discussed in the following chapter.

4.3 Retroreflection control and stabilization

In order to achieve the wavefront-retracing retroreflection in the AFR, it is necessary to adjust the distance between the fiber and the collimator (collimation distance) such that the position of the flat wavefront of the collimated beam is at the HR mirror. Moreover, the horizontal and vertical (tip-tilt) directions of the HR mirror need to be oriented such that the wave vectors of the forward and backward propagating waves are antiparallel to each other. If both conditions (collimation and tip-tilt alignment) are optimized, the backcoupled light fraction is maximized.

The stabilization of the HR mirror tip-tilt orientation is described in detail in the previous work [197]. In short, modulating the two piezo actuators for the tip-tilt movement of the HR mirror mount with weak signals of different frequencies (producing maximal angular

misalignment of $\sim \pm 1\,\mu\text{rad}$) and detecting this modulation in the backcoupled light with two lock-in amplifiers, two error signals are generated which are used for the tip and tilt stabilization feedback loops. We tried improving the bandwidth of the feedback by using higher modulation frequencies. Mechanical resonances cause a crosstalk between the otherwise linearly independent horizontal and vertical piezo actuators. In order to find frequencies with minimal crosstalk between horizontal and vertical modulation, we measure the corresponding transfer functions of the HR mirror assembly. For this measurement we use an auxiliary laser beam reflected off the HR mirror from the back side to allow for an in-situ measurement (with PMT being removed) under a small ($\simeq 5°$) angle, and detect the reflection with a position-sensitive detector while sweeping the frequency of horizontal and vertical piezo actuators. Though higher modulation frequencies of 1.52 kHz (vertical) and 2.09 kHz (horizontal) with minimal crosstalk (typically 10–30 % amplitude ratio of horizontal to vertical error signals) could be identified, the feedback bandwidth could not be improved due to large mechanical resonances around 30 Hz caused by the rotatable geometry of the whole AFR setup.

Fig. 4.13 shows the performance of the tip-tilt stabilization, where in (a) and (b) the in-loop error signals are plotted. The bandwidth of stabilization as deduced from the in-loop error signals is around 10 Hz. However, no significant noise suppression is observed in the spectrum of the backcoupled light shown in (c), with even a slight increase of noise visible for low frequencies when the tip-tilt stabilization is switched on. Only a small decrease of noise is visible on the backcoupled light for resonances around 30 Hz. Apart from Rayleigh scattering from fiber discussed below, the unobserved noise suppression in the backcoupled light could originate from the large amount of noise common to both directions which cannot be suppressed due to large cross-talk. Though for inspection of this issue no out-of-loop measurement of the tip-tilt stabilization is available in our setup, the performance of the tip-tilt feedback is clearly observed in the backcoupled light when scanning the piezo actuator controlling the fiber-collimator distance as described below and shown in Fig. 4.14. Likewise, during a typical hour-long precision spectroscopy measurement, the tip-tilt feedback maintains the retro-reflecting condition.

In the previous setup [197] the collimation distance was adjusted by using a remote-controlled motor and maximizing the observed signal on the backcoupling APD. With this procedure the backcoupled signal could typically be optimized within $\sim 1\,\%$. We improved the distance control by adding a piezo actuator to the precision motor, which is now used for pre-alignment only. In order to determine the optimal piezo voltage, we typically scan the applied voltage with a frequency of 1 Hz over a period of 30 s such that the fluctuations on the backcoupling APD are averaged out, see Fig 4.14. Due to the not exactly on axis translation of the fiber, we observe tip-tilt misalignment on the in-loop error signals shown in (c) and (d), resulting in a large drop of the backcoupled light fraction ($\sim 3\,\%$) shown in (a) with tip-tilt stabilization switched off (brown curves). With the tip-tilt stabilization switched on (blue and orange curves), the drop of the backcoupled light fraction by $\pm 0.5\,\%$ for $\pm 1.5\,\mu\text{m}$ around $\delta d_{\text{fc}} = 0$ agrees with simulations from Fig. 4.6. From the fitted dashed line the optimal piezo voltage is determined, allowing to set the fiber-collimator distance to within $\sim \pm 0.2\,\mu\text{m}$ of the optimal value corresponding to $\pm 0.1\,\%$ of the maximum backcoupled light fraction value. In our setup we observe only slow drifts of the optimal collimation distance on the order of $0.2\,\mu\text{m}$ per hour (correlated with temperature) such that typically an adjustment is performed every 1–2 hours with no need of active stabilization.

The observed modulation on the backcoupled light fraction in Fig. 4.14(a) demonstrates how in addition to the precise distance control, the piezo actuator provides the possibility

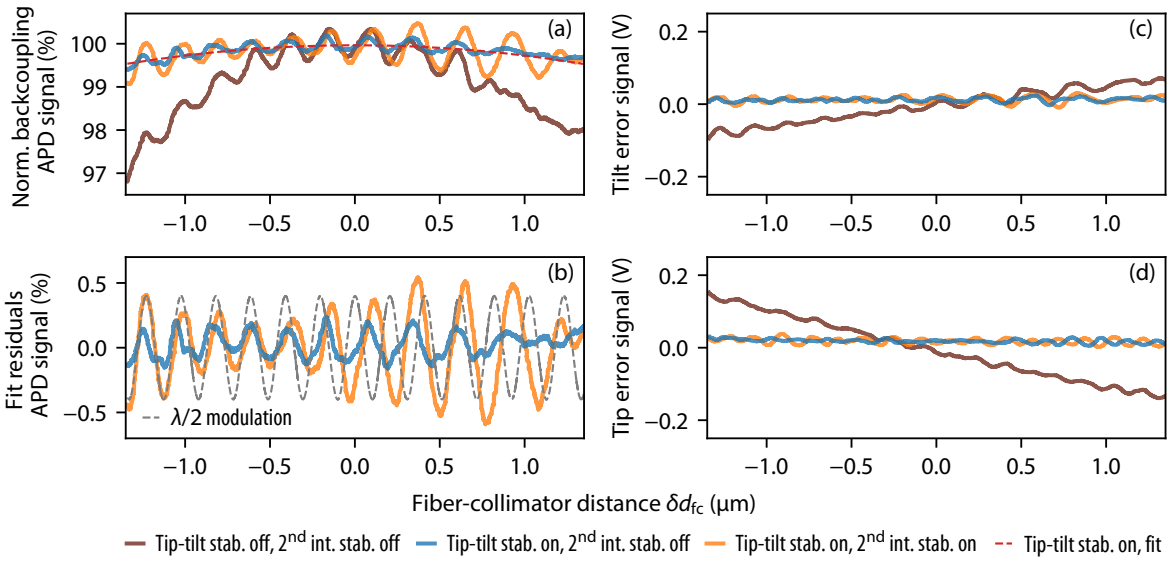

Figure 4.14: Demonstration of the improved fiber-collimator distance control using a piezo actuator. All plots show the recorded data when scanning the voltage of the piezo actuator with a frequency of 1 Hz over an averaging time of 30 s. The common x-axis has been converted from the applied voltage and leverage factor to the fiber-collimator displacement δd_{fc}, with zero δd_{fc} corresponding to maximum backcoupling. In (a) the normalized signal of the backcoupled light is shown. If the tip-tilt stabilization is switched off (brown curves), clear tip-tilt misalignment is observed on the in-loop error signals of the tip-tilt stabilization shown in (c) and (d), leading to a large drop in the backcoupled light fraction of $\sim 3\,\%$ in (a) over the full distance range. With tip-tilt being stabilized (blue and orange curves), this drop is reduced to $\sim 0.5\,\%$ in agreement with simulations from Fig. 4.6. The dashed curve in (a) shows a quadratic fit to the data with tip-tilt stabilization switched on. Clear modulation is observed on all of the signals, originating from Rayleigh scattering inside the fiber leading to an etalon effect. Along with the fit residuals of the backcoupled fraction in (b), the expected $\lambda/2$ modulation is drawn (dashed gray curve) which also reveals the nonlinearity of the piezo actuator. As expected, the modulation is stronger when the 2^{nd} intensity stabilization (to the PMT after the HR mirror) is switched on (orange curve), as compared to the case with intensity not stabilized (blue curve).

to inspect the AFR for optical etalons. The corresponding $\lambda/2$ modulation is depicted along with fit residuals in (b), not exactly matching all the data due to expected nonlinearities of the piezo actuator of $\sim 20\,\%$ over the full range. In order to avoid etalons, we use only AR-coated optics and place all photo-detectors at large angles ($\gtrsim 10°$). The fiber tips are angle-cleaved under 8° and AR-coated. After a thorough investigation, we found that the modulation we observe originates from Rayleigh scattering inside the fiber. A small fraction on the order of 10^{-3} of the scattered light from randomly distributed scattering points inside the fused silica of the fiber is guided backward in the fiber mode [232, 233, 234], interfering with the strong reflection from the HR mirror. As expected, stabilizing the intensity after the fiber leads to an increased modulation (orange curves) as compared to the case with the stabilization switched off (blue curves). The phasor of total back scattered Rayleigh light corresponds to a random walk due to the random distribution of scattering points. Therefore, the modulation depth ξ_{back} of the backcoupled light increases with the square-root of the fiber length, and we use an as short as possible fiber. More details on investigating this effect is given in the next section.

4.4 Etalon effect from Rayleigh backscattering in fiber

The obvious reason for the observed modulation in Fig. 4.14 would be a single Fabry-Perot etalon in the AFR, e.g. arising from a single parasitic reflection from the coupling lens or the fiber tips. Therefore, we first discuss this case. However, we could not identify any single parasitic reflection in the AFR leading to such an etalon. We then found that Rayleigh backscattering in the fiber produces multiple parasitic reflections leading to an etalon effect responsible for the modulation observed in Fig. 4.14. We carefully investigated this effect which is presented in Section 4.4.2. Interestingly, we find that the effective behavior of the multiple reflections from Rayleigh backscattering in the fiber can be modelled as a single Fabry-Perot etalon.

4.4.1 Case of a single Fabry-Perot etalon

Let us first consider a Fabry-Perot etalon from a single parasitic reflection with reflectance $R_1 = r_1^2 \ll 1$ (field transmission coefficient $t_1 \simeq 1$) from somewhere in the AFR between the backcoupling APD and the HR mirror, which has reflectance $R_2 = r_2^2 \simeq 1$ (field transmission coefficient $t_2 \ll 1$), see Fig. 4.15(a). The length l between the parasitic reflection and the HR mirror leads to an accumulated round-trip phase of $2\phi = 2l\omega n/c$, where n is the refractive index (i.e. the optical path length is $n\,l$). We also take into account a transmission factor of a^2 per round-trip for the electric field (which corresponds to a half-round-trip (single path) transmission factor in the intensity). The transmission factor of $a^2 < 1$ mainly originates from imperfect AR coatings as well as from the fiber attenuation in our setup[1] and is approximated for our setup with the four-lens collimator to $a^2 \approx 0.95$. The bottom scheme in Fig. 4.15(a) illustrates how the circulating field E_{circ}, the transmitted field E_{trans}, as well as the reflected field E_{back} can be derived from the incoming field E_0 following the reflection, transmission, absorption and phase difference factors. The backcoupling APD measures a signal proportional to $|E_{\mathrm{back}}|^2$, and the PMT after the HR mirror measures a signal proportional to $|E_{\mathrm{trans}}|^2 \propto |E_{\mathrm{circ}}|^2$. As the bottom scheme illustrates, the circulating field E_{circ} is derived[2] to be [169, 168]

$$E_{\mathrm{circ}} = \mathrm{i}E_0 t_1 \left(1 + a^2 r_1 r_2 e^{\mathrm{i}2\phi} + (a^2 r_1 r_2 e^{\mathrm{i}2\phi})^2 + \cdots\right) = \frac{\mathrm{i}E_0 t_1}{1 - a^2 r_1 r_2 e^{\mathrm{i}2\phi}}. \tag{4.17}$$

Note that we took into account the phase difference factor [235] of $\exp(\mathrm{i}\,\pi/2) = \mathrm{i}$. For $r_2 \simeq 1$ and $r_1 \ll 1$ it is sufficient to keep the leading term in r_1, such that the above expression simplifies to

$$E_{\mathrm{circ}} \simeq \mathrm{i}E_0 t_1 + \mathrm{i}E_0 t_1 a^2 r_1 r_2 e^{\mathrm{i}2\phi}. \tag{4.18}$$

[1] From the specifications of the corresponding AR coatings, we can estimate the transmission due to reflection losses from fiber tips to be 98.4(2)%, the transmission of the collimator (8 AR-coated surfaces) to be 98.3(4)% (note that the coupling lens transmission of 99.0(2)% does not enter the factor a since the etalon does not pass the coupling lens multiple times). The fiber transmission from attenuation ($\alpha = 30 \pm 5$ dB/km) inside the fiber yields for a 0.8 meter-long fiber 99.4(1)%. Together these factors give a transmission factor of $a^2 \simeq 0.961(5)$ (single path in the power of the field, i.e. squared amplitude). Note that this assumes perfect backcoupling from the collimator which is a good approximation for the four-lens collimator presented in Section 4.2, but not for the three-lens collimator where additional losses of ∼5% would need to be taken into account. Alternatively, the modulation depth in the backcoupling can serve as a measure of the total losses in the system and hence can be used to extract the backcoupling fraction produced by the collimator which indicates its performance.

[2] The same expression can be also derived from the self-consistent expression $E_{\mathrm{circ}} = \mathrm{i}E_0 t_1 + a^2 r_1 r_2 e^{\mathrm{i}2\phi} E_{\mathrm{circ}}$, where $E_{\mathrm{inc}} = \mathrm{i}E_0 t_1$ is the incoming field in the cavity and $g_{\mathrm{rt}} = a^2 r_1 r_2 e^{\mathrm{i}2\phi}$ the complex round-trip gain [169].

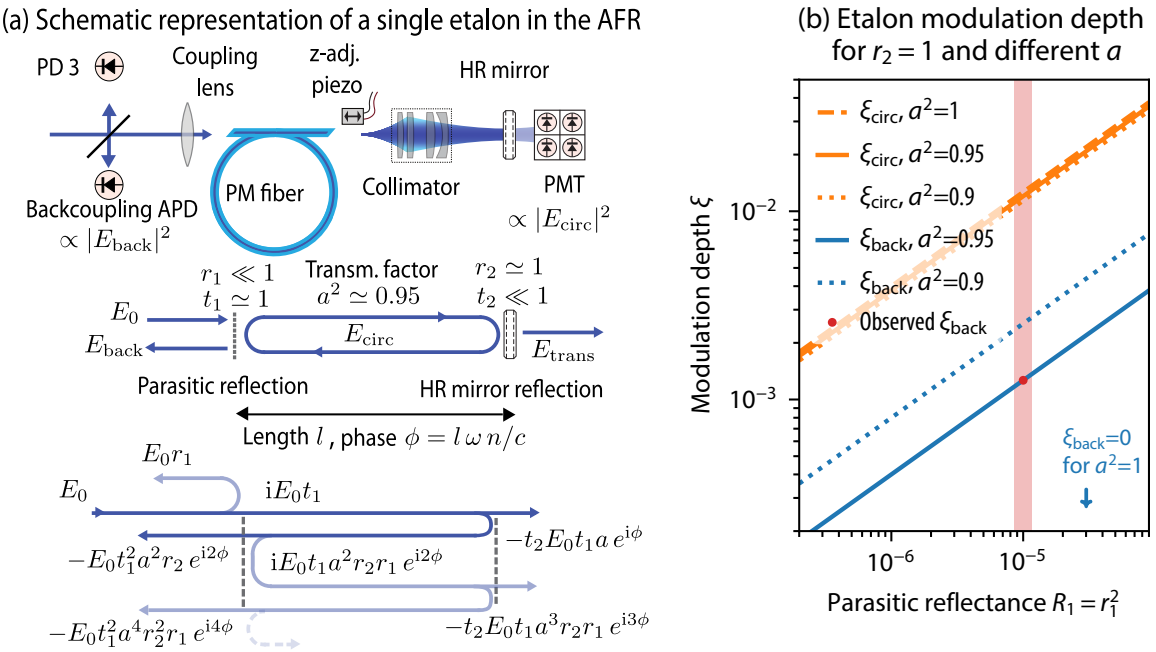

Figure 4.15: (a) Schematic representation of a single Fabry-Perot etalon in the AFR. An optical resonator is formed by a parasitic reflection $r_1 \ll 1$ (originating from somewhere between the Backcoupling APD and the HR mirror) together with the HR mirror with $r_2 \simeq 1$. The length l between the parasitic reflection and the HR mirror enters the accumulated round-trip phase $2\phi = 2l\omega n/c$, where n is the refractive index. A transmission factor of a^2 per round-trip of the electric field is taken into account, mainly originating from imperfect AR coatings and the fiber attenuation. The bottom scheme shows how the circulating field E_{circ}, the back-reflected field E_{back} and the transmitted field E_{trans} can be derived from the interference of the reflected and transmitted fields from the incoming field E_0. The backcoupling APD measures a signal proportional to $|E_{\mathrm{back}}|^2$ and the PMT measures a signal proportional to $|E_{\mathrm{circ}}|^2$ since $|E_{\mathrm{trans}}|^2 \propto |E_{\mathrm{circ}}|^2$. (b) Etalon modulation depth in the circulating light intensity (ξ_{circ} from Eq. (4.20), orange curves) and the backcoupled intensity (ξ_{back} from Eq. (4.23)) for $r_2 \simeq 1$ (HR mirror) and different transmission factors. The solid curve represents the case of our setup with $a^2 \sim 0.95$. Note that the modulation in the backcoupling vanishes for the case of no losses ($a^2 = 1$). In contrast to ξ_{back}, ξ_{circ} does not strongly depend on the transmission factor. The observed modulation depth of $\xi_{\mathrm{back}} \sim 0.1\%$ (red point) from the blue curve in Fig. 4.14(b) would correspond to a parasitic reflectance of $R_1 \sim 10^{-5}$ (faint red bar).

The transmitted field through the HR mirror is proportional to the circulating field:

$$E_{\mathrm{trans}} = \mathrm{i}at_2 e^{\mathrm{i}\phi} E_{\mathrm{circ}}. \tag{4.19}$$

Therefore, the modulation depth detected on the PMT is equal to the modulation depth ξ_{circ} for the circulating field (as seen by the atoms during the spectroscopy). We define the modulation depth ξ to be the relative peak-to-peak modulation in the light intensity, which can be derived from the above expression where $|E_{\mathrm{circ}}|$ reaches its maximum and minimum values for $\phi = 0$ and $\phi = \pi/2$:

$$\xi_{\mathrm{circ}} = 2\frac{|E_{\mathrm{circ,max}}|^2 - |E_{\mathrm{circ,min}}|^2}{|E_{\mathrm{circ,max}}|^2 + |E_{\mathrm{circ,min}}|^2} = \frac{4a^2 r_1 r_2}{1 + a^4 r_1^2 r_2^2} \simeq 4a^2 r_1, \tag{4.20}$$

where in the last step we kept the leading term for $r_1 \ll 1$ and $r_2 \simeq 1$.

The back-reflected field E_{back} is given by[1]:

$$E_{\text{back}} = E_0 r_1 - E_0 t_1^2 a^2 r_2 e^{\mathrm{i}2\phi}\left(1 + a^2 r_1 r_2 e^{\mathrm{i}2\phi} + \cdots\right) = E_0\left(r_1 - \frac{t_1^2 r_2 a^2 e^{\mathrm{i}2\phi}}{1 - a^2 r_1 r_2 e^{\mathrm{i}2\phi}}\right). \quad (4.21)$$

As in Eq. (4.18), for $r_2 \simeq 1$ and $r_1 \ll 1$ it is sufficient to keep the leading term in r_1, such that the above expression simplifies to:

$$E_{\text{back}} \simeq E_0 r_1 - E_0 t_1^2 a^2 r_2 e^{\mathrm{i}2\phi} - E_0 t_1^2 a^4 r_2^2 r_1 e^{\mathrm{i}4\phi}. \quad (4.22)$$

Similarly to Eq. (4.20), the modulation depth ξ_{back} in the intensity of reflected light (detected at the backcoupling APD) yields with $t_1^2 = 1 - r_1^2$:

$$\xi_{\text{back}} = 2\frac{|E_{\text{back,max}}|^2 - |E_{\text{back,min}}|^2}{|E_{\text{back,max}}|^2 + |E_{\text{back,min}}|^2} = \frac{4a^2 r_1 r_2 (1 - r_1^2)(1 - a^4 r_2^2)}{r_1^2 + a^4(1 - 4r_1^2 + r_1^4) r_2^2 + a^8 r_1^2 r_2^2} \simeq 8 r_1 (1 - a^2), \quad (4.23)$$

where in the last step we again kept the leading order term for $a^2 \approx 1$, $r_1 \ll 1$ and $r_2 \simeq 1$ (HR mirror).

In our case ($r_1 \ll 1$ and $r_2 \simeq 1$) the modulation depth in the backcoupling, ξ_{back}, strongly depends on the transmission factor a, and for the case of no losses ($a^2 = 1$) no modulation would be detected on the backcoupling APD ($\xi_{\text{back}} = 0$), see Fig. 4.15(b), where blue curves show ξ_{back} and orange curves show ξ_{circ}. In contrast to ξ_{back}, the modulation depth for the circulating (or transmitted) light ξ_{circ} seen by the atoms during spectroscopy does not strongly depend on a. The observed modulation depth on the order of $\xi_{\text{back}} \sim 0.1\%$ (red point) from the blue curve in Fig. 4.14(b) would correspond to a parasitic reflectance on the order of $R_1 \sim 10^{-5}$ (faint red bar). This in agreement with a modulation on the order of $\xi_{\text{circ}} \sim 1\%$ which we observed on the PMT when scanning the piezo actuator for the fiber-collimator distance.

Note that $\xi_{\text{back}} = 0$ occurs only for $r_2 = 1$ and $a^2 = 1$, which can be intuitively understood from energy conservation: independent of the round-trip phase 2ϕ, all light must be reflected since no light is transmitted through or lost in the cavity. The opposite case of maximally possible modulation of reflected light, $\xi_{\text{back}} = 2$, corresponds to an impedance matched Fabry-Perot cavity where $r_1 = r_2 a^2$ [168]. On resonance, the circulating power is then maximized while the reflected power is exactly zero, $|E_{\text{back,min}}| = 0$. For $r_2 = 1$, the impedance matched cavity has $r_1 = a^2$, and for the case of no losses ($a^2 = 1$) the impedance matched cavity has equal mirror reflectivities $r_1 = r_2$. Therefore, our case of $a^2 \approx 1$ with $r^2 \simeq 1$ and $r_1 \ll 1$ corresponds to maximally impedance mismatched case where $\xi_{\text{back}} \approx 0$. This case of a Fabry-Perot cavity, $r_1 \ll 1$ and $r_2 \simeq 1$, has a finesse close to zero, as opposed to a typical Fabry-Perot cavity with $r_1 \simeq 1$ and $r_2 \simeq 1$ with finesse larger than one. In the latter case the circulating or reflected intensities obtained from Eq. (4.17) or Eq. (4.21) yield an Airy function with well separated peaks or valleys. In our case of a finesse close to zero, this modulation becomes simply a sinusodial modulation, as evident from Eq. (4.18) and Eq. (4.22).

It is worth realizing that for a Fabry-Perot etalon in the AFR, i.e. one strong reflection ($r_2 \simeq 1$) combined with a small parasitic reflection ($r_1 \ll 1$), the dominating physical effect does not arise from multiple reflections off the parasitic reflectance r_1, but only from a single parasitic reflection r_1 of the forward- and backward-propagating beams. Therefore, only two

[1] We can also obtain this expression directly from Eq. (4.17) with $E_{\text{back}} = E_0 r_1 + \mathrm{i} t_1 r_2 a^2 e^{\mathrm{i}2\phi} E_{\text{circ}}$.

terms need to be taken into account for the 'circulating' field, see Eq. (4.18), namely the interference of a strong forward propagating field $\propto E_0$ with the parasitic reflection of the backward propagating field $\propto r_1 r_2 E_0$. Similarly, for the backcoupled field, only three terms dominate the behavior (see Eq. (4.22)), namely the interference of the parasitic reflection of the forward-propagating field $\propto r_1 E_0$ with the strong reflection from the HR mirror $\propto r_2 E_0$ and the parasitic reflection of the backward-propagating field strongly reflected by the HR mirror $\propto r_1 r_2^2 E_0$. This is illustrated in the bottom of Fig. 4.15(a) where only the relevant field contributions are shown with solid arrows for $\propto \mathcal{O}(1)E_0$, while terms $\propto \mathcal{O}(r_1)E_0$ are shown in a faint color. All parasitic reflections of order $\propto \mathcal{O}(r_1^2)E_0$ and higher (indicated by the dashed curved arrow of fainter color) can be neglected. This realization makes it easier in Section 4.4.2 to derive the equations for multiple parasitic reflections as is the case for Rayleigh backscattering.

When we first observed the modulation in the AFR while scanning the piezo actuator, the origin of this etalon effect was unknown and we investigated various possible sources for a parasitic reflectance. The same modulation depth was also observed when scanning the frequency of the laser. We found that the visibility and the free spectral range $\mathrm{FSR} = c/(2n\,l)$ (where c is the speed of light, n the refractive index and l the etalon length) changes on the time scale of seconds. The dominant FSR was compatible with an etalon length l including the full length of the fiber[1]. We then suspected that parasitic reflections of the coupling lens lead to this etalon and replaced the coupling lens by a reflective collimator using a parabolic mirror[2], which however did not remove or suppress the observed modulation. We next tested the possible parasitic reflection from the fiber tips which are AR-coated and angle-cleaved under 8° such that the reflected beam is under an angle of 24° w.r.t. the incoming beam. No difference was observed with non-AR coated angle-cleaved fiber tips. Finally, after excluding all other possible sources for parasitic reflections, we found that Rayleigh backscattering in the fiber is responsible for the observed etalon effect, as treated in the next section.

4.4.2 Multiple etalons from Rayleigh backscattering in fiber

Rayleigh scattering is present in any medium and can be seen as the physical origin of the refractive index. If the medium is dense and homogenous, all the light scattered not in exactly the forward direction interferes destructively, such that the light does not scatter laterally [236]. However, this is not the case for an optical fiber since amorphous solids including glass are inhomogeneous. These non-homogeneities mainly originate from frozen density fluctuations produced during fiber drawing when the melted glass cools down [228]. The fused silica fiber core then forms randomly distributed scattering points along the fiber. The small-scale inhomogeneities in an optical fiber can be even viewed with a microscope [237]. Rayleigh scattered light along the fiber leads to damping and is for most wavelengths (especially in the near UV) the limiting and dominant source of fiber attenuation[3], leading to an attenuation of $\alpha_s = A/\lambda^4$ with $A = 0.63\,\mathrm{dB}\,\mu\mathrm{m}^4/\mathrm{km}$ for pure silica [228], which yields

[1] The AFR setup first had a fiber with a length of $l \sim 5\,\mathrm{m}$, such that we observed $\mathrm{FSR} \sim 18(1)\,\mathrm{MHz}$ giving an optical length of $n\,l \sim 8.3(4)\,\mathrm{m}$ which is in agreement with the fiber length plus the additional 0.3 m distance from the fiber to the HR mirror (using the refractive index of our fused silica fiber, $n = 1.51$). Furthermore, the fiber was initially not thermally isolated such that the etalon modulation changed on the timescale of seconds rather than several minutes.

[2] Protected Silver Reflective FC/APC Collimator for 2 mm diameter beam, Thorlabs RC02APC-P01.

[3] According to [236, 238], Rayleigh scattering is usually responsible for $\sim 85\%$ of losses for operation at small enough optical power, whereas the remaining $\sim 15\%$ are due to Raman and Brillouin scattering.

$\alpha_s = 22\,\mathrm{dB/km}$ for $\lambda = 410\,\mathrm{nm}$, close to $\alpha = 28\,\mathrm{dB/km}$ for low-loss silica fibers [239][1] and in agreement with the specified value for our fiber[2]. Doped fibers have a higher attenuation since doping adds additional scattering centers [236], just as increased radiation exposure also leads to additional scattering [240]. One can estimate the attenuation from Rayleigh scattering in fibers for both the glass and doping inhomogeneities with an analytical expression [236], which is outside the scope of this thesis. If the total attenuation α is dominated by scattering, $\alpha \simeq \alpha_s$, the scattered power fraction P_s/P_{in} for a fiber length l (where P_s is the total scattered power and P_{in} the ingoing power into the fiber) is [228]

$$\frac{P_s}{P_{\mathrm{in}}} = 1 - 10^{-\alpha_s l/10} \simeq l\,\alpha_s \frac{\ln 10}{10} \sim 5 \times 10^{-3}, \tag{4.24}$$

where in the last step we approximated the expression for small fiber lengths such that $P_s/P_{\mathrm{in}} \ll 1$ and used the numerical values $l = 0.8\,\mathrm{m}$ and $\alpha_s \sim 30\,\mathrm{dB/km}$. What is important for the discussion here is the fraction η of the scattered light that is guided in the backward-propagating direction through the fiber [228, 236]:

$$\eta = \frac{3}{8\pi^2 n_{\mathrm{core}}^2 (w_0/\lambda)^2} \sim 10^{-3}, \tag{4.25}$$

with the numerical value given for our parameters (mode field radius $w_0 \simeq 1.7\,\mu\mathrm{m}$, core refractive index $n_{\mathrm{core}} \simeq 1.47$, wavelength $\lambda = 410\,\mathrm{nm}$). Combining the two above equations we can give the power fraction R_s of guided Rayleigh backscattered light from the fiber as

$$R_s = \frac{P_s}{P_{\mathrm{in}}} \times \eta = l \times \frac{3\,\alpha_s \ln 10}{80\,\pi^2 n_{\mathrm{clad}}^2 (w_0/\lambda)^2} \sim 5 \times 10^{-6}. \tag{4.26}$$

One may ask whether some fraction of total scattered light is also guided in the forward-propagating direction and adds on top of the transmitted light. However, one can argue that Rayleigh scattering in the forward-propagating direction is not an additional term but simply how light propagates through the medium. Rayleigh scattering can be seen classically as oscillating dipoles re-emitting the incoming field, and the same model applies when deriving the refractive index of a medium. From this argument no additional contribution from Rayleigh scattering is added on top of the forward propagating beam in the fiber, since it is effectively included in the refractive index or reduced propagation velocity of the transmitted field through the medium. Another possible contribution in the forward direction is from Rayleigh scattering under a small angle w.r.t. the forward propagating mode which may excite higher-order modes in the fiber. However, for our fiber[3] the attenuation of the next

[1] This publication reports a total loss of 0.265 dB/km at 1310 nm which can be scaled with λ^4-dependency to 410 nm, assuming that the dominant source of attentuation is due to Rayleigh scattering.

[2] The model PM-S405-XP has a specified attenuation of $\alpha < 30\,\mathrm{dB/km}$ at 488 nm, but a newer model PM-S405-XP+ specifies $\alpha < 50\,\mathrm{dB/km}$ at 405 nm. The model PM-S405-XP distributed by Schäfter+Kirchhoff (sold under PMC-400Si-3.1-NA010) has a specified attenuation of 16.6 dB/km at 488 nm which is closer to the limit from Rayleigh scattering at this wavelength (11.3 dB/km). Scaling this value to 410 nm yields 33.3 dB/km which is close to the value for a similar fiber (Corning PM 40-U40D) for which the inspection report states $\alpha = 37.2\,\mathrm{dB/km}$. Therefore, it is reasonable to assume that for the PM-S405-XP fiber used in the experiment, the attenuation is around $30 - 35\,\mathrm{dB/km}$. The test measurements with the Corning PM 40-U40D fiber indicate that there are $\sim 10\,\mathrm{dB/km}$ losses unrelated to Rayleigh scattering, such that the contribution of the attenuation from Rayleigh scattering would be $25 - 30\,\mathrm{dB/km}$ which is closer to the Rayleigh scattering limit for pure silica.

[3] V-number $V = 2.18$, core radius $a = 1.5\,\mu\mathrm{m}$, relative refractive index difference between core and cladding of 0.25%.

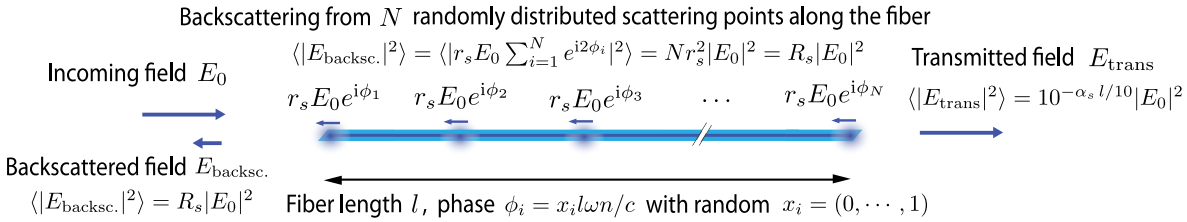

Figure 4.16: Model of Rayleigh backscattering in a fiber. The incoming field E_0 is scattered at N scattering points along the fiber with length l. At each point the backward scattered guided field is $r_s E_0 e^{\mathrm{i}\phi_i}$, where $\phi_i = x_i\, l\omega n/c$ is the phase of the incoming field at the i^{th} scattering center along the fiber, with $\omega = 2\pi\nu$ where ν is the frequency of light, c is the speed of light, n is the refractive index and x_i is a length fraction of the fiber with $x_1 = 0$, $x_N = 1$, and x_i for $1 < i < N$ a random number between 0 and 1. The average of total backscattered guided light through the fiber is $\langle|E_{\text{backsc.}}|^2\rangle = N r_s^2 |E_0|^2$, where $R_s = N r_s^2$ is the fraction from Eq. (4.26).

higher mode (LP_{11}) can be estimated [241] to be 145 dB/m which is many orders of magnitude larger that α_s (the attenuation of higher modes LP_{02}, LP_{12}, LP_{31}, ... is even larger). The strongly suppressed contribution from forward scattering would then predominantly arise from scattering at the two fiber facets, which we neglect in the following model.

The order of magnitude for R_s approximately agrees with the expected value for R_1 from the observed modulation discussed in the previous section, see Fig. 4.15. We shall now explore why this is the case. Initially, we thought that Rayleigh backscattering could not lead to a clearly observed modulation when scanning the fiber-collimator distance or the frequency of the laser, since the interference from randomly distributed points along the fiber should average out, not being able to produce a dominant modulation with a certain free spectral range. However, this is not correct. For example, in gravitational wave detectors the backscattering from the fiber produces non-reciprocal phase noise which does not average out and requires to use a balanced detection scheme [242, 243]. Furthermore, a similar effect has been reported to convert the phase noise of the laser into intensity noise through multiple Rayleigh scattering events [244]. To illustrate how the scattering from randomly distributed points leads to an observed modulation in our case, let us consider the following model.

Model for guided backscattering in the fiber

First, consider the case of back-scattering from the fiber only, i.e. without a retroreflection from the HR mirror as in the AFR. We model the Rayleigh scattering as N randomly distributed scattering points along the fiber starting from one scattering point at the beginning of the fiber, and one scattering point at the end of the fiber, see Fig. 4.15. With an incoming field E_0, each scattering point couples a field $r_s E_0 e^{\mathrm{i}\phi_i}$ backward into the fiber with a phase $\phi_i = x_i\, l\omega n/c$ relative to the incoming field, where l is the fiber length, $\omega = 2\pi\nu$ where ν is the frequency of light, c is the speed of light and n is the refractive index. x_i is a length fraction of the fiber with $x_1 = 0$, $x_N = 1$ and x_i for $1 < i < N$ a random number following a uniform distribution between 0 and 1. The total backscattered field is then given by:

$$E_{\text{backsc.}} = r_s E_0 \sum_{i=1}^{N} e^{\mathrm{i}\,2\phi_i}. \tag{4.27}$$

Note that the contribution of each scattering center to the total backscattered field at the fiber input comes along with a phase factor corresponding to twice the distance x_i to the scattering center: the incoming field propagates to the i^{th} scattering center accumulating a phase ϕ_i, and the scattered field accumulates an additional phase ϕ_i on the backward path to the fiber input.

The above expression corresponds to a random walk in two dimensions or the complex plane [245, 246]. The average of the field is zero, $\langle E_{\text{backsc.}} \rangle = 0$, but the expectation value for the squared absolute value (intensity) scales with the number of scattering centers N, $\langle |E_{\text{backsc.}}|^2 \rangle = N r_s^2 |E_0|^2$. This result can be related to the guided backscattered fraction as $R_s = N r_s^2$. Assuming that the density of scattering points is constant, we expect the total backscattered power fraction to increase linearly with fiber length l. Note that we neglect the transmission losses from each scattering center, that is the scattered light that is not guided, but for clarity include the total loss in the absolute value of the transmitted field in Fig. 4.16, $\langle |E_{\text{trans}}|^2 \rangle = 10^{-\alpha_s l/10} |E_0|^2 \simeq (1 - l\alpha_s \ln 10/10) |E_0|^2$.

The above model is evaluated in Fig. 4.17, where in (a) the backscattered power fraction is calculated for different numbers of scattering centers N and a fiber length of 5 m assuming the total backscattered guided fraction of $R_s \sim 2.5 \times 10^{-5}$, thereby determining $r_s = \sqrt{R_s/N}$. The left plot shows the modulation when changing the frequency of light (with $\lambda \simeq 410\,\text{nm}$) sent through the fiber. For the simple case of only two scattering centers ($N = 2$, black curve), one at the beginning of the fiber ($x_1 = 0$) and one at the end ($x_2 = 1$), the modulation arises from the interference of two fields with a phase difference of $l\omega/c$. We define the free spectral range FSR to be the frequency period of the signal modulation when the laser frequency is detuned, which yields $\text{FSR} = c/(2\,l\,n) \simeq 20\,\text{MHz}$. The right plot shows the distribution of free spectral ranges, obtained from a Fourier transform of the left plot. For larger N (e.g. $N = 12$ in blue or $N = 10^4$ in orange) the phase difference between the interfering fields can be $< l\omega/c$ and hence $\text{FSR} > c/(l\,n)$. Note that the experimentalist would still dominantly deduce $\text{FSR} \sim c/(l\,n)$ since a typical setup makes it difficult to separate the higher FSR components from various noise sources and drifts in the system. Fig. 4.17(b) shows how for a fixed number of scattering centers but different fiber lengths the modulation and the FSR spectrum relate to the fiber length.

Experimental test of the model for guided scattering in the fiber

To test the above model, we used a ∼45 m long angle-cleaved bare fiber of similar type as the one used in our experiment[1]. The setup is shown in Fig. 4.18. By splitting off a light fraction with a non-polarizing beamsplitter and detecting it on the intensity stabilization photodiode (PD), we stabilize the power of the 410 nm laser light before the fiber to 0.2 mW. The power launched into the fiber P_{in} can only be inferred from the transmitted power through the full length fiber. The transmitted power through the full length fiber ($l_0 = 45\,\text{m}$) was measured to be $P_{\text{trans}}^{l_0} = 81\,\mu\text{W}$. Assuming the attenuation of $\alpha = 37\,\text{dB/km}$ from the manufacturer's inspection report leads to $P_{\text{in}} = P_{\text{trans}}^{l_0}/10^{-\alpha\, l_0/10} = 119\,\mu\text{W}$ of power coupled into the fiber, corresponding to a coupling efficiency of only ∼60% due to the non-optimal distance between the fiber tip and the coupling lens (which was optimized to reduce the background from the angle-cleaved fiber tip reflection as explained below). The beamsplitter is also used on the

[1] Distributed by Fujikura, Corning product description 03518800001 PM 40-U40D, Fujikura description SC40-PS-U40D, Fiber ID SNOYGFK00074, specified attenuation at 410 nm is $\alpha < 50\,\text{dB/km}$, test result from the Fujikara inspection report at 410 nm is $\alpha = 37.22\,\text{dB/km}$ (no uncertainty on the value is given).

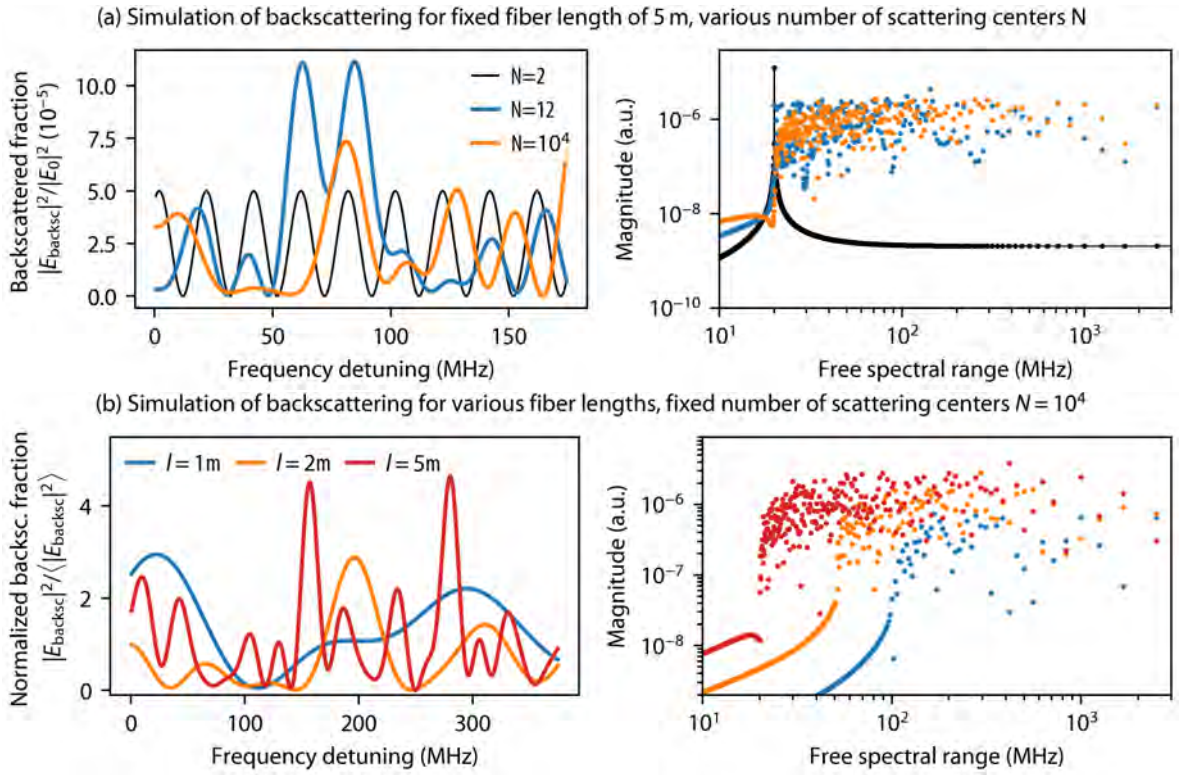

Figure 4.17: Simulations of backscattered light from a fiber using the model from Fig. 4.16. In (a) the fiber length is kept constant at 5 m, resulting in a fixed average value of total backscattered guided fraction $R_s \sim 2.5 \times 10^{-5}$, thereby determining $r_s = \sqrt{R_s/N}$. The left plot shows the backscattered fraction $|E_{\text{backsc.}}|^2/|E_0|^2$ evaluated for different numbers of scattering centers as a function of frequency detuning for $\lambda = 410\,\text{nm}$ and $n = 1.5$. Having only two scattering centers (one at the beginning of the fiber and one at the end, $N = 2$, black curve) produces a modulation with a free spectral range of FSR $= c/(2\,l\,n) = 20\,\text{MHz}$. The right plot shows the FSR distribution obtained from a Fourier transform of a similar left plot (using a larger frequency detuning up to 5 GHz for a denser spacing in the FSR domain). For a larger number of scattering centers N (blue and orange) the free spectral range distribution has a cutoff $\text{FSR}_{\text{min}} = 20\,\text{MHz}$ (this cutoff is smoothed out due to finite sampling points). In (b) the number of scattering centers is kept constant, $N = 10^4$, and the fiber length is varied. The backscattered fraction in the left plot is now normalized to the average $\langle|E_{\text{backsc.}}|^2\rangle = R_s|E_0|^2$. The FSR distribution on the right demonstrates how the total fiber length is manifested in the lowest possible $\text{FSR}_{\text{min}} = c/(2\,l\,n)$.

returning path to split a fraction $r_{\text{BS}} \simeq 0.45$ of the backscattered light from the fiber and measure it on the backreflection photodiode[1]. We took the factor r_{BS} into account along with the power calibration, such that the given signal corresponds to the backreflected power directly from the fiber before the beamsplitter. The backreflection from the fiber is measured non-destructively[2] for different guided fiber lengths by introducing bend loss at different

[1]Thorlabs PDA36A operated at 70 dB gain (5 kHz bandwidth) with a pre-amplifier of gain 100 and 3 kHz (6 dB roll-off) low-pass filter.

[2]Since the fiber is very strongly bent, care has to be taken not to bend the fiber at the same positions too often. However, since many measurements were performed with the fiber, this could not be fully prevented such that the fiber broke several times. Fortunately, this happened closer to one of the fiber ends such that the experiment could be restored with almost the full initial fiber length.

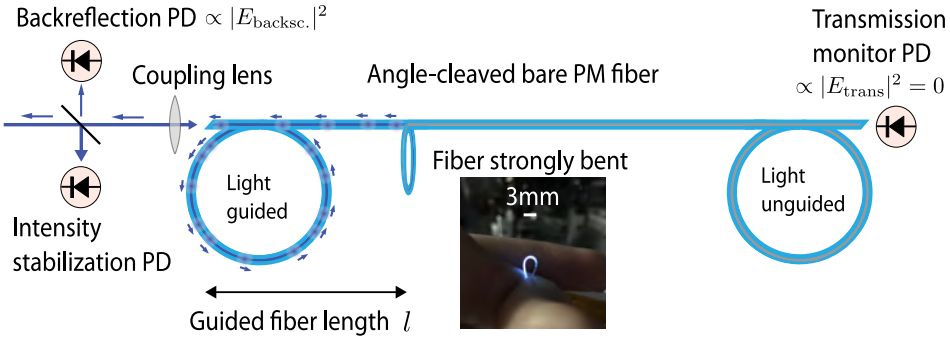

Figure 4.18: Setup to measure Rayleigh backscattering in the fiber and to test the model shown in Fig. 4.16 and Fig. 4.17. Laser light is sent through a beamsplitter to stabilize its intensity before being coupled into an angle-cleaved bare fiber. After a certain fiber length l the fiber is strongly bent (bend radius of $< 3\,\text{mm}$) such that no light is guided after this point. The point where the fiber is bent is systematically varied while the backscattered light is detected at the backreflection photodiode (PD). The transmission monitor PD placed after the fiber is used to ensure that the fiber is bent strongly enough such that no light is transmitted through the fiber.

positions: when strongly bending the fiber (bend radius less than 3 mm), the light escapes into the cladding and is not guided in the core anymore.

The results for the average power measured at the backreflection PD for each (guided) fiber length l are shown in Fig. 4.19(a). When the laser is blocked (faint diamond points) we detect a $\sim$30 nW signal from the stray light as well as electronic background noise which has been subtracted here such that with the laser blocked the signal value is around zero. Furthermore, when the laser is unblocked, a fraction of light coupled into the fiber is reflected from the non-AR coated angle-cleaved fiber tip (Fresnel reflection of 4% $\sim 8\,\mu\text{W}$), reaches the edge of the coupling lens and is focused onto the backreflection PD. Care has been taken to minimize this spurious signal to around $P_{\text{bkg}} \sim 10\,\text{nW}$ by changing the distance from the fiber tip to the coupling lens (thereby resulting in a non-optimal fiber coupling efficiency). The approximately linear increase in the average backreflected signal for different fiber lengths is then attributed to the backscattering, $P_{\text{backsc}} \simeq p_l \times l$. From the linear fit (gray dotted line), $P = p_l \times l + P_{\text{bkg}}$ we obtain a slope of $p_l = 0.578\,\text{nW/m}$, which gives the following guided backscattered power fraction from the fiber per meter fiber length ($l = 1\,\text{m}$):

$$R_s^{410\,\text{nm}} \simeq \frac{p_l \times l}{(P_{\text{in}} + P_{\text{trans}}^{l_0})/2} \simeq 5.8 \times 10^{-6}, \tag{4.28}$$

in good agreement with the expected value from Eq. (4.26). Assuming $\eta = 9.65 \times 10^{-4}$ (Eq. (4.25) with $n_{\text{core}} \sim 1.470$ and measured $w_0 \simeq 1.75(5)\,\mu\text{m}$ at $\lambda = 410\,\text{nm}$), the above fraction gives $\alpha_s \simeq 26.0\,\text{dB/km}$. In the above equation we assumed an average power inside the fiber $P_{\text{in}}(\int_0^{l_0} 10^{-\alpha l/10})/l_0 \simeq (P_{\text{in}} + P_{\text{trans}}^{l_0})/2$ for all fiber lengths. More accurately, one can fit the backscattered power based on a Beer-Lambert law:

$$P = P_{\text{in}} \times 10^{-(\alpha-\alpha_s)l/10} \times (1 - 10^{-\alpha_s l/10}) \times \eta + P_{\text{bkg}}, \tag{4.29}$$

where the launched power into the fiber is calculated from $P_{\text{in}} = P_{\text{trans}}^{l_0}/10^{-\alpha\, l_0/10}$ with mea-

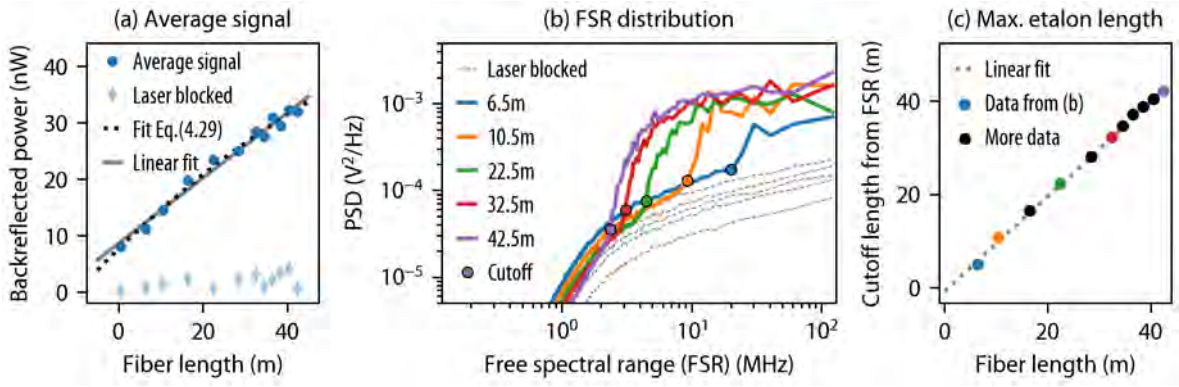

Figure 4.19: Measurement of fiber backscattering at 410 nm with the setup shown in Fig. 4.18. In (a) the average backreflected power is shown for different (guided) fiber lengths. The blue data points are fit linearly (gray curve), and with a more accurate model (black dotted curve) from Eq. (4.29) based on the Beer-Lambert law. In (b) the power spectral density (PSD) is plotted for different free spectral ranges (FSR) obtained from a Fourier transform of the time-resolved signal of backscattered light when periodically detuning the frequency (see text for details). Data for only five fiber lengths are shown for the sake of clarity. For each fiber length a cutoff FSR can be determined (colored points). This cutoff $\mathrm{FSR}_{\mathrm{cutoff}}$ can be related to the maximal etalon length l_{cutoff} from $\mathrm{FSR}_{\mathrm{cutoff}} = c/(2\,l_{\mathrm{cutoff}}\,n)$ where c is the speed of light and n the refractive index. These cutoff lengths are plotted in (c) against the (guided) fiber length, where colored points show the data from (b) and black points show additional data. As expected, the cutoff etalon length corresponds to the guided fiber length.

sured P_{trans} for $l_0 \simeq 45\,\mathrm{m}$ assuming[1] the value of the total attenuation $\alpha = 37\,\mathrm{dB/km}$. The factor $10^{-(\alpha-\alpha_s)l/10}$ accounts for all other attenuation losses leading to the reduced power in the fiber. Since the fiber length in our case is not as large such that the exponential function deviates strongly from the linear approximation, the parameter η from the above equation cannot be fitted reliably due to a strong correlation with α_s and must be set as an known input parameter. With $\eta = 9.65 \times 10^{-4}$ and measured $P_{\mathrm{in}} = 119\,\mu\mathrm{W}$, the fit yields $\alpha_s \simeq 27.7\,\mathrm{dB/km}$, giving $R_s^{410\,\mathrm{nm}} \simeq 6.4 \times 10^{-6}$ for $l = 1\,\mathrm{m}$. The uncertainty of this measurement is dominated by the accuracy of the power meter. The uncertainty of the power measurement is estimated to be $\sim 7\%$ from the specifications of the power meter[2], yielding an uncertainty of $\sim 1.5\,\mathrm{dB/km}$ for α_s. The measured value for α_s is close to the expected value for pure silica, $\alpha_s = A/\lambda^4 = 22\,\mathrm{dB/km}$ for $\lambda = 410\,\mathrm{nm}$ with $A = 0.63\,\mathrm{dB}\mu\mathrm{m}^4/\mathrm{km}$ [228]. A higher value for α_s is expected due to impurities which add additional scattering centers.

We also measured the time-resolved signal of the backscattered light while periodically detuning the laser frequency. The frequency of the light coupled into the fiber is periodically swept with a 120 MHz span in 20 ms. From the Fourier transform of the average signal within

[1] Another assumption could be to identify the total attenuation only with attenuation from Rayleigh scattering, $\alpha = \alpha_s$ (i.e. assuming that all the attenuation is caused by Rayleigh scattering) which can be then fitted along in the above equation. However, we find that this assumption is not appropriate for our fiber. For the fiber used here, an additional attenuation of $\alpha \sim 10\,\mathrm{dB/km}$ from absorption and bend losses is present as indicated by the data. If we assume $\alpha = \alpha_s$, the fit yields $\alpha = \alpha_s \simeq 27.8\,\mathrm{dB/km}$, which would then be inconsistent with the value of $\alpha = 37\,\mathrm{dB/km}$ from the manufacturer's inspection report at 410 nm. For measurements at 486 nm we measured $\alpha = 27(2)\,\mathrm{dB/km}$. Again we would find from Rayleigh backscattering data $\alpha = \alpha_s \simeq 14.4\,\mathrm{dB/km}$ assuming $\alpha = \alpha_s$, which would then be inconsistent with the measured total attenuation.

[2] Thorlabs PM160: calibration uncertainty ±5%, power linearity ±1%, active area uniformity ±1%.

a sweep period of 20 ms, the distribution of free spectral ranges (i.e. modulation frequencies when detuning the laser) is calculated, see Fig. 4.18(b) showing only five different fiber lengths for clarity. The measured distribution resembles the theoretical prediction from Fig. 4.17. The 3 kHz low-pass filter in the system corresponds to a free spectral range of FSR ~ 2 MHz, below which the signal rapidly drops. The gray dashed curves show the background signals with blocked laser light. For each fiber length, the cutoff free spectral range (colored marker points) can be converted into the maximal etalon length, $l_{\max}$, using FSR $= c/(2\,n\,l_{\max})$, where c is the speed of light and $n \simeq 1.5$ the fiber core refractive index. These cutoff lengths from Fig. 4.18(b) are shown as colored points in Fig. 4.18(c). Additional data points not plotted in Fig. 4.18(b) are shown in black as well as a linear fit to all data point taken together (gray dashed curve). The fit yields a ratio of $l_{\max}$ to the fiber length l which is in agreement with the expected ratio of one within 2%. This measurement confirms the model prediction that the information about the fiber length is encoded in the time-resolved backscattered signal when periodically detuning the frequency of light sent into the fiber.

We also repeated the above measurement at a longer wavelength of 486 nm. The transmitted power for $l_0 \simeq 38$ m was measured to be $P^{l_0}_{\text{trans}} \simeq 76\,\mu$W, leading to

$$P_{\text{in}} = P^{l_0}_{\text{trans}}/10^{-\alpha\, l_0/10} \simeq 96\,\mu\text{W} \tag{4.30}$$

of light power coupled into the fiber assuming[1] $\alpha = 27$ dB/km. From the linear model we measured $p_l = 0.293$ nW/m which leads to the guided backscattered power fraction per meter fiber length ($l =$1 m) of:

$$R_s^{486\,\text{nm}} \simeq \frac{p_l \times l}{(P_{\text{in}} + P^{l_0}_{\text{trans}})/2} \simeq 3.4 \times 10^{-6}. \tag{4.31}$$

Assuming $\eta = 1.1 \times 10^{-3}$ (Eq. (4.25) with $n_{\text{core}} \sim 1.465$ and measured $w_0 \simeq 1.95(5)\,\mu$m at $\lambda = 486$ nm) the above fraction gives $\alpha_s \simeq 13.4$ dB/km. Fitting the data with Eq. (4.29) yields $\alpha_s \simeq 14.4$ dB/km, giving $R_s^{410\,\text{nm}} \simeq 3.6 \times 10^{-6}$ for $l = 1$ m. As above, the uncertainty for the determination of α_s is dominated by the power measurement and is around ~ 1 dB/km. As for 410 nm, the measured value for α_s is slightly higher than the expected value for pure silica, $\alpha_s = A/\lambda^4 = 11.3$ dB/km for $\lambda = 486$ nm with $A = 0.63\,\text{dB}\mu\text{m}^4/\text{km}$ [228]. From the scaling of Rayleigh scattering one would expect a factor of $(486\text{nm}/410\text{nm})^4 \simeq 1.97$ for the ratio of α_s at the two wavelength, which is in agreement with the observed ratio. Note that R_s does not necessarily scale the same as α_s with the wavelength. According to Eq. (4.25) the parameter η explicitly depends on the wavelength. Typically, also the mode radius w_0 depends on the wavelength which is not explicitly taken into account Eq. (4.25), but included in the above estimation with different values of w_0 for the two wavelengths. Moreover, n_{core} from Eq. (4.25) also depends on the wavelength, though this dependency is negligible here.

AFR case: interference with a strong reflection

Using the above model for Rayleigh backscattering, we can now investigate its effect on the AFR. In the AFR, the effect of Rayleigh backscattering from the fiber is combined with the strong reflection from the HR mirror which we assume to be at a distance l_{HR} from the fiber

[1] There is no specified value for the attenuation at 486 nm. However, we measured the attenuation to be $\alpha = 27(2)$ dB/km from the transmission at three different fiber lengths ($l \simeq 38\,\text{m}, 5\,\text{m}, 0.5\,\text{m}$) without changing the fiber coupling, i.e. when the fiber broke off at $l \simeq 5\,\text{m}, 0.5\,\text{m}$.

of length l with refractive index n. Each scattering center forms a Fabry-Perot etalon with the HR mirror. We can extend the model of a single etalon in Section 4.4.1 to N Fabry-Perot etalons by calculating the circulating field of each scattering center and taking it as the incoming field for the next scattering center. We neglect the losses in the fiber but only take into account a field transmission factor of a on a single path from the end of the fiber to the HR mirror[1]. We then obtain the following expression:

$$\begin{aligned} E_{\text{circ}} &\simeq \mathrm{i}E_0 e^{\mathrm{i}l\omega n/c} \times \left(1 + a^2 r_2 r_s e^{\mathrm{i}2(l_{\text{HR}}\omega/c + l\omega n/c - \phi_1)} + (a^2 r_2 r_s e^{\mathrm{i}\,2l_{\text{HR}}\omega/c + l\omega n/c - \phi_1)})^2 + \cdots\right) \\ &\quad \times \left(1 + a^2 r_2 r_s e^{\mathrm{i}\,2(l_{\text{HR}}\omega/c + l\omega n/c - \phi_2)} + \cdots\right) \times \left(1 + a^2 r_2 r_s e^{\mathrm{i}\,2(l_{\text{HR}}\omega/c + l\omega n/c - \phi_3)} + \cdots\right) \times \cdots \\ &= \frac{\mathrm{i}E_0 e^{\mathrm{i}l\omega n/c}}{\prod_{i=1}^{N}(1 - a^2 r_2 r_s e^{\mathrm{i}2(l_{\text{HR}}\omega/c + l\omega n/c - \phi_i)})}, \end{aligned} \tag{4.32}$$

where each sum in the parantheses multiplies the incoming field after each scattering center by the geometrical sum analogously to Eq. (4.17). Compared to Eq. (4.17), here we consider the circulating field at the fiber end facing the HR mirror and for clarity include the overall phase factor $e^{\mathrm{i}l\omega n/c}$ relative to the fiber input. The optical distance from the HR mirror to each scattering center is $l_{\text{HR}} + nl(1 - x_i)$ since we number the scattering centers from the fiber end facing the input field (as in Fig. 4.16). The round-trip phase for each scattering center is therefore $2(l_{\text{HR}}\omega/c + l\omega n/c - \phi_i)$, where $\phi_i = x_i\, l\omega n/c$. Note that in the above calculation we neglected the multiple scattering events of distinct scattering centers within each etalon. However, from the discussion in Section 4.4.1 we found that for the case of a Fabry-Perot etalon with an HR mirror ($r_2 \simeq 1$) and a small parasitic reflection ($r_1 = r_s \ll 1$) the physical effect of the etalon is dominated only by terms of order $\mathcal{O}(r_1)E_0$. Therefore, we can also neglect all other multiple scattering events of order $\mathcal{O}(r_s^2)E_0$ in the above expression, such that the circulating field is simply given by the interference of the incoming field with the backscattering of the beam reflected by the HR mirror:

$$E_{\text{circ}} \simeq \mathrm{i}E_0 e^{\mathrm{i}l\omega n/c} + \mathrm{i}E_0 a^2 r_2 r_s e^{\mathrm{i}(3ln + 2l_{\text{HR}})\omega/c} \sum_{i=1}^{N} e^{-\mathrm{i}\,2\phi_i}. \tag{4.33}$$

The power fraction $|E_{\text{circ}}|^2/\langle|E_{\text{circ}}|^2\rangle$ using the above equation is evaluated in Fig. 4.20 for different numbers of scattering centers as well as $l = 0.8\,\text{m}$, $n = 1.5$, $l_{\text{HR}} = 0.3\,\text{m}$, $\lambda = 410\,\text{nm}$, $R_s = 5 \times 10^{-6}$, $a^2 = 0.95$ and $r_2 = 1$. Consider first the simple case of only one scattering center at each fiber end: $x_1 = 0$ and $x_2 = l$ ($N = 2$), shown in black in Fig. 4.20. For $a^2 \simeq 1$ and $r_2 \simeq 1$, the circulating field is proportional to:

$$E_{\text{circ}}(N = 2) \propto 1 + r_s e^{\mathrm{i}2(ln + l_{\text{HR}})\omega/c} + r_s e^{\mathrm{i}\,2l_{\text{HR}}\omega/c}. \tag{4.34}$$

Neglecting the terms of order $\mathcal{O}(r_s^2)$, there are two modulation frequencies when detuning the laser frequency: $\text{FSR}_{\text{max}} = c/(2l_{\text{HR}})$ and $\text{FSR}_{\text{min}} = c/(2ln + 2l_{\text{HR}})$. This is what is visible in the right plot showing the free spectral range distribution. If we now add more scattering centers within the fiber, the dominant interference with the strong field component produces modulations with a free spectral range in between those two values (blue and orange points

[1] This is a good approximation for our short 0.8 m fiber since only 0.6% of light power is lost in the fiber assuming 30 dB/km loss, but around 4% are lost due to imperfect AR coatings of the fiber tips and 8 surfaces of the collimator.

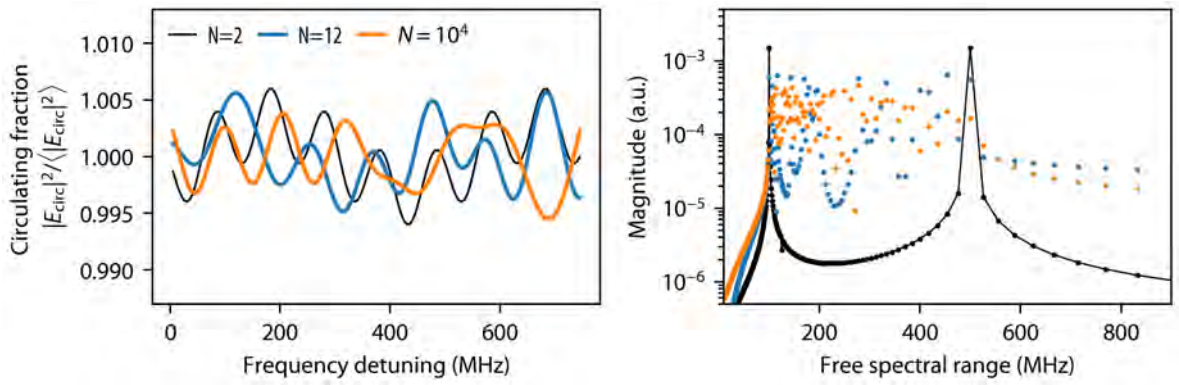

Figure 4.20: Simulations of the circulating power in the AFR with Rayleigh backscattering from a fiber according to Eq. (4.33) with parameters $l = 0.8\,\mathrm{m}$, $n = 1.5$, $l_{\mathrm{HR}} = 0.3\,\mathrm{m}$, $\lambda = 410\,\mathrm{nm}$, $R_s = 5 \times 10^{-6}$, $a^2 = 0.95$ and $r_2 = 1$, for different number of scattering centers N. The left plot shows the modulation whereas the right plot shows the distribution of the free spectral ranges. For $N = 2$ (two scattering centers at each end of the fiber), only two modulation frequencies are present, and for more scattering centers distributed along the fiber (blue and orange curves) the free spectral ranges lie approximately in between these two frequencies.

for $N = 12$ and $N = 10^4$, respectively). The experimentalist would mainly deduce the lower free spectral range from the simulated signal in the left plot, since modulations with a higher free spectral range are difficult to separate from the typical noise in the setup.

Similar to Eq. (4.22) for the case of a single etalon, the backcoupled beam in the AFR includes the interference of the strong reflection from the HR mirror with the backscattered light before the HR mirror reflection, and with the backscattered light of the backward-propagating beam reflected by the HR mirror:

$$E_{\mathrm{back}} = E_0 r_s \sum_{i=1}^{N} e^{\mathrm{i}\,2\phi_i} - E_0 a^2 r_2 e^{\mathrm{i}2(ln+l_{\mathrm{HR}})\omega/c} - E_0 a^4 r_2^2 r_s e^{\mathrm{i}4(ln+l_{\mathrm{HR}})\omega/c} \sum_{i=1}^{N} e^{-\mathrm{i}\,2\phi_i}. \tag{4.35}$$

The different terms from Eq. (4.33) and Eq. (4.35) are visualized in Fig. 4.21(a), where we neglect all second-order reflections of the scattering centers based on the discussion in Section 4.4.1. Fig. 4.21(b) shows an example of the modulation for $N = 10^4$, $R_s = 10^{-5}$ and $a^2 = 0.95$. Note that the modulation in the backcoupling is much smaller as compared to the circulating intensity, and in fact the modulation in the backcoupling would exactly vanish for $a^2 = 1$ and $r_2 = 1$ just as in the case of a single etalon. In Fig. 4.21(c) the average peak-to-peak modulation depth $\langle\xi\rangle$ for the circulating intensity (orange points) and the backcoupled intensity (blue points) has been calculated from the standard deviation σ of the corresponding modulated intensity fraction:

$$\langle\xi_{\mathrm{circ}}\rangle = 2\sqrt{2}\,\sigma_{|E_{\mathrm{circ}}|^2/\langle|E_{\mathrm{circ}}|^2\rangle}, \quad \langle\xi_{\mathrm{back}}\rangle = 2\sqrt{2}\,\sigma_{|E_{\mathrm{back}}|^2/\langle|E_{\mathrm{back}}|^2\rangle}. \tag{4.36}$$

The factor $2\sqrt{2}$ is justified by comparing to a single sinusoidal modulation, where the peak-to-peak value is a factor of $2\sqrt{2}$ larger than the standard deviation. The calculation has been performed for $a^2 = 0.95$ as a function of the total backscattering fraction R_s for fixed value of scattering centers $N = 10^4$, thereby defining $r_s = \sqrt{R_s/N}$. The solid curves show ξ_{circ} (orange) and ξ_{back} (blue) for a single etalon with $r_1 = \sqrt{R_s}$, which match the average modulation depth well. Therefore, we find that the average modulation depth of the circulating

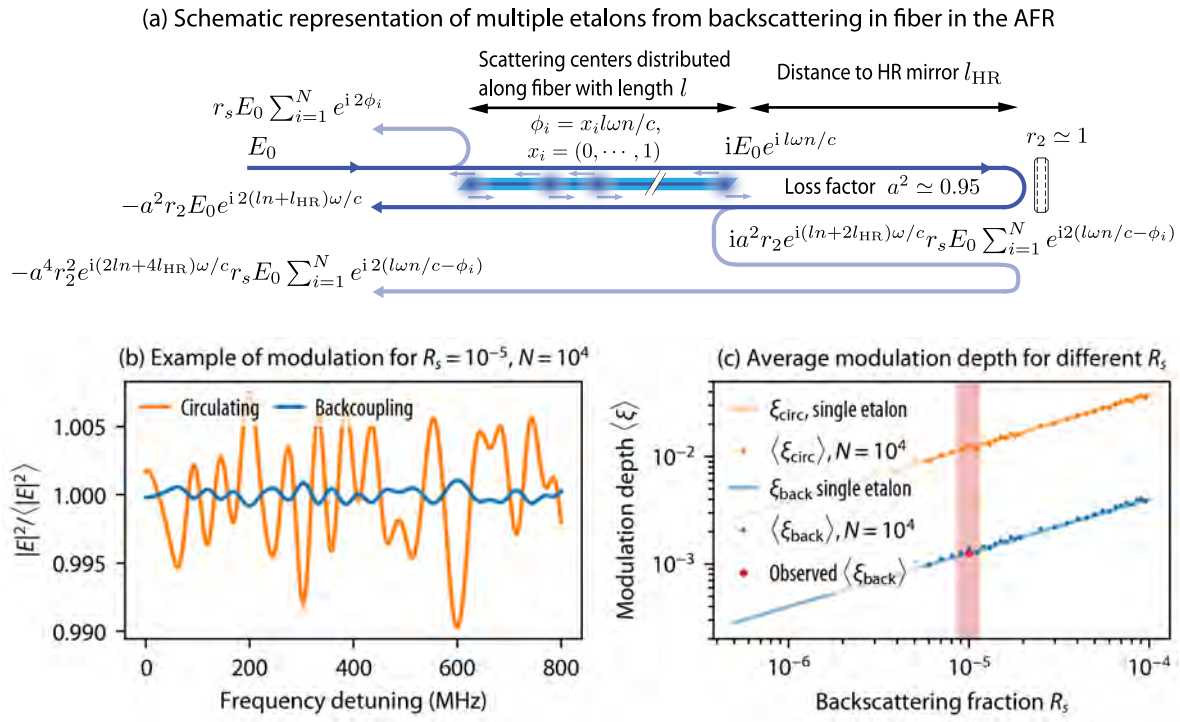

Figure 4.21: (a) Scheme of multiple etalons in the AFR from Rayleigh backscattering in the fiber. The model of backscattering in the fiber of length l from Fig. 4.16 is combined with a reflection r_2 from the HR mirror at a distance l_{HR} to the fiber. Since $r_2 \simeq 1$ and $r_s \ll 1$, based on the discussion of a single etalon in Section 4.4.1 and Fig. 4.15, all second-order reflection from the scattering centers are neglected. Therefore, the circulating field has only two contributions: the incoming field and the backscattered field from the backward-propagating beam through the fiber. The backcoupled beam has three terms: the backscattered field from the forward-propagating beam, the backward-propagating strong reflection of the HR mirror, and the backscattered field of the backward-propagating beam which is reflected back by the HR mirror. No losses are assumed in the fiber but the field transmission factor $a^2 \simeq 0.95$ on the round-trip path $2l_{HR}$ is taken into account. (b) Example of a modulation in the circulating (orange) and backcoupled (blue) intensity fraction for $N = 10^4$, $R_s = 10^{-5}$ and $a^2 = 0.95$. (c) Average modulation depth for the circulating (orange) and backcoupled (blue) intensity calculated as a function of the total backscattered fractions R_s. The solid curves show the expectation assuming a single etalon with $R_1 = R_s$, same as solid curves in Fig. 4.15(b), thereby demonstrating that the etalon effect from backscattering of the fiber can be viewed as a single etalon with the parasitic reflectance corresponding to the total backscattered fraction.

and backcoupled field is given by the value for a single etalon (Eq. (4.20) and Eq. (4.23)) assuming a parasitic reflection of the total backscattered light fraction from the fiber:

$$\langle\xi_{\text{circ}}\rangle = 4a^2\sqrt{R_s}, \quad \langle\xi_{\text{back}}\rangle = 8\sqrt{R_s}(1-a^2). \tag{4.37}$$

The observed modulation (red point) leads to $R_s \sim 10^{-5}$ which is the same order of magnitude as expected from Eq. (4.26) and measured (for a similar but different fiber) in Eq. (4.28). The difference might be due to a higher fraction of scattered light guided into the fiber than approximated by Eq. (4.25), where a Gaussian beam is assumed. However, a whole factor of two is unlikely since Eq. (4.25) gave good agreement with the measurements in Eq. (4.28) testing the backscattering model.

It shall be noted that $\langle\xi_{\text{back}}\rangle$ strongly depends on the transmission factor which is only estimated. Also note that $\langle\xi_{\text{back}}\rangle$ and $\langle\xi_{\text{circ}}\rangle$ are average modulation depths, but the measurement in Fig. 4.14 shows only a single modulation value from a 30 s long signal. We typically observe that with our thermally insulated fiber, the intensity fluctuations of the backcoupled signal due to Rayleigh scattering are on the order of $\sim 5-20$ minutes. On the other hand, we observe that if the fiber is intentionally heated or scrambled, the modulation averages out over a typical fiber-collimator piezo actuator averaging time of 30 s (30 piezo actuator scans with 1 Hz periodicity). More measurements could be performed in the future to determine $\langle\xi_{\text{back}}\rangle$ and $\langle\xi_{\text{circ}}\rangle$ more accurately from repeated measurements throughout the day.

The average modulation depth scales with the square root of the fiber length:

$$\langle\xi_{\text{back}}\rangle, \langle\xi_{\text{circ}}\rangle \propto \sqrt{R_s} \propto \sqrt{l}. \tag{4.38}$$

We first observed the modulation with a longer fiber ($l = 5\,\text{m}$) and the three-lens collimator which has higher losses due to reduced backcoupled fraction of the collimator ($a^2 \simeq 0.9$). Therefore, in this configuration we observed a larger modulation on the order of $\xi_{\text{back}} \sim 1\%$ and $\xi_{\text{circ}} \sim 3\%$, leading to the conclusion of $R_1 \sim 5 \times 10^{-5}$ in agreement with the expected scaling from the above. We also tested the etalon behavior for different losses, e.g. by reducing the backcoupled fraction with the horizontal or vertical piezo actuators on the HR mirror, and confirmed the expected behavior: while ξ_{circ} remained the same, ξ_{back} strongly increased for higher losses (reduced backcoupled fraction).

To suppress the etalon effect from Rayleigh backscattering in the fiber, we therefore used a shorter fiber length of $l = 0.8\,\text{m}$ compared to the previous setup with $l = 5\,\text{m}$, suppressing the modulation as seen by atoms by a factor of 2.5. However, the previous setup was used at the wavelength of 486 nm (hydrogen 2S-4P transition measurement). Assuming the same fraction η of scattered light coupled back into the fiber, the backscattered fraction approximately scales as $R_s \propto 1/\lambda^4$, such that $R_s(\lambda = 410\,\text{nm}) \sim 2R_s(\lambda = 486\,\text{nm})$ which leads to approximately the same modulation depth with the longer fiber of the previous setup at the higher wavelength as compared to the modified setup with a shorter fiber at the lower wavelength. To further suppress the etalon effect from the fiber, we stabilized the circulating intensity, which is discussed in the next section.

4.5 Intensity stabilization

Since the spectroscopy signal depends on the intensity of the exciting laser beams, it is advantageous to implement an intensity stabilization in the AFR. Various sources like pointing fluctuations, polarization drifts, electronic noise in the laser system or frequency-dependent AOM efficiencies lead to intensity fluctuations already before the light reaches the AFR fiber. In the previous setup only the intensity of this light before the fiber was stabilized [197]. However, the intensity of the wavefront-retracing beams in the AFR is then still affected by the coupling efficiency of the AFR fiber, subject to pointing fluctuations, as well as by the frequency-dependent interference from the Rayleigh scattering discussed in the previous section. In order to stabilize the intensity of the wavefront-retracing beams, we use the summed signal of all four quadrants of the PMT behind the HR mirror (see Fig. 4.1). Due to the low power reaching the PMT (70–400 pW) and the resulting large shot noise, only a low-bandwidth stabilization can be achieved such that the high-bandwidth first intensity stabilization (with PD1 in Fig. 4.1 serving as detector) is still needed to suppress

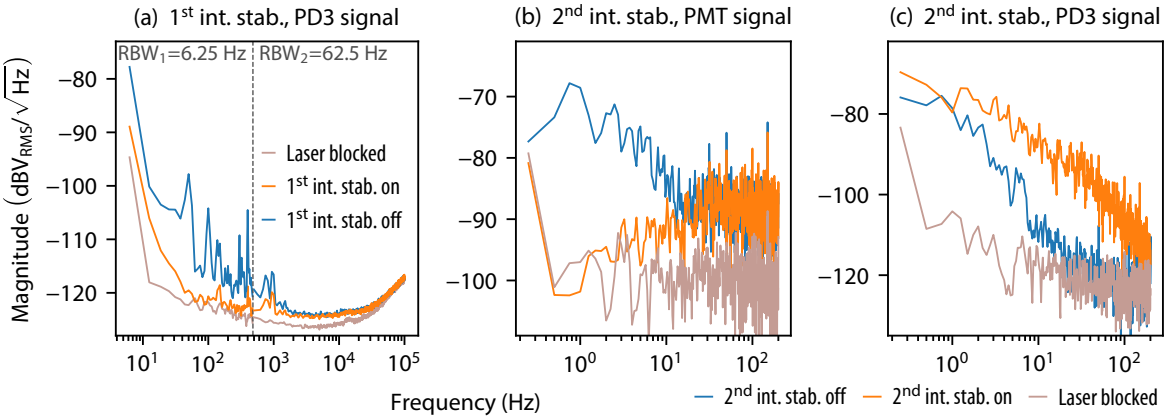

Figure 4.22: Spectra of the PMT and PD3 photodetector signals showing the performance of the two intensity stabilizations of the AFR, shown for active stabilization on (orange line) or off (blue line) along with the background noise (gray line). (a): Spectrum on the out-of-loop PD3 detector demonstrating the performance of the first high-bandwidth (∼30 kHz) intensity stabilization to PD1 (with second intensity stabilization switched off). The frequency interval up to 500 Hz is plotted with a resolution bandwidth (RBW_1) of 6.25 Hz and with $\mathrm{RBW}_2 = 62.5$ Hz for higher frequencies. (b) and (c): Second intensity stabilization of wavefront-retracing beams using the PMT signal after the HR mirror (with first intensity stabilization switched on). The in-loop PMT spectrum in (b) demonstrates the bandwidth of around 10 Hz while additional noise is imprinted on PD3 as shown in (c).

other noise. Two electro-optic modulators[1] (EOM 1 and EOM 2 in Fig. 4.1) are used as voltage-controlled waveplates and, combined with polarizing beamsplitters, serve as actuators for the two intensity stabilizations. A low-pass filter is placed before EOM 2 to adapt for the lower feedback bandwidth.

Fig. 4.22 shows the performance of the two intensity stabilizations by comparing the spectra for the corresponding stabilization switched on (orange line) and off (blue line). In (a) the spectrum of the out-of-loop detector PD3 demonstrates the ∼30 kHz bandwidth of the first intensity stabilization (with the second intensity stabilization switched off). The spectrum of the PMT signal which is the in-loop detector of the second intensity stabilization is shown in (b), where the feedback bandwidth of ∼10 Hz is observed from the merging point of the blue and orange data lines. The second intensity stabilization imprints the noise of the stabilized signal on the PMT to the light before the fiber, which is observed on the spectrum of the PD3 signal in (c). Note that also shot noise from the PMT signal is imprinted which cannot be fully avoided. By using a low-pass filter with a corner frequency of 80 Hz in the second intensity stabilization, we found a compromise between a sufficient suppression of noise and an acceptable additional imprinting of shot noise at lower frequencies.

When scanning over the atomic resonance, at each point the frequency applied to the AOM in Fig. 4.1 is switched, thereby causing a short dead time (in our case ∼400 µs using the signal generator Rohde & Schwarz SMC100A) where no light is diffracted by the AOM. The error signal generated from noise during that dead time perturbs the feedback loops. To avoid this, we use a pulse generator triggered to the frequency switching, which places the feedback loops on hold during and after the dead time. This hold time is adapted to each of the feedback loops (20 ms for 1st int. stab., 22 ms for 2nd int. stab., 50 ms for tip-tilt stab.).

[1] Conoptics KD*P (potassium dideuterium phosphate) Crystal Series 350-50.

Furthermore, we implemented the possibility to automatically switch the power of the spectroscopy laser beams by using digital step attenuators[1] connected in series at the output of the photodiodes. In this way, the signal levels of the feedback loops remain unchanged without the need to modify the feedback loop parameters. The power switching allows us to perform nearly simultaneous spectroscopy measurements with different laser powers, thereby investigating the effect of light-force induced line distortions and systematic frequency shifts in the spectroscopy measurement [205, 71].

4.6 Polarization monitor

Achieving the best possible linear polarization of the wavefront-retracing beams is important for both the hydrogen and deuterium spectroscopy of 2S-nP transitions. For both isotopes, the residual circularly polarized light leads to the first-order Zeeman shift which vanishes for fully linearly polarized light. Recalling Chapter 2, for deuterium the residual circular polarization may lead to a systematic shift from the simultaneous excitation of different hyperfine components in combination with the initial state population asymmetry. The linear polarization rotation angle ψ is especially important for resolved quantum interference between the two fine structure components as has been discussed in Chapter 2. One way to achieve a well-controlled polarization in the AFR would be to place a polarizer after the collimator. However, such a polarizer might lead to optical etalons, wavefront distortions, and residual intensity fluctuations, and requires additional space currently not available in our setup. Therefore, we choose to work only with a well-characterized polarization-maintaining (PM) fiber.

In the following, we assume monochromatic, fully coherent and thus fully polarized laser light described by a Stokes vector $\vec{S} = (S_0, S_1, S_2, S_3)$. Using the Stokes formalism, the residual circularly polarized light is given by S_3/S_0, where S_0 is the total intensity and S_3 is the intensity difference between right and left circularly polarized light [133]. The linear polarization rotation angle ψ is given by the other two Stokes parameters as $\tan 2\psi = S_2/S_1$. For fully polarized light (zero unpolarized light fraction), the polarization extinction ratio PER of the beam (defined in the same way as for polarizers, see Section 4.1) is related to the residual circular polarized light fraction as $|S_3/S_0| \sim 2\sqrt{1/\mathrm{PER}}$ for $\mathrm{PER} \gg 1$.

Since the main component of our system leading to polarization imperfections (i.e. linearly polarized light, which remains fully polarized but acquires a certain circularly polarized fraction) is the polarization-maintaining (PM) fiber, we first consider the physical origin of the polarization imperfections in Section 4.6.1. In Section 4.6.2 a model for the determination of the polarization state after the fiber from the polarization state of backcoupled light is developed. It is found that only the absolute value of circularly polarized fraction can be determined unless its sign or the linear polarization rotation angle are known otherwise. Section 4.6.3 presents experimental tests of the model, and Section 4.6.4 concludes with polarimetry data during spectrosopy measurements.

4.6.1 Limitations of the polarization-maintaining (PM) fiber

In theory, a perfectly symmetric single-mode fiber preserves polarization, but in reality manufacturing imperfections (leading to a not perfectly symmetric core and cladding along the

[1] Mini-Circuits ZX76-31R5A-PPS+.

whole fiber) as well as imperfections such as micro-stresses or perturbations of the environment distort the symmetry. The distorted symmetry introduces coupling between the two (in the ideal symmetric case degenerate) orthogonally polarized modes of the fundamental (TEM_{00}) mode which changes the polarization state along the fiber [247]. Therefore, polarization-maintaining (PM) specialty fibers which we use in our AFR setup have been developed.

Two different effects may lead to imperfectly preserved linear polarization in a PM fiber: first, the alignment of the input polarization with the PM axis of the fiber and second, the random polarization mode coupling. The first effect can in principle always be minimized, while the latter limits the performance of PM fibers due to intrinsic properties. The imperfect alignment of the input polarization can be caused by not exactly matching the linear polarization rotation angle of the input polarization with the orientation of the PM axis. Furthermore, stress-induced birefringence of various components (e.g. the fiber connectors or the coupling lens) can distort the launched polarization into the fiber. However, even if the polarization launched into the fiber is perfectly linear (zero circularly polarized fraction), and its linear polarization rotation angle is perfectly aligned with the PM axis, the outgoing polarization will still have a small circularly polarized fraction due to random polarization mode coupling.

In the following, we describe both effects of polarization imperfections from the PM fiber in more detail. In our setup, we minimize imperfections due to alignment such that the imperfections due to random mode coupling dominate the outgoing circularly polarized fraction.

4.6.1.1 Aligning the input polarization with the polarization-maintaining axis of the fiber

In order to achieve a high PER after a PM fiber[1], it is important to use incoming light with a high PER, and to align the linear polarization rotation angle of the incoming light to the polarization-maintaining axis of the fiber. For our PM fiber, this alignment has to be better than 1°, which we achieve by placing the polarizers in the PSPU (see Fig. 4.1) on rotation mounts. However, typically the input polarization is not limited by how accurately the linear polarization can be rotated, but by the stress-induced birefringence of the fiber connectors which distort the launched polarization into the fiber. Furthermore, in our setup we find that the coupling lens as well as mirrors and beamsplitters after the polarizers may distort the input polarization due to stress-induced birefringence. In principle, the net effect of stress-induced birefringence of all components (including the connectors) can always be compensated. We minimize this effect by also placing the fiber onto a rotation mount, and systematically varying the orientation of both the polarizers and the fiber mount. For their optimal orientations, the polarization is aligned to both the stress-induced birefringence axis of optical components after the polarizers (such that the resulting effect from their birefringence is minimized), and the polarization-maintaining axis of the fiber.

Let us now consider how the alignment of the input polarization influences the outgoing polarization. Polarization-maintainting fibers feature a large instrinsic birefringence:

$$\delta_{\mathrm{PM}} = \frac{2\pi}{\lambda}\,\Delta n\, l = \frac{2\pi}{\lambda}\, l\, \gamma\, (T_0 - T), \tag{4.39}$$

[1]Note that though the polarization-maintaining properties of the PM fiber are typically characterized by the PER, the PM fiber does not “extinct” any polarization component (in contrast to polarizers or polarizing fibers).

where λ is the wavelength of light, l is the fiber length, and $\Delta n = n_{\text{slow}} - n_{\text{fast}}$ is the refractive index difference between the orthogonal axes of the fiber, which are called the slow and the fast axis depending on which refractive index is higher. For our PM fiber at room temperature this difference is $\Delta n \simeq 2 \times 10^{-4}$. For the PANDA-based PM fibers this high birefringence is achieved through stress-inducing rods made of doped silica glass which have a different coefficient of thermal expansion than the fiber cladding. The refractive index difference can then be expressed by $\Delta n = \gamma(T_0 - T)$ where T is the temperature of the fiber, $T_0 \simeq 600\,\text{K}$ is the softening temperature of the stress-inducing glass rods and $\gamma \simeq 5{\times}10^{-7}\,\text{K}^{-1}$ is the thermal coefficient of the birefringence of the PM fiber [248]. Since the two orthogonal polarization modes propagate at different velocities along the fiber, the cross-coupling between the polarization modes averages out due to the intereference between the fields which add up with both positive and negative phases. The prerequisite for this polarization maintenance is that all the light is coupled into only one of the polarization modes (i.e. the incoming linear polarization is aligned with either of the two polarization-maintaining axes of the fiber) and that the fiber length is much longer than the beat length $L_p = \lambda/\Delta n \simeq 2\,\text{mm}$ (where we used $\lambda = 410\,\text{nm}$ for the laser wavelength) for which the phase shift between the fast and the slow propagating mode is equal to 2π.

For non-optimal coupling, the PM fiber is therefore described by a waveplate with retardance δ_{PM} and the birefrigence axis orientation β_{PM}. Since δ_{PM} is large (for $l = 1\,\text{m}$ from above: $\delta_{\text{PM}} \sim 10^3\pi$) and fluctuating due to environmental perturbations, non-optimal coupling ($\beta_{\text{PM}} \neq 0$) strongly influences the polarization behavior. When coupling both polarization modes into the PM fiber, $\beta_{\text{PM}} = \pi/4$, the outgoing polarization from the PM fiber is extremely sensitive to stress and temperature, which makes the PM fiber ideal for either force/pressure or temperature sensor applications [249, 250]. Instead, for optimal coupling $\beta_{\text{PM}} = 0$ and zero incoming circularly polarized fraction, the model predicts that the PM fiber does not change the incoming linear polarization since a waveplate with perfectly aligned birefringence axis to the incoming linearly polarized light does not change the polarization.

Fig. 4.23 shows the magnitude of typical polarization fluctuations (e.g. polarization variations due to deformation, twisting and heating of the fiber) in dependence on the relative orientation β_{PM} between the linear polarization rotation before the fiber and the PM axis, corresponding to the orientation of the polarizer before the fiber. The offset was chosen such that $\beta_{\text{PM}} \bmod \pi/2 \simeq 0$ corresponds to the optimal alignment. The top plots show the fluctuations of circularly polarized fraction S_3/S_0, and the bottom plots the fluctuations in the linear polarization rotation angle ψ, with error bars representing all possible polarization values. The left plots show the coupling into the slow axis of the fiber ($\beta_{\text{PM}} \simeq 0$) and the right plots show the coupling into the fast axis of the fiber ($\beta_{\text{PM}} \simeq \pi/2$. For each polarizer orientation the fiber was deformed, heated and twisted to ensure that all possible polarization states are reached. Using the above model, for nearly optimal coupling, $\beta_{\text{PM}} \simeq 0$, one finds $S_3/S_0 \simeq \sin\delta_{\text{PM}} \times 2\beta_{\text{PM}}$, such that S_3/S_0 fluctuates between $\pm 2\beta_{\text{PM}}$ for all possible δ_{PM}, see dashed curves on the upper plots. Similarly, for $\beta_{\text{PM}} \simeq 0$ one finds that the linear polarization rotation angle ψ fluctuates between $\pm\delta_{\text{PM}}$, see dashed curves on the bottom plots. For $\beta \simeq \pi/4$ (not shown here) all possible polarization states would be reached such that the circularly polarized fraction fluctuates between $S_3/S_0 = -1$ and $S_3/S_0 = +1$ and the linear polarization angle between $\psi = -\pi/2$ and $\psi = +\pi/2$.

The magnitude of polarization fluctuations for optimal alignment, as is typically the case for connectorized fibers, depends on which fiber end the light is coupled in. In Fig. 4.23, orange data corresponds to coupling into one fiber end (named B) and blue data correspond

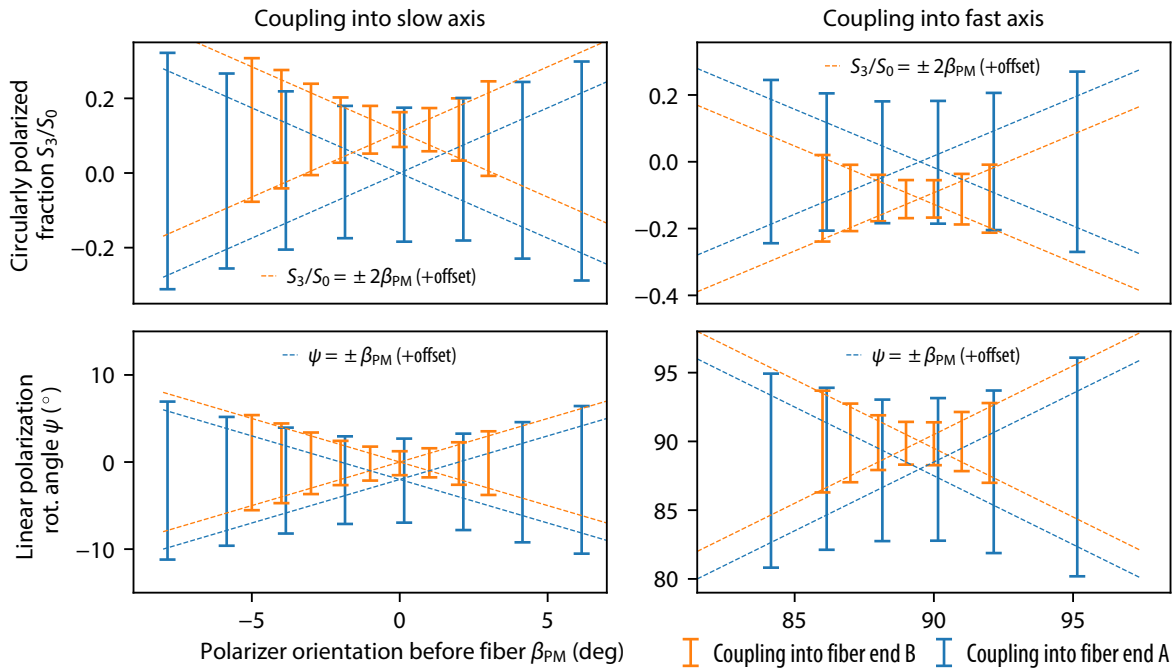

Figure 4.23: Polarization fluctuations after the fiber for different angles around the optimal coupling into the slow (left) or fast (right) polarization-maintaining axes of the fiber, $\beta_{PM} \simeq 0$ or $\pi/2$. The top figures show the fluctuations of circularly polarized fraction S_3/S_0, the bottom figures show the fluctuations of linearly polarized rotation angle ψ. Dashed curves show the maximum and minimum values $S_3/S_0 \sim \pm 2\beta_{PM}$ and $\psi \sim \pm\beta_{PM}$ expected from the model for non-optimal coupling described in the text, plus a possible offset. The fluctuations are represented by error bars giving all possible polarization values for a given polarizer orientation before the fiber. At each polarizer orientation the fiber was deformed, twisted and heated for a few minutes to ensure that all possible polarzation states are reached. Blue bars show the data for coupling into one fiber end A, orange bars show the data for coupling into the other fiber end B. The polarization fluctuations are minimized but non-zero for both fiber ends when the polarizer orientation matches the polarization maintaining axis. When coupled into the fiber end B, the fluctuations are smaller than for the other end and show an offset of $\pm \sim 0.1$ in the circularly polarized fraction. This offset is attributed to the stress-induced birefringence of the connector at the fiber end A. Therefore, when coupled into the fiber end A, the fluctuations are larger since the stress-induced birefringence at the connector disturbs the purity of coupled polarization into the fiber. On the other hand, the much smaller residual polarization fluctuations for coupling into fiber end B are predominantly attributed to random polarization mode coupling which cannot be avoided and limit the performance of PM fibers.

to coupling into the other fiber end (named A). Coupling into fiber end A produces much stronger fluctuations as compared to coupling into fiber end B. Furthermore, the fluctuations are in much better agreement with expectation from the model for the fiber end B (orange dashed curve), though an offset is present. This is in agreement with what one would expected if one of the fiber connectors has much stronger stress-induced birefringence. In this case, the connector at fiber end A produces an offset in the circularly polarized fraction on the order of $S_3/S_0 \sim \pm 0.1$ when the light is coupled into fiber end B. The sign is opposite between the slow and fast axes of the fiber, as expected from modelling the fiber connector as a waveplate with a small retardance on the order of $\delta_{con} \sim 0.1$ rad. For the linear polarization orientation β_{con} w.r.t. the birefrigence axis, such a waveplate produces an offset of $S_3/S_0 \sim \delta_{con} \sin 2\beta_{con}$,

resulting in $S_3/S_0 \sim \pm\delta_{\mathrm{con}}$ for orthogonal linear polarizations maximally misaligned with the birefringence axis. If, on the other hand, light is coupled into the fiber end A, the purity of linear polarization is decreased resulting in a reduced PER $\sim 4/\beta_{\mathrm{con}}^2 \sim 26\,\mathrm{dB}$ of light coupled into the fiber. The situation is then equivalent to a misaligned linear polarization rotation before the fiber with $\beta_{\mathrm{PM}} \sim \delta_{\mathrm{con}}/2 \sim 3°$, resulting in light coupled into both the fast and the slow axis, and hence giving rise to much stronger fluctuations.

For optimal alignment of linear polarization as well as minimized or compensated stress-induced birefringence before the fiber, the above model of the fiber (waveplate with retardance δ_{PM} and birefringence axis β_{PM}) predicts vanishing polarization fluctuations. However, as seen from the orange data in Fig. 4.23, this is not the case. The origin of these residual polarization fluctuations is called random polarization mode coupling which we discuss in the next section.

4.6.1.2 Limitation from random polarization mode coupling

Typically, for connectorized PM fibers in the near UV, the specified PER of the output polarization (for optimal alignment of input polarization) is around 20 dB, corresponding to a circularly polarized fraction of $|S_3/S_0| < 20\,\%$. Typically, stress-induced birefringence at the fiber connectors mostly limits the achieved extinction ratio. The resulting stress after connectorizing the fiber cannot be fully controlled. However, in a sample of commercial, connectorized fibers[1] we find that some have a higher extinction ratio of up to 26 dB corresponding to $|S_3/S_0| < 10\,\%$. Even for perfect coupling into a polarization-maintaining axis of the PM fiber ($\beta_{\mathrm{PM}} = 0$ or $\beta_{\mathrm{PM}} = \pi/2$) and large enough fiber length ($l \gg L_p$), the linear polarization is not perfectly maintained. The polarization-maintaining property is then limited by the cross-talk of the two polarization modes which is described by the random mode coupling theory [251, 252]. For optimal coupling, the residual imperfections are therefore not adequatly described by modelling the fiber as a waveplate with δ_{PM} and β_{PM}.

The effect of random mode coupling is summarized in the parameter h describing the rate of power transfer to the cross-polarization state, which has typically values around $h \sim 10^{-3}\,\mathrm{m}^{-1}$. This parameter gives the ultimate limitation of polarization-maintaining properties of the bare fiber (i.e. without any connector) excluding all possible imperfections from non-optimal input polarization. Using the h-parameter one can express the extinction ratio of a bare PM fiber as $\mathrm{PER} = P_{\max}/P_{\min} = 2/(1 - \exp(-2\,h\,l)) \simeq 1/(h\,l)$, where $P_{\max}$ and $P_{\min}$ are the maximal and minimal transmitted optical powers in the two orthogonal polarization directions, yielding PER $\sim 30\,\mathrm{dB}$ for a $l = 1\,\mathrm{m}$ long fiber, in good agreement with our observations. Therefore, the polarization imperfections, which we aim to monitor, mainly arise from random polarization mode coupling along the fiber and not from imperfect alignment of the incoming polarization into the fiber. Note that this extinction ratio is only achieved when the effect of mixed polarization modes coupled into the fiber is minimized. In order for this condition to be satisfied, the stress-induced birefringence of fiber connectors has to be minimized or compensated, the purity of incoming linear polarization has to be maximized, and the incoming linear polarization rotation angle has to be aligned with a polarization-maintaining axis of the PM fiber.

The effect of random polarization mode coupling for perfect input polarization can be

[1] We ordered our connectorized fibers from the company Diamond GmbH. Twice as many connectorized fibers were ordered (6 pieces with 0.8 m length and 4 pieces with 0.4 m length) before sending the remaining fibers with the best extinction ratio (3 pieces and 2 pieces, respectively) to the AR coating (organized by the same company).

modelled as follows. Consider the electric field $\vec{\mathcal{E}} = \hat{x}\mathcal{E}_{0x}\cos(\omega t - kz + \varphi) + \hat{y}\mathcal{E}_{0y}\cos(\omega t - kz)$ of a fully polarized plane wave traveling in the z direction with frequency ω and wavenumber k, where $\mathcal{E}_{0x}$ and $\mathcal{E}_{0y}$ are the amplitudes of the orthogonal field components, and φ is the phase difference between the two orthogonal components (in reality φ depends on z, though this is not relevant here as we consider only a certain propagation length at the output of the fiber). $\hat{x}$ and $\hat{y}$ are the unit vectors along the two orthogonal PM axes of the fiber. Let us consider that a field $\vec{\mathcal{E}}_{\text{in}} = \hat{x}\mathcal{E}_{x,\text{in}}$ is coupled into one of the PM axes (i.e. $\mathcal{E}_{y,\text{in}} = 0$). At the output of the fiber, a small part of the orthogonal field component $\mathcal{E}_y \equiv \mathcal{E}_{y,\text{out}}$ is present, with the phase difference $\varphi = \delta_{\text{PM}}$ corresponding to the retardance between the slow and fast axes. The squared amplitude ratio can be related to the extinction ratio as $\text{PER} = \mathcal{E}_x^2/\mathcal{E}_y^2 = \mathcal{E}_{0x}^2/\mathcal{E}_{0y}^2$, with the field components $\mathcal{E}_{0x}$ and $\mathcal{E}_{0y}$ at the output of the fiber. From these electric field components we can calculate the Stokes vector [133]:

$$\vec{S} = \begin{pmatrix} S_0 \\ S_1 \\ S_2 \\ S_3 \end{pmatrix} = \begin{pmatrix} \mathcal{E}_{0x}^2 + \mathcal{E}_{0y}^2 \\ \mathcal{E}_{0x}^2 - \mathcal{E}_{0y}^2 \\ 2\,\mathcal{E}_{0x}\mathcal{E}_{0y}\cos\varphi \\ 2\,\mathcal{E}_{0x}\mathcal{E}_{0y}\sin\varphi \end{pmatrix}. \tag{4.40}$$

Using the polarization extinction ratio we can obtain the circularly polarized fraction as:

$$S_3/S_0 = \frac{2\,\mathcal{E}_{0x}\mathcal{E}_{0y}\sin\varphi}{\mathcal{E}_{0x}^2 + \mathcal{E}_{0y}^2} \simeq \frac{2\,\mathcal{E}_{0y}\sin\varphi}{\mathcal{E}_{0x}} = 2\sqrt{\eta}\sin(\phi_0 + 2\pi\, l\,\gamma\Delta T\,/\lambda), \tag{4.41}$$

where in the last step we used the inverse polarization extinction ratio $\eta = 1/\text{PER}$ and expressed the phase difference using δ_{PM} from Eq. (4.39) with a temperature difference ΔT and a constant phase offset ϕ_0.

Typical fluctuations in the circularly polarized fraction with the PM fiber used in the AFR are shown in Fig. 4.24(a). We observe that after thermally insulating the part of the fiber outside of vacuum, only slow polarization drifts occur. For the measurement shown here, the vacuum chamber was openend and a polarimeter was placed after the fiber. The fluctuations of the circularly polarized fraction are then on the timescale of 15 min, shown on the upper plot in Fig. 4.24(a). The bottom plot shows the temperature at the fiber[1]. A clear correlation between the temperature and polization is observed. At the time around 11:30 in Fig. 4.24(a) the air around the fiber was heated up (using a heat gun) to $\sim 45°\text{C}$, resulting in fast polarization fluctuations. The circularly polarized fraction from this time period is plotted in Fig. 4.24(b) against the temperature around the fiber, clearly matching the expected behaviour from the above model. Eq. (4.41) is used along with an offset (accounting for possible stress-indunced birefringence of the connector and/or the collimator) to fit the data with fixed $l = 0.8\,\text{m}$ and $\lambda = 410\,\text{nm}$, see gray curve. The parameters $\eta \sim 10^{-3}$ ($\text{PER} \sim 30\,\text{dB}$) and $\gamma \sim 10^{-7}\,\text{K}^{-1}$ agree with the order of magnitude for typical values [248].

[1]For this measurement a small temperature sensor (AD590) was placed inside the thermal insulation of the fiber. Note that the small AD590 sensor is more sensitive to air fluctuations than typical temperature sensors used to monitor the lab temperature (e.g. TE Connectivity HTM2500LF). In our lab, the air conditioning system periodically exhausts cold air, such that the air temperature directly at the air conditioning outlet periodically varies between $\sim 14°\text{C}$ and $\sim 23°\text{C}$ with a period of around 15 min. The sensor monitoring the lab temperature (TE Connectivity HTM2500LF) measures temperature fluctuations of only $\sim 0.5°\text{C}$, since the housing of the sensor acts as a low-pass filter smoothing out the air fluctuations. Therefore, the temperature fluctuations recorded at the fiber inside the thermal isolation with the AD590 sensor are higher at around 2°C. If the AD590 is placed outside the thermal insulation of the fiber, the measured temperature fluctuations are around 4°C.

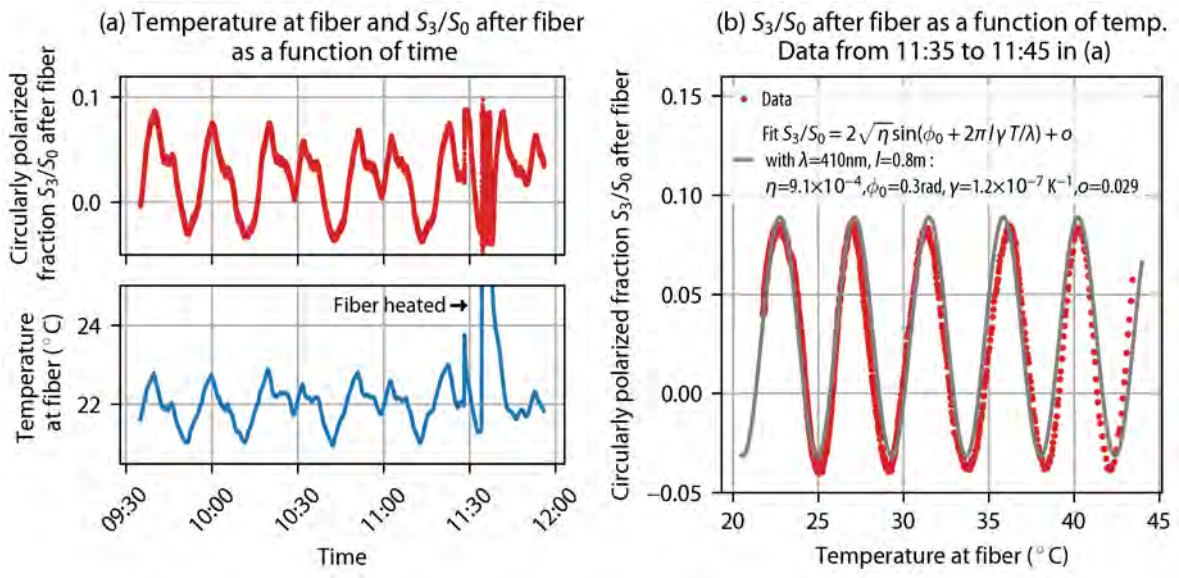

Figure 4.24: Temperature dependence of polarization fluctuations after the PM fiber for optimal alignment of incoming linear polarization w.r.t. the PM axis of the fiber ($\beta_{\mathrm{PM}} \simeq 0$). The residual polarization fluctuations are then due to random mode coupling described by Eq. (4.41). In (a) typical fluctuations of the circularly polarized fraction S_3/S_0 are shown on the upper plot, whereas the lower plot shows the air temperature at the fiber against the shared time axis. At around 11:30 the fiber was heated up to ~ 45°C outside the range of the shown plot. The circularly polarized fraction for this time period is plotted in (b) against the temperature, well described by Eq. (4.41) used to fit the data (see gray curve) for fixed $l = 0.8\,\mathrm{m}$ and $\lambda = 410\,\mathrm{nm}$, and extract the parameters η and γ. An offset o accounts for possible stress-induced birefringence of optical components after the fiber (e.g. the connector and the collimator).

In principle, if the temperature along the fiber is accurately known, this temperature dependence of polarization can be used to extract some information about the polarization after the fiber. However, the fiber must be then also subject to the same bending, mechanical stress and twist all the time, since small perturbations may change the random mode coupling along the fiber and result in a shift of the phase ϕ_0. This condition is difficult to achieve reliably and not possible in our setup where the vacuum part of the fiber moves when the angle between the atomic beam and the laser beam is adjusted (the rotatable cylinder RC shown in Fig. 4.2 rotates and moves the fiber). Though some information, as for example the sign of circularly polarized light, could still probably be extracted, a reliable determination of S_3/S_0 is not possible. Therefore, in the next section we describe how to monitor the polarization after the fiber (as seen by atoms during spectroscopy) from polarimetry of the backcoupled light.

4.6.2 Polarization monitor model

To monitor the polarization in the AFR, we implemented polarimetry of the backcoupled light by placing a polarimeter[1] in the unused beam path before BS 2 as depicted in Fig. 4.1. Note that the same information could be obtained from polarimetry of the light after the

[1] Schäfter+Kirchhoff SK010PA-UV.

HR mirror. However, this would further increase the complexity of the setup and require an in-vacuum polarimeter for $< 100\,\mathrm{pW}$ of laser power. In the following, we summarize how the measured polarization of backcoupled light relates to the polarization after the collimator in the AFR.

Before the light reaches the polarimeter, it passes various optical components, the fiber, and the collimator in the forward- and backward-traveling directions. Independent of the physical origin of polarization imperfections[1], the total birefringence of all non-polarizing components (mirrors, polarization-maintaining fiber, collimator lenses etc.) on the same path for the forward- and backward-traveling directions can be described by the combined Mueller matrix $\hat{R}(\phi)\,\hat{\Gamma}(\delta,\beta)$, where $\hat{R}(\phi)$ is the Mueller matrix of circular birefringence (rotator) and $\hat{\Gamma}(\delta,\beta)$ is the Mueller matrix of a single linear retarder (waveplate) with retardance δ and the birefringence axis oriented at an angle β:

$$\hat{\Gamma}(\delta,\beta) = \begin{pmatrix} 1 & 0 & 0 & 0 \\ 0 & \cos^2 2\beta + \cos\delta \sin^2 2\beta & \sin 4\beta \sin^2 \frac{\delta}{2} & -\sin 2\beta \sin\delta \\ 0 & \sin 4\beta \sin^2 \frac{\delta}{2} & \cos\delta \cos^2 2\beta + \sin^2 2\beta & \cos 2\beta \sin\delta \\ 0 & \sin 2\beta \sin\delta & -\cos 2\beta \sin\delta & \cos\delta \end{pmatrix}, \tag{4.42}$$

$$\hat{R}(\phi) = \begin{pmatrix} 1 & 0 & 0 & 0 \\ 0 & \cos 2\phi & -\sin 2\phi & 0 \\ 0 & \sin 2\phi & \cos 2\phi & 0 \\ 0 & 0 & 0 & 1 \end{pmatrix}. \tag{4.43}$$

The circular birefringence matrix (rotator) is equivalent to a rotation in the plane of polarization by an angle ϕ, and hence is the same matrix as for the coordinate transformation for a rotated lab frame. It can be shown [253, 254] that any non-polarizing birefringent system is described by the combined matrix $\hat{R}(\phi)\,\hat{\Gamma}(\delta,\beta)$. Note that though the matrices $\hat{R}(\phi)$ and $\hat{\Gamma}(\delta,\beta)$ do not commute, the order does not matter since we can always write $\hat{R}(\phi)\,\hat{\Gamma}(\delta,\beta) = \hat{\Gamma}(\delta,\beta')\hat{R}(\phi')$ with $\beta' = \phi + \beta$ and $\phi' = -\phi - 2\beta$, where we used the identities $\hat{\Gamma}(\delta,\beta) = \hat{R}(\beta)\hat{\Gamma}(\delta,0)\hat{R}(-\beta)$ and $\hat{R}(x)\hat{R}(y) = \hat{R}(x+y)$.

The circular birefrigence matrix $\hat{R}(\phi)$ does not change the circularly polarized fraction S_3/S_0, but only the linear polarization rotation angle. For single-mode fibers, one finds that the polarization plane at the output of the fiber is rotated by $\sim 0.07°$ per degree of the fiber's mechanical twist [255, 256]. For polarization-maintaining fibers, this relation is more complicated and depends on various parameters [257]. However, the parameters ϕ, δ and β are only effective parameters describing the overall polarization behaviour of the system, and are not necessarily linked to the circular or linear birefringence of each element (e.g the fiber). The term $\hat{R}(\phi)$ can be non-zero even if none of the physical objects in the system exhibit circular birefringence, e.g. when cascading multiple linear retarders.

Furthermore, it shall be remarked that the matrix $\hat{R}(\phi)$ is similar, but not equal to the matrix of a $\lambda/2$ waveplate, $\hat{\Gamma}(\pi,\beta)$. Though the ideal $\lambda/2$ waveplate also rotates the linear polarization and keeps $|S_3/S_0|$ unchanged, it flips the sign of S_3/S_0. However, one can write $\hat{R}(\phi)$ as a combination of two $\lambda/2$ waveplates: $\hat{R}(\phi) = \hat{\Gamma}(\pi,\phi/2)\hat{\Gamma}(\pi,0)$, where the latter

[1] Note that we assume monochromatic, fully coherent, and fully polarized laser light. If, for example, a pulsed laser source is used, a distinction between uniformly and non-uniformly distributed birefringence has to be made [236]. For our case, non-uniformly distributed birefringence can always be modelled as multiple segments of uniformly distributed birefringence [236], which is equivalent to a single birefringent element.

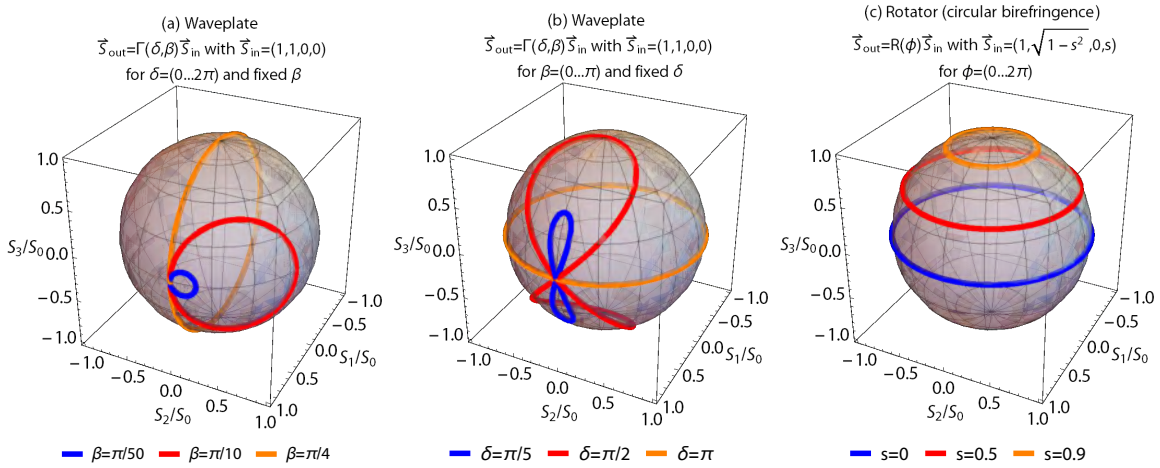

Figure 4.25: Visualization of polarization changes due to linear and circular birefringence on a Poincaré sphere, where the poles represent fully left- or right-handed circularly polarized light states ($S_3/S_0 = \pm 1$). (a) The state of outgoing polarization $\vec{S}_{\text{out}} = \hat{\Gamma}(\delta,\beta)\vec{S}_{\text{in}}$ with $\hat{\Gamma}(\delta,\beta)$ from Eq. (4.42) represents the effect of a linear birefringent element for horizontal linear incoming polarization, $\vec{S}_{\text{in}} = (1,1,0,0)$. The colored curves representing $\vec{S}_{\text{out}}$ are drawn for all possible values of δ and for a fixed β each. The reached polarization states are described by circles on the Poincaré sphere, corresponding to a rotation around a vector lying in the equatorial plane. (b) Same as (a) but with curves for all possible values of β for a fixed δ each. (c) The state of outgoing polarization $\vec{S}_{\text{out}} = \hat{R}(\phi)\vec{S}_{\text{in}}$ with $\hat{R}(\delta,\beta)$ from Eq. (4.43) represents the effects of a circular birefringent element. The curves show $\vec{S}_{\text{out}}$ for all possible values of ϕ for different incoming circularly polarized fraction s in $\vec{S}_{\text{in}} = (1,\sqrt{1-s^2},0,s)$. The circular birefringence does not change the state of circularly polarized light for any incoming polarization, but changes only the rotation of linear polarization. Therefore, it can be viewed simply as a coordinate transformation of the horizontal and vertical linear polarization vectors, which is a rotation around the poles on the shown Poincaré sphere.

matrix also represents the mirror, $\hat{M} = \hat{\Gamma}(\pi,0)$, which flips back the sign[1] of S_3/S_0 after the first $\lambda/2$ waveplate.

The effects of linear and circular birefringence can be visualized on the Poincaré sphere, where the poles represent fully left- or right-handed circularly polarized light states, $S_3/S_0 = \pm 1$. Fig. 4.25(a) and (b) show the effect of linear birefringence described by Eq. (4.42). In (a) the angle β is fixed at three different values (represented by different colors), while the curves are drawn for all possible retardance values δ between 0 and 2π. The reached polarization states are described by circles on the Poincaré sphere, resulting from a rotation around a vector lying in the equatorial plane. In (b) the retardance δ is kept constant at three different values, while the angle β is varied between 0 and π. The case $\delta = \pi/2$ (red) represents a $\lambda/4$ waveplate capable of transforming purely linearly polarized into purely circularly polarized light. The case of a $\lambda/2$ waveplate ($\delta = \pi$) is shown in orange, which rotates the linear polarization only. Also the circular birefringence visualized in Fig. 4.25(c) rotates the linear polarization only. Here, the states of outgoing polarization $\vec{S}_{\text{out}} = \hat{R}(\phi)\vec{S}_{\text{in}}$ with $\hat{R}(\delta,\beta)$ from Eq. (4.43) describe rotations around the poles. The curves show $\vec{S}_{\text{out}}$ for

[1]Note that the mirror flips the sign of S_3/S_0 because the Stokes vector is defined in the coordinate system referenced to the propagation direction of light. However, for the atoms the propagation direction does not matter, such that circularly polarized light drives the same Zeeman transitions (e.g. σ^+) after a reflection.

all possible values of ϕ between 0 and 2π for different incoming circularly polarized fraction s in $\vec{S}_{\text{in}} = (1, \sqrt{1-s^2}, 0, s)$. The rotation around the pole in the equatorial plane for $s = 0$ has the same effect as $\delta = \pi$ (orange curve) in (b), however note the factor of two difference in the angles β vs ϕ (besides, the rotation is in the opposite direction not visible here).

As we will derive below, the case of small β and arbitrary δ (blue circle in Fig. 4.25(a)) corresponds to the case of a PM fiber. The circular birefringence (rotation around the poles as in Fig. 4.25(c)) represents the orientation of the PM axis of the fiber. If the output end of the PM fiber is rotated (in our setup by using the rotation mount of the fiber-collimator system, (RM) in Fig. 4.2), any linear polarization rotation can be reached without changing the magnitude of circularly polarized fraction. This corresponds to transforming the horizontal/vertical lab frame, visualized as rotation of the Poincaré sphere around the poles: the blue circle Fig. 4.25(a) can then be moved in the equatorial plane by rotating the PM axis of the fiber. Constant stress-induced birefringence at the output of the fiber (e.g. the connector or the collimator) corresponds to a fixed rotation around a vector lying in the equatorial plane: the blue circle then moves out of the equatorial plane towards one of the poles resulting in a constant offset in the circularly polarized fraction as e.g. in the case of orange data in Fig. 4.23 for $\beta_{\text{PM}} \simeq 0$ or $\simeq \pi/2$. Since the total birefringence effect can still be described by a single waveplate combined with a rotator, $\hat{R}(\phi)\,\hat{\Gamma}(\delta, \beta)$, at any instant point in time (frozen environmental fluctuations) it is always possible to adjust β by rotating the input linear polarization such that the circularly polarized fraction is zero. However, this then changes the coupling into the PM axis of the fiber and increases the magnitude of circular polarization fluctuations (increased radius of the circle as e.g. the red circle in Fig. 4.25(a)). Therefore, when the PM fiber is combined with a fixed waveplate at the output of the fiber (e.g. from stress-induced birefringence of the fiber connector), the orientation of linear input polarization before the fiber which minimizes the magnitude of circular polarization fluctuations does not necessarily correspond to the orientation of linear polarization which reduces the circularly polarized fraction to zero.

In our original manuscript [110] we presented the polarization monitor model assuming small linear birefringence $\delta \ll 1$ arguing that the linear polarization is known be approximately preserved such that the outgoing circularly polarized fraction after the fiber and the collimator, $(S_3/S_0)_{\text{atom}}$, is small. However, we realized that δ does not have to be small in order to preserve linear polarization, and in fact a waveplate oriented at small β and large δ also preserves linear polarization. Since for both cases, large β and small δ, as well as small β and large δ, the polarization of light stays approximately linear, it is a priori unclear which assumptions can be made (unless one identifies δ with δ_{PM} which is not necessarily true since δ is an effective parameter describing the overall polarization behavior). We therefore perform a general calculation of the problem without any assumptions on β, δ or ϕ. From this calculation we find that there is a unique solution for the absolute value (but not its sign) of circularly polarized light fraction, $|(S_3/S_0)_{\text{atom}}|$, if the circular polarization fraction of outgoing light is known to not exceed $|(S_3/S_0)_{\text{atom}}| < 1/\sqrt{2}$ which is satisfied for preserved linear polarization. We then find that for even smaller circularly polarized light fractions, $|(S_3/S_0)_{\text{atom}}| \lesssim 0.3$, this solution is well approximated by the simple solution for $\beta \ll 1$ in agreement with the intuitive picture and the simple model for random mode coupling from Eq. (4.41). These corrections are summarized in the published erratum [111].

4.6.2.1 Circularly polarized fraction

Consider first a perfect incoming horizontal or linear polarization, $(S_1/S_0)_{\text{in}} = \pm 1$, $(S_2/S_0)_{\text{in}} = (S_3/S_0)_{\text{in}} = 0$. The Stokes vector before the HR mirror as seen by atoms is given by

$$\vec{S}_{\text{atom}} = \hat{R}(\phi)\,\hat{\Gamma}(\delta,\beta)\vec{S}_{\text{in}} = \begin{pmatrix} 1 \\ \pm\cos 2\beta\cos(2\beta+2\phi) \pm \cos\delta\sin 2\beta\sin(2\beta+2\phi) \\ \pm\cos 2\beta\sin(2\beta+2\phi) \mp \cos\delta\sin 2\beta\cos(2\beta+2\phi) \\ \pm\sin 2\beta\sin\delta \end{pmatrix}. \tag{4.44}$$

The Stokes vector of backcoupled light is given by

$$\begin{aligned} \vec{S}_{\text{back}} &= \hat{\Gamma}(\delta,-\beta)\,\hat{R}(\phi)\,\hat{M}\,\vec{S}_{\text{atom}} = \hat{\Gamma}(\delta,-\beta)\,\hat{M}\,\hat{\Gamma}(\delta,\beta)\,\vec{S}_{\text{in}} \\ &= \begin{pmatrix} 1 \\ \pm\cos^2 2\beta \;\; \pm\cos 2\delta\sin^2 2\beta \\ \mp\sin 4\beta\sin^2\delta \\ \mp\sin 2\beta\sin 2\delta \end{pmatrix}, \end{aligned} \tag{4.45}$$

where $\hat{M} = \hat{\Gamma}(\pi,0)$ is the Mueller matrix of the mirror (which can be modelled as a $\lambda/2$ waveplate with a fixed orientation, however, note that the mirror also changes the propagation direction which needs to be taken into account for the following matrices as described below). Note that in the above expression we assume the birefringence system to be reciprocal. Though non-reciprocal effects such as the Faraday rotation or time-dependent temperature gradients ('Shupe-effect') may in principle be present [236, 258], these effects are negligible in our case. The reciprocity of polarization-maintaining fibers can even be exploited to passively remove birefringence fluctuations after the backprogapagation through the same fiber after a reflection by a Faraday mirror [259]. The Mueller matrix $\hat{\Gamma}(\delta,\beta)$ is referenced to the propagation direction and since after the reflection the laboratory coordinate system is reversed, the linear birefringence axis angle β is reversed. However, the rotation angle ϕ due to circular birefringence remains unchanged since it is always referenced to the propagation direction [133].

Consider now the general problem of determining the circular polarization fraction before the mirror (as seen by the atoms), $(S_3/S_0)_{\text{atom}}$, from the measured incoming polarization $\vec{S}_{\text{in}}$ and backcoupled polarization $\vec{S}_{\text{back}}$. Given the measured Stokes parameters of the backcoupled light, $(S_2/S_0)_{\text{back}}$ and $(S_3/S_0)_{\text{back}}$, we found that in general $(S_3/S_0)_{\text{atom}}$ cannot be determined without a sign ambiguity. Furthermore, for the absolute value $|(S_3/S_0)_{\text{atom}}|$ there are two solutions regardless of the values for δ and β:

$$|(S_3/S_0)_{\text{atom}}|_{\pm} = A_{\pm}|s_3|\sqrt{s_3^4 \pm s_2^2\left(2\sqrt{1-s_2^2-s_3^2}\pm 2 \pm s_3^2\right)}, \tag{4.46}$$

with

$$A_{\pm} = \sqrt{\frac{2s_2^2+s_3^2 \pm s_3^2\sqrt{1-s_2^2-s_3^2}}{2s_3^2(s_2^2+s_3^2)(4s_2^2+s_3^4)}}, \tag{4.47}$$

where

$$s_2 \equiv (S_2/S_0)_{\text{back}} + (S_2/S_0)_{\text{in}}, \quad s_3 \equiv (S_3/S_0)_{\text{back}} - (S_3/S_0)_{\text{in}}, \tag{4.48}$$

where we took into account the small measured imperfections of the incoming polarization $(S_2/S_0)_{\text{in}} \lesssim 0.1$ and $(S_3/S_0)_{\text{in}} \lesssim 0.1$ (e.g. in our setup between BS 2 and BS 3 in Fig. 4.1, we

measured $(S_3/S_0)_{\mathrm{in}} \simeq -0.024$ and $(S_2/S_0)_{\mathrm{in}} \simeq -0.036$ for vertical input polarization). We find that the inequality $|(S_3/S_0)_{\mathrm{atom}}|_- \leq 1/\sqrt{2}$ and $|(S_3/S_0)_{\mathrm{atom}}|_+ \geq 1/\sqrt{2}$ is always valid, such that the solution $|(S_3/S_0)_{\mathrm{atom}}|_-$ is unique if the polarization is known to remain approximately linear, as in the case for our AFR with a properly coupled polarization-maintaining fiber. Furthermore, we found that the approximation of the solution $|(S_3/S_0)_{\mathrm{atom}}|_-$ for small circularly polarized light fractions, $|(S_3/S_0)_{\mathrm{atom}}| \lesssim 0.3$, is equivalent to the solution within the approximation[1] $\beta \ll 1$:

$$|(S_3/S_0)_{\mathrm{atom}}|_- \overset{\beta\ll 1}{\simeq} \frac{1}{2}\sqrt{\left((S_3/S_0)_{\mathrm{back}} - (S_3/S_0)_{\mathrm{in}}\right)^2 + \left((S_2/S_0)_{\mathrm{back}} + (S_2/S_0)_{\mathrm{in}}\right)^2}. \quad (4.49)$$

The above equation is accurate to ~ 0.02 for $|(S_3/S_0)_{\mathrm{atom}}| < 0.3$. For $\beta \ll 1$ we then also obtain a simple expression for δ:

$$\delta = \arctan\left(\frac{(S_2/S_0)_{\mathrm{back}} + (S_2/S_0)_{\mathrm{in}}}{(S_3/S_0)_{\mathrm{back}} - (S_3/S_0)_{\mathrm{in}}}\right). \quad (4.50)$$

The above expression determines δ only modulo π, which illustrates the sign ambiguity in determining $(S_3/S_0)_{\mathrm{atom}}$.

Comparing S_3/S_0 from Eq. (4.44) with Eq. (4.41) we find that if the polarization imperfections solely arise from random mode coupling of the PM fiber, we can relate $\sin 2\beta = 2\sqrt{\eta} \ll 1$ and $\delta = \delta_{\mathrm{PM}}$ which again gives an intuitive reason for $\beta \ll 1$. Since δ_{PM} takes any value, this approximation also agrees with the intuitive picture that for a given waveplate with arbitrary values of δ, a linear input polarization is only (approximately) preserved if $\beta \ll 1$. However, in general not only random mode coupling, but also other effects like stress-induced birefrigence may contribute to overall polarization imperfections. Furthermore, the model from Eq. (4.41) describes the effect of random mode coupling only for perfect input polarization in the fiber. In general, the effects of random mode coupling are mixed with an imperfect alignment of the PM axis and/or impure linear polarization before the fiber.

It shall be remarked that for $(S_2/S_0)_{\mathrm{out}} + (S_2/S_0)_{\mathrm{in}} \ll (S_3/S_0)_{\mathrm{back}} - (S_3/S_0)_{\mathrm{in}}$ the above equation is approximately similar to the Eq. (10) of [110] derived with our initial approximation $\delta \ll 1$, however with the important distinction that the above equation only gives the absolute value of $(S_3/S_0)_{\mathrm{atom}}$. In our AFR setup we observe that this condition happens to be usually satisfied such that the absolute value of the (in general incorrect) approximation $\delta \ll 1$ is usually in agreement with the approximation $\beta \ll 1$ within the experimental uncertainty.

4.6.2.2 Linear polarization rotation angle

We found that from the polarimetry of the backcoupled light it is not possible to deduce the linear polarization angle or its variations. The polarization after back-propagation is identical with and without including the circular birefringence term, since $\hat{R}(\phi)\,\hat{M}\,\hat{R}(\phi) = \hat{M}$, where $\hat{M}$ is the Mueller matrix of the mirror. The linear polarization rotation angle ψ_{atom} in the AFR is coarsely given by the orientation of the polarization-maintaining axis of the fiber, which we align by using the rotation mount of the fiber-collimator system (RM in Fig. 4.2). Therefore, the main effect of the linear polarization rotation from the PM fiber for optimal coupling can

[1] Since β can be negative, the approximation is actually $|\beta| \ll 1$. However, we can always choose β to be positive, such that the results on $|(S_3/S_0)_{\mathrm{atom}}|$ remain unaffected. Therefore, in the following we refer to this approximation as $\beta \ll 1$.

simply be described by the orientation ϕ_{PM} of the polarization-maintaining axis at the output of the fiber such that $\phi \approx \phi_{\mathrm{PM}}$. From the polarimetry of the backcoupled light we thus would not aim to determine the absolute value of the linear polarization rotation angle ψ_{atom}, but only its small variations $\Delta\psi_{\mathrm{atom}}$. Comparing Eq. (4.44) to Eq. (4.45), this is only possible as long as the circular birefringence ϕ in the system stays constant. However, recall that the parameter ϕ is only an effective parameter describing the overall polarization behavior, and is not necessarily linked to the circular birefringence of the fiber. Therefore, even though for optimal coupling the approximation $\phi \approx \phi_{\mathrm{PM}}$ is satisfied, the circular birefringence term ϕ cannot generally be assumed to be constant such that small fluctuations of ϕ around ϕ_{PM} are possible. This means that in general also the variations of the linear rotation angle cannot be inferred from the backcoupled light beam.

However, even if ϕ could be assumed to be constant, we found that in general it would not be possible to determine the linear polarization rotation angle changes $\Delta\psi_{\mathrm{atom}}$ unless δ is known to modulo 2π, or equivalently, the sign of $(S_3/S_0)_{\mathrm{atom}}$ is known otherwise or determined with other methods. For $\beta \ll 1$ and for constant ϕ, one finds that the change in the linear polarization angle of the backcoupled light, $\Delta\psi_{\mathrm{back}}$, relates to the change $\Delta\psi_{\mathrm{atom}}$ as seen by the atoms as:

$$\Delta\psi_{\mathrm{back}} \simeq -2\,\Delta\psi_{\mathrm{atom}}\,(1+\cos\delta)\,, \tag{4.51}$$

with the retardance δ from Eq. (4.50). Since Eq. (4.50) determines δ only modulo π, in general it is not possible to determine $\Delta\psi_{\mathrm{atom}}$ unless $\cos\delta$ is known without a sign ambiguity. Furthermore, if $\delta \simeq \pi$ such that $\cos\delta \simeq -1$, from the above equation we find $\Delta\psi_{\mathrm{back}} \simeq 0$ such that the uncertainty on determining $\Delta\psi_{\mathrm{atom}}$ from $\Delta\psi_{\mathrm{back}}$ diverges around these values of δ. Though the variations of the linear polarization rotation angle $\Delta\psi_{\mathrm{atom}}$ cannot be in general determined from the polarimetry of backcoupled light, from the properties of the polarization-maintaining fiber (characterization of polarization fluctuations as in Fig. 4.23) we know that $\Delta\psi_{\mathrm{atom}} \lesssim 3°$, which is sufficient for our experiment.

4.6.3 Experimental test of the polarization monitor model

Initially, we tested our polarization model from [110] (with the incorrect approximation $\delta \ll 1$) by measuring the polarization after the collimator (which blocks the laser beam before the HR mirror and therefore cannot be done in-situ), and comparing it to the derived result from the subsequent measurement of the backcoupled polarization. We found good agreement with our model. However, as demonstrated below, in our spectroscopy AFR setup we observed a special case where the generally incorrect approximation $\delta \ll 1$ is in good agreement with the correct approximation $\beta \ll 1$. As we mentioned in the outlook of [110], we then explored integrating circular polarization in the AFR setup. The tests with circular polarization revealed that the polarization monitor leads to incorrect results, which drew us to rethink our model and lead to the general treatment of the problem and detailed consideration of polarization imperfections from the PM fiber as described in the previous sections. In order to better test our polarization model, we then used a second polarimeter[1] which is capable to measure down to 1 nW laser power and therefore can be placed after the HR mirror to simultaneously measure the polarization as seen by atoms while measuring the backcoupling polarization with the other polarimeter. For this measurement we removed the four-quadrant PMT shown in Fig. 4.2. Furthermore, we increased the laser power before the HR mirror (transmission

[1] Thorlabs PAX1000VIS.

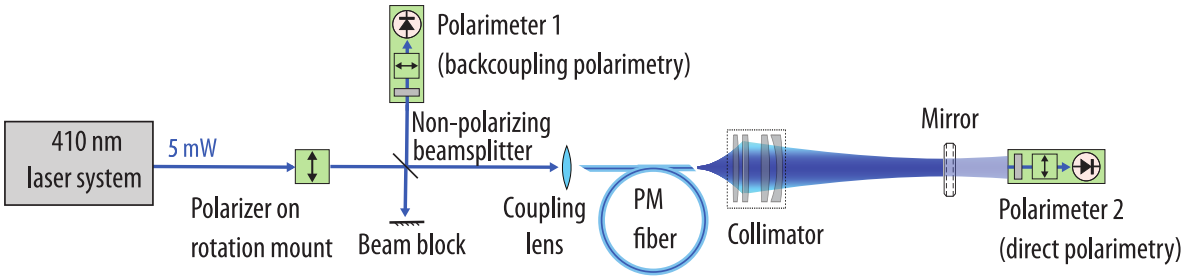

Figure 4.26: Setup for testing the polarization monitor model of light collimated after a PM fiber from polarimetry of backcoupled light. The laser light is first sent through a polarizer on a rotation mount which purifies the linear polarization coupled into the PM fiber and adjusts its rotation angle to match the polarization-maintaining axis of the PM fiber. After being collimated, the light is retroreflected by a mirror while the transmission signal is measured by polarimeter 2 (direct polarimetry of polarization before the mirror). A non-polarizing beamsplitter is placed before the fiber to split one part of the returning laser light to measure its polarization in the polarimeter 1 (backcoupling polarimetry).

$T \simeq 2 \times 10^{-5}$) to $1 - 2\,\mathrm{mW}$ since the typical spectroscopy laser power of $5 - 30\,\mu\mathrm{W}$ is too low for a large enough transmission signal for the polarimeter.

In addition to testing the polarization monitor with a second polarimeter in our spectroscopy setup, we built a separate test setup where we used a less ideal polarization-maintaining fiber (with polarization extinction ratio of $\sim$20 dB) to observe a significant difference between our initial and corrected models. This simple setup in shown in Fig. 4.26. We start with the same narrow-linewidth laser at 410 nm and purify the polarization by sending the light through a Glan-Thompson polarizer. This polarizer is placed on a rotation mount to adjust the linear polarization rotation angle relative to the polarization-maintaining axis of the fiber. Then the light passes a non-polarizing 50:50 beamsplitter[1] which is needed to split one part of the backward-propagating light for measuring the polarization of the backcoupled light with the first polarimeter[2]. After the light is coupled into and sent through the PM fiber, it is collimated and retroreflected by the mirror (in the test setup we used a 90:10 beamsplitter[3] as a mirror). The transmission signal is measured by a second polarimeter (polarimeter 2, "direct polarimetry").

Typically, all mounted optics are subject to stress-induced birefringence which distorts the polarization and needs to be characterized separately. Similar to the spectroscopy setup, also in the test setup of Fig. 4.26 the non-polarizing beamsplitter and/or the mirror would distort the polarimetry measurements from the first and/or the second polarimeter. To minimize these imperfections, we mounted these optics very loosely while measuring the polarization of transmitted or reflected light through the optic to ensure that no stress-induced birefringence effects change the measured Stokes parameters on a level above $\sim 1\%$, which corresponds to the accuracy of our polarimeters[4].

[1] Thorlabs BSW10.

[2] Schäfter+Kirchhoff SK010PA-UV, the same polarimeter as used in the spectroscopy setup for measuring the polarization of backcoupled light.

[3] Thorlabs BSX11.

[4] In principle, a more accurate self-calibrating polarimeter [260] can be used in the future for more accurate measurements. However, though an order of magnitude more accurate, due to the precision rotation stages required for higher accuracy, this self-calibrating polarimeter is more than two orders of magnitude slower compared to the commercial polarimeters ($\sim$ 100 s measurement time for a single polarization measurement compared to $<$ 1 s measurement time).

In contrast to the test setup with minimized imperfections from stress-induced birefringence, in our spectroscopy setup, the imperfections from the beamsplitter and the HR mirror are characterized separately. The effect of the beamsplitter is described in the next section. For direct polarimetry in the spectroscopy setup, we also characterized the HR mirror and measured that the HR mirror acts in transmission as a waveplate with a retardance of ~ 0.35 rad. We also tested the potential birefringence effect of the coating and found no polarization distortion in the HR mirror reflection (retardance < 0.005 rad), thereby demonstrating that the stress-induced birefringence originates in the substrate. Note that if the HR mirror would be mounted incorrectly with the HR surface facing the PMT but not the atoms, the polarimetry of backcoupled light would not determine the polarization as seen by atoms, but the distorted polarization within the HR mirror substrate.

Note that if the non-polarizing beamsplitter is used in reflection for backcoupling polarimetry as shown in Fig. 4.26, then the sign of measured Stokes parameters S_2/S_0 and S_3/S_0 at polarimeter 1 is flipped compared to the backcoupled polarization before the beamsplitter. Just as the mirror, the beamsplitter flips the sign of S_2/S_0 and S_3/S_0 in reflection. Intuitively, it can be understood as the change in propagation direction: whenever circular polarized light is reflected, right-handed polarization becomes left-handed and vice versa (similar for diagonal and anti-diagonal linearly polarized light). This sign is important since the relative sign between $(S_2/S_0)_{\mathrm{back}}$ and $(S_2/S_0)_{\mathrm{in}}$ enters Eq. (4.49). Note also that the sign of measured Stokes parameters S_1/S_0 and S_2/S_0 depends on the orientation of the polarimeter which may be opposite, as is the case for the two polarimeters we use from two different companies. Furthermore, the relative orientation of the polarimeter needs to be aligned when the polarimeter is moved to measure $(S_2/S_0)_{\mathrm{in}}$ before the fiber relative to its position in Fig. 4.26 to determine $(S_2/S_0)_{\mathrm{back}}$.

The results of the polarization model tests with two polarimeters as described above are shown in Fig. 4.27(a) for the spectroscopy setup and in Fig. 4.27(b) for the test setup. On the top, the absolute value of the circularly polarized fraction before the mirror (as seen by the atoms in the AFR), $|(S_3/S_0)_{\mathrm{atom}}|$, is shown. The center plots show the variation of the linear polarization rotation angle $\Delta\psi_{\mathrm{atom}}$, and the bottom plots show the deduced retardance δ modulo π based on Eq. (4.50). The red points show the polarization deduced from the direct measurement by polarimeter 2 placed after the mirror, the orange points show the deduced polarization from backcoupling polarimetry using the approximation $\delta \ll 1$ from Eqs. (10)-(11) of [110], and the faint blue points the corrected model $\beta \ll 1$ from Eqs. (4.49) and (4.51). Furthermore, for the test setup polarimetry the bright blue points in Fig. 4.27(b) show the exact solution from Eqs. (4.46)-(4.47) which shows deviations from the $\beta \ll 1$ solution only for $|(S_3/S_0)_{\mathrm{atom}}| \gtrsim 0.3$. Since no significant difference between the exact solution and the $\beta \ll 1$ solution is visible for $|(S_3/S_0)_{\mathrm{atom}}| < 0.1$, the exact solution is not shown for the spectroscopy setup where the circularly polarized fraction is smaller than in the test setup.

The difference between the $\beta \ll 1$ and $\delta \ll 1$ solutions for $|(S_3/S_0)_{\mathrm{atom}}|$ in the spectroscopy setup are only on the order of the absolute accuracy of the measurement ($\sim 2\%$). The differences are much more pronounced in the test setup and for higher circularly polarized fractions the $\delta \ll 1$ solution can lead to incorrect results as high as $\sim 40\%$. Comparing to the deduced retardance on the bottom plot, one can see that the $\beta \ll 1$ and $\delta \ll 1$ solutions agree when the calculated retardance is around zero which demonstrates the consistency of the measurement. The disagreement is stronger for larger $|(S_3/S_0)_{\mathrm{atom}}|$ and for $|(S_3/S_0)_{\mathrm{atom}}| \gtrsim 0.3$ the $\beta \ll 1$ approximation starts to not be a good approximation anymore, with $\sim 5\%$ deviations to the exact solution being observed.

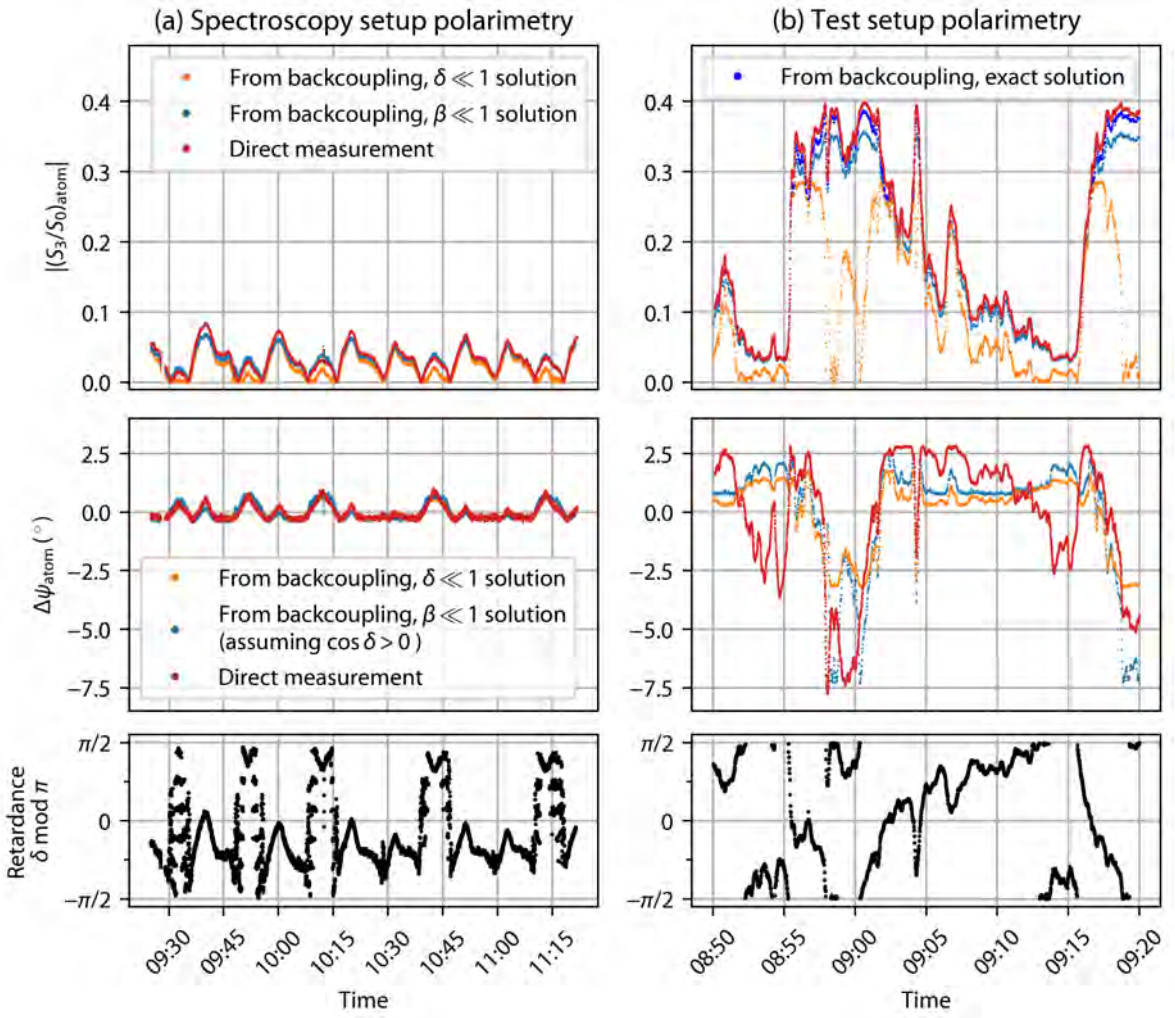

Figure 4.27: Experimental tests of the polarization monitor model according to the setup presented in Fig. 4.26 with two simultaneous polarimeter measurements. In the left plots (a) the data from the AFR spectroscopy vacuum setup is shown, in the right plots (b) the data from the test setup with a less ideal PM fiber is depicted. The top plots show the data for the deduced absolute value of circularly polarized fraction before the mirror (as seen by atoms), $|(S_3/S_0)_{\mathrm{atom}}|$, the center plots show the linear polarization rotation angle changes $\Delta\psi_{\mathrm{atom}}$, and the bottom plots show the retardance δ modulo π from Eq. (4.50). Red points show the data from the direct polarimetry of the mirror transmission (e.g. polarimeter 2 in Fig. 4.26). Faint blue points show the data as deduced from the backcoupling polarimetry (polarimeter 1 in Fig. 4.26), using the approximation $\beta \ll 1$ from Eqs. (4.49) and (4.51), where for the determination of $\Delta\psi_{\mathrm{atom}}$ in addition $\cos\delta > 0$ is assumed. Orange points show the data as deduced from the backcoupling polarimetry using the approximation $\delta \ll 1$ reported in our original publication, Eqs. (10)-(11) of [110]. For the test setup polarimetry the data based on the exact solution from Eqs. (4.46)-(4.47) is shown, where deviations to the approximated $\beta \ll 1$ solution are only visible for higher circularly polarized fraction $|(S_3/S_0)_{\mathrm{atom}}| \gtrsim 0.3$. As detailed in Section 4.6.2.2, no agreement is expected for the linear polarization rotation angle monitor, and the agreement for the spectroscopy setup is believed to be a coincidence.

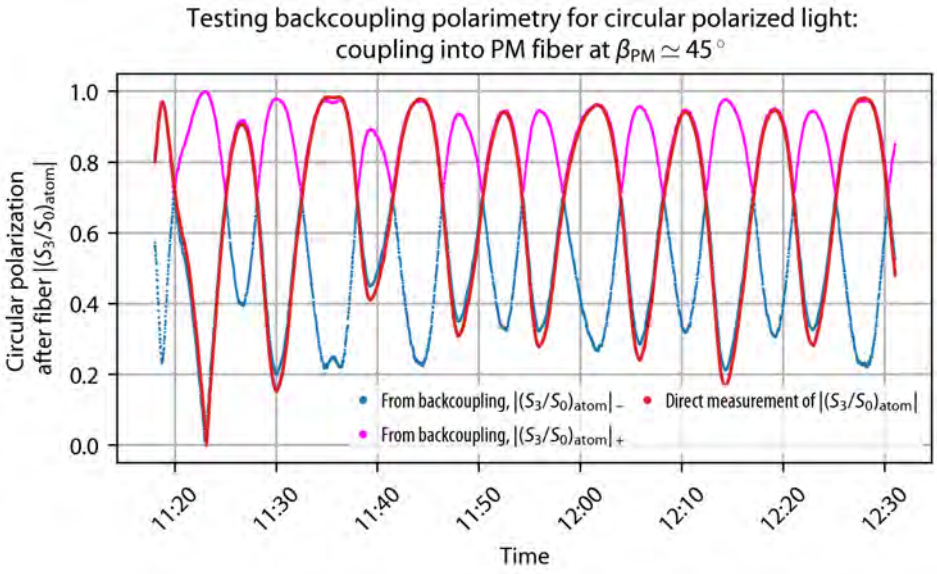

Figure 4.28: Test of polarization monitor model for circularly polarized light. Using the setup presented in Fig. 4.26 with two simultaneous polarimetery measurements, the linear polarization before the fiber was maximally misaligned with the PM axis of the fiber ($\beta_{\mathrm{PM}} \simeq \pi/4$) resulting in all possible polarization states after the fiber (orange curve in Fig. 4.25(a)). The PM fiber was thermally isolated for this measurement such that the polarization fluctuations are relatively slow and can be well resolved by both polarimeters. Red data points show the direct measurement of circularly polarized fraction $|(S_3/S_0)_{\mathrm{atom}}|$ after the fiber. Blue and magneta points show the two solutions $|(S_3/S_0)_{\mathrm{atom}}|_\pm$ for the determination of circularly polarized fraction after the fiber from polarimetry of backcoupled light according to Eqs. 4.46-4.48. As expected, the direct measurement agrees with $|(S_3/S_0)_{\mathrm{atom}}|_-$ for $|(S_3/S_0)_{\mathrm{atom}}| < 1/\sqrt{2}$ and with $|(S_3/S_0)_{\mathrm{atom}}|_+$ for $|(S_3/S_0)_{\mathrm{atom}}| > 1/\sqrt{2}$.

Surprisingly, we found during polarization monitor tests in our spectroscopy setup (see Fig. 4.27(a)) that the linear polarization angle changes determined from Eq. (4.51) with Eq. (4.50) assuming $\cos\delta > 0$ are in good agreement with the direct measurement of $\Delta\psi_{\mathrm{atom}}$. We believe that this agreement is by coincidence. However, this might also be a hint that in some special cases, the circular birefringence term can indeed be assumed constant. In our test setup we find strong disagreement with the direct measurement (see Fig. 4.27(b)) which demonstrates that in general the linear polarization angle changes cannot be determined from polarimetry of backcoupled light.

Since for the future deuterium measurements also circularly polarized light may be used, we also tested the polarization monitor for this case. The setup from Fig. 4.26 was used with maximally misaligned linear polarization into the PM axis of the fiber ($\beta_{\mathrm{PM}} \simeq \pi/4$) resulting in all possible polarization states after the fiber (orange curve in Fig. 4.25(a)). The PM fiber was thermally isolated for this measurement such that the polarization fluctuations are relatively slow and can be well resolved by both polarimeters. The results of this measurement are presented in Fig. 4.28, where red data points show the direct measurement of circularly polarized fraction $|(S_3/S_0)_{\mathrm{atom}}|$ after the fiber. Blue and magneta points show the two solutions $|(S_3/S_0)_{\mathrm{atom}}|_\pm$ for the determination of circularly polarized fraction after the fiber from polarimetry of backcoupled light according to Eqs. 4.46-4.48. As expected, the direct measurement agrees with $|(S_3/S_0)_{\mathrm{atom}}|_-$ for $|(S_3/S_0)_{\mathrm{atom}}| < 1/\sqrt{2}$ and with $|(S_3/S_0)_{\mathrm{atom}}|_+$ for $|(S_3/S_0)_{\mathrm{atom}}| > 1/\sqrt{2}$. The slight discrepancy on the order of $\sim 3-5\%$ at the points where

the drift of circularly polarization reverses the direction might be due to the non-reciprocity in the system (e.g. 'Shupe-effect' [258]), but needs to be further investigated. The PM fiber with maximally misaligned input polarization is very sensitive to environmental fluctuations and hence the non-reciprocal effects may also be enhanced.

4.6.4 Polarization monitor data at the spectroscopy setup

Typically, mirrors and non-polarizing beamsplitters before the polarimeter[1] are subject to stress-induced birefringence, as well as a polarization-dependent transmission and reflectivity (thereby acting as partial polarizers). Note that Eq. (4.49) does not include the stress-induced birefringence of uncommon components for the forward- and backward-traveling directions, e.g. BS 2 (see Fig. 4.1) may introduce a different retardance in transmission than in reflection. Therefore, the remaining distinct path of the backward-traveling beam to the polarimeter needs to be taken into account separately. If the polarizing effects can be neglected, one can again model the total birefringence of optical components between the place where $(S_3/S_0)_{\mathrm{in}}$ and $(S_2/S_0)_{\mathrm{in}}$ are measured and the polarimeter with a single waveplate of retardance δ_{BS} and orientation β_{BS}. For mostly horizontal or vertical linear polarization ($|S_1/S_0| \simeq 1$, $|S_2/S_0| \ll 1$, $|S_3/S_0| \ll 1$) as well as small δ_{BS} (in our setup $\delta_{\mathrm{BS}} \lesssim 0.3\,\mathrm{rad}$) and small β_{BS} (due to optics mounts of our setup, which mostly lead to horizontal or vertical forces due to the corresponding orientations of the setscrews, we find $\beta_{\mathrm{BS}} \lesssim 0.1\,\mathrm{rad}$), the measured Stokes parameters are related to the Stokes parameters of the backcoupled light from Eq. (4.49) as:

$$\begin{aligned}
(S_1/S_0)_{\mathrm{back}} &\simeq (S_1/S_0)_{\mathrm{meas}} + 2\delta_{\mathrm{BS}}\beta_{\mathrm{BS}}(S_3/S_0)_{\mathrm{meas}},\\
(S_2/S_0)_{\mathrm{back}} &\simeq (S_2/S_0)_{\mathrm{meas}} - \delta_{\mathrm{BS}}(S_3/S_0)_{\mathrm{meas}},\\
(S_3/S_0)_{\mathrm{back}} &\simeq (S_3/S_0)_{\mathrm{meas}} + \delta_{\mathrm{BS}}(S_2/S_0)_{\mathrm{meas}} - 2\delta_{\mathrm{BS}}\beta_{\mathrm{BS}}(S_1/S_0)_{\mathrm{meas}}.
\end{aligned} \tag{4.52}$$

For the incorrect polarization monitor model presented in [110], only $(S_3/S_0)_{\mathrm{back}}$ and $(S_3/S_0)_{\mathrm{in}}$ need to be known in order to determine $(S_3/S_0)_{\mathrm{atom}}$, see Eq. (10) in [110]. However, for the correct polarization monitor model (Eq. (4.49)) also $(S_2/S_0)_{\mathrm{back}}$ and $(S_2/S_0)_{\mathrm{in}}$ need to be determined. While testing how well $(S_2/S_0)_{\mathrm{back}}$ can be determined from $(S_2/S_0)_{\mathrm{meas}}$ we found that the polarizing effects of BS 2 from Fig. 4.1 might need to be included for a more accurate determination of $(S_2/S_0)_{\mathrm{back}}$, since it was found that BS 2 has a much larger polarizing effect of $\sim 20\%$ as opposed to the $\sim 2\%$ which we measured for BS 3.[2] The more accurate determination of $(S_2/S_0)_{\mathrm{back}}$ from $(S_2/S_0)_{\mathrm{meas}}$ should then include the $\sim$20% polarization-dependent transmission and reflection. Alternatively, BS 2 can be replaced by another beamsplitter (or placed in a modified setup under a smaller incidence angle of $\ll 45°$) such that the polarizing effects remain negligible and Eq. (4.52) remains an accurate model.

The system with polarization-dependent transmission and reflection can be modelled as a combination of a partial polarizer in between two different waveplates and an additional rotator [253]. Instead, we simply measured the Mueller matrix $\hat{M}_{\mathrm{BS}}$ of the backward travelling path. This Mueller matrix $\hat{M}_{\mathrm{BS}}$ then describes the backward travelling path between the point where $(S_2/S_0)_{\mathrm{in}}$ and $(S_3/S_0)_{\mathrm{in}}$ are measured (between BS 2 and BS 3 in Fig. 4.1) and

[1] Compared to the test setup with only one beamsplitter on the way to polarimeter 1 for backcoupling polarimetry, in our spectroscopy setup two beamsplitters and several mirrors are placed between the fiber and the polarimeter (see Fig. 4.2 for the simplified scheme).

[2] Both BS 2 and BS 3 are Thorlabs BSW10 50:50 non-polarizing beamsplitters, but placed under different incidence angles ($\sim$45° for BS 2 and $\sim$10° for BS 3) and subject to different mechanical stresses.

the polarimeter. Note that the backward travelling paths are different for the horizontal and vertical polarizations, such that the corresponding Mueller matrices are different, $\hat{M}_{\mathrm{BS,H}}$ and $\hat{M}_{\mathrm{BS,V}}$, respectively.

The measurement of $\hat{M}_{\mathrm{BS}}$ can be performed as follows[1]. An auxiliary polarizer[2] is placed on a rotation mount[3] with adjustable angle γ at the place where the input polarization is characterized (between BS 2 and BS 3 in Fig. 4.1). An auxiliary laser[4] at 405 nm wavelength is placed such that the auxiliary laser beam is polarized by this auxiliary polarizer. The auxiliary laser beam is then overlapped with the forward-traveling laser beam of the experiment, such that the input polarization[5] of the auxiliary laser beam is $\vec{S}_{\mathrm{back}} = (1, -\cos 2\gamma, -\sin 2\gamma, 0)$. For a general Mueller matrix $\hat{M}_{\mathrm{BS}}$, the polarization at the polarimeter $\vec{S}_{\mathrm{meas}} = \hat{M}_{\mathrm{BS}}\,\vec{S}_{\mathrm{back}}$ is then given by:

$$\vec{S}_{\mathrm{meas}} = \begin{pmatrix} m_{00} & m_{01} & m_{02} & m_{03} \\ m_{10} & m_{11} & m_{12} & m_{13} \\ m_{20} & m_{21} & m_{22} & m_{23} \\ m_{30} & m_{31} & m_{32} & m_{33} \end{pmatrix} \begin{pmatrix} 1 \\ -\cos 2\gamma \\ -\sin 2\gamma \\ 0 \end{pmatrix} = \begin{pmatrix} m_{00} - m_{01}\cos 2\gamma - m_{02}\sin 2\gamma \\ m_{10} - m_{11}\cos 2\gamma - m_{12}\sin 2\gamma \\ m_{20} - m_{21}\cos 2\gamma - m_{02}\sin 2\gamma \\ m_{30} - m_{31}\cos 2\gamma - m_{32}\sin 2\gamma \end{pmatrix}. \quad (4.53)$$

Since we are interested in the relative Stokes parameters only, we can set $m_{00} = 1$. Fitting the above equation to the data for various angles γ (see Fig. 4.29) determines all matrix elements except m_{03}, m_{13}, m_{23} and m_{33}. These matrix elements can be measured by adding a quarter waveplate to the setup with the auxiliary polarizer in order to produce fully left- and right-handed circular polarization states $\vec{S}_{\mathrm{back}} = (1, 0, 0, \pm 1)$ leading to $\vec{S}_{\mathrm{meas}} = (m_{00} \pm m_{03}, m_{10} \pm m_{13}, m_{20} \pm m_{23}, m_{30} \pm m_{33})$. From the measurement of $\vec{S}_{\mathrm{meas}}$ the matrix elements are extracted. Using the above methods, we measured the following matrices $\hat{M}_{\mathrm{BS,V}}$ and $\hat{M}_{\mathrm{BS,H}}$ for the vertical and horizontal polarization paths, respectively:

$$\hat{M}_{\mathrm{BS,V}} = \begin{pmatrix} 1 & -0.228(1) & -0.010(2) & 0.001(6) \\ -0.230(2) & 0.999(1) & 0.011(14) & -0.017(12) \\ 0.008(2) & 0.006(13) & -0.965(1) & -0.144(19) \\ 0.005(4) & -0.032(2) & 0.131(8) & -0.965(1) \end{pmatrix},$$

$$\hat{M}_{\mathrm{BS,H}} = \begin{pmatrix} 1 & 0.256(5) & 0.007(9) & -0.007(8) \\ 0.258(2) & 1.000(1) & 0.021(2) & 0.000(1) \\ 0.003(10) & -0.019(1) & 0.895(1) & -0.361(3) \\ 0.000(3) & -0.001(9) & 0.364(6) & 0.894(2) \end{pmatrix}. \quad (4.54)$$

[1] The matrix $\hat{M}_{\mathrm{BS}}$ can also be measured in the opposite direction along with the forward-propagating laser beam in the setup. Then the polarizer and the polarimeter are swapped. Note that in this case not the inverse $\hat{M}_{\mathrm{BS}}^{-1}$ matrix is measured but $\hat{M}_{\mathrm{BS}}$: not only the positions are swapped, but also the propagation direction inverting the matrix twice. This measurement can serve as a consistency check.

[2] Thorlabs GTH5M-A.

[3] Thorlabs CRM1T/M.

[4] Thorlabs CPS405 used with an aperture resulting in approximately the same beam width as the laser beam of the experiment (which is important to prevent possible inconsistensies due to possible polarization gradients).

[5] Care has to be taken by choosing the right sign depending on the rotation direction of γ. Furthermore, the offset rotation angle needs to be determined separately, e.g. by placing the polarimeter directly after the polarizer, or included in the model as an additional parameter. Here, we measured the offset angle and show the equations only with this approach for simplicity.

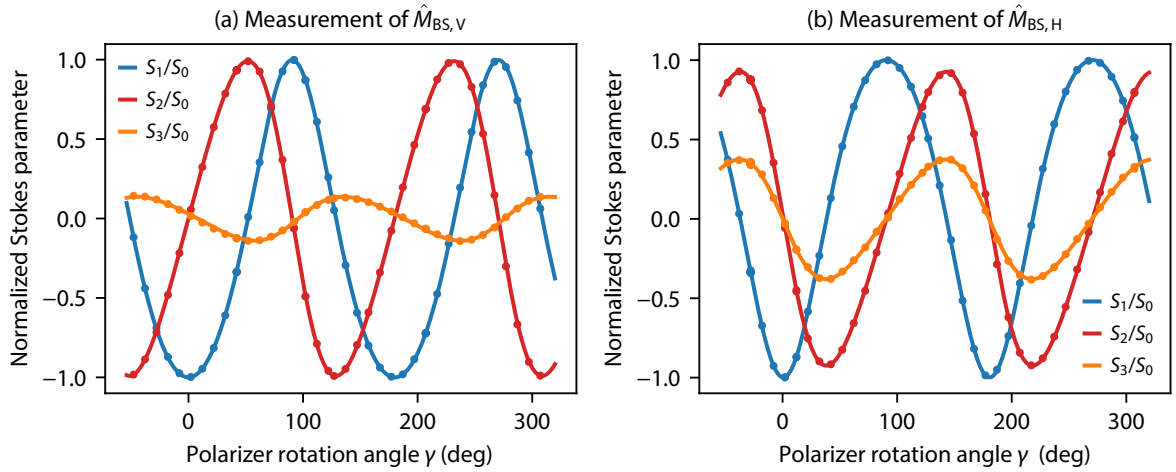

Figure 4.29: Measurement of the Mueller matrix for the vertical (a) and horizontal (b) back-coupled polarization paths. For this measurement, a polarizer is placed on a rotation mount with adjustable angle γ at the place where the input polarization is characterized (between BS 2 and BS 3 in Fig. 4.1). An auxiliary laser is placed before the polarizer and the laser beam is overlapped with the forward-traveling laser beam of the experiment, such that the Stokes vector after the polarizer is $\vec{S}_{\mathrm{back}} = (1, -\cos 2\gamma, -\sin 2\gamma, 0)$ (here, γ is calibrated such that $\gamma = 0$ corresponds to the Stokes parameters $S_1/S_0 = -1$, $S_2/S_0 = S_3/S_0 = 0$ after the polarizer). Having passed through the optical components on the back-coupled polarization path to the polarimeter (described by Mueller matrices $\hat{M}_{\mathrm{BS,V}}$ and $\hat{M}_{\mathrm{BS,H}}$), the polarization changes according to Eq. (4.53). Fits of this equation (curves) to the data (points) for the normalized Stokes parameters S_1/S_0 (blue), S_2/S_0 (red), and S_3/S_0 (orange) determines all matrix elements except m_{03}, m_{13}, m_{23} and m_{33}. The latter are measured with circularly polarized light as described in the main text.

The measured Stokes vector $\vec{S}_{\mathrm{meas}}$ is then related to the Stokes vector $\vec{S}_{\mathrm{back}}$ of the back-coupled light needed for Eq. (4.49) using the inverse of the matrix $\hat{M}_{\mathrm{BS}}$ as

$$\vec{S}_{\mathrm{back}} = \hat{M}_{\mathrm{BS}}^{-1}\, \vec{S}_{\mathrm{meas}}, \tag{4.55}$$

with the measured inverse matrices $\hat{M}_{\mathrm{BS,V}}^{-1}$ and $\hat{M}_{\mathrm{BS,H}}^{-1}$ calculated from Eq. (4.54) for the vertical and horizontal polarization paths, respectively:

$$\hat{M}_{\mathrm{BS,V}}^{-1} = \begin{pmatrix} 1 & 0.228(1) & -0.008(2) & -0.002(3) \\ 0.230(2) & 1.000(1) & 0.007(12) & -0.018(13) \\ 0.010(2) & 0.013(12) & -0.962(3) & 0.143(19) \\ -0.001(5) & -0.030(2) & -0.131(7) & -0.962(3) \end{pmatrix},$$
$$\hat{M}_{\mathrm{BS,H}}^{-1} = \begin{pmatrix} 1 & -0.256(5) & -0.004(11) & 0.006(4) \\ -0.258(2) & 1.000(1) & -0.018(1) & -0.009(1) \\ -0.008(10) & 0.019(1) & 0.896(1) & 0.362(4) \\ 0.003(3) & -0.007(9) & -0.365(6) & 0.897(1) \end{pmatrix}. \tag{4.56}$$

Eq. (4.55) is a general form of Eq. (4.52) including polarizing effects. Eqs. (4.49) and (4.52) or (4.55) allow then to monitor the circular polarization as seen by atoms from polarimetry of backcoupled light and the characterized polarization effect of optical components before the polarimeter. Based on the uncertainties for Stokes parameter measurements ($\sim 1\,\%$) combined

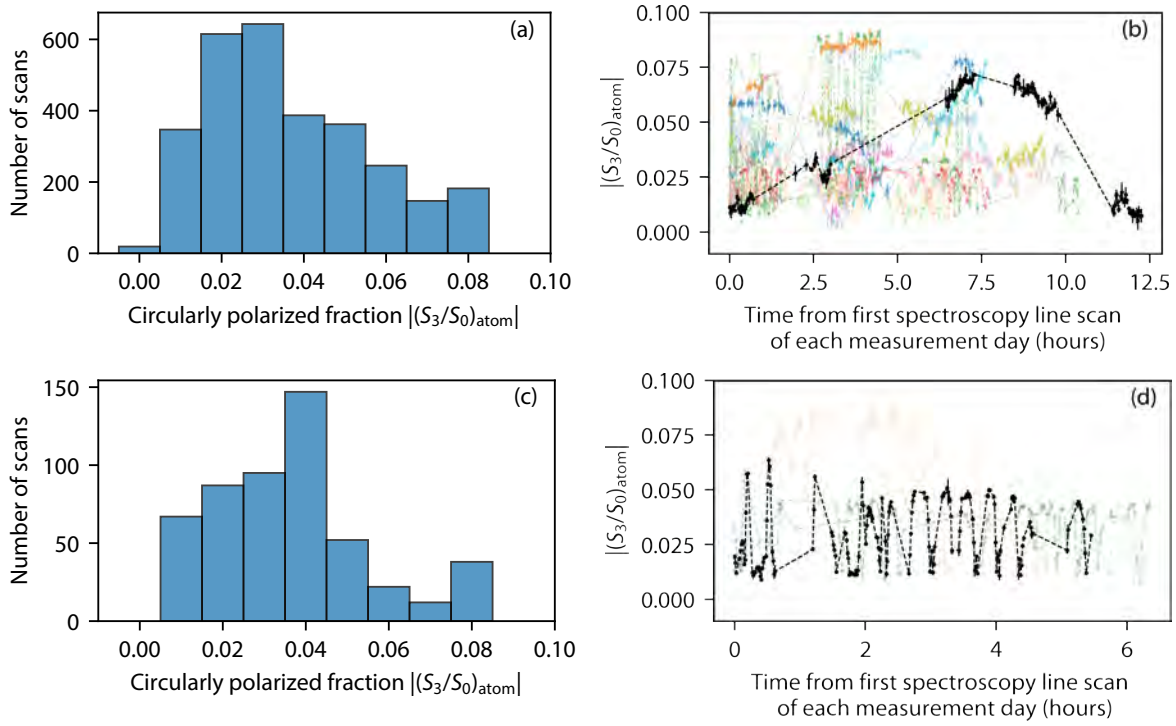

Figure 4.30: Circularly polarized fraction $|(S_3/S_0)_{\mathrm{atom}}|$ in the AFR (as seen by the atoms) as deduced from polarimetry of backcoupled light according to Eqs. (4.49) and (4.55). (a) and (b) show the polarization data during the hydrogen 2S-6P measurement campaign in 2019 (3035 spectroscopy line scans from 22 measurement days), whereas (c) and (d) show the polarization data during the deuterium 2S-6P measurement campaign in 2021 (527 spectroscopy line scans from 5 measurement days). From the histograms in (a) and (c), the circularly polarized fraction is always $|(S_3/S_0)_{\mathrm{atom}}| \lesssim 10\%$ corresponding to an extinction ratio of PER $\gtrsim 26\,\mathrm{dB}$. For most spectroscopy line scans, $|(S_3/S_0)_{\mathrm{atom}}| \lesssim 5\%$ corresponding to PER $\gtrsim 32\,\mathrm{dB}$. In (b) and (d), the polarimetry data is plotted versus time for several days (from the first spectroscopy line scan of the day). Each point respresents one spectroscopy line scan, while the different faint colors represent different measurement days, with one exemplary day being highlighted in black (227 line scans in (b) and 167 line scans in (d)). Error bars show the variation within a line scan, which is much smaller than the $\sim 2\%$ absolute accuracy on the determination of $|(S_3/S_0)_{\mathrm{atom}}|$.

with uncertainties for matrix element of $\hat{M}_{\mathrm{BS}}$, we estimate the absolute accuracy on deducing $(S_3/S_0)_{\mathrm{atom}}$ to be $\sim 2\,\%$.

We continuously took polarimetry data during our hydrogen and deuterium 2S-6P spectroscopy measurement campaigns. In Fig. 4.30(a) and (b), the circularly polarized fraction after the collimator (as seen by the atoms) is shown for the hydrogen 2S-6P measurement in 2019, as deduced from polarimetry of the backcoupled light according to the above equations. Similar polarimetry data for the 2S-6P deuterium measurement in 2021 is shown in Fig. 4.30(c) and (d). The histograms in Fig. 4.30(a) and (c) show the values for $(S_3/S_0)_{\mathrm{atom}}$ for all the days of the measurement campaign with a total number of 3035 spectroscopy line scans in (a), and 527 spectroscopy line scans in (c). For all of the data, we observe $|(S_3/S_0)_{\mathrm{atom}}| \lesssim 10\,\%$ corresponding to PER $\gtrsim 26\,\mathrm{dB}$. For most spectroscopy line scans, $|(S_3/S_0)_{\mathrm{atom}}| \lesssim 5\%$ corresponding to PER $\gtrsim 32\,\mathrm{dB}$. The time variation of polarization data is shown in Fig. 4.30(b) and (d), where the circularly polarized fraction is plotted for each

measurement day starting from the first spectroscopy line scan of the day, with one single day highlighted in black. The polarization for the deuterium measurement in (c) typically varied on a faster time scale of $\sim 15\,\mathrm{min}$ than for the hydrogen measurement in (b) where the fluctuations are on the timescale of hours. This is attributed to the ambient laboratory temperature, which unfortunately was less stable in 2021 due to the different air conditioning system. However, still the polarization fluctuations occured on a much larger timescale compared to the $\sim 2\,\mathrm{min}$ time scale of a single line scan. The polarization within a line scan typically fluctuates by less than $|(S_3/S_0)_{\mathrm{atom}}| \lesssim 0.5\,\%$ which is smaller than the total uncertainty of $\sim 2\%$ on determining $|(S_3/S_0)_{\mathrm{atom}}|$. Due to slow drifts within a line scan and well-known polarization deduced from in-situ monitoring, it is possible, if needed, to extract spectroscopy data with $(S_3/S_0)_{\mathrm{atom}} \lesssim 2\,\%$ corresponding to PER $\gtrsim 40\,\mathrm{dB}$. In the future, if the accuracy of the polarization monitor limits the uncertainty for precision spectroscopy, a more accurate self-calibrating polarimeter [260] could be used to improve the accuracy of polarization monitor, though such a polarimeter would be much slower and require a modification of the setup because of its larger size.

Chapter 5

Preliminary Measurement of the 2S-6P Transition in Atomic Deuterium

This chapter presents the preliminary measurement of the 2S-6P transition in atomic deuterium, which was conducted in July 2021. The main purpose of this measurement campaign was the feasibility study for planning a future precision measurement campaign, along with characterization measurements. The focus lied on measuring the 2S-6$P_{1/2}$ fine structure component.

Section 5.1 presents the overview of the collected data. Over the course of the measurement campaign, also resonance line scans of the 1S-2S transition were collected, which is discussed in Section 5.2. The 1S-2S measurement helps to find the optimal laser frequency for the maximum 2S-6P signal, but also serves as a consistency check of the absolute frequency determination with a frequency comb. Furthermore, comparisons with simulations of the 1S-2S resonance line check the numerical modelling of the experiment. Section 5.3 discusses how the atomic beam is aligned w.r.t. the counter-propagating 2S-6P laser beams in the active fiber-based retroreflector, which also tests the numerical modelling of the experiment and identifies nozzle misalignments. Another fraction of the measurement time is needed for the in-situ determination of the stray electric field in the interaction region, which has been introduced in Section 3.5.2. In this chapter, Section 5.4 presents the results of the stray electric field measurements throughout the measurement campaign. Section 5.5 discusses the preliminary analysis of precision line scans, along with a summary of the preliminary uncertainty budget.

5.1 Overview of the collected data

The overview of the collected data is presented in Table 5.1. The first two columns list the measurement day number and the date. Next, the number of 1S-2S line scans is listed (see Section 5.2). The addressed fine-structure component is given in the column "FS", where $6P_{1/2}$ or $6P_{3/2}$ stand for measuring the 2S-6$P_{1/2}$ or 2S-6$P_{3/2}$ transitions, respectively. The power of the 2S-6P laser beams is listed in the column "$P_{2S\text{-}6P}$". The columns "$\delta\alpha$-al. scans" or "E-Field scans" give the number of line scans for the alignment of the angle between the atomic beam and the 2S-6P laser beam (see Section 5.3), or the number of line scans for in-

Table 5.1: Overview of the collected data for the preliminary measurement of the 2S-6P transition in deuterium. "1S-2S scans": number of 1S-2S transition line scans (see Section 5.2). "FS": addressed fine-structure component, where $6P_{1/2}$ or $6P_{3/2}$ stands for measuring the 2S-$6P_{1/2}$ or 2S-$6P_{3/2}$ transitions, respectively. "$P_{2S\text{-}6P}$": power of the 2S-6P laser beam. "$\delta\alpha$-al. scans": number of line scans for the alignment of the angle $\alpha = 90° + \delta\alpha$ between the atomic beam and the 2S-6P laser beam (see Section 5.3). "E-Field scans": number of line scans for the in-situ measurements of stray electric field (see Section 3.5.2). "Excluded precision scans": number of excluded precision line scans due to corrupted data points (e.g. laser lock failure or nozzle temperature instability). "Valid precision scans": number of valid precision line scans entering the preliminary analysis (see Section 5.5).

Meas. day	Date (2021)	1S-2S scans	FS	$P_{2S\text{-}6P}$ (µW)	$\delta\alpha$-al. scans	E-Field scans	Excluded precision scans	Valid precision scans
0	20.7	6	$6P_{1/2}$	30	31	–	(13)	–
1	21.7	8	$6P_{1/2}$	30	36	46	6(+35)	31
2	22.7	11	$6P_{1/2}$	10, 20, 30	12	36	9, 5, 25	21, 4, 99
3	23.7	8	$6P_{1/2}$	10, 20, 30	12	36	3, 1, 13	35, 19, 97
4	26.7	9	$6P_{1/2}$	10, 20, 30	11	49	5, 1, 10	36, 8, 61
			$6P_{3/2}$	10, 15	–	10	1, 1	2, 14
5	27.7	4	$6P_{1/2}$	30	19	24	1	29
			$6P_{3/2}$	5, 10, 15	6	24	1, 1, 10	9, 10, 81
Total		46	$6P_{1/2}$	10			17	92
				20			7	31
				30	121	191	55	317
			$6P_{3/2}$	5			1	9
				10			3	11
				15	6	34	10	96
					127	225	93	556

situ measurements of stray electric fields (see Section 3.5.2), respectively. Both "$\delta\alpha$-al. scans" and "E-Field scans" were performed at $P_{2S\text{-}6P} = 30\,\mu W$ (2S-$6P_{1/2}$) or $P_{2S\text{-}6P} = 15\,\mu W$ (2S-$6P_{3/2}$) laser powers. The number of excluded precision scans (e.g. due to a failure of the laser locks or the nozzle temperature instability) is shown next[1]. The last column gives the number of precision line scans at each laser power entering the preliminary analysis discussed in Section 5.5.

The first two days of the measurement campaign (Days 0 and 1 in Table 5.1) were mostly used for the characterization of the apparatus, as for instance for the temperature dependence studies of the cryogenic deuterium atomic beam, which are presented in Section 3.6. Line scans were taken at different nozzle temperatures to investigate the temperature dependence of the deuterium 2S-6P signal and the background (see Fig. 3.21). These line scans are listed in paranthesis under "Excluded precision scans". The remaining days focused on collecting precision line scans at the 2S-6P laser power of $P_{2S\text{-}6P} = 30\,\mu W$ in order to reach a low

[1] In principle, the so far excluded precision scans can be included in the future analysis, since mostly only a few data points are corrupted. However, then these line scans need to be corrected for an additional possible sampling bias.

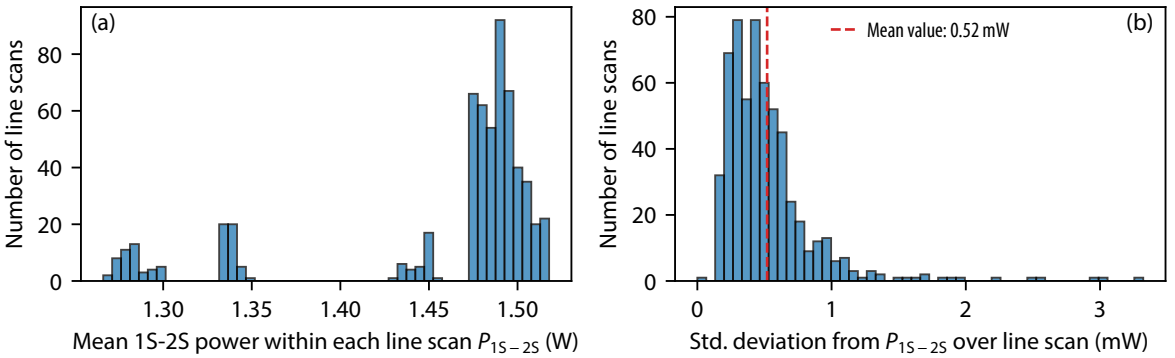

Figure 5.1: Mean 1S-2S intracavity power and stability for deuterium 2S-6P precision line scans during the July 2021 measurement campaign. The histogram in (a) shows the mean 1S-2S intracavity power P_{1S-2S} within minute-long line scans. The uncertainty on the absolute scale of $P_{1S\text{-}2S}$ due to calibration is 12%. For most line scans $P_{1S-2S} = 1.50(18)$ W. Over the course of the measurement campaign, the mirrors of the 1S-2S cavity degraded, such that the experiment needed to be operated at lower 1S-2S powers. The histogram in (b) shows the standard deviation from the mean intracavity power within the line scans. The mean value for this deviation for all line scans is 0.5 mW (vertical red line).

statistical uncertainty of the 2S-6P$_{1/2}$ transition frequency measurement within a relatively short measurement time. Around 150 line scans were also taken at lower laser powers of $P_{2S\text{-}6P} = 10\,\mu W$ or $P_{2S\text{-}6P} = 20\,\mu W$. Furthermore, with around 150 line scans the 2S-6P$_{3/2}$ transition was addressed. However, most of them were measured on the last day (Day 5) of the measurement campaign, where the 1S-2S mirrors were re-aligned to maintain the higher 1S-2S intracavity power. This seemed to have increased the misalignment of the apparatus, which resulted in a significant residual Doppler shift[1]. Therefore, Section 5.5 presents only the preliminary analysis of the 2S-6P$_{1/2}$ line scans. The last days of the measurement campaign were also challenged by the deteriorating cryostat performance, where it became more and more difficult to maintain the stable nozzle temperature, as discussed in Section 3.6.3. For the future measurement campaign, it is hoped that the cryostat performance can be improved, and the 1S-2S cavity mirror degradation can be prevented (either by upgrading the apparatus to flush the mirrors with oxygen combined with differential pumping, and/or by using the fluoride coatings instead of oxide coatings as discussed in Section 3.2.1.1).

The 1S-2S intracavity power $P_{1S\text{-}2S}$ is one of the parameters affecting the mean speed of atoms in each delay group (see Table 3.1), and thus it is important to measure $P_{1S\text{-}2S}$. Fig. 5.1 shows $P_{1S\text{-}2S}$ and its stability for the precision line scans. As described in Section 3.2.1.1, $P_{1S\text{-}2S}$ is stabilized using a fast photodiode measuring the transmission through the cavity. The signal on this photodiode is sensitive to pointing fluctuations, which occur on a slow timescale of several minutes and result in signal fluctuations on the order of few percent. As a result, $P_{1S\text{-}2S}$ remains stable within each line scan, while slow pointing drifts are responsible for percent-fluctuations of $P_{1S\text{-}2S}$ between the line scans. The integrating sphere is mostly insensitive to these pointing fluctuations and is used to monitor $P_{1S\text{-}2S}$ out-of-loop. The histogram of the mean values for $P_{1S\text{-}2S}$ within each line scan, as deduced from the integrating sphere along with calibration measurements, is shown in Fig. 5.1(a). Fig. 5.1(b) demonstrates that the

[1]The preliminary analysis of the 2S-6P$_{3/2}$ line scans shows a Doppler slope of $\kappa \sim 40(10)$Hz/(m/s), resulting in an average Doppler shift of ~ 10 kHz. However, in principle, the absolute frequency can still be extracted free from the Doppler shift using the velocity extrapolation.

deviations from the mean power within the line scans are on average 0.5 mW, which is less than 0.05%. The uncertainty from the calibration factor[1] results in a 12% uncertainty on the absolute scale of $P_{\text{1S-2S}}$. Most line scans were measured at $P_{\text{1S}-\text{2S}} = 1.50(18)\,\text{W}$. Over the course of the measurement campaign, the 1S-2S cavity mirrors degraded, such that at the end of day 4 (26.7) this power could not be maintained anymore. Therefore, some precision line scans were taken at a lower power of $P_{\text{1S}-\text{2S}} \sim 1.3\,\text{W}$. As mentioned above, on day 5 (27.7) the 1S-2S cavity was re-aligned to a slightly different position on the mirror, such that $P_{\text{1S}-\text{2S}} \sim 1.5\,\text{W}$ could be reached again.

All the measurements were performed with a linear polarization rotation angle $\theta_L = 56.5(3.0)\,\text{deg}$ (alignment uncertainty of $\pm 3\,\text{deg}$), where θ_L is the angle of the polarization vector from the axis of the detector cylinder. This value of θ_L approximately corresponds to the "magic angle", where the line shifts due to the resolved quantum interference are minimal (see Sec. 6.2.3 of [71]). Therefore, similar to the preliminary analysis of the hydrogen 2S-6P data presented in [71], we here use the symmetric Voigt fit function (see Eq. (2.73)). The asymmetric fit function such as the the Fano-Voigt function would result in an increased uncertainty of the center frequency due to correlations between the additional asymmetry parameter and the center frequency. Since the resolved quantum interference has been studied in detail in the 2S-4P measurement [14, 71], we minimize its effect by aligning the polarization to the magic angle and use a symmetric fit function for more accurate center frequency determinations. The remaining small corrections of resolved quantum interference are then taken into account with "Big Model" simulations. In the final analysis, also the asymmetric fit functions such as the Fano-Voigt can be used for consistency checks.

Fig. 5.2(a) shows an example of the deuterium 2S-6P$_{1/2}$ line scan. Different colors represent the five exemplary delays 2, 10, 13, 15, and 16. The points show the number of counts for the top detector as a function of the laser frequency detuning $\Delta\nu_{\text{2S-6P}}$, which we here define such that zero $\Delta\nu_{\text{2S-6P}}$ corresponds to the laser frequency prediction from theory[2] with a random blind offset[3]. The error bars represent the shot noise (square root of the number of counts). The resonance is sampled with 30 frequency detuning points[4]. The curves show the Voigt fits to the data, with fit results for the center frequency ν_0, the linewidths Γ_{F} and Γ_{G},

[1] The calibration factor for $P_{\text{1S-2S}}$ from the signal of the integrating sphere (which was used in Fig. 5.1) is 1.74(21) W/V. These uncertainty on the calibration factor is composed from the 7.5% uncertainty in the power measurement and the 9% uncertainty in the transmission factor $T_{\text{OC}}T_{\text{path}} = 5.6(5)\times 10^{-5}$ (see Section 3.2.1.1).

[2] The theory prediction (following QED theory with fundamental constants according to [8] with hyperfine structure according to [116]) for the hyperfine center frequency of the $2\text{S}_{1/2}^{F=1/2}$-$6\text{P}_{1/2}$ transition with linearly polarized light is $\nu_{\text{2S-6P}} = \nu_{\text{A,0 (F=1/2)}} + \eta_{1/2}\Delta_{\text{HFS}_{1/2}} + \Delta\nu_{\text{rec}} \simeq 730\,888\,824\,058.5\,\text{kHz}$, where $\nu_{\text{A,0 (F=1/2)}}$ is the unperturbed transition frequency of the $2\text{S}_{1/2}^{F=1/2}$-$6\text{P}_{1/2}^{F=1/2}$ transition, $\Delta_{\text{HFS}_{1/2}}$ is the hyperfine splitting, $\Delta\nu_{\text{rec}}$ is the recoil shift (see Table 2.4 for the values of the latter three), and $\eta_{1/2} = 8/9$ is the fraction defined in Eq. (2.49). As has been discussed in Table 2.3, the total uncertainty on the prediction in $\sim$1.5 kHz.

[3] The blind offset is randomly drawn from a normal distribution centered around zero with a standard deviation of 12 kHz. The numerical value of the blind offset is encoded using the base64 python module in characters, such that the offset is not given in numbers, but as a string of characters to the input settings of the analysis code.

[4] See Sec. 5.1.3 in [71] for details on the sampling of the resonance line. Here, the same frequency detunings $\Delta\nu_{\text{2S-6P}}$ as for the hydrogen 2S-6P measurement campaign with offset angles $\alpha_0 = 0\ldots 6\,\text{mrad}$ were used (first columns in Table 5.2 in [71]). The sign and value of $\Delta\nu_{\text{2S-6P}}$ is chosen randomly during the line scan, always with zero $\Delta\nu_{\text{2S-6P}}$ at the beginning and at the end of the resonance line scans, which results in 30 frequency detunings in total. Due to a mistake in the center frequency calculation (which did not take into account the recoil shift $\Delta\nu_{\text{rec}}$), the resonance lines were sampled by $\Delta\nu_{\text{rec}} \simeq 589\,\text{kHz}$ off-center. This results in a sampling bias of the center frequency determination, which must be taken into account through simulations and has to be carefully investigated for the final analysis.

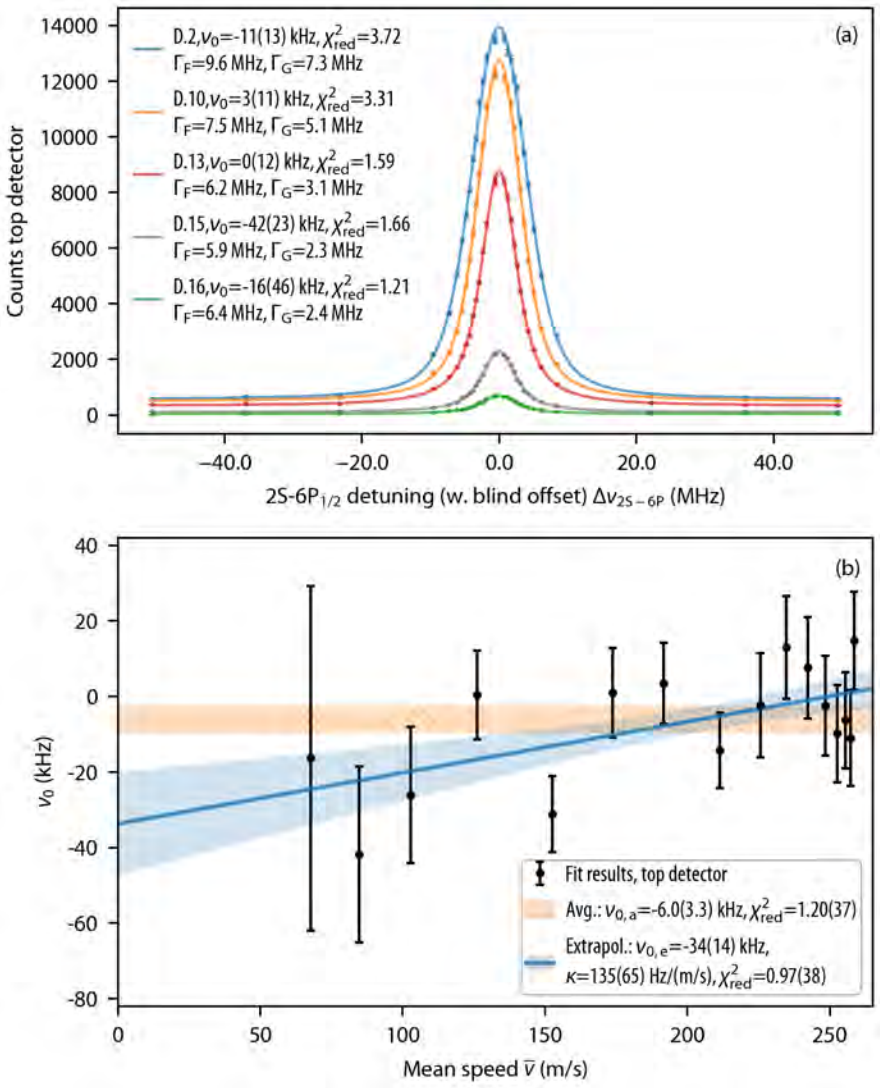

Figure 5.2: Example of the deuterium 2S-6P$_{1/2}$ resonance line scan. (a) The points show the number of counts for the top detector in five selected delays (D. 2, 10, 13, 15, 16) versus the laser frequency detuning $\Delta\nu_{2S\text{-}6P}$ (zero detuning is here defined to correspond to the theory prediction including the recoil shift and a blind offset), with the error bars showing the shot noise. The curves show the Voigt fits (see Eq. (2.73)) to the data, with fit results for the center frequency ν_0 (relative to zero detuning), the linewidths Γ_F and Γ_G (see Eq. (2.74)), as well as the reduced chi-square per degree of freedom χ^2_{red} given for each fit in the legend. In (b), the points show the center frequency fit results for each delay (with the error bar deduced from the fit) versus the mean atomic speed $\overline{v}$ determined from simulations for each delay (similar to Table 3.2 with parameters $P_{1S\text{-}2S} = 1.5\,W$, $\Delta\nu_{1S\text{-}2S} = 0.8\,kHz$, $v_{cutoff} = 100\,m/s$, $T_N = 7.1\,K$, as well as other fixed parameters from Table 3.1). The horizontal orange bar shows the center frequency $\nu_{0,a}$ averaged over all velocities, with the vertical size of the bar representing the uncertainty (the value of $\nu_{0,a}$ and the χ^2_{red} are given in the legend). The blue line shows the fit to ν_0 assuming a linear velocity dependence, i.e. $\nu_0 = \kappa\,\overline{v} + \nu_{0,e}$, where κ is the slope and $\nu_{0,e}$ the extrapolated center frequency for zero $\overline{v}$. The fit results for $\nu_{0,e}$ and κ are given in the legend, and the faint blue region shows the one standard deviation (1σ) uncertainty region calculated from the covariance matrix values resulting from the fit.

as well as the reduced chi-square per degree of freedom χ^2_{red} given for each fit in the legend. Slower atoms experience a smaller Doppler broadening, which is seen in the smaller value for the Gaussian width Γ_{G} for larger delay numbers. The increased $\chi^2_{\mathrm{red}} > 1$ is attributed to atomic flux fluctuations due to temperature fluctuations, which are the main cause of the signal noise in our experiment (see Section 3.6). As has been demonstrated in Fig. 3.21, faster atoms (smaller delay numbers) are more sensitive to temperature fluctuations than slow atoms (larger delay numbers). Therefore, χ^2_{red} is closer to one for larger delay numbers.

The points in Fig. 5.2(b) show the fit results for the center frequency ν_0 in each delay as a function of the atomic mean speed $\overline{v}$, which is determined for each delay from simulations (similar to Table 3.2 with parameters $P_{\text{1S-2S}} = 1.5\,\mathrm{W}$, $\Delta\nu_{\text{1S-2S}} = 0.8\,\mathrm{kHz}$, $v_{\mathrm{cutoff}} = 100\,\mathrm{m/s}$, $T_{\mathrm{N}} = 7.1\,\mathrm{K}$, as well as other fixed parameters from Table 3.1). The orange bar is the average $\nu_{0,a}$ of the center frequencies from all delays, where the vertical size of the bar represents the one standard deviation (1σ) uncertainty (values are given in the legend). The blue line is a fit to the center frequencies assuming a linear velocity dependence as

$$\nu_0 = \kappa\,\overline{v} + \nu_{0,\mathrm{e}}, \tag{5.1}$$

where κ is the slope and $\nu_{0,\mathrm{e}}$ the extrapolated center frequency for atoms at rest. For example, this velocity dependence of the center frequency is present for a first-order Doppler shift $\Delta\nu_{\mathrm{D}} = \kappa\,\overline{v}$, where κ is then identified with the Doppler slope from Eq. (2.28). However, note that also more subtle velocity-dependent effects such as the light force shift may be present, as well as possible non-linear effects due to the misalignment of the apparatus (see Fig. 5.6). For the example line scan in Fig. 5.2, the results for κ and $\nu_{0,\mathrm{e}}$ are given in the legend of Fig. 5.2(b). The faint blue region shows the one standard deviation (1σ) uncertainty region calculated from the covariance matrix values resulting from the fit[1].

5.2 1S-2S transition line scans

The 1S-2S laser frequency needs to be accurately matched to the 1S-2S resonance in order to achieve the maximal number of metastable 2S atoms, thereby maximizing the 2S-6P signal. The natural linewidth of the 1S-2S transition is only 1.3 Hz, but the broadening mechanisms due to ionization, time-of-flight, as well as the ac-Stark and second-order Doppler effects, lead to the experimental linewidth of $\sim 4 - 5\,\mathrm{kHz}$. Recalling Section 3.2.1, the 243 nm laser light for the two-photon excitation of the 1S-2S transition originates from the master laser at 972 nm. Therefore, the transition linewidth in units of the detuning of the master laser is $2 \times 2 \times 2 = 8$ times smaller (two frequency doublings and the two-photon excitation), which is $\sim 5\,\mathrm{kHz}/8 \simeq 0.6\,\mathrm{kHz}$. As discussed in Section 3.2.3, the master laser frequency drifts by $\sim 0.1\,\mathrm{kHz/h}$, and thus needs to be adjusted on the timescale of hours during the measurement. During the 2S-6P measurement campaign, we regularly perform line scans of the 1S-2S resonance and adjust the laser frequency to the maximal signal. Comparing the

[1] For a linear function $y(x) = a + b\,x$ with fit parameters a and b, the variance in y is given by: $\sigma_y^2 = \sigma_a^2(\partial y/\partial a)^2 + \sigma_b^2(\partial y/\partial b)^2 + \sigma_{ab}(\partial y/\partial a)(\partial y/\partial b) + \sigma_{ba}(\partial y/\partial b)(\partial y/\partial a) = \sigma_a^2 + x^2\sigma_b^2 + 2x\sigma_{ab}$, where σ_a^2 and σ_b^2 are the variances of parameters a and b, and $\sigma_{ab} = \sigma_{ba}$ are their covariances, which are determined from the covariance matrix $((\sigma_a^2, \sigma_{ab}), (\sigma_{ba}, \sigma_b^2))$ of the fit. The 1σ uncertainty region is given by $y \pm \sigma_y$.

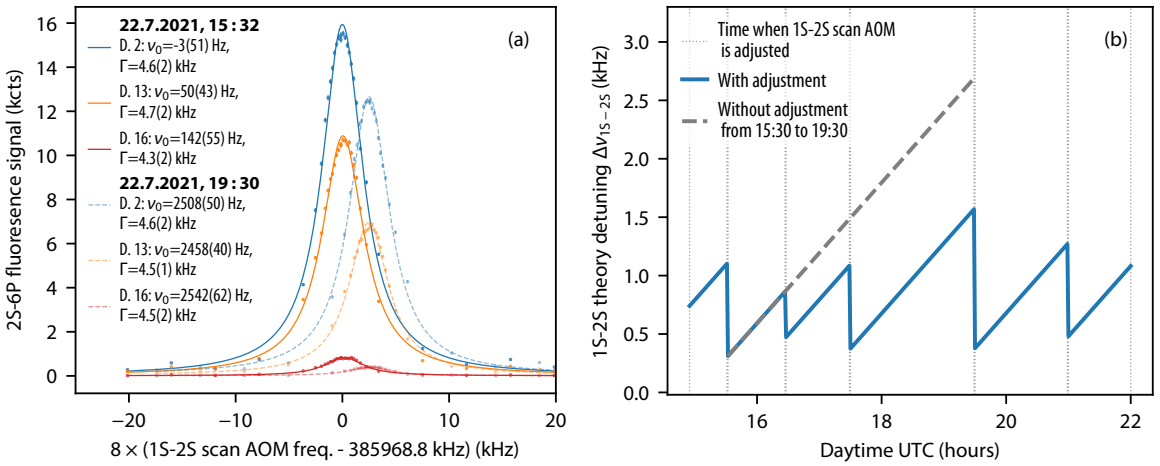

Figure 5.3: Example of the 1S-2S resonance line scans and the drift of the 1S-2S laser detuning throughout the measurement day. (a) Solid curves show the Lorentzian fits to the data (markers with error bars representing shot noise) on a specific day and time (22.7.2021, 15:32) from the 2S-6P fluorescence signal in dependence on the 1S-2S Scan AOM (see Fig. 3.5) detuning as seen by atoms. Three delays are exemplarily shown: delay 2 (D. 2, blue), delay 13 (D. 13, orange) and delay 16 (D. 16, red). The frequency offset is here chosen such that the center frequency for the delay 2 is approximately zero at this time of the measurement day. The Lorentzian fit results for the center frequency ν_0 and the linewidth Γ are given in the legend. However, note that the Lorentzian does not describe the data properly since the resonance lines are distorted, which is expected from simulations (see Fig. 5.4). Faint dashed curves show the fits to the data on the same measurement day but around 4 hours later. The center frequency is different by ∼2.5 kHz due to the linear drift of the laser frequency (see Section 3.2.3). (b) The blue line shows the laser detuning relative to the prediction of the unperturbed resonance frequency ("1S-2S theory detuning" $\Delta\nu_{1S-2S}$) in dependence on the daytime (the uncertainty on $\Delta\nu_{1S-2S}$ is ∼0.2 kHz due to the absolute frequency reference, see Section 3.2.3). Gray vertical dotted lines represent the times when the 1S-2S Scan AOM was adjusted to compensate for the drift of the laser frequency. The gray dashed line shows how $\Delta\nu_{1S-2S}$ would drift without the adjustment of the laser detuning between the two times from (a).

measured line center to the prediction[1], the detuning $\Delta\nu_{1S-2S}$ from the unperturbed resonance frequency ("1S-2S theory detuning") can be extracted, which is one of the input parameters for the simulations for the determination of the mean speed in each delay (recall Table 3.1). This detuning is on the order of ∼1 kHz and mainly originates from the ac-Stark and the second-order Doppler shifts.

Fig. 5.3 shows an example of two 1S-2S resonance line scans during a measurement day, and illustrates how the 1S-2S Scan AOM (see Fig. 3.5) is adjusted to compensate for the drifting laser frequency. In Fig. 5.3(a), solid curves show the Lorentzian fits to the data on a specific day and time (22.7.2021, 15:32). The signal originates from the 2S-6P fluorescence signal, and is shown in dependence on the 1S-2S Scan AOM detuning as seen by atoms (which is 8 times larger than the detuning of the 972 nm master laser). Different colors represent

[1] As discussed in Table 2.2, theory predicts the 1S-2S transition frequency only with an uncertainty of few kHz. However, the 1S-2S frequency in deuterium has been measured more accurately, resulting in the $1S_{1/2}$-$2S_{1/2}$ hyperfine centroid frequency of $\nu_{1S-2S,centr.} = 2\,466\,732\,407\,521\,641(25)$ Hz [54]. Together with the hyperfine splittings of the 1S and 2S states of $\Delta_{HFS,1S} = 327\,384\,352.5222(17)$ Hz and $\Delta_{HFS,2S} = 40\,924\,454(7)$ Hz, the prediction for the $1S_{1/2}^{F=1/2}$-$2S_{1/2}^{F=1/2}$ transition frequency with linearly polarized light excitation (see Fig. 2.2) is $\nu_{1S-2S,centr.} + \frac{2}{3}\Delta_{HFS,1S} - \frac{2}{3}\Delta_{HFS,2S} = 2\,466\,732\,598\,494\,907(26)$ Hz.

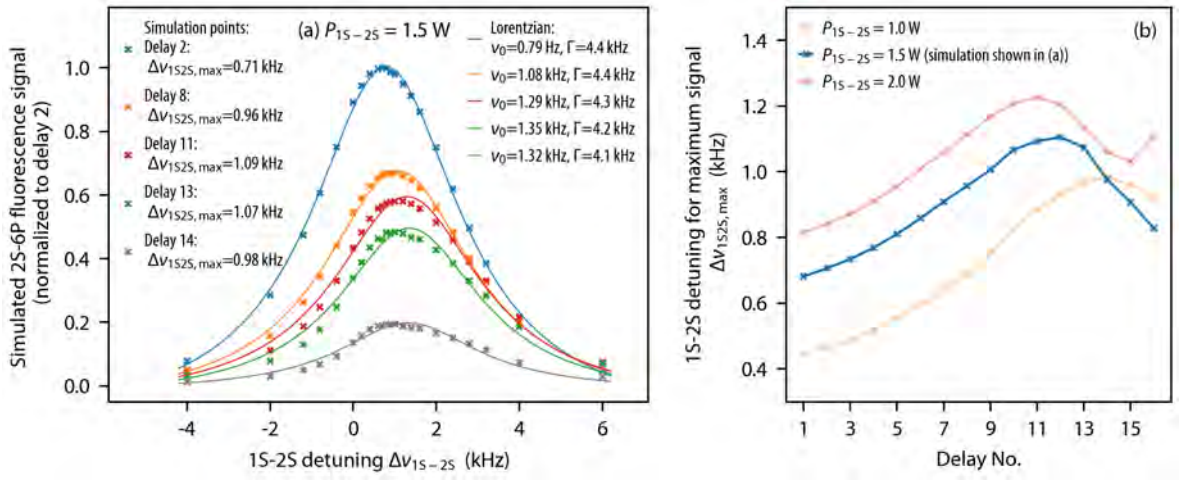

Figure 5.4: Simulation of the 1S-2S resonance from the 2S-6P fluorescence signal following the procedure described in Section 3.3. (a) The simulated 2S-6P fluorescence signal is shown as crossed markers in dependence on the 1S-2S theory detuning $\Delta\nu_{\text{1S-2S}}$ for the 1S-2S laser power of $P_{\text{1S-2S}} = 1.5\,\text{W}$, nozzle temperature $T_{\text{N}} = 7.1\,\text{K}$, cutoff speed $v_{\text{cutoff}} = 120\,\text{m/s}$ (for other simulation parameters see Table 3.1). Five different delays are represented by different colors. For each delay, the legend shows the 1S-2S theory detuning $\Delta\nu_{\text{1S2S,max}}$, where the 2S-6P fluorescence signal is maximal. To guide the eye, the curves show the Lorentzian fit with the center frequency ν_0 given in the legend. Since the resonance lines are distorted, the center frequency of the Lorentzian fit does not correspond to $\Delta\nu_{\text{1S2S,max}}$. (b) $\Delta\nu_{\text{1S2S,max}}$ is shown in dependence on the delay number for three values of $P_{\text{1S-2S}}$ (other parameters same as in (a)), where the case from (a), $P_{\text{1S-2S}} = 1.5\,\text{W}$, is represented in blue.

the three different delays, for which the fit results for the center frequency and the linewidth are given in the legend. Note that the Lorentzian fits do not properly describe the distorted resonance lineshapes, and hence are here only used as a rough estimate of the center frequency. The frequency offset is chosen such that the center frequency for the delay 2 approximately corresponds to zero for the line scan at 15:32. Faint markers with faint dashed curves show the 1S-2S line scan around 4 hours laser during the same day. The center frequency is here different by $\sim 2.5\,\text{kHz}$ due to the drift of the laser frequency. The reduced amplitude is attributed to changing atomic beam formation over time (see Section 3.6.1).

Comparing to the prediction of the unperturbed transition frequency, for the line scans from Fig. 5.3(a), we find that the frequency with maximum signal corresponds to the 1S-2S theory detuning of $\Delta\nu_{\text{1S-2S}} = 0.9(2)\,\text{kHz}$, with the uncertainty from the absolute frequency reference (see Section 3.2.3). At 15:32, the frequency of the "Scan AOM" has been set such that $\Delta\nu_{\text{1S-2S}} = 0.3(2)\,\text{kHz}$ in order to pre-compensate the laser drift out of resonance. Fig. 5.3(b) shows the linear drift of $\Delta\nu_{\text{1S-2S}}$ in between the laser detuning adjustments (vertical dotted lines represent the time when the frequency of the 1S-2S scan AOM (see Fig. 3.5) is adjusted). If the laser detuning would have been not adjusted in between the two times shown in Fig. 5.3(a), $\Delta\nu_{\text{1S-2S}}$ would have changed by $\sim 2.5\,\text{kHz}$, which would result in a reduced 2S-6P fluorescence signal. With adjustments, $\Delta\nu_{\text{1S-2S}}$ is usually kept between $\Delta\nu_{\text{1S-2S}} = 0.5 \ldots 1.5\,\text{kHz}$, such that the 2S-6P signal is nearly optimal. For the data analysis, one has to bear in mind that $\Delta\nu_{\text{1S-2S}}$ is one of the parameters which affects the velocity distribution of atoms in each delay (see Table 3.1).

It is instructive to compare the measured 1S-2S resonance lines to simulations, which

are shown in Fig. 5.4. Fig. 5.4(a) shows the simulation of a 1S-2S resonance line scan, where the 2S-6P fluorescence signal (crossed markers) has been simulated as described in Section 3.3 for different $\Delta\nu_{\text{1S-2S}}$. Other parameters are: 1S-2S laser power $P_{\text{1S-2S}} = 1.5\,\text{W}$, nozzle temperature $T_{\text{N}} = 7.1\,\text{K}$, cutoff speed $v_{\text{cutoff}} = 120\,\text{m/s}$, as well as the remaining fixed parameters from Table 3.1. Different colors exemplarily show five delays. For each delay, one can determine the 1S-2S detuning $\Delta\nu_{\text{1S2S,max}}$, for which the 2S-6P fluorescence signal is maximal. These values are given in the legend. To guide the eye, solid curves show the Lorentzian fits, with the center frequency ν_0 and the linewidth Γ given in the legend. In agreement with the measurement from Fig. 5.3(a), the resonance lineshapes are distorted. Therefore, the Lorentzian center frequency does not correspond to $\Delta\nu_{\text{1S2S,max}}$. Note that since the Lorentzian function does not properly describe the lineshape, the fit result depends on the specific sampling of simulation points and the detuning range. Nevertheless, the approximate agreement of the resonance linewidth between the simulation in Fig. 5.4(a) and the measurement in Fig. 5.3(a) confirms the modeling of the experiment. Furthermore, in agreement with observations, we find the optimal detuning of $\Delta\nu_{\text{1S-2S,max}} \sim 1\,\text{kHz}$. This agreement is also a crosscheck of the absolute laser frequency determination, where the 1S-2S transition can be considered as a clock.

Fig. 5.4(b) shows the optimal detuning $\Delta\nu_{\text{1S-2S,max}}$ (crossed markers connected by straight lines to guide the eye) in dependence on the delay number. Three different 1S-2S laser power values are represented by different colors, with other simulation parameters same as in Fig. 5.4(a). The case $P_{\text{1S-2S}} = 1.5\,\text{W}$ from Fig. 5.4(a) is shown in blue. Between the delays, $\Delta\nu_{\text{1S-2S,max}}$ varies by $\sim 0.4\,\text{kHz}$, with the tendency of higher $\Delta\nu_{\text{1S-2S,max}}$ for slower atoms (larger delay numbers). This can be attributed to the fact that slower atoms experience a smaller second-order Doppler shift (given by Eq. (2.29) with $\nu_{\text{A},0} \simeq 2.47 \times 10^{15}\,\text{Hz}$). For mean speeds between $\sim 60\,\text{m/s}$ (delay 16) and $\sim 280\,\text{m/s}$ (delay 2), the second-order Doppler shift varies between $-0.05\,\text{kHz}$ and $-1.1\,\text{kHz}$, which compensates the positive ac-Stark shift. However, the general behavior is a complex interplay between various effects for each delay, for instance between the second-order Doppler shift, the ac-Stark shift, the ionization broadening, the time-of-flight broadening and the atomic trajectories through the approximately Gaussian 1S-2S laser beam.

Relying on the simulations, it is in principle conceivable to extract the 1S-2S transition frequency from the acquired 1S-2S line scans during the 2S-6P measurement campaign. Note that to extract the Rydberg constant and the deuteron radius from the 2S-6P measurement in combination with the 1S-2S measurement (without significant reduction of uncertainty), the 1S-2S transition frequency only needs to be known within a moderate uncertainty of $\sim 0.5\,\text{kHz}$. In principle, one could fit the simulated distorted resonance lineshapes to the data for a more accurate determination of the transition frequency. For a future measurement campaign, one may plan for additional 1S-2S line scans at different 1S-2S laser powers to extrapolate the 1S-2S transition frequency at zero laser power, thereby additionally testing the numerical modelling of the experiment as well as experimentally determining the ac-Stark shift.

5.3 Alignment of the atomic beam

The active fiber-based retroreflector (AFR, see Chapter 4) needs to be accurately aligned w.r.t. the atomic beam, such that the angle $\alpha = 90^\circ + \delta\alpha$ between the counter-propagating

2S-6P laser beams and the atomic beam is as close as possible to 90°, i.e. $|\delta\alpha|$ as small as possible. Note that for the perfect AFR, any non-zero $\delta\alpha$ still leads to a complete cancellation of the Doppler shift. However, even in the case of a perfect AFR, it is advantageous to minimize $\delta\alpha$ to achieve the minimal linewidth of the resonance. As outlined in Chapter 4, we try to minimize all imperfections such as spherical aberrations in the AFR. However, some imperfections remain, such as the "orange-peel" structure of the collimated beam (see Fig. 4.12) or the residual astigmatism (see Fig. 4.9). Therefore, in reality the AFR has only a finite suppression factor of the Doppler shift, such that minimizing $\delta\alpha$ through accurate alignment is important to minimize the Doppler shift.

At the beginning of each freezing cycle, the variable atomic beam apertures are calibrated and set to the center position with the typical width of 1.2 mm using the alignment laser, which itself is aligned to co-propagate with the 1S-2S laser beam (see Section 3.1.2). Then the nozzle is aligned with the 1S-2S laser beam. The goal is to position the nozzle such that the 1S-2S laser beam passes through the center of the nozzle. For the deuterium 2S-6P measurement campaign, this positioning was performed with the help of the alignment stage of the new cryostat. Using the cryostat alignment stage, the nozzle is moved in both horizontal and vertical directions while the transmission of the 1S-2S laser is monitored. The positions where the nozzle begins to clip the 1S-2S beam are identified, from which the horizontal and vertical center positions are determined. The hydrogen 2S-6P measurement campaign was performed with the old cryostat, which did not have an accurate alignment stage. Instead, the positioning of the nozzle was performed with the help of the nozzle imaging system (see Sec. 4.5.2.5 of [71]). In the beginning of the deuterium 2S-6P measurement campaign, both alignment methods were compared. It was observed that the nozzle positioning using the nozzle imaging system was inconsistent with the nozzle positioning using the cryostat alignment stage by ~ 0.2 mm in both horizontal and vertical directions, i.e. by $\sim 10\%$ of the 2 mm nozzle diameter. If the nozzle alignment was performed with the nozzle imaging system, for the AFR "switched off" (with closed shutter (SH) in Fig. 4.2, such that only the forward-propagating 2S-6P is present and the atoms experience the full Doppler shift) differrent velocity classes of atoms were observed to have different Doppler slopes, as shown below. If the nozzle alignment was performed with the cryostat alignment stage, this effect was less pronounced, such that for the remaining measurement campaign the nozzle was aligned with the cryostat alignment stage. The discrepancy between the two alignment methods reveals an asymmetry present in the apparatus, which may originate from the imperfect alignment of the 1S-2S (243 nm) cavity w.r.t. the atomic beam apertures attached to the vacuum chamber floor, as described in Section 3.1.2. In the future, the vacuum chamber may be more reliably aligned after the planned upgrade of the apparatus for differential pumping, where the core part of the vacuum setup (including the AFR) will be placed on the rods holding the 1S-2S cavity ((ER) spacer Invar rods in Fig. 3.3) with special screws allowing for an accurate alignment.

After the nozzle has been aligned to the 1S-2S laser beam, the AFR is aligned w.r.t. the atomic beam. This is achieved with the alignment actuator, which changes the angle $\alpha = 90° + \delta\alpha$ between the atomic beam and the 2S-6P laser beam in the AFR ((AA) in Fig. 3.4 and Fig. 3.3). In the following, we denote the alignment angle which is set by the actuator as $\delta\tilde{\alpha}$. The goal is to find the actuator position $\delta\tilde{\alpha}_0$, which corresponds to zero $\delta\alpha$. This can be done in two ways. First, using a shutter before the mirror reflecting the 2S-6P laser beam ((SH) in Fig. 4.2), the AFR is "switched off", such that only the forward-propagating laser beam is present. The atoms therefore experience the full first-order Doppler shift, which can be measured for different actuator angles $\delta\tilde{\alpha}$. The minimal Doppler shift then corresponds

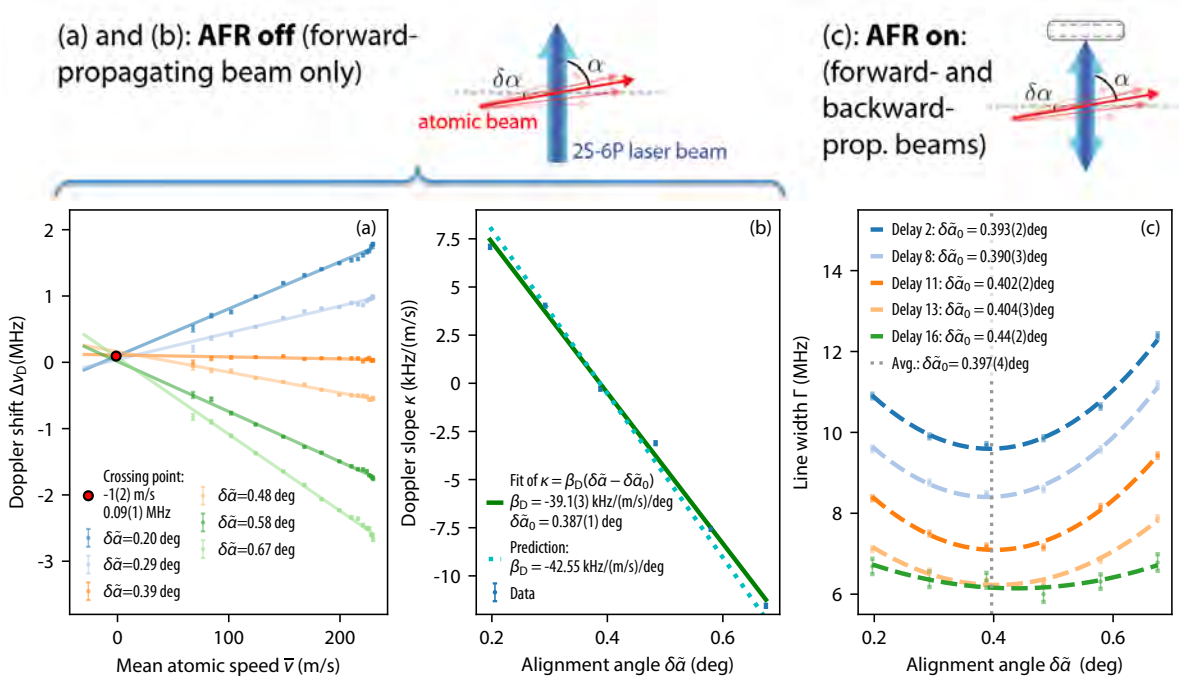

Figure 5.5: Alignment of the angle $\alpha = 90° + \delta\alpha$ between the atomic beam and the 2S-6P laser beam in the AFR with two methods. (a) and (b) show the data with AFR "switched off", where only the forward-propagating beam is present, as illustrated by the upper scheme. In (a), the Doppler shift $\Delta\nu_D$ is plotted versus the mean atomic speed $\overline{v}$ of each delay for different values of the alignment angle $\delta\tilde{\alpha}$ set by the actuator. The lines show linear fits from which the Doppler slope κ for each value of $\delta\tilde{\alpha}$ is determined. The red circle shows the average value for the crossing point between each pair of the lines. The legend shows the corresponding colors for each value of $\delta\tilde{\alpha}$, as well as the average values of the crossing point. In (b), the Doppler slope κ as determined from the fits in (a) is plotted versus $\delta\tilde{\alpha}$. The linear fit $\kappa = \beta_D(\delta\tilde{\alpha} - \delta\tilde{\alpha}_0)$ (green line) determines the actuator position $\delta\tilde{\alpha}_0$ with zero κ, which corresponds to zero $\delta\alpha$ ($\alpha = 90°$). The theoretical prediction for β_D is shown as a dotted line. (c) shows the data with AFR "switched on", i.e. where the Doppler shift is suppressed by the superimposed forward- and backward-propagating laser beams. The finite atomic beam divergence leads to the Doppler-broadened resonance linewidth Γ, which is plotted versus $\delta\tilde{\alpha}$ for five exemplary delays (different colors). Dashed curves show quadratic fits to the data, where the minimum determines $\delta\tilde{\alpha}_0$ given in the legend. The dashed vertical line shows the average value for all delays. The values for $\delta\tilde{\alpha}_0$ between the two methods in (b) and (c) disagree by ~ 0.01 deg, which is attributed to the residual misalignment effects discussed in Fig. 5.6 and Fig. 5.7.

to the actuator angle $\delta\tilde{\alpha}_0$ (where $\delta\alpha$ is zero). Second, with the AFR "switched on", where both forward- and backward-propagating beams are present, the Doppler-broadend 2S-6P resonance linewidth Γ is measured for different actuator angles $\delta\tilde{\alpha}$. The minimal linewidth Γ then determines $\delta\tilde{\alpha}_0$.

An example of the α angle alignment with both methods is shown Fig. 5.5. For this measurement, the alignment actuator is moved to the lowest value of $\delta\tilde{\alpha}$, and then $\delta\tilde{\alpha}$ is incrementally increased, where for each value of $\delta\tilde{\alpha}$ the 2S-6P resonance is measured with AFR "switched on" and AFR "switched off". Therefore, the actuator is incrementally moved in one direction, which removes errors due to the absolute on-axis accuracy or backlash. In Fig. 5.5(a) and (b) the AFR is "switched off", i.e. the shutter blocks the backward-propagating beam.

Fig. 5.5(a) shows the Doppler shift (relative to the theoretical prediction of the resonance line center) for different values of $\delta\tilde{\alpha}$ (represented by different colors) versus the mean atomic speed $\overline{v}$ from each delay. For each value of $\delta\tilde{\alpha}$, the Doppler slope κ from Eq. (5.1) is determined, which is shown in Fig. 5.5(b). The green line shows the linear fit of $\kappa = \beta_{\mathrm{D}}(\delta\tilde{\alpha} - \delta\tilde{\alpha}_0)$, with fit results for β_{D} and the optimal angle $\delta\tilde{\alpha}_0$ given in the legend. The value of β_{D} can be compared to the prediction $\beta_{\mathrm{D}} = -\nu_{\mathrm{A},0}/c \simeq -42.55\,\mathrm{kHz/(m/s)/deg}$, shown as dotted line in Fig. 5.5(b), where $\nu_{\mathrm{A},0}$ is the 2S-6P resonance frequency (see Eq. (2.28)). This comparison checks the numerical modeling of the experiment, which determines the mean atomic speed in each delay (see Section 3.3). However, also the conversion factor of the linear alignment actuator to the angular scale enters the comparison, as well as possible systematic uncertainties from misalignment of the apparatus (see below) and the systematic effects from the resonance line fits. Here, the disrepancy between measured and calculated β_{D} is around $\sim 3\,\mathrm{kHz/(m/s)/deg}$, which is $\sim 10\%$ of the slope. This discrepancy is mainly attributed to systematic shifts of resonance lines with large Doppler shifts, which are fitted with a symmetric fit function but have a slightly asymmetric line shape[1]. Another check is the crossing point of linear fits from Fig. 5.5(a). In the ideal case, all slopes should cross at zero mean speed and zero Doppler shift. The data from Fig. 5.5(a) gives an average crossing point at $-1(2)\,\mathrm{m/s}$, which is compatible with zero, and $0.09(1)\,\mathrm{MHz}$, which disagrees with zero Doppler shift by $\sim 0.1\,\mathrm{MHz}$. However, the chi-square per degree of freedom for both horizontal and vertical average values[2] is $\chi^2_{\mathrm{red}} \sim 7$, which indicates a scatter due to systematic effects.

Fig. 5.5(c) shows the data with the AFR "switched on", i.e. with both forward- and backward-propagating beams, such that the Doppler shift is suppressed. The finite atomic beam divergence leads to the Doppler-broadend linewidth Γ, which is plotted as a function of $\delta\tilde{\alpha}$ for five exemplary delays represented by different colors. The dashed curves show the quadratic fits, from which the angle $\delta\tilde{\alpha}_0$ with minimal Γ is determined for each delay. Note that there is a slight inconsistency of values between different delays ($\sim 0.01\,\mathrm{deg}$ between delay 2 and 13), which is attributed to the residual misalignment effects discussed below. The vertical dashed line shows the average over all delays (see legend for the value). The values for $\delta\tilde{\alpha}_0$ between the two methods (compare Fig. 5.5(b) with Fig. 5.5(c)) agree within $\sim 0.01\,\mathrm{deg}$. This number approximately corresponds to the possible backlash error of the actuator for setting $\delta\tilde{\alpha}_0$ after the alignment[3].

The alignment procedure described above is also important to identify possible nozzle misalignments in the apparatus. An example of the data where nozzle misalignment is clearly observed is presented in Fig. 5.6. The Doppler shifts shown in Fig. 5.6(a) clearly do not scale linearly with the mean atomic speed. In other words, different velocity groups of atoms are subject to different Doppler slopes, such that the alignment angle for zero Doppler shift differs between the velocity groups. Therefore, the linear fit does not adequately describe the data. This systematic error manifests in a crossing point which is off by $\sim 1\,\mathrm{MHz}$ from the expected zero Doppler shift (relative to the theoretical prediction of the resonance line

[1] The resonance line shape of atoms is convoluted with the speed distribution of the atomic beam, and thus leads to line shape distortions in the case of the "AFR switched off" with large Doppler shifts, which has been simulated to cause $\sim 10\%$ systematic effects (see Chapter 7 in [71]).

[2] The uncertainties for the crossing point values given in the legend of Fig. 5.5(a) have been scaled by $\sqrt{\chi^2_{\mathrm{red}}}$.

[3] The absolute on-axis accuracy of the alignment actuator is $0.13\,\mathrm{mm} \hat{=} 0.12\,\mathrm{deg}$ (see footnote in Section 3.1.2 for specification details), which is the most conservative limit on setting the actuator to $\delta\tilde{\alpha}_0$ after the alignment. However, here only the relative accuracy w.r.t. the first alignment value of $\delta\tilde{\alpha}$ matters. Such a relative accuracy is not specified, but may be expected to be at least on the same order as the backlash of $8\,\mu\mathrm{m}$.

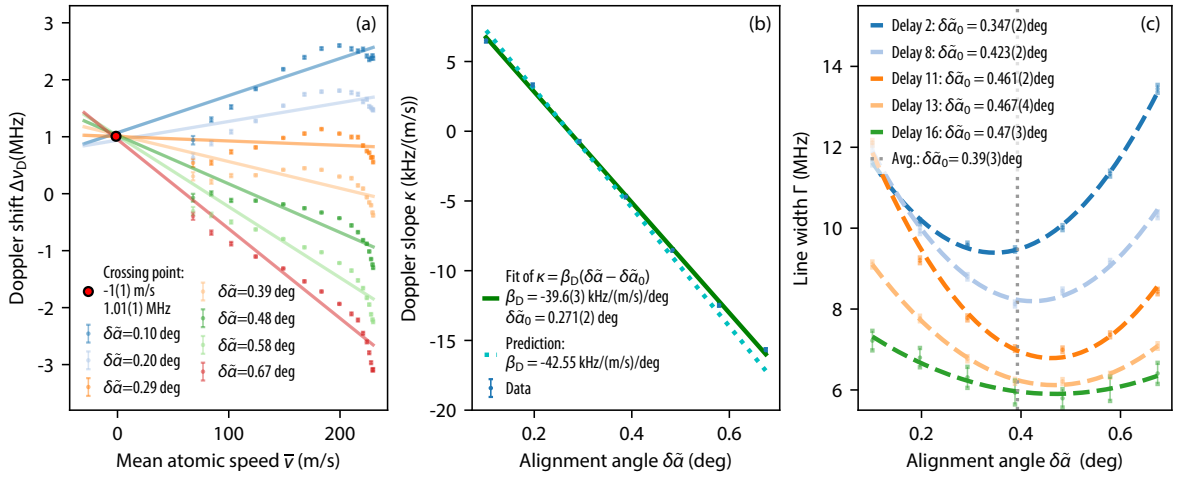

Figure 5.6: Similar to Fig. 5.5, here showing the data where clear nozzle misalignment is observed. The 1S-2S laser beam is estimated here to be off-center by ~ 0.2 mm or $\sim 10\%$ of the 2 mm nozzle diameter. In (a), it is observed that different velocity groups of atoms experience different Doppler slopes, such that the linear fits do not adequately describe the data. The value for $\delta\tilde{\alpha}_0$ determined in (b) is therefore strongly subject to this systematic error, and is discrepant with the average value for $\delta\tilde{\alpha}_0$ from (c) by ~ 0.1 deg. The data in (c) also confirms that the angle $\delta\tilde{\alpha}_0$ differs between different velocity groups of atoms.

center), as well as in the ~ 0.1 deg discrepancy of the value for $\delta\tilde{\alpha}_0$ from the fit in Fig. 5.6(b) compared to the average value of $\delta\tilde{\alpha}_0$ from Fig. 5.6(c). Furthermore, Fig. 5.6(c) confirms that the optimal angle $\delta\tilde{\alpha}_0$ differs between the different velocity groups of atoms, i.e. the values $\delta\tilde{\alpha}_0$ are inconsistent in between the delays (~ 0.12 deg between delay 2 and 13 which is an order of magnitude larger than in Fig. 5.5(c)).

The data set in Fig. 5.6 was obtained with the nozzle being aligned using the nozzle imaging system, whereas in Fig. 5.5 the nozzle was aligned using the cryostat alignment stage[1]. The cryostat alignment lead to similar alignment results as shown in Fig. 5.5 throughout the whole measurement campaign. However, it is not fully resolved why the nozzle imaging system did not agree with the cryostat alignment and lead to Doppler shift asymmetries[2]. The difference in the nozzle position between the two alignment methods is ~ 0.2 mm or $\sim 10\%$ of the 2 mm nozzle diamter. In hydrogen 2S-6P test measurements similar Doppler shift inconsistencies between velocity groups ("kink" of Doppler shifts for fast atoms) were observed for nozzle misalignments on the order of $\sim 10\%$ of the nozzle diameter. If the nozzle is misaligned in the opposite direction, the "kink" also changes direction. Note that in

[1]The data from Fig. 5.6 is from a different measurement day than Fig. 5.5, such that the values for $\delta\tilde{\alpha}_0$ are also subject to day-to-day fluctuation.

[2]One possible reason could be that the incoming 1S-2S laser beam was not aligned to the center of the 1S-2S incoupler cavity mirror, such that some asymmetries could enter the imaging of the nozzle. Another reason could be that the atomic beam apertures are not perfectly aligned with the 1S-2S laser beam, which leads to asymmetries of the nozzle imaging. In the hydrogen 2S-6P measurement, the higher-order modes of the 1S-2S cavity (up to the $\mathrm{TEM}_{n,m}$ modes with $n + m = 10$) could be used to check for the alignment of the apertures. However, for the deuterium 2S-6P apparatus, the 1S-2S laser system was upgraded, such that the mode-matching was modified (see Section 3.2.1). The mode-matching was optimized to minimize the contribution of higher-order modes. However, with this better mode-matching, the higher order modes which were used for the alignment of the vacuum chamber are not visible anymore. In the future, one may think of worsening the mode-matching to allow for this possibility again.

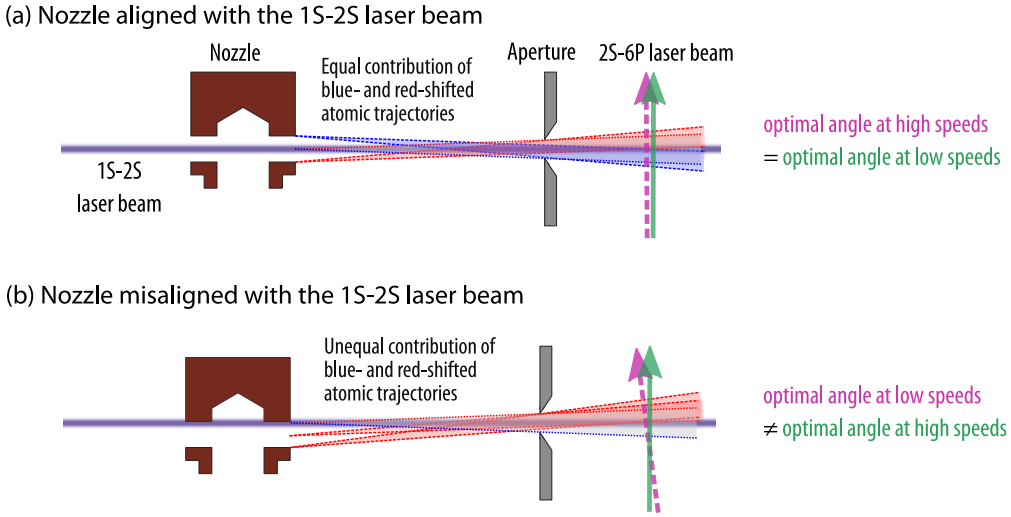

Figure 5.7: Illustration of aligned (a) and misaligned (b) nozzle w.r.t. the 1S-2S laser beam. Three exemplary fans of atomic beam trajectories are drawn for each case: one fan of trajectories originating from the center of the 1S-2S laser beam, and two fans of trajectories originating from either of the nozzle edges. For both cases, it is assumed that the 1S-2S laser beam is perfectly aligned with the aperture which collimates the atomic beam. Trajectories which lead to a Doppler blueshift of the 2S-6P resonance in case of the orthogonal configuration between the 2S-6P laser beam and the 1S-2S laser beam ("blue-shifted trajectories") are drawn in blue, and the trajectories which lead to a Doppler redshift ("red-shifted trajectories") are drawn in red. In (a), the nozzle is aligned such that the 1S-2S laser beam passes through the center of the nozzle. Due to the symmetry, there is exactly the same number of blue- and red-shifted atomic trajectories, such that the total Doppler shift is cancelled if the 1S-2S laser beam is perfectly orthogonal to the 2S-6P laser beam. The optimal angle of the 2S-6P laser beam is equal for all speeds of atoms ($\alpha = 90°$). In (b), the nozzle is misaligned, here exaggeratedly such that the 1S-2S laser beam passes through the edge of the nozzle. The contribution of blue- and red-shifted trajectories is unequal, such that the orthogonal configuration between the 1S-2S and the 2S-6P laser beams is not optimal. For the case shown here, there is an angle $\alpha < 90°$ between the 1S-2S and the 2S-6P laser beams, for which the total Doppler shift of the resonance is zero. This angle depends on the mean speed of atoms, since the excitation and ionization dynamics differ between the various velocity groups of atoms. This situation is observed in Fig. 5.6.

Fig. 5.5(a), for values of $\delta\tilde{\alpha}$ with large Doppler shifts, also small "kinks" are visible. However, they are symmetric and can be explained by the non-perfect assignment of mean speeds to the delays[1]. On the other hand, the asymmetric "kinks" from Fig. 5.6(a) cannot be explained by the different assignment of mean speeds.

The effect of different Doppler slopes for different velocity groups of atoms can be understood as follows. Fig. 5.7(a) illustrates the case where the nozzle is perfectly aligned, such that the 1S-2S laser beam passes through the center of the nozzle. The 1S-2S laser beam is here shown to be perfectly orthogonal to the 2S-6P laser beam. The aperture between the nozzle and the 2S-6P laser beam is assumed to be perfectly aligned with the 1S-2S laser beam. Three exemplary fans of atomic beam trajectories are drawn: one fan of trajectories originating from the center point of the nozzle, as well as two fans of trajectories from the edge

[1]In fact, in the future one may use this data to correct the mean speeds in each delay and infer more information about the velocity distribution.

of the nozzle[1]. The trajectories which are oriented towards the incoming 2S-6P laser beam experience a Doppler shift towards a higher resonance frequency ("blue-shifted trajectories") and are drawn in blue. The opposite case is drawn in red ("red-shifted trajectories"). If the aperture size is smaller than the nozzle diameter, all trajectories which originate from the edge of the nozzle are here either blue- or red-shifted, which is illustrated by the corresponding color of the fan. In the perfectly symmetric case, there is an equal number of red- and blue-shifted trajectories, such that the optimal angle (where the Doppler shift of the resulting resonance from all trajectories is cancelled) between the 1S-2S laser beam and the 2S-6P laser beam is $\alpha = 90°$ for both slow and fast atoms.

Fig. 5.7(b) shows the case of a misaligned nozzle, again in an exaggerated fashion, where the 1S-2S laser beam passes close to one edge of the nozzle. There is now an imbalance between the red- and blue-shifted trajectories. Therefore, the optimal angle α between the 1S-2S laser beam and the 2S-6P laser beam, for which the total Doppler shift is zero, is not $\alpha = 90°$ anymore, but for the example here $\alpha < 90°$. The relative contribution between the trajectories originating within and outside the 1S-2S laser beam depends on the excitation and ionization dynamics, which differs between the various velocity groups of atoms. This illustrates how atoms with different mean speeds can observe different Doppler slopes. The angle between the 1S-2S laser beam and the 2S-6P laser beam, where the total Doppler shift is zero, is then different depending on the velocity group, which is observed in Fig. 5.6. Slow atoms tend to be more likely ionized if they spend too much time in the 1S-2S laser beam, such that the signal contribution of trajectories crossing the 1S-2S laser beam under an angle is larger than for fast atoms[2]. On the other hand, the signal contribution of fast atoms is dominated by trajectories along the 1S-2S laser beam, since for fast atoms the ionization is negligible. Therefore, with increasing speed, the center of weight of the atomic beam shifts towards trajectories propagating along the 1S-2S laser beam.

In the case of a perfect AFR with two counter-propagating beams (perfect Doppler shift suppression), the above nozzle misalignment does not give rise to a systematic line shift, because the Doppler shift is cancelled independent of the atomic angle. However, as discussed in the beginning of this section, in reality the AFR has only a finite Doppler shift suppression factor. Therefore, nozzle misalignments can affect the 2S-6P frequency measurement. Indeed, the precision data from Fig. 5.10 indicates a non-linear structure of the center frequency in dependence on the mean speed, similar to what is exaggeratedly observed in Fig. 5.6.

5.4 Stray electric fields measurements

The procedure for in-situ stray electric field measurements has been explained in Section 3.5.2. Here, Fig. 5.8 shows the results for all stray electric field data throughout the measurement campaign. Each measurement determines the stray electric field value ΔF, the effective dc-

[1]Note that the situation is here greatly exaggerated for illustration purposes. In reality, only very few atomic beam trajectories originate from the edge of the nozzle due to geometrical constraints, as there is no direct line of sight to the nozzle walls for most of possible trajectories. The majority of atomic trajectories originates from atom-atom collisions in the nozzle, which have a direct line of sight to the 2S-6P interaction region.

[2]One way to quantify this is to calculate the average distance $\bar{l}_{1S-2S,i} = \overline{T}_{\text{1S-2S},i} \times \overline{v}_i$, which the atom spends in the 1S-2S for each delay i, where $\overline{T}_{\text{1S-2S},i}$ is the average interaction time of those trajectories which interacted with the laser, and $\overline{v}_i$ is the mean speed. From simulations we find that $\bar{l}_{\text{1S-2S},i}$ rapidly drops from $\bar{l}_{\text{1S-2S},1} \sim 0.15\,\text{m}$ for the first delay (fast atoms) to $\bar{l}_{\text{1S-2S},13} \sim 0.04\,\text{m}$ for the last delays (slow atoms).

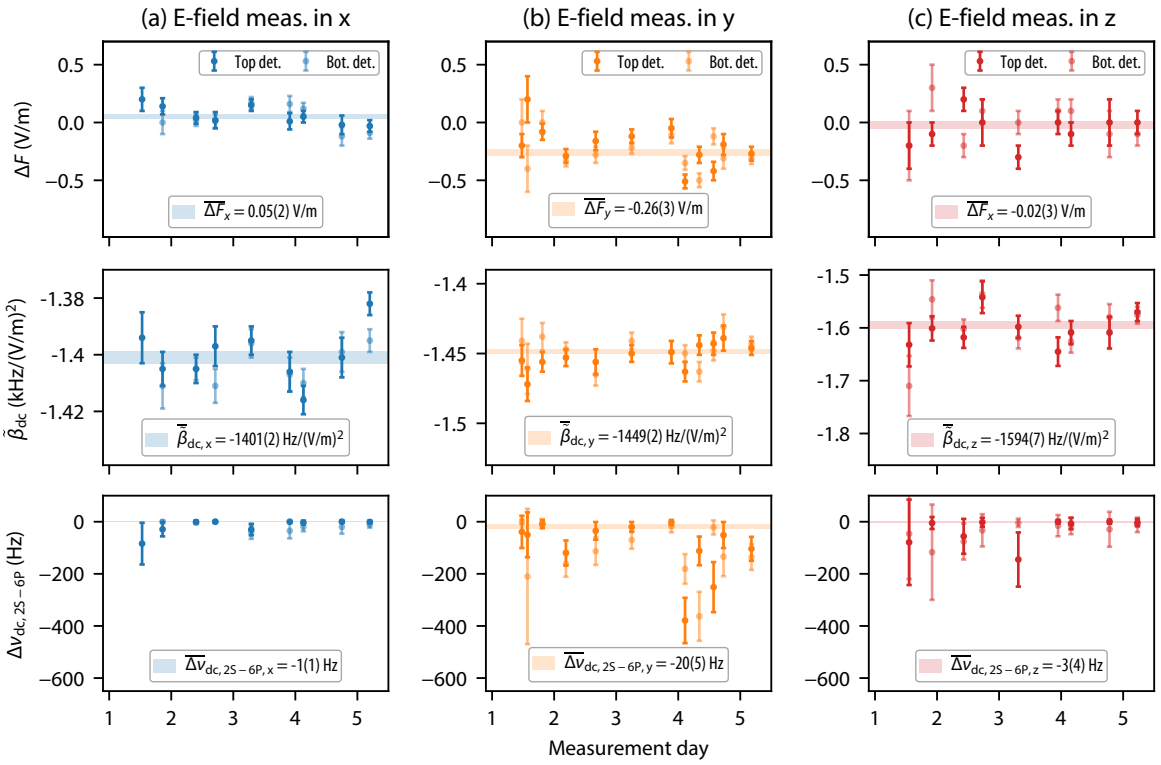

Figure 5.8: In-situ stray electric field measurement results for each measurement day. The procedure for the determination of stray electric fields is explained in Section 3.5.2. For a given spatial direction, each stray electric field measurement yields the stray electric field value ΔF, the effective dc-Stark coefficient $\tilde{\beta}_{\mathrm{dc}}$ and the dc-Stark shift $\Delta\nu_{\mathrm{dc,2S-6P}}$. These three quantities are shown for the measurements in the x, y, and z directions in (a), (b) and (c), respectively. The horizontal bars show the weighted average results.

Stark coefficient $\tilde{\beta}_{\mathrm{dc}}$ and the dc-Stark shift $\Delta\nu_{\mathrm{dc,2S-6P}}$. Typically, on each measurement day two stray electric field determinations in each of the three spatial directions are performed. In the x and z directions, the average stray electric field is consistent with zero. In the vertical y direction, the average value is significantly above zero: $\overline{\Delta F}_y = -0.26(3)\,\mathrm{V/m}$. This electric field corresponds to a dc-Stark shift of around $-0.1\,\mathrm{kHz}$. Note that the average value for the dc-Stark shift from Fig. 5.8 does not correspond to the dc-Stark shift with the average value for the stray electric field, because the electric field enters quadratically to the dc-Stark shift calculation.

For the preliminary uncertainty budget, it is assumed that the stray electric field is constant throughout the whole measurement campaign, with the corresponding average values $\overline{\Delta F}_x$, $\overline{\Delta F}_y$, $\overline{\Delta F}_z$ as determined in Fig. 5.8. Assuming these values, we compute the dc-Stark shift with the corresponding measured average coefficients (see Eq. (3.16)) $\tilde{\beta}_{\mathrm{dc,x}} \equiv \overline{\tilde{\beta}}_{\mathrm{dc,x}}$, $\tilde{\beta}_{\mathrm{dc,y}} \equiv \overline{\tilde{\beta}}_{\mathrm{dc,y}}$, and $\tilde{\beta}_{\mathrm{dc,z}} \equiv \overline{\tilde{\beta}}_{\mathrm{dc,z}}$ as:

$$\Delta\nu_{\mathrm{dc,2S\text{-}6P}} = -\sqrt{\left(\tilde{\beta}_{\mathrm{dc,x}}\overline{\Delta F}_x^2\right)^2 + \left(\tilde{\beta}_{\mathrm{dc,y}}\overline{\Delta F}_y^2\right)^2 + \left(\tilde{\beta}_{\mathrm{dc,z}}\overline{\Delta F}_z^2\right)^2} = -98(25)\,\mathrm{Hz}, \tag{5.2}$$

where in the last step we gave the number with the values from Fig. 5.8. Note that this

estimation of the dc-Stark shift gives a more conservative limit as compared to the averaged dc-Stark shift from the bottom plots in Fig. 5.8, which would yield $-20(6)$ Hz.

A non-zero electric field in the vertical y direction has also been repeatedly observed in the hydrogen 2S-6P measurement campaign and is suspected to be caused by the temperature gradient along the detector, as has been mentioned in Section 3.5.2. Therefore, for the final data analysis, it may be more appropriate to correct the data for each day with the corresponding value of the dc-Stark shift separately. During the deuterium 2S-6P measurement campaign, the apparatus was not in operation for two days between measurement day 3 and measurement day 4, which may have caused the small drop of observed dc-Stark shift in Fig. 5.8(b). In this case, one may also divide the data into two groups (day 1-3 and day 4-5), with separate dc-Stark shift corrections. However, as summarized in Table 5.3, the dc-Stark shift correction is small compared to other corrections, such that for the preliminary measurement presented here, these different ways of analyzing the dc-Stark shift do not make a notable difference. Note that the largest observed dc-Sark shift from Fig. 5.8 is $-0.3(1)$ kHz (average of top and bottom detectors for the first measurement in the y direction on day 4), which is $\sim$20% of the total uncertainty according to Table 5.3. However, the future deuterium 2S-6P precision measurement may reach the similar uncertainty as the hydrogen 2S-6P measurement (0.6 kHz according to the preliminary analysis in [71]), where the different ways of analyzing the dc-Stark shift would become important.

5.5 Preliminary analysis of precision line scans

Here, the preliminary analysis of the precision line scans for the 2S-6P$_{1/2}$ transition measurement data is presented. The majority of precision line scans was collected at the 2S-6P laser power of $P_{\text{2S-6P}} = 30\,\mu\text{W}$ (see Table 5.1), which contribute most significantly to the result. Therefore, first we show the analysis of this data group in order to demonstrate the analysis procedure. In total, the preliminary analysis includes 317 precision line scans at $P_{\text{2S-6P}} = 30\,\mu\text{W}$. Two ways of performing the extrapolation for different mean speeds of atoms of the 16 delays are presented: first, one can analyze each line scan separately (as in Fig. 5.2), and then average the results of all line scans. This approach is carried out in Section 5.5.1. Second, one can average the center frequencies of all line scans for each delay, and then perform the extrapolation, which is demonstrated in Section 5.5.2. Section 5.5.3 summarizes the analysis results of the precision line scans at all laser powers along with simulation corrections. Section 5.5.4 presents the preliminary uncertainty budget and corrections for determining the hyperfine centroid of the 2S$_{1/2}$-6P$_{1/2}$ transition.

As introduced in Section 5.1, we here define the center frequencies $\nu_{0,\text{a}}$ and $\nu_{0,\text{e}}$ to be the difference to the theoretical laser frequency prediction with a random blind offset, which is created from a normal distribution centered around zero with a standard deviation of 12 kHz. The numerical value of the blind offset is encoded in the analysis scripts in characters, such that the blind offset is not given in numbers, but as a string of characters to the input settings of the analysis code. For each line scan, as in Fig. 5.2, the center frequencies are determined relative to the detuning of the 2S-6P$_{1/2}$ transition, which is calculated from the measured laser frequency (see Section 3.2.3) relative to the prediction including the blind offset.

5.5.1 Extrapolation of delay center frequencies for individual line scans

As shown in the example line scan of Fig. 5.2, for each line scan one can determine the average center frequency $\nu_{0,\mathrm{a}}$ over all delays, as well as the extrapolated frequency $\nu_{0,\mathrm{e}}$ along with the slope κ according to Eq. (5.1). Fig. 5.9 shows the results for all 317 precision line scans at $P_{\text{2S-6P}} = 30\,\mu\mathrm{W}$, where the data from the top (blue markers) and bottom (orange markers) detectors is shown along with the error bars according to the fit uncertainties. The averages of all data from both detectors are shown as gray lines. The legends list the corresponding averages over all line scans with the χ^2_{red} values. The histograms on the right show the distributions of the data from the top (blue) and botton (orange) detectors, where curves show the normal distribution fits, with mean values μ and standard deviations σ given in the legends. The average value for $\nu_{0,\mathrm{a}}$ has a statistical uncertainty of $\sim 0.2\,\mathrm{kHz}$ and shows an excess scatter with $\chi^2_{\mathrm{red}} \sim 3$. The statistical uncertainty of the average value for $\nu_{0,\mathrm{e}}$ is $\sim 0.7\,\mathrm{kHz}$ with a lower $\chi^2_{\mathrm{red}} \sim 1.6$. The main origin of excess scatter is attributed to the atomic flux fluctuations caused by nozzle temperature fluctuations, which are expected to have a larger effect on $\nu_{0,\mathrm{a}}$ than on the extrapolation.

Note that the extrapolation depends on the mean speeds $\overline{v}$ assigned to each delay. As explained in Section 3.3, these mean speeds are determined from simulations, which depend on various experimental parameters (see Table 3.1). There are four parameters which vary throughout the measurement campaign: the 1S-2S laser power $P_{\text{1S-2S}}$, the 1S-2S laser detuning $\Delta\nu_{\text{1S-2S}}$, the cutoff velocity v_{cutoff}, and the nozzle temperature T_{N}. For the analysis in Fig. 5.9, these parameters are set for all line scans to be equal to $P_{\text{1S-2S}} = 1.5\,\mathrm{W}$, $\Delta\nu_{\text{1S-2S}} = 0.8\,\mathrm{kHz}$, $v_{\text{cutoff}} = 100\,\mathrm{m/s}$, $T_{\mathrm{N}} = 7.1\,\mathrm{K}$. The sensitivity of the result to these simulation parameters is evaluated in Table 5.2, which shows the average values for $\nu_{0,\mathrm{e}}$ and κ for different simulation parameter sets. The parameters are varied within the most conservative ranges $P_{\text{1S-2S}} = 1.1 \ldots 1.7\,\mathrm{W}$, $\Delta\nu_{\text{1S-2S}} = 0.0 \ldots 2.0\,\mathrm{kHz}$, $v_{\text{cutoff}} = 0 \ldots 300\,\mathrm{m/s}$, $T_{\mathrm{N}} = 7.0 \ldots 7.5\,\mathrm{K}$. For each parameter set, the mean speeds $\overline{v}$ in each delay are determined and the data analysis is repeated. Table 5.2 lists the simulation results for $\overline{v}$ in three exemplary delays (2, 13, and 16). The last two columns in Table 5.2 give the measurement result for $\nu_{0,\mathrm{e}}$ and κ, which have been determined with the corresponding delay velocities. The first row lists the result from Fig. 5.9. Compared to other simulation parameter sets, $\nu_{0,\mathrm{e}}$ varies maximally by $\sim 0.5\,\mathrm{kHz}$, and κ by $\sim 4\,\mathrm{Hz/(m/s)}$. Therefore, even for these most conservative simulation parameter ranges, the result for $\nu_{0,\mathrm{e}}$ varies only within a fraction of the total estimated uncertainty ($\sim 1.7\,\mathrm{kHz}$, see Table 5.3). The result is most sensitive to the 1S-2S detuning $\Delta\nu_{\text{1S-2S}}$, which is measured to $\sim 0.2\,\mathrm{kHz}$ as discussed in Section 5.2. Therefore, for the final analysis, each line scan can be evaluated with a different set of mean speeds according to the parameter set which best describes the experimental condition at the corresponding measurement time.

5.5.2 Extrapolation of averaged delay center frequencies

Another way of analyzing the data is to average the center frequencies in each delay separately for all line scans, and then average or extrapolate over these averaged frequencies. This analysis is presented in Fig. 5.10, where the averaged center frequency ν_0 is plotted versus the mean speed $\overline{v}$ assigned to each delay (with simulation parameters same as for the analysis in Fig. 5.9). As expected, the delay-averaged frequency $\nu_{0,\mathrm{a}}$ gives exactly the same result, though with a slightly different χ^2_{red}. The extrapolation yields the values for $\nu_{0,\mathrm{e}}$ and κ, which differ by $\sim 0.3\,\mathrm{kHz}$ and $\sim 2\,\mathrm{Hz/(m/s)}$, respectively, which are fractions of the uncertainties

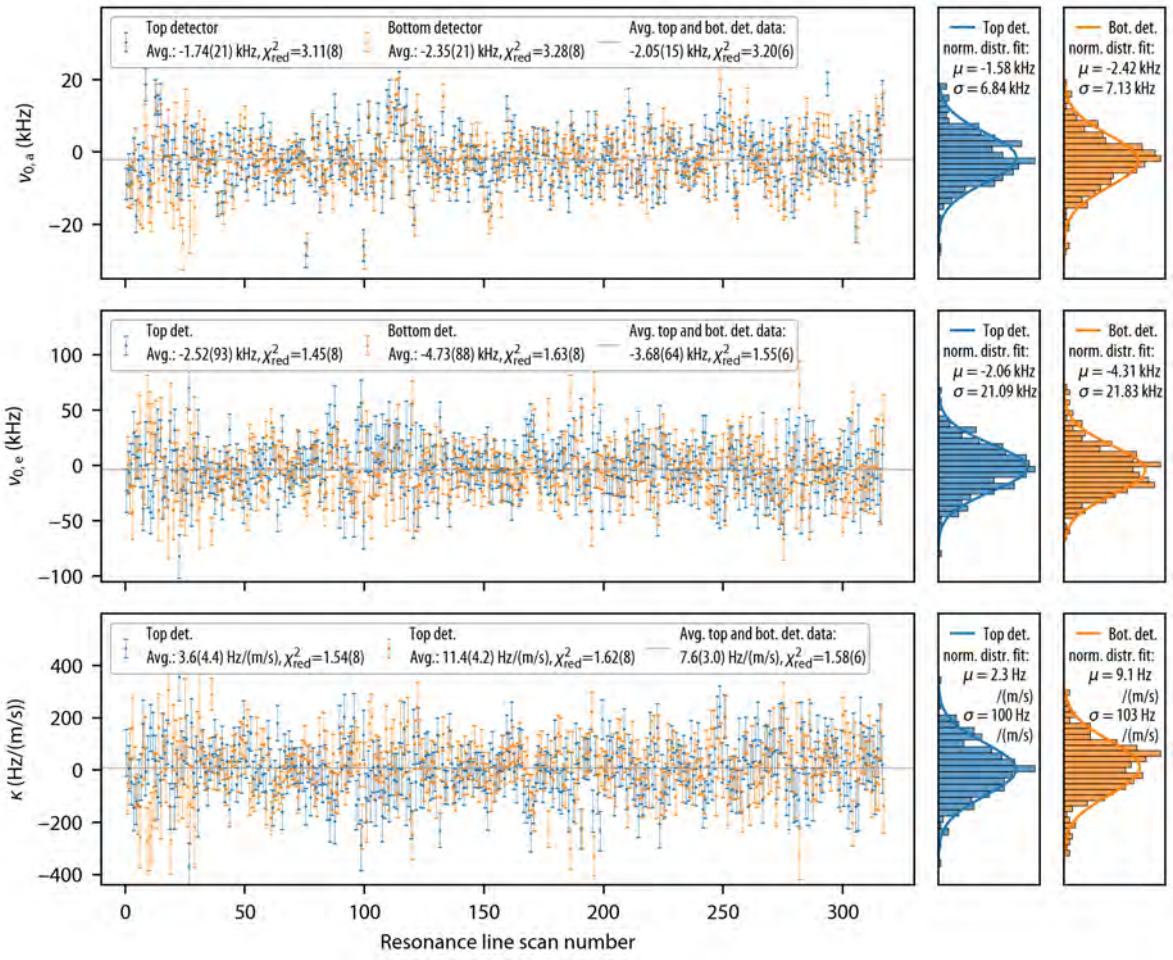

Figure 5.9: Preliminary analysis of 317 precision line scans at $P_{\text{2S-6P}} = 30\,\mu\text{W}$. Each line scan is analyzed separately (as in Fig. 5.2) to extract the averaged center frequency $\nu_{0,\text{a}}$ over all delays, as well as the extrapolated frequency $\nu_{0,\text{e}}$ together with the the Doppler slope κ from the extrapolation according to Eq. (5.1). The mean speeds for each delay have been simulated with parameters $P_{\text{1S-2S}} = 1.5\,\text{W}$, $\Delta\nu_{\text{1S-2S}} = 0.8\,\text{kHz}$, $v_{\text{cutoff}} = 100\,\text{m/s}$, $T_{\text{N}} = 7.1\,\text{K}$, as well as other fixed parameters from Table 3.1. Here, for each line scan, the results for $\nu_{0,\text{a}}$, $\nu_{0,\text{e}}$ and κ are plotted versus the resonance line scan number for the top (blue) and bottom (orange) detectors. The corresponding averages with the χ^2_{red} values are given in the legends. The gray lines show the average of the data from both detectors. The histograms on the right show the distributions of the data from the top (blue) and botton (orange) detectors, where curves show the normal distribution fits, with mean values μ and standard deviations σ given in the legends.

from Fig. 5.9. Most importantly, the extrapolation yields a higher $\chi^2_{\text{red}} \sim 2{-}3$ compared to $\chi^2_{\text{red}} \sim 1.6$ from Fig. 5.9. This might be an indicitation of a residual non-linear dependence of the center frequency on $\overline{v}$, which may originate from misalignment. Indeed, one may recognize a similar non-linear structure on the data from Fig. 5.10, which is exaggeratedly present in Fig. 5.6(a). Note that one would expect that such a small non-linear dependence would not be observed in the analysis from Fig. 5.9, where each line scan is extrapolated individually. The statistical uncertainty of each line scan is then much larger than the residual non-linearity, and hence is statistically not resolved. On the other hand, when each delay is averaged

Simulation parameters				Simulation result for $\overline{v}$ (m/s) in delay number			Measurement result	
$P_{\text{1S-2S}}$ (W)	$\Delta\nu_{\text{1S-2S}}$ (kHz)	T_{N} (K)	v_{cutoff} (m/s)	2	13	16	$\nu_{0,\text{e}}$ (kHz)	κ (Hz/(m/s))
1.5	0.8	7.1	100	257.4	126.1	67.7	-3.68(64)	7.6(3.0)
1.1	0.0	7.0	0	242.1	116.4	61.2	-3.66(72)	8.0(3.6)
1.1	0.0	7.5	0	247.1	116.6	60.5	-3.58(70)	7.5(3.5)
1.1	0.0	7.0	300	282.9	138.7	72.5	-3.68(73)	7.0(3.1)
1.1	0.0	7.5	300	288.3	138.2	73.5	-3.60(71)	6.5(3.0)
1.1	2.0	7.0	0	223.2	120.5	66.8	-4.29(82)	11.7(4.3)
1.1	2.0	7.5	0	227.5	121.3	66.2	-4.19(81)	11.0(4.2)
1.1	2.0	7.0	300	263.3	138.8	74.7	-4.16(80)	9.4(3.6)
1.1	2.0	7.5	300	267.6	139.3	77.4	-4.07(78)	8.9(3.5)
1.7	0.0	7.0	0	258.6	119.7	61.8	-3.53(69)	7.0(3.3)
1.7	0.0	7.5	0	265.5	120.7	61.9	-3.43(67)	6.4(3.1)
1.7	0.0	7.0	300	301.9	142.4	77.4	-3.54(70)	6.0(2.8)
1.7	0.0	7.5	300	308.3	142.6	77.6	-3.45(68)	5.5(2.7)
1.7	2.0	7.0	0	244.0	125.6	67.7	-4.01(78)	9.5(3.8)
1.7	2.0	7.5	0	249.3	125.6	67.4	-3.90(76)	8.9(3.6)
1.7	2.0	7.0	300	282.0	143.3	77.5	-3.92(76)	7.9(3.2)
1.7	2.0	7.5	300	287.1	143.0	74.6	-3.83(74)	7.4(3.1)

Table 5.2: Measurement results for the extrapolated frequency $\nu_{0,\text{e}}$ along with the slope κ (average values of 317 line scans at $P_{\text{2S-6P}} = 30\,\mu\text{W}$ for the top and bottom detectors). This extrapolation depends on the mean speed of atoms in each delay, and thus on the simulation parameters responsible for the simulated velocity distribution. Therefore, $\nu_{0,\text{e}}$ and κ are evaluated for different simulation parameter sets of the 1S-2S laser power $P_{\text{1S-2S}}$, 1S-2S detuning $\Delta\nu_{\text{1S-2S}}$, nozzle temperature T_{N}, and cutoff velocity v_{cutoff} (for other simulation parameters see Table 3.1). For each set of simulation parameters, the simulation result for the mean speed $\overline{v}$ is exemplarily given for three delays. The first row lists the most probable case of simulation parameters (used in Fig. 5.9). Compared to this parameter set, the result for $\nu_{0,\text{e}}$ varies maximally by $\sim 0.5\,\text{kHz}$, and for κ by $\sim 4\,\text{Hz/(m/s)}$ within the given range of simulation parameters.

separately for all line scans, the statistical uncertainty becomes small enough to resolve the small non-linear dependence on $\overline{v}$.

This possible non-linear dependence of the center frequency on the mean speed of atoms needs to be futher investigated. Note that in the simulations presented in Section 3.3, the perfect symmetric alignment is assumed between the 1S-2S laser beam, the atomic beam apertures, and the nozzle. As demonstrated in Section 5.3, an asymmetry present in the apparatus can lead to the non-linear dependence of the center frequency on the mean speed of atoms if the AFR is switched off, and thus a residual effect might be present if the AFR is switched on but does not perfectly suppress the Doppler shift. In the future, such an asymmetry can be included in simulations, which may help to better understand and model these effects. For the preliminary analysis presented here, we increase the uncertainty by an additional factor of $\sqrt{\chi^2_{\text{red}}} \sim \sqrt{3}$ to account for the possible distortion of the extrapolation as observed in Fig. 5.10.

The measurement results from Fig. 5.10 need to be corrected by the following three effects

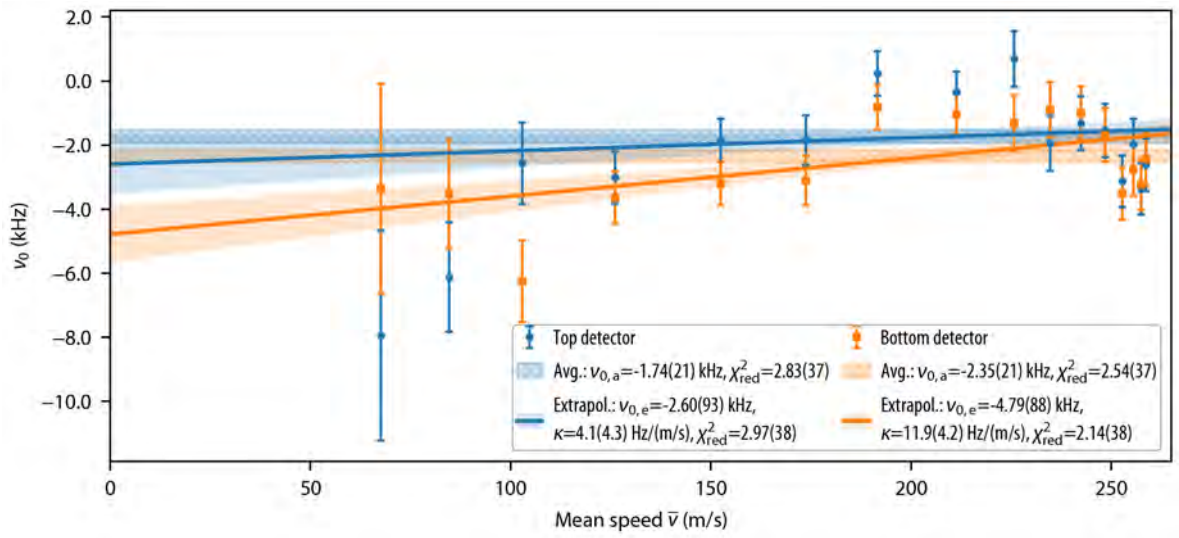

Figure 5.10: Preliminary analysis of the 317 precision line scans at $P_{\text{2S-6P}} = 30\,\mu\text{W}$ (average in each delay). The separately averaged center frequencies ν_0 are shown in dependence on the mean speed in each delay for all line scans with the top (blue circular markers) and bottom (orange square markers) detectors. The mean speeds have been assigned for each delay with parameters $P_{\text{1S-2S}} = 1.5\,\text{W}$, $\Delta\nu_{\text{1S-2S}} = 0.8\,\text{kHz}$, $v_{\text{cutoff}} = 100\,\text{m/s}$, $T_{\text{N}} = 7.1\,\text{K}$, as well as other fixed parameters from Table 3.1. The values for the delay-averaged frequency $\nu_{0,\text{a}}$ as well as the extrapolation according to Eq. (5.1) which yields $\nu_{0,\text{e}}$ and κ are given in the legend (see main text for discussion).

based on simulations: the "Big Model" (BM) effects, the light force shift (LFS) and the second-order Doppler shift (SOD), which are shown in Fig. 5.11. Fig. 5.11(a) shows the "Big Model" (BM) simulations from the procedure described in Section 3.3. Here, the value of the center frequency $\nu_{0,\text{BM}}$ from the BM simulations is evaluated relative to the $2\text{S}_{1/2}^{F=1/2}$-$6\text{P}_{1/2}^{F=3/2}$ hyperfine transition. Therefore, the observed hyperfine center correction of $(1-\eta_{1/2})\Delta_{\text{HFS},1/2} = 56.105\,\text{kHz}$ (see Eq. (2.49)) is included in the BM correction. In order to quantify the remaining effects, we define the shift $\Delta\nu_{\text{BM-HFC}}$, where the hyperfine center correction are excluded from $\nu_{0,\text{BM}}$, as following:

$$\Delta\nu_{\text{BM-HFC}} = \nu_{0,\text{BM}} + (1-\eta_{1/2})\Delta_{\text{HFS},1/2} = \nu_{0,\text{BM}} + \frac{1}{9}\Delta_{\text{HFS},1/2} = \nu_{0,\text{BM}} + 56.105\,\text{kHz}, \quad (5.3)$$

which is shown on the right axis in Fig. 5.11(a). The BM includes fit corrections as those discussed in Fig. 2.14 (here, the Voigt fit has been used as for the experimental data). In the BM results presented here, the signals from $\sigma^{\pm}$ and π decay channels are weighted equally, i.e. no detection efficiency is taken into account, which influences the quantum interference. For the final analysis, the detection efficiency should be taken into account as described in Sec. 6.2.3 of [71] to appropriately take the resolved quantum interference into account, which is expected to be on the order of $\sim 0.2\,\text{kHz}$ based on the results from the hydrogen 2S-6P simulations in [71]. Furthermore, here the detector is assumed to be perfectly linear. In the future, one may also model the non-linearity of the detector, which has been treated in Section 3.5.3. The legend in Fig. 5.11(a) gives the results on the total corrections from the BM for $\nu_{0,\text{a}}$, $\nu_{0,\text{e}}$ and κ, determined from the weighted average or extrapolation with experimental uncertainties for the top or bottom detectors from the top plot. Similar to the

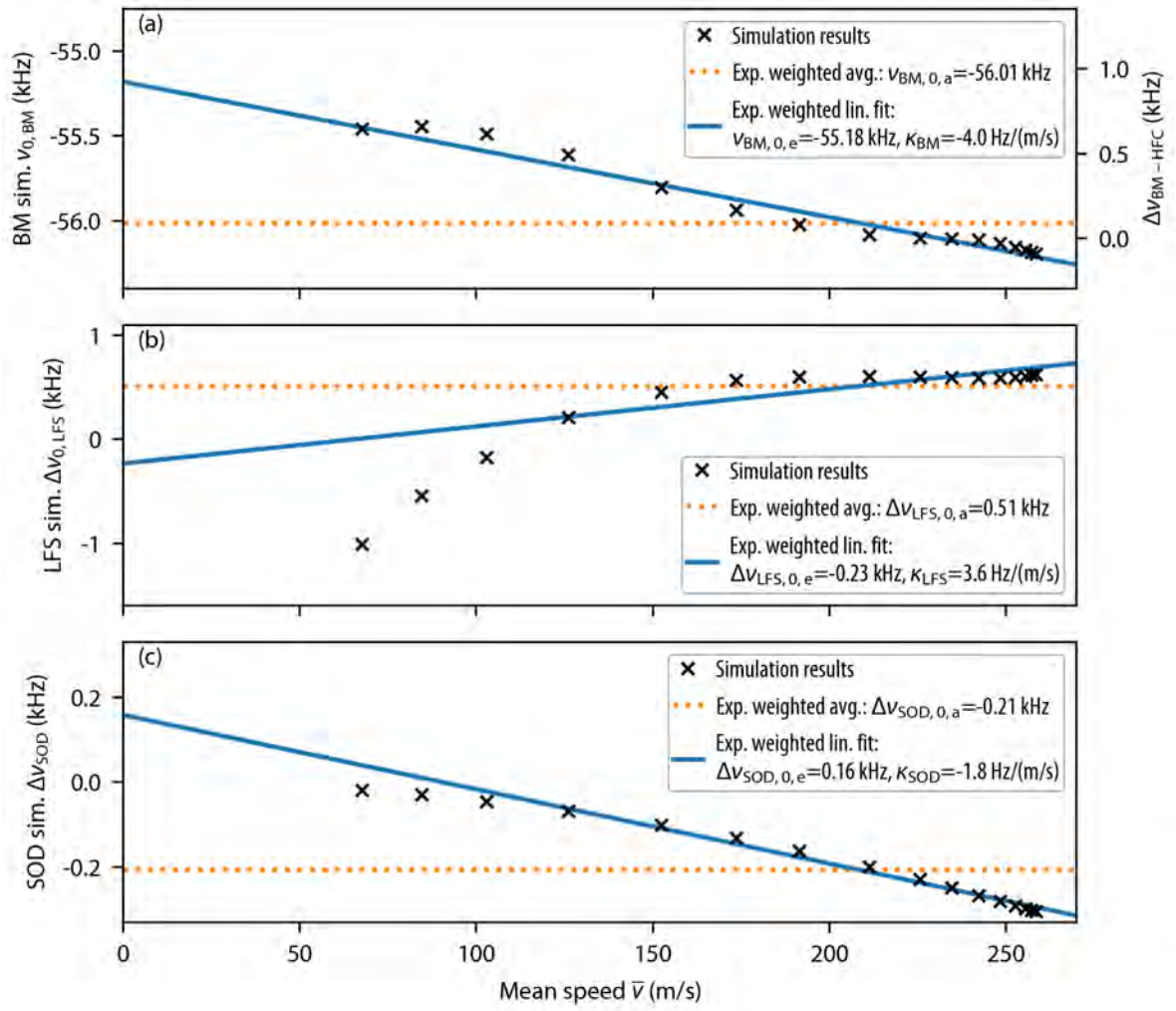

Figure 5.11: "Big Model" (BM), light force shift (LFS) and second-order Doppler shift (SOD) simulations for the 2S-6P laser power of $P_{2S\text{-}6P} = 30\,\mu W$. The mean speeds have been assigned for each delay with parameters $P_{1S\text{-}2S} = 1.5\,W$, $\Delta\nu_{1S\text{-}2S} = 0.8\,kHz$, $v_{cutoff} = 100\,m/s$, $T_N = 7.1\,K$, as well as other fixed parameters from Table 3.1. (a) The BM simulation gives the center frequency $\nu_{0,BM}$ relative to the $2S_{1/2}^{F=1/2}$-$6P_{1/2}^{F=3/2}$ hyperfine transition, i.e. including the observed hyperfine center shift of $(1-\eta_{1/2})\Delta_{HFS,1/2} \simeq 56.105\,kHz$ (see Eq. (2.49)). The right axis shows the shift $\Delta\nu_{BM-HFC}$ (see Eq. (5.3)), which excludes this hyperfine center shift. The BM simulation assumes perfect cancellation of the first-order Doppler shift and does not include the second-order Doppler shift. The signals from $\sigma^{\pm}$ and π decay channels are weighted equally, i.e. no detection efficiency is taken into account here. The detector is also assumed to be perfectly linear. The legend gives the correction results for $\nu_{0,a}$, $\nu_{0,e}$ and κ, determined from the weighted average or extrapolation with experimental uncertainties for the top detector from Fig. 5.10 (the uncertainties for the bottom detector are almost the same). Similarly, in (b) the LFS shift simulation results are shown (see Section 2.6.6). In (c), the second-order Doppler shift $\Delta\nu_{SOD}$ is calculated from the simulated root-mean-square speed of atoms in each delay according to Eq. (5.4).

BM simulations, Fig. 5.11(b) shows the simulation of the light force shift (LFS) $\Delta\nu_{0,\mathrm{LFS}}$ as explained in Section 2.6.6.

The second-order Doppler shift (SOD) has been discussed in Section 2.2.2. For each delay, this shift is given by

$$\Delta\nu_{\mathrm{SOD}} = -\frac{\overline{v}_{\mathrm{RMS}}^2}{2c^2}\nu_{\mathrm{A},0} \simeq -19\ldots-305\,\mathrm{Hz}, \tag{5.4}$$

where $\overline{v}_{\mathrm{RMS}}$ is the root-mean-square speed of atoms[1], and $\nu_{\mathrm{A},0} \simeq 730.889\,\mathrm{THz}$ the (approximate) 2S-6P resonance frequency. For the simulation parameters used here (first row in Table 5.2), $\overline{v}_{\mathrm{RMS}} \simeq 69\ldots274\,\mathrm{m/s}$, which gives the above values for $\Delta\nu_{\mathrm{SOD}}$ for delays $16\ldots1$.

Note that the values of the simulated effects from Fig. 5.11 need to be substracted from the measurement results from Fig. 5.10, i.e. the added correction value is of the opposite sign of the simulated value. For example, the corrected value $\nu_{0,\mathrm{e}}(\mathrm{corr.})$ for measured value $\nu_{0,\mathrm{e}}(\mathrm{meas.})$ is:

$$\nu_{0,\mathrm{e}}(\mathrm{corr.}) = \nu_{0,\mathrm{e}}(\mathrm{meas.}) - \Delta\nu_{\mathrm{BM-HFC},0,\mathrm{e}} - \Delta\nu_{\mathrm{LFS},0,\mathrm{e}} - \Delta\nu_{\mathrm{SOD},0,\mathrm{e}}. \tag{5.5}$$

5.5.3 Measurement results and simulation corrections for precision line scans at all 2S-6P laser powers

Fig. 5.12 shows the measurement results of all precision line scans (including those at $P_{\text{2S-6P}} = 10\,\mu\mathrm{W}$ and $P_{\text{2S-6P}} = 20\,\mu\mathrm{W}$) and the corresponding simulation corrections in dependence on the 2S-6P laser power $P_{\text{2S-6P}}$. Fig. 5.12(a) shows the measurement result from the average of the separate analysis of individual line scans as in Fig. 5.9. The error bars for $\nu_{0,\mathrm{a}}$ have been scaled by $\sqrt{\chi^2_{\mathrm{red}}} = \sqrt{2.6}, \sqrt{3.0}, \sqrt{3.3}$, and for $\nu_{0,\mathrm{e}}$ and κ by $\sqrt{\chi^2_{\mathrm{red}}} = \sqrt{1.3}, \sqrt{1.2}, \sqrt{1.6}$ for the power values $P_{\text{2S-6P}} = 10, 20, 30\,\mu\mathrm{W}$, respectively. Note that this scaling accounts for the excess scatter due to atomic flux caused by temperature fluctuations, but not for a possible non-linearity in the extrapolation, which has been discussed above.

Fig. 5.12(b) shows the different contributions from simulation corrections: the Big Model correction excluding the hyperfine center correction (BM-HFC, faint triangular markers), the light force shift correction (LFS, faint crossed markers), and the second-order Doppler shift correction (SOD, faint diamond markers). The total correction is the sum of these three contributions (square markers). Each correction is calculated for the delay-averaged frequency $\nu_{0,\mathrm{a}}$ (orange markers) and the extrapolation, which yields corrections for $\nu_{0,\mathrm{e}}$ (blue markers, top plot) and κ (bottom plot). Note that the correction is of opposite sign compared to the value of the simulated effect, e.g. the points in Fig. 5.12(b) for $P_{\text{2S-6P}} = 30\,\mu\mathrm{W}$ correspond to values from Fig. 5.11 with an opposite sign, because the value for each of the effects needs to be substracted from the measured value, such that the added correction value is of opposite sign compared to the simulated value.

As discussed above and shown in Fig. 5.11(a), the Big Model correction $\nu_{0,\mathrm{BM}}$ is evaluated relative to the $2\mathrm{S}_{1/2}^{F=1/2}$-$6\mathrm{P}_{1/2}^{F=3/2}$ hyperfine transition. Therefore, the observed hyperfine center correction of $(1-\eta_{1/2})\Delta_{\mathrm{HFS},1/2} \simeq 56.105\,\mathrm{kHz}$ (see Eq. (2.49)) dominates the values of $\nu_{0,\mathrm{BM}}$. In order to quantify the remaining effects, we therefore exclude the hyperfine center correction from $\nu_{0,\mathrm{BM}}$ (see Eq. (5.3)), the value of which is shown with triangular markers in Fig. 5.12(b). These corrections are $-\Delta\nu_{\text{BM-HFC},0,\mathrm{a}} \simeq -0.1\ldots-0.5\,\mathrm{kHz}$ for $\nu_{0,\mathrm{a}}$ (orange

[1]Note that $\overline{v}_{\mathrm{RMS}}$ is slightly different from $\overline{v}$, here by $\sim 15\,\mathrm{m/s}$ for delay 2, by $\sim 4\,\mathrm{m/s}$ for delay 13, and by $\sim 1\,\mathrm{m/s}$ for delay 16.

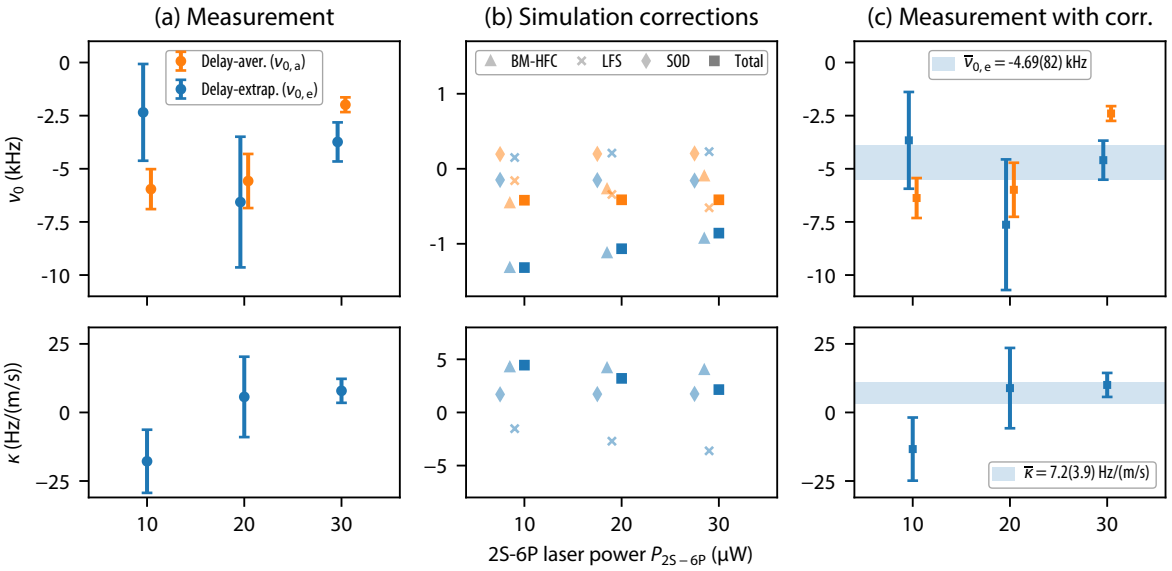

Figure 5.12: Simulation corrections and results for all precision line scans in dependence on the 2S-6P laser power $P_{\text{2S-6P}}$. (a) The measured delay-averaged frequency $\nu_{0,\text{a}}$ (orange) and delay-extrapolated frequency $\nu_{0,\text{e}}$ (blue) from the average of the separate analysis of individual line scans (as in Fig. 5.9) are shown on the top. The bottom plot shows the slope κ from the extrapolation. The error bars have been scaled by $\sqrt{\chi^2_{\text{red}}} = \sqrt{2.6} \dots \sqrt{3.3}$ for $\nu_{0,\text{a}}$, and by $\sqrt{\chi^2_{\text{red}}} = \sqrt{1.2} \dots \sqrt{1.6}$ for $\nu_{0,\text{e}}$ and κ. (b) Different contributions of simulation corrections for the delay-averaged frequency $\nu_{0,\text{a}}$ (orange) and extrapolation (blue, $\nu_{0,\text{e}}$ on the top and κ on the bottom plot): Big Model correction excl. the hyperfine center correction (BM-HFC, faint triangular markers, see Eq. (5.3)), light force shift correction (LFS, faint crossed markers), and second-order Doppler shift (SOD, faint diamond markers, see Eq. (5.4). The total correction (square markers) is the sum of these three contributions. Note that the corrections are of opposite sign compared to the values of the simulated effects, e.g. the points in (b) for $P_{\text{2S-6P}} = 30\,\mu\text{W}$ correspond to values from Fig. 5.11 with an opposite sign. (c) The measurement result from (a) corrected by the total correction from (b) (e.g. as given in Eq. (5.5)). The horizontal bars show the weighted averages for $\nu_{0,\text{e}}$ and κ for all three laser powers, with the values given in the legend.

triangular markers) and $-\Delta\nu_{\text{BM-HFC},0,\text{e}} \simeq -0.9 \dots -1.3\,\text{kHz}$ for $\nu_{0,\text{e}}$ (blue triangular markers), depending on $P_{\text{2S-6P}}$. Note that these corrections include the fit correction from fitting a single Voigt function to two unresolved hyperfine resonances (see Fig. 2.14), which is on the order of $\sim -1\,\text{kHz}$. This correction is mostly independent of $P_{\text{2S-6P}}$. The total absolute value of $\Delta\nu_{\text{BM-HFC}}$ becomes smaller with the higher laser power, because different effects such as the saturation and fit correction can have opposite signs. The correction on κ from the Big Model simulations is only slightly dependent on $P_{\text{2S-6P}}$ between $-\kappa_{\text{BM}} \simeq 4.0 \dots 4.3\,\text{Hz/(m/s)}$, see triangular markers in the bottom plot of Fig. 5.12(b).

The LFS correction has most influence on the power dependence of the total correction for the slope, varying between $-\kappa_{\text{LFS}} \simeq -1.5 \dots -3.6\,\text{Hz/(m/s)}$ for the 2S-6P laser powers between $P_{\text{2S-6P}} = 10 \dots 30\,\mu\text{W}$. The correction for $\nu_{0,\text{a}}$ is $-\Delta\nu_{\text{LFS},0,\text{a}} \simeq -0.2 \dots -0.5\,\text{kHz}$, and for $\nu_{0,\text{e}}$ is $-\Delta\nu_{\text{LFS},0,\text{e}} \simeq 0.15 \dots 0.23\,\text{kHz}$.

The SOD shift from Eq. (5.4) results in a correction of $-\Delta\nu_{\text{SOD},0,\text{a}} \sim 0.2\,\text{kHz}$ for $\nu_{0,\text{a}}$ and $-\Delta\nu_{\text{SOD},0,\text{e}} \sim -0.16\,\text{kHz}$ for $\nu_{0,\text{e}}$, which is mostly independent of $P_{\text{2S-6P}}$. The speed-dependence of $\Delta\nu_{\text{SOD}}$ yields a small correction for the slope κ of $-\kappa_{\text{SOD}} \sim 1.8\,\text{Hz/(m/s)}$, see diamond markers in the bottom plot of Fig. 5.12(b).

Note that similar to Table 5.2, the simulation corrections also depend on the mean speeds for each delay, which depend on simulation parameters. In Fig. 5.12, the same parameters as for Fig. 5.9 (first row in Table 5.2) have been used[1]. For the parameter ranges in Table 5.2, the SOD correction varies by $< 0.05\,\mathrm{kHz}$, the BM correction by $< 0.3\,\mathrm{kHz}$, and the LFS correction also by $< 0.3\,\mathrm{kHz}$ for $\nu_{0,\mathrm{e}}$. Nevertheless, for the future analysis the corrections can be evaluated for each line scan separately with a different set of mean speeds according to the parameter set which best describes the experimental condition at the corresponding measurement time.

Fig. 5.12(c) shows the measurement result from Fig. 5.12(a), which has been corrected by the total correction from Fig. 5.12(b), i.e. the correction values from (b) are added to the measured values from (a). The horizontal bar shows the weighted averages for $\nu_{0,\mathrm{e}}$ and κ, with the values given in the legend. Since the data at lower laser powers has a larger statistical uncertainty, the result mostly corresponds to the value at $P_{\text{2S-6P}} = 30\,\mu\mathrm{W}$ from Fig. 5.9. The uncertainty for $\nu_{0,\mathrm{e}}$ is 0.82 kHz. The residual slope κ is consistent with zero within approximately two standard deviations. However, in light of a possible non-linear dependence of the center frequency on the mean speed, which has been discussed in Section 5.5.2, the interpretation of κ must be treated with care until this possible non-linearity has been further investigated.

5.5.4 Preliminary uncertainty budget and corrections

Table 5.3 summarizes the preliminary uncertainty budget and corrections for the $2S_{1/2}$-$6P_{1/2}$ transition frequency measurement in deuterium. The statistical uncertainty is the result for $\nu_{0,\mathrm{e}}$ from Fig. 5.12(c), which is scaled by $\sqrt{3}$ to account for a possible non-linear dependence of the center frequency on the mean speed of atoms, as the increased $\chi^2_{\mathrm{red}} \sim 2\text{–}3$ from Fig. 5.10 may indicate (see discussion in Section 5.5.2). Note that the extrapolated frequency $\nu_{0,\mathrm{e}}$ includes the linear Doppler shift, but not any possible non-linearities, which can effectively be manifested as a speed-dependent Doppler slope.

Next the simulation corrections are listed, where the corrections for $\nu_{0,\mathrm{e}}$ from Fig. 5.12(b) (blue markers) have been calculated from the weighted sum with the corresponding experimental uncertainties for the three different laser powers. Of the three simulation corrections, the second-order Doppler shift correction is the smallest with $-0.16\,\mathrm{kHz}$ and an estimated uncertainty of 0.05 kHz due to the possible variation of the mean speeds assigned to each delay. The Big Model corrections excluding the hyperfine center (see Eq. (5.3)) are around $-1\,\mathrm{kHz}$, and depend on the linear polarization angle θ_{L} having an uncertainty of 3°, which is the main origin of the uncertainty for the Big Model corrections (see Fig. 6.8 in [71]).

The light force shift simulation has been confirmed experimentally within $\sim 40\%$ (see Fig. 6.6 in [71]). Here, we multiply this fractional uncertainty with the $\sim$1.6 kHz shift between the slowest and fastest atoms for the laser power of 30 µW (see Fig. 5.11(b)), which yields the uncertainty of $\sim$0.6 kHz. In the future, it is planned to test the light force shift model more accurately. Furthermore, here most precision line scans are taken at a higher laser power of 30 µW, and the future precision measurement can be performed at lower laser powers where the light force shift correction is smaller.

The dc-Stark shift has been discussed in Section 5.4. In Table 5.3, the result from Eq. (5.2)

[1] The delay velocities also depend on the 2S-6P laser power $P_{\text{2S-6P}}$, which has been set to the corresponding value for the three laser power data groups in Table 5.2. However, this dependence is negligible compared to the sensitivity to other parameters shown in Table 5.2: the mean speed varies by $\sim 5\,\mathrm{m/s}$ for delay 2, by $\sim 2\,\mathrm{m/s}$ for delay 13, and by $\sim 1\,\mathrm{m/s}$ for delay 16.

Contribution (kHz)	Correction	Uncertainty
Statistical uncertainty Fig. 5.12(c) scaled with $\sqrt{3}$	—	1.42
"Big Model" corr. excl. HF center (BM-HFC), $-\overline{\Delta\nu}_{\text{BM-HFC,0,e}}$	−0.99	∼0.8
Light force shift (LFS), $-\overline{\Delta\nu}_{\text{LFS,0,e}}$	0.21	∼0.6
Second-order Doppler shift (SOD), see Eq. (5.4), $-\overline{\Delta\nu}_{\text{SOD,0,e}}$	−0.16	0.05
Stray electric fields (dc-Stark shift), see Eq. (5.2), $-\Delta\nu_{\text{dc,2S-6P}}$	0.10	0.03
Blackbody-radiation-induced shift Table I in [261] assuming T^4 scaling and $T = 295(15)\,\text{K}$	0.27	0.08
Zeeman shift Eq. (2.41) with $\iota < 10^{-6}$, $s < 0.1$, $B < 1\,\text{mG}$	0.00	0.05
Pressure shift	0.00	0.01
Frequency standard	0.00	0.07
Hyperfine center shift Eq. (2.51) with $\iota < 10^{-6}$, $s < 0.1$	0.00	0.00
Unresolved quantum interference Eq. (2.69) with $\iota < 10^{-6}$, $\xi_\circ < 0.3$	0.00	0.00
Total without recoil and hyperfine structure corr.	−0.57	1.7
Recoil shift	588.785	0.000
Hyperfine (HF) structure corrections		
HF center relative to $2S_{1/2}^{F=1/2}$-$6P_{1/2}^{F=3/2}$ $(+\frac{1}{9}\Delta_{\text{HFS},6P_{1/2}})$	56.105	0.005
HF centroid of $6P_{1/2}$ levels $(-\frac{1}{3}\Delta_{\text{HFS},6P_{1/2}})$	−168.314	0.005
HF centroid of $2S_{1/2}$ levels $(-\frac{2}{3}\Delta_{\text{HFS},2S_{1/2}})$	−27 282.969	0.007
Off-diag. HFS shift $(-\Delta\nu_{\text{HFS}}^{\text{o.-d.}})$	0.021	0.000
Quadrupole HFS shift $(-\Delta\nu_{\text{HFS}}^{\text{quad}})$	0.000	0.000
Total correction and uncertainty on HF centroid	−26 806.942	1.7

Table 5.3: Preliminary uncertainty budget and corrections for the $2S_{1/2}$-$6P_{1/2}$ transition frequency measurement in deuterium presented in this thesis. The statistical uncertainty for $\nu_{0,\text{e}}$ from Fig. 5.12(c) has been scaled by a factor of $\sqrt{3}$ motivated by a possible non-linear dependence of the center frequency on the mean speed as discussed in Section 5.5.2. See main text for the discussion of other contributions.

is used. The surrounding blackbody radiation induces a dynamical Stark shift of energy levels, which has been calculated in [261]. Here, we use the result for the $6P_{1/2}$ levels from Table I in [261], where this shift is calculated for a temperature of $T = 300\,\text{K}$. The walls of our vacuum chamber are at room temperature of around $T = 295\,\text{K}$. However, the bottom of the vacuum chamber is cooled by the cryopump, where we measure a temperature of around 285 K. We assume a temperature of 295 K with a more conservative uncertainty of 15 K, and scale the result from Table I in [261] assuming a T^4-dependence[1], which yields a correction of 0.27(8)kHz.

The Zeeman shift is given by Eq. (2.41), with one term which depends on the initial state asymmetry ι and another term which depends on the circularly polarized fraction s.

[1] In [261], the scaling is shown to be T^n with $n < 4$ for higher states, but here we use $n = 4$ which gives the most conservative estimate on the uncertainty.

Both terms scale linearly with the magnetic field B. Here we assume $\iota < 10^{-6}$ based on the estimate from Eq. (2.37), which makes the term with ι negligible. The magnetic field in the 2S-6P interaction region is suppressed to $B < 1\,\mathrm{mG}$ (see Fig. 3.13). Together with the circularly polarized fraction of $s \equiv |(S_3/S_0)_{\mathrm{atom}}| < 0.1$ (see Fig. 4.30), the uncertainty due to the Zeeman shift is $< 0.05\,\mathrm{kHz}$.

For the pressure shift, we use the same estimate as in Sec. 6.2.4.4 of [71], giving a pressure shift of $< 0.01\,\mathrm{kHz}$ (see also Sec. 2.9 in supplementary materials of [14] for the discussion).

The frequency standard (passive hydrogen maser) for the laser frequency measurement using a frequency comb (see Section 3.2.3) introduces an uncertainty of 0.07 kHz.

The hyperfine center shift (see Section 2.4) and the shift due to unresolved quantum interference (see Section 2.5) lead to negligible shifts below 1 Hz, assuming the initial state assymmetry of $\iota < 10^{-6}$ based on the estimated from Eq. (2.37). In the future, one may also place an experimental limit on ι, as discussed in Appendix A.4.2. The measured residual circularly polarized fraction of $s \equiv |(S_3/S_0)_{\mathrm{atom}}| < 0.1$ (see Fig. 4.30) further suppresses the hyperfine center shift, and the most conservative limit on the possible polarization sensitivity of the detector of $\xi_\circ < 0.3$ (see Section 2.3.3) further suppresses the shift due to unresolved quantum interference.

The recoil shift (see Eq. (2.30)) is known with an accuracy of $< 1\,\mathrm{Hz}$. Also the hyperfine structure corrections have a negligible uncertainty. The hyperfine splitting of the $6\mathrm{P}_{1/2}$ level $\Delta_{\mathrm{HFS},6\mathrm{P}_{1/2}} \equiv \Delta_{\mathrm{HFS},1/2}$ is known with an uncertainty of 5 Hz and the hyperfine splitting of the $2\mathrm{S}_{1/2}$ level $\Delta_{\mathrm{HFS},2\mathrm{S}_{1/2}}$ is known with an uncertainty of 7 Hz [116]. In order to determine the correction for the hyperfine centroid, consider first the observed hyperfine center of the unresolved $2\mathrm{S}_{1/2}^{F=1/2}$-$6\mathrm{P}_{1/2}^{F=1/2}$ and $2\mathrm{S}_{1/2}^{F=1/2}$-$6\mathrm{P}_{1/2}^{F=3/2}$ transitions, which has been discussed in Section 2.4. We here choose to determine the correction for the $2\mathrm{S}_{1/2}^{F=1/2}$-$6\mathrm{P}_{1/2}^{F=3/2}$ transition frequency, which is given by $(1-\eta_{1/2})\Delta_{\mathrm{HFS},1/2} = \frac{1}{9}\Delta_{\mathrm{HFS},1/2} = 56.105\,\mathrm{kHz}$. The excited $6\mathrm{P}_{1/2}^{F=3/2}$ state is $\frac{1}{3}\Delta_{\mathrm{HFS},6\mathrm{P}_{1/2}}$ above the $6\mathrm{P}_{1/2}$ hyperfine centroid, and the initial $2\mathrm{P}_{1/2}^{F=3/2}$ state is $\frac{2}{3}\Delta_{\mathrm{HFS},2\mathrm{S}_{1/2}}$ below the $2\mathrm{S}_{1/2}$ hyperfine centroid. Therefore, the $2\mathrm{S}_{1/2}^{F=1/2}$-$6\mathrm{P}_{1/2}^{F=3/2}$ transition frequency is higher by these two numbers than the $2\mathrm{S}_{1/2}$-$6\mathrm{P}_{1/2}$ hyperfine centroid transition frequency. Furthermore, the determination of the hyperfine centroid requires to substract the small off-diagonal hyperfine structure shift from the measured frequency (see Table 2.4), which has a negligible uncertainty below 1 Hz [117]. The total off-diagonal hyperfine structure shift is calculated from the individual shifts of the two hyperfine transitions $2\mathrm{S}_{1/2}^{F=1/2}$-$6\mathrm{P}_{1/2}^{F=1/2}$ and $2\mathrm{S}_{1/2}^{F=1/2}$-$6\mathrm{P}_{1/2}^{F=3/2}$, which are weighted with the relative strengths of these two hyperfine transitions. Note that the electric quadrupole hyperfine structure shift $\Delta\nu_{\mathrm{HFS}}^{\mathrm{quad}}$ vanishes for the $2\mathrm{S}_{1/2}$-$6\mathrm{P}_{1/2}$ transition, but needs to be included for the future measurement of the $2\mathrm{S}_{1/2}$-$6\mathrm{P}_{3/2}$ transition (see Table 2.5). The total uncertainty on the hyperfine centroid is unaffected by all the hyperfine corrections and remains $\sim 1.7\,\mathrm{kHz}$, where all uncertainty contributions have been summed in quadrature.

Chapter 6

Conclusion and Outlook

This thesis contributes to the precision spectroscopy of the 2S-nP transitions in hydrogen and deuterium, with a particular focus on the 2S-6P transition in deuterium. In Chapter 1, it is described how the precision spectroscopy of simple atomic systems is an important test of the bound-state quantum electrodynamics theory, which is a fundamental building block of the Standard Model. Since we know that our fundamental understanding of nature is incomplete, there is a need to test the current state-of-the-art theories in order to find how they can eventually be modified or extended. Moreover, there is currently an inconsistency of around three standard deviations between the measurements in muonic deuterium and electronic deuterium. More data is needed to strengthen or weaken this discrepancy. Furthermore, precision spectroscopy of higher principal quantum number states can be sensitive to certain types of new particles.

In Chapter 2, it is shown how the precision spectroscopy 2S-nP transitions in deuterium is complicated as compared to hydrogen by the simulationeus excitation of transitions between unresolved hyperfine components, which can also lead to the effect of unresolved quantum interference. Possible line shifts are quantified in dependence on the possible asymmetry between initial states, the residual circularly polarized fraction of the excitation light, and the polarization sensitivity of the fluorescence detector. It is derived and confirmed by supercomputer simulations that these effects are highly suppressed, which makes precision spectroscopy possible. These results are valid for all 2S-nP transitions in deuterium. Furthermore, the light force shift is investigated in deuterium, and is simulated to be comparable to hydrogen despite of the complications arising from several state manifolds.

Chapter 3 explains the apparatus, which is used to measure the 2S-6P transition in deuterium. Since the experiment has been described in detail in the thesis by Lothar Maisenbacher [71], which treats the 2S-nP transitions in hydrogen, here the focus lies on the differences to deuterium and the modifications of the apparatus since 2019, as for instance the modifications of the laser systems. A particular focus is given to the cryogenic deuterium atomic beam generation and the high performance cryostat. Furthermore, this chapter presents characterization results from the test measurements with deuterium, in particular the observed non-linearity of the fluorescence detector and the temperature dependence of the deuterium 2S-6P spectroscopy signal along with the characterization of the speed distribution of the flux of atoms.

The main contribution of this thesis to the apparatus is the improved active fiber-based retroreflector (AFR), which is used to suppress the first-order Doppler shift. Chapter 4 follows

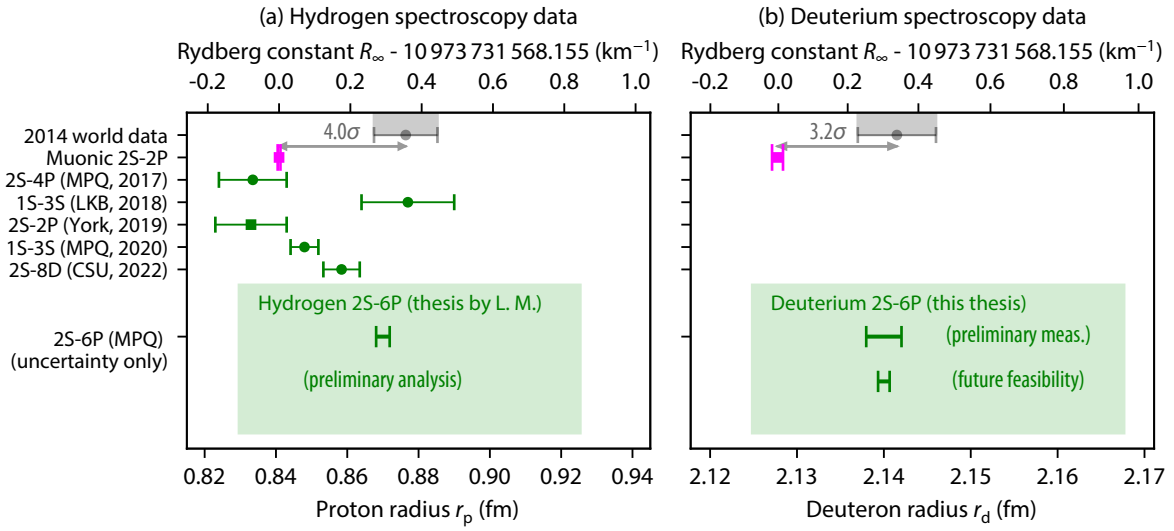

Figure 6.1: Similar to Fig. 1.1, the Rydberg constant and proton or deuteron charge radii extracted from precision spectroscopy of hydrogen or deuterium, in (a) or (b), respectively. Here, Fig. 1.1 is extended by the preliminary uncertainty result from the 2S-6P transition measurement in hydrogen (see thesis by Lothar Maisenbacher [71]), and by the uncertainty results from the 2S-6P transition measurement in deuterium which is treated in this thesis. The preliminary measurement presented in Chapter 5 results in an uncertainty lower than the average of all the previous data from electronic deuterium. In the future, a measurement with a comparable uncertainty as in hydrogen seems feasible, which would be comparable to the uncertainty result from muonic deuterium.

the corresponding publication [110], which summarizes the results. Here, some topics are treated in more detail. A particular focus lies on the etalon effect from Rayleigh backscattering within the fiber. Furthermore, the polarization monitor is explained in detail, which turned out to be more complicated than initially thought, such that a correction was published [111]. The improved AFR presented in this thesis can be used for all 2S-nP transitions in hydrogen and deuterium with $4 \leq n \leq 10$. Moreover, the results of this work can be applied not only to precision spectroscopy, but also to other experiments where a high beam quality or wavefront-retracing beams are important. The detailed examination of weak aberrations with a caustic measurement, as well as the design of a fiber collimator providing a high beam quality, can be of interest to other applications and experiments such as [30]. Likewise, the precise fiber-collimator distance control, the intensity stabilization of wavefront-retracing beams, as well as in-situ polarimetry of retroreflected light can be used separately from the AFR in other optical setups. The AFR presented in this thesis has been successfully used to measure the 2S-6P transition in hydrogen, which is treated in [71], where the first-order Doppler shift was demonstrated to be consistent with zero within the $\sim 500\,\mathrm{Hz}$ uncertainty of the measurement according to the preliminary data analysis. Possible limitations of the improved AFR are mid-spatial frequency errors of lens surfaces leading to the "orange-peel" structure on the collimated beam profile, the residual astigmatism due to the stress applied on the lenses in the collimator mount, as well as the not exactly Gaussian beam profile from the single-mode fiber. In the future, some of these imperfections may be further reduced.

Chapter 5 presents the preliminary measurement of the 2S-6P transition in deuterium. The main purpose of this measurement was the feasibility study in order to plan a future pre-

cision measurement campaign. It is demonstrated that a precision measurement of the 2S-6P transition in deuterium with a similar uncertainty than in hydrogen is feasible. According to the preliminary uncertainty budget, the test measurement determines the $2S_{1/2}$-$6P_{1/2}$ transition frequency in deuterium to $\delta\nu_{\mathrm{exp}}^{\mathrm{2S\text{-}6P}} \simeq 1.7\,\mathrm{kHz}$. Together with the 1S-2S measurement, this result can enable the most accurate determinations of the deuteron radius and the Rydberg constant from the electronic deuterium: according to Eq. (2.17), the resulting uncertainties of the Rydberg constant and the deuteron radius are $\delta R_\infty \simeq 5 \times 10^{-5}\,\mathrm{m}^{-1}$ and $\delta r_d \simeq 0.002\,\mathrm{fm}$, respectively. This is visualized in Fig. 6.1(b). It seems feasible for a future precision measurement to determine the 2S-6P transition frequency with the same accuracy as in hydrogen. The preliminary analysis of the 2S-6P transition frequency measurement in hydrogen, which is treated in [71], estimates an uncertainty $\delta\nu_{\mathrm{exp}}^{\mathrm{2S\text{-}6P}} \simeq 0.6\,\mathrm{kHz}$, which would correspond to $\delta R_\infty \simeq 2 \times 10^{-5}\,\mathrm{m}^{-1}$ and $\delta r_d \simeq 0.0007\,\mathrm{fm}$ in deuterium.

The preliminary analysis of the 2S-6P transition measurement in deuterium has been performed with a blind offset to the data, such that only the uncertainty is given here. It is important to carry out different consistency checks before unblinding the data. For example, the data can be fitted with different fit functions, which have different simulation corrections. In particular, the Voigt doublet function with a fixed sepearation between the two unresolved resonances can be used, along with an assumption of the fixed dipole ratio between the two resonances. Another important point is the careful investigation of the sampling bias, with consistency checks by using different fit functions and removing a different number of data points to increase or decrease the sampling bias while comparing to simulations of these different cases (similar to the 2S-4P measurement [14]). Furthermore, correlations between various quantities should be investigated. The most important issue is the possible non-linear velocity dependence of the center frequency, which might be caused by misalignment of the nozzle w.r.t. the 1S-2S preparation laser beam. In the preliminary analysis, this possible systematic effect has been taken into account by increasing the uncertainty by the factor of $\sqrt{3}$, which corresponds to the increased $\chi^2_{\mathrm{red}} \sim 2\text{–}3$ from Fig. 5.10 indicating such an effect. In the future, numerical modelling of the experiment can be extended to account for such misalignments, which may help to quantify the experimental data for these effects.

The preliminary measurement of this thesis focused on measuring the 2S-$6P_{1/2}$ fine-structure component of 2S-6P transitions. The future precision measurement campaign of the 2S-6P deuterium should be equally distributed between measuring the 2S-$6P_{1/2}$ and 2S-$6P_{3/2}$ fine-structure components. The combination of both transition frequencies suppresses effects due to resolved quantum interference, as has been shown in [14] and [71]. Furthermore, the measurement campaign could include the 1S-2S measurement in deuterium, in order to extract the Rydberg constant and the deuteron radius from the same experiment. Another measurement campaign can be planned to measure the light force shift in deuterium, similar to the measurement presented in [71].

An important quantity for 2S-nP measurements in deuterium is the possible initial state population asymmetry. The preliminary uncertainty budget uses a theoretical estimate (Section 2.3.1). In the future, various measurements can be performed to place an experimental limit on this quantity, possibly together with techniques creating such an asymmetry in order to test the understanding of the systematic effects related to the simultaneous excitation of different hyperfine components. Some ideas for such measurements are presented in Appendix A.2 and Appendix A.4.2.

Appendix A

Appendix

A.1 Stokes formalism of light polarization

Here we summarize the Stokes formalism for the description of the polarization of light, see e.g. [133] for details. We use the Stokes parameters because they are related to directly measurable quanitities. Furthermore, the Stokes formalism gives directly the circularly polarization fraction, which is important in our experiment as discussed in Section 4.6.

The Stokes vector $\vec{S}$ is defined from four parameters which can be characterized by intensities transmitted after the light passes through each of four simple configurations of optical elements:

$$\vec{S} = \begin{pmatrix} S_0 \\ S_1 \\ S_2 \\ S_3 \end{pmatrix} = \begin{pmatrix} I \\ I(0^\circ) - I(90^\circ) \\ I(45^\circ) - I(-45^\circ) \\ I_{\mathrm{RHC}} - I_{\mathrm{LHC}} \end{pmatrix}. \tag{A.1}$$

The total intensity $S_0 = I = I(0^\circ) + I(90^\circ) = I(45^\circ) + I(-45^\circ) = I_{\mathrm{RHC}} + I_{\mathrm{LHC}}$, and the two intensities of linear polarization, S_1 and S_2, are given in terms of intensities $I(\varphi)$ measured after the light passes through a perfect linear polarizer whose transmission axis is oriented at an angle φ with respect to the polarization of the incoming light. The circularly polarized intensity S_3 is the difference between the intensity of right- and left-handed circularly polarized light, I_{RHC} and I_{LHC}, and hence describes the amount of circular polarization present in the light beam.[1] In the context of atomic physics, S_3 is very practical since it directly relates to the rate difference in driving the σ^+ and σ^- one-photon transitions.

Optical elements typically change the Stokes vector. A Mueller matrix $\hat{O}$ transforms an input Stokes vector into the Stokes vector for the light leaving the optical elements,

$$\vec{S}_{\mathrm{out}} = \hat{O}\ \vec{S}_{\mathrm{in}}. \tag{A.2}$$

Using the Cauchy-Schwarz inequality together with averaged electric field representation of the Stokes parameters, one finds the following relation to be true:

$$S_1^2 + S_2^2 + S_3^2 \leq S_0^2, \tag{A.3}$$

[1] S_3 can be measured by putting a quarter-waveplate before the linear polarizer. If $I_{\mathrm{QWP}}(\alpha, \beta)$ is the intensity of light after the beam first passes through a perfect quarter-waveplate with the fast axis given by the angle β and then through a linear polarizer whose axis is given by the angle α, the last Stokes parameter is given by: $S_3 = I_{\mathrm{RHC}} - I_{\mathrm{LHC}} = 2I_{\mathrm{QWP}}(45^\circ, 0^\circ) - I$ where I is obtained from Eq. (A.1). A more accurate way to determine S_3 along with all other Stokes components is to use a simple rotating-waveplate polarimeter [260].

with equality in the case of fully polarized light. The degree of polarization P that survives the averaging is defined as:

$$P = \frac{\sqrt{S_1^2 + S_2^2 + S_3^2}}{S_0} \leq 1. \tag{A.4}$$

In our case we deal with fully polarized light ($P = 1$). Typically, one is not interested in the total intensity but rather in the dimensionless quantities S_1/S_0, S_2/S_0 and S_3/S_0 which determine the polarization state of light, which is represented by relative Stokes parameters summarized in the relative Stokes vector:

$$\vec{s} = \begin{pmatrix} S_1/S_0 \\ S_2/S_0 \\ S_3/S_0 \end{pmatrix}. \tag{A.5}$$

The linear polarization rotation angle is given by $\tan 2\psi = S_2/S_1$ and the ellipticity angle by $S_3/S_0 = \sin 2\chi$. The linearly polarized fraction is

$$L/S_0 = \sqrt{(S_1/S_0)^2 + (S_2/S_0)^2}, \tag{A.6}$$

whereas the circularly polarized fraction is simply S_3/S_0. The following relation is therefore true between the linearly and circularly polarized fractions:

$$(L/S_0)^2 + (S_3/S_0)^2 = P^2 \leq 1. \tag{A.7}$$

Because the relative intensities of circularly and linearly polarized light are summed in quadrature, in the case of fully polarized light ($P = 1$) nearly complete linear polarization corresponds to a still substantial circular polarization (e.g. $S_3/S_0 = 14\%$ for $L/S_0 = 99\%$). Typically, linearly polarized light is produced by optical components (e.g. polarizes or polarization-maintaining fibers) with a specified extinction ratio $\mathrm{PER} = I_{\max}/I_{\min}$ defined via the minimum ($I_{\min}$) and maximum ($I_{\max}$) transmitted intensities after sending the light emerging from the optical component through a rotatable perfect polarizer, after which $I_{\min}$ and $I_{\max}$ are measured. The fraction of circularly polarized light with the extinction ratio PER is then given by[1]:

$$S_3/S_0 = \pm\frac{2\sqrt{1/\mathrm{PER}}}{1 + 1/\mathrm{PER}} \simeq \pm 2\sqrt{1/\mathrm{PER}} + \mathcal{O}(\mathrm{PER}^{-3/2}), \tag{A.8}$$

where the approximation is valid for high extinction ratios $\mathrm{PER} \gg 1$. Typically, the specified extinction ratio of polarization-maintaining fibers is around $\mathrm{PER} \simeq 20\,\mathrm{dB}$ (100 : 1) corresponding to a substantiation circularly polarized light fraction of $S_3/S_0 \simeq 20\%$. The limitation typically originates from the stress-induced birefringence of the connectors, which cannot be fully controlled during the production process. However, we found that in a pack of several fibers, some of them may have significantly higher extinction ratios than others (where the connector induces luckily less stress). The highest extinction ratios we observed with our

[1] The Stokes vector emerging from the optical component can be modelled as $\vec{S}_{\mathrm{in}} = (1, \sqrt{1-s^2}, 0, s)$, where $s \equiv S_3/S_0$ is the residual circular polarization of light. The Stokes vector after sending the light through the rotatable perfect linear polarizer is then $\vec{S}_{\mathrm{out}} = \hat{P}(\alpha)\vec{S}_{\mathrm{in}} = (I(\alpha), \cos(\alpha), \sin(\alpha), 0$, where $\hat{P}(\alpha)$ is the Mueller matrix for a perfect linear polarizer rotated by angle α (given by Eq. (36) from [260] with $r = 0$), and $I(\alpha) = (\cos(2\alpha)\sqrt{1-s^2} + 1)/2$ is the normalized intensity transmitted through the polarizer. The maximum intensity is then $I_{\max} = (1 + \sqrt{1-s^2})/2$ and the minimum intensity is $I_{\min} = (1 - \sqrt{1-s^2})/2$, from which $\mathrm{PER} = I_{\max}/I_{\min}$ is calculated. Inverting the equation for s and then yields Eq. (A.8).

Nufern PM-S405-XP fibers were around PER $\simeq$ 30 dB leading to maximally $S_3/S_0 \approx 5\%$. When coupling light into the fiber, also the coupling lens may introduce some stress-induced birefringence. Sometimes, one can partly compensate for the stress-induced birefringence of the connector and the coupling lens by introducing slightly circular polarized light before the coupling lens.

A.2 Generating asymmetry of the 2S states in deuterium

For future measurements of the 2S-nP transitions in deuterium, it may be advantageous to generate an asymmetry in the 2S Zeeman sublevels in deuterium to investigate systematic effects related to this state asymmetry. Here, two general ideas are discussed: first, through radiofrequency (RF) radiation combined with a static magnetic field, and second, through a circularly polarized laser beam driving the 2S-4P transition.

A.2.1 Creating asymmetry through RF radiation combined with static magnetic field

The first idea to introduce population asymmetry is through circular polarized RF radiation and applied static magnetic field. Consider the Zeeman splitting of the 1S and 2S hyperfine levels illustrated in Fig. A.1. The Zeeman energy shift with the corresponding g_F factor has been introduced in Eq. (2.32) and Eq. (2.33). Since $g_{1/2} = -g_{3/2}$, the transition $(m_F = -1/2, F = 1/2) \to (m_F = 1/2, F = 3/2)$ does not shift. In contrast, the energy difference to the case with no magnetic field for the transition $(m_F = 1/2, F = 1/2) \to (m_F = 3/2, F = 3/2)$ is:

$$\Delta E = E^Z_{3/2,3/2} - E^Z_{1/2,1/2} = \frac{4}{3}\mu_\mathrm{B} B, \tag{A.9}$$

which gives a frequency shift of around 2 MHz/G. Assuming the velocity of $v \simeq 200$ m/s and the RF beam width of $w \simeq 2$ cm, the time-of-flight broadening is $v/w \simeq 10$ kHz. This would require a magnetic field of larger than 5 mG which is easily achievable in our setup, where with the compensation coils we can apply a magnetic field up to 50 mG in the horizontal direction transversal to atomic beam. The production of circularly polarized 41 MHz radiation (which corresponds to the wavelength of 7.3 m) could be achieved with compact split-ring resonators (which can have orders of magnitude smaller dimensions that the resonant wavelength [262, 263]).

Note that for the 1S ground state, the approach to depopulate the sub-states is less efficient because all the hyperfine levels of the ground state are being populated incoherently. If the transition $(F = 1/2, m_F = -1/2) \to (F = 3/2, m_F = 1/2)$ is driven, nothing will change because the same amount of atoms in the upper level is pumped down as in the lower level pumped up. Therefore, to introduce any population asymmetry one has to make use of the fact that the 1S-2S two-photon excitation populates only the $F = 1/2$ states. There are not many 2S atoms which can be depopulated in the region after the nozzle, such that the asymmetry introduced in the state population is small.

One could also exploit a similar spin-filtering technique as described in [264], where the simultaneous interaction with a magnetic field, an electric field and RF radiation allows to depopulate certain Zeeman-sublevels via the short-lived $2\mathrm{P}_{1/2}$ state.

A.2.2 Creating asymmetry through circular polarized 2S-4P light blade

Another possibility to introduce the initial state asymmetry is through circular polarized excitation of 2S-nP transitions itself, see Fig. A.2 where the two initial states are labelled as $i1$ and $i2$ and the excited states accessed by σ^+ light as $e3$, $e4$ and $e6$. Here we can use the different strengths of transitions from the $m_F = \pm 1/2$ initial states for circular polarized light. Calculating the relative matrix elements (see Tab. A.1) we find that the transitions $i1 \rightarrow e3$, $i1 \rightarrow e4$ and $i2 \rightarrow e6$ are driven with relative strengths of $2 : 1 : 6$ for 2S-$n\mathrm{P}_{1/2}$ and of $16 : 5 : 15$ for 2S-$n\mathrm{P}_{3/2}$. Therefore, for the 2S-$n\mathrm{P}_{1/2}$ transition, $i2$ is depopulated twice more than $i1$ (ratio $3 : 6$), and for the 2S-$n\mathrm{P}_{3/2}$ transition, $i1$ is 1.4 times more depopulated than $i2$ (ratio $21 : 15$). This opposite asymmetry is advantageous since one can flip the sign of the asymmetry between $i1$ and $i2$ simply by switching between the 2S-$n\mathrm{P}_{1/2}$ and 2S-$n\mathrm{P}_{3/2}$ transitions.

In our setup, we already have the so-called "light blade" which was installed for a possible 1S-2S measurement (see (QB) in Fig. 3.4). This light blade consists of an elongated beam of 486 nm light, which is resonant with the 2S-4P transition. The light blade is placed before atoms enter the magnetically and electrically shielded region. For the 1S-2S measurement, the idea is to depopulate most of already excited atoms, which could experience larger magnetic and stray electric fields in the nozzle region before they enter the magnetically and electrically

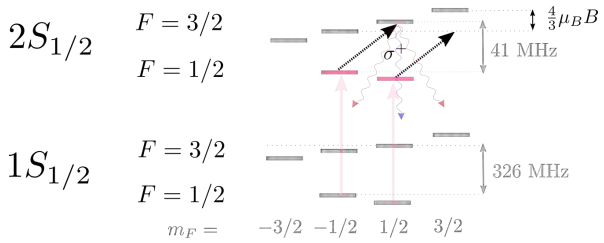

Figure A.1: Level scheme of Zeeman shifted hyperfine splitting of 1S and 2S levels in deuterium. Since the transition $(m_F = 1/2, F = 1/2) \rightarrow (m_F = 3/2, F = 3/2)$ shifts by $\frac{4}{3}\,\mu_\mathrm{B}\,B$ relative to the transition $(m_F = 1/2, F = 1/2) \rightarrow (m_F = 3/2, F = 3/2)$, this Zeeman energy difference can be exploited to depopulate the 2S, $m_F = -1/2$ state by circular polarized σ^+ RF radiation of 41 MHz. Note that this approach is less efficient for the ground state where all the six hyperfine levels are populated equally.

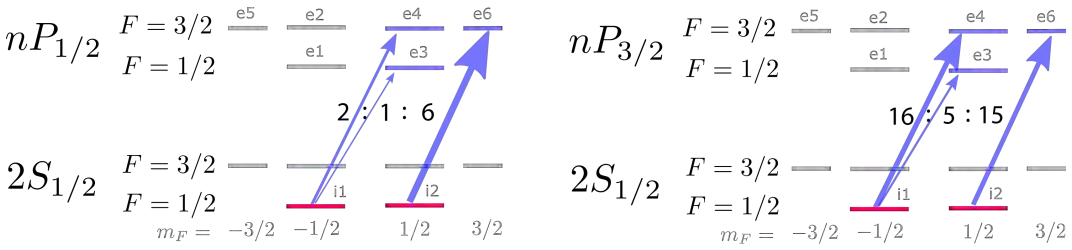

Figure A.2: Level schemes of the 2S-$n\mathrm{P}_{1/2}$ (left) and 2S-$n\mathrm{P}_{3/2}$ (right) transitions in deuterium with σ^+ excitation light. The relative strength of transitions (squared matrix elements) is illustrated through different thicknesses of arrows representing the excitation. For the 2S-$n\mathrm{P}_{1/2}$ transitions, two times more atoms are excited from the $m_F = 1/2$ initial state ($i2$) than from the $m_F = -1/2$ state ($i1$). For the 2S-$n\mathrm{P}_{3/2}$ transitions, the ratio is opposite with 1.4 times more atoms being depopulated from $i1$. Therefore, one can introduce opposite asymmetries in the population of the initial states $i1$ and $i2$ by driving the two different fine structure components of nP states (besides polarization switching between σ^+ and σ^- light).

shielded region. Through this quenching of 2S atoms, Stark and Zeeman shifts are minimized. For the deuterium 2S-nP measurement, one can use this light blade in combination with a quarter-waveplate for a similar process as described above, i.e. asymmetrical depopulation of 2S atoms with two different initial states. Implementing the polarization switching for the 2S-4P laser would allow to switch between σ^+ and σ^- light to flip the asymmetry. This could be combined with frequency switching between the fine structure components (which also flips the sign of initial state asymmetry as described above) for another cross-check.

The asymmetry introduced through 2S-nP quenching is limited by the following: some of the atoms, which decay back to the ground state, are excited again until they reach the detection region. Furthermoe, some of the atoms decay back to the 2S state. Which maximal asymmetry can be reached depends on the parameters and geometry of the setup and can be simulated with optical Bloch equations. It shall be remarked that atoms which decayed back to the 2S state have a different momentum since they absorbed a photon. This should be taken into account in the simulation.

In principle, it is also possible to use the spectroscopy light directly to introduce the asymmetry first and then perform the spectroscopy measurement by separating the signals. However, as described in Section 4.6, creating fully circular polarized light of the spectroscopy beam comes along with the difficulties related to the ambiguity between left- and right-circular polarized light in the polarization monitor of the backcoupled light. Furthermore, rebuilding the setup back and forth between linear and circular polarized light can be time-consuming. Apart from that, using the 2S-4P excitation instead of the 2S-6P (or higher transitions) would be anyway better because of the larger line width, which allows to address more atoms. In the procedure of creating asymmetry between the 2S Zeeman sublevels, it is important not to remove all the 2S atoms (in contrast to the desired quenching of all 2S atoms for the 1S-2S transition measurement). Otherwise no 2S atoms with prepared population asymmetry are left in the beam, such that the 2S-6P signal solely comes from the 2S atoms which have been re-excited after quenching (exactly the purpose for the 1S-2S measurement, but not for preparing asymmetry in the 2S states for the 2S-6P measurement). Therefore, the larger line width of the light blade transition helps to access more atoms without increasing the laser power.

Finally, we remark that one may learn about the polarization sensitivity of the detector from creating asymmetry between the initial states with the help of the circular polarized 2S-4P light blade. Having the time-resolved excitation and detection, one could make use of the fact that the asymmetry of the 2S state develops gradually, so that one would see a shift as a function of observation time if the detector is polarization-sensitive. Since we already have the time-resolved detection, one would only have to pulse the spectroscopy laser for that purpose. Fast polarization-switching between left- and right-handed circular polarization of the 2S-4P light blade (as well as switching the frequency between addressing the $4P_{1/2}$ and $4P_{3/2}$ fine structure components) would reverse the asymmetry, which can be helpful to look for polarization-sensitivity of the detector despite of the noise in the system.

A.3 Angular distribution and polarization of atomic fluorescence

Here we consider the angular distribution and polarization of atomic fluorescence. Furthermore, we consider the projected momentum distribution of emitted photons onto a particular axis (i.e. derivation of Eq. (2.82) and Eq. (2.83)). The discussion in Appendix A.3.1 and Appendix A.3.2 mostly follows problem 3.8 from [265].

A.3.1 Angular distribution

We consider an atom in an excited state which can decay to three different final states via σ^+, σ^- and π decay channels, see left of Fig. 2.4. The projected value of the total atomic angular momentum m_F onto the quantization axis $\hat{z}$ does not matter for this discussion, only the difference $\Delta m_F = \{-1, 0, +1\}$ from the excited to the three final states is relevant. To be specific for the case of deuterium, consider that the atom is in the excited state with $m_F = 1/2$. With $\hat{z}$ as the quantization axis[1] and the atom being at the origin of our coordinate system, due to the symmetry we can restrict ourselves to the $\hat{x}\hat{z}$-plane as shown on the right of Fig. 2.4, i.e. in spherical coordinates we set the azimuthal angle $\varphi = 0$. Denoting $\hat{k}$ as the direction of fluorescence light propagation, the inclination angle θ is the angle between $\hat{z}$ and $\hat{k}$. The vectors

$$\hat{\epsilon}_s \equiv \hat{\varphi} = -\hat{x}\sin\varphi + \hat{y}\cos\varphi \overset{\varphi=0}{=} \hat{y}, \tag{A.10}$$

$$\hat{\epsilon}_p \equiv \hat{\theta} = \hat{x}\cos\theta\cos\varphi + \hat{y}\cos\theta\sin\varphi - \hat{z}\sin\theta \overset{\varphi=0}{=} \hat{x}\cos\theta - \hat{z}\sin\theta \tag{A.11}$$

are the s- and p-polarization components, which are the polarization components perpendicular (s from the German word *senkrecht*) and parallel to the incidence plane (the $\hat{x}\hat{z}$-plane in Fig. 2.4). The basis vectors for right- and left-circular polarized light ($\hat{\epsilon}_R$ and $\hat{\epsilon}_L$, respectively) are then[2]

$$\hat{\epsilon}_R = -(\hat{\varphi} + i\hat{\theta})/\sqrt{2} \overset{\varphi=0}{=} -(\hat{y} + i\hat{x}\cos\theta - i\hat{z}\sin\theta)/\sqrt{2}, \tag{A.12}$$

$$\hat{\epsilon}_L = (\hat{\varphi} - i\hat{\theta})/\sqrt{2} \overset{\varphi=0}{=} (\hat{y} - i\hat{x}\cos\theta + i\hat{z}\sin\theta)/\sqrt{2}. \tag{A.13}$$

The polarization vectors of emitted σ^+, σ^- and π light are:

$$\hat{\epsilon}_\pi = \hat{z}, \quad \hat{\epsilon}_{\sigma^+} = -(\hat{x} + i\hat{y})/\sqrt{2}, \quad \hat{\epsilon}_{\sigma^-} = (\hat{x} - i\hat{y})/\sqrt{2}. \tag{A.14}$$

Using the above expressions, we can derive the angular distribution of the emitted fluorescence intensity, which is given by the sum of squared amplitudes[3] of the two orthogonal electric

[1] Note that in our experimental setup (see Fig. 3.1) the $\hat{z}$ axis from Fig. 2.4 does not necessarily correspond to the vertical axis of the fluorescence detector: the orientation of the $\hat{x}\hat{z}$-plane from Fig. 2.4 relative to the fluorescence detector depends on the rotation angle of the linear polarization of excitation light.

[2] The imaginary unit vector represents a phase shift of $\pi/2$ in the time dependence.

[3] Note that in particular cases, the coherences between the emitted fluorescence photons should be taken into account. For example, if the π fluorescence is described in the different quantization basis, it corresponds to the coherent superposition of σ^+ and σ^- light, which, due to interference, leads to the same emission pattern as the π fluorescence. Here, we assume no coherence between the fluorescence light from the different decay channels.

field components:

$$I_\pi \propto I_\pi^s + I_\pi^p = |\hat{\epsilon}_s \cdot \hat{\epsilon}_\pi|^2 + |\hat{\epsilon}_p \cdot \hat{\epsilon}_\pi|^2 = \sin^2\theta, \tag{A.15}$$

$$I_{\sigma^\pm} \propto I_{\sigma^\pm}^s + I_{\sigma^\pm}^p = |\hat{\epsilon}_s \cdot \hat{\epsilon}_{\sigma^\pm}|^2 + |\hat{\epsilon}_p \cdot \hat{\epsilon}_{\sigma^\pm}|^2 = \frac{1+\cos^2\theta}{2}. \tag{A.16}$$

In the above equation, the relative intensities I_π^s and I_π^p of the s- and p-polarizations for the π decay channel, respectively, are:

$$I_\pi^s = 0, \quad I_\pi^p = \sin^2\theta. \tag{A.17}$$

The π decay channel does not contribute to s-polarization. The relative intensities $I_{\sigma^\pm}^s$ and $I_{\sigma^\pm}^p$ of the s- and p-polarizations for the $\sigma^\pm$ decay channels, respectively, are:

$$I_{\sigma^\pm}^s = \frac{1}{2}, \quad I_{\sigma^\pm}^p = \frac{\cos^2\theta}{2}. \tag{A.18}$$

Note that the intensity fractions of s- and p-polarizations are the same for σ^+ and σ^- decays.

A.3.2 Stokes parameters

To examine the polarization of detected light, we compute the relative Stokes parameters. From symmetry, it is clear that the second relative Stokes parameter (S_2/S_0), which describes diagonal vs. anti-diagonal linear polarization, vanishes for $\sigma^\pm$ and π light:

$$(S_2/S_0)_\pi = (S_2/S_0)_{\sigma^\pm} = 0. \tag{A.19}$$

Note that the above equation is only valid in the chosen coordinate system, e.g. if the atoms are excited with diagonal linear polarization, S_2/S_0 of emitted fluorescence light is not zero. However, we can always rotate the coordinate system accordingly. Here, our simple choice of the coordinate system allows to directly compute the degree of linearly polarized fraction: the first relative Stokes parameter S_1/S_0 for horizontal and vertical linear polarization is then equal to the linearly polarized fraction L/S_0 (defined in Eq. (A.6)):

$$(L/S_0)_\pi = (S_1/S_0)_\pi = \frac{|\hat{\epsilon}_H \cdot \hat{\epsilon}_\pi|^2 - |\hat{\epsilon}_V \cdot \hat{\epsilon}_\pi|^2}{I_\pi} = -1, \tag{A.20}$$

$$(L/S_0)_{\sigma^\pm} = (S_1/S_0)_{\sigma^\pm} = \frac{|\hat{\epsilon}_H \cdot \hat{\epsilon}_{\sigma^\pm}|^2 - |\hat{\epsilon}_V \cdot \hat{\epsilon}_{\sigma^\pm}|^2}{I_{\sigma^\pm}} = \frac{1-\cos^2\theta}{1+\cos^2\theta}. \tag{A.21}$$

The circular polarization fraction is then calculated to be the following:

$$\begin{aligned}(S_3/S_0)_\pi &= \frac{|\hat{\epsilon}_R \cdot \hat{\epsilon}_\pi|^2 - |\hat{\epsilon}_L \cdot \hat{\epsilon}_\pi|^2}{I_\pi} = 0, \\ (S_3/S_0)_{\sigma^\pm} &= \frac{|\hat{\epsilon}_R \cdot \hat{\epsilon}_{\sigma^\pm}|^2 - |\hat{\epsilon}_L \cdot \hat{\epsilon}_{\sigma^\pm}|^2}{I_{\sigma^\pm}} = \pm\frac{2\cos\theta}{1+\cos^2\theta}.\end{aligned} \tag{A.22}$$

Combining the above equations, it is instructive to check the relation between the Stokes parameters for fully polarized light (see Eq. (A.3)):

$$(S_1/S_0)_\pi^2 + (S_2/S_0)_\pi^2 + (S_3/S_0)_\pi^2 = 1 + 0 + 0 = 1, \tag{A.23}$$

$$(S_1/S_0)_{\sigma^\pm}^2 + (S_2/S_0)_{\sigma^\pm}^2 + (S_3/S_0)_{\sigma^\pm}^2 = \frac{(2\cos\theta)^2}{(1+\cos^2\theta)^2} + 0 + \frac{(1-\cos^2\theta)^2}{(1+\cos^2\theta)^2} = 1. \tag{A.24}$$

A.3.3 Probability distributions of projected photon momenta

The angular probability distributions for the emission of π and $\sigma^{\pm}$ fluoresence photons are:

$$\mathcal{N}_{\pi}(\theta,\phi) = \frac{3}{8\pi}\sin^2\theta, \tag{A.25}$$

$$\mathcal{N}_{\sigma^{\pm}}(\theta,\phi) = \frac{3}{16\pi}\left(1+\cos^2\theta\right). \tag{A.26}$$

The above equations are obtained from Eq. (A.15) and Eq. (A.16) together with the normalization requirement of the angular probability distribution:

$$\int_0^{2\pi} \mathrm{d}\phi \int_0^{\pi} \sin\theta \mathrm{d}\theta\, \mathcal{N}(\theta,\phi) = 1. \tag{A.27}$$

Now we wish to determine the probability distribution of the projected photon momenta onto the $\hat{z}$ and $\hat{x}$ axes as defined in Fig. 2.4. In spherical coordinates, it is easiest to compute the projection onto the $\hat{z}$ axis, which we do first. As a next step we rotate the distribution such that the rotated $\hat{x}$ axis corresponds to the $\hat{z}$ axis and repeat the calculation with the rotated distribution.

The probability $\mathrm{d}P$ to find the projected momenta between the fractions z and $z+\mathrm{d}z$ of the total photon momentum can be calculated from the surface area $\mathrm{d}A$ of the slice with width $\mathrm{d}z$,, where all the vectors giving this projected momenta lie:

$$\mathrm{d}A = \int_0^{2\pi} \mathrm{d}\phi \int_{\theta_z}^{\theta_{z+\mathrm{d}z}} \sin\theta \mathrm{d}\theta\, \mathcal{N}(\theta,\phi), \tag{A.28}$$

where $\theta_z = \arccos z$ and $\theta_{z+\mathrm{d}z} = \arccos(z+\mathrm{d}z)$ correspond to the polar angles of the projected fractions z and $z+\mathrm{d}z$. Since the total area is normalized to one ($A=1$), the probability $\mathrm{d}P$ is equal to $\mathrm{d}P = \mathrm{d}A/A = \mathrm{d}A$. The evaluation of the above expression for the π and $\sigma^{\pm}$ distributions yields:

$$\mathrm{d}P_{\pi} = \mathrm{d}z\,\frac{3}{4}(1-z^2) + \mathcal{O}(\mathrm{d}z^2), \tag{A.29}$$

$$\mathrm{d}P_{\sigma^{\pm}} = \mathrm{d}z\,\frac{3}{8}(1+z^2) + \mathcal{O}(\mathrm{d}z^2). \tag{A.30}$$

The probability distribution is given by $\mathrm{d}P/\mathrm{d}z$. Therefore, the normalized probability density for having a spontaneous photon with linear momentum $\Delta p \in [-\hbar K_L, \hbar K_L]$ along the $\hat{z}$ axis is:

$$\mathcal{N}_{\pi}^{\hat{z}}(\Delta p) = \frac{3}{4}\left(1-\Delta p^2/(\hbar K_{\mathrm{L}})^2\right), \tag{A.31}$$

$$\mathcal{N}_{\sigma^{\pm}}^{\hat{z}}(\Delta p) = \frac{3}{8}\left(1+\Delta p^2/(\hbar K_{\mathrm{L}})^2\right), \tag{A.32}$$

where $\hbar K_{\mathrm{L}}$ is the total photon momentum. This result is in agreement with Eq. (74) and Eq. (75) of [152].

For the case of our experiment, as for instance for the description of the light force shift in Section 2.6, we choose the quanzitation axis $\hat{z}$ to be along the linear polarization direction, such that the laser light drives π transitions ($\Delta m_F = 0$). The quantization axis $\hat{z}$ is then perpendicular to the laser propagation direction $\hat{x}$. For the evaluation of the light force shift,

we then need to project the photon momentum onto the laser propagation direction ($\hat{x}$ axis), which is perpendicular to the quanzitation axis $\hat{z}$. This case is different from Eq. (74) and (75) of [152] derived above, where the photon momentum is projected onto the quantization axis $\hat{z}$. We now wish to determine the analogous expressions for the projection on the the $\hat{x}$ axis. For this calculation, we rotate the distributions from Eq. (A.25) and Eq. (A.26) such that the rotated $\hat{x}$ axis corresponds to the new $\hat{\tilde{z}}$ axis:

$$\tilde{\mathcal{N}}_{\pi}(\theta,\phi) = \frac{3}{8\pi}\left(1-\cos^2\phi\sin^2\theta\right), \tag{A.33}$$

$$\tilde{\mathcal{N}}_{\sigma^{\pm}}(\theta,\phi) = \frac{3}{16\pi}\left(1+\cos^2\phi\sin^2\theta\right). \tag{A.34}$$

Repeating the calculation with the above distributions yields the normalized probability density for having a spontaneous photon with linear momentum $\Delta p \in [-\hbar K_L, \hbar K_L]$ along the $\hat{x}$ axis before rotating the distribution (for the rotated distribution this is the new $\hat{\tilde{z}}$ axis):

$$\mathcal{N}_{\pi}^{\hat{x}}(\Delta p) = \frac{3}{8}\left(1+\Delta p^2/(\hbar K_{\mathrm{L}})^2\right), \tag{A.35}$$

$$\mathcal{N}_{\sigma^{\pm}}^{\hat{x}}(\Delta p) = \frac{3}{16}\left(3-\Delta p^2/(\hbar K_{\mathrm{L}})^2\right). \tag{A.36}$$

Since the π transitions correspond to a superposition of $\sigma^{\pm}$ transitions in the rotated quantization basis, Eq. (A.35) for π transitions corresponds to $\sigma^{\pm}$ transitions from Eq. (A.32), i.e. $\mathcal{N}_{\sigma^{\pm}}^{\hat{x}}(\Delta p) = \mathcal{N}_{\pi}^{\hat{z}}(\Delta p)$. Since there is no such simple correspondance for $\sigma^{\pm}$ transitions (which are a combination of $\sigma^{\pm}$ and π transitions in the rotated quantization basis), Eq. (A.36) is different from Eq. (A.31).

A.4 Derivation of hyperfine center shifts for 2S-nP transitions in deuterium

A.4.1 Derivation of the hyperfine center for imperfect polarization and asymmetry in the initial states

The excitation amplitudes are determined from the dipole matrix elements given by (derived from Eq. (4.120) and Eq. (4.175) in [129]):

$$\begin{aligned} d_p(i\to e) =&(-1)^{F_e-m_e}\begin{pmatrix} F_e & 1 & F_i \\ -m_e & p & m_i \end{pmatrix} \\ &\times(-1)^{J_e+I+F_i+1}\begin{Bmatrix} J_e & F_e & I \\ F_i & J_i & 1 \end{Bmatrix}\times(-1)^{l_e+S+J_i+1}\begin{Bmatrix} l_e & J_e & S \\ J_i & l_i & 1 \end{Bmatrix} \\ &\times\sqrt{(2F_e+1)(2F_i+1)(2J_e+1)(2J_i+1)}\times\langle n_e,l_e||d||n_i,l_i\rangle, \end{aligned} \tag{A.37}$$

where $(\cdots)$ and $\{\cdots\}$ denote the Wigner 3-j and 6-j symbols, respectively [128, 129]. p denotes the spherical component of exciting light ($p=0$ for π-light and $p=\pm1$ for $\sigma^{\pm}$-light). The quantum numbers for initial (subscript i) and excited (subscript e) states are: nuclear spin $I=1$, electron spin $S=1/2$, principal quantum numbers $n_i=2$ and $n_e=n$, orbital angular momenta $l_i=0$ and $l_e=1$, spin-orbital angular momenta $J_i=1/2$ and $J_e=\{1/2,3/2\}$, total atomic angular momenta $F_i=1/2$ and $F_e=\{1/2,3/2\}$ (here, we do not consider the $F_e=5/2$ state manifold since it is not addressed in our excitation scheme, see Fig. 2.2), and projections of total atomic angular momenta $m_i=\{-1/2,1/2\}$ and $m_e=\{-3/2,-1/2,1/2,3/2\}$. According to the labelling of initial and excited states in Fig. 2.8 we denote the dipole matrix elements in short with an abbreviated subscript $iIeE$ where $I=\{1,2\}$ (not to be confused with the same symbol for the nuclear spin above) and $E=\{1,2,3,4,5,6\}$. The last factor in Eq. (A.37), called the reduced matrix element, can be omitted as long as the quantum numbers n_e, l_e, n_i and l_i do not change for the considered transitions, which is the case here. The remaining factors (relative matrix elements) are summarized in Tab. A.1.

We define the center frequency of the total resonance line $\nu_c=\nu_0+\eta\Delta_{\mathrm{HFS}}$ as shown in orange in Fig. 2.8, where ν_0 is the resonance frequency of the $2\mathrm{S}_{1/2}^{F=1/2}$-$n\mathrm{P}_{1/2}^{F=1/2}$ transition, and η is the fraction of the hyperfine splitting by which the $2\mathrm{S}_{1/2}^{F=1/2}$-$n\mathrm{P}_{1/2}^{F=3/2}$ transition increases the total resonance line center:

$$\nu_c=\nu_0+\eta\Delta_{\mathrm{HFS}}. \tag{A.38}$$

The fraction η can be calculated from the fraction of atoms in the $F=3/2$ and $F=3/2$ states of the nP level manifold, $N_{F=3/2}$ and $N_{F=1/2}$ respectively, as:

$$\eta=\frac{N_{F=3/2}}{N_{F=1/2}+N_{F=3/2}}, \tag{A.39}$$

where $N_{F=1/2}=N_{e1}+N_{e3}$ and $N_{F=3/2}=N_{e2}+N_{e4}+N_{e5}+N_{e6}$ according to the population in the corresponding excited states of Fig. 2.8. In the low-excitation regime, the number of atoms brought into the excited state is proportional to the squared Rabi frequency (see Eq. (2.24)). Therefore, the population in the excited state eE is proportional to the intensity of excitation light I, the number of atoms in the initial states N_{iI}, and the squared relative

$iIeE$	Initial state m_F	Excited state F and m_F	Polarization p	Matrix element d_{iIeE} $J_e = 1/2$	$J_e = 3/2$
$i1e1$	$m_i = -1/2$	$F_e = 1/2$, $m_e = -1/2$	π	$-1/9$	$2\sqrt{2}/9$
$i1e2$	$m_i = -1/2$	$F_e = 3/2$, $m_e = -1/2$	π	$-2\sqrt{2}/9$	$\sqrt{10}/9$
$i2e3$	$m_i = 1/2$	$F_e = 1/2$, $m_e = 1/2$	π	$1/9$	$-2\sqrt{2}/9$
$i2e4$	$m_i = 1/2$	$F_e = 3/2$, $m_e = 1/2$	π	$-2\sqrt{2}/9$	$\sqrt{10}/9$
$i1e3$	$m_i = -1/2$	$F_e = 1/2$, $m_e = 1/2$	σ^+	$-\sqrt{2}/9$	$4/9$
$i1e4$	$m_i = -1/2$	$F_e = 3/2$, $m_e = 1/2$	σ^+	$-2/9$	$\sqrt{5}/9$
$i1e5$	$m_i = -1/2$	$F_e = 3/2$, $m_e = -3/2$	σ^-	$-2/(3\sqrt{3})$	$\sqrt{5/3}/3$
$i2e6$	$m_i = 1/2$	$F_e = 3/2$, $m_e = 3/2$	σ^+	$-2/(3\sqrt{3})$	$\sqrt{5/3}/3$
$i2e1$	$m_i = 1/2$	$F_e = 1/2$, $m_e = -1/2$	σ^-	$\sqrt{2}/9$	$-4/9$
$i2e2$	$m_i = 1/2$	$F_e = 3/2$, $m_e = -1/2$	σ^-	$-2/9$	$\sqrt{5}/9$

Table A.1: Relative matrix elements for the excitation of the $2S_{1/2}^{F=1/2}$-nP ($l_i = 0$, $J_i = 1/2$, $F_i = 1/2$, $l_e = 1$) transitions in deuterium (nuclear spin $I = 1$, electron spin $S = 1/2$). The first column denotes the abbreviation for corresponding transition according to Fig. 2.8, the second and third columns show the three varying quantum numbers for the initial and excited states m_i, F_e, m_e. The next column states the corresponding polarization of the excitation light ($p = \pm 1$ corresponds to $\sigma^\pm$ and $p = 0$ to π). The calculated values of the reduced matrix elements (Eq. (A.37) without the factor $\langle n_e, l_e || d || n_i, l_i \rangle$) for the 2S-$nP_{1/2}$ ($J_e = 1/2$) or the 2S-nP$_{3/2}$ ($J_e = 3/2$) transitions are written in the last two columns.

matrix element d_{iIeE}:

$$N_{eE} \propto I\, N_{iI} |d_{iIeE}|^2. \tag{A.40}$$

For the quantization basis with π-light[1] (left of Fig. 2.8), we obtain:

$$\begin{aligned} \eta_\pi =& \frac{N_{i1}|d_{i1e2}|^2 + N_{i2}|d_{i2e4}|^2}{N_{i1}|d_{i1e1}|^2 + N_{i2}|d_{i2e3}|^2 + N_{i1}|d_{i1e2}|^2 + N_{i2}|d_{i2e4}|^2} \\ =& \frac{|d_{i1e2}|^2}{|d_{i1e1}|^2 + |d_{i1e2}|^2}, \end{aligned} \tag{A.41}$$

where in the last step we assumed equal populations $N_{i1} = N_{i2}$ and used the fact that the absolute values of the matrix elements are equal for $i1$ and $i2$. With numbers from Table A.1, we find for $\eta_{1/2,\pi}$ (2S-nP$_{1/2}$ transition) and $\eta_{3/2,\pi}$ (2S-nP$_{3/2}$ transition) in case of perfectly linearly polarized light:

$$\eta_{1/2,\pi} = \frac{8}{9}, \quad \eta_{3/2,\pi} = \frac{5}{9}. \tag{A.42}$$

In the rotated quantization basis (right of Fig. 2.8), the corresponding populations of the excited states driven by σ^+ and σ^- light are proportional to the right- and left-handed

[1] Note that when considering the excitation only, we can always choose the coordinate system such that linear polarization of any linear polarization rotation angle drives the π transitions only (independent of the rotation of the detector).

circular polarization intensities I_{RHC} and I_{LHC}. Therefore, η is given by:

$$\begin{aligned}\eta =& \frac{I_{\mathrm{LHC}}(N_{i1}|d_{i1e5}|^2 + N_{i2}|d_{i2e2}|^2) + I_{\mathrm{RHC}}(N_{i1}|d_{i1e4}|^2 + N_{i2}|d_{i2e6}|^2)}{I_{\mathrm{RHC}}(N_{i1}(|d_{i1e3}|^2 + |d_{i1e4}|^2) + N_{i2}|d_{i2e6}|^2) + I_{\mathrm{LHC}}(N_{i1}|d_{i1e5}|^2 + N_{i2}(|d_{i2e2}|^2 + |d_{i2e1}|^2))} \\ =& \frac{|d_{i1e4}|^2 + |d_{i1e5}|^2 + (I_{\mathrm{LHC}}/I_{\mathrm{RHC}})(N_{i2}/N_{i1})(|d_{i1e5}|^2 - |d_{i1e4}|^2)}{|d_{i1e3}|^2 + |d_{i1e4}|^2 + |d_{i1e5}|^2 + (I_{\mathrm{LHC}}/I_{\mathrm{RHC}})(N_{i2}/N_{i1})(|d_{i1e5}|^2 - |d_{i1e4}|^2 - |d_{i1e3}|^2)}, \end{aligned} \tag{A.43}$$

where $N_{i2}/N_{i1} = (1+\iota)/(1-\iota)$ and $I_{\mathrm{LHC}}/I_{\mathrm{RHC}} = (1+s)/(1-s)$ according to Eq. (2.31) and Eq. (2.38), respectively. We made use of the fact that absolute values of corresponding relative matrix elements are equal for $i1$ and $i2$, e.g. $|d_{i2e6}| = |d_{i1e5}|$. In the case of small initial population asymmetry ι or small residual circlar polarization fraction s ($\iota \ll 1$ or $s \ll 1$), Eq. (A.43) simplifies to:

$$\eta \simeq \frac{|d_{i1e4}|^2 + |d_{i1e5}|^2}{|d_{i1e3}|^2 + |d_{i1e4}|^2 + |d_{i1e5}|^2} + 2\,s\,\iota\,\frac{|d_{i1e3}|^2|d_{i1e5}|^2}{(|d_{i1e3}|^2 + |d_{i1e4}|^2 + |d_{i1e5}|^2)^2}, \tag{A.44}$$

where the first term represents the case of perfect linear polarization and is equal to Eq. (A.41). With numbers from Table A.1 we obtain η with population asymmetry and imperfect linear polarization for 2S-nP$_{1/2}$ and 2S-nP$_{3/2}$:

$$\eta_{1/2} = \frac{8 + 4\,s\,\iota}{9 + 3\,s\,\iota} \simeq \frac{8}{9} + \frac{4}{27}\,s\,\iota, \quad \eta_{3/2} = \frac{5 + 2.5\,s\,\iota}{9 - 1.5\,s\,\iota} \simeq \frac{5}{9} + \frac{10}{27}\,s\,\iota, \tag{A.45}$$

where the approximation is valid for small initial population asymmetry or small residual circlar polarization fraction ($\iota \ll 1$ or $s \ll 1$).

A.4.2 Switching between right- and left-handed circular polarized light

Switching between right- and left-handed circular polarized light with $\pm s_\iota$, i.e. in the extreme case between $s = -1$ and $s = +1$ as shown on the left of Fig. A.3, results in a shift of the hyperfine center which we denote as Δ_ι. Using Eq. (A.45), we obtain the following expression for the 2S-nP$_{1/2}$ ($\Delta_{\iota,1/2}$) and 2S-nP$_{3/2}$ ($\Delta_{\iota,3/2}$) transitions:

$$\Delta_{\iota,1/2} = \frac{8\,s_\iota\,\iota\,\Delta_{\mathrm{HFS}_{1/2}}}{27 - 3\,s_\iota^2\,\iota^2} \simeq \frac{8}{27}\,s_\iota\,\iota\,\Delta_{\mathrm{HFS}_{1/2}}, \tag{A.46}$$

$$\Delta_{\iota,3/2} = \frac{20\,s_\iota\,\iota\,\Delta_{\mathrm{HFS}_{3/2}}}{27 - 3\,s_\iota^2\,\iota^2/4} \simeq \frac{20}{27}\,s_\iota\,\iota\,\Delta_{\mathrm{HFS}_{3/2}}, \tag{A.47}$$

where the approximated value is valid for small $\iota \ll 1$. $\Delta_{\mathrm{HFS}_{1/2}}$ and $\Delta_{\mathrm{HFS}_{3/2}}$ are the hyperfine splittings of the 2S-nP$_{1/2}$ and 2S-nP$_{3/2}$ transitions respectively. Since $\Delta_{\mathrm{HFS}_{1/2}} \simeq \Delta_{\mathrm{HFS}_{3/2}}/5$, where Γ_{nP} is the natural linewidth of the 2S-nP transition (see Fig. 2.2), the shift is approximately the twice as large for the 2S-nP$_{1/2}$ transition than for the 2S-nP$_{3/2}$ transition:

$$\Delta_{\iota,1/2} \simeq 0.039\,s_\iota\,\iota\,\Gamma_{\mathrm{nP}}, \quad \Delta_{\iota,3/2} \simeq 0.019\,s_\iota\,\iota\,\Gamma_{\mathrm{nP}}. \tag{A.48}$$

Eq. (A.48) allows to estimate the required measurement precision to place a limit on ι. Fig. A.3(b) shows the shift $\Delta_\iota \equiv \Delta_{\iota,1/2}$ is plotted in units of $10^{-3}\,\Gamma_{\mathrm{nP}}$ in dependence on the initial state population asymmetry ι. For switching between fully right- and left-handed circular polarized light ($s_\iota = 1$), the resonance line center has to be determined to better than

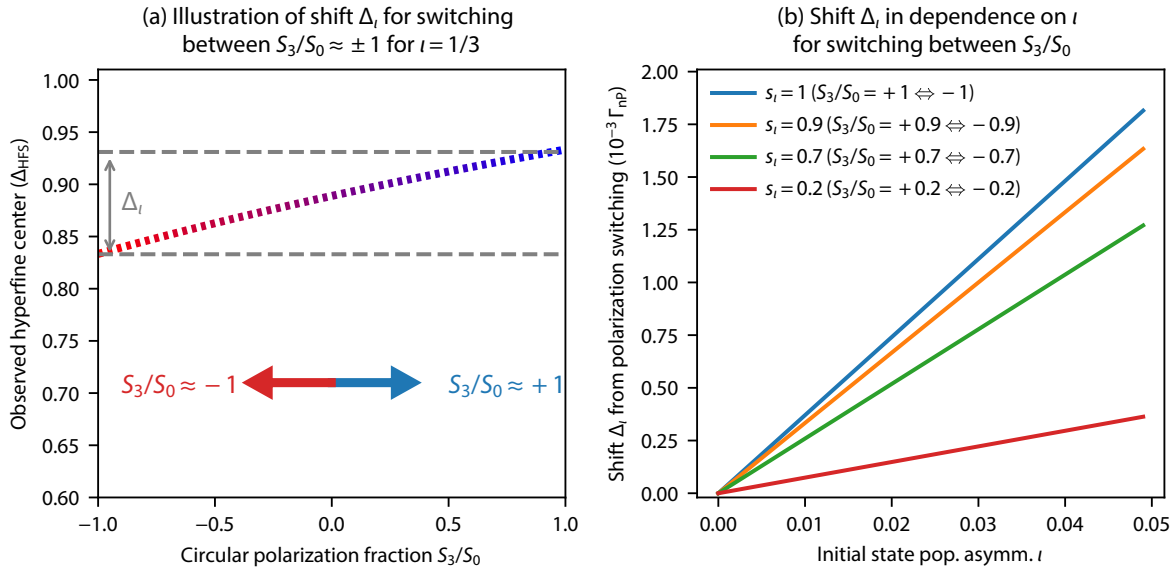

Figure A.3: Shift $\Delta_\iota \equiv \Delta_{\iota,1/2}$ of the hyperfine center when switching the polarization of excitation light between the left- and right-handed circular polarization for the 2S-nP$_{1/2}$ transition, see Eq. (A.48). In (a), Δ_ι is illustrated for the case of fully circular polarized light for an examplary initial state population asymmetry of $\iota = 1/3$. In (b), Δ_ι is plotted in dependence on the initial state population asymmetry ι. For example, switching between fully left- and right-handed circular polarizations requires to determine the line center to around $2 \times 10^{-3}\,\Gamma_{\mathrm{nP}}$ in order to place the experimental limit on $\iota < 0.05$

$2 \times 10^{-3}\,\Gamma_{\mathrm{nP}}$ in order to place the experimental limit $\iota < 5\%$. Note that for this measurement the circular polarization fraction does not need to be accurately known: 10% accuracy would be enough, as the difference to the orange curve with $s_\iota = 0.9$ illustrates.

For a measurement with fully circular polarized light, the fiber in the active fiber-based retroreflector can be replaced by a non-polarization maintaining fiber (possibly in combination with an in-line fiber polarization controller). However, as discussed in Section 4.6, the polarization monitor does not distinguish between the right- and left-handed circular polarization. A potentially easier way could be to make use of the existing stress-induced birefringence of the collimator. For our collimators, we observed the retardance to be on the order of $\delta_{\mathrm{coll}} \simeq 0.1 - 0.3\,\mathrm{rad}$ (see Section 4.2.4). For one of our collimators we found that for a certain orientation w.r.t. the fiber a circular polarization fraction of $S_3/S_0 \approx 0.3$ could be achieved. The sign ambiguity in the polarization monitor is then overcome by the properties of the PM fiber which is known to produce less than 10% variation in S_3/S_0 for optimal alignment (see Fig. 4.23). The collimator can then be rotated to produce circular polarization between $S_3/S_0 = -0.2 \ldots -0.3$ and $S_3/S_0 = +0.2 \ldots +0.3$. In Fig. A.3(b), this case approximately corresponds to $s_\iota = 0.2$ (red curve), which reduces the sensitivity to the experimental limit on ι by a factor of $6 - 7$ compared to the case with fully circular polarized light.

Which of the above scenarios is most suitable for the measurement of ι depends on the statistics and the time needed to rebuilt the setup. Note that a factor of $6 - 7$ in sensitivity to ι means a factor of $36 - 49$ for measurement time in order to reach the same statistical uncertainty. The scenario with mostly circular polarized light requires to replace the vacuum fiber at least two times: first from the polarization-maintaining fiber in the setup to the non-polarization maintaining fiber (in combination with a polarization-controller or waveplates

before the fiber) and then back to the polarization-maintaining fiber for precision-data taking. Furthermore, one has to repeat the alignment procedure for the collimator-fiber system each time the fiber is replaced. In addition, due to limited space in the vacuum chamber setup, the collimator needs to be removed from the AFR setup in order to replace the fiber. This introduces some risk to capture dust in the collimator. Furthermore, the ambiguity between left- and right-circular polarized light has to be handled, e.g. with additional methods such as a thin polarizing element before the photomultiplier after the HR mirror. Therefore, it may be more efficient to operate in the scenario with a smaller circularly polarized fraction, i.e. use the existing setup ready for precision-data taking and invest more measurement days for data with introduced polarization imperfections from collimator birefringenc ($s_\iota \approx 0.2$). In order to place an experimental limit $\iota < 0.05$, one would have to determine the line center to better than $3 \times 10^{-4}\,\Gamma_{\mathrm{nP}}$ (see Fig. A.3(b)).

A.4.3 Derivation of the hyperfine center with quantum interference

As shown in Eq. (2.62), the evaluation of quantum interference involves the factor of the exciting dipole matrix element from Eq. (A.37) as well as the emitting dipole matrix element given by (analagous to Eq. (A.37)):

$$\begin{aligned} d_q(e \to f) =& (-1)^{F_f - m_f} \begin{pmatrix} F_f & 1 & F_e \\ -m_f & q & m_e \end{pmatrix} \\ & \times (-1)^{J_f + I + F_e + 1} \begin{Bmatrix} J_f & F_f & I \\ F_e & J_e & 1 \end{Bmatrix} \times (-1)^{l_f + S + J_e + 1} \begin{Bmatrix} l_f & J_f & S \\ J_e & l_e & 1 \end{Bmatrix}, \\ & \times \sqrt{(2F_f+1)(2F_e+1)(2J_f+1)(2J_e+1)} \langle n_f, l_f || d || n_e, l_e \rangle \end{aligned} \tag{A.49}$$

where $(\cdots)$ and $\{\cdots\}$ denote the Wigner 3-j and 6-j symbols, respectively [128, 129]. q denotes the spherical component of emitting light polarization ($q = 0$ for π decay and $q = \pm 1$ for $\sigma^{\pm}$ decays). The quantum numbers for excited (subscript e) and final (subscript f) states for our case of the decay from the nP state to the $1\mathrm{S}_{1/2}$ ground state are: nuclear spin $I = 1$, electron spin $S = 1/2$, principal quantum numbers $n_e = n$ and $n_f = 1$, orbital angular momenta $l_e = 1$ and $l_f = 0$, spin-orbital angular momenta $J_e = \{1/2, 3/2\}$ and $J_f = 1/2$, total atomic angular momenta $F_e = \{1/2, 3/2\}$ and $F_f = \{1/2, 3/2\}$, and projections of total atomic angular momenta $m_e = \{-3/2, -1/2, 1/2, 3/2\}$ and $m_f = \{-3/2, -1/2, 1/2, 3/2\}$. According to the labelling of excited and final states in Fig. A.4 we denote the dipole matrix elements in short with an abbreviated subscript $eEfF$ where $E = \{1, 2, 3, 4, 5, 6\}$ and $F = \{1, 2, 3, 4, 5, 6\}$ number the excited and final states, respectively. The factor $\langle n_f, l_f || d || n_e, l_e \rangle$ can be omitted as long as the quantum numbers n_e, l_e, n_f and l_f do not change for the considered transitions, which is the case here. The remaining factors (relative matrix elements) are evaluated in Table A.2.

Consider now the example shown in Fig. A.4, where the atom is excited to the states $e1$ and $e2$ from the initial state $i1$. Using the quantum mechanical perturbative model, the signal for laser excitation with only one of the standard polarizations is given by Eq. (2.63), where the unresolved quantum interference occurs between the two paths involving the same initial and final states but the two different excited hyperfine states $e1$ and $e2$. The contribution for the different final states as well as different spherical components q enters the sum incoherently, such that it corresponds to the incoherent sum of many unresolved Lorentzians which can be approximated by a single Lorentzian with a line center according to Eq. (2.59). For the

$eEfF$	Excited state		Final state		Emitting polar.	Matrix element d_{eEfF}	
	F_e	m_e	F_f	m_f	q	$J_e = 1/2$	$J_e = 3/2$
$e1f1$	1/2	−1/2	1/2	−1/2	π	$1/9$	$-2\sqrt{2}/9$
$e1f2$				1/2	σ^+	$\sqrt{2}/9$	$-4/9$
$e1f3$			3/2	−3/2	σ^-	$2/(3\sqrt{3})$	$1/(3\sqrt{6})$
$e1f4$				−1/2	π	$2\sqrt{2}/9$	$1/9$
$e1f5$				1/2	σ^+	$2/9$	$1/(9\sqrt{2})$
$e2f1$	3/2	−1/2	1/2	−1/2	π	$2\sqrt{2}/9$	$-\sqrt{10}/9$
$e2f2$				1/2	σ^+	$-2/9$	$\sqrt{5}/9$
$e2f3$			3/2	−3/2	σ^-	$\sqrt{2/3}/3$	$2\sqrt{2/15}/3$
$e2f4$				−1/2	π	$-1/9$	$-2/(9\sqrt{5})$
$e2f5$				1/2	σ^+	$-2\sqrt{2}/9$	$-4\sqrt{2/5}/9$
$e3f1$	1/2	1/2	1/2	−1/2	σ^-	$-\sqrt{2}/9$	$4/9$
$e3f2$				1/2	π	$-1/9$	$2\sqrt{2}/9$
$e3f4$			3/2	−1/2	σ^-	$2/9$	$1/(9\sqrt{2})$
$e3f5$				1/2	π	$2\sqrt{2}/9$	$1/9$
$e3f6$				3/2	σ^+	$2/(3\sqrt{3})$	$1/(3\sqrt{6})$
$e4f1$	3/2	1/2	1/2	−1/2	σ^-	$-2/9$	$\sqrt{5}/9$
$e4f2$				1/2	π	$2\sqrt{2}/9$	$-\sqrt{10}/9$
$e4f4$			3/2	−1/2	σ^-	$2\sqrt{2}/9$	$4\sqrt{2/5}/9$
$e4f5$				1/2	π	$1/9$	$2/(9\sqrt{5})$
$e4f6$				3/2	σ^+	$-\sqrt{2/3}/3$	$-2\sqrt{2/15}/3$
$e5f3$	3/2	−3/2	3/2	−3/2	π	$-1/3$	$-2/(3\sqrt{5})$
$e5f4$				−1/2	σ^+	$-\sqrt{2/3}/3$	$-2\sqrt{2/15}/3$
$e5f1$			1/2	−1/2	σ^+	$-2/(3\sqrt{3})$	$\sqrt{5/3}/3$
$e6f6$	3/2	3/2	3/2	3/2	π	$1/3$	$2/(3\sqrt{5})$
$e6f5$				1/2	σ^-	$\sqrt{2/3}/3$	$2\sqrt{2/15}/3$
$e6f2$			1/2	1/2	σ^-	$-2/(3\sqrt{3})$	$\sqrt{5/3}/3$

Table A.2: Relative matrix elements for the decays from the nP excited state ($l_e = 1$) to the $1S_{1/2}$ ground state ($l_f = 0$, $J_f = 1/2$) in deuterium (nuclear spin $I = 1$, electron spin $S = 1/2$). The excited and final states are denoted as eE and fF with $E = \{1, 2, 3, 4, 5, 6\}$ and $F = \{1, 2, 3, 4, 5, 6\}$ according to Fig. A.4. The first column names the corresponding decay from the eE state to the fF state. The quantum numbers F and m_F for the excited (F_e, m_e) and final states (F_f, m_f) are listed thereafter. Next, the emitting polarization q is given ($q = \pm 1$ corresponds to the $\sigma^\pm$ decays and $q = 0$ to the π decay). The last two columns give the value for the reduced matrix element d_{eEfF} (Eq. (A.49) without the factor $\langle n_f, l_f || d || n_e, l_e \rangle$) for the $nP_{1/2}$ ($J_e = 1/2$) and the $nP_{3/2}$ ($J_e = 3/2$) fine-structure components.

contribution of the unresolved quantum interference, we can use the result of Eq. (2.60) with $D_1 = d_{i1e1} d_{e1fF}$ and $D_2 = d_{i1e2} d_{e2fF}$ for each final state F. The fractional shift η of the total line center in units of the hyperfine splitting (see Eq. (A.38)), including unresolved quantum

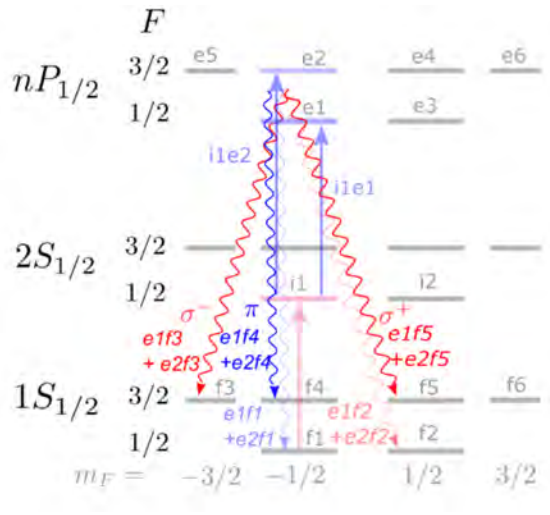

Figure A.4: Example of the level scheme for the derivation of the line center with unresolved quantum interference for 2S-nP transitions in deuterium. The $2S_{1/2}$ ($F = 1/2$, $m_F = -1/2$) state is the initial state $i1$, from which the two excited $nP_{1/2}$ ($F = 1/2$ and $F = 3/2$, $m_F = -1/2$) states $e1$ and $e2$ are driven. The π decays (blue wavy arrows) occur to the $1S_{1/2}$ ($F = 1/2$ and $F = 3/2$, $m_F = -1/2$) ground states (final states $f1$ and $f4$). Unresolved quantum interference for the π decays involves terms with $(d_{i1e1}d_{e1f1})(d_{i1e2}d_{e2f1})$ and $(d_{i1e1}d_{e1f4})(d_{i1e2}d_{e2f4})$, where d_{iIeE} are the reduced matrix elements from the initial state iI to the excited state eE (evaluated in Table A.1) and d_{eEfF} are the reduced matrix elements from the excited state eE to the final state fF (evaluated in Table A.2). Similarly, the $\sigma^{\pm}$ decays are shown with red wavy arrows.

interference, is then given by:

$$\eta = \frac{\mathcal{S}_2 + \mathcal{S}_Q}{\mathcal{S}_1 + \mathcal{S}_2 + 2\mathcal{S}_Q} \tag{A.50}$$

with

$$\mathcal{S}_2 = \sum_F (d_{i1e2}d_{e2fF})^2, \quad \mathcal{S}_1 = \sum_F (d_{i1e1}d_{e1fF})^2, \quad \mathcal{S}_Q = \sum_F d_{i1e1}d_{e1fF}\, d_{i1e2}d_{e2fF}. \tag{A.51}$$

For the example shown in Fig. A.4, the above terms yield:

$$\mathcal{S}_1 = (d_{i1e1}d_{e1f3})^2 + (d_{i1e1}d_{e1f4})^2 + (d_{i1e1}d_{e1f1})^2 + k_\xi(d_{i1e1}d_{e1f5})^2 + k_\xi(d_{i1e1}d_{e1f2})^2, \tag{A.52}$$

$$\mathcal{S}_2 = (d_{i1e2}d_{e2f3})^2 + (d_{i1e2}d_{e2f4})^2 + (d_{i1e2}d_{e2f1})^2 + k_\xi(d_{i1e2}d_{e2f5})^2 + k_\xi(d_{i1e2}d_{e2f2})^2, \tag{A.53}$$

$$\begin{aligned}\mathcal{S}_Q = {} & (d_{i1e1}d_{e1f3})(d_{i1e2}d_{e2f3}) + (d_{i1e1}d_{e1f4})(d_{i1e2}d_{e2f4}) + (d_{i1e1}d_{e1f1})(d_{i1e2}d_{e2f1}) \\ & + k_\xi(d_{i1e1}d_{e1f5})(d_{i1e2}d_{e2f5}) + k_\xi(d_{i1e1}d_{e1f2})(d_{i1e2}d_{e2f2}),\end{aligned} \tag{A.54}$$

where we included the factor k_ξ describing the polarization sensitive detector, which detects a factor k_ξ more σ^+ than σ^- photons. The factor k_ξ converts to the asymmetry parameter introduced in Eq. (2.44) as follows:

$$k_\xi = (1 - \xi_\circ)/(1 + \xi_\circ). \tag{A.55}$$

Similarly, we can also include the excitation from the state $i2$ with a state asymmetry ι. With the reduced matrix elements from Table A.2, we then find the following line center fractions

$\eta_{1/2}$ ($n\mathrm{P}_{1/2}$ level) and $\eta_{3/2}$ ($n\mathrm{P}_{3/2}$ level):

$$\eta_{1/2} = \frac{24 + 8\xi_\circ\iota}{27 + 15\xi_\circ\iota} \simeq \frac{8}{9} - \frac{16}{81}\xi_\circ\iota, \quad \eta_{3/2} = \frac{15 + 13\xi_\circ\iota}{27 + 21\xi_\circ\iota} \simeq \frac{5}{9} + \frac{4}{81}\xi_\circ\iota. \tag{A.56}$$

The above equation shows that there is only a shift if the states i_1 and i_2 are unequally populated ($\iota \neq 0$) and the detector detects σ^- photons with a different quantum efficiency than σ^+ photons ($\xi_\circ \neq 0$), which is independent of the detector geometry. Due to the discussed cancellation of unresolved quantum interference there is no dependence on the detector geometry, and there is no shift proportional only to $\xi_\circ$ or only to ι.

A.5 Piezo-mirror for the 1S-2S enhancement cavity

The possible future upgrade of the 1S-2S enhancement cavity (see Section 3.2.1.1) to differential pumping may require a higher feedback bandwidth of the cavity lock (due to the increased cavity length and the vacuum chamber extensions for the cavity mirrors, which may be more sensitive to vibrations). Therefore, a piezo-mirror with higher bandwidth than the previous design was explored. Fig. A.5(a) shows the drawing for the most promising design of the mount (new design denoted as V6), which is a modified design based on [266]. Contrary to [266], here we require a mirror mount with a through-hole, and which has smaller dimensions. The drawing of the previous piezo-mirror design (denoted as V0) is shown in Fig. A.5(b). The photograph in Fig. A.5(c) shows these designs manufactured from copper or steel, where the mirror (7.75 mm diameter, 4.0 mm thickness) is glued with TorrSeal® epoxy onto the ring-piezo (PI PD080.31, 4.5 mm inner diameter, 8 mm outer diameter), which is in turn glued onto the mount. The epoxy also serves as the insulator between the piezo electrodes and the mount. The photograph in Fig. A.5(d) shows how the mirror can be glued using 3 cubic piezos (PI PL022.31, 2x2x2 mm) similar to [266].

Fig. A.6 shows the frequency response of different configurations. As in [266], these

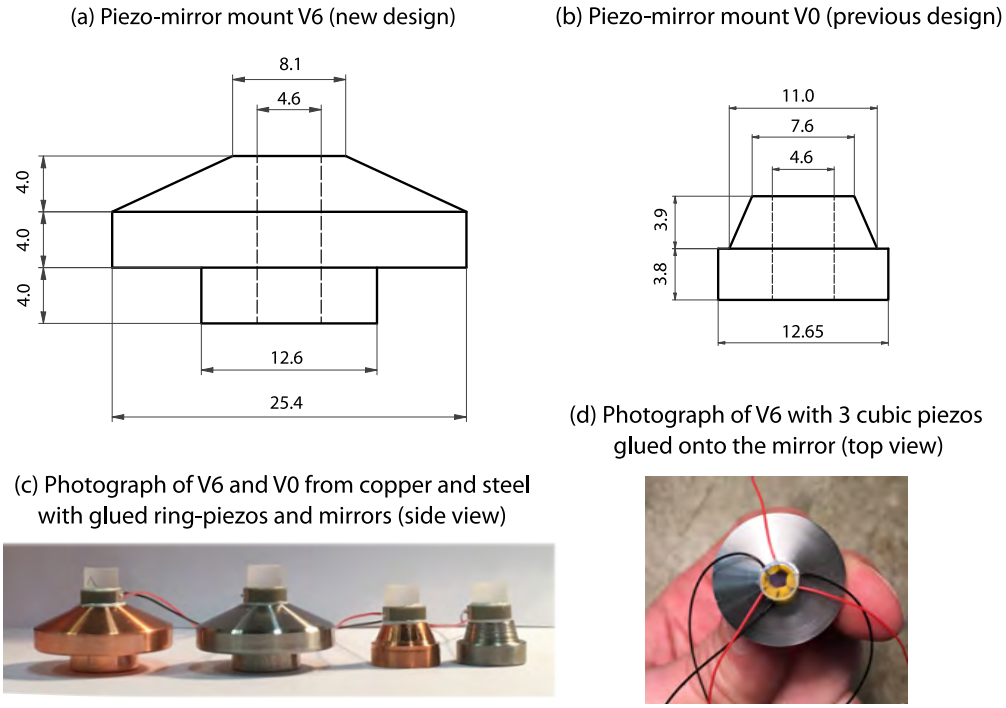

Figure A.5: Drawings and photographs of the previous and new designs of the piezo-mirror which serves as the incoupling mirror for the 1S-2S enhancement cavity. (a) Drawing of the new piezo-mirror mount design V6 (modified design from [266] with smaller dimensions and a through-hole). (b) Drawing of the previous piezo-mirror design V0. The values of dimensions in (a) and (b) are given in mm. (c) Photograph (side view) of the piezo-mirror mounts from (a) and (b), manufactured from copper or stainless steel, with glued ring-piezos (PI PD080.31, 4.5 mm inner diameter, 8 mm outer diameter) and mirrors (7.75 mm diameter, 4.0 mm thickness). (d) Photograph (top view) of the piezo-mirror design from (a), where the mirror is glued onto the mount with 3 cubic piezos (PI PL022.31, 2x2x2 mm) similar to the configuration in [266].

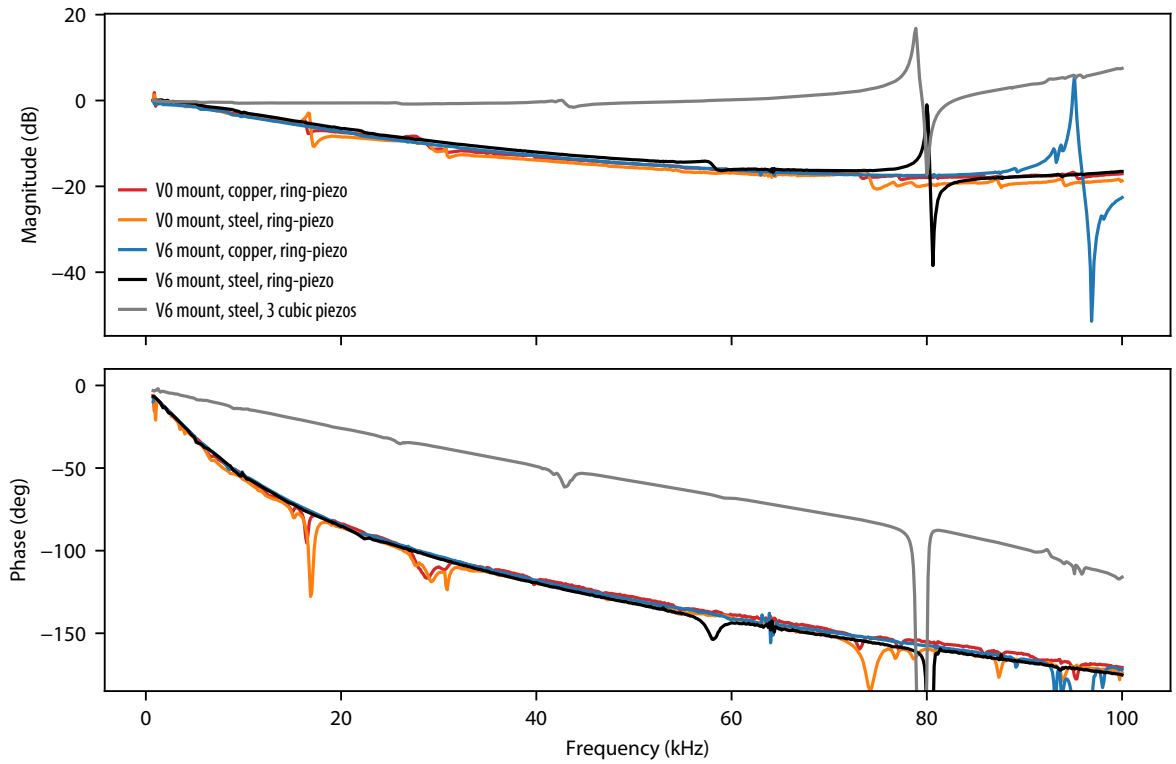

Figure A.6: Frequency response of different piezo-mirror designs. The amplitude is shown on the top plot, the phase on the bottom plot. All curves except the gray curve show different configurations with the ring-piezo (PI PD080.31, 4.5 mm inner diameter, 8 mm outer diameter) glued onto the mirror (7.75 mm diameter, 4.0 mm thickness) as shown in Fig. A.5(c). This ring-piezo has a capacitance of 300 nF, which forms a lowpass filter together with the 50 Ω output resistance of the high voltage amplifier for the piezo (resuling in a −3 dB cutoff frequency around 10 kHz, where the phase shift is −45 deg). The gray curve shows the response for a similar mirror glued onto the mount with three cubic piezos (PI PL022.31, 2x2x2 mm) as in [266], having a smaller capacitance of 25 nF. For this configuration, the response is approximately flat up to the resonance around 80 kHz, where the first phase shift of −90 deg occurs. The frequency responses of the V0 designs from Fig. A.5(b) from copper (red) and steel (orange) with the ring-piezo both show a resonance around 17 kHz. The V6 design from Fig. A.5(a) has an approximately smooth response up to around 80 kHz for steel (black) or up to around 95 kHz for copper (blue), with higher amplitude for copper. However, note that for the configuration with the ring-piezo the lowpass behaviour might limit the bandwidth to 20 kHz, where the phase shift reaches −90 deg (together with the phase shift of −90 deg from the integrator of the feedback loop this results in the −180 deg phase shift).

measurements were performed by using a Michelson interferometer[1]. The gray curve shows the data for the V6 mount manufactured from steel with 3 cubic piezos, whereas other curves show the data for the V0 or V6 mounts with the ring-piezo. The ring-piezo has a capacitance of 300 nF, which forms a lowpass filter together with the 50 Ω output resistance of the high voltage amplifier for the piezo. This lowpass results in a −3 dB cutoff frequency around 10 kHz, where the phase shift is −45 deg. The cubic piezos have a smaller capacitance of 25 nF, which has the advantage of shifting the lowpass cutoff to higher frequency. For this configuration,

[1]The frequency response was measured with the Ono-Sokki CF-9200 FFT-Analyser with the CF-0971 signal output module, which enables the measurement of the transfer function.

the response is approximately flat up to the resonance around around 80 kHz, where the first phase shift of −90 deg occurs. Note that typically the phase shift of −90 deg in the frequency response of the piezo-mirror limits the bandwidth (without any additional techniques such as notch filters), since the integrator adds another phase shift of −90 deg, which results in the −180 deg total phase shift. The responses of the V0 design from Fig. A.5(b) with the ring-piezo both from copper (red) and steel (orange) show a resonance around 17 kHz. The V6 design from Fig. A.5(a) has an approximately smooth response up to around 80 kHz for steel (black) or up to around 95 kHz for copper (blue). Here, the resonance has a smaller amplitude for the mount from steel as compared to copper, which was found to be typically the case for different designs similar to V6. For this configuration, the lowpass behavior of the ring-piezo is limiting the bandwidth. In principle, this could be improved by a lower output resistance of the high voltage amplifier.

Though the design with 3 cubic piezos has the best frequency response curve, it turned out that our cubic piezos are less reliable when gluing them onto the mirror, since the small connection leads were sensitive to break during the assembly process. In addition, it may be necessary to compensate for the tilt resulting from the slightly different response of the three piezos, such that three high voltage amplifiers with an adjustable gain are needed. Since in the current configuration of the 1S-2S enhancement cavity, a locking bandwidth of around 10-20 kHz turned out to be sufficient, the V6 mount design from steel (due to the smaller amplitude of the resonance as compared to copper) with a ring-piezo was used for now in the apparatus. However, for the future upgrade, it may turn out to be necessary to use this mount with 3 cubic piezos.

List of Figures

List of Tables

Bibliography

[1] V. Mukhanov, *Physical Foundations of Cosmology*. Cambridge University Press, 2005.

[2] L. Canetti, M. Drewes, and M. Shaposhnikov, "Matter and antimatter in the universe," *New Journal of Physics*, vol. 14, p. 095012, 2012.

[3] G. Börner, *The Early Universe*. Springer, 2002.

[4] T. Kajita, "Nobel Lecture: Discovery of atmospheric neutrino oscillations," *Reviews of Modern Physics*, vol. 88, p. 030501, 2016.

[5] S. Weinberg, "The cosmological constant problem," *Reviews of Modern Physics*, vol. 61, pp. 1–23, 1989.

[6] S. G. Karshenboim, "Precision physics of simple atoms: QED tests, nuclear structure and fundamental constants," *Physics Reports*, vol. 422, pp. 1–63, 2005.

[7] M. I. Eides, H. Grotch, and V. A. Shelyuto, *Theory of Light Hydrogenic Bound States*. Springer, 2007.

[8] E. Tiesinga, P. J. Mohr, D. B. Newell, and B. N. Taylor, "CODATA recommended values of the fundamental physical constants: 2018," *Reviews of Modern Physics*, vol. 93, p. 025010, 2021.

[9] S. G. Karshenboim, "Precision Physics of Simple Atoms and Constraints on a Light Boson with Ultraweak Coupling," *Physical Review Letters*, vol. 104, p. 220406, 2010.

[10] T. Udem, R. Holzwarth, and T. W. Hänsch, "Optical frequency metrology," *Nature*, vol. 416, p. 5, 2002.

[11] T. W. Hänsch, "Nobel lecture: Passion for precision," *Rev. Mod. Phys.*, vol. 78, pp. 1297–1309, 2006.

[12] A. Grinin, A. Matveev, D. C. Yost, L. Maisenbacher, V. Wirthl, R. Pohl, T. W. Hänsch, and T. Udem, "Two-photon frequency comb spectroscopy of atomic hydrogen," *Science*, vol. 370, pp. 1061–1066, 2020.

[13] C. G. Parthey, A. Matveev, J. Alnis, B. Bernhardt, A. Beyer, R. Holzwarth, A. Maistrou, R. Pohl, K. Predehl, T. Udem, T. Wilken, N. Kolachevsky, M. Abgrall, D. Rovera, C. Salomon, P. Laurent, and T. W. Hänsch, "Improved Measurement of the Hydrogen 1S–2S Transition Frequency," *Physical Review Letters*, vol. 107, p. 203001, 2011.

[14] A. Beyer, L. Maisenbacher, A. Matveev, R. Pohl, K. Khabarova, A. Grinin, T. Lamour, D. C. Yost, T. W. Hänsch, N. Kolachevsky, and T. Udem, "The Rydberg constant and proton size from atomic hydrogen," *Science*, vol. 358, pp. 79–85, 2017.

[15] H. Fleurbaey, S. Galtier, S. Thomas, M. Bonnaud, L. Julien, F. Biraben, F. Nez, M. Abgrall, and J. Guéna, "New Measurement of the 1S–3S Transition Frequency of Hydrogen: Contribution to the Proton Charge Radius Puzzle," *Physical Review Letters*, vol. 120, p. 183001, 2018.

[16] A. D. Brandt, S. F. Cooper, C. Rasor, Z. Burkley, A. Matveev, and D. C. Yost, "Measurement of the $2S_{1/2} - 8D_{5/2}$ Transition in Hydrogen," *Phys. Rev. Lett.*, vol. 128, p. 023001, 2022.

[17] M. Herrmann, M. Haas, U. D. Jentschura, F. Kottmann, D. Leibfried, G. Saathoff, C. Gohle, A. Ozawa, V. Batteiger, S. Knünz, N. Kolachevsky, H. A. Schüssler, T. W. Hänsch, and T. Udem, "Feasibility of coherent xuv spectroscopy on the $1S-2S$ transition in singly ionized helium," *Phys. Rev. A*, vol. 79, p. 052505, 2009.

[18] G. Clausen, P. Jansen, S. Scheidegger, J. A. Agner, H. Schmutz, and F. Merkt, "Ionization Energy of the Metastable 2 $^1S_0$ State of ^{4}He from Rydberg-Series Extrapolation," *Phys. Rev. Lett.*, vol. 127, p. 093001, 2021.

[19] S. Alighanbari, G. S. Giri, F. L. Constantin, V. I. Korobov, and S. Schiller, "Precise test of quantum electrodynamics and determination of fundamental constants with HD+ ions," *Nature*, vol. 581, pp. 152–158, 2020.

[20] S. Patra, M. Germann, J.-P. Karr, M. Haidar, L. Hilico, V. I. Korobov, F. M. J. Cozijn, K. S. E. Eikema, W. Ubachs, and J. C. J. Koelemeij, "Proton-electron mass ratio from laser spectroscopy of HD $^+$ at the part-per-trillion level," *Science*, vol. 369, pp. 1238–1241, 2020.

[21] M. Beyer, N. Hölsch, J. A. Agner, J. Deiglmayr, H. Schmutz, and F. Merkt, "Metrology of high-n Rydberg states of molecular hydrogen with $\Delta\nu/\nu = 2\times10^{-10}$ accuracy," *Phys. Rev. A*, vol. 97, p. 012501, 2018.

[22] J. Hussels, N. Hölsch, C.-F. Cheng, E. J. Salumbides, H. L. Bethlem, K. S. E. Eikema, C. Jungen, M. Beyer, F. Merkt, and W. Ubachs, "Improved ionization and dissociation energies of the deuterium molecule," *Physical Review A*, vol. 105, p. 022820, 2022.

[23] A. Antognini, F. Kottmann, and R. Pohl, "Laser spectroscopy of light muonic atoms and the nuclear charge radii," *SciPost Phys. Proc.*, p. 21, 2021.

[24] G. S. Adkins, D. B. Cassidy, and J. Pérez-Ríos, "Precision spectroscopy of positronium: Testing bound-state QED theory and the search for physics beyond the Standard Model," *Physics Reports*, vol. 975, pp. 1–61, 2022.

[25] Mu-MASS Collaboration, "Precision Measurement of the Lamb Shift in Muonium," *Physical Review Letters*, vol. 128, p. 011802, 2022.

[26] A. Sótér, H. Aghai-Khozani, D. Barna, A. Dax, L. Venturelli, and M. Hori, "High-resolution laser resonances of antiprotonic helium in superfluid ^{4}He," *Nature*, vol. 603, pp. 411–415, 2022.

[27] M. Ahmadi, B. X. R. Alves, C. J. Baker, W. Bertsche, A. Capra, C. Carruth, C. L. Cesar, M. Charlton, S. Cohen, R. Collister, S. Eriksson, A. Evans, N. Evetts, J. Fajans, T. Friesen, M. C. Fujiwara, D. R. Gill, J. S. Hangst, W. N. Hardy, M. E. Hayden, C. A. Isaac, M. A. Johnson, J. M. Jones, S. A. Jones, S. Jonsell, A. Khramov, P. Knapp, L. Kurchaninov, N. Madsen, D. Maxwell, J. T. K. McKenna, S. Menary, T. Momose, J. J. Munich, K. Olchanski, A. Olin, P. Pusa, C. . Rasmussen, F. Robicheaux, R. L. Sacramento, M. Sameed, E. Sarid, D. M. Silveira, G. Stutter, C. So, T. D. Tharp, R. I. Thompson, D. P. van der Werf, and J. S. Wurtele, "Characterization of the 1S–2S transition in antihydrogen," *Nature*, vol. 557, pp. 71–75, 2018.

[28] E. G. Myers, "*CPT* tests with the antihydrogen molecular ion," *Phys. Rev. A*, vol. 98, p. 010101, 2018.

[29] R. H. Parker, C. Yu, W. Zhong, B. Estey, and H. Müller, "Measurement of the fine-structure constant as a test of the Standard Model," *Science*, vol. 360, pp. 191–195, 2018.

[30] L. Morel, Z. Yao, P. Cladé, and S. Guellati-Khélifa, "Determination of the fine-structure constant with an accuracy of 81 parts per trillion," *Nature*, vol. 588, pp. 61–65, 2020.

[31] P. Asenbaum, C. Overstreet, M. Kim, J. Curti, and M. A. Kasevich, "Atom-Interferometric Test of the Equivalence Principle at the 10^{-12} Level," *Physical Review Letters*, vol. 125, p. 191101, 2020.

[32] D. Hanneke, S. Fogwell, and G. Gabrielse, "New Measurement of the Electron Magnetic Moment and the Fine Structure Constant," *Physical Review Letters*, vol. 100, p. 120801, 2008.

[33] X. Fan and G. Gabrielse, "Driven one-particle quantum cyclotron," *Phys. Rev. A*, vol. 103, p. 022824, 2021.

[34] R. S. Van Dyck, S. L. Zafonte, S. Van Liew, D. B. Pinegar, and P. B. Schwinberg, "Ultraprecise Atomic Mass Measurement of the α Particle and ^{4}He," *Phys. Rev. Lett.*, vol. 92, p. 220802, 2004.

[35] S. Sturm, F. Köhler, J. Zatorski, A. Wagner, Z. Harman, G. Werth, W. Quint, C. H. Keitel, and K. Blaum, "High-precision measurement of the atomic mass of the electron," *Nature*, vol. 506, pp. 467–470, 2014.

[36] F. Heiße, F. Köhler-Langes, S. Rau, J. Hou, S. Junck, A. Kracke, A. Mooser, W. Quint, S. Ulmer, G. Werth, K. Blaum, and S. Sturm, "High-Precision Measurement of the Proton's Atomic Mass," *Physical Review Letters*, vol. 119, p. 033001, 2017.

[37] D. J. Fink and E. G. Myers, "Deuteron-to-Proton Mass Ratio from Simultaneous Measurement of the Cyclotron Frequencies of H_2^+ and D^+," *Physical Review Letters*, vol. 127, p. 243001, 2021.

[38] K. Blaum, S. Eliseev, and S. Sturm, "Perspectives on testing fundamental physics with highly charged ions in Penning traps," *Quantum Science and Technology*, vol. 6, p. 014002, 2020.

[39] M. Pospelov and A. Ritz, "Electric dipole moments as probes of new physics," *Annals of Physics*, vol. 318, pp. 119–169, 2005.

[40] C. Abel, S. Afach, N. Ayres, C. Baker, G. Ban, G. Bison, K. Bodek, V. Bondar, M. Burghoff, E. Chanel, Z. Chowdhuri, P.-J. Chiu, B. Clement, C. Crawford, M. Daum, S. Emmenegger, L. Ferraris-Bouchez, M. Fertl, P. Flaux, B. Franke, A. Fratangelo, P. Geltenbort, K. Green, W. Griffith, M. van der Grinten, Z. Grujić, P. Harris, L. Hayen, W. Heil, R. Henneck, V. Hélaine, N. Hild, Z. Hodge, M. Horras, P. Iaydjiev, S. Ivanov, M. Kasprzak, Y. Kermaidic, K. Kirch, A. Knecht, P. Knowles, H.-C. Koch, P. Koss, S. Komposch, A. Kozela, A. Kraft, J. Krempel, M. Kuźniak, B. Lauss, T. Lefort, Y. Lemière, A. Leredde, P. Mohanmurthy, A. Mtchedlishvili, M. Musgrave, O. Naviliat-Cuncic, D. Pais, F. Piegsa, E. Pierre, G. Pignol, C. Plonka-Spehr, P. Prashanth, G. Quéméner, M. Rawlik, D. Rebreyend, I. Rienäcker, D. Ries, S. Roccia, G. Rogel, D. Rozpedzik, A. Schnabel, P. Schmidt-Wellenburg, N. Severijns, D. Shiers, R. Tavakoli Dinani, J. Thorne, R. Virot, J. Voigt, A. Weis, E. Wursten, G. Wyszynski, J. Zejma, J. Zenner, and G. Zsigmond, "Measurement of the Permanent Electric Dipole Moment of the Neutron," *Physical Review Letters*, vol. 124, p. 081803, 2020.

[41] ACME Collaboration, "Improved limit on the electric dipole moment of the electron," *Nature*, vol. 562, pp. 355–360, 2018.

[42] D. Aybas, J. Adam, E. Blumenthal, A. V. Gramolin, D. Johnson, A. Kleyheeg, S. Afach, J. W. Blanchard, G. P. Centers, A. Garcon, M. Engler, N. L. Figueroa, M. G. Sendra, A. Wickenbrock, M. Lawson, T. Wang, T. Wu, H. Luo, H. Mani, P. Mauskopf, P. W. Graham, S. Rajendran, D. F. J. Kimball, D. Budker, and A. O. Sushkov, "Search for Axionlike Dark Matter Using Solid-State Nuclear Magnetic Resonance," *Physical Review Letters*, vol. 126, p. 141802, 2021.

[43] C. Frugiuele, E. Fuchs, G. Perez, and M. Schlaffer, "Constraining new physics models with isotope shift spectroscopy," *Physical Review D*, vol. 96, p. 015011, 2017.

[44] C. Sanner, N. Huntemann, R. Lange, C. Tamm, E. Peik, M. S. Safronova, and S. G. Porsev, "Optical clock comparison for Lorentz symmetry testing," *Nature*, vol. 567, pp. 204–208, 2019.

[45] X. Rong, M. Wang, J. Geng, X. Qin, M. Guo, M. Jiao, Y. Xie, P. Wang, P. Huang, F. Shi, Y.-F. Cai, C. Zou, and J. Du, "Searching for an exotic spin-dependent interaction with a single electron-spin quantum sensor," *Nature Communications*, vol. 9, p. 739, 2018.

[46] M. Safronova, D. Budker, D. DeMille, D. F. J. Kimball, A. Derevianko, and C. W. Clark, "Search for new physics with atoms and molecules," *Reviews of Modern Physics*, vol. 90, p. 025008, 2018.

[47] D. Griffiths, *Introduction to Elementary Particles*. Wiley, 2005.

[48] CMS Collaboration, "Observation of a new boson at a mass of 125 GeV with the CMS experiment at the LHC," *Physics Letters B*, vol. 716, pp. 30–61, 2012.

[49] ATLAS Collaboration, "Observation of a new particle in the search for the Standard Model Higgs boson with the ATLAS detector at the LHC," *Physics Letters B*, vol. 716, pp. 1–29, 2012.

[50] T. Aoyama, M. Hayakawa, T. Kinoshita, and M. Nio, "Tenth-Order QED Contribution to the Electron $g-2$ and an Improved Value of the Fine Structure Constant," *Phys. Rev. Lett.*, vol. 109, p. 111807, 2012.

[51] T. Aoyama, T. Kinoshita, and M. Nio, "Revised and improved value of the QED tenth-order electron anomalous magnetic moment," *Phys. Rev. D*, vol. 97, p. 036001, 2018.

[52] S. Volkov, "Calculating the five-loop qed contribution to the electron anomalous magnetic moment: Graphs without lepton loops," *Phys. Rev. D*, vol. 100, p. 096004, 2019.

[53] G. Gabrielse, "The standard model's greatest triumph," *Physics Today*, vol. 66, pp. 64–65, 2013.

[54] R. Pohl, F. Nez, T. Udem, A. Antognini, A. Beyer, H. Fleurbaey, A. Grinin, T. W. Hänsch, L. Julien, F. Kottmann, J. J. Krauth, L. Maisenbacher, A. Matveev, and F. Biraben, "Deuteron charge radius and Rydberg constant from spectroscopy data in atomic deuterium," *Metrologia*, vol. 54, pp. L1–L10, 2017.

[55] B. J. Mount, M. Redshaw, and E. G. Myers, "Atomic masses of ^{6}Li,^{23} Na,^{39,41} K,^{85,87} Rb, and ^{133}Cs," *Physical Review A*, vol. 82, p. 042513, 2010.

[56] S. Rau, F. Heiße, F. Köhler-Langes, S. Sasidharan, R. Haas, D. Renisch, C. E. Düllmann, W. Quint, S. Sturm, and K. Blaum, "Penning trap mass measurements of the deuteron and the HD^+ molecular ion," *Nature*, vol. 585, pp. 43–47, 2020.

[57] C. G. Parthey, A. Matveev, J. Alnis, R. Pohl, T. Udem, U. D. Jentschura, N. Kolachevsky, and T. W. Hänsch, "Precision Measurement of the Hydrogen-Deuterium 1S–2S Isotope Shift," *Physical Review Letters*, vol. 104, p. 233001, 2010.

[58] G. Newton, D. A. Andrews, and P. J. Unsworth, "A Precision Determination of the Lamb Shift in Hydrogen," *Philosophical Transactions of the Royal Society of London. Series A, Mathematical and Physical Sciences*, vol. 290, no. 1373, pp. 373–404, 1979.

[59] S. R. Lundeen and F. M. Pipkin, "Separated Oscillatory Field Measurement of the Lamb Shift in H, $n = 2$," *Metrologia*, vol. 22, pp. 9–54, 1986.

[60] E. W. Hagley and F. M. Pipkin, "Separated oscillatory field measurement of hydrogen $2S_{1/2}$-$2P_{3/2}$ fine structure interval," *Physical Review Letters*, vol. 72, pp. 1172–1175, 1994.

[61] D. J. Berkeland, E. A. Hinds, and M. G. Boshier, "Precise Optical Measurement of Lamb Shifts in Atomic Hydrogen," *Physical Review Letters*, vol. 75, pp. 2470–2473, 1995.

[62] M. Weitz, A. Huber, F. Schmidt-Kaler, D. Leibfried, W. Vassen, C. Zimmermann, K. Pachucki, T. W. Hänsch, L. Julien, and F. Biraben, "Precision measurement of the 1S ground-state Lamb shift in atomic hydrogen and deuterium by frequency comparison," *Physical Review A*, vol. 52, pp. 2664–2681, 1995.

[63] S. Bourzeix, B. de Beauvoir, F. Nez, M. D. Plimmer, F. de Tomasi, L. Julien, F. Biraben, and D. N. Stacey, "High Resolution Spectroscopy of the Hydrogen Atom: Determination of the 1S Lamb Shift," *Physical Review Letters*, vol. 76, pp. 384–387, 1996.

[64] B. de Beauvoir, F. Nez, L. Julien, B. Cagnac, F. Biraben, D. Touahri, L. Hilico, O. Acef, A. Clairon, and J. J. Zondy, "Absolute Frequency Measurement of the 2S–8S/D Transitions in Hydrogen and Deuterium: New Determination of the Rydberg Constant," *Physical Review Letters*, vol. 78, pp. 440–443, 1997.

[65] C. Schwob, L. Jozefowski, B. de Beauvoir, L. Hilico, F. Nez, L. Julien, F. Biraben, O. Acef, J.-J. Zondy, and A. Clairon, "Optical frequency measurement of the $2S-12D$ transitions in hydrogen and deuterium: Rydberg constant and lamb shift determinations," *Physical Review Letters*, vol. 82, pp. 4960–4963, 1999.

[66] O. Arnoult, F. Nez, L. Julien, and F. Biraben, "Optical frequency measurement of the 1S–3S two-photon transition in hydrogen," *The European Physical Journal D*, vol. 60, pp. 243–256, 2010.

[67] A. Antognini, F. Nez, K. Schuhmann, F. D. Amaro, F. Biraben, J. M. R. Cardoso, D. S. Covita, A. Dax, S. Dhawan, M. Diepold, L. M. P. Fernandes, A. Giesen, A. L. Gouvea, T. Graf, T. W. Hänsch, P. Indelicato, L. Julien, C.-Y. Kao, P. Knowles, F. Kottmann, E.-O. L. Bigot, Y.-W. Liu, J. A. M. Lopes, L. Ludhova, C. M. B. Monteiro, F. Mulhauser, T. Nebel, P. Rabinowitz, J. M. F. d. Santos, L. A. Schaller, C. Schwob, D. Taqqu, J. F. C. A. Veloso, J. Vogelsang, and R. Pohl, "Proton Structure from the Measurement of 2S-2P Transition Frequencies of Muonic Hydrogen," *Science*, vol. 339, pp. 417–420, 2013.

[68] CREMA Collaboration, "Laser spectroscopy of muonic deuterium," *Science*, vol. 353, no. 6300, pp. 669–673, 2016.

[69] M. Kalinowski, "Deuteron charge radius from the Lamb-shift measurement in muonic deuterium," *Physical Review A*, vol. 99, p. 030501, 2019.

[70] N. Bezginov, T. Valdez, M. Horbatsch, A. Marsman, A. C. Vutha, and E. A. Hessels, "A measurement of the atomic hydrogen Lamb shift and the proton charge radius," *Science*, vol. 365, pp. 1007–1012, 2019.

[71] L. Maisenbacher, *Precision Spectroscopy of the 2S-nP Transitions in Atomic Hydrogen*. PhD thesis, LMU Munich, 2020.

[72] P. J. Mohr, D. B. Newell, and B. N. Taylor, "CODATA recommended values of the fundamental physical constants: 2014," *Reviews of Modern Physics*, vol. 88, p. 035009, 2016.

[73] R. Pohl, A. Antognini, F. Nez, F. D. Amaro, F. Biraben, J. M. R. Cardoso, D. S. Covita, A. Dax, S. Dhawan, L. M. P. Fernandes, A. Giesen, T. Graf, T. W. Hänsch, P. Indelicato, L. Julien, C.-Y. Kao, P. Knowles, E.-O. Le Bigot, Y.-W. Liu, J. A. M. Lopes, L. Ludhova, C. M. B. Monteiro, F. Mulhauser, T. Nebel, P. Rabinowitz, J. M. F. dos Santos, L. A. Schaller, K. Schuhmann, C. Schwob, D. Taqqu, J. F. C. A. Veloso, and F. Kottmann, "The size of the proton," *Nature*, vol. 466, pp. 213–216, 2010.

[74] M. P. A. Jones, R. M. Potvliege, and M. Spannowsky, "Probing new physics using Rydberg states of atomic hydrogen," *Physical Review Research*, vol. 2, p. 013244, 2020.

[75] B. L. Cosens, "Remeasurement of the Lamb Shift in D, $n = 2$," *Phys. Rev.*, vol. 173, pp. 49–55, 1968.

[76] A. van Wijngaarden and G. W. F. Drake, "Deuterium Lamb shift via quenching-radiation anisotropy measurements," *Phys. Rev. A*, vol. 17, pp. 1366–1374, 1978.

[77] B. Acharya, V. Lensky, S. Bacca, M. Gorchtein, and M. Vanderhaeghen, "Dispersive evaluation of the Lamb shift in muonic deuterium from chiral effective field theory," *Physical Review C*, vol. 103, p. 024001, 2021.

[78] J. J. Krauth, M. Diepold, B. Franke, A. Antognini, F. Kottmann, and R. Pohl, "Theory of the n=2 levels in muonic deuterium," *Annals of Physics*, vol. 366, pp. 168–196, 2016.

[79] K. Pachucki, V. Patkóš, and V. A. Yerokhin, "Three-photon-exchange nuclear structure correction in hydrogenic systems," *Physical Review A*, vol. 97, p. 062511, 2018.

[80] O. J. Hernandez, A. Ekström, N. Nevo Dinur, C. Ji, S. Bacca, and N. Barnea, "The deuteron-radius puzzle is alive: A new analysis of nuclear structure uncertainties," *Physics Letters B*, vol. 778, pp. 377–383, 2018.

[81] V. A. Yerokhin, K. Pachucki, and V. Patkóš, "Theory of the Lamb Shift in Hydrogen and Light Hydrogen-Like Ions," *Annalen der Physik*, vol. 531, no. 5, p. 1800324, 2019.

[82] G. A. Miller, "Defining the proton radius: A unified treatment," *Physical Review C*, vol. 99, p. 035202, 2019.

[83] Y.-H. Lin, H.-W. Hammer, and U.-G. Meißner, "Dispersion-theoretical analysis of the electromagnetic form factors of the nucleon: Past, present and future," *The European Physical Journal A*, vol. 57, p. 255, 2021.

[84] W. Xiong, A. Gasparian, H. Gao, D. Dutta, M. Khandaker, N. Liyanage, E. Pasyuk, C. Peng, X. Bai, L. Ye, K. Gnanvo, C. Gu, M. Levillain, X. Yan, D. W. Higinbotham, M. Meziane, Z. Ye, K. Adhikari, B. Aljawrneh, H. Bhatt, D. Bhetuwal, J. Brock, V. Burkert, C. Carlin, A. Deur, D. Di, J. Dunne, P. Ekanayaka, L. El-Fassi, B. Emmich, L. Gan, O. Glamazdin, M. L. Kabir, A. Karki, C. Keith, S. Kowalski, V. Lagerquist, I. Larin, T. Liu, A. Liyanage, J. Maxwell, D. Meekins, S. J. Nazeer, V. Nelyubin, H. Nguyen, R. Pedroni, C. Perdrisat, J. Pierce, V. Punjabi, M. Shabestari, A. Shahinyan, R. Silwal, S. Stepanyan, A. Subedi, V. V. Tarasov, N. Ton, Y. Zhang, and Z. W. Zhao, "A small proton charge radius from an electron–proton scattering experiment," *Nature*, vol. 575, pp. 147–150, 2019.

[85] M. Mihovilovič, P. Achenbach, T. Beranek, J. Beričič, J. C. Bernauer, R. Böhm, D. Bosnar, M. Cardinali, L. Correa, L. Debenjak, A. Denig, M. O. Distler, A. Esser, M. I. Ferretti Bondy, H. Fonvieille, J. M. Friedrich, I. Friščić, M. Hoek, S. Kegel, H. Merkel, D. G. Middleton, U. Müller, J. Pochodzalla, B. S. Schlimme, M. Schoth, F. Schulz, C. Sfienti, S. Širca, S. Štajner, Y. Stöttinger, M. Thiel, A. Tyukin, M. Vanderhaeghen, and A. B. Weber, "The proton charge radius extracted from the initial-state radiation experiment at MAMI," *The European Physical Journal A*, vol. 57, p. 107, 2021.

[86] M. Mihovilovič, D. W. Higinbotham, M. Bevc, and S. Širca, "Reinterpretation of Classic Proton Charge Form Factor Measurements," *Frontiers in Physics*, vol. 8, 2020.

[87] Y.-H. Lin, H.-W. Hammer, and U.-G. Meißner, "New Insights into the Nucleon's Electromagnetic Structure," *Physical Review Letters*, vol. 128, p. 052002, 2022.

[88] I. Sick and D. Trautmann, "On the rms radius of the deuteron," *Nuclear Physics A*, p. 17, 1998.

[89] J. Zhou, V. Khachatryan, H. Gao, D. W. Higinbotham, A. Parker, X. Bai, D. Dutta, A. Gasparian, K. Gnanvo, M. Khandaker, N. Liyanage, E. Pasyuk, C. Peng, and W. Xiong, "Advanced extraction of the deuteron charge radius from electron-deuteron scattering data," *Physical Review C*, vol. 103, p. 024002, 2021.

[90] E. Cline, J. Bernauer, E. J. Downie, and R. Gilman, "MUSE: The MUon Scattering Experiment," *SciPost Physics Proceedings*, p. 023, 2021.

[91] N. Kaiser, Y.-H. Lin, and U.-G. Meißner, "Radiative corrections to elastic muon-proton scattering at low momentum transfers," *Physical Review D*, vol. 105, p. 076006, 2022.

[92] Muon g–2 Collaboration, "Measurement of the Positive Muon Anomalous Magnetic Moment to 0.46 ppm," *Physical Review Letters*, vol. 126, p. 141801, 2021.

[93] N. Hasan, J. Green, S. Meinel, M. Engelhardt, S. Krieg, J. Negele, A. Pochinsky, and S. Syritsyn, "Computing the nucleon charge and axial radii directly at Q 2 = 0 in lattice QCD," *Physical Review D*, vol. 97, p. 034504, 2018.

[94] D. Djukanovic, T. Harris, G. von Hippel, P. Junnarkar, H. Meyer, D. Mohler, K. Ottnad, T. Schulz, J. Wilhelm, and H. Wittig, "Isovector electromagnetic form factors of the nucleon from lattice QCD and the proton radius puzzle," *Physical Review D*, vol. 103, p. 094522, 2021.

[95] U. Jentschura, A. Matveev, C. Parthey, J. Alnis, R. Pohl, T. Udem, N. Kolachevsky, and T. Hänsch, "Hydrogen-deuterium isotope shift: From the 1S–2S -transition frequency to the proton-deuteron charge-radius difference," *Physical Review A*, vol. 83, p. 042505, 2011.

[96] M. Ahmadi, B. X. R. Alves, C. J. Baker, W. Bertsche, E. Butler, A. Capra, C. Carruth, C. L. Cesar, M. Charlton, S. Cohen, R. Collister, S. Eriksson, A. Evans, N. Evetts, J. Fajans, T. Friesen, M. C. Fujiwara, D. R. Gill, A. Gutierrez, J. S. Hangst, W. N. Hardy, M. E. Hayden, C. A. Isaac, A. Ishida, M. A. Johnson, S. A. Jones, S. Jonsell, L. Kurchaninov, N. Madsen, M. Mathers, D. Maxwell, J. T. K. McKenna, S. Menary, J. M. Michan, T. Momose, J. J. Munich, P. Nolan, K. Olchanski, A. Olin, P. Pusa, C. . Rasmussen, F. Robicheaux, R. L. Sacramento, M. Sameed, E. Sarid, D. M. Silveira, S. Stracka, G. Stutter, C. So, T. D. Tharp, J. E. Thompson, R. I. Thompson, D. P. van der Werf, and J. S. Wurtele, "Observation of the 1S–2S transition in trapped antihydrogen," *Nature*, vol. 541, pp. 506–510, 2017.

[97] STAR Collaboration, "$\overline{d}$ and $^3\overline{\mathrm{he}}$ production in $\sqrt{s_{\mathrm{NN}}} = 130 GeV\, Au + Au$ collisions," *Phys. Rev. Lett.*, vol. 87, p. 262301, 2001.

[98] S. G. Karshenboim, "Precision study of positronium: Testing bound state QED theory," *Int. J. Mod. Phys. A*, vol. 19, pp. 3879–3896, 2004.

[99] G. S. Adkins and R. N. Fell, "Positronium hyperfine splitting at order $m\alpha^7$: Light-by-light scattering in the two-photon-exchange channel," *Phys. Rev. A*, vol. 89, p. 052518, 2014.

[100] F. Schmid, *Towards high resolution spectroscopy on trapped helium ions.* PhD thesis, LMU Munich, 2022.

[101] J. J. Krauth, K. Schuhmann, M. A. Ahmed, F. D. Amaro, P. Amaro, F. Biraben, T.-L. Chen, D. S. Covita, A. J. Dax, M. Diepold, L. M. P. Fernandes, B. Franke, S. Galtier, A. L. Gouvea, J. Götzfried, T. Graf, T. W. Hänsch, J. Hartmann, M. Hildebrandt, P. Indelicato, L. Julien, K. Kirch, A. Knecht, Y.-W. Liu, J. Machado, C. M. B. Monteiro, F. Mulhauser, B. Naar, T. Nebel, F. Nez, J. M. F. dos Santos, J. P. Santos, C. I. Szabo, D. Taqqu, J. F. C. A. Veloso, J. Vogelsang, A. Voss, B. Weichelt, R. Pohl, A. Antognini, and F. Kottmann, "Measuring the α-particle charge radius with muonic helium-4 ions," *Nature*, vol. 589, pp. 527–531, 2021.

[102] V. I. Korobov, L. Hilico, and J.-P. Karr, "Fundamental Transitions and Ionization Energies of the Hydrogen Molecular Ions with Few ppt Uncertainty," *Physical Review Letters*, vol. 118, p. 233001, 2017.

[103] V. I. Korobov, J. C. J. Koelemeij, L. Hilico, and J.-P. Karr, "Theoretical hyperfine structure of the molecular hydrogen ion at the 1 ppm level," *Phys. Rev. Lett.*, vol. 116, p. 053003, 2016.

[104] J.-P. Karr, M. Haidar, L. Hilico, Z.-X. Zhong, and V. I. Korobov, "Higher-order corrections to spin-spin scalar interactions in HD^+ and H_2^+," *Phys. Rev. A*, vol. 102, p. 052827, 2020.

[105] V. I. Korobov, J.-P. Karr, M. Haidar, and Z.-X. Zhong, "Hyperfine structure in the H_2^+ and HD^+ molecular ions at order $m\alpha^6$," *Phys. Rev. A*, vol. 102, p. 022804, 2020.

[106] V. c. v. Patkóš, V. A. Yerokhin, and K. Pachucki, "Complete $\alpha^7 m$ Lamb shift of helium triplet states," *Phys. Rev. A*, vol. 103, p. 042809, 2021.

[107] V. I. Korobov and J.-P. Karr, "Rovibrational spin-averaged transitions in the hydrogen molecular ions," *Phys. Rev. A*, vol. 104, p. 032806, 2021.

[108] J. Biesheuvel, J.-P. Karr, L. Hilico, K. S. E. Eikema, W. Ubachs, and J. C. J. Koelemeij, "High-precision spectroscopy of the HD+ molecule at the 1-p.p.b. level," *Applied Physics B*, vol. 123, p. 23, 2016.

[109] M. Puchalski, J. Komasa, and K. Pachucki, "Hyperfine Structure of the First Rotational Level in H_2, D_2 and HD Molecules and the Deuteron Quadrupole Moment," *Phys. Rev. Lett.*, vol. 125, p. 253001, 2020.

[110] V. Wirthl, L. Maisenbacher, J. Weitenberg, A. Hertlein, A. Grinin, A. Matveev, R. Pohl, T. W. Hänsch, and T. Udem, "Improved active fiber-based retroreflector with intensity stabilization and a polarization monitor for the near UV," *Optics Express*, vol. 29, p. 7024, 2021.

[111] V. Wirthl, L. Maisenbacher, J. Weitenberg, A. Hertlein, A. Grinin, A. Matveev, R. Pohl, T. W. Hänsch, and T. Udem, "Improved active fiber-based retroreflector with intensity stabilization and a polarization monitor for the near UV: erratum," *Optics Express*, vol. 30, p. 7340, 2022.

[112] H. A. Bethe and E. E. Salpeter, *Quantum Mechanics of One- and Two-Electron Atoms*. Dover Publications, 2008.

[113] K. Pachucki, D. Leibfried, M. Weitz, A. Huber, W. König, and T. W. Hänsch, "Theory of the energy levels and precise two-photon spectroscopy of atomic hydrogen and deuterium," *Journal of Physics B: Atomic, Molecular and Optical Physics*, vol. 29, pp. 177–195, 1996.

[114] U. D. Jentschura and G. S. Adkins, *Quantum Electrodynamics: Atoms, Lasers and Gravity*. World Scientific Publishing, 2022.

[115] M. Horbatsch and E. A. Hessels, "Tabulation of the bound-state energies of atomic hydrogen," *Phys. Rev. A*, vol. 93, p. 022513, 2016.

[116] A. Kramida, "A critical compilation of experimental data on spectral lines and energy levels of hydrogen, deuterium, and tritium," *Atomic Data and Nuclear Data Tables*, vol. 96, pp. 586–644, 2010.

[117] A. Kramida, "Erratum to "A critical compilation of experimental data on spectral lines and energy levels of hydrogen, deuterium, and tritium" [At. Data Nucl. Data Tables 96 (2010) 586–644]," *Atomic Data and Nuclear Data Tables*, vol. 126, pp. 295–298, 2019.

[118] S. J. Brodsky and R. G. Parsons, "Precise Theory of the Zeeman Spectrum for Atomic Hydrogen and Deuterium and the Lamb Shift," *Phys. Rev.*, vol. 163, pp. 134–146, 1967.

[119] E. Latvamaa, L. Kurittu, P. Pyykko, and L. Tataru, "On second-order magnetic hyperfine interactions in one-electron atoms: connections between the Schrodinger, Dirac and quantum electrodynamical perturbation calculations," *Journal of Physics B: Atomic and Molecular Physics*, vol. 6, pp. 591–600, 1973.

[120] A. Beyer, L. Maisenbacher, K. Khabarova, A. Matveev, R. Pohl, T. Udem, T. W. Hänsch, and N. Kolachevsky, "Precision spectroscopy of 2S–nP transitions in atomic hydrogen for a new determination of the Rydberg constant and the proton charge radius," *Physica Scripta*, vol. T165, p. 014030, 2015.

[121] F. G. Brickwedde, "Harold Urey and the discovery of deuterium," *Physics Today*, vol. 35, pp. 34–39, 1982.

[122] E. Segré, *Die großen Physiker und ihre Entdeckungen – Von Röntgen bis Weinberg*. Piper, 2004.

[123] W. E. Lamb and R. C. Retherford, "Fine structure of the hydrogen atom by a microwave method," *Phys. Rev.*, vol. 72, pp. 241–243, 1947.

[124] S. G. Karshenboim, A. Ozawa, and V. G. Ivanov, "Higher-order logarithmic corrections and the two-loop self-energy of a 1s electron in hydrogen," *Phys. Rev. A*, vol. 100, p. 032515, 2019.

[125] S. G. Karshenboim and V. A. Shelyuto, "Three-loop radiative corrections to the 1s lamb shift in hydrogen," *Phys. Rev. A*, vol. 100, p. 032513, 2019.

[126] U. D. Jentschura, "Proton radius, Darwin-Foldy term and radiative corrections," *The European Physical Journal D*, vol. 61, pp. 7–14, 2011.

[127] C. J. Foot, *Atomic Physics*. Oxford University Press, 2005.

[128] I. I. Sobelman, *Introduction to the Theory of Atomic Spectra*. Pergamon Press, 1972.

[129] I. I. Sobelman, *Atomic Spectra and Radiative Transitions*. Springer, 1992.

[130] R. Loudon, *The Quantum Theory of Light*. Oxford University Press, 1983.

[131] J. Baker, "Transition probabilities for one electron atoms," Tech. Rep. NBS TN 1612, National Institute of Standards and Technology, Gaithersburg, MD, 2008.

[132] J. L. Hall, C. J. Bordé, and K. Uehara, "Direct Optical Resolution of the Recoil Effect Using Saturated Absorption Spectroscopy," *Physical Review Letters*, vol. 37, pp. 1339–1342, 1976.

[133] D. Goldstein, *Polarized Light*. CRC, 2011.

[134] F. P. Fehlner and N. F. Mott, "Low-temperature oxidation," *Oxidation of Metals*, vol. 2, pp. 59–99, 1970.

[135] M. L. Scott, P. N. Arendt, B. J. Cameron, J. M. Saber, and B. E. Newnam, "Extreme ultraviolet reflectance degradation of aluminum and silicon from surface oxidation," *Appl. Opt.*, vol. 27, pp. 1503–1507, 1988.

[136] S. Moser, "An experimentalist's guide to the matrix element in angle resolved photoemission," *Journal of Electron Spectroscopy and Related Phenomena*, vol. 214, pp. 29–52, 2017.

[137] H. Zhang, T. Pincelli, C. Jozwiak, T. Kondo, R. Ernstorfer, T. Sato, and S. Zhou, "Angle-resolved photoemission spectroscopy," *Nature Reviews Methods Primers*, vol. 2, p. 54, 2022.

[138] T. Zhu, J. Bie, C. Ji, X. Zhang, L. Li, X. Liu, X.-Y. Huang, W. Fa, S. Chen, and J. Luo, "Circular polarized light-dependent anomalous photovoltaic effect from achiral hybrid perovskites," *Nature Communications*, vol. 13, p. 7702, 2022.

[139] G. W. Fraser, M. D. Pain, J. F. Pearson, J. E. Lees, C. R. Binns, P.-S. Shaw, and J. R. Fleischman, "Polarization sensitivity of x-ray photocathodes in the 60-200eV band," in *Production and Analysis of Polarized X Rays*, vol. 1548, pp. 132–148, SPIE, 1991.

[140] A. Nichols, J. Pearson, and G. Fraser, "The x-ray vectorial effect revisited," *Nuclear Instruments and Methods in Physics Research Section A: Accelerators, Spectrometers, Detectors and Associated Equipment*, vol. 454, no. 2, pp. 506–511, 2000.

[141] E. D. Palik, *Handbook of Optical Constants of Solids, Volume 2*. Academic Press, 1991.

[142] H.-J. Hagemann, W. Gudat, and C. Kunz, "Optical constants from the far infrared to the x-ray region: Mg, Al, Cu, Ag, Au, Bi, C, and Al_2O_3," *JOSA*, vol. 65, pp. 742–744, 1975.

[143] T. Udem, L. Maisenbacher, A. Matveev, V. Andreev, A. Grinin, A. Beyer, N. Kolachevsky, R. Pohl, D. C. Yost, and T. W. Hänsch, "Quantum Interference Line Shifts of Broad Dipole-Allowed Transitions," *Annalen der Physik*, vol. 531, p. 1900044, 2019.

[144] U. D. Jentschura and P. J. Mohr, "Nonresonant effects in one- and two-photon transitions," *Canadian Journal of Physics*, vol. 80, no. 6, pp. 633–644, 2002.

[145] C. J. Sansonetti, C. E. Simien, J. D. Gillaspy, J. N. Tan, S. M. Brewer, R. C. Brown, S. Wu, and J. V. Porto, "Absolute Transition Frequencies and Quantum Interference in a Frequency Comb Based Measurement of the ^{6,7}Li D Lines," *Physical Review Letters*, vol. 107, p. 023001, 2011.

[146] R. C. Brown, S. Wu, J. V. Porto, C. J. Sansonetti, C. E. Simien, S. M. Brewer, J. N. Tan, and J. D. Gillaspy, "Quantum interference and light polarization effects in unresolvable atomic lines: Application to a precise measurement of the ^{6,7}Li D_2 lines," *Physical Review A*, p. 032504, 2013.

[147] Z. Ficek and S. Swain, *Quantum interference and coherence: Theory and experiments*. Springer, 2005.

[148] J. J. Olivero and R. L. Longbothum, "Empirical fits to the Voigt line width: A brief review," *Journal of Quantitative Spectroscopy and Radiative Transfer*, vol. 17, no. 2, pp. 233–236, 1977.

[149] H. J. Metcalf and P. van der Straten, *Laser cooling and trapping*. Springer, 1999.

[150] C. Salomon, J. Dalibard, A. Aspect, H. Metcalf, and C. Cohen-Tannoudji, "Channeling atoms in a laser standing wave," *Physical Review Letters*, vol. 59, pp. 1659–1662, 1987.

[151] M. Born and E. Wolf, *Principles of Optics*. Cambridge University Press, 1999.

[152] K. Mølmer, Y. Castin, and J. Dalibard, "Monte Carlo wave-function method in quantum optics," *Journal of the Optical Society of America B*, vol. 10, p. 524, 1993.

[153] M. Fleischhauer, A. Imamoglu, and J. P. Marangos, "Electromagnetically induced transparency: Optics in coherent media," *Reviews of Modern Physics*, vol. 77, pp. 633–673, 2005.

[154] D. Leibfried, *Präzisionsspektroskopie an atomarem Wasserstoff*. PhD thesis, LMU Munich, 1995.

[155] K. Jousten, *Wutz Handbuch Vakuumtechnik*. Vieweg, 2004.

[156] V. Nemanic, "The influence of a hot cathode vacuum gauge on the residual gas composition," *Vacuum*, vol. 70, pp. 523–530, 2003.

[157] K. Jousten and P. Röhl, "Comparison of the sensitivities of ionization gauges to hydrogen and deuterium," *Vacuum*, vol. 46, pp. 9–12, 1995.

[158] J. T. M. Walraven and I. F. Silvera, "Helium-temperature beam source of atomic hydrogen," *Review of Scientific Instruments*, vol. 53, pp. 1167–1181, 1982.

[159] C. T. Archer, "Thermal conduction in hydrogen-deuterium mixtures," *Proceedings of the Royal Society of London. Series A. Mathematical and Physical Sciences*, vol. 165, pp. 474–485, 1938.

[160] S. C. Saxena and V. K. Saxena, "Thermal conductivity data for hydrogen and deuterium in the range 100-1100 degrees C," *Journal of Physics A: General Physics*, vol. 3, pp. 309–320, 1970.

[161] C. Kroll, "A low divergence atomic beam for 2S-nP hydrogen spectroscopy," Bachelor's thesis, LMU Munich, 2016.

[162] J. Alnis, A. Matveev, N. Kolachevsky, T. Wilken, R. Holzwarth, and T. W. Hänsch, "Stable diode lasers for hydrogen precision spectroscopy," *The European Physical Journal Special Topics*, vol. 163, pp. 89–94, 2008.

[163] J. Alnis, A. Matveev, N. Kolachevsky, T. Udem, and T. W. Hänsch, "Subhertz linewidth diode lasers by stabilization to vibrationally and thermally compensated ultralow-expansion glass Fabry-Pérot cavities," *Physical Review A*, vol. 77, p. 053809, 2008.

[164] N. Kolachevsky, J. Alnis, C. G. Parthey, A. Matveev, R. Landig, and T. W. Hänsch, "Low phase noise diode laser oscillator for 1S–2S spectroscopy in atomic hydrogen," *Optics Letters*, vol. 36, p. 4299, 2011.

[165] R. W. P. Drever, J. L. Hall, F. V. Kowalski, J. Hough, G. M. Ford, A. J. Munley, and H. Ward, "Laser phase and frequency stabilization using an optical resonator," *Applied Physics B Photophysics and Laser Chemistry*, vol. 31, pp. 97–105, 1983.

[166] F. Riehle, *Frequency Standards: Basics and Applications*. Wiley, 2006.

[167] L.-S. Ma, P. Jungner, J. Ye, and J. L. Hall, "Delivering the same optical frequency at two places: accurate cancellation of phase noise introduced by an optical fiber or other time-varying path," *Optics Letters*, vol. 19, p. 1777, 1994.

[168] W. Nagourney, *Quantum Electronics for Atomic Physics and Telecommunication*. Oxford University Press, 2014.

[169] A. E. Siegman, *Lasers*. University Science Books, 1986.

[170] Z. Burkley, L. de Sousa Borges, B. Ohayon, A. Golovozin, J. Zhang, and P. Crivelli, "Stable high power deep-uv enhancement cavity in ultra-high vacuum with fluoride coatings," *Optics Express*, vol. 29, p. 27450, 2021.

[171] T. Hansch and B. Couillaud, "Laser frequency stabilization by polarization spectroscopy of a reflecting reference cavity," *Optics Communications*, vol. 35, pp. 441–444, 1980.

[172] M. Giunta, M. Fischer, W. Hänsel, T. Steinmetz, M. Lessing, S. Holzberger, C. Cleff, T. W. Hänsch, M. Mei, and R. Holzwarth, "20 Years and 20 Decimal Digits: A Journey With Optical Frequency Combs," *IEEE Photonics Technology Letters*, vol. 31, pp. 1898–1901, 2019.

[173] S. A. Diddams, K. Vahala, and T. Udem, "Optical frequency combs: Coherently uniting the electromagnetic spectrum," *Science*, vol. 369, 2020.

[174] W. Hänsel, H. Hoogland, M. Giunta, S. Schmid, T. Steinmetz, R. Doubek, P. Mayer, S. Dobner, C. Cleff, M. Fischer, and R. Holzwarth, "All polarization-maintaining fiber laser architecture for robust femtosecond pulse generation," *Applied Physics B*, vol. 123, p. 41, 2017.

[175] M. Giunta, W. Hänsel, M. Fischer, M. Lezius, T. Udem, and R. Holzwarth, "Real-time phase tracking for wide-band optical frequency measurements at the 20th decimal place," *Nature Photonics*, vol. 14, pp. 44–49, 2020.

[176] W. Hänsel, M. Giunta, M. Lezius, M. Fischer, and R. Holzwarth, "Electro-optic modulator for rapid control of the carrier-envelope offset frequency," in *Conference on Lasers and Electro-Optics*, p. SF1C.5, Optica Publishing Group, 2017.

[177] G. Kramer and W. Klische, "Extra high precision digital phase recorder," in *2004 18th European Frequency and Time Forum (EFTF 2004)*, pp. 595–602, 2004. ISSN: 0537-9989.

[178] S. F. Cooper, A. D. Brandt, C. Rasor, Z. Burkley, and D. C. Yost, "Cryogenic atomic hydrogen beam apparatus with velocity characterization," *Review of Scientific Instruments*, vol. 91, p. 013201, 2020.

[179] P. Forman, "Atomichron®: The atomic clock from concept to commercial product," *Proceedings of the IEEE*, vol. 73, pp. 1181–1204, 1985.

[180] I. Estermann, O. C. Simpson, and O. Stern, "The Free Fall of Atoms and the Measurement of the Velocity Distribution in a Molecular Beam of Cesium Atoms," *Physical Review*, vol. 71, pp. 238–249, 1947.

[181] G. Scoles, *Atomic and Molecular Beam Methods, Volume 1.* Oxford University Press, 1988.

[182] N. F. Ramsey, *Molecular beams.* Oxford University Press, 1956.

[183] W. H. Press, S. A. Teukolsky, W. T. Vetterling, and B. P. Flannery, *Numerical Recipies: The Art of Scientific Computing (Third Edition).* Cambridge University Press, 2007.

[184] Burle Industries Inc., *Channeltron Electron Multiplier Handbook for Mass Spectrometry Applications.* Galileo Electro-Optics Corp., 1991.

[185] D. Singy, P. Schmelzbach, W. Grüebler, and W. Zhang, "Study of the surface recombination in the production of a dense polarized hydrogen atomic beam at low temperature," *Nuclear Instruments and Methods in Physics Research Section B: Beam Interactions with Materials and Atoms*, vol. 47, pp. 167–180, 1990.

[186] A. Gelb and S. K. Kim, "Theory of Atomic Recombination on Surfaces," *The Journal of Chemical Physics*, vol. 55, pp. 4935–4939, 1971.

[187] B. F. Hansen and G. D. Billing, "Hydrogen and deuterium recombination rates on a copper surface," *Surface Science*, vol. 373, pp. L333–L338, 1997.

[188] T. Nagasaki, R. Yamada, and H. Ohno, "Recombination coefficients of deuterium on metal surfaces evaluated from ion-driven permeation," *Journal of Nuclear Materials*, vol. 191-194, pp. 258–262, 1992.

[189] I. Čadež, S. Markelj, Z. Rupnik, and P. Pelicon, "Processes with neutral hydrogen and deuterium molecules relevant to edge plasma in tokamaks," *Journal of Physics: Conference Series*, vol. 133, p. 012029, 2008.

[190] P. C. Souers, C. K. Briggs, J. W. Pyper, and R. T. Taugawa, *Hydrogen Vapor Pressures from 4 to 30K Review*. Lawrence Livermore Laboratory, 1977.

[191] S. B. Crampton, "Resonance studies of h atoms adsorbed on frozen H_2 surfaces," *Le Journal de Physique Colloques*, vol. 41, pp. C7–249–C7–255, 1980.

[192] Advanced Research Systems Inc., Helitran® Advanced Features.

[193] V. Altov, E. Blagov, N. Kulysov, and V. Sytchev, "The influence of nucleate to film boiling transition in liquid helium on the stability of composite superconductors under ac conditions," *Cryogenics*, vol. 21, pp. 555–558, 1981.

[194] O. Tsukamoto and S. Kobayashi, "Transient heat transfer characteristics of liquid helium," *J. Appl. Phys.*, vol. 46, p. 7, 1975.

[195] H. Furci, B. Baudouy, A. Four, and C. Meuris, "Transient boiling in two-phase helium natural circulation loops," *AIP Conference Proceedings*, vol. 1573, no. 1, pp. 1490–1497, 2014.

[196] A. N. Pavlenko, E. A. Tairov, V. E. Zhukov, A. A. Levin, and A. N. Tsoi, "Investigation of transient processes at liquid boiling under nonstationary heat generation conditions," *Journal of Engineering Thermophysics*, vol. 20, pp. 380–406, 2011.

[197] A. Beyer, L. Maisenbacher, A. Matveev, R. Pohl, K. Khabarova, Y. Chang, A. Grinin, T. Lamour, T. Shi, D. C. Yost, T. Udem, T. W. Hänsch, and N. Kolachevsky, "Active fiber-based retroreflector providing phase-retracing anti-parallel laser beams for precision spectroscopy," *Optics Express*, vol. 24, p. 17470, 2016.

[198] A. Beyer, *The Rydberg Constant and Proton Size from Atomic Hydrogen*. PhD thesis, LMU Munich, 2016.

[199] R. Carriles, D. N. Schafer, K. E. Sheetz, J. J. Field, R. Cisek, V. Barzda, A. W. Sylvester, and J. A. Squier, "Invited Review Article: Imaging techniques for harmonic and multiphoton absorption fluorescence microscopy," *Review of Scientific Instruments*, vol. 80, p. 081101, 2009.

[200] J. F. Sherson, C. Weitenberg, M. Endres, M. Cheneau, I. Bloch, and S. Kuhr, "Single-atom-resolved fluorescence imaging of an atomic Mott insulator," *Nature*, vol. 467, pp. 68–72, 2010.

[201] E. A. Salim, S. C. Caliga, J. B. Pfeiffer, and D. Z. Anderson, "High-Resolution Imaging and Optical Control of Bose-Einstein Condensates in an Atom Chip Magnetic Trap," *Applied Physics Letters*, vol. 102, p. 084104, 2013.

[202] T. van Leent, M. Bock, R. Garthoff, K. Redeker, W. Zhang, T. Bauer, W. Rosenfeld, C. Becher, and H. Weinfurter, "Long-Distance Distribution of Atom-Photon Entanglement at Telecom Wavelength," *Physical Review Letters*, vol. 124, p. 010510, 2020.

[203] V. Schkolnik, B. Leykauf, M. Hauth, C. Freier, and A. Peters, "The effect of wavefront aberrations in atom interferometry," *Applied Physics B*, vol. 120, pp. 311–316, 2015.

[204] A. Gauguet, B. Canuel, T. Lévèque, W. Chaibi, and A. Landragin, "Characterization and limits of a cold-atom Sagnac interferometer," *Physical Review A*, vol. 80, p. 063604, 2009.

[205] X. Zheng, Y. R. Sun, J.-J. Chen, J.-L. Wen, and S.-M. Hu, "Light-force-induced shift in laser spectroscopy of atomic helium," *Physical Review A*, vol. 99, p. 032506, 2019.

[206] L. Semeria, P. Jansen, G.-M. Camenisch, F. Mellini, H. Schmutz, and F. Merkt, "Precision Measurements in Few-Electron Molecules: The Ionization Energy of Metastable $^4He_2$ and the First Rotational Interval of $^4He_2^+$," *Physical Review Letters*, vol. 124, p. 213001, 2020.

[207] W. T. Welford, *Aberrations of Optical Systems*. Hilger, 1986.

[208] P. Hamilton, M. Jaffe, J. M. Brown, L. Maisenbacher, B. Estey, and H. Müller, "Atom Interferometry in an Optical Cavity," *Physical Review Letters*, vol. 114, p. 100405, 2015.

[209] V. Xu, M. Jaffe, C. D. Panda, S. L. Kristensen, L. W. Clark, and H. Müller, "Probing gravity by holding atoms for 20 seconds," *Science*, vol. 366, pp. 745–749, 2019.

[210] C. P. Wang and R. L. Sandstrom, "Three-mirror stable resonator for high power and single-mode lasers," *Appl. Opt.*, vol. 14, pp. 1285–1289, 1975.

[211] H. Carstens, S. Holzberger, J. Kaster, J. Weitenberg, V. Pervak, A. Apolonski, E. Fill, F. Krausz, and I. Pupeza, "Large-mode enhancement cavities," *Optics Express*, vol. 21, p. 11606, 2013.

[212] J. Kruschwitz, "Technology boost in precision optics: The story of QED technologies inc.," *Optics and Photonics News*, vol. 17, pp. 10–13, 2006.

[213] S. N. Shafrir, H. J. Romanofsky, M. Skarlinski, M. Wang, C. Miao, S. Salzman, T. Chartier, J. Mici, J. C. Lambropoulos, R. Shen, H. Yang, and S. D. Jacobs, "Zirconia-coated carbonyl-iron-particle-based magnetorheological fluid for polishing optical glasses and ceramics," *Applied Optics*, vol. 48, p. 6797, 2009.

[214] C. Kumari and S. K. Chak, "A review on magnetically assisted abrasive finishing and their critical process parameters," *Manufacturing Review*, vol. 5, p. 13, 2018.

[215] A. E. Siegman, "New developments in laser resonators," in *Optical Resonators*, vol. 1224, pp. 2 – 14, International Society for Optics and Photonics, SPIE, 1990.

[216] C. Wang, X. Dun, Q. Fu, and W. Heidrich, "Ultra-high resolution coded wavefront sensor," *Optics Express*, vol. 25, p. 13736, 2017.

[217] J.-C. Chanteloup, "Multiple-wave lateral shearing interferometry for wave-front sensing," *Applied Optics*, vol. 44, p. 1559, 2005.

[218] T. Ling, J. Jiang, R. Zhang, and Y. Yang, "Quadriwave lateral shearing interferometric microscopy with wideband sensitivity enhancement for quantitative phase imaging in real time," *Scientific Reports*, vol. 7, p. 9, 2017.

[219] ISO Standard 11146, "Lasers and laser-related equipment – Test methods for laser beam widths, divergence angles and beam propagation ratios" (2005).

[220] H. W. N. Hodgson, *Laser Resonators and Beam Propagation. Fundamentals, Advanced Concepts and Applications*. Springer, 2005.

[221] P. A. Bélanger, "Beam propagation and the ABCD ray matrices," *Opt. Lett.*, vol. 16, pp. 196–198, 1991.

[222] A. E. Siegman, "Analysis of laser beam quality degradation caused by quartic phase aberrations," *Applied Optics*, vol. 32, p. 5893, 1993.

[223] J. Weitenberg, *Transversale Moden in optischen Resonatoren für Anwendungen hoher Laserintensität*. PhD thesis, RWTH Aachen, 2017.

[224] R. Paschotta, "Beam quality deterioration of lasers caused by intracavity beam distortions," *Optics Express*, vol. 14, no. 13, p. 6069, 2006.

[225] N. Bey, "Spektal aufgelöste Strahlqualitätsmessung," Master's thesis, RWTH Aachen, 2013.

[226] J. Weitenberg, P. Rußbüldt, I. Pupeza, T. Udem, H.-D. Hoffmann, and R. Poprawe, "Geometrical on-axis access to high-finesse resonators by quasi-imaging: a theoretical description," *Journal of Optics*, vol. 17, p. 025609, 2015.

[227] B. Saleh and M. Teich, *Fundamentals of Photonics*. Wiley, 1991.

[228] A. Mendez and T. Morse, *Single Mode Fibers*. Springer, 1988.

[229] S. Amarande, A. Giesen, and H. Hügel, "Propagation analysis of self-convergent beam width and characterization of hard-edge diffracted beams," *Applied Optics*, vol. 39, p. 3914, 2000.

[230] A. Hertlein, "Laserstrahlcharakterisierung für die Wasserstoffpräzisionsspektroskopie," Bachelor's thesis, LMU Munich, 2018.

[231] S. Bade, L. Djadaojee, M. Andia, P. Cladé, and S. Guellati-Khelifa, "Observation of Extra Photon Recoil in a Distorted Optical Field," *Physical Review Letters*, vol. 121, p. 073603, 2018.

[232] E. Brinkmeyer, "Backscattering in single-mode fibres," *Electronics Letters*, vol. 16, pp. 329–330, 1980.

[233] E. Brinkmeyer, "Analysis of the backscattering method for single-mode optical fibers," *Journal of the Optical Society of America*, vol. 70, p. 1010, 1980.

[234] M. Nakazawa, "Rayleigh backscattering theory for single-mode optical fibers," *Journal of the Optical Society of America*, vol. 73, p. 1175, 1983.

[235] V. Degiorgio, "Phase shift between the transmitted and the reflected optical fields of a semireflecting lossless mirror is $\pi/2$," *American Journal of Physics*, vol. 48, pp. 81–81, 1980.

[236] L. Thevanaz, *Advanced Fiber Optics: Concepts and Technology*. EPFL Press, 2011.

[237] C. A. Burrus and R. D. Standley, "Viewing Refractive-Index Profiles and Small-Scale Inhomogeneities in Glass Optical Fibers: Some Techniques," *Applied Optics*, vol. 13, p. 2365, 1974.

[238] E. Lichtman, R. Waarts, and A. Friesem, "Stimulated Brillouin scattering excited by a modulated pump wave in single-mode fibers," *Journal of Lightwave Technology*, vol. 7, pp. 171–174, 1989.

[239] Y. Chigusa, Y. Yamamoto, T. Yokokawa, T. Sasaki, T. Taru, M. Hirano, M. Kakui, M. Onishi, and E. Sasaoka, "Low-loss pure-silica-core fibers and their possible impact on transmission systems," *Journal of Lightwave Technology*, vol. 23, pp. 3541–3550, 2005.

[240] J. Max Rohr, S. Ast, O. Gerberding, J. Reiche, and G. Heinzel, "Fiber backscatter under increasing exposure to ionizing radiation," *Optics Express*, vol. 28, p. 34894, 2020.

[241] O. Wallner, W. R. Leeb, and P. J. Winzer, "Minimum length of a single-mode fiber spatial filter," *J. Opt. Soc. Am. A*, vol. 19, pp. 2445–2448, 2002.

[242] R. Fleddermann, F. Steier, M. Tröbs, J. Bogenstahl, C. Killow, G. Heinzel, and K. Danzmann, "Measurement of the non-reciprocal phase noise of a polarization maintaining single-mode optical fiber," *Journal of Physics: Conference Series*, vol. 154, p. 012022, 2009.

[243] R. Fleddermann, C. Diekmann, F. Steier, M. Tröbs, G. Heinzel, and K. Danzmann, "Sub-pm/$\sqrt{\text{Hz}}$ non-reciprocal noise in the LISA backlink fiber," *Classical and Quantum Gravity*, vol. 35, p. 075007, 2018.

[244] S. Wu, A. Yariv, H. Blauvelt, and N. Kwong, "Theoretical and experimental investigation of conversion of phase noise to intensity noise by Rayleigh scattering in optical fibers," *Applied Physics Letters*, vol. 59, pp. 1156–1158, 1991.

[245] W. H. McCrea and F. J. W. Whipple, "XXII.—Random Paths in Two and Three Dimensions," *Proceedings of the Royal Society of Edinburgh*, vol. 60, no. 3, pp. 281–298, 1940.

[246] E. W. Weisstein, "Random Walk–2-Dimensional," MathWorld - A Wolfram Web Resource.

[247] A. Mendez and T. Morse, *Specialty Optical Fibers Handbook*. Elsevier Academic Press, 2007.

[248] Z. Ding, Z. Meng, X. S. Yao, X. Chen, T. Liu, and M. Qin, "Accurate method for measuring the thermal coefficient of group birefringence of polarization-maintaining fibers," *Optics Letters*, vol. 36, p. 2173, 2011.

[249] P. Hao, C. Yu, T. Feng, Z. Zhang, M. Qin, X. Zhao, H. He, and X. S. Yao, "PM fiber based sensing tapes with automated 45° birefringence axis alignment for distributed force/pressure sensing," *Optics Express*, vol. 28, p. 18829, 2020.

[250] H. Afkhamiardakani, L. Horstman, L. Arissian, and J.-C. Diels, "Low-power (mW) nonlinearities of polarization maintaining fibers," *Photonics Research*, vol. 7, p. 1386, 2019.

[251] I. P. Kaminow, "Polarization in optical fibers," *IEEE Journal of Quantum Electronics*, vol. 17, no. 1, pp. 15–22, 1981.

[252] S. C. Rashleigh, R. Ulrich, W. K. Burns, and R. P. Moeller, "Polarization holding in birefringent single-mode fibers," *Optics Letters*, vol. 7, p. 40, 1982.

[253] H. Hurwitz and R. C. Jones, "A New Calculus for the Treatment of Optical Systems. II. Proof of Three General Equivalence Theorems," *J. Opt. Soc. Am.*, vol. 31, pp. 493–499, 1941.

[254] S.-Y. Lu and R. A. Chipman, "Interpretation of Mueller matrices based on polar decomposition," *Journal of the Optical Society of America A*, vol. 13, p. 1106, 1996.

[255] R. Ulrich and A. Simon, "Polarization optics of twisted single-mode fibers," *Applied Optics*, vol. 18, p. 2241, 1979.

[256] V. Budinski and D. Donlagic, "Fiber-Optic Sensors for Measurements of Torsion, Twist and Rotation: A Review," *Sensors*, vol. 17, p. 443, 2017.

[257] M. W. Shute, C. S. Brown, and J. Jarzynski, "Polarization model for a helically wound optical fiber," *Journal of the Optical Society of America A*, vol. 14, p. 3251, 1997.

[258] D. M. Shupe, "Thermally induced nonreciprocity in the fiber-optic interferometer," *Appl. Opt.*, vol. 19, pp. 654–655, 1980.

[259] C. Vinegoni, M. Wegmuller, B. Huttner, and N. Gisin, "Measurement of nonlinear polarization rotation in a highly birefringent optical fibre using a Faraday mirror," *Journal of Optics A: Pure and Applied Optics*, vol. 2, pp. 314–318, 2000.

[260] V. Wirthl, C. Panda, P. Hess, and G. Gabrielse, "Simple Self-calibrating Polarimeter for Measuring the Stokes Parameters of Light," *OSA Continuum*, vol. 4, pp. 2949–2969, 2021.

[261] J. W. Farley and W. H. Wing, "Accurate calculation of dynamic Stark shifts and depopulation rates of Rydberg energy levels induced by blackbody radiation. Hydrogen, helium, and alkali-metal atoms," *Physical Review A*, vol. 23, pp. 2397–2424, 1981.

[262] W. N. Hardy and L. A. Whitehead, "Split-ring resonator for use in magnetic resonance from 200–2000 MHz," *Review of Scientific Instruments*, vol. 52, no. 2, pp. 213–216, 1981.

[263] E. Widmann, "In-beam hyperfine spectroscopy of antihydrogen, hydrogen and deuterium," in *9th Meeting on CPT and Lorentz Symmetry*, 2022.

[264] M. P. Westig, R. Engels, K. Grigoryev, M. Mikirtytchiants, F. Rathmann, H. Paetz gen. Schieck, G. Schug, A. Vasilyev, and H. Ströher, "Hydrogen spectroscopy with a Lamb-shift polarimeter: An alternative approach towards anti-hydrogen spectroscopy experiments," *The European Physical Journal D*, vol. 57, pp. 27–32, 2010.

[265] D. Budker, D. K. Kimball, and D. P. DeMille, *Atomic Physics – An Exploration through Problems and Solutions*. Oxford University Press, 2008.

[266] E. Magnan, J. Maslek, C. Bracamontes, A. Restelli, T. Boulier, and J. V. Porto, "A low-steering piezo-driven mirror," *Review of Scientific Instruments*, vol. 89, no. 7, p. 073110, 2018.

Publications and conference contributions

Publications

The following publications were published before the name change (as V. Andreev):

- **V. Andreev**, D. G. Ang, D. DeMille, J. M. Doyle, G. Gabrielse, J. Haefner, N. R. Hutzler, Z. Lasner, C. Meisenhelder, B. R. O'Leary, C. D. Panda, A. D. West, E. P. West, and X. Wu (ACME Collaboration), "Improved limit on the electric dipole moment of the electron", Nature **562**, pages 355–360 (2018)
- T. Udem, L. Maisenbacher, A. Matveev, **V. Andreev**, A. Grinin, A. Beyer, N. Kolachevsky, R. Pohl, D. C. Yost, and T. W. Hänsch, "Quantum interference line shifts of broad dipole-allowed transitions", Annalen der Physik **531**, 1900044 (2019)

The following publications were published after the name change (as V. Wirthl):

- A. Grinin, A. Matveev, D. C. Yost, L. Maisenbacher, **V. Wirthl**, R. Pohl, T. W. Hänsch, and T. Udem, "Two-photon frequency comb spectroscopy of atomic hydrogen", Science **370**, 1061–1065 (2020)
- **V. Wirthl**, C. D. Panda, P. W. Hess, and G. Gabrielse, "Simple self-calibrating polarimeter for measuring the Stokes parameters of light", OSA Continuum **4**, 2949-2969 (2021)
- **V. Wirthl**, L. Maisenbacher, J. Weitenberg, A. Hertlein, A. Grinin, A. Matveev, R. Pohl, T. W. Hänsch, and T. Udem, "Improved active fiber-based retroreflector with intensity stabilization and polarization monitor for the near UV", Opt. Express **29**, 7024-7048 (2021)

Conference contributions

Oral presentations

- "Precision spectroscopy of atomic hydrogen and deuterium at MPQ", International STRONG-2020 Workshop on the Proton Charge Radius and related topics, Sorbonne University, Paris, June 2022
- "Precision spectroscopy of the 2S-6P transition in atomic hydrogen and deuterium", 53rd Annual Meeting of the Division of Atomic, Molecular and Optical Physics of the American Physical Society (APS DAMOP), Online, June 2022
- "Towards precision spectroscopy of the 2S-6P transition in atomic deuterium", 52th Annual Meeting of the Division of Atomic, Molecular and Optical Physics of the American Physical Society (APS DAMOP), Online, June 2021
- "Towards precision spectroscopy of the 2S-6P transition in atomic deuterium", 52nd Conference of the European Group on Atomic Systems (EGAS), Online, July 2021

Poster presentations

- "Precision spectroscopy of the 2S-6P transition in atomic deuterium", 766. Wilhelm-und-Else-Heraeus-Seminar "High-precision measurements and searches for New Physics", Physikzentrum Bad Honnef, May 2022
- "Precision spectroscopy of one-photon 2S-nP transitions in atomic hydrogen", Gordon Research Conference on Atomic Physics, Salve Regina University, Newport, RI, USA, June 2019
- "Towards precision spectroscopy of the 2S-6P transition in atomic hydrogen", 26th International Conference on Atomic Physics (ICAP), Barcelona, Spain, July 2018
- "Towards precision spectroscopy of the 2S-6P transition in atomic hydrogen", 10th International Conference on Precision Physics of Simple Atomic Systems (PSAS), Vienna, Austria, May 2018

Danksagung

Ganz herzlich danke ich Theodor W. Hänsch, dass ich in seiner Abteilung an diesem spannenden Experiment promovieren durfte und eine hervorragende wissenschaftliche Atmosphäre sowie exzellente Rahmenbedingungen genießen durfte.

Ein großer Dank gilt meinem Doktorvater Thomas Udem für die vielen tiefgründigen Physikdiskussionen, für seine intuitiven Denkweisen und Erklärungen, für Ratschläge, das sehr gründliche Lesen meiner Doktorarbeit und die vielen hilfreichen Kommentare und Anmerkungen dazu sowie für die tolle Gruppenatmosphäre. Auch bin ich meinem Zweitgutachter Randolf Pohl für all die fruchtbaren Diskussionen, die wertvollen Anregungen und Inspirationen sehr dankbar, die mich immer wieder ermutigt und frischen Wind gebracht haben.

Vielen lieben aufrichtigen Dank an meinen „großen Laborbruder“ Lothar Maisenbacher, mit dem ich während meiner Doktorarbeit im Wasserstoff-Spektroskopie-Team am engsten zusammenarbeiten durfte und von dem ich so vieles lernen und übernehmen durfte. Zusammen mit ihm verbrachte ich unzählige dankbare Stunden im Labor, u.a. bei der Vorbereitung und Durchführung der Wasserstoff 2S-6P Messkampagne und bei der Deuterium 2S-6P Messung, die ich in dieser Doktorarbeit vorstelle. Ich bin sehr froh darüber, dass Lothar das Experiment (schon bevor ich angefangen hatte) in so vielen Bereichen erneuert und verbessert hatte, worauf ich mich stützen konnte. Als herausragendes Beispiel dafür möchte ich die komplette Erneuerung der Datenaufnahme mit dem von ihm entwickelten Software-Paket „Pythonic Hydrogen“ erwähnen. Lothars Programmierarbeit war auch maßgeblich für die komplexen Simulationen und damit verbundenen Analysen, die ich übernehmen und auf denen ich aufbauen konnte. Auch nach seinem Ortswechsel für den Post-Doc in Berkeley blieb er stets bereit, mir gründlich zu helfen und wertvolle Hinweise und Anregungen anzumerken, sowie durchdachte Kommentare zu meiner Doktorarbeit zu geben.

Herzlich danken möchte ich auch Arthur Matveev, der mir nicht nur immer unterstützend in allen experimentellen und theoretischen Fragen zur Seite stand, sondern der auch die „Big Model“ Simulationen für die Wasserstoff-Experimente ins Leben gerufen hat. Vor seinem Jobwechsel im September 2020 hat er sich viele Stunden Zeit genommen, um mir das „Big Model“ zu erklären, sodass ich es dank seiner Hilfe übernehmen und für die Deuterium 2S-6P Simulationen anpassen konnte.

Einen umarmenden Dank möchte ich Alexey Grinin geben, mit dem es eine Freude war im Wasserstoff-Team zu sein, der stets zu helfen bereit war, mich immer wieder ermutigt hat und mit seiner herzlichen Art viel Segen im Doktorarbeits-Alltag gebracht hat. Seinem Nachfolger Derya Taray möchte ich auch ganz herzlich danken, der die gutherzige Atmosphäre des 1S-3S-Labors bewahrt hat und mich auch in den letzten beiden Jahren meiner Doktorarbeit mit einem Lächeln im Gesicht begleitet hat und auch wertvolle Kommentare in den Meetings und zu meinen Aufschrieben gegeben hat.

Es war für mich eine besondere Freude im Zusammenhang mit der Charakterisierung der Aberrationen des Kollimators im AFR mit Johannes Weitenberg zusammenzuarbeiten und von ihm alles über die Gouy-Phase und vieles andere zu lernen. Seine lebendige, freudvolle,

unkomplizierte, ehrliche und ermutigende Art war auch darüber hinaus für mich ein großer Segen während meiner ganzen Doktorarbeitszeit und erfüllt mich mit großer Dankbarkeit. Im Zusammenhang mit dem AFR möchte ich auch Alexander Hertlein herzlich danken, der im Rahmen seiner Bachelorarbeit ein sehr praktisches M^2-Messgerät gebaut hat, welches für die Arbeit mit dem AFR von großem Nutzen war. Außerdem danke ich vielmals Jakob Silbermann von der B. Halle Nachfl. GmbH für die sehr nette Zusammenarbeit am Kollimator.

Sehr dankbar bin ich Fabian Schmid für die vielen technischen Hilfestellungen, seine unkomplizierte und freundliche Art sowie das sorgfältige Gegenlesen meiner Doktorarbeit. Außerdem bedanke ich mich herzlich bei Akira Ozawa, der ebenfalls immer zu helfen bereit war und auch eine große Bereicherung für unsere Gruppe ist.

Ganz herzlich danken möchte ich Savely Karshenboim für die vielen Diskussionen rund um die Theorie sowie seine wichtigen Hinweise und Kommentare zu der Einleitung meiner Doktorarbeit. Es ist eine große Bereicherung so einen genialen Theoretiker in unserer Gruppe zu haben, der zudem auch für eine heitere Stimmung sorgt. Ein herzliches Dankeschön auch an Hans Schüssler, der Teile meiner Arbeit gelesen hat und an der ein oder anderen Stelle einen wertvollen Hinweis gegeben hat.

Das Experiment in dieser Doktorarbeit wäre ohne tatkräftige technische Unterstützung nicht möglich gewesen. Ich danke daher ganz herzlich unserem Feinmechaniker Wolfgang Simon, ein Pionier der Perfektion in der technischen Präzision und Machbarkeit mit einem Feingefühl für die Technik, seinem Kollegen Karl Linner, der immer alles unkompliziert, schnell und auf eine herzliche Art und Weise gemacht hat, und Helmut Brückner, der mir mit seinen reichen Elektronik-Kenntnissen und praktischen Lösungen immer zur Seite stand.

Auch für die exzellenten administrativen und organisatorischen Tätigkeiten von Ingrid Hermann und Gabriele Gschwendtner möchte ich mich ganz herzlich bedanken. Zudem war ich froh in der International Max Planck Research School on Advanced Photon Science (IMPRS-APS) zu sein – vielen Dank an alle, die zum Gelingen dieser Doktorandenschule beigetragen haben und tolle Treffen mit anderen Doktoranden organisiert haben, bei denen ich mich auch bedanke. Dank sei auch allen anderen Mitgliedern der Hänsch-Gruppe am MPQ und an der LMU für die wissenschaftliche und zwischenmenschliche Freude bei verschiedenen Begegnungen wie z.B. bei Gruppenseminaren, Doktorfeiern oder zwischendurch.

In meinem privaten Umfeld gilt mein innigster und tiefster Dank meiner Ehefrau Barbara, die mich immer bedingungslos auf allen Ebenen unterstützt hat, die ganze Doktorarbeitszeit mitgetragen hat und mich im Herzen immer wieder ermutigt und motiviert hat. Mit wärmstem Dank bedanke ich mich auch bei meiner Mutter, die mich während des ganzen Physikstudiums unterstützt hat, mir das Leben in Deutschland überhaupt erst ermöglicht hat und mich mit mütterlicher Liebe getragen hat. Mit inniger Dankbarkeit erfüllt denke ich an meinen Großvater, der mich schon als Kind für die Wissenschaft und Technik im Allgemeinen und die Physik im Speziellen begeistert hat. Schließlich geht ein herzliches Vergelt's Gott an all meine Freunde und meine Geschwister in der Gemeinschaft Emmanuel für die seelische Unterstützung und das aufrichtige Gebet.

All mein Dank wäre unvollständig, wenn ich nicht meinem Herrn und Schöpfer gedankt hätte, der mich ins Dasein rief, mir die Begeisterung für das Erforschen der Naturgesetze ins Herz gelegt hat und mich auf all meinen Wegen sicher und treu geführt hat. Dank sei dem Heiligen Josef, der mich durch seine Fürsprache als himmlischer Doktorvater begleitet hat und mich in der Arbeit immer wieder zu Jesus Christus (zurück-)geführt hat. Dank, Lob, Preis und Ehre sei dem dreieinen Gott, der die Naturgesetze so wunderbar geschaffen hat und mich mit der Gabe ausgestattet hat, sie zu erforschen!